I. R. IRAN

ISSN: 1728-144X
e-ISSN: 1735-9244

International Journal of Engineering

Journal Homepage: www.ije.ir

MERC

TRANSACTIONS B: APPLICATIONS

Volume 36, Number 05, May 2023

Materials and Energy Research Center

In the Name of God

INTERNATIONAL JOURNAL OF ENGINEERING
Transactions B: Applications

DISCLAIMER
The publication of papers in International Journal of Engineering does not imply that the editorial board, reviewers or publisher accept, approve or endorse the data and conclusions of authors.

International **J**ournal of **E**ngineering *Transactions A: Basics* (ISSN 1728-1431) (EISSN 1735-9244)
International **J**ournal of **E**ngineering *Transactions B: Applications* (ISSN 1728-144X) (EISSN 1735-9244)
International **J**ournal of **E**ngineering *Transactions C: Aspects* (ISSN 2423-7167) (EISSN 1735-9244)
Web Sites: www.ije.ir & www.ijeir.info E-mails: ije.editor8@gmail.com, Tel: (+9821) 88771578, Fax: (+9821) 88773352
Materials and Energy Research Center (MERC)

ISSN: 1728-144X, e-ISSN: 1735-9244

International Journal of Engineering, Volume 36, Number 05, May 2023

CONTENTS

Transactions B: Applications

ISSN: 1728-144X, e-ISSN: 1735-9244

International Journal of Engineering, Volume 36, Number 05, May 2023

International Journal of Engineering

Journal Homepage: www.ije.ir

Challenges of Generation and Transmission Expansion Planning Considering Power System Resilience and Provide Solutions

M. Rezaei, M. Tolou-Askari*, M. Amirahmadi, V. Ghods

Department of Electrical and Electronic Engineering, Semnan Branch, Islamic Azad University, Semnan, Iran

PAPER INFO

Paper history:
Received 9 July 2022
Received in revised form 5 February 2023
Accepted 21 February 2023

Keywords:
Disastrous Incidents
Energy Hub
Generation and Transmission Expansion Planning
Micro Grid Power System
Resilience

ABSTRACT

Since power systems are susceptible to damages induced by disastrous incidents, the assessment and improvement of system resilience are unavoidable as a new goal of planning and operation. On the other hand, the expansion of generation and transmission grids constitute an essential part of power system planning as it needs a huge budget. So, a primary concern of researchers has always been the optimal planning of power systems. This paper studies the emerging concept of resilience, its criteria, and indicators, how to enhance it, and the identification of its strengths and weaknesses. It also reviews the strategies recommended in the literature to improve power system resilience. The paper briefly reports the models for expansion plan analysis and the generation and transmission expansion planning (GTEP) tools with or without the target of resilience enhancement, which can be instrumental in future research and can be used to estimate the effectiveness of different tools. Furthermore, the paper discusses the planning problems, thereby opening the way for further work in future studies. Finally, the study presents the most eminent challenges of GTEP to accomplish better, resilient, and innovative plans to escalate power system resilience.

***doi**: 10.5829/ije.2023.36.05b.01*

1. INTRODUCTION

Given the growing energy consumption in the contemporary world, the investigation into the development of power systems has become inevitable. A power system refers to a complicated grid composed of instruments to meet consumer needs. These facilities automatically protect the power systems upon detecting a violation of the electrical constraints. In this encoding, the operator separates components from the grid to protect them against any damage given the system evolutions and the implications of a set of predefined events. As load increases, operators should adopt proper strategies for the long-term development of the power systems by systematic planning for the inclusion of grid components. On the other hand, the opt performance results from decisions on precise planning. Various methods have so far been used to provide the best grid expansion design. Accordingly, this paper aims to comprehensively explore generation and transmission expansion planning (GTEP) to improve the resilience of power systems. The study focuses on expanding the power systems in the generation, transmission, and distribution sections. However, investment is more significant in the generation and transmission sections than in the distribution sections. Although GTEP is interdependent, it can be planned separately or concurrently. The GTEP is a complicated problem with nonlinear and binary variables, and time-consuming calculations. Restructured electricity markets exhibit further uncertainties, e.g., random and logical uncertainty, which should consider in the GTEP optimization problem. Power systems constantly expose to perturbations, so it is necessary to enhance system resilience to ensure its capability. Also, rapid fault detection and system recovery to normal conditions in the shortest possible time are significant factors in maintaining the security of a power system. In this case, the static and dynamic effects of hundreds of events should be examined in power systems. Table 1 briefly presents a review of some models with their advantages and disadvantages.

*Corresponding Author Institutional Email: m.askari@semnaniau.ac.ir (M. Tolou Askari)

Please cite this article as: M. Rezaei, M. Tolou-Askari, M. Amirahmadi, V. Ghods, Challenges of Generation and Transmission Expansion Planning Considering Power System Resilience and Provide Solutions, ***International Journal of Engineering, Transactions B: Applications***, Vol. 36, No. 05, (2023) 824-841

TABLE 1. Review of some models with their advantages and disadvantages

Models	Advantages	Disadvantages
1. Topological model	• Power system analysis • Quick detection of unexpected emergency behavior • Consider some basic electrical properties.	• Lack of electrical properties
1.1. Modified topology model	• Provide criteria for combined electrical topology. • Rapid assessment of vulnerability, risk probability, and robustness	
1.2. Maximum flow model	• Use the maximum flow method • Consider the weight of the line and the node	
2. Stochastic simulation model	• Pay attention to the most uncertainties during the waterfall	• Lack of attention to dynamic stability and waterfall details
2.1. Model (practice)	• Introducing single-track and multi-track modes • Adopt an incident tree-based approach	
2.2. Markov China model	• Indicates non-local diffusion	
3. High-level statistical model	• Able to enable risk assessment • Simple and compact	• Ignores all the details of the waterfall
3.1 Cascade model	• The probability of failure is related to the load level	
3.2 Branch process model	• Can be considered as an improved CASCADE model • It considers each component of failure from an early stage through a specific distribution	
4. Dynamic simulation model	• Simulation of most of the dynamic mechanisms in the waterfall • Provides a deeper understanding of cascade failure	• Detailed information on the power system is required • Slow simulation • The network of this model has a small number of nodes, which is very different from the real system. • In this model, it is assumed that all elements of the system are the same
4.1. model OPA	• Considers the effects of the operation, automation, communications, relay protection, mode of operation, and planning • Tree contact, line failure due to line heating, and UVM model	• System control is done with only a small number of parameters • There is no clear relationship between the model parameters and the actual system • The protection system is not modeled • This model cannot cover the self-organized crisis caused by the interactions between the power plant, the operator, and the control system
4.2. Manchester model	• Approve AC power flow • Monte Carlo methods are used for risk assessment	
4.3. COSMIC model	• Considers the mechanism of nonlinear dynamics • Different relay and load models are involved	
4.4. Quasi-dynamic multi-time model	• Uses a quasi-dynamic approach • The approximate time of evolution is considered • Improved reuse simulation	
4.5. ASSESS MODEL	• Optimal AC power flux is provided with security restrictions • Use of quasi-steady state dynamic model simulator • Modeling control in the system through time domain simulator access to statistical tools	
4.6. TRELSS model	• Considers the actions of breakers • Voltage problems are modeled using quasi-steady state AC power flux	
4.7. PRA dynamic model	• Two levels of cascade failure are simulated using two different models • The effect of various changes in the system is simulated	
5. Interdependent models	• Interaction analysis between network connections	• Validation is difficult

5.1. Interconnected models based on complex networks	• The vulnerability of the entire system connection has been investigated and analyzed • Interdependencies are depicted • Computer and cyber risks are considered	• Precise mechanisms are ignored
5.2. Interrelated Markov chain models	• Able to predict system level with tracking details	
5.3. Hierarchical physics-cyber models based on congestion	• Dynamic nodes, PMU, and local cyber-controlled model • Frequency, phase angle, and other related parameters are involved • Control strategies are presented	
6. Other models	• Focuses on specific parts of the mechanism	• It focuses only on parts of the cascade failure mechanisms.
6.1. Potential waterfall model	• The "cluster" approach is used • The goal is to predict possible cascade fractures	
6.2. Hidden error model	• Considers hidden failure and reuse of the generator	
6.3. Models based on historical data	• Accurately reproduce historical events • Complementary models available	

This study provides an up-to-date review of GTEP models and tools and concentrates on the essential role of this scientific discipline in improving power system resilience. Unlike previous studies, this review emphasizes the effect of GTEP models on enhancing the resilience of power systems. Another contribution of the paper is the analysis of the trend of previous studies and the challenges that need new expansion models with/without considering the power system resilience.

The remaining parts of the paper are structured as below. Section 2 reviews resilience concepts, assessment frameworks, and enhancement, as well as its indices. Section 3 deals with models and their applications in expansion planning. Section 4 discusses the literature on the planning of GTEP that aimed at enhancing power system resilience, or did not consider this perspective. Section 5 lists and analyzes the challenges of GTEP. Section 6 finally concludes the paper with some final points.

2. THE CONCEPT OF RESILIENCE

Resilience is a dynamic, complicated, and multidimensional concept in the field of power systems, which has emerged relatively late [1]. Recently, disastrous incidents research has focused on the concept of 'resilience' [2]. Different definitions have been put forth for resilience, but they all have similar natures [3]. The word resilience is rooted in the Latin word resilio, means 'leaping back' as a system feature, and implies the capability of improvement against destructive events. In the simplest sense, power system resilience is defined as the capacity of a grid for the timely management of high-impact, low probability (HILP) incidents, e.g., atmospheric incidents and natural disasters [4]. Arghandeh et al. [5] resilience defines as 'the capability of a system to keep a continuous flow of power to customers by load prioritization.' The UK Energy Research Centre (UKERC) defines resilience as 'the capacity of a power system to tolerate disturbance and continue to deliver affordable energy services to consumers [6].' The US office [7] defines this concept as 'the capacity of grids to anticipate, absorb, adapt to, or/and rapidly recover from a destructive incident'. Also, resilience has been described in terms of the power system consistency and recovery during and after a disaster [8]. According to Presidential Policy Directive (PPD-21), resilience is 'the ability to prepare for or adapt to changing conditions and recover rapidly from disruptions' including 'deliberate attacks, accidents, or naturally occurring threats or incidents' [9]. In 2009, the American Society of Mechanical Engineers (ASME) defined resilience as 'the ability of a system to recover to its normal operating conditions after the occurrence of disruptive events' [10]. In 2011, an effective strategy was proposed for resilience enhancement. In 2013, a paper was published on the economic advantages of a resistant power grid focused on grid resilience during natural incidents [11]. NIAC's description of resilience encompasses robustness (ability to absorb), which implies the ability to absorb shocks and continue to work, defined as the system's resilience against disruption to minimize loss. According to Ouyang and Duenas-Osorio [12], resilience is the ability of the network to withstand damage, continue to work in the event of damage, and recover quickly from blackouts. It also includes adaptability, i.e., the ability to reduce future losses by using learning lessons to reinforce resilience. It refers to the endogeneity of the system and minimizes the consequences by self-organizing. Finally, the reinforcement of any of these four features will strengthen the power system's resilience [13].

Over 70 definitions can be found for the emerging concept of resilience in different papers in different disciplines. These definitions shift between the two features of adaptation and recovery [14]. The term resilience was first introduced in 1973 by Holling [15] to

describe how to change perspective on environmental systems and behaviors and to describe different approaches to resource management. Today, however, it has gained more importance in other disciplines [16]. For example, extensive effort has been made to describe and measure the resilience of power systems. In 2011, resilience was defined using the concepts of power system reliability and recovery [17]. In fact, 'the time dimension' distinguishes resilience from reliability. Expansion planning mainly aims to prevent incidents and protect the equipment thoroughly. Recently, research has been conducted on 'timely response and rapid recovery' from destructive incidents. Therefore, attaining arrangements for resilience has become a chief priority, and practical actions should be taken before, during, and after incidents to assist the safe operation of power systems. After planning, system resilience measurement is the main issue [18].

Therefore, a review paper that describes challenges in this field can help the power engineer community to develop standard indices and create a framework for its assessment and reinforcement. This paper tries to shed light on the concept of resilience and its improvement in planning for the expansion of power systems during disastrous incidents, which has become a hot issue today. In this section, we provide a general framework for assessing and reinforcing power system resilience based on a comprehensive review of authentic literature. Due to reinforce system resilience, we first need to determine resilience and a proper method for its measurement. So, this paper provides a literature review on the definitions and measurement of resilience. Then, we discuss them as a tool for enhancing power system resilience with an emphasis on modern technologies.

2. 1. Key Features of Resilience Since disturbances are unpredictable and may have disastrous impacts on vital infrastructure rapidly, resulting in considerable losses in the system, so it is very complicated and time-consuming to recover the system [1]. An important characteristic of power system resilience is how to recover it. A resilient power system should have the following features. Figure 1 depicts a resilience curve [4]:

1) Before the incident, the system should be consistent and resilient enough, and the operator should estimate the location and severity of the incident to prepare with a series of preventive actions.

2) After the incident, the operator is informed about the situation by advanced information systems, and since the system has entered the destruction phase, the resilience is jeopardized. At this stage, the key features of resilience, including capability, redundancy, and adaptive self-organizing, help reinforce resilience and reduce vulnerability.

3) As the disturbance advances, the system is damaged. At this stage, emergency prioritization, preparation, and coordination adjustment allow the operator to identify the main components for the recovery system as soon as possible and estimate the damages of the incident.

4) As the impact of the incident is minimized ($r_0 - r_b$), the system enters the recovery phase at t_c, and the units are re-installed. Then, the system will enter the post-recovery phase (r_d), at which stage the resilience may no longer be as remarkable as the pre-incident resilience (r_0), i.e., $r_d < r_0$. The recovery duration depends on the incident intensity and the power system's resilience features ($t_f - t_e > t_d - t_c$). So, having the critical resilience features, the power system can predict the following incidents and improve from destruction to the resilient stage. Also, it can adapt its performance and structure to alleviate the impact of the subsequent incidents.

2. 2. Evaluate the Resilience of the Power System Power system assessment and resilience have dominated research in recent years, but the present methods in the resilience measurement still need development and revision. This subsection discusses power system resilience assessment. Since research on resilience assessment has a multidimensional nature and includes both quantitative and qualitative aspects, they are dealt with below.

2. 2. 1. Qualitatively Evaluating the Resilience of a Power System The qualitative methods allow investigation of power system resilience from engineering, social, and organizational perspectives. Library work, questionnaires, and personal ratings are used as introduced by Carlson et al. [19] to study resilience. Analytical methods, e.g., the analytic hierarchy process (AHP), can be easily applied in decision-making as employed according to Orencio and Fujii, [20]. The qualitative assessment of the system formulated by Roege et al. [21], and a qualitative evaluation of resilience by events analysis is focused [22].

2. 2. 2. Quantitative Evaluation of Power System Resilience Quantitative evaluation methods include simulation-based, analytical, and statistical analysis methods, among which simulation-based methods can easily be combined with incident scenarios and allow easy calculation of incident implications. The complicated network model was used by Chanda and Srivastava [23], and outage records are used as Maliszewski and Perrings [24] for data analysis. An analytical method is adopted from Whitson and Ramirez-Marquez [25] to estimate power outage duration, and a statistical model is used as introduced by Nateghi et al. [26]. A quantitative assessment method is proposed by Nan and Sansavini [27] for resilience composed of two

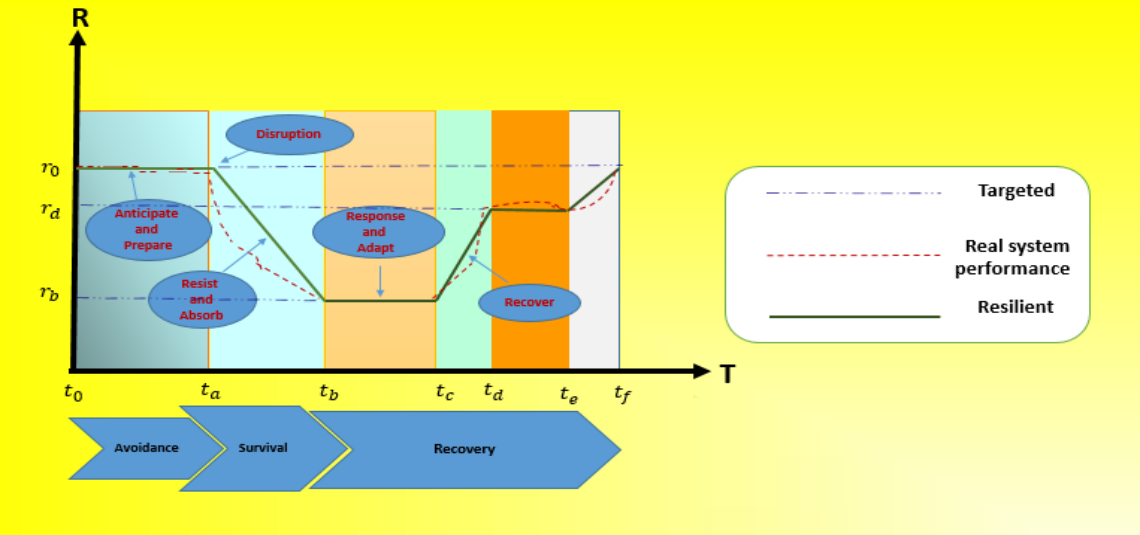

Figure 1. Events-related trapezoidal curve [4]

components an integrated metric to measure resilience and a hybrid model to show the failure behavior of the infrastructural systems.

2. 3. Framework Assessing and Improve Resilience Research is growing on the assessment and enhancement of power system resilience. However, no unique framework for resilience has been agreed upon, and it still seems necessary to study methodologies and research challenges, formulate resilience reinforcement strategies, and develop definitions and indices. In 2007, the 'resilience triangle' (see Figure 2) was introduced as a guideline for resilience assessment. The resilience of engineering systems is proposed by Ren et al. [28] by using the resilience triangle model developed by MCEER. Panteli et al. [29], indices are presented for resilience quantification in which the resilience triangle is developed into a 'resilient trapezoid'. Francis and Bekera [30] proposed a framework for resilience assessment, which includes identifying and prioritizing the system, defining the system domain, describing main goals of the system, describing physical, chemical, spatial, and social properties, identifying analytical purposes, and analyzing system vulnerability and dynamic behavior. Then, considering the system performance, resilience goals are

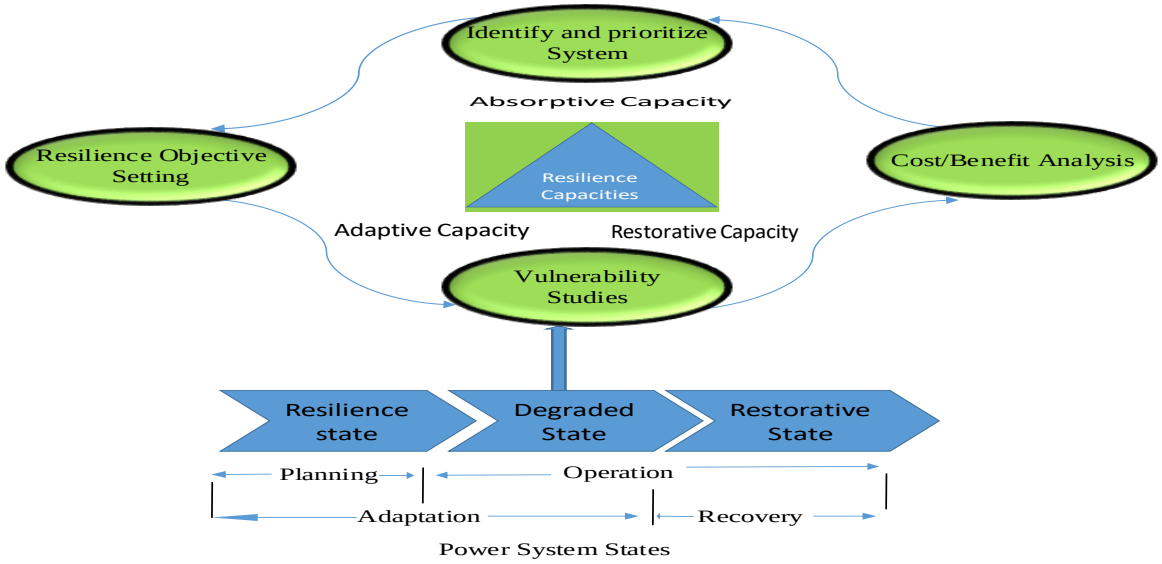

Figure 2. Power system resilience framework

set, and the stakeholders (profit/cost analysis) participate. The last component of the framework is resilience capacities, which encompasses absorption, adaptive, and recovery capacity. Engineering system resilience was explored by Mehrpouyan et al. [31] using the spectral graph approach. Engineering system redundancy, which enables increasing system reliability and decreasing vulnerability, was studied by Wang and Li [32]. A quantitative framework was proposed by Amirioun et al. [33] for the assessment of resilience and the application of microgrids in which destruction index (DI), recovery index (REI), and microgrid resilience index (MRI) are presented for describing the performance of system resilience. As depicted in Figure 3, the assessment of grid resilience, which is employed to assess grid status, compare the grid, and adopt arrangements for its resilience reinforcement, includes risk modeling.

Research around the world has focused on the assessment and reinforcement of the resilience of power systems against disasters [34]. On the other hand, engineers have been challenged by power system complexity and the range of incidents. Ouyang et al. [35], the features of severe incidents are ignored in resilience assessment. The resilience assessment and reinforcement strategies are expressed in details through the CIM method [36]. This part of the paper mentions solutions for resilience reinforcement (see Figure 4). All methods of resilience quantification cannot cover all resilience stages and overlap with other concepts, e.g., robustness and vulnerability [37]. Furthermore, some quantification methods for resilience estimation are inconsistent with the concept of resilience [38]. So, when responding to disturbances, it is necessary to develop a method for infrastructure resilience assessment. Zhang et al. [39] calculated the resilience during an incident within a three-stage framework, and the capacity of grid recovery is evaluated by the Monte Carlo simulation after the incident. The paper proposed an artificial metric system to calculate power system resilience performance. Indeed, contemporary research aims to develop infrastructures or minimize the losses of disastrous incidents [40].

2. 4. Resilience Metrics Some definitions of resilience indices are provided by Ayyub [41] and discussed in detail by Hosseini et al. [42]. Two indices are provided by Barker et al. [43] for resilience, and one

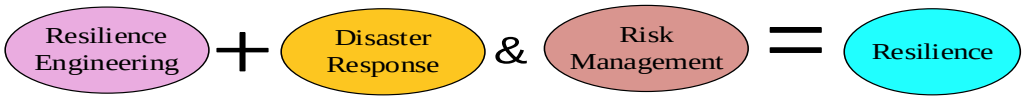

Figure 3. Strengthening the resilience of the power system

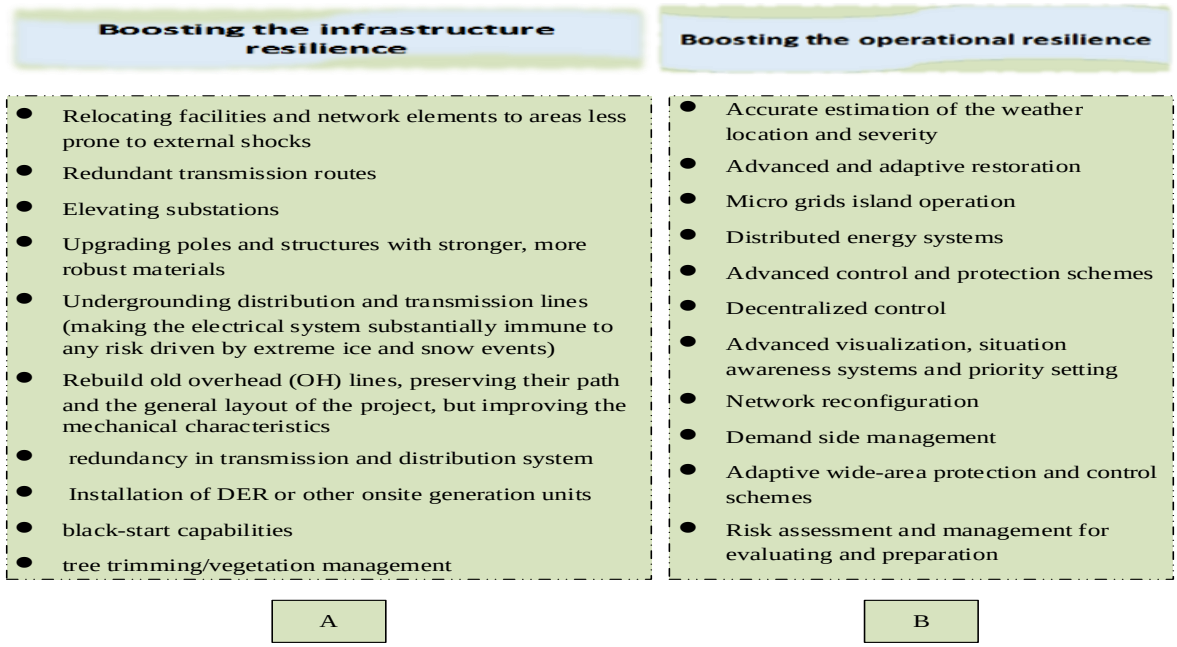

Figure 4. A) The solution to strengthening the resilience of infrastructure. B) The solution to strengthening exploitation resilience [36]

new criterion of resilience was discussed by Hu et al. [44]. A benchmark was proposed by Zhao and Zeng [45] for resilience, considering the impacts of weariness and different vulnerability scenarios. Figure 5 displays resilience indices.

3. MODELS AND THEIR APPLICATIONS IN PLANNINGy

A wide range of studies have addressed the modeling of vulnerability, outage duration during disasters, and post-disaster system restoration, and most proposed methods assess post-incident damages. This section discusses some models used in expansion planning. Various models have been presented for resilience assessment, e.g., the OPA-based DC model [46] and the AC power flux model [47]. The storms damage to a power system is estimated by Guikema et al. [48]. Various methods have so far been proposed for GEP, including mathematical optimization methods, e.g., analytic hierarchy process [49], decision tree [50], dynamic planning [51], decomposition method [52], meta-exploratory optimization methods, e.g., evolutionary planning, ant colony optimization, frog leaping algorithm [53], and PSO [54], and exploratory methods [55]. Furthermore, GEP models are based on robust optimization in which unknown parameters are displayed by an uncertainty set introduced by Mejía-Giraldo and McCalley [56]. In 1997, linear planning was first used by Garver to solve a TEP problem in which transmission losses were ignored, and all constraints were linear [57]. Robust optimization (RO) determines unknown parameters by a set of uncertainties and uses renewable energy resources to describe the unknown nature [58]. RO needs less data than SP [59]. TEP has also been solved by using mathematical optimization techniques,

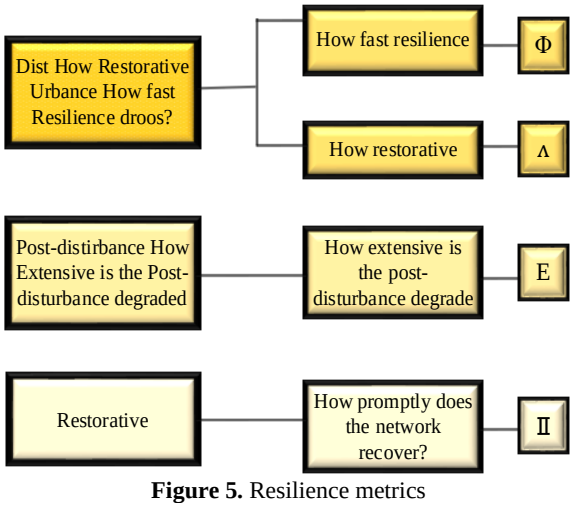

Figure 5. Resilience metrics

which are harder to use because of nonlinearity and the number of constraints and variables. Branch-dependent method [60] and Benders decomposition techniques [61] have been used too. Two-stage optimization was used by Zhang and Conejo [62] as a framework to address uncertainty in TEP. It is also observed that meta-exploratory optimization methods are employed, such as the honeybee algorithm by Meza et al. [63], the chaos theory by Hedman et al. [64], the evolutionary differential system by Limbu et al. [65], the frog leaping algorithm by Roh et al. [66], smart systems such as genetic algorithms by Rahimzadeh et al. [67], all are useful to find globally optimal solutions but suffer from very slow convergence. In addition to classic methods, the decomposition methods mentioned above have also been employed for analyzing TEP problems. Although the Benders decomposition technique exhibits better performance when analytic methods are used, other methods have also been used to solve TEP problems, such as the internal point method to solve linear and nonlinear problems and the branch and bound method based on the Benders analytic decomposition.

3. 1. Planning to Improve, Evaluate, and Resilience

Resilience reinforcement plans are divided into long-term, medium-term, and short-term plans. They are also categorized into single-stage problems (static planning) or multi-stage problems (dynamic planning). In static planning, no time horizon is set, and a plan is developed for a certain year, in which it is assumed that all new lines should be installed in the first year of the planning horizon. But, in dynamic planning, horizon years are studied separately, and new lines are specified for each year. Indeed, power system planning aims to establish resilience in the grid against natural disasters in a more robust manner. Studies have presented different optimization models, from mixed integer programming to quadratic planning and the more complicated stochastic planning, and more robust optimization, to facilitate the decision process. On the other hand, grid resilience should be improved in critical conditions (i.e., its capacity to cope with incidents and rapidly recover after disturbances) by corrective action – to minimize losses and recover the power system to its normal state after an incident – and remedial actions – to lead the power system to its normal state before an incident after load elimination [68]. Resource allocation is another key strategy for resilience planning. To minimize the effects of natural disasters and improve power system resilience, the use of distributed generation (DG) resources was proposed by Wang et al. [1], and the operational strategies that are converted into mixed integer linear programming by the linear scaling method were focused by Wang et al. [69]. As well the failure caused by the incident has been assessed. Defensive islanded schemes

are used by Panteli et al. [70] in which the risk severity index, which can record the random and spatial impact, is employed to determine the application of these schemes. Also, the concept of the fragility curve, which expresses the probability of failure as a function of meteorological parameters, has been used. When natural disasters strike, operation strategies consisting of maintenance planning [71] and wide-area control, should adjust in response to communication failures [72] based on the present status of the system and related equipment, as well as the likely future states related to the climatic conditions. A power and natural gas system is suggested by Shao et al. [73] by replacing the underground gas lines to enhance resilience. However, no suggestion has made to eliminate the risk of fire. Gao et al. [74] found that structure, dynamics, and failure mechanisms of a grid determine its resilience. A system of systems (SoS) resilience assessment is proposed by Han et al. [75]. The dominant and analytical Markov chain technique is used by Kwasinski et al. [76] to evaluate and analyze resilience with the availability of fuel, and it used by Song et al. [77] with the availability of photovoltaics. To assess and reinforce the resilience of a three-step system, a metric is defined by Li et al. [78] for resilience and simulated different scenarios to analyze the grid structure against natural incidents. Despite the simplicity of these approaches, the simulation techniques, e.g., the Monte Carlo simulation, used by Arab et al. [79]; results show that they are more appropriate for studies on power system resilience. Panteli et al. [80] used mixed integer programming to evaluate incident effects on power system resilience. A robust optimization model is proposed by Xu et al. [81] to minimize restoration time and improve resilience. Lei et al. [82]presented a scenario-based two-stage stochastic optimization model before a natural disaster. In [83], reliability indices, such as loss of load probability (LOLP) and expected demand not supplied (EDNS) in the presence of microgrids, are employed to reinforce power system resilience. Since modern intelligent network technologies are effective in improving power system resilience and reinforcing power systems against extreme incidents [1], modern systems should be resistant in addition to purposefulness [84]. In research, systems have been hardened by underground electricity lines, vegetation cover management, so on, which also have been effective in resilience enhancement [85]. Wang et al. [86] proposed three-level planning to harden power and natural gas systems against disastrous incidents. A robust defense method is employed. Operation activities to reinforce resilience and to make a comparison for distinguishing system hardening and operating activities are given by Panteli et al. [87], in which frequency load shedding is employed for resilience assessment. Research has also used preventive strategies, e.g., grid topology re-adjustment, to enhance resilience. In [88], using a two-stage integer planning and an analysis-based algorithm, it is concluded that preventive response is preferred to emergency response in terms of resilience enhancement. Resilience can also be increased by topology switching. Other methods used to increase resilience and minimize outage costs include dynamic circuit reconfiguration [89], portable energy storage systems [90], emergency generators in the power grid [91], and back-start unit preparation [92]. Abbasi et al. [93] performed mixed integer nonlinear programming (MINLP) and the post-outage system restoration is discussed with the aim of resilience maximization. Offline restoration planning is performed by Golshani et al. [94] to reinforce grid resilience. The plan formulated is stochastic two-stage mixed integer linear programming with wind energy generation scenarios; the L-shaped integer algorithm is used. It is observed that the optimal wind harnessing strategy can contribute to improving both the restoration process and system resilience. MINLP is performed by Sarkar et al. [95] with a grid restoration approach. Stochastic planning is performed by Su et al. [96] to enhance resilience against disastrous incidents and minimize microgrid costs. Various methods have presented to model restoration and recovery time during natural disasters [97]. Bie et al. [98] proposed resilience assessment methods are explored, and a load restoration method. In [99], five restoration strategies are used for restorating the power and gas grids to analyze resilience. It is revealed that the ‘stochastic restoration’ strategy brings about the lowest resilience for both systems, and the ‘gas aimed’ restoration strategy is related to the highest resilience for the gas system. The estimation of system infrastructure failure and its post-incident restoration was addressed by Marnay et al. [100]. Liang et al. [101], proposed microgrids to enhance resilience in which loss of load reduction is regarded as the most effective resilient source, which has been subject to extensive research. Islanded microgrids were utilized by Pashajavid et al. [102] with centralized and decentralized approaches. A two-level optimization problem was studied by Hussain et al. [103] in the presence of multiple energy carrier microgrids, subjected to power and natural gas grid disturbances. In [104], investment cost and resilience enhancements are considered the constraint and objective function, respectively. However, investment cost and resilience enhancement are the objective functions [105] in which stochastic planning is performed considering the demand response plan and aiming to improve the resilience of microgrids, and solving the model by the constraint ε method. Resilience planning was carried out by He et al. [106] to improve the resilience of an integrated energy system. Recommendations were provided by Chen et al. [107] for solving resilience gaps. Indeed, resilience responses are divided into preventive responses (actions before incident scenarios) and emergency responses (actions

taken due to the incident). They play a significant role in reinforcing resilience. In coordinated regional-district operation, an integrated energy system was used by Yan et al. [108] for resilience enhancement. Threat description, vulnerability assessment, recovery, and restoration were addressed by Paredes et al. [109]. In [110], a risk-aversion framework is proposed for more resilient planning and operation. Some studies have also investigated the impacts of critical conditions on power systems [111]. A model called CRISP is presented by Kelly-Gorham et al. [112] to measure power system resilience. In 2012, several parameters of resilience measurement were identified, and the resilience of a transmission grid was assessed for disastrous conditions by Henry and Ramirez-Marquez [113]. In 2017, grid resilience was evaluated under probability scenarios by two-level mixed-integer stochastic programming [114]. Also, two-stage stochastic optimization is proposed by Nagarajan et al. [115], in which the first level is grid investments and the second is the assessment of resilience enhancement related to the grid investment. Three-level optimization is proposed by Ma et al. [116] to minimize investment costs and to lose load. Planning was made by Gholami et al. [117] to enhance resilience in the presence of microgrids using the CVR technique. Power systems caused by cascading failure are analyzed by Xiao and Yeh [118]. Post-earthquake power system restoration planning is performed by Xu et al. [119], and seismic resilience is assessed by Anghel et al. [120]. Two criteria of repair time and resilience reduction are proposed by Fang et al. [121] to evaluate the criticality of power system components from their contribution to the system resilience viewpoint. Also, this method establishes a balance between risk and cost [122]. A mixed integer linear programming model is proposed by Teymouri et al. [123] for closed-loop controlled islanded systems in real-time to enhance resilience. In this paper, AC power flux reinforces resilience, and the recommended method exhibits saving on losing the load. Also, the sensitivity analysis indicates that the total loss of load increases as the delay time increases between line switching and loss of load. In recent decades, as power systems have been exposed to disastrous incidents, it has become imperative to use effective mechanisms for system resilience enhancement. Since most studies have focused on post-disturbance control intending to maximize demand, they are reviewed and analyzed here.

4. EXPANSION PLANNING

Developing goals of resilience, considering different scenarios, and expressing gaps provide opportunities for resilience enhancement, performed in three groups of GTEP and DEP. A comprehensive plan should reduce capacity and location of capacities, initiation time, frequency, severity, and duration of disasters, and improve resilience. The factors that should be considered in stochastic generation and transmission expansion planning are demand rate, availability of existing and candidate resources, and the capacity of the transmission lines.

4. 1. GEP Problem GEP is the most basic model in planning, and the type, location, and time of construction of generators must be determined in a time horizon of 20 or 30 years to meet the demand for projected loads. In generation expansion planning, the goal is to provide adequacy at the lowest cost. In 1955, the first long-term expansion planning was done in French. In 1957, Danzig and Taylor translated it into English, introducing the first linear planning (LP). Anderson, in 1972, showed that the nature of multi-stage generation expansion planning is similar to previous methods in dynamic planning. In 1976, linear expansion planning was to minimize investment and operating costs. Dehghan et al. [58] proposed linear programming of one-step and two-step integers with uncertainty in mind. A multi-stage generation expansion planning considering wind uncertainty has been used. A comprehensive review of generation expansion planning was conducted. Among which, Benders decomposition and Dantzig-Wolfe decomposition are more popular [124]. Also, stochastic optimization models based on scenario generation techniques with different uncertainties have been used [125]. In some studies, exploitation constraints have been included in generation expansion planning [126, 127]. Chen et al. studied GEP [128].

4. 1. 1. Uncertainty in GEP Some prevalent uncertainties in expansion planning include price volatility, reliability of generation units, demand evolution, investment, operating costs, and fuel and electricity prices. Dual uncertainty in the objective and constraint function is also presented by Hu et al. [129]. In GEP, the MCS method is commonly used to deal with uncertainties [130].

4. 2. TEP Problem Recently, transmission expansion planning has become a complex nonlinear optimization problem by determining which, where, and when new lines are to be built at the lowest total cost. In order to develop and strengthen transmission network capacity as well as ensuring future demand and integrating new power units with existing units have been considered by many researchers more than before due to technical/financial constraints along the planning horizon [131] and analysis of two critical issues of network reliability and security modeling [132]. Lumbreras and Ramos [133] presented a literature review up to 2016. Stochastic planning and robust optimization have been

used to solve the problem of transmission and storage systems planning [135], for the development of transmission and storage systems, robust optimization reported in literature [134]. A multi-stage random model is used. Conejo et al. [136] presented a model for the simultaneous development of energy transfer and storage with a distinction between long-term and short-term uncertainty in a stochastic planning framework. Zhang and Conejo [137] presented a robust optimization framework that includes random scheduling. A robust optimization model was proposed by Moreira et al. [138] in the possible conditions although the security criterion of the worst-case n-k, and the decomposition algorithm is solved using the column and constraint method [139, 140]. The robust optimization model presented by Chen and Wang [141] identified uncertainties related to the development of future production capacity and the decommissioning of existing generation units. In, The AR-TEP model was presented by Mínguez and García-Bertrand [142] due to the uncertainty of load demand and production capacity. A two-stage AR-TEP model was proposed by Jabr [143], to introduce the uncertainty of loads and renewable energy sources using a decomposition algorithm that finds the optimal investment and minimum cost of fines related to limiting renewable energy loads and sources.

4. 2. 2. Uncertainty in TEP The problem of TEP is usually with the uncertainty of load forecasting and availability of power system equipment, market uncertainty [144], energy and risk [145], and technology and new forms of production. Based on the results, the researchers found that considering uncertainty leads to better transmission expansion planning. The most common methods for dealing with uncertainties are the mathematical model [146]. The fuzzy approach is used to model uncertainty [147]. The application of DG in transmission development planning has also been investigated.

4. 2. 3 TEP and Improve Resilience Enhancing resilience and reducing the density of TEP have been increasingly considered by researchers and have been addressed by Zhao et al. [148]. In 2015, transmission network optimization was carried out by Fang ey al. [149] to strengthen the resilience of the power system against cascading errors and minimize investment costs. The impact of fire on transmission development planning was presented by Choobineh et al. [150]. The optimization framework is illustrated by providing the formula of MILP to track the redistribution of power flow DC and the evolution of the theoretical diagram of the network topology during cascade failures and, in the next step, determine the effect of acceleration [151]. Interaction after disruption of system resilience has been suggested to be the worst case of disorder. Whereas some lines are overloaded and some lines have empty capacities after redistribution of power flow due to line interruption, optimal changes in line reactance reduce the flux in overloaded lines and transfer them to lines that have unused capacity. Romero et al. [152] presented the (MIP) model for investment arrangements under terrorist threats. Panteli et al. [153] also presented MCS to evaluate the impact of weather on power system equipment focusing on the effect of wind on transmission lines, using fragility curves that express the probability of equipment failure as a function of wind speed. Arroyo and Galiana [154], Motto et al. [155] used two-level TEP to identify the power system's key elements and to identify the sensitive transmission lines. One of the crucial advantages of transmission expansion planning is its resilience to the worst-case scenarios, which is vital for strengthening the resilience of power system infrastructure.

4. 3. GTEP Problem GTEP is the most important part of power system planning. Recently, extensive research has addressed concurrent generation and transmission expansion planning (CGTEP) [156], but we are trying to provide a more comprehensive paper. Multi-objective CGTEP was conducted by Tekiner et al. [157] to minimize operational, investment, and emission costs. A three-level model of decentralized GEP and centralized TEP was studied by Javadi and Esmaeel Nezhad [158] using the epsilon method, in which multiple stochastic points are considered along with the load demand uncertainty. A two-level model was presented by Jenabi et al. [159], for the trade between generation and transmission investment and is transformed into a single-level mixed integer linear problem. Probabilistic multi-objective planning was performed by Mavalizadeh et al. [160] to reduce investment costs and adverse environmental impacts. Guerra et al. [161] presented coordinated planning under the constraints on pollutant emissions, storage, and load response programs. Coordinated planning was addressed by Zhang et al. [162] considering load response plans. In the coordinated expansion of power systems and gas grids was planned by Hu et al. [163] under uncertainty and the effect of a wind turbine. Muñoz-Delgado et al. [164] presented a dynamic planning considering grid uncertainty and reliability. Integrated generation and transmission expansion planning models were designed by Baringo and Baringo [165], considering uncertainty. The critical advantage of optimal expansion planning models is the calculation of uncertainty parameters with large dimensions, which does not need probabilistic models or the application of specific probability distributions. Unsihuay-Vila et al. [166] discussed on linear planning of mixed integer coordinated generation and transmission expansion. An exploratory algorithm was used by Alizadeh and Jadid [167] for dynamic

CGTEP in which the power system reliability is assessed within a linear framework. The same method was used by Alizadeh and Jadid [168] in the static form. Interested readers can find more details on GTEP problem-solving [169].

4. 3. 1. GTEP and Improve Resilience To strengthen resilience, a static GTEP was developed by Romero et al. [170] with a scenario-based approach for the analysis of earthquake effects. Studies have dealt with cost reduction, system losses, and increasing grid reliability. However, the alleviating of power system vulnerabilities to deliberate invasions should also be considered [171]. The static model of coordinated planning for GTEP [172], which aims to reduce the side effects of deliberate attacks on the transmission lines and minimize investment and operational costs, can also reduce the power system vulnerability. A scenario-based framework was described by Vaziri et al. [173] in response to seismic incidents. To reduce earthquake-induced power outages, a maintenance plan was studied by Çağnan et al. [174] in which the incident damages are ignored. A four-level planning model was described by Shivaie et al. [175] to reinforce a 400-kV grid in Iran for assessing seismic events. In An instrument was used by Cervigni et al. [176], to investigate the strategies for enhancing infrastructure resilience in Africa against natural disasters. The optimization of integrated GTEP is dealt with in the US in a time frame extending to 2050 [177].

5. TRENDS AND CHALLENGES

Since electricity cannot be stored, the operator will be faced to multiple challenges in any planning horizon. Therefore, optimal power system operation needs optimal planning. Since a resilient power system is capable of predicting possible disasters, taking practical actions to reduce losses and damages to the system components, and restoring the system to the pre-incident state, the investigation of its different aspects is crucial for organizing future research. On the other hand, researchers try to transform societies into resilient societies against disasters, in which case the infrastructure will be operated more efficiently. Still, it will result in system vulnerability and cascading errors. As power engineers, we can build reliable and resistant grids. The most obvious way is to build resilient grids, and an economical practice is to make further investments. With more information on the concept of resilience, this problem can be solved. Rezaei et al. [178], have listed the key challenges, constraints of modeling, and resilience enhancement activities. The first step to accomplishing resilience is to study vulnerability. Resilience enhancement activities are first prioritized based on their significance. Some activities are better in terms of resilience, and others are more economical. Eventually, a profit/cost analysis is undertaken. In the next step, the resilience activities can be categorized and fulfilled based on the resilience indices, which will contribute to building power infrastructure and satisfying resilience needs and the need for being economical. When or after a disturbance happens, resilience is analyzed to understand the infrastructure behavior to be more capable of preventing damage. Presently, the deployment of sensors for data collection has opened a new way to understand system resilience reinforcement by data analysis. For instance, machine learning can be used to analyze the collected data. However, there is still a huge gap between big data and significant impacts, while research is rare on it. Factors such as reliability, electricity market [179], uncertainty [180], environment, distributed generation, modeling, line density, reactive power planning, FACTS instruments, and demand-side management (DSM) are effective in resilient planning. On the other hand, the investigation of GTEP challenges in this paper lays the ground for future research. Based on the literature, the presence of distributed generation resources in planning helps develop an optimal plan and reduce costs [181]. As well, reactive power is essential for GTEP, which should be considered by researchers in their attempts to accomplish optimal planning. On the other hand, integrating reactive power planning with GEP will result in more optimal planning, so it is better to consider it in future studies. Research should explore uncertainties and FACTS instruments, e.g., TCSC, SSSC, UPFC, and IPFC, in TEP. Demand management programs, e.g., DSM, are mainly influential in the result of planning, but they have not been adequately studied in research on generation and transmission expansion planning. Microgrids have extensively been used in generation and transmission expansion planning in the studies, which has had good results too, so it has been presented as the most effective way of resilience enhancement. On the other hand, research has shown that energy hubs will be very effective. It is an emerging concept in the issue of power system resilience. This is a contribution of this article, which the authors will address in their future studies. It should be noted that some studies have neglected reliability and security in planning. In contrast the inclusion of reliability contributes to developing a resilient and reliable plan, as many researchers have mentioned as a pressing issue. Almost all studies have considered investment costs to minimize costs or maximize social welfare. However, operational costs are also crucial for a significant planning horizon, so they should also be studied within the model. Therefore, generation and transmission expansion planning are a key factor in long-term power system operation. On the other hand, it has been revealed

by the studies that multiple energy supply systems will also help enhance resilience.

6. CONCLUSIONS

Power systems have recently been exposed to disturbances induced by natural disasters, have influenced global security and economic benefits. So, we have to use techniques to assess the effect of these incidents. On the other hand, it is crucial to plan power systems that are resistant to high-impact, low-probability events. Since incidents may have irreparable consequences for power systems and their components, the issue of enhancing system resilience against disasters has become an essential requirement for smart grids. This paper provided resilience definitions and indicators in detail and identified different strategies and technologies for resilience enhancement. Also, the research papers on models were comprehensively reviewed, and the assessment of GTEP separately and concurrently, which is sophisticated and challenges the analysis of the results, was discussed. Finally, the paper mentioned the trends and challenges of the expansion models and my contribution. Indeed, the authors intended to provide a comprehensive review of concurrent GTEP aimed at improving grid resilience and give a general understanding of its effectiveness in improving system performance. In other words, a system is resilient when it can tolerate unexpected disturbances or restore itself rapidly after the incidents. So, it is vital to be able to assess incidents to evaluate and enhance power system resilience against them. This paper is a comprehensive context to find different ideas for future work.

7. REFERENCES

1. Wang,Y., Chen, C., Wang, J. and Baldick, R., "Research on resilience of power systems under natural disasters—A review", ***IEEE Transactions on Power Systems***, Vol. 31, No. 2, (2015), 1604-1613. doi: 10.1109/TPWRS.2015.2429656
2. Obama. B., "Presidential policy directive 21: Critical infrastructure security and resilience", (2013).
3. Hussain, A., Bui, V.-H. and Kim, H.-M., "Microgrids as a resilience resource and strategies used by microgrids for enhancing resilience", ***Applied Energy***, Vol. 240, (2019), 56-72. doi: 10.1016/j.apenergy.2019.02.055
4. Panteli, M. and Mancarella, P., "The grid: Stronger, bigger, smarter?: Presenting a conceptual framework of power system resilience", ***IEEE Power and Energy Magazine***, Vol. 13, No. 3, (2015), 58-66. doi: 10.1109/MPE.2015.2397334
5. Arghandeh, R., Meier, A. V., Mehrmanesh, L. and Mili, L., "On the definition of cyber-physical resilience in power systems", ***Renewable and Sustainable Energy Reviews***, Vol. 58, (2016), 1060-1069. doi: 10.1016/j.rser.2015.12.193
6. Chaudry, M., Ekins, P., Ramachandran, K. and Shakoor, A., "Building a resilient UK energy system", (2011).
7. Office, C., "Keeping the country running: Natural hazards and infrastructure", (2011).
8. Stockton, P., "Resilience for black sky days", Report prepared for the National Association of Regulatory Utility Commissioners and the US Department of Energy, (2014).
9. Rieger, C. and Manic, M., "On Critical Infrastructures, Their Security and Resilience-Trends and Vision", (2018). doi: 10.48550/arXiv.1812.02710
10. RAMCAP, P. "All hazard risk and resilience, prioritizing critical infrastructure by using the RAMCAP Plus SM approach", ASME Inno, (2009).
11. House, W., "Economic benefits of increasing electric grid resilience to weather outages", *Washington, DC: Executive Office of the President*, (2013).
12. Ouyang, M. and Duenas-Osorio, L., "Multi-dimensional hurricane resilience assessment of electric power systems", ***Structural Safety***, Vol. 48, (2014), 15-24. doi: 10.1016/j.strusafe.2014.01.001
13. Preston, B. L., Backhaus, S. N. and Ewers, M., "Resilience of the US electricity system: a multi-hazard perspective", DOE Report, *August*,(2016).
14. Fisher, L., "More than 70 ways to show resilience", ***Nature***, Vol. 518, No. 7537, (2015), 35-35. doi: 10.1038/518035a
15. Holling, C. S., "Resilience and stability of ecological systems", ***Annual Review of Ecology and Systematics***, Vol. 4, No. 1, (1973), 1-23. doi: 10.1146/annurev.es.04.110173.000245
16. Baroud, H., Barker, K., Ramirez-Marquez, J. E. and Rocco, C. M., "Inherent costs and interdependent impacts of infrastructure network resilience", ***Risk Analysis***, Vol. 35, No. 4, (2015), 642-662. doi: 10.1111/risa.12223
17. Youn, B. D., Hu, C. and Wang, P., "Resilience-driven system design of complex engineered systems", ***Journal of Mechanical Design***, Vol. 133, No. 10, (2011). doi: 10.1115/1.4004981
18. Mancarella, P., "MES (multi-energy systems): An overview of concepts and evaluation models", ***Energy***, Vol. 65, 1-17, (2014). doi: 10.1016/j.energy.2013.10.041
19. Carlson, J., Haffenden, R., Bassett, G. and Buehring, W., "Resilience: Theory and Application", Argonne National Lab.(ANL), Argonne, IL (United States), (2012).
20. Orencio, P. M. and Fujii, M., "A localized disaster-resilience index to assess coastal communities based on an analytic hierarchy process (AHP)", ***International Journal of Disaster Risk Reduction***, Vol. 3, (2013), 62-75. doi: 10.1016/j.ijdrr.2012.11.006
21. Roege, P. E., Collier, Z. A., Mancillas, J., McDonagh, J. A. and Linkov, I., "Metrics for energy resilience", ***Energy Policy***, Vol. 72, (2014), 249-256. doi: 10.1016/j.enpol.2014.04.012
22. Carvalho, P. V., dos Santos, I. L., Gomes, J. O. and Borges, M. R., "Micro incident analysis framework to assess safety and resilience in the operation of safe critical systems: a case study in a nuclear power plant", ***Journal of Loss Prevention in the Process Industries***, Vol. 21, No. 3, (2008), 277-286. doi: 10.1016/j.jlp.2007.04.005
23. Chanda, S. and Srivastava, A. K., "Defining and enabling resiliency of electric distribution systems with multiple microgrids", ***IEEE Transactions on Smart Grid***, Vol. 7, No. 6, (2016), 2859-2868. doi: 10.1109/TSG.2016.2561303
24. Maliszewski, P. J. and . Perrings, C., "Factors in the resilience of electrical power distribution infrastructures", ***Applied Geography***, Vol. 32, No. 2, (2012), 668-679. doi: 10.1016/j.apgeog.2011.08.001
25. Whitson, J. C. and Ramirez-Marquez, J. E., "Resiliency as a component importance measure in network reliability",

Reliability Engineering & System Safety, Vol. 94, No. 10, (2009), 1685-1693. doi: 10.1016/j.ress.2009.05.001

26. Nateghi, R., Guikema, S. D. and Quiring, S. M., "Forecasting hurricane-induced power outage durations", ***Natural hazards***, Vol. 74, No. 3, (2014), 1795-1811. doi: 10.1007/s11069-014-1270-9
27. Nan, C. and Sansavini, G., "A quantitative method for assessing resilience of interdependent infrastructures", ***Reliability Engineering & System Safety***, Vol. 157, (2017), 35-53. doi: 10.1016/j.ress.2016.08.013
28. Ren, F., Zhao, T., Jiao, J. and Hu, Y., "Resilience optimization for complex engineered systems based on the multi-dimensional resilience concept", ***IEEE Access***, Vol. 5, (2017), 19352-19362. doi: 10.1109/ACCESS.2017.2755043
29. Panteli, M., Mancarella, P., Trakas, D. N., Kyriakides, E. and Hatziargyriou, N. D., "Metrics and quantification of operational and infrastructure resilience in power systems", ***IEEE Transactions on Power Systems***, Vol. 32, No. 6, (2017), 4732-4742. doi: 10.1109/TPWRS.2017.2664141
30. Francis, R. and Bekera, B., "A metric and frameworks for resilience analysis of engineered and infrastructure systems", ***Reliability Engineering & System Safety***, Vol. 121, (2014), 90-103. doi: 10.1016/j.ress.2013.07.004
31. Mehrpouyan, H., Haley, B., Dong, A., Tumer, I. Y. and Hoyle, C., "Resiliency analysis for complex engineered system design", ***AI EDAM***, Vol. 29, No. 1, (2015), 93-108. doi: 10.1017/S0890060414000663
32. Wang, J. and Li, M., "Redundancy Allocation Optimization for Multistate Systems With Failure Interactions Using Semi-Markov Process", ***Journal of Mechanical Design***, Vol. 137, No. 10, (2015). doi: 10.1115/1.4031297
33. Amirioun, M., Aminifar, F., Lesani, H. and Shahidehpour, M., "Metrics and quantitative framework for assessing microgrid resilience against windstorms", ***International Journal of Electrical Power & Energy Systems***, Vol. 104, (2019), 716-723. doi: 10.1016/j.ijepes.2018.07.025
34. Gao, H., Chen, Y., Xu, Y. and Liu, C.-C., "Resilience-oriented critical load restoration using microgrids in distribution systems", ***IEEE Transactions on Smart Grid***, Vol. 7, No. 6, (2016), 2837-2848. doi: 10.1109/TSG.2016.2550625
35. Ouyang, M., Dueñas-Osorio, L. and Min, X., "A three-stage resilience analysis framework for urban infrastructure systems", ***Structural Safety***, Vol. 36, (2012), 23-31. doi: 10.1016/j.strusafe.2011.12.004
36. Bhusal, N., Abdelmalak, M., Kamruzzaman, M. and Benidris, M., "Power system resilience: Current practices, challenges, and future directions", ***IEEE Access***, Vol. 8, (2020),18064-18086. doi: 10.1109/ACCESS.2020.2968586
37. Alessandri, A. and Filippini, R., "Evaluation of resilience of interconnected systems based on stability analysis", in *Critical Information Infrastructures Security*: ***Springer***, (2013), 180-190. doi: 10.1007/978-3-642-41485-5_16
38. Khodaei, A., "Resiliency-oriented microgrid optimal scheduling", ***IEEE Transactions on Smart Grid***, Vol. 5, No. 4, (2014), 1584-1591. doi: 10.1109/TSG.2014.2311465
39. Zhang, H., Yuan, H., Li, G. and Lin, Y., "Quantitative resilience assessment under a tri-stage framework for power systems", ***Energies***, Vol. 11, No. 6, (2018), 1427. doi: 10.3390/en11061427
40. Gritzalis, D. and Theocharidou, M., "Critical Infrastructure Security and Resilience", (2019).
41. Ayyub, B. M., "Systems resilience for multihazard environments: Definition, metrics, and valuation for decision making", ***Risk Analysis***, Vol. 34, No. 2, (2014), 340-355. doi: 10.1111/risa.12093
42. Hosseini, S., Barker, K. and Ramirez-Marquez, J. E., "A review of definitions and measures of system resilience", ***Reliability Engineering & System Safety***, Vol. 145, (2016), 47-61. doi: 10.1016/j.ress.2015.08.006
43. Barker, K., Ramirez-Marquez, J. E. and Rocco, C. M., "Resilience-based network component importance measures", ***Reliability Engineering & System Safety***, Vol. 117, (2013), 89-97. doi: 10.1016/j.ress.2013.03.012
44. Hu, Z. and Mahadevan, S., "Resilience assessment based on time-dependent system reliability analysis", ***Journal of Mechanical Design***, Vol. 138, No. 11, (2016). doi: 10.1115/1.4034109
45. Zhao, L. and Zeng, B., "Vulnerability analysis of power grids with line switching", ***IEEE Transactions on Power Systems***, Vol. 28, No. 3, (2013), 2727-2736. doi: 10.1109/TPWRS.2013.2256374
46. Dobson, I., Carreras, B. A., Lynch, V. E. and Newman, D. E., "Complex systems analysis of series of blackouts: Cascading failure, critical points, and self-organization", *Chaos: An **Interdisciplinary Journal of Nonlinear Science***, Vol. 17, No. 2, (2007). doi: 10.1063/1.2737822
47. Kirschen, D. S., Jayaweera, D., Nedic, D. P. and Allan, R. N., "A probabilistic indicator of system stress", ***IEEE Transactions on Power Systems***, Vol. 19, No. 3, (2004), 1650-1657. doi: 10.1109/TPWRS.2004.831665
48. Guikema, S. D., Davidson, R. A. and Liu, H., "Statistical models of the effects of tree trimming on power system outages", ***IEEE Transactions on Power Delivery***, Vol. 21, No. 3, (2006), 1549-1557. doi: 10.1109/TPWRD.2005.860238
49. Meza, J. L. C., Yildirim, M. B. and Masud, A. S., "A model for the multiperiod multiobjective power generation expansion problem", ***IEEE Transactions on Power Systems***, Vol. 22, No. 2, (2007), 871-878. doi: 10.1109/TPWRS.2007.895178
50. Feng, Y. and Ryan, S. M., "Scenario construction and reduction applied to stochastic power generation expansion planning", ***Computers & Operations Research***, Vol. 40, No. 1, (2013), 9-23. doi: 10.1016/j.cor.2012.05.005
51. Tafreshi, S. M., Lahiji, A. S., Aghaei, J. and Rabiee, A., "Reliable generation expansion planning in pool market considering power system security", ***Energy Conversion and Management***, Vol. 54, No. 1, (2012), 162-168. doi: 10.1016/j.enconman.2011.10.008
52. Sirikum, J., Techanitisawad, A. and Kachitvichyanukul, V., "A new efficient GA-benders' decomposition method: For power generation expansion planning with emission controls", ***IEEE Transactions on Power Systems***, Vol. 22, No. 3, (2007), 1092-1100. doi: 10.1109/TPWRS.2007.901092
53. Jadidoleslam, M., Bijami, E., Amiri, N., Ebrahimi, A. and Askari, J., "Application of shuffled frog leaping algorithm to long term generation expansion planning", ***International Journal of Computer and Electrical Engineering***, Vol. 4, No. 2, (2012), 115.
54. Moghddas-Tafreshi, S., Shayanfar, H., Lahiji, A. S., Rabiee, A. and Aghaei, J., "Generation expansion planning in Pool market: A hybrid modified game theory and particle swarm optimization", ***Energy Conversion and Management***, Vol. 52, No. 2, (2011), 1512-1519. doi: 10.1016/j.enconman.2010.10.019
55. Munoz, F. D. and Watson, J.-P., "A scalable solution framework for stochastic transmission and generation planning problems", ***Computational Management Science***, Vol. 12, No. 4, (2015), 491-518. doi: 10.1007/s10287-015-0229-y
56. Mejía-Giraldo, D. and McCalley, J., "Adjustable decisions for reducing the price of robustness of capacity expansion planning", ***IEEE Transactions on Power Systems***, Vol. 29, No. 4, (2014), 1573-1582. doi: 10.1109/TPWRS.2013.2295166
57. Careri, F., Genesi, C., Marannino, P., Montagna, M., Rossi, S. and Siviero, I., "Generation expansion planning in the age of green

economy", ***IEEE Transactions on Power Systems***, Vol. 26, No. 4, (2011), 2214-2223. doi: 10.1109/TPWRS.2011.2107753

58. Dehghan, S., Amjady, N. and Conejo, A. J., "Adaptive robust transmission expansion planning using linear decision rules", ***IEEE Transactions on Power Systems***, Vol. 32, No. 5, (2017), 4024-4034. doi: 10.1109/TPWRS.2017.2652618
59. Bertsimas, D., Litvinov, E., Sun, X. A., Zhao, J. and Zheng, T., "Adaptive robust optimization for the security constrained unit commitment problem", ***IEEE Transactions on Power Systems***, Vol. 28, No. 1, (2012), 52-63. doi: 10.1109/TPWRS.2012.2205021
60. Rudkevich, A. M., "A nodal capacity market for co-optimization of generation and transmission expansion", in *2012 50th Annual Allerton Conference on Communication ,Control, and Computing (Allerton)*, (2012), 1080-1088. doi: 10.1109/Allerton.2012.6483338
61. Pozo, D., Sauma, E. E. and Contreras, J., "A three-level static MILP model for generation and transmission expansion planning", ***IEEE Transactions on Power Systems***, Vol. 28, No. 1, (2012), 202-210. doi: 10.1109/TPWRS.2012.2204073
62. Zhang, X. and Conejo, A. J., "Robust transmission expansion planning representing long-and short-term uncertainty", ***IEEE Transactions on Power Systems***, Vol. 33, No. 2, (2017), 1329-1338. doi: 10.1109/TPWRS.2017.2717944
63. Meza, J. L. C., Yildirim, M. B. and Masud, A. S., "A multiobjective evolutionary programming algorithm and its applications to power generation expansion planning", ***IEEE Transactions on Systems***, Vol. 39, No. 5, (2009), 1086-1096. doi: 10.1109/TSMCA.2009.2025868
64. Hedman, K. W., Ferris, M. C., O'Neill,R. P., Fisher, E. B. and Oren, S. S., "Co-optimization of generation unit commitment and transmission switching with N-1 reliability", ***IEEE Transactions on Power Systems***, Vol. 25, No. 2, (2010), 1052-1063. doi: 10.1109/TPWRS.2009.2037232
65. Limbu, T., Saha,T. and McDonald, J., "Value-based allocation and settlement of reserves in electricity markets", ***IET Generation, Transmission & Distribution***, Vol. 5, No. 4, (2011), 489-495. doi: 10.1049/iet-gtd.2010.0467
66. Roh, J. H., Shahidehpour, M. and Wu, L., "Market-based generation and transmission planning with uncertainties", ***IEEE Transactions on Power Systems***, Vol. 24, No. 3, (2009), 1587-1598. doi: 10.1109/TPWRS.2009.2022982
67. Rahimzadeh, S., Bina, M. T. and Viki, A., "Simultaneous application of multi-type FACTS devices to the restructured environment: achieving both optimal number and location", ***IET generation, transmission & Distribution***, Vol. 4, No. 3, (2010), 349-362. doi: 10.1049/iet-gtd.2009.0287
68. Yuan, W., Wang, J., Qiu, F., Chen, C., Kang, C. and Zeng, B., "Robust optimization-based resilient distribution network planning against natural disasters", ***IEEE Transactions on Smart Grid***, Vol. 7, No. 6, (2016), 2817-2826. doi: 10.1109/TSG.2015.2513048
69. Wang, C., Hou, Y., Qiu, F., Lei, S. and Liu, K., "Resilience enhancement with sequentially proactive operation strategies", ***IEEE Transactions on Power Systems***, Vol. 32, No. 4, (2016), 2847-2857. doi: 10.1109/TPWRS.2016.2622858
70. Panteli, M., Trakas, D. N., Mancarella, P. and Hatziargyriou, N. D., "Boosting the power grid resilience to extreme weather events using defensive islanding", ***IEEE Transactions on Smart Grid***, Vol. 7, No. 6, (2016), 2913-2922. doi: 10.1109/TSG.2016.2535228
71. Wang, C., Hou,Y., Qin, Z., Peng, C. and Zhou, H., "Dynamic coordinated condition-based maintenance for multiple components with external conditions", ***IEEE Transactions on Power Delivery***, Vol. 30, No. 5, (2015), 2362-2370. doi: 10.1109/TPWRD.2015.2442291
72. Zhang, S. and Vittal, V., "Design of wide-area power system damping controllers resilient to communication failures", ***IEEE Transactions on Power Systems***, Vol. 28, No. 4, (2013), 4292-4300. doi: 10.1109/TPWRS.2013.2261828
73. Shao, C., Shahidehpour, M., Wang, X., Wang, X. and Wang, B., "Integrated planning of electricity and natural gas transportation systems for enhancing the power grid resilience", ***IEEE Transactions on Power Systems***, Vol. 32, No. 6, (2017), 4418-4429. doi: 10.1109/TPWRS.2017.2672728
74. Gao, J., Liu, X., Li, D. and Havlin, S., "Recent progress on the resilience of complex networks", ***Energies***, Vol. 8, No. 10, (2015), 12187-12210. doi: 10.3390/en81012187
75. Han, S. Y., Marais, K. and DeLaurentis, D., "Evaluating system of systems resilience using interdependency analysis", in 2012 IEEE International Conference on Systems, (2012), 1251-1256. doi: 10.1109/ICSMC.2012.6377904
76. Kwasinski, A., Krishnamurthy, V., Song, J. and Sharma, R., "Availability evaluation of micro-grids for resistant power supply during natural disasters", ***IEEE Transactions on Smart Grid***, Vol. 3, No. 4, (2012), 2007-2018. doi: 10.1109/TSG.2012.2197832
77. Song, J., Krishnamurthy, V., Kwasinski, A. and Sharma, R., "Development of a Markov-chain-based energy storage model for power supply availability assessment of photovoltaic generation plants", ***IEEE Transactions on Sustainable Energy***, Vol. 4, No. 2, (2012), 491-500. doi: 10.1109/TSTE.2012.2207135
78. Li, B., Roche, R. and Miraoui, A., "System resilience improvement using multiple energy supply systems under natural disasters", in *IECON 2016-42nd Annual Conference of the IEEE Industrial Electronics Society*, (2016), 3912-3917. doi: 10.1109/IECON.2016.7793278
79. Arab, A., Khodaei, A., Khator, S. K., Ding, K., Emesih, V. A. and Han, Z., "Stochastic pre-hurricane restoration planning for electric power systems infrastructure", ***IEEE Transactions on Smart Grid***, Vol. 6, No. 2, (2015), 1046-1054. doi: 10.1109/TSG.2015.2388736
80. Panteli, M., Pickering, C., Wilkinson, S., Dawson, R. and Mancarella, P., "Power system resilience to extreme weather: fragility modeling, probabilistic impact assessment, and adaptation measures", ***IEEE Transactions on Power Systems***, Vol. 32, No. 5, (2016), 3747-3757. doi: 10.1109/TPWRS.2016.2641463
81. Xu, Y., Liu, C.-C., Schneider, K. P. and Ton, D. T., "Placement of remote-controlled switches to enhance distribution system restoration capability", ***IEEE Transactions on Power Systems***, Vol. 31, No. 2, (2015), 1139-1150. doi: 10.1109/TPWRS.2015.2419616
82. Lei, S., Wang, J., Chen, C. and Hou, Y., "Mobile emergency generator pre-positioning and real-time allocation for resilient response to natural disasters", ***IEEE Transactions on Smart Grid***, Vol. 9, No. 3, (2016), 2030-2041. doi: 10.1109/TSG.2016.2605692
83. Liu, X., Shahidehpour, M., Li, Z., Liu ,X., Cao, Y. and Bie, Z., "Microgrids for enhancing the power grid resilience in extreme conditions", ***IEEE Transactions on Smart Grid***, Vol. 8, No. 2, (2016), 589-597. doi: 10.1109/TSG.2016.2579999
84. Chen, C., Wang, J. and Ton, D., "Modernizing distribution system restoration to achieve grid resiliency against extreme weather events: an integrated solution", Proceedings of the IEEE, Vol. 105, No. 7, (2017), 1267-1288. doi: 10.1109/JPROC.2017.2684780
85. Arab, A., Tekin, E., Khodaei, A., Khator, S. K. and Han, Z., "System hardening and condition-based maintenance for electric power infrastructure under hurricane effects", ***IEEE Transactions on Reliability***, Vol. 65, No. 3, (2016), 1457-1470. doi: 10.1109/TR.2016.2575445

86. Wang, C., Wei, W., Wang, J., Liu, F., Qiu, F. and Carlos, M., "Robust defense strategy for gas–electric systems against malicious attacks", ***IEEE Transactions on Power Systems***, Vol. 32, No. 4, (2016), 2953-2965. doi: 10.1109/TPWRS.2016.2628877
87. Panteli, M., Trakas, D. N., Mancarella, P. and Hatziargyriou, N. D., "Power systems resilience assessment: Hardening and smart operational enhancement strategies", ***Proceedings of the IEEE***, Vol. 105, No. 7, (2017), 1202-1213. doi: 10.1109/JPROC.2017.2691357
88. Huang, G., Wang, J., Chen, C., Qi, J. and Guo, C., "Integration of preventive and emergency responses for power grid resilience enhancement", ***IEEE Transactions on Power Systems***, Vol. 32, No. 6, (2017), 4451-4463. doi: 10.1109/TPWRS.2017.2685640
89. Amirioun, M. H., Aminifar, F. and Lesani, H., "Towards proactive scheduling of microgrids against extreme floods", ***IEEE Transactions on Smart Grid***, Vol. 9, No. 4, (2017), 3900-3902. doi: 10.1109/TSG.2017.2762906
90. Yao, S., Wang, P. and Zhao, T., "Transportable energy storage for more resilient distribution systems with multiple microgrids", ***IEEE Transactions on Smart Grid***, Vol. 10, No. 3, (2018), 3331-3341. doi: 10.1109/TSG.2018.2824820
91. Sun, W., Liu, C.-C. and Liu, S., "Black start capability assessment in power system restoration", in *2011 IEEE Power and Energy Society General Meeting*, (2011), 1-7. doi: 10.1109/PES.2011.6039752
92. Sun, W., Liu, C.-C. and Zhang, L., "Optimal generator start-up strategy for bulk power system restoration", ***IEEE Transactions on Power Systems***, Vol. 26, No. 3, (2010), 1357-1366. doi: 10.1109/TPWRS.2010.2089646
93. Abbasi, S., Barati, M. and Lim, G. J., "A parallel sectionalized restoration scheme for resilient smart grid systems", ***IEEE Transactions on Smart Grid***, Vol. 10, No. 2, (2017), 1660-1670. doi: 10.1109/TSG.2017.2775523
94. Golshani, A., Sun, W., Zhou, Q., Zheng, Q. P. and Hou, Y., "Incorporating wind energy in power system restoration planning", ***IEEE Transactions on Smart Grid***, Vol. 10, No. 1, (2017), 16-28. doi: 10.1109/TSG.2017.2729592
95. Sarkar, R., Gusrialdi, A. and Qu, Z., "An adaptive restorative method for resilient power distribution networks", in 2016 IEEE Power and Energy Society General Meeting (PESGM), (2016), 1-5. doi: 10.1109/PESGM.2016.7741994
96. Su, W., Wang, J. and Roh, J., "Stochastic energy scheduling in microgrids with intermittent renewable energy resources", ***IEEE Transactions on Smart grid***, Vol. 5, No. 4, (2013), 1876-1883. doi: 10.1109/TSG.2013.2280645
97. Liu, Y. and Singh, C., "A methodology for evaluation of hurricane impact on composite power system reliability", ***IEEE Transactions on Power Systems***, Vol. 26, No. 1, (2010), 145-152. doi: 10.1109/TPWRS.2010.2050219
98. Bie, Z., Lin, Y., Li, G. and Li, F., "Battling the extreme: A study on the power system resilience", ***Proceedings of the IEEE***, Vol. 105, No. 7, (2017), 1253-1266. doi: 10.1109/JPROC.2017.2679040
99. Ouyang, M. and Wang, Z., "Resilience assessment of interdependent infrastructure systems: With a focus on joint restoration modeling and analysis", ***Reliability Engineering & System Safety***, Vol. 141, (2015), 74-82. doi: 10.1016/j.ress.2015.03.011
100. Marnay, C., Aki, H., Hirose, K., Kwasinski, A., Ogura, S. and Shinji, T., "Japan's pivot to resilience: How two microgrids fared after the 2011 earthquake", ***IEEE Power and Energy Magazine***, vol. 13, No. 3, (2015), 44-57. doi: 10.1109/MPE.2015.2397333
101. Liang, L., Hou,Y., Hill, D. J. and Hui, S. Y. R., "Enhancing resilience of microgrids with electric springs", ***IEEE Transactions on Smart Grid***, Vol. 9, No. 3, (2016), 2235-2247. doi: 10.1109/TSG.2016.2609603
102. Pashajavid, E., Shahnia, F. and Ghosh, A., "Development of a self-healing strategy to enhance the overloading resilience of islanded microgrids", ***IEEE transactions on smart grid***, Vol. 8, No. 2, (2015), 868-880. doi: 10.1109/TSG.2015.2477601
103. Hussain, A., Bui, V.-H. and Kim, H.-M., "Optimal operation of hybrid microgrids for enhancing resiliency considering feasible islanding and survivability", ***IET Renewable Power Generation***, Vol. 11, No. 6, (2017), 846-857. doi: 10.1049/iet-rpg.2016.0820
104. Najafi, J., Peiravi, A. and Guerrero, J. M., "Power distribution system improvement planning under hurricanes based on a new resilience index", ***Sustainable Cities and Society***, Vol. 39, (2018), 592-604. doi: 10.1016/j.scs.2018.03.022
105. Najafi, J., Peiravi, A., Anvari-Moghaddam, A. and Guerrero, J. M., "Power-heat generation sources planning in microgrids to enhance resilience against islanding due to natural disasters", in 2019 IEEE 28th International Symposium on Industrial Electronics (ISIE), (2019), 2446-2451. doi: 10.1109/ISIE.2019.8781415
106. He,Y., Shahidehpour, M., Li, Z., Guo, C. and Zhu, B., "Robust constrained operation of integrated electricity-natural gas system considering distributed natural gas storage", ***IEEE Transactions on Sustainable Energy***, Vol. 9, No. 3, (2017), 1061-1071. doi: 10.1109/TSTE.2017.2764004
107. Chen, C., Wang, J., Qiu, F .and Zhao, D., "Resilient distribution system by microgrids formation after natural disasters", ***IEEE Transactions on Smart Grid***, Vol. 7, No. 2, (2015), 958-966. doi: 10.1109/TSG.2015.2429653
108. Yan, M., He, Y., Shahidehpour, M., Ai, X., Li, Z. and Wen, J., "Coordinated regional-district operation of integrated energy systems for resilience enhancement in natural disasters", ***IEEE Transactions on Smart Grid***, Vol. 10, No. 5, (2018), 4881-4892. doi: 10.1109/TSG.2018.2870358
109. Paredes, R. and Dueñas-Osorio, L., "A time-dependent seismic resilience analysis approach for networked lifelines", in Proceedings of the 12th International Conference on Applications of Statistics and Probability in Civil Engineering (ICASP12), Vancouver, BC, Canada, (2015), 12-15. doi: 10.14288/1.0076219
110. Strbac, G., Kirschen, D. and Moreno, R., "Reliability standards for the operation and planning of future electricity networks", Vol. 1: No. 3, (2016), 143-219. doi: 10.1561/3100000001
111. Davis, C. M. and Overbye, T. J., "Multiple element contingency screening", ***IEEE Transactions on Power Systems***, Vol. 26, No. 3, (2010), 1294-1301. doi: 10.1109/TPWRS.2010.2087366
112. Kelly-Gorham, M. R., Hines,P. and Dobson, I., "Using historical utility outage data to compute overall transmission grid resilience", ***IEEE Transactions on Power Systems***, (2019). doi: 10.1109/MEPS46793.2019.9395039
113. Henry, D. and Ramirez-Marquez, J. E., "Generic metrics and quantitative approaches for system resilience as a function of time", ***Reliability Engineering & System Safety***, Vol. 99, (2012), 114-122. doi: 10.1016/j.ress.2011.09.002
114. Fotouhi, H., Moryadee, S. and Miller-Hooks, E., "Quantifying the resilience of an urban traffic-electric power coupled system", ***Reliability Engineering & System Safety***, Vol. 163, (2017), 79-94. doi: 10.1016/j.ress.2017.01.026
115. Nagarajan, H., Yamangil, E., Bent, R., Van Hentenryck, P. and Backhaus,S., "Optimal resilient transmission grid design", in 2016 Power Systems Computation Conference (PSCC), (2016), 1-7. doi: 10.1109/PSCC.2016.7540988
116. Ma,S., Chen, B. and Wang, Z., "Resilience enhancement strategy for distribution systems under extreme weather events", ***IEEE Transactions on Smart Grid***, Vol. 9, No. 2, (2016), 1442-1451. doi: 10.1109/TSG.2016.2591885

117. Gholami, A., Shekari, T., Aminifar, F. and Shahidehpour, M., "Microgrid scheduling with uncertainty: The quest for resilience", ***IEEE Transactions on Smart Grid***, Vol. 7, No. 6, (2016), 2849-2858. doi: 10.1109/TSG.2016.2598802

118. Xiao, H. and Yeh, E. M., "Cascading link failure in the power grid: A percolation-based analysis", in *2011 IEEE International Conference on Communications Workshops (ICC)*, (2011), 1-6. doi: 10.1109/iccw.2011.5963573

119. Xu, N., Guikema, S. D., Davidson, R. A., Nozick, L. K., Çağnan, Z. and Vaziri, K., "Optimizing scheduling of post-earthquake electric power restoration tasks", *Earthquake engineering & structural dynamics*, Vol. 36, No. 2, (2007), 265-284. doi: 10.1002/eqe.623

120. Anghel, M., Werley, K. A. and Motter, A. E., "Stochastic model for power grid dynamics", in *2007 40th Annual Hawaii International Conference on System Sciences (HICSS'07)*, (2007), 103-113. doi: 10.1109/HICSS.2007.500

121. Fang, Y.-P., Pedroni, N. and Zio, E., "Resilience-based component importance measures for critical infrastructure network systems", ***IEEE Transactions on Reliability***, Vol. 65, No. 2, (2016), 502-512. doi: 10.1109/TR.2016.2521761

122. Wang,Y., Zhao, S., Zhou, Z., Botterud, A., Xu, Y. and Chen R., "Risk adjustable day-ahead unit commitment with wind power based on chance constrained goal programming", ***IEEE Transactions on Sustainable Energy***, Vol. 8, No. 2, (2016), 530-541. doi: 10.1109/TSTE.2016.2608841

123. Teymouri, F., Amraee, T., Saberi, H. and Capitanescu, F., "Toward controlled islanding for enhancing power grid resilience considering frequency stability constraints", ***IEEE Transactions on Smart Grid***, Vol. 10, No. 2, (2017), 1735-1746. doi: 10.1109/TSG.2017.2777142

124. Baringo, L. and Conejo, A. J., "Wind power investment: A Benders decomposition approach", ***IEEE Transactions on Power Systems***, Vol. 27, No. 1, (2011), 433-441. doi: 10.1109/TPWRS.2011.2167764

125. Gil, E., Aravena, I. and Cárdenas, R., "Generation capacity expansion planning under hydro uncertainty using stochastic mixed integer programming and scenario reduction", ***IEEE Transactions on Power Systems***, Vol. 30, No. 4, (2014), 1838-1847. doi: 10.1109/TPWRS.2014.2351374

126. Jin, S., Botterud, A. and Ryan, S. M., "Temporal versus stochastic granularity in thermal generation capacity planning with wind power", ***IEEE Transactions on Power Systems***, Vol. 29, No. 5, (2014), 2033-2041. doi: 10.1109/TPWRS.2014.2299760

127. Johnston, J., Henriquez-Auba, R., Maluenda, B. and Fripp, M., "Switch 0.2: a modern platform for planning high-renewable power systems", ***SoftwareX***, Vol. 10, (2019). doi: 10.1016/j.softx.2019.100251

128. Chen, Q., Kang, C., Xia, Q. and Zhong, J., "Power generation expansion planning model towards low-carbon economy and its application in China", ***IEEE Transactions on Power Systems***, Vol. 25, No. 2, (2010), 1117-1125. doi: 10.1109/TPWRS.2009.2036925

129. Hu, Q., Huang, G., Cai, Y. and Huang, Y., "Feasibility-based inexact fuzzy programming for electric power generation systems planning under dual uncertainties", ***Applied Energy***, Vol. 88, No. 12, (2011), 4642-4654. doi: 10.1016/j.apenergy.2011.06.004

130. Pereira, A. J. and Saraiva, J. T., "A decision support system for generation expansion planning in competitive electricity markets", ***Electric Power Systems Research***, Vol. 80, No. 7, (2010), 778-787. doi: 10.1016/j.epsr.2009.12.003

131. Dehghan, S., Kazemi, A. and Amjady, N., "Multi-objective robust transmission expansion planning using information-gap decision theory and augmented ε-constraint method", ***IET Generation, Transmission & Distribution***, Vol. 8, No. 5, (2014), 828-840. doi: 10.1049/iet-gtd.2013.0427

132. Ploussard, Q., Olmos, L. and Ramos, A., "A search space reduction method for transmission expansion planning using an iterative refinement of the DC load flow model", ***IEEE Transactions on Power Systems***, Vol. 35, No.1, (2019), 152-162. doi: 10.1109/TPWRS.2019.2930719

133. Lumbreras, S. and Ramos, A., "The new challenges to transmission expansion planning .Survey of recent practice and literature review", ***Electric Power Systems Research***, Vol. 134, (2016), 19-29 .doi: 10.1016/j.epsr.2015.10.013

134. Qiu,T., Xu, B., Wang, Y., Dvorkin, Y. and Kirschen, D. S., "Stochastic multistage coplanning of transmission expansion and energy storage", ***IEEE Transactions on Power Systems***, Vol. 32, No. 1, (2016), 643-651. doi: 10.1109/TPWRS.2016.2553678

135. Dehghan, S. and Amjady, N., "Robust transmission and energy storage expansion planning in wind farm-integrated power systems considering transmission switching", ***IEEE Transactions on Sustainable Energy***, Vol. 7, No. 2, (2015), 765-774. doi: 10.1109/TSTE.2015.2497336

136. Conejo, A. J., Cheng, Y., Zhang, N. and Kang, C., "Long-term coordination of transmission and storage to integrate wind power", ***CSEE Journal of Power and Energy Systems***, Vol. 3, No. 1, (2017), 36-43. doi: 10.17775/CSEEJPES.2017.0006

137. Zhang, X. and Conejo, A. J., "Coordinated investment in transmission and storage systems representing long-and short-term uncertainty", ***IEEE Transactions on Power Systems***, Vol. 33, No. 6, (2018), 7143-7151. doi: 10.1109/TPWRS.2018.2842045

138. Moreira, A., Street, A. and Arroyo, J. M., "An adjustable robust optimization approach for contingency-constrained transmission expansion planning", ***IEEE Transactions on Power Systems***, Vol. 30, No. 4, (2014), 2013-2022. doi: 10.1109/TPWRS.2014.2349031

139. Chen, B., Wang, J., Wang, L., He, Y. and Wang, Z., "Robust optimization for transmission expansion planning: Minimax cost vs. minimax regret", ***IEEE Transactions on Power Systems***, Vol. 29, No. 6, (2014), 3069-3077. doi: 10.1109/TPWRS.2014.2313841

140. Ruiz, C. and Conejo, A. J., "Robust transmission expansion planning", ***European Journal of Operational Research***, Vol. 242, No. 2, (2015), 390-401. doi: 10.1016/j.ejor.2014.10.030

141. Chen, B. and Wang, L., "Robust transmission planning under uncertain generation investment and retirement", ***IEEE Transactions on Power Systems***, Vol. 31, No. 6, (2016), 5144-5152. doi: 10.1109/TPWRS.2016.2538960

142. Mínguez, R. and García-Bertrand, R., "Robust transmission network expansion planning in energy systems: Improving computational performance", ***European Journal of Operational Research***, Vol. 248, No. 1, (2016), 21-32. doi: 10.1016/j.ejor.2015.06.068

143. Jabr, R. A., "Robust transmission network expansion planning with uncertain renewable generation and loads", ***IEEE Transactions on Power Systems***, Vol. 28, No. 4, (2013), 4558-4567. doi: 10.1109/TPWRS.2013.2267058

144. Akbari, T., Heidarizadeh, M., Siab, M. A. and Abroshan, M., "Towards integrated planning: Simultaneous transmission and substation expansion planning", ***Electric Power Systems Research***, Vol. 86, (2012), 131-139. doi: 10.1016/j.epsr.2011.12.012

145. Buygi, M. O., Shanechi, H. M., Balzer, G., Shahidehpour, M. and Pariz, N., "Network planning in unbundled power systems", ***IEEE Transactions on Power Systems***, Vol. 21, No. 3, (2006), 1379-1387. doi: 10.1109/TPWRS.2006.873016

146. Yu, H., Chung, C., Wong, K. and Zhang, J., "A chance constrained transmission network expansion planning method with consideration of load and wind farm uncertainties", ***IEEE***

Transactions on Power Systems, Vol. 24, No. 3, (2009), 1568-1576. doi: 10.1109/TPWRS.2009.2021202

147. Braga, A. S. D. and Saraiva, J. T., "A multiyear dynamic approach for transmission expansion planning and long-term marginal costs computation", ***IEEE Transactions on Power Systems***, Vol. 20, No. 3, (2005), 1631-1639. doi: 10.1109/TPWRS.2005.852121
148. Zhao, J. H., Foster, J., Dong, Z. Y. and Wong, K. P., "Flexible transmission network planning considering distributed generation impacts", ***IEEE Transactions on Power Systems***, Vol. 26, No.3, (2010), 1434-1443. doi: 10.1109/TPWRS.2010.2089994
149. Fang,Y., Pedroni, N. and Zio, E., "Optimization of cascade-resilient electrical infrastructures and its validation by power flow modeling", ***Risk Analysis***, Vol. 35, No. 4, (2015), 594-607. doi: 10.1111/risa.12396
150. Choobineh, M., Ansari, B. and Mohagheghi, S., "Vulnerability assessment of the power grid against progressing wildfires", ***Fire Safety Journal***, Vol. 73, (2015), 20-28. doi: 10.1016/j.firesaf.2015.02.006
151. Faghih, A. and Dahleh, M. A., "On Enhancing Resilience to Cascading Failures via Post-Disturbance Tweaking of Line Reactances", **IEEE *Transactions on Power Systems***, Vol. 34, No. 6, (2019), 4921-4930. doi: 10.1109/TPWRS.2019.2922288
152. Romero, N., Xu, N., Nozick, L. K., Dobson, I. and Jones, D., "Investment planning for electric power systems under terrorist threat", ***IEEE Transactions on Power Systems***, Vol. 27, No. 1, (2011), 108-116. doi: 10.1109/TPWRS.2011.2159138
153. Panteli, M., Mancarella, P., Wilkinson, S., Dawson, R. and Pickering, C., "Assessment of the resilience of transmission networks to extreme wind events", in 2015 IEEE Eindhoven PowerTech, (2015), 1-6. doi: 10.1109/PTC.2015.7232484
154. Arroyo, J. M. and Galiana, F. D., "On the solution of the bilevel programming formulation of the terrorist threat problem", ***IEEE transactions on Power Systems***, Vol. 20, No. 2, (2005),789-797. doi: 10.1109/TPWRS.2005.846198
155. Motto, A. L., Arroyo, J. M. and Galiana, F. D., "A mixed-integer LP procedure for the analysis of electric grid security under disruptive threat", ***IEEE Transactions on Power Systems***, Vol. 20, No. 3, (2005), 1357-1365. doi: 10.1109/TPWRS.2005.851942
156. Motamedi, A., Zareipour, H., Buygi, M. O. and Rosehart, W. D., "A transmission planning framework considering future generation expansions in electricity markets", ***IEEE Transactions on Power Systems***, Vol. 25, No. 4, (2010), 1987-1995. doi: 10.1109/TPWRS.2010.2046684
157. Tekiner, H., Coit, D. W. and Felder, F. A., "Multi-period multi-objective electricity generation expansion planning problem with Monte-Carlo simulation", ***Electric Power Systems Research***, Vol. 80, No. 12, (2010), 1394-1405. doi: 10.1016/j.epsr.2010.05.007
158. Javadi, M. S. and Esmaeel Nezhad, A., "Multi-objective, multi-year dynamic generation and transmission expansion planning-renewable energy sources integration for Iran's National Power Grid", ***International Transactions on Electrical Energy Systems***, Vol. 29, No. 4, (2019). doi: 10.1002/etep.2810
159. Jenabi ,M., Ghomi, S. M. T. F. and Smeers, Y., "Bi-level game approaches for coordination of generation and transmission expansion planning within a market environment", ***IEEE Transactions on Power systems***, Vol. 28, No. 3, (2013), 2639-2650. doi: 10.1109/TPWRS.2012.2236110
160. Mavalizadeh, H., Ahmadi, A. and Heidari, A., "Probabilistic multi-objective generation and transmission expansion planning problem using normal boundary intersection", ***IET Generation, Transmission & Distribution***, Vol. 9, No. 6, (2014), 560-570. doi: 10.1049/iet-gtd.2014.0278
161. Guerra, O. J., Tejada, D. A. and Reklaitis, G. V., "An optimization framework for the integrated planning of generation and transmission expansion in interconnected power systems", ***Applied Energy***, Vol. 170, (2016), 1-21. doi: 10.1016/j.apenergy.2016.02.014
162. Zhang, N., Hu, Z., Shen, B., Dang, S., Zhang, J. and Zhou,Y., "A source–grid–load coordinated power planning model considering the integration of wind power generation", ***Applied Energy***, Vol. 168, (2016), 13-24. doi: 10.1016/j.apenergy.2016.01.086
163. Hu, Y., Bie, Z., Ding, T. and Lin, Y., "An NSGA-II based multi-objective optimization for combined gas and electricity network expansion planning", ***Applied Energy***, Vol. 167, (2016), 280-293. doi: 10.1016/j.apenergy.2015.10.148
164. Muñoz-Delgado, G., Contreras, J. and Arroyo, J. M., "Multistage generation and network expansion planning in distribution systems considering uncertainty and reliability", ***IEEE Transactions on Power Systems***, Vol. 31, No. 5, (2015), 3715-3728. doi: 10.1109/TPWRS.2015.2503604
165. Baringo L. and Baringo, A., "A stochastic adaptive robust optimization approach for the generation and transmission expansion planning", ***IEEE Transactions on Power Systems***, Vol. 33, No. 1, (2017), 792-802. doi: 10.1109/TPWRS.2017.2713486
166. Unsihuay-Vila, C., Marangon-Lima, J. W., De Souza, A. Z., Perez-Arriaga, I. J. and Balestrassi, P. P., "A model to long-term, multiarea, multistage, and integrated expansion planning of electricity and natural gas systems", ***IEEE Transactions on Power Systems***, Vol. 25, No. 2, (2010), 1154-1168. doi: 10.1109/TPWRS.2009.2036797
167. Alizadeh, B. and Jadid, S., "A dynamic model for coordination of generation and transmission expansion planning in power systems", ***International Journal of Electrical Power & Energy Systems***, Vol. 65, (2015), 408-418. doi: 10.1016/j.ijepes.2014.10.007
168. Alizadeh, B. and Jadid, S., "Reliability constrained coordination of generation and transmission expansion planning in power systems using mixed integer programming", ***IET Generation, Transmission & Distribution***, Vol. 5 , No. 9, (2011), 948-960. doi: 10.1049/iet-gtd.2011.0122
169. Khodaei, A. and Shahidehpour, M., "Microgrid-based co-optimization of generation and transmission planning in power systems", ***IEEE Transactions on Power Systems***, Vol. 28, No. 2, (2012), 1582-1590. doi: 10.1109/TPWRS.2012.2224676
170. Romero, N. R., Nozick, L. K., Dobson, I. D., Xu, N. and Jones, D. A., "Transmission and generation expansion to mitigate seismic risk", ***IEEE Transactions on Power Systems***, Vol. 28, No. 4, (2013), 3692-3701. doi: 10.1109/TPWRS.2013.2265853
171. Carrión, M., Arroyo, J. M. and Alguacil, N., "Vulnerability-constrained transmission expansion planning: A stochastic programming approach", ***IEEE Transactions on Power Systems***, Vol. 22, No. 4, (2007), 1436-1445. doi: 10.1109/TPWRS.2007.907139
172. Nemati, H., Latify, M. A. and Yousefi, G. R., "Coordinated generation and transmission expansion planning for a power system under physical deliberate attacks", ***International Journal of Electrical Power & Energy Systems***, Vol. 96, (2018), 208-221. doi: 10.1016/j.ijepes.2017.09.031
173. Vaziri, P., Davidson, R., Apivatanagul, P. and Nozick, L., "Identification of optimization-based probabilistic earthquake scenarios for regional loss estimation", ***Journal of Earthquake Engineering***, Vol. 16, No. 2, (2012), 296-315. doi: 10.1080/13632469.2011.597486
174. Çağnan, Z., Davidson, R. A. and Guikema, S. D., "Post-earthquake restoration planning for Los Angeles electric power", ***Earthquake Spectra***, Vol. 22, No. 3, (2006), 589-608. doi: 10.1193/1.2222400
175. Shivaie, M., Kiani-Moghaddam, M. and Weinsier, P. D., "A vulnerability-constrained quad-level model for coordination of

generation and transmission expansion planning under seismic- and terrorist-induced events", ***International Journal of Electrical Power & Energy Systems***, Vol. 120, (2020). doi: 10.1016/j.ijepes.2020.105958

176. Cervigni, R., Liden, R., Neumann, J. E. and Strzepek, K. M., "Enhancing the climate resilience of Africa's infrastructure: the power and water sectors", (2015).
177. Jayadev, G., Leibowicz, B. D. and Kutanoglu, E., "US electricity infrastructure of the future: Generation and transmission pathways through 2050", ***Applied Energy***, Vol. 260, (2020). doi: 10.1016/j.apenergy.2019.114267
178. Rezaei, M., Askari, M. T., Amirahmadi, M. and Ghods, V., "Dynamic Multi-Level Generation and Transmission Expansion Planning Model of Multi-Carrier Energy System to Improve Resilience of Power System", ***Journal of Industrial Electronics Control and Optimization***, (2023). doi: 10.22111/ieco.2023.42385.1428
179. Askari, M. T., Ab Kadir, M. Z. A., Hizam, H. and Jasni, J., "A new comprehensive model to simulate the restructured power market for seasonal price signals by considering on the wind resources", ***Journal of Renewable and Sustainable Energy 6***, No. 2, (2014). doi: 10.1063/1.4869141
180. Askari, M. T., Ab Kadir, M. Z. A., Tahmasebi, M. and Bolandifar, E., "Modeling optimal long-term investment strategies of hybrid wind-thermal companies in restructured power market", ***Journal of Modern Power Systems and Clean Energy 7***, No. 5, (2019), 1267-1279. doi: 10.1007/s40565-019-0505-x
181. Hosseini Mola, J., Barforoshi, T. and Adabi Firouzjaee, J., "Distributed generation expansion planning considering load growth uncertainty: A novel multi-period stochastic model", ***International Journal of Engineering, Transactions C: Aspects***, Vol.31, No. 3, (2018), 405-414. doi: 10.5829/ije.2018.31.03c.02

Persian Abstract

چکیده

از آنجایی که سیستم‌های قدرت در معرض آسیب‌های ناشی از حوادث فاجعه‌بار هستند، ارزیابی و بهبود تاب آوری سیستم به عنوان یک هدف جدید برنامه‌ریزی و عملیات اجتناب‌ناپذیر است. از سوی دیگر، توسعه شبکه‌های تولید و انتقال، بخش مهمی از برنامه‌ریزی سیستم قدرت را تشکیل می‌دهد، زیرا نیاز به بودجه هنگفتی دارد. بنابراین، یکی از دغدغه های اصلی محققان همواره برنامه ریزی بهینه سیستم های قدرت بوده است. این مقاله به بررسی مفهوم نوظهور تاب‌آوری، معیارها و شاخص‌های آن، نحوه ارتقای آن و شناسایی نقاط قوت و ضعف آن می‌پردازد. همچنین استراتژی های توصیه شده در مطالعات برای بهبود تاب آوری سیستم قدرت را بررسی می کند. این مقاله به طور خلاصه مدل‌های تحلیل طرح توسعه و ابزارهای برنامه‌ریزی توسعه تولید و انتقال را با یا بدون هدف تقویت تاب آوری گزارش می‌کند، که می‌تواند در تحقیقات آینده ابزاری باشد و جهت تخمین اثربخشی ابزارهای مختلف استفاده شود. علاوه بر این، این مقاله مشکلات برنامه ریزی را مورد بحث قرار می دهد و در نتیجه راه را برای کار بیشتر در مطالعات آینده باز می کند. در نهایت، این مقاله مهم‌ترین چالش‌های برنامه‌ریزی توسعه تولید و انتقال را برای انجام برنامه‌های بهتر، تاب آور و نوآورانه جهت تقویت تاب آوری سیستم قدرت ارائه می‌کند.

IJE TRANSACTIONS B: Applications Vol. 36, No. 05, (May 2023) 842-857

International Journal of Engineering

Journal Homepage: www.ije.ir

Market-based Real Time Congestion Management in a Smart Grid Considering Reconfiguration and Switching Cost

I. Ehsani, M. Amirahmadi*, M. Tolou-Askari, V. Ghods

Department of Electrical and Electronic Engineering, Semnan Branch, Islamic Azad University, Semnan, Iran

P A P E R I N F O

Paper history:
Received 21 September 2022
Received in revised form 18 December 2022
Accepted 22 February 2023

Keywords:
Microgrid
Smart Grid
Real-Time Congestion Management
Generation Rescheduling
Soccer League Algorithm

A B S T R A C T

Network Real-Time Congestion (RTC) is a bottleneck that limits energy transfer from the generation units or up-grid to the loads. Some factors, such as intermittent generation of renewable resources and forced outages of generating units and load forecasting errors, can lead to Real-Time Congestion Management (RTCM) in a smart grid network. RTCM is a set of methods to eliminate congestion in real-time. To implement RTCM, some approaches can be employed, including network reconfiguration by Remote Control Switches (RCS), load shedding generation and up-grid power rescheduling. In this paper, a two-stage programming model is proposed to find the optimal solution for RTCM using the integration of reconfiguration and market-based approaches. Therefore, following the occurrence of congestion, at the first stage, microgrid central controller (MGCC) or central energy manager implements reconfiguration as the lowest-cost approach to mitigating RTC. The Soccer League (SL) algorithm is employed at the first stage to find the optimal network topology. Subsequently, based on the results obtained from the first stage, a programming model is applied at the second stage to completely eliminate the RTC. The proposed model minimizes a weighted objective function that includes the generation and up-grid rescheduling cost, load shedding cost, switching cost, and congestion clearing time. In order to model switching costs, a new index is defined to prevent risky switching and the depreciation caused by frequent switching. This index is determined based on the critical locations in the network and the age of RCSs. The numerical results demonstrate the efficacy of the proposed model.

doi: *10.5829/ije.2023.36.05b.02*

NOMENCLATURE

$Bid_{g,t}^{Real-time}$	Bid of the *g*th generator at time t	$Bid_{L,t}^{Rael-time}$	Bid of the *L*th load at time t
$F_t^{penalty}$	The product of $f_{l,t}^{penalty}$	$\pi_{p,t}$	Cost of the *p*th switch action at time t
N_L^{Resch}	Number of the participated loads in CM	$\boldsymbol{SeP_l^{WM}}$	Line active power flow sensitivity with respect to the up-grid active power
N_g^{Resch}	Number of the participated generators in CM.	$\boldsymbol{SeP_l^L}$	Line active power flow sensitivity with respect to active power load
$N_{p,max}^{sw}$	Maximum allowable number of switching actions for RCS *p* per day.	$\boldsymbol{w_t}$	Congestion clearing time weighting factor
P_{WM}^0	Initial value of active power flow of the wholesale market	Q_g^0	Initial value of reactive power flow of the *g*th generator
Q_{WM}^0	Initial value of reactive power flow of the wholesale market	P_{WM}^{max}	Maximum allowable active power purchased from wholesale market
$\boldsymbol{E_p^{dis}}.\boldsymbol{E_p^{age}}$	Distance index, age index	P_g^0	Initial value of active power flow of the *g*th generator
$\boldsymbol{E_p^{sw}}$	Switching index	$\boldsymbol{s_{p,t}}$	Status of RCS *p* at time *t* (1: when the related RCS is opened, and 0: otherwise).
$\boldsymbol{F_l^{max}}$	Maximum apparent flow of the *l*th line (MVA).	$\boldsymbol{f_{l,t}^{penalty}}$	Thermal rate penalty function of the *lth* line at time *t*
$\boldsymbol{I_{E,t}^{max}}$	Emergency-tern thermal rate	$\boldsymbol{t_{clear}}$	Congestion clearing time
$\boldsymbol{I_{L,t}^{max}}$	Long-tern thermal rate	$\boldsymbol{C_L(\Delta P_L)}$	Cost of change in active power of the *L*th load
$\boldsymbol{I_{s,t}^{max}}$	Short-tern thermal rate	$\boldsymbol{C_g(\Delta P_g)}$	Cost of change in active power of the *g*th generator

Corresponding Author Institutional Email:
m.amirahmadi@semnaniau.ac.ir (M. Amirahmadi)

Please cite this article as: I. Ehsani, M. Amirahmadi, M. Tolou-Askari, V. Ghods, Market-based Real Time Congestion Management in a Smart Grid Considering Reconfiguration and Switching Cost, ***International Journal of Engineering, Transactions B: Applications***, Vol. 36, No. 05, (2023) 842-857

N_l	Number of branches
N_p	Number of RCSs
P_L^{max}	Maximum allowed active power consumed by the *L*th load (MW).
P_L^{min}	Minimum allowed active power consumed by the *L*th load (MW).
P_{WM}^{min}	Minimum allowable active power purchased from wholesale market
P_g^{max}	Maximum allowed active power generation of the *g*th generator (MW).
P_g^{min}	Minimum allowed active power generation of the *g*th generator (kW).
Q_{WM}^{max}	Maximum allowable reactive power purchased from wholesale market
Q_{WM}^{min}	Minimum allowable reactive power purchased from the wholesale market
Q_g^{max}	Maximum allowed reactive power generation of the *g*th generator (kVar).
Q_g^{min}	Minimum allowed reactive power generation of the *g*th generator (kVar).
R_g^{Down}	Ramp down rate of the *g*th generator (kW/h).
R_g^{up}	Ramp up rate of the *g*th generator (kW/h).
$t_{clear,E}^{max}$	Maximum Emergency-tern clearing time
$t_{clear,L}^{max}$	Maximum Long-tern clearing time
$t_{clear,s}^{max}$	Maximum Short-tern clearing time
D	Set of scenarios that guarantee the radial topology of the network
L	Index of load
g	Index of DGs
k	Number of scenarios that guarantee the radial topology of the network
l	Index of branches
m	Index of PVs
n	Index of WTs
p	Index of switch
t	Index of hour
ΔP_g	Change in active power of the *g*th generator (kW).
$C_{WM}(\Delta P_{WM})$	Cost of change in purchased active power from the wholesale market
SeQ_l^L	Line reactive power flow sensitivity with respect to reactive power load
SeQ_l^{WM}	Line reactive power flow sensitivity with respect to the up-grid reactive power
Q_l	Reactive power flow of the *l*th line (kVar).
P_l	Active power flow of the *l*th line(kW).
ΔP_l	Variation in active power flow in the *l*th line (kW)
t_{recon}	Reconfiguration Times
t_{est}	Estimated time to solve reconfiguration equation
Q_l^0	Initial value of reactive power flow of the *l*th line (kVar).
P_l^0	Initial value of active power flow of the *l*th line(kW)
$t_{clear,Resch}$	Rescheduling Time
ΔQ_l	Variation in reactive power flow in the *l*th line (kVar)
t_{clear}^{max}	Maximum allowed time for congestion clearing time
$s_{p,t,recon}$	Status of RCS *p*th at time t after reconfiguration
w_k	Switch action weighting factor
w_f	Thermal-Rate weighting factor
w_c	Congestion management cost weighting factor.
SeP_l^g	Line active power flow sensitivity with respect to the generator active power
ΔP_L	Change in the active power of the *L*th load (kW).
ΔQ_L	Change in reactive power of the *L*th load (kVar).
SeQ_l^g	Line reactive power flow sensitivity with respect to generator reactive power
ΔQ_g	Change in reactive power of the *g*th generator (kVar).
ΔQ_{WM}	Change in reactive power of up-grid (kVar).
ΔP_{WM}	Change in the active power of up-grid (kW).
$P_{L,t}$	Total power demand *L*th load at time *t* (kW)

1. INTRODUCTION

Microgrid congestion is a bottleneck that limits energy transferring from the generation units or up-grid to the loads. It occurs when the transmission line cannot be operated in a specific configuration of generation and consumption [1, 2]. More attention on renewable units and increasing connections between them for supplying power raise the probability of congestion resulting from forecasting errors [3]. Therefore, it is necessary to use an efficient method for solving this problem [4]. Generally, there are two main procedures for Congestion Management (CM), the first being the pre-real time by system operator almost performed by motivational methods. Wu and Oren [5], O'Connell et al. [6] and Verzijlbergh et al. [7] proposed the dynamic tariff method. Huang and Wu [8] suggested the dynamic subside method by modifying the drawbacks of the dynamic tariff method. Andersen et al. [9], Hu et al. [10] proposed the capacity market, and Zhang et al. [11] have proposed the ancillary services market to solve the pre-real time congestion problem. All the mentioned proposals are based on giving financial incentives to consumers for shifting their consumption to other less congested hours [12]. In fact, these methods determine rewards to flexible demand for shifting their consumption to confront probable congestion [13]. The second process of CM is called RTCM which includes methods to remove the congestion-inducing RT by forecasting error, contingences and cascading failure. The proposed methods are based on motivation and reconfiguration. Biegel et al. [3], Huang and Wu [3, 14] suggested the motivation method by making a real-time market that acts based on flexible load shifts. Another research proposed a reconfiguration method and reactive power control method for RTCM [15]. Viawan and Karlsson [16], Ramesh and Ranjith Babu [17] reported that congestion is managed by reactive power control such as the operation of transformer taps, Flexible Alternating Current Transmission System

(FACTS) devices, or phase shifters. Generally, in research that has used the reactive power control methods for RTCM, voltage constraints take precedence over thermal constraints, as a voltage problem is more critical than a thermal problem while ignoring thermal problems can cause irreparable damage to the system. Another method for RTCM is through network reconfiguration [18]. Huang et al. [19] provided a prioritization based on congestion management costs, and according to this prioritization, free (or almost free) reconfiguration methods are preferred to CM because of lower defined DR cost and development investment.

Microgrid networks are designed in the form of a ring to have appropriate reliability but are operated in the form of a radius to maintain the voltage and balance of the system [20]. With the advancement in technology and communication and power system monitoring in smart distribution networks, the option of using RCSs to reduce the cost of losses was proposed. In this respect, several investigators [21-27] have tried to solve this optimization problem by different methods. Some studies have proposed genetic algorithms to solve this problem. Later, researchers thought of using RCSs to solve the congestion problem [28], but optimization for this purpose is an integer nonlinear optimization problem that is generally hard to solve. There are many methods to solve this problem; for instance, Franco et al. [29] recommended Mix Integer Linear Programing (MILP), Abur [30] suggested Linear Programing (LP), Baran and Wu [31] focussed on forward None Linear Programing (NLP) that has started from one executable point and moved to the next point, which has reduced the cost function more than the previous one (by changing only one pair of switches). Notably, in these methods, the global minimum points may not be found. Enacheanu et al. [32] suggested Genetic Algorithm (GA) to solve this optimization problem by the nonlinear integer latency problem and the tendency to reach a general minimum. However, due to the nature of these methods, there is no guarantee to determine the overall optimal point [33].

To summarize the reviewed studies, the following research gaps can be classified:

• A few studies have analyzed the congestion problem for transmission networks, while there are some differences between congestion problems in distribution networks and transmission networks. One difference is that, unlike the distribution network, transmission systems aren't operated radially. The other difference is that –considering deregulation in the power system –in transmission network, the congestion management is considered an economical issue while in the distribution network, it is regarded as a technical problem. Moreover, generally, RTCM is considered in the N−1 security level in a transmission network. However, in distribution systems, it is commonly not required to take this level of security into account. However, solving the congestion problem for the distribution network seems to be a greater challenge.

•Some studies have tried to solve the congestion problem pre-real time, while the congestion problem in a real-time is a greater challenge for distribution system operators.

•Some papers have proposed RTCM based on the network reconfiguration model, but the main problem in all of these methods proposed is that they may not solve the congestion problem due to poor network infrastructure or compression congestion.

•Another drawback of the literature review on the reconfiguration method is the lack of due attention to this subject. In this regard, some RCSs are located in critical branches of the microgrid system and changing their status in short-term scheduling will cause intolerable disturbances or significant loss of power which are not desirable for MGO.

•Some papers have proposed RTCM based on the market-based model, which is an expensive solution.

• There is an evident lack of a suitable model in most studies to optimize important objective functions simultaneously.

Table 1 provides a comparison of contributions offered by the proposed model with models studied in the literature.

In this paper, a 2-stage optimization problem is defined to reduce microgrid costs while solving congestion problems. The output is the RCSs situation, rate of load shedding for each curtailable load, rate of generation rescheduling, the range changes of the purchase from the wholesale market, and finally reaching the optimal point. To achieve this purpose, congestion is divided into three types, each solved based on the predicted scenarios. The solution to this problem is based on the integration of a reconfiguration method with load shedding, generation rescheduling and purchased changes. The integration of these two independent methods can solve a wide range of congestion problems with any intensity and under any type of network infrastructure to ultimately reach an

TABLE 1. Comparison between the proposed model and similar researches

Ref.	Distribution	Real-Time	Market-base	Reconfiguration	Switch cost
[5-12]	✓		✓		
[3, 14]	✓	✓	✓		
[15-17]	✓	✓			
[28-32]	✓	✓		✓	
[34]		✓	✓		
Proposed method	✓	✓	✓	✓	✓

optimal point in the optimization problem. Importantly, unlike previous methods, in this method, all possible scenarios are inspected and the most optimal solution is selected. Moreover, a new switching index based on the critical locations in the network and switch ages is defined to assign allowable RCS actions for each.

Given the previous analysis, the main contributions of this paper are as follows:

1) Integrating the reconfiguration method with the market-based method to solve the congestion problem.
2) Minimizing the elimination cost of RTC in a microgrid using a new approach
3) Proposing a new index for switching action based on switch ages and critical locations to maintain the reliability of the RCS switching procedure.

The rest of this paper is organized as follows: Section 2 deals with the problem and problem formulation; in section 3 the proposed algorithm is discussed; numerical results and discussions on a test system are dealt with in section 4; and finally in section 5, conclusions are presented.

2. MODELLING

2. 1. Problem Discussion In this paper, the congestion problem is solved in real time and the corrections are performed in real time, too. RTCM is proposed because we have a day-ahead planning and a series of forecasting errors is likely to occur in this planning, which causes real-time congestion. For this purpose, we assume that based on load forecasting and switch index, the amount of generation scheduling, consumption scheduling, purchasing from the wholesale market, and situation of RCSs considering switch constraints are determined for the next 24 hours in a day-ahead manner. In the next step based on literature [35], the thermal rate is obtained which is a defined amount of current that flows in the line and induces the maximum allowed temperature in the conductor. Also, based on its intensity, it is divided into three categories: short-term, long-term and emergency time, considering the thermal rate in the three mentioned categories. Then, the real-time load, generation and switch situation are considered based on real data. Afterward, the system is managed based on a 2-stage optimization problem when faced with congestion caused by overload, generator outages, and changes in weather conditions in real time. Loads and generation variations during the RTCM process are taken into account by classifying the clearing time into subsequent subintervals. The proposed RTCM in this paper is performed in two stages. The first stage is network reconfiguration based on minimizing the load of the congested line which is solved by the Soccer league algorithm considering minimizing switch cost. In the second stage, an optimization problem is proposed to plan the changing of the pattern of generation, consumption and purchase from the wholesale market to minimize the cost of RTCM based on the generator bid strategy, power price in the wholesale market, and load shedding cost at cleaning time. This problem is solved by defining the sensitivity coefficient of each line for a change in the generation of each generator, load of each consumption, and purchase from the wholesale market. In this model, the cleaning time is obtained by thermal rates and the problem solution is solved according to the cleaning time and the generators as well as the ramp rate and down rate of loads.

2. 2. Problem Formulation In this section, a 2-stage optimization problem is proposed in accordance with the switching cost for the RTCM based on the network reconfiguration in the first step. Also, in the second step, it is proposed for changing the pattern of generation, consumption, and purchase from the wholesale market. The purpose of this optimization problem is to solve the real-time congestion problem in the shortest time and by the lowest possible cost. At all times, the conductor currents in all microgrid lines must be lower than the thermal rates obtained by the multi-level method to determine the allowable current of the lines in the short-, long- and emergency term. Otherwise, the proposed model in this paper solves real-time congestion, depending on the type of congestion, before the end of clearing time. Therefore, in times of potential congestion (short-term, long-term or emergency) according to the penalty coefficient, the main priority minimizes additional current on the congested lines by reconfiguration and, if necessary, by changing the pattern of generation, consumption and purchase from the wholesale market. Thus, if the current of the lines of the microgrid is less than the long-term thermal rate, the thermal limits are not violated because the lowest thermal rate is the long-term thermal rate.

$$I_{l,t} \le I_{L,t}^{max} \rightarrow safe\ mod \tag{1}$$

Otherwise, there are three cases where RTCM must be performed in each case according to the clearing time.

Emergency time congestion:

$$I_{l,t} \ge I_{E,t}^{max} \rightarrow t_{clear} \le t_{clear,E}^{max} = 5min \tag{2}$$

Short time congestion:

$$I_{s,t}^{max} \le I_{l,t} < I_{E,t}^{max} \rightarrow t_{clear} \le t_{clear,s}^{max} = 15min \tag{3}$$

Long time congestion:

$$I_{L,t}^{max} \le I_{l,t} < I_{s,t}^{max} \rightarrow t_{clear} \le t_{clear,l}^{max} = 2h \tag{4}$$

If any congestion is detected, the type is first determined, and then the clearance time is determined accordingly. This time is mentioned as the conductor

tolerance threshold for this overcurrent in the congested line. Therefore, before reaching this threshold, the congested line can withstand this overcurrent. Often for long-term congestion, without any action, the congestion problem is solved due to the passage of the peak time or the elimination of events without any action for network reconfiguration or changing the pattern of generation, consumption and purchase. So, basically, the occurrence of this type of congestion is not a difficult problem for microgrids. In this paper, the principle is to solve short-term and emergency-term congestion. Emergency and short-term congestions are managed by a two-stage optimization problem. This problem is solved through the soccer league algorithm to minimize overcurrent in the congested line by network reconfiguration in the first stage and determining the amount of change in generation, consumption and purchase pattern as decision variables in the second stage for minimizing the cost of RTCM.

2. 2. 1. The First Stage of RTCM Microgrids are designed in the form of a ring to enhance reliability but by putting RCSs, there are operated in the form of a radius. On the other hand, RCSs are used to improve system parameters such as power balancing and voltage profile [22]. The configuration of a microgrid should remain radial after the reconfiguration of operations. Thus, the main constraint in the use of RCSs is maintaining the radial structure of the network; to do so, the states of RCSs are arranged in a way that ultimately leads to maintaining the radial structure of the network. In this respect, first, all the different states of open or closed RCSs are examined. Then, based on the graph theory, all the scenarios that lead to the preservation of the radial structure of the network are collected in a set. Also, scenarios outside this set are not used in the algorithm, so a group of configuration scenarios that have a radial structure is collected in the following set, and scenarios outside this set are not used in the algorithm.

$$D = \{D(1), D(2), \ldots\ldots, D(k)\} \tag{5}$$

The thermal rate penalty function helps to select scenarios in which there are no congested lines in the network as the optimal scenario. In addition, as far as possible, scenarios with the lowest penalty coefficient should be determined. The amount of penalty coefficient for the thermal rate of lines, depending on types of congestion, is shown in Figure 1.

$$F_t^{penalty} = \prod_{l=1}^{N_l} f_{l,t}^{penalty} \tag{6}$$

After detecting a short-term or emergency-term congestion, the algorithm should change the status of RCSs to reduce the currents of the congested lines in such a way that, ideally, not only is the congestion eliminated ($F_t^{penalty}$=1) but also the winning scenario has the least RCSs change compared to the planned scenario for the desired time.

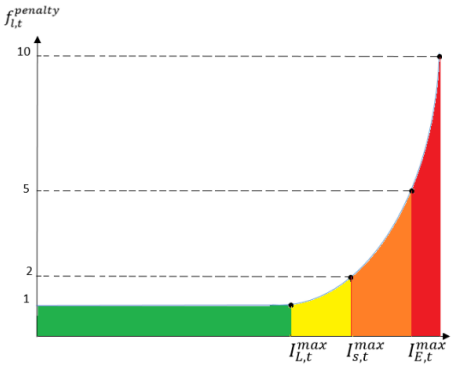

Figure 1. Amount of penalty coefficient for the thermal rate of lines

$$OF = Min\left[w_f\left(\prod_{l=1}^{N_l} f_{penalty,T}^{l}\right) + w_k\left(\sum_{p=1}^{N_p} \pi_{p,t}\left|N_{p,t}^{sw}\right|\right)\right] \quad \forall D(k) \in \{D\} \tag{7}$$

$$N_{p,t}^{sw} = s_{p,t} - s_{p,t-1} \tag{8}$$

Some of the RCSs are located in critical branches of the microgrid system and changing their status in short-term scheduling will cause intolerable disturbances or significant loss of power which are not desirable for MGO. Another scenario that prevents short-term reconfiguration is the RCS ages according to asset management monitoring data. To address these issues, a new index for switching action of each RCS is defined as follows:

$$E_p^{sw} = E_p^{dis}.E_p^{age} \tag{9}$$

$$E_p^{dis} = \begin{cases} 0 & Distance < a \\ \frac{distance-a}{b-a} & a \le dis \le b \\ 1 & Distance > b \end{cases} \tag{10}$$

$$E_p^{age} = \begin{cases} 1 & age < c \\ \frac{d-Age}{d-c} & c \le Age \le d \\ 0 & Age > d \end{cases} \tag{11}$$

$$N_{p,max}^{sw} = \lfloor E_{p,max}^{sw} N_{max} \rfloor \tag{12}$$

$N_{p,max}^{sw}$ is an integer value. N_{max} can be calculated by the expected lifetime of RCSs and the maximum number of switching in the lifetime. Considering an expected lifetime of 30 years for each RCS [36, 37], the possible maximum switching actions are computed as 12 times per day where ten operations are assumed for reconfiguration and two operations are devoted to fault detection, isolation and maintenance duties. The number of switching actions per day must be limited as follows:

$$N_{p,day}^{sw} \le N_{p,max}^{sw} \tag{13}$$

In this paper, according to the current generation, consumption and purchased scheduling, the scenario which has the lowest amount of thermal rate penalty function and the least change of RCSs, compared to the initial situation, is selected as the winning scenario (ideally, by changing a pair of switches, the thermal rate penalty function equals one). The difficulty of solving this optimization problem is to reach the global optimal solution. Therefore, the use of an algorithm with high-performance speed and accuracy and appropriate structure to solve this optimization problem seems necessary. For this purpose, the soccer league algorithm is proposed. The theory of this algorithm is comprehensively demonstrated by Moosavian and Roodsari [38]. In this section, while briefly explaining the rules of the algorithm, based on the existing conditions in this optimization problem, adaptation is carried out. The rules of this algorithm are based on soccer leagues and the principles of competition between teams (scenarios). Thus, the champion team of the league is selected as the preferred scenario. In this algorithm, each team participates in a k-1 match and (k * (k-1))/ 2 matches are held in one season, where *k* is the number of scenarios that maintained the radial structure of the microgrid. The teams get closer to the top of the league table with each win, but their position in the league table goes lower with each loss. There is a competition at the bottom of the league table at the end of the season. Here, the two last teams in the league are relegated (Falling points), and the two top teams in the second division (promotion points) will replace the relegated teams from the first division. In this special optimization problem, the second division league is designed to increase the speed of convergence so that weaker teams (scenarios) for different hours compete in parallel with the stronger teams (scenarios) in the first division league. The final position of each team is determined at the end of the competition based on their total score. Competition between teams is used to win the league championship, and internal competition of players is used to progress to converge to the global optimal point (to increase the speed of performance) which is mentioned in the algorithm by Imitation and Provocation.

One advantage of soccer league algorithm is using a combination of coarse and fine scale search processes. There is a rather similar process in the particle swarm optimization (PSO), but the soccer league algorithm uses different operators for evaluating the search space. On the other hand, PSO applies only one population while the soccer league uses several populations or teams in the searching process. In addition, the soccer league takes into account the best player of the league or superstar player (SSP), while all players should imitate him.

Based on the proposed method in this step, the scenario with the lowest amount of penalty function and the least change in the RCSs state, compared to the planned configuration, is selected as the reconfiguration scenario. In most cases, only by the reconfiguration method proposed in this step is the congestion problem managed, and this problem is completely solved ($F_t^{penalty}$=1). However, sometimes due to poor network infrastructure or intensity of congestion, free methods (reconfiguration) alone cannot solve real-time congestion problems in the microgrid. Therefore, it is necessary to integrate this method with market-based methods to have a principled RTCM. Under these conditions, first, the network configuration is changed based on the reduction of congested lines current and the winning scenario replaces the planned scenario. Then, if the congestion problem is not solved, the proposed method in the second step is employed to generate rescheduling, load shedding, and changing the pattern of purchase from the wholesale market to solve real-time congestion problems.

2. 2. 2. The Second Stage of RTCM In the second step, the line active and reactive power flow sensitivity for the generator, load and purchased active and reactive power, is initially calculated. Then, an optimization problem is proposed to solve the congestion problem in real time based on reducing the costs of RTCM by an optimal change in the pattern of generation, consumption and purchase from the wholesale market, as elaborated in this section. In this optimization problem, the congestion clearing time is determined according to the type of congestion, and the variation of the reactive power in the congested lines is considered. Furthermore, the downtime of Curtailable load and the ramp-down and ramp-up rates of the generating is taken into the RTCM problem. Therefore, in this proposed model, the operation conditions are considered more realistic than in other models. In addition, the multi-level thermal rate increases reliability and makes RTCM process more economical.

$$SeP_l^g = \frac{\Delta P_l}{\Delta P_g} \quad l = 1,2,\dots,N_l \quad g = 1,2,\dots,N_g^{Resch} \tag{14}$$

$$SeQ_l^g = \frac{\Delta Q_l}{\Delta Q_g} \quad l = 1,2,\dots,N_l \quad g = 1,2,\dots,N_g^{Resch} \tag{15}$$

$$SeP_l^L = \frac{\Delta P_l}{\Delta P_L} \quad l = 1,2,\dots,N_l \quad L = 1,2,\dots,N_L^{Resch} \tag{16}$$

$$SeQ_l^L = \frac{\Delta Q_l}{\Delta Q_L} \quad l = 1,2,\dots,N_l \quad L = 1,2,\dots,N_L^{Resch} \tag{17}$$

$$SeP_l^{WM} = \frac{\Delta P_l}{\Delta P_{WM}} \quad l = 1,2,\dots,N_l \tag{18}$$

$$SeQ_l^{WM} = \frac{\Delta Q_l}{\Delta Q_{WM}} \quad l = 1,2,\dots,N_l \tag{19}$$

These sensitivity factors are calculated in real time before beginning the optimization process, by Equations (14-19) with the proposed method by Esfahani and Yousefi [34], immediately after the occurrence of congestion and by the full Newton–Raphson method. Therefore, during the optimization process, power flow solutions are not required, which accelerated the solution of RTCM. The calculation method for obtaining these factors is based on power flow equations neglecting Q − ϑ and P − V coupling as described by Dutta and Singh [39].

Hence, the second step of RTCM can be formulated as follows:

$$min\left\{w_c\left(\sum_{g=1}^{N_g^{Resch}} C_g(\Delta P_g)+\sum_{L=1}^{N_L^{Resch}} C_L(\Delta P_L)+ C_{WM}(\Delta P_{WM})\right)+w_t.t_{clear,Resch}\right\} \quad (20)$$

This optimization problem is performed aimed at minimizing the RTCM costs and the congestion clearing time by considering generation rescheduling cost, load shedding cost, and cost of change in the purchased pattern.

Although minimizing the RTCM costs is the main goal of this problem, in emergency congestion occurrence, quick solution of this problem might be required. Thus, congestion-clearing time is added to the objective function of this optimization problem. Here, w_t and w_c are the weight factors which have different values depending on the intensity of congestion, and t_{clear}^{max} is defined as the maximum allowed time for congestion clearing time determined according to the worst condition of congested lines as formulated in Equations (22) and (23).

$$w_t = 20\max f_{l,t}^{penalty} \quad l = 1,2,\dots,N_l \quad (21)$$

$$t_c=\begin{cases} t_{clear,s}^{max} & if: \quad I_{s,t}^{max}\le I_{l,t}<I_{E,t}^{max} \\ t_{clear,E}^{max} & if: \quad I_{l,t}\ge I_{E,t}^{max}\end{cases} \quad \forall\, l\in congestion\ line \quad (22)$$

$$t_{clear}^{max} = \min t_c \quad (23)$$

The constraints of this optimization problem are formulated as follows:

$$t_{clear,Resch} \le t_{clear}^{max} - t_{recon} - t_{est} \quad (24)$$

$$P_l^2 + Q_l^2 \le (F_l^{max})^2 \quad (25)$$

$$(P_g^{min} - P_g^0) \le \Delta P_g \le (P_g^{max} - P_g^0) \quad (26)$$

$$(Q_g^{min} - Q_g^0) \le \Delta Q_g \le (Q_g^{max} - Q_g^0) \quad (27)$$

$$(10\times R_g^{Down}.t_{clear}^{max}) \le \Delta P_g \le (10\times R_g^{Down}.t_{clear}^{max}) \quad (28)$$

$$(P_{WM}^{min} - P_{WM}^0) \le \Delta P_{WM} \le (P_{WM}^{max} - P_{WM}^0) \quad (29)$$

$$(Q_{WM}^{min} - Q_{WM}^0) \le \Delta Q_{WM} \le (Q_{WM}^{max} - Q_{WM}^0) \quad (30)$$

$$P_L^{min} - P_L^{max} \le \Delta P_L \le 0 \quad (31)$$

$$\sum_{g=1}^{N_g^{Resch}}(\Delta P_g)+\sum_{L=1}^{N_L^{Resch}}(\Delta P_L)+\Delta P_{WM}=0 \quad (32)$$

Congestion clearing time is limited by Equation (24) in order to achieve a reliable answer. The line flow limit with regards to load shedding, generation rescheduling and changes of purchase from the wholesale market is shown in Equation (25). The allowed changes in generators' active and reactive power are determined by Equations (26) and (27) respectively. However, in Equation (28), acceptable variation in the active power of generators is represented according to t_{clear}^{max} and their ramp rates. Allowed changes of purchased active and reactive power from the wholesale market are determined by Equations (29) and (30), respectively. Load variation constraints are presented in Equation (31). Also, the power balance according to changes in active power at the slack bus is addressed in Equation (32).

The cost of load shedding and generation rescheduling are calculated below:

$$C_g(\Delta P_g) = Bid_{g,t}^{Real-time}\times(\Delta P_{g,t}) \quad g = 1,2,\dots,N_g^{Resch} \quad (33)$$

$$C_L(\Delta P_L) = Bid_{L,t}^{Rael-time}\times(\Delta P_{L,t}) \quad L = 1,2,\dots,N_L^{Resch} \quad (34)$$

where:

$$P_l = P_l^0 + \sum_{g=1}^{N_g^{Resch}}(\Delta P_g.SeP_l^g)+\sum_{L=1}^{N_L^{Resch}}(\Delta P_L.SeP_l^L)+SeP_l^{WM}.\Delta P_{WM} \quad (35)$$

$$Q_l = Q_l^0 + \sum_{g=1}^{N_g^{Resch}}(\Delta Q_g.SeQ_l^g)+\sum_{L=1}^{N_L^{Resch}}(\Delta Q_L.SeQ_l^L)+SeQ_l^{WM}.\Delta Q_{WM} \quad (36)$$

After the convergence of this optimization process, the final generation at the slack bus is achieved by a full AC power flow solution. At this power flow, the generation of each generator (except the slack bus) and the amount of purchase from the wholesale market and load shedding are set to the outcome values obtained from this optimization process.

3. PROPOSED ALGORITHM

The proposed algorithm for real-time congestion management based on reconfiguration (red color) and generation rescheduling, load shedding, changing the pattern of purchase from the wholesale market (blue color) and considering switch action is shown in Figure 2. Since the base of this paper is an RTCM with the

lowest cost and considering that rescheduling tools are an expensive method to solve congestion, priority is given to cheaper methods for the RTCM. Therefore, the first stage of RTCM is solving this problem through the reconfiguration method and the second stage includes load shedding, generation rescheduling and changing the pattern of purchase. Congestion clearing time is subdivided into subintervals in order to evaluate the effects of power system variations or load change on the congested line current. In step 4 of this algorithm, the number of switching actions per day is considered. During the RTCM procedure, if the power system variations lead to incrementing the current of the congested line, the commands will be stopped and updated based on solving the congestion problem in the new conditions. Stage 2 of this model is divided into two steps. In the first step, reactive power change is ignored (ΔQ=0). If this problem is solved in the first step, the answer feasibility must be evaluated by power system operation constraints and the power flow solution should be checked (such as the power flow of branches and voltage magnitude of buses). If the answers do not satisfy system constraints or the solver fails to find a reliable solution, reactive power changes must be taken into the formulation to find out a feasible and reliable solution in step 2 ($\Delta Q \neq 0$).

4. NUMERICAL RESULTS

A microgrid test system with four dispatchable DGs, thirty-two buses, one wind unit, one photovoltaic unit and five load points (four load points with adjustable consumption) are considered for studying the performance of the RTCM model. The microgrid, presented by Shirmohammadi and Hong [23] which has thirty-two sectionalizing switches and five tie switches, is shown in Figure 3. A Pentium V, 4-GHz, 6-GB RAM computer is used for real-time congestion management

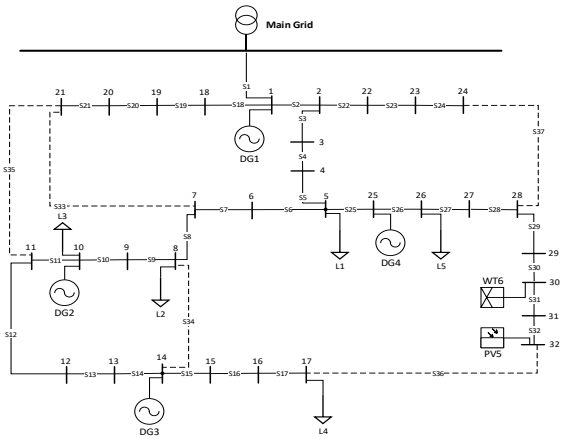

Figure 3. The diagram of the test microgrid

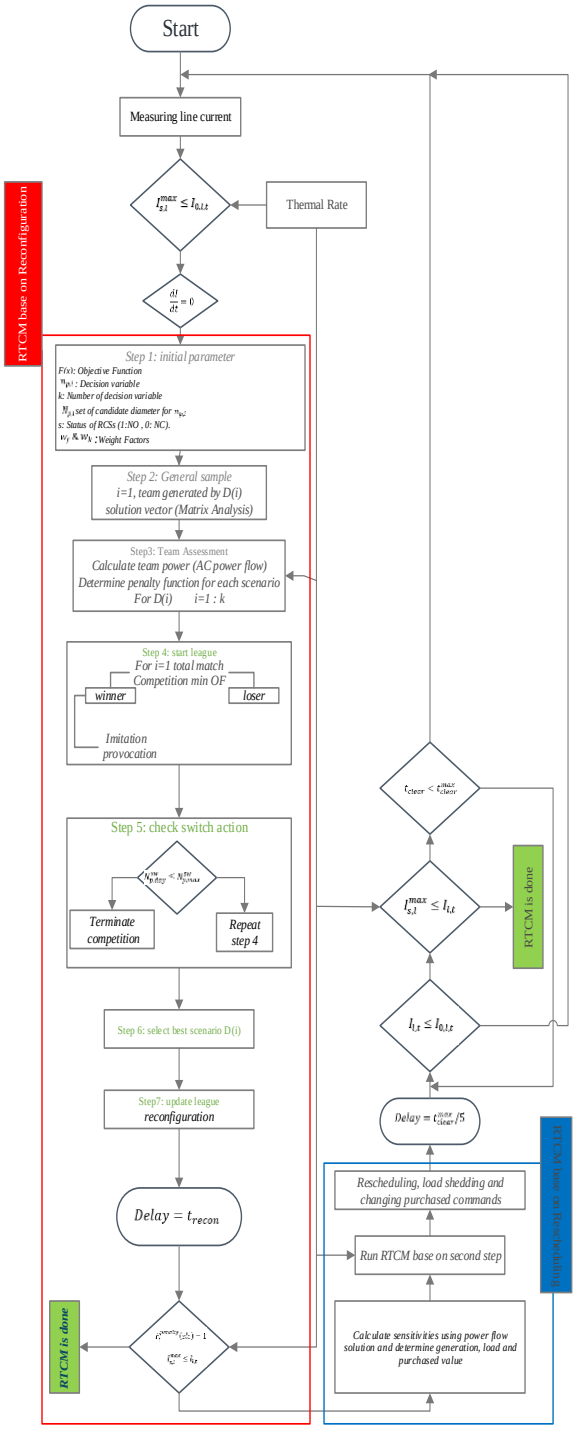

Figure 2. The proposed RTCM algorithm

calculations in this paper. Power flow solution and system modeling are performed using DIgSILENT software.

With regards to the network shown in Figure 3, initially, generation, consumption and purchase rescheduling as well as the situation of RCSs are determined for 24 hours a day (in a day-ahead manner)

considering network constraints. In addition, the generation, rescheduling constraint, and load-shedding constraints are specified. Then, the allowable line current for the next one-hour intervals is determined. The proposed algorithm can be used for both considering the switch cost and non-considering the switch cost. In this section, both strategies are used to solve the RTCM problem and show that considering this factor has a notable effect on the RTCM costs in the RTCM problem. Then, the network under this configuration and power flow are examined in real-time and in encountering scenarios that eventually create specific contingencies. These defined scenarios are the result of forecast errors and the faults which lead to generator outages. The scenarios chosen can cause congestion in one or more lines under this certain condition. Afterward, the proposed model in section 3 is applied to managing real-time congestion for these cases and the obtained results are analyzed. The defined cases that lead to congestion are as follows:

Case 1. L2 increase 35% at times 8-9

Case 2. outage of G3 due to a fault occurrence at times. 24-25

These cases are defined as events that happen in real time and lead to real-time congestion in the network, which can be managed by the proposed RTCM in this paper.

As mentioned, initially, generation, consumption and purchase rescheduling as well as the situation of RCSs are determined 24 hours a day. Since displaying these figures for 24 hours a day confuses the reader, this information is only displayed for the cases (and hours) where the scenario occurs. Table 2 shows the switching schedule for each case (D9 and D4 configuration), as well as the maximum allowable and planned switching actions for each RCSs. The characteristic of DGs and the limitation of each unit for each case are displayed in Table 3. Moreover, Table 4 summarizes the characteristics of loads in each case. Also, the line loading limitations are shown in Table 5.

Figure 4 shows the calculated amounts of age index, distance index, and switching index for all RCSs. As can be seen, RCSs with lower values of age index (e.g., RCS 7, 12, 36) or with lower values of distance index (e.g., RCS 6) create lower amounts of switching index. According to Equation (12), the maximum allowable switching actions for each RCSs can be extracted as shown in Table 1.

TABLE 2. Planned configuration for each case

	***P* (switch number)**	**Max allowable switch action** $N^{sw}_{p,max}$	**Planned switch action** $N^{sw}_{p,day}$	$s_{p,t}$ **case2 (8-9) D9**	$s_{p,t}$ **case3 (17-18) D4**
Sectionalizing	4	8	4	1	0
	6	3	2	0	0
	7	7	5	0	1
	8	9	6	1	0
	9	5	3	0	0
	10	8	6	0	0
	11	3	0	0	0
	12	9	3	1	0
	13	1	0	0	0
	15	2	0	0	0
	16	9	0	0	0
	17	4	0	0	0
	22	2	0	0	0
	23	1	0	0	0
	24	3	0	0	0
	28	2	0	0	0
	33	6	4	0	0
	34	8	6	0	1
Tie	35	9	5	0	1
	36	6	4	1	1
	37	9	5	1	1

TABLE 3. Characteristics of DGs

	Generation unit	$Bid_g^{day-a-head}(\frac{\$}{kWh})$	$Bid_g^{Real-time}(\frac{\$}{kWh})$	$P_{g,t}(kW)$	$P_g^{max}(kW)$	$R_g^{up}(\frac{kW}{min})$	$R_g^{Down}(\frac{kW}{min})$
Case1 (8-9)	DG1	0.148	0.653	4000	5000	350	-350
	DG2	0.142	-	5000	5000	112	-112
	DG3	0.187	0.793	2500	4000	251	-251
	DG4	0.228	0.859	700	٧900	458	-458
	PV5	-	-	1200	3000	-	-
	WT6	-	-	2100	3500	-	-
	P_{upgrid}	0.128	0.225	0	-	-	-
case3 (22-23)	DG1	0.159	--	5000	5000	350	-350
	DG2	0.164	0.912	4500	5000	112	-112
	DG3	0.198	0.583	3000	4000	251	-251
	DG4	0.238	0.847	600	٧900	458	-458
	PV5	-	-	1000	3000	-	-
	WT6	-	-	2000	3500	-	-
	P_{upgrid}	0.161	0.312	0	-	-	

TABLE 4. Characteristics of loads

	Load	Type	P_{Li}	$Bid_{L,t}^{Real-time}(\frac{\$}{kWh})$	Min-max capacity (Kw)	Down Time (kW/min)
Case1 (8-9)	L1	Curtailable	3000	1.466	0-700	150
	L2	Curtailable	2700	1.129	0-600	125
	L3	Curtailable	3100	0.989	200-600	160
	L4	Curtailable	3500	1.108	100-700	117
	L5	Uncurtailable	3200	-	-	-
Case2 (22-23)	L1	Curtailable	2900	1.927	0-800	150
	L2	Curtailable	3500	1.832	0-800	125
	L3	Curtailable	3200	1.174	200-800	160
	L4	Curtailable	3800	1.437	100-500	117
	L5	Uncurtailable	2700	-	-	-

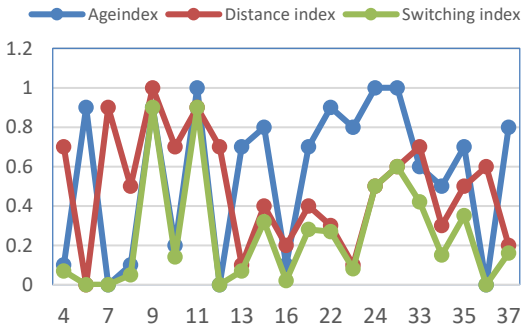

Figure 4. Switching indices for each RCS

In these studies, we assumed that cost function of load shedding and generation rescheduling for RTCM is as Equation (37).

$$cost\ of\ RTCM = \sum_{g=1}^{N_g^{Resch}} (\Delta P_{g,t} \times Bid_{g,t}^{Real-time}) + \sum_{L=1}^{N_L^{Resch}} |\Delta P_{L,t}| \times Bid_{L,t}^{Real-time} + \sum_{p=1}^{N_p} \pi_{p,t} |N_{p,t}^{sw}| \quad (37)$$

4. 1. Obtained Results in Case 1 At times 8-9, the network topology is predetermined as D9 (as depicted in Figure 5 and Table 2). The characteristics of DGs and loads as well as their limitation are displayed in Tables 3 and 4, respectively. The number of switch actions at time t ($N_{p,t,day}^{SW}$) in Table 6 includes the number of planned switch actions in day-ahead in addition to switch actions due to RTCM before 8 o'clock.

Under these conditions, L2 increases by 35% and leads to additional power supplied from the up-grid

system at 945kW. In this case, before an increase of L2 in D9 configuration, a power equal to 4000 kW and a current of 200 A flowed in lines 18,19 and 20. Under the new conditions, a power equal to 4945 kW and a current of 247.2 A flow in them. Also, a power equal to 3700 kW and a current of 185A flow in lines 9 and 10. In this respect, a power of 4645 kW and a current equal to 232 A are transmitted through them.

By comparing these currents with the thermal rate (Table 5), we find that these lines are congested. Lines 18, 19 and 20 have emergency congestion and lines 9 and 10 have short-term congestion.

Under these conditions, as shown in Table 8, the solution of the Soccer League algorithm in the first stage of RTCM is network reconfiguration by providing the D37 if we consider the switch cost factor or D19 configuration without considering this factor. Accordingly, the transmission power of the mentioned lines is reduced, and the real-time congestion problem is solved at $F_t^{penalty} = 1$ accordingly. As observed, an RTCM is performed for this case by changing three pairs of switches.

Table 6 compares the configuration of D9, D19 and D37. Figure 5 shows the topological structure of the network in D9, D19 and D37 configurations.

As can be seen, the network configuration in D37 and D19 are similar and the difference lies in the cost of the switch action.

4. 2. Obtained Results in Case 2 At times 22-23, the network topology is predetermined as D4 (as shown in Figure 6 and Table 2). The characteristics of DGs and loads as well as their limitation are displayed in Tables 3 and 4, respectively.

In this case, the outage of G3 due to a fault occurrence leads to additional power supplied from the up-grid system at 3000kW to maintain voltage and frequency and prevent blackouts. In this case, before the outage of G3 in D4 configuration, lines 18, 19, 20, 8 and 33 transmit a power equal to 4000 kW and a current of 200 A. In this connection, a power of 6000 kW and a current equal to 300 A transmit through them. By comparing these currents with the thermal rate (Table 5), we find that these lines are congested. All these lines have an emergency. Under these conditions, the solution of the

TABLE 5. The thermal rate of the line obtained by SR & MR methods

Line	Line Current Rate		
	$I_{L,t}^{max}$	$I_{s,t}^{max}$	$I_{E,t}^{max}$
Lines (1-8)	194	207	237
Lines (9-13)	198	215	252
Lines (14-17)	229	242	270
Lines (18-24)	203	214	245
Lines (25-32)	237	250	278
Lines (33)	194	206	235
Lines (34)	238	251	280
Lines (35)	191	207	240
Lines (36)	195	211	243
Lines (37)	242	254	282

TABLE 6. Switch cost for change, number of switch actions at time *t* and Network configuration in D9, D19 and D37

	P (switch number)	$\pi_{p,t}$ ($)	$N_{p,t,day}^{sw}$	D9	D19	D37
Sectionalizing	4	2.1	3	1	0	0
	6	1.8	1	0	0	1
	7	3.4	3	0	1	0
	8	2.3	2	1	0	0
	9	1.5	1	0	0	1
	10	4.8	3	0	1	0
	11	6.0	0	0	0	0
	12	3.4	2	1	0	0
	13	7.0	0	0	0	0
	15	5.9	0	0	0	0
	16	4.7	0	0	0	0
	17	6.3	0	0	0	0
	22	7.2	0	0	0	0
	23	4.6	0	0	0	0
	24	3.2	0	0	0	0
	28	3.9	0	0	0	0
	33	3.9	1	0	0	0
Tie	34	2.8	3	0	1	1
	35	7.8	2	0	0	0
	36	4.3	2	1	1	1
	37	6.8	1	1	1	1

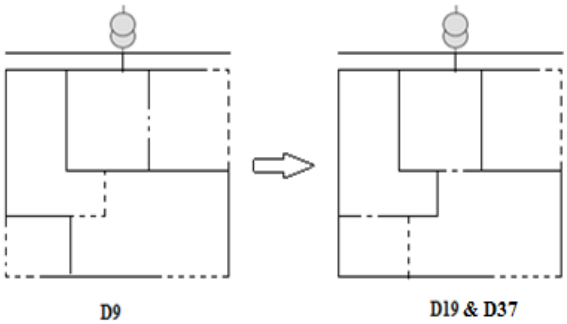

Figure 5. Network structure for D9 & D19 & D37 configuration

Soccer League algorithm is network reconfiguration by providing the D24 with considering the switch cost factor and D46 without considering this factor instead of D4 (as shown in Figure 6). Table 7 compares the configuration of D4, D46 and D24. As a result of this reconfiguration, the amount of $F_t^{penalty}$ penalty has significantly decreased from 43776 to 3672 by considering the switch action factor or 43776 to 3895 by not considering this factor (as shown in Table 8) and the congestion in the mentioned lines has been eliminated. Nevertheless, this reconfiguration causes the congestion of lines 2, 3, 4 and 5 in full RTCM and lines 22, 23, 24, 34, 27, and 28 regardless of the switch action factor. Therefore, to completely solve the congestion problem, the performance of the second stage of RTCM is needed based on the proposed model in this paper. The solution of the second stage determines generation scheduling, load shedding, and changes purchased from the up-grid system. For this case, if the switch cost factor is used in the calculations, the solution is the decrease of 1820 kW purchased from the up-grid system and an increase of 1820 kW in the generation of DG4. The duration of this change is equal to 1820÷458=3.9 min where 458 is the ramp rate of G4 and the cost to $1820 \times 0.847 = \$\,1541$where 0.847 is G4 real-time bid at time 22-23. In addition, without considering this factor, the cost of this change is $1640 \times 0.847 = \$1388$.

In addition, if the switch action factor is used in the RTCM, there is a 1820kW increase in DG4 generation by the same amount, which will eliminate this congestion and the $153 RTCM cost. Yet, it should be noted that if the switch action factor is ignored, it will lead to irreparable damages to the system according to Table 1. The maximum allowable switch action of switch No. 34 (RCS$N_{p,max}^{sw}$) during the day is equal to 8, while the number of switch actions has reached its maximum value before 22:00 ($N_{p,t,day}^{sw}$ in Table 7), while this switch cannot act at the desired time.

4. 3. Discussion As mentioned, the proposed model in this paper is based on the integration of marketing with the reconfiguration method, for the RTCM in a microgrid. Now, for principled validation, we

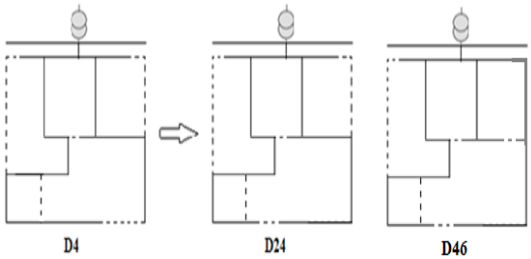

Figure 6. Network structure for D4, D24 and D46 configuration

TABLE 7. Network configuration in D4 and D24

	p (switch number)	$\pi_{p,t}$	$N_{p,t,day}^{sw}$	D4	D24	D46
Sectionalizing	4	2.5	4	0	0	0
	6	2.3	2	0	0	0
	7	4.4	4	1	1	1
	8	3.1	2	0	0	0
	9	1.8	1	0	0	0
	10	5.3	4	0	0	0
	11	6.4	0	0	0	0
	12	2.4	3	0	0	0
	13	6.0	0	0	0	0
	15	5.5	0	0	0	0
	16	4.9	1	0	1	1
	17	6.8	0	0	0	0
	22	7.7	1	0	0	0
	23	5.0	0	0	0	0
	24	3.7	0	0	0	0
	28	3.3	0	0	0	1
	33	3.1	4	0	0	0
Tie	34	9.8	8	1	1	0
	35	8.4	3	1	1	1
	36	4.9	5	1	0	0
	37	7.8	3	1	1	1

TABLE 8. RTCM by generation scheduling, load shedding and supplied power from up-grid

/		Full RTCM With considering switch cost		RTCM based on just Rescheduling		RTCM based on Reconfiguration and Rescheduling Without considering switch cost	
Case No.		**Case1**	**Case 2**	**Case1**	**Case 2**	**Case1**	**Case 2**
Type of congestion for each line before RTCM	long-term congestion						
	short-term congestion	S9, S10		S9, S10		S9, S10	

	emergency congestion	S18, S19, S20	S8, S18, S19, S20, S33	S18, S19, S20	S8, S18, S19, S20, S33	S18, S19, S20	S8, S18, S19, S20, S33
	Selected configuration	D9	D4	D9	D4	D9	D4
	$F_t^{penalty}$ before reconfiguration	1722	43776	1722	43776	1722	43776
	t_{clear}^{max} (min)	5	5	5	5	5	5
	Select best reconfiguration	D37	D24	_	_	D19	D46
	$F_t^{penalty}$ after Reconfiguration	1	3895	_	_	1	3672
First Stage	$\sum_{k=1}^{n_p} \lvert \Delta s_{p,t} \rvert$	6	2	_	_	6	4
	t_{recon} (min)	1	1	_	_	1	1
	Reconfiguration cost ($)	13.2	7.3	_	_	32.0	20.4
	w_c	_	1	1	1	_	1
	w_t	_	176	122	53	_	169
	ΔP_{G1}	_	0	0	0	_	0
	ΔP_{G2}	_	0	0	+500	_	0
	ΔP_{G3}	_	0	+885	0	_	0
Second Stage	ΔP_{G4}	_	1820	0	0	_	+1640
	ΔP_{upgrid}	_	-1820	-885	-2120	_	-1640
	$\sum_{g=1}^{N_g^{Resch}} (\Delta P_g)$	_	1820	+885	+500	_	+1640
	$\sum_{L=1}^{N_L^{Resch}} \lvert \Delta P_L \rvert$	_	0	0	1620	_	0
	$t_{clear,Resch}$ (min)	_	3.9	3.5	0	_	3.5
	Rescheduling cost ($)	_	1541	701.8	2699	_	1388
Total cost ($)		13.9	1548	701.8	2699	32.0	1408.4
t_{clear}(min)		1	4.9	3.5	5	1	4.5

consider the cases for the above microgrid in a situation where the reconfiguration method or the marketing method is used alone. To implement the method of reconfiguration for RTCM, regarding the red part of Table 8, this method cannot solve the congestion problem alone in all the cases, e.g., case 2.

In column 2 of Table 8, the mentioned cases in this section for RTCM were examined based merely on the market-based model as proposed in this paper (stage 2 of the proposed model in this paper). Finally, in this way, we understand the effect of the integration of marketing methods with the reconfiguration of RTCM. In the first case, if the reconfiguration is not performed, 885 kW of the supplied power from the up-grid system must be reduced and added to Generator G3 to solve the real-time congestion problem. Regarding Equation (35), the cost of congestion management is equal to \$701.8. However, if the complete model presented in this paper is employed, this value will reach \$13.9. The congestion clearance time also increased to 3.5 minutes due to the ramp-up rate of Generator G3, which was one minute in the integrated model. Calculations are performed similarly for case 2 and the results are generalized. Now, to understand the effectiveness of using the integration model of reconfiguration methods with market-base, it suffices to compare the last two rows and column 2 of Table 8 with the last two rows of Table 8. This comparison eliminates unnecessary costs in the proposed model to solve the real-time congestion problem, and at the same time enhances the effectiveness of this method in the RTCM.

On the other hand, in this paper, a new index for switching action is proposed to prevent risky switching and the depreciation caused by frequent switching. For principled validation, it has been considered that the cases for the above microgrid in a situation where switching action is not considered. The first and third columns of Table 8 show RTCM by the proposed model in this paper, with and without considering the switching cost. In the first case, the network configuration in D37 and D19 are similar and the difference lies in the cost of switch action. As can be seen, the reconfiguration cost is lower when the switching cost is considered. But in the second case, despite taking into account the switching cost, the reconfiguration cost has increased. Yet, it should be noted that if the switch action factor is ignored, it will lead to irreparable damages to the system according to

Table 2, because the number of switch action of switch No. 34 has reached its maximum value and this switch is not able to act at the desired time.

The distinction between considering switch action factor and without considering this factor in RTCM calculations is evident in both cases.

5. CONCLUSION

The high penetration of Distributed Energy Resources (DER) raises new challenges in microgrid operation due to stochastic and intermittent characteristics. This exacerbates the difficulty of congestion management of microgrids in comparison with conventional power systems. On the other hand, with the development of microgrids as well as increased investment for telecommunication infrastructure, distribution networks can be operated online and in real time. In this situation, using the proposed method in this paper can solve a wide range of congestion problems with any intensity and under any type of network infrastructure, and finally reach an optimal point in the optimization problem. This paper proposed real-time congestion management in accordance with the switch cost factor based on integrating a reconfiguration method with the marketing method in the microgrid. The model presented in this paper solves the real-time congestion problem in two steps. In the first step, based on a structural method and switch cost factor, the status of RCSs is determined by the reconfiguration of the microgrid and to reach the global optimal point. This is done to reduce the current in congested lines and thus solve the real-time congestion problem. Then, if the congestion problem is not solved in the first step, a fast, feasible and inexpensive solution is proposed to solve the real-time congestion problem in the next step by considering the ramp-up and ramp-down time of the generators and loads and also determining the sensitivity of each line to these changes. The integration of these two independent methods can solve a wide range of congestion problems with any intensity and under any type of network infrastructure, and finally reach a general optimal point in the optimization problem. Importantly, unlike previous methods, in this method, all possible scenarios are inspected and the most optimal solution is selected. In addition, the division of congestion into long-term, short-term and emergency time and the definition of the congestion clearing time parameter prevent unnecessary costs for RTCM. Numerical results showed that through the method proposed in this paper, the congestion problem in the microgrid is solved at a lower cost and shorter time than other methods. In future work, the energy losses of the distribution lines during congestion management will be studied.

6. REFERENCES

1. Barbulescu, C., Kilyeni, S., Cristian, D.P. and Jigoria-Oprea, D., "Congestion management using open power market environment electricity trading", in 45th international universities power engineering conference UPEC2010, IEEE., (2010), 1-6.
2. Babagheibi, M., Jadid, S. and Kazemi, A., "Distribution locational marginal pricing for congestion management of an active distribution system with renewable-based microgrids under a privacy-preserving market clearing approach and load models", ***Sustainable Energy, Grids and Networks***, Vol. 32, (2022), 100935. https://doi.org/10.1016/j.segan.2022.100935
3. Biegel, B., Andersen, P., Stoustrup, J. and Bendtsen, J., "Congestion management in a smart grid via shadow prices", ***IFAC Proceedings Volumes***, Vol. 45, No. 21, (2012), 518-523. https://doi.org/10.3182/20120902-4-FR-2032.00091
4. Fattaheian-Dehkordi, S., Rajaei, A., Abbaspour, A., Fotuhi-Firuzabad, M. and Lehtonen, M., "Distributed transactive framework for congestion management of multiple-microgrid distribution systems", ***IEEE Transactions on Smart Grid***, Vol. 13, No. 2, (2021), 1335-1346. https://doi.org/10.3182/201209024-FR-2032.00091
5. Li, R., Wu, Q. and Oren, S.S., "Distribution locational marginal pricing for optimal electric vehicle charging management", ***IEEE Transactions on Power Systems***, Vol. 29, No. 1, (2013), 203-211. https://doi.org/10.1109/TPWRS.2013.2278952
6. O'Connell, N., Wu, Q., Østergaard, J., Nielsen, A.H., Cha, S.T. and Ding, Y., "Day-ahead tariffs for the alleviation of distribution grid congestion from electric vehicles", ***Electric Power Systems Research***, Vol. 92, (2012), 106-114. https://doi.org/10.1016/j.epsr.2012.05.018
7. Verzijlbergh, R.A., De Vries, L.J. and Lukszo, Z., "Renewable energy sources and responsive demand. Do we need congestion management in the distribution grid?", ***IEEE Transactions on Power Systems***, Vol. 29, No. 5, (2014), 2119-2128. https://doi.org/10.1109/TPWRS.2014.2300941
8. Huang, S. and Wu, Q., "Dynamic subsidy method for congestion management in distribution networks", ***IEEE Transactions on Smart Grid***, Vol. 9, No. 3, (2016), 2140-2151. https://doi.org/10.1109/TSG.2016.2607720
9. Andersen, P.B., Hu, J. and Heussen, K., "Coordination strategies for distribution grid congestion management in a multi-actor, multi-objective setting", in 2012 3rd IEEE PES Innovative Smart Grid Technologies Europe (ISGT Europe), IEEE. (2012), 1-8.
10. Hu, J., You, S., Lind, M. and Østergaard, J., "Coordinated charging of electric vehicles for congestion prevention in the distribution grid", ***IEEE Transactions on Smart Grid***, Vol. 5, No. 2, (2013), 703-711. https://doi.org/10.1109/TSG.2013.2279007
11. Zhang, C., Ding, Y., Nordentoft, N.C., Pinson, P. and Østergaard, J., "Flech: A danish market solution for dso congestion management through der flexibility services", ***Journal of Modern Power Systems and Clean Energy***, Vol. 2, No. 2, (2014), 126-133. https://doi.org/10.1007/s40565-014-0048-0
12. Aljohani, T.M., Ebrahim, A.F. and Mohammed, O.A., "Dynamic real-time pricing mechanism for electric vehicles charging considering optimal microgrids energy management system", ***IEEE Transactions on Industry Applications***, Vol. 57, No. 5, (2021), 5372-5381. https://doi.org/10.1109/TIA.2021.3099083
13. Vergara-Fernandez, L., Aguayo, M.M., Moran, L. and Obreque, C., "A milp-based operational decision-making methodology for demand-side management applied to desalinated water supply systems supported by a solar photovoltaic plant: A case study in

agricultural industry", ***Journal of Cleaner Production***, Vol. 334, (2022), 130123. https://doi.org/10.1016/j.jclepro.2021.130123

14. Huang, S. and Wu, Q., "Real-time congestion management in distribution networks by flexible demand swap", ***IEEE Transactions on Smart Grid***, Vol. 9, No. 5, (2017), 4346-4355. https://doi.org/10.1109/TSG.2017.2655085
15. Daroj, K. and Limpananwadi, W., "Reactive power dispatch scheme evaluation for synchronous based distributed generators to reduce real power loss in distribution systems", in 2008 IEEE International Conference on Sustainable Energy Technologies, IEEE., (2008), 1178-1183.
16. Viawan, F.A. and Karlsson, D., "Voltage and reactive power control in systems with synchronous machine-based distributed generation", ***IEEE Transactions on Power Delivery***, Vol. 23, No. 2, (2008), 1079-1087. https://doi.org/10.1109/TPWRD.2007.915870
17. Ramesh, G. and Ranjith Babu, V., "Combined facts and microgrid-based congestion management in transmission lines", in Advances in Electrical and Computer Technologies: Select Proceedings of ICAECT 2020, Springer., (2021), 1063-1073.
18. Thakar, S., Vijay, A. and Doolla, S., "System reconfiguration in microgrids", ***Sustainable Energy, Grids and Networks***, Vol. 17, (2019), 100191. https://doi.org/10.1016/j.segan.2019.100191
19. Huang, S., Wu, Q., Liu, Z. and Nielsen, A.H., "Review of congestion management methods for distribution networks with high penetration of distributed energy resources", ***IEEE PES Innovative Smart Grid Technologies, Europe***, (2014), 1-6. https://doi.org/10.1109/ISGTEurope.2014.7028811
20. Keshavarz, M., Doroudi, A., Kazemi, M. and Mahdian Dehkordi, N., "A new consensus-based distributed adaptive control for islanded microgrids", ***International Journal of Engineering, Transactions A: Basics***, Vol. 34, No. 7, (2021), 1725-1735.oi. https://doi.org/10.5829/ije.2021.34.07a.17
21. Merlin, A. and Back, H., "Search for a minimal-loss operating spanning tree configuration in an urban power distribution system", in Proc. 5th Power System Computation Conf., Cambridge, UK., (1975), 1-18.
22. Mendoza, J., López, R., Morales, D., López, E., Dessante, P. and Moraga, R., "Minimal loss reconfiguration using genetic algorithms with restricted population and addressed operators: Real application", ***IEEE Transactions on Power Systems***, Vol. 21, No. 2, (2006), 948-954. https://doi.10.1109/TPWRS.2006.873124
23. Shirmohammadi, D. and Hong, H.W., "Reconfiguration of electric distribution networks for resistive line losses reduction", ***IEEE Transactions on Power Delivery***, Vol. 4, No. 2, (1989), 1492-1498. https://doi.10.1109/61.25637
24. Glamocanin, V., "Optimal loss reduction of distributed networks", ***IEEE Transactions on Power Systems***, Vol. 5, No. 3, (1990), 774-782. https://doi.10.1109/59.65905
25. Toune, S., Fudo, H., Genji, T., Fukuyama, Y. and Nakanishi, Y., "Comparative study of modern heuristic algorithms to service restoration in distribution systems", ***IEEE Transactions on Power Delivery***, Vol. 17, No. 1, (2002), 173-181. https://doi.10.1109/61.974205
26. Nara, K., Shiose, A., Kitagawa, M. and Ishihara, T., "Implementation of genetic algorithm for distribution systems loss minimum re-configuration", ***IEEE Transactions on Power Systems***, Vol. 7, No. 3, (1992), 1044-1051. https://doi.10.1109/59.207317
27. Savier, J. and Das, D., "A multi-objective method for network reconfiguration", ***International Journal of Engineering, Transactions A: Basics,*** , Vol. 22, No. 4, (2009).
28. Shariatkhah, M.H. and Haghifam, M.R., "Using feeder reconfiguration for congestion management of smart distribution network with high dg penetration", (2012). https://doi.10.1049/cp.2012.0863
29. Franco, J.F., Rider, M.J., Lavorato, M. and Romero, R., "A mixed-integer lp model for the reconfiguration of radial electric distribution systems considering distributed generation", ***Electric Power Systems Research***, Vol. 97, (2013), 51-60. https://doi.org/10.1016/j.epsr.2012.12.005
30. Abur, A., "A modified linear programming method for distribution system reconfiguration", ***International Journal of Electrical Power & Energy Systems***, Vol. 18, No. 7, (1996), 469-474. https://doi.org/10.1016/0142-0615(96)00005-1
31. Baran, M.E. and Wu, F.F., "Network reconfiguration in distribution systems for loss reduction and load balancing", ***IEEE Transactions on Power Delivery***, Vol. 4, No. 2, (1989), 1401-1407. https://doi.10.1109/61.25627
32. Enacheanu, B., Raison, B., Caire, R., Devaux, O., Bienia, W. and HadjSaid, N., "Radial network reconfiguration using genetic algorithm based on the matroid theory", ***IEEE Transactions on Power Systems***, Vol. 23, No. 1, (2008), 186-195. https://doi.10.1109/PES.2008.4596321
33. Shariatkhah, M., Haghifam, M.-R. and Arefi, A., "Load profile based determination of distribution feeder configuration by dynamic programming", in 2011 IEEE Trondheim PowerTech, IEEE., (2011), 1-6.
34. Esfahani, M.M. and Yousefi, G.R., "Real time congestion management in power systems considering quasi-dynamic thermal rating and congestion clearing time", ***IEEE Transactions on Industrial Informatics***, Vol. 12, No. 2, (2016), 745-754. https://doi.10.1109/TII.2016.2530402
35. 738, I.S., "Ieee standard for calculating the current temperature relationship of bare overhead conductors", (2006). https://doi.10.1109/IEEESTD.2013.6692858
36. Esmaeili, S., Anvari-Moghaddam, A., Jadid, S. and Guerrero, J.M., "A stochastic model predictive control approach for joint operational scheduling and hourly reconfiguration of distribution systems", ***Energies***, Vol. 11, No. 7, (2018), 1884. https://doi.org/10.3390/en11071884
37. Kavousi-Fard, A. and Khodaei, A., "Efficient integration of plug-in electric vehicles via reconfigurable microgrids", ***Energy***, Vol. 111, (2016), 653-663. https://doi.org/10.1016/j.energy.2016.06.018
38. Moosavian, N. and Roodsari, B.K., "Soccer league competition algorithm, a new method for solving systems of nonlinear equations", ***International Journal of Intelligence Science***, Vol. 4, No. 01, (2013), 7. https://doi.10.4236/ijis.2014.41002
39. Dutta, S. and Singh, S., "Optimal rescheduling of generators for congestion management based on particle swarm optimization", ***IEEE Transactions on Power Systems***, Vol. 23, No. 4, (2008), 1560-1569. https://doi.10.1109/TPWRS.2008.922647

Persian Abstract

چکیده

در ریزشبکه‌ها از تراکم بعنوان یک محدودیت نام برده می‌شود که مانع از رسیدن انرژی از ژنراتورها به بارها شده و زمانی به‌وجود می‌آید که سیستم نتواند در یک الگوی خاص تولید، مصرف و انتقال بصورت ایمن عمل کند. این درحالی است که تمرکز بیشتر روی واحدهای تجدیدپذیر و مشارکت روزافزون آن‌ها برای تامین توان ریزشبکه‌ها، احتمال وقوع تراکم ناشی از خطای پیش‌بینی را افزایش داده است. لذا با توجه به ضرورت مطلب لزوم استفاده از یک روش کارآمد، برای حل موضوع تراکم زمان واقعی غیر قابل انکار است. استفاده از نقاط مانور شبکه‌های توزیع به همراه تغییر الگوی تولید مصرف و خرید از بالا دست می‌تواند از آپشن‌های اصلی برطرف کردن تراکم در محدوده زمانی زمان واقعی باشد. در این مقاله یک مساله بهینه‌سازی دو مرحله‌ای بمنظور حل مشکل تراکم زمان واقعی در یک ریزشبکه ارائه شده است. مساله بهینه سازی شامل بازآرایی ساختار توپولوژیک شبکه توسط نقاط مانور در مرحله اول وهمچنین ادغام آن با برنامه های شیفت مصرف و پخش بار بهینه برای کمینه کردن هزینه های میکروگرید در مرحله دوم، در فاصله زمانی مشخص و در نهایت رسیدن به یک نقطه بهینه کلی است. بنابراین پس از وقوع تراکم، نخست تغییر در پیکربندی شبکه بمنظور کاهش حداکثری میزان تراکم به‌عنوان یک روش ارزان بکار گرفته می‌شود. الگوریتم لیگ فوتبال برای حل این مساله بهینه‌سازی در مرحله اول بمنظور یافتن توپولوژی بهینه شبکه پیشنهاد شده است. سپس بر اساس نتایج بدست آمده از مرحله اول، مدل ارائه شده در مرحله دوم بمنظور رفع کامل تراکم با کمترین هزینه اعمال می‌شود. مدل ارائه شده یک تابع هدف وزنی را کمینه می‌کند که شامل هزینه برنامه ریزی مجدد تولید و خرید از بالادست، هزینه کاهش بار، هزینه سوئیچینگ و زمان پاکسازی تراکم است. در این مقاله بمنظور مدل سازی هزینه‌های سوییچینگ شاخص جدیدی بر اساس موقعیت مکانی و همچنین طول عمر آن تعریف شده است. مطالعات موردی تاثیر گذاری این روش را در کاهش هزینه ها وحل مساله تراکم نشان می‌دهد و این فرصت را برای ریز شبکه‌ها فراهم می‌آورد تا با کمترین هزینه و بدون سرمایه گذاری برای توسعه خطوط و ادوات شبکه و تنها با بازآرایی به همراه کنترل میزان تولید و مصرف و خرید از بالادست در ساعات مشخص، نیازهای شبکه را چه در زمان وقوع تراکم چه در زمان‌های غیر متراکم برآورده کند.

International Journal of Engineering

Journal Homepage: www.ije.ir

Integrating Building Information Modeling and Virtual Reality to Develop Real-time Suitable Cost Estimates using Building Visualization

S. M. Omaran, A. S. J. Al-Zuheriy*

Civil Engineering Department, University of Technology Iraq, Baghdad, Iraq

P A P E R I N F O

Paper history:
Received 18 November 2022
Received in revised form 24 January 2023
Accepted 18 February 2023

Keywords:
Building Information Modeling
Virtual Reality
Visualization
Cost Estimation

A B S T R A C T

The literature and previous research revealed that reducing the variation order by selecting the favorite material visually by the project's owner in the design stage is not available recently. As a problem, the cost estimates in real-time from walk-through interactions selecting multi-alternative building components are a potential threat to projects' success unless there is a visualization system helping to decide the costs of different building items and the items' suitability. This research is a powerful tool that allows the project's owner to reduce the variation order by visually selecting his favorite material in the design stage. It expresses the application of Building Information Modeling (BIM) with Virtual Reality (VR) to improve Cost Estimation (CE) and the material selection process. The authors utilize BIM and virtual reality technology to enhance the visualization and processing of project cost estimation in the construction industry. In this study, the primary goal is to develop a BIM-VR-CE system that helps construction stakeholders to visualize and quickly to decide the costs of different building items and the items' suitability. Accordingly, the authors developed a BIM-VR-CE system that integrates BIM and virtual reality technology using Unity 3D. Navigating building environments in real-time with the ability to select the cost and items suitable for elements of projects is now available to construction stakeholders through the BIM-VR prototype developed in this paper. To evaluate the effectiveness of the proposed preliminary model, a questionnaire was created, and 85 evaluations were collected. The findings of this paper show significant potential to utilize the proposed model in construction projects to deal with cost, reduce the variation orders, and select the favorite elements.

***doi**: 10.5829/ije.2023.36.05b.03*

1. INTRODUCTION

The accuracy of project cost estimating is one of the most important factors for the success of construction projects [1]. To determine the financial resources, resources, and scope of work, construction projects need efficient cost estimation [2]. Estimation should be considered before construction; otherwise, an incorrect approximation could lead to the failure of the project [3]. Also, the cost estimates help track the progress of development and can assist in decision-making regarding project termination [3]. Project failures have increased due to inaccuracies in cost estimation. Problems encountered in construction estimates include cost overrun, failure to initially define the scope of the work, unrealistic assumptions, lack of estimation knowledge, poor technologies for estimation, and even inflation. At project completion, the initial costs differ by a more significant margin than expected [3].

The technological advancement in the construction industry recently created an important term; BIM, integrated with virtual reality. BIM is an illustration of the physical features of buildings that enable the making of decisions during the project's lifetime [4]. The BIM can be expanded to consider the full construction cost and scheduled activities. Initially, the contractors and building owners used CAD documents from engineers and architects. The drawings did not integrate the schedule and cost with the technology advancements that have been incorporated to reduce the costs. Therefore, using a 3D model can help contractors as well as owners

*Corresponding Author Institutional Email: ahmed.sh.jeber@uotechnology.edu.iq (A. S. J. Al-Zuheriy)

Please cite this article as: S. M. Omaran, A. S. J. Al-Zuheriy, Integrating Building Information Modeling and Virtual Reality to Develop Real-time Suitable Cost Estimates using Building Visualization, ***International Journal of Engineering, Transactions B: Applications***, Vol. 36, No. 05, (2023) 858-869

to create a 3D environment to deal with the cost and schedule of projects effectively. Also, virtual study construction of 3D modeling helps ensure a more efficient understanding of buildings. The digital models will effectively change the construction industry, especially when the visual analysis proficiencies become repetitive [5]. When clients incorporate this technology, they end up saving on the cost of the project.

There have been various studies documenting the importance of VR technologies. However, VR has not been used effectively in the design process. VR use has been limited to some projects of importance. In the recent past, this was because of a lack of computing hardware that was affordable. This meant that VR at that time needed time-consuming and costly to create different 3D models [6]. the initial design was done on a 2D model. The original design from the 2D could then be taken to the 3D model, and this had to be done by someone else. It consequently affected the integration of technology conversion to a suitable real-time optimized visualization. Therefore, utilizing BIM in the construction industry has enhanced new capabilities in construction. Evolution from the 2D to 3D models has now made it easier to describe buildings in detail [7]. Now it is easier to integrate BIM models into VR without creating a separate model.

2. LITERATURE REVIEW

Virtual Reality (VR) has numerous applications in construction [8]. It has the potential to navigate freely in 3D models. It communicates ideas ideally regarding upcoming projects and enhances understanding of tasks in a detailed manner [9]. For individuals with fixed experience in interpreting ancient designs, the VR helps avoid misunderstandings that can arise and helps enable a thorough comprehension of all buildings [10]. The BIM method can maintain and generate all the information produced during the construction process from design to maintenance. The prototyping supports the solicitation of the BIM data in developing several multi-dimensional BIM models. It also hastens the process of delivering and refining designs [11]. The nD-BIM applications are described below.

a) 3D-BIM model involves modeling the development of architecture, piping, and electrical [12].

b) The 4D-BIM model relates to construction planning and scheduling. Also, it supports the visualization of constructing, monitoring, and controlling the project. 4D-BIM mode is achieved by links from the 4D application with the 3D elements such as links between Naviswork and Revit to visualize the schedule of the project [13].

c) The 5D-BIM model is mainly related to cost estimation [14].

d) The 6D-BIM model is related to energy and sustainability. It is used to estimate the energy consumption of the project, and to measure and verify energy utilization in the life span of a building [14].

e) The 7D-BIM model is used to support facility management and maintenance activities [15].

Communication among individuals at a high - level comes from data design. From existing reports, many companies recorded quick project approvals, increased workers' interactions, and enhanced productivity. For efficient work of the BIM technology, the software combines other advanced technologies like Virtual Reality (VR) enhancing defect analysis and management. Linking the VR and BIM blends expertly to the design of the BIM. The process improves architecture and engineers' activities in construction [16]. The VR blends with additional fields that aid the use of visualization recognized by the BIM. This study examines the number of accomplishments permissible by the genuine software to execute numerous tasks merging VR and BIM, primarily in two indispensable uses: the 4D model aiding building activity and the 7D model regarding conservation [16]. In the distinct building segment, VR and BIM knowledge lead to main players' upgraded communication, grounded on the visualization of superior design, relevant to the best indulgence of the augmenting BIM blend with VR. The reality of different data that can be related to other factors which classify every single BIM progression is of immense significance once the workers want to investigate hitches and deliberate alternate solutions [16]. The simulation of the life-cycle cost (LCC) supports by integrating BIM and the game engine model. To envisage LCC analysis, owners, stakeholders, and students depend on the BIM-game prototype [17].

Combining the BIM and VR models to help visualize the characteristics of the sorts and access to information is an evolutionary improvement of the entire project. Approval of virtual reality in the building field has risen. VR facilitates the operator to engage in a 1-to-1, 3D, and BIM scale with significant influence [18]. To view designs earlier for customers, construction experts are aware that virtual reality apps are making it possible, thus lowering material costs and shrinking the total number of laborers required for a specific project. Alternatively, the BIM/4D model the VR can help BIM methodology given that it permits the user to interact with 3D and BIM models in two important ways [18]:

a) A walkthrough is popularly used because it enables the user to use 3D in a completely simulated environment from numerous buildings, whether inside or outside of the building [18].

b) Consulting data is concerned with the possibility of retrieving the data already centralized in the BIM model that is composed of the parametric steps involved in the modeling.

In the walkthrough, the building viability can be tested by using human judgment and scale models. However, judgment cannot always be accurate. In VR, the final model can be expressed in 3-D. The user is now allowed to observe an artificial environment which is enhancing architects' efforts [18]:

• Samsung Gear VR is a VR that enables exploration of the virtual environment at construction sites or in meetings. A BIM model is required along with site pictures to allow follow-up of construction [19].

• Oculus Rift is enabled with interactive capacities that can be executed as a plugin in Revit. It can provide a realistic overview of the actual scale of a building that was not possible with traditional systems [20].

In consulting data, the model VR materials such as the furniture, and other small details are incorporated.

• Autodesk 360 permits a combination of the group in joint projects because each adjustment in the BIM model is demonstrated at a convenient time for every individual to view. Autodesk produces a comprehensive web-based clarification for studying BIM composition [21-24].

• Augment software allows the operator to realize the 3D/BIM model from a human viewpoint. It can as well be downloaded on a Smartphone to help in consultation about the BIM data [22-25].

Construction design 4D CAD models incorporate 3D components with time. They have been widely used in construction phases and have shown benefits in some activities with stakeholders like evaluating project constructability as well as, ascertaining spatial conflicts in construction [23].

The administration and conservation 7D model merging BIM with VR help enable efficient collaboration because the information can be envisioned, referred to, and distorted while the client and even the team are inside the building. The use of BIM in material estimation, labor, and cost of construction equipment will help to estimate the value of projects and any other costs accurately. Students studying BIM estimation are more prepared for the daily changing building industry. It will also help boost the technological know-how and help them stay relevant [23-26].

Using Building Information Modeling (BIM) capabilities, A novel method was proposed to identify cost and energy-efficient building envelope materials within a region over the life cycle. By replacing conventionally used materials with the available high-performance building materials, the results showed 31%and 28% for the potential energy performance enhancement and a life cycle cost improvement, respectively [27].

To minimize the expected project cost, time, and risk as well as to maximize the expected quality, a set of project activities were selected to be stopped in such a way as to reach the abovementioned goal through executive each project activity in a specific mode [28].

Building Information Modeling (BIM) and Virtual Reality (VR) are two technologies that have been increasingly used in the architecture, engineering, and construction (AEC) industry. BIM is a process for creating and managing digital building models, while VR is a technology that allows users to experience a digital environment as if it were real. The integration of these two technologies has the potential to enhance collaboration, communication, and decision-making in the AEC industry.

Ghanem [29] found the use of VR technology in particular can provide a more immersive and interactive experience for project stakeholders, which can improve the understanding of the building and the design process. However, the study has not considered all possible factors and challenges that may affect the integration of BIM and VR in the construction industry

Abbasnejad et al. [30] presented a research on how to use BIM and VR technologies for construction project management. In their study, found that the integration of BIM and VR can improve the management of construction projects. However, the study has a limitation in that the research was conducted on a small scale and the results may not be generalizable to other projects or situations [30].

Sampaio [21] discussed about the potential benefits of integrating virtual reality (VR) technology with building information modeling (BIM) methodology, such as improved communication, collaboration, and visualization. However, it may also mention some of the challenges and limitations of using VR in BIM, such as lack of standardization, user adoption, integration with other systems, and challenges in terms of implementation, cost, and availability of VR technology and software [21].

Kamari et al. [31] focused on the advantages of using BIM-enabled VR technology in this context, such as improved visualization, collaboration, and communication, as well as the ability to simulate and analyze different scenarios. It could also potentially demonstrate how the use of BIM-enabled VR technology can lead to more sustainable building design and construction and improved cost-efficiency. However, the limitations of this paper were less explored interactive charcuteries with VR due to the lab shutdown and the project cost being unavailable such as indirect costs, direct costs, and other costs that could affect the decision-making [31].

Natephra et al. [32] investigated on how to use BIM and VR technologies for construction site safety planning. The study found that the integration of BIM and VR can improve the effectiveness and efficiency of safety planning. However, the study has a limitation in that the research was conducted on a small scale and the repeated lighting design processes were limited in the software and this software needs special knowledge and technical skills to handle the models [32].

This research is an effective tool that allows the project's owner to reduce the variation order by visually selecting his favorite material in the design stage. This study is unique from previous research because no other study has attempted to integrate cost estimating with the game engine and produce the (5-D) environment. Also, this paper appropriates an open game platform that helps owners, stakeholders, and students create their cost estimates in real-time from walkthrough interactions selecting multi-alternative building components.

3. METHODOLOGY

This study has a methodology that can be integrated with BIM with VR in 5 dimensions (i.e., 3D, time, and cost) for estimating project cost. Therefore, the project owner can use this system to navigate each item's cost in his project through VR visually. Figure 1 illustrates the BIM-VR system supporting project cost-estimating (CE). The BIM-VR-CE system included two main phases. BIM is the first phase that used AutoCAD, SketchUp, and Revit software to design 3-D models. The Revit software is utilized to create the project and accessories of the project (i.e., fences, trees, and furniture). All these 3-D models are running under the unity game engine software. These 3-D models have geometric information such as scale, and dimensions, and non-geometric details such as material types that be used internally and externally for the project. material types cannot be recognized by the Unity game engine unless they are not modified to the standard material types. The 3D-model files are exported to FBX files by using SketchUp or Revit software. The FBX file is opened through 3Ds Max software. The project materials are transformed into standard material types by using 3Ds Max software and then exported to FBX files. Also, it creates a database for all elements of the building. The process of creating the database is started by exporting the 3D-Models to an IFC file using SketchUp or Revit software. the IFC extracts the properties of each element (i.e., Absorptance, area, assembly code, assembly description, base extension distance, base offset, family name, length, extension distance, top offset, type name, unconnected height, and width). Also, it adds the cost estimate for each element and then adds the element alternatives and their costs to the database.

The second phase is VR. First, by using the Unity game engine imported the FBX file that was created by SketchUp or Revit software. then the real environment is set up for the project such as collision, gravity, and detection. Also, for navigating the project is set up the first-person controller is represented as the project's owner. To complete the virtual reality environment for the project, some game components are added to the project (e.g., land, cameras, streets, and lights). In this phase, C# scripts language is utilized. Developing a database with C# scripts allows the user to see the properties of the element when he looks at the element. Figure 2 shows the pseudo-code of developing a database. The C# script programming is utilized to allow the owner to select various material types for any element in the project. when this change occurs properties and cost estimates of the element are changed and calculate the difference in costs between the original element and the new element and save for the final step (i.e., Report).

Figure 3 shows the pseudo-code of changing materials, and properties and estimates the cost. It uses C# scripts to create the shaded element when the user looks at the element using the VR device to allow the user to select the right element. Once the users are satisfied and made their decisions, they go to the finish button to get the report; otherwise, all cost-estimating options can be iterated by the users until satisfaction is reached. To create the final report on the computer by the users, The C# scripts are used. The pseudo-code for creating the report is shown in Figure 4. The user can find the report on the computer in a specific folder. The report includes the final decision made by them such as the names of elements that were changed with new elements, the name of the new element, the estimated difference in cost between two elements, the total of all differences in costs, and the total cost of the project after the changes. These data are collected from previous steps. The report goes to the designer to make the changes in Revit, SketchUp, or AutoCAD.

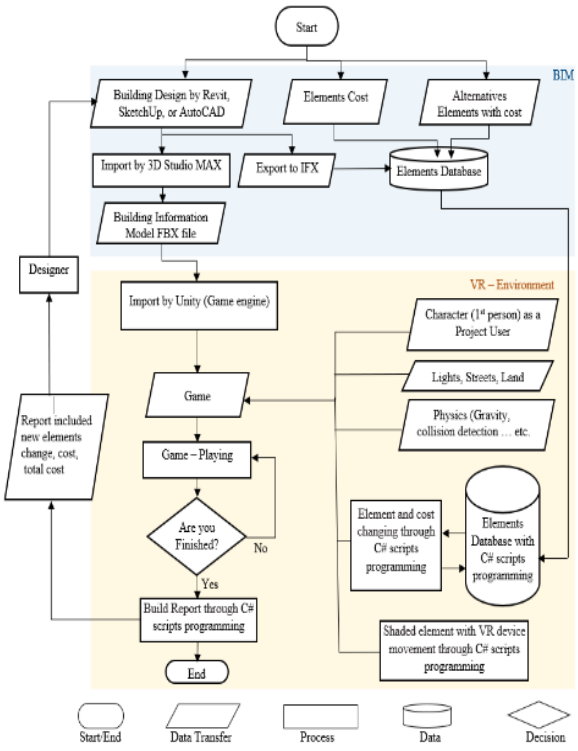

Figure 1. BIM-VR prototyping supports the process diagram for estimating costs

```
BEGIN
string d
case select element name #1
Output Display d = element descriptions "Absorptance, Area, Assembly Code, Assembly
Description, Base Extension Distance, Base Offset, Family Name, Length, Top Extension
Distance, Top Offset, Type Name, Unconnected Height, Width, Element Cost, Total cost.
break;
case select element name #2
Output Display d = element descriptions "Absorptance, Area, Assembly Code, Assembly
Description, Base Extension Distance, Base Offset, Family Name, Length, Top Extension
Distance, Top Offset, Type Name, Unconnected Height, Width, Element Cost, Total cost.
break;
.
.
.
case select element name #n
Output Display d = element descriptions "Absorptance, Area, Assembly Code, Assembly
Description, Base Extension Distance, Base Offset, Family Name, Length, Top Extension
Distance, Top Offset, Type Name, Unconnected Height, Width, Element Cost, Total cost.
break;
END
```

Figure 2. The pseudo-code of developing a database

```
BEGIN
String GameObject alternative 1
String GameObject alternative 2
.
.
String gameobject alternative n
double  a1
double  a2
.
.
Private double  an
Onmousedown
Display alternative texture and description
Hidden all other alternative textures and descriptions
If index.name = element 1 then
If Display existed element then a1 = 0
Else if Display alternative1 then a1 = cost of alternative1
.
.
Else if Display alternative1 then a1 = cost of alternative n
Open File
Write File (alternative name + " instead of " + existed element name + a1)
Close File
Open File
Write File (a1)
Close File
End if
If index.name = element 2 then
If Display existed element then a2 = 0
Else if Display alternative1 then a2 = cost of alternative1
.
.
Else if Display alternative1 then a2 = cost of alternative n
Open File
Write File (alternative name + " instead of " + existed element name + a2)
Close File
Open File
Write File (a2)
Close File
End if
.
If index.name = element n then
If Display existed element then an = 0
Else if Display alternative1 then an = cost of alternative1
.
.
Else if Display alternative1 then an = cost of alternative n
Open File
Write File (alternative name + " instead of " + existed element name + an)
Close File
Open File
Write File (a3)
Close File
End if
END
```

Figure 3. The pseudo-code of changing materials, properties, and estimating the cost

4. IMPLEMENTATION

The application of this study is designed to utilize VR for cost estimating of projects in a 5-D environment. The

```
BEGIN
string sa 1
string sa 2
.
.
string sa n
string ma 1
string ma 2
.
.
string ma n

OnMouseOver
sa 1 = Read File 1
sa 2 = Read File 2
.
.
sa n = Read File n

ma 1 = Read File n+1
ma 2 = Read File n+2
.
.
ma n = Read File m

OnMouseDown
Open File
Write File (" Report of changing materials and cost" sa 1 + sa 2 + … + sa n)
Write File ("The total differences in cost= " ma 1 + ma 2 + … + ma m)
Write File ("The Total Project cost = " exist total cost + ma 1 + ma 2 + … + ma m)
Close File
END
```

Figure 4. The pseudo-code for creating the report

BIM-VR is required when the project's owner needs to realize how the cost estimates influence the project. A VR device (i.e., Oculus Rift headsets + Joystick) is used to allow the client to navigate his project, and change any element in the project, as shown in Figure 5. There are many users had navigation capabilities which include forward and backward movement as well as turning right, or left, and jumping. The project's owner also interacts with the environment in real time. He cannot penetrate the wall of walls because of the activation of collision detection through the game engine. When the player walks into his project, he or she can deal with many alternatives for building, materials, furniture, or landscape. He can just look at any object and click it, the object will be changed, and its cost and feature will change simultaneously. The system can work under the Microsoft Windows system, the Xbox One system, the IOS system, and the Android system. the users used real building and put in the system and then made their decision. The results of using the system, the projects were less cost and better finishing selection, and fewer variation orders. There are four applications in this study.

In the first implementation, the project's owner can change the project's accessories such as gates, fences, landscape, and so on. The user puts on the VR headset

Figure 5. The user navigates the project with Oculus Rift headsets and Joystick devices

and looks at the construction accessory; simultaneously, it is shaded. the properties appear as information in the upper left corner, and then the client clicks on the construction accessory. The construction accessory is switched with an alternative construction accessory, and the information in the upper left corner informs the user of the new properties, the cost estimate of the construction accessory, and the total cost of the project. For example, the project's owner walks to the gate and looks and clicks on the gate. He or she can select from three different alternatives. The selections under each replacement are gate type (i.e., wood gate, steel gate, and modern gate), and the properties (i.e., height, length, material, cost per meter, and total cost), as shown in Figure 6.

In the second implementation, the project's owner can change objects in the landscape for the project such as a flower garden, garden shed, trees, children's play set, and so on. The player looks at an object, simultaneously the object is shaded, and the properties appear as information in the upper left corner, and then the client clicks on the object. The object is switched with an alternative object, and information in the upper left corner describes the new properties, cost estimate of the object, and total cost of the project. For example, the project's owner walks to the trees and looks and clicks on the trees. He or she can select from three different alternatives. The selections under each replacement are tree type (i.e., Palm, ForestVision_Lite_tree, and Pond pine), and the properties (i.e., Height, radius, cost each, number, cost, and total cost), as shown in Figure 7.

The most important application is the third application when the client wants to change elements in the building, like exterior walls, interior walls, stairs, roofs, and so on. The player looks at an element and simultaneously it is shaded, and the properties appear as information at the upper left corner, and then the client clicks on the element. The element is switched with the alternative element, and information at the upper left corner describes the new properties, cost estimate of the element, and total cost of the project. For example, the user moves to the front of the exterior wall, interior wall, and floor and looks and clicks on them. He or she can select from four different alternatives; a click shows each alternative. The selections under each replacement are exterior wall type (i.e., Exterior_Brick_on_CMU_30 _ [236056], Exterior_Stone siding _on_CMU_30, Exterior_Stuccosiding_on_CMU_30, and Exterior_Aluminumsiding_on CMU_30), the properties (i.e., Absorptance, area, assembly code, assembly description, base extension distance, base offset, family name, top extension distance, top offset, type name, unconnected height, width, cost, and total cost) as shown in Figure 8(a). The options under each alternative are interior wall type (i.e., Interior_-_4_7/8 inch_Partition_(1 - hr)_[248137], Interior_Marble Texture Wall Mural, Interior_Slate Wall Mural, and Interior_PVC Leandros EnduraWall Decorative 3D Wall Panel), the properties (i.e., Absorptance, area, assembly code, assembly description, base extension distance, base offset, family name, top extension distance, top offset, type name, unconnected height, width, cost, and total cost) as shown in Figure 8(b). The options under each alternative are exterior wall type (i.e., Generic_-_12 inch_10_[458745], Wood Flooring, Terrazzo (Marble Chips) Flooring, and Marble Flooring), the properties (i.e., Absorptance, area, assembly code, assembly description, thickness, elevation at bottom, elevation at

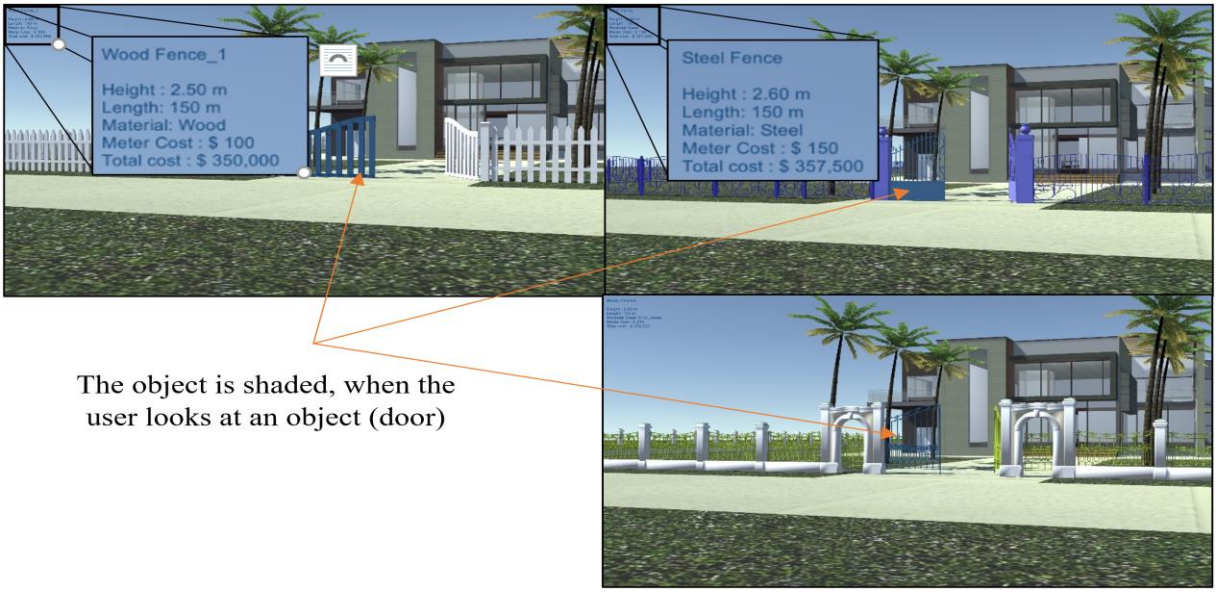

Figure 6. The first application shows the three alternatives for the fence

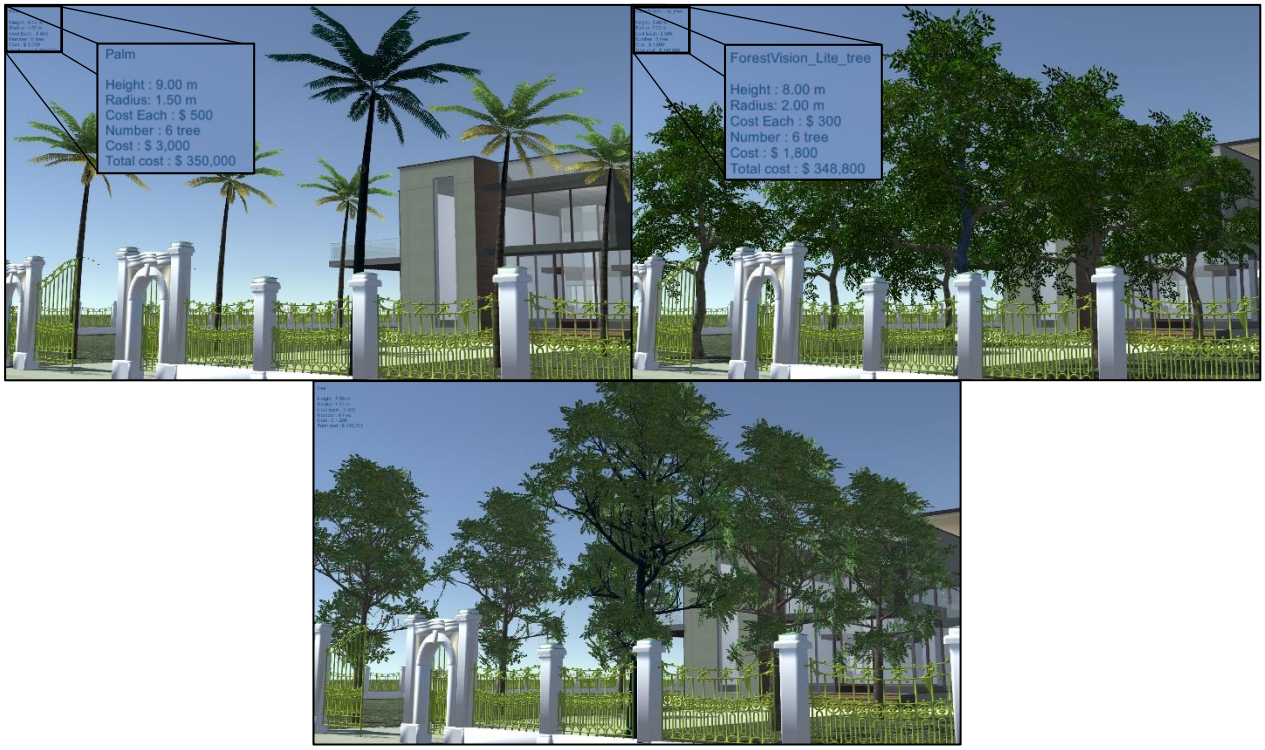

Figure 7. The second application shows the three alternatives for trees

top, family name, height offset from level, perimeter, thickness, type name, meter cost, total cost) as shown in Figure 8(c).

The fourth application is when the client wants to change the furniture in the buildings like kitchen furniture, sofas, dining tables, bedroom furniture, and so on. The user looks at an item of furniture; simultaneously the furniture is shaded, and the properties appear as information in the upper left corner, and then the client clicks on the furniture. The object is switched with alternative furniture and the information in the upper left corner informs the new properties, the cost estimate of the furniture, and the total cost of the project. For example, the user walks to the dining table and looks and clicks on it. He or she can select from four different alternatives.

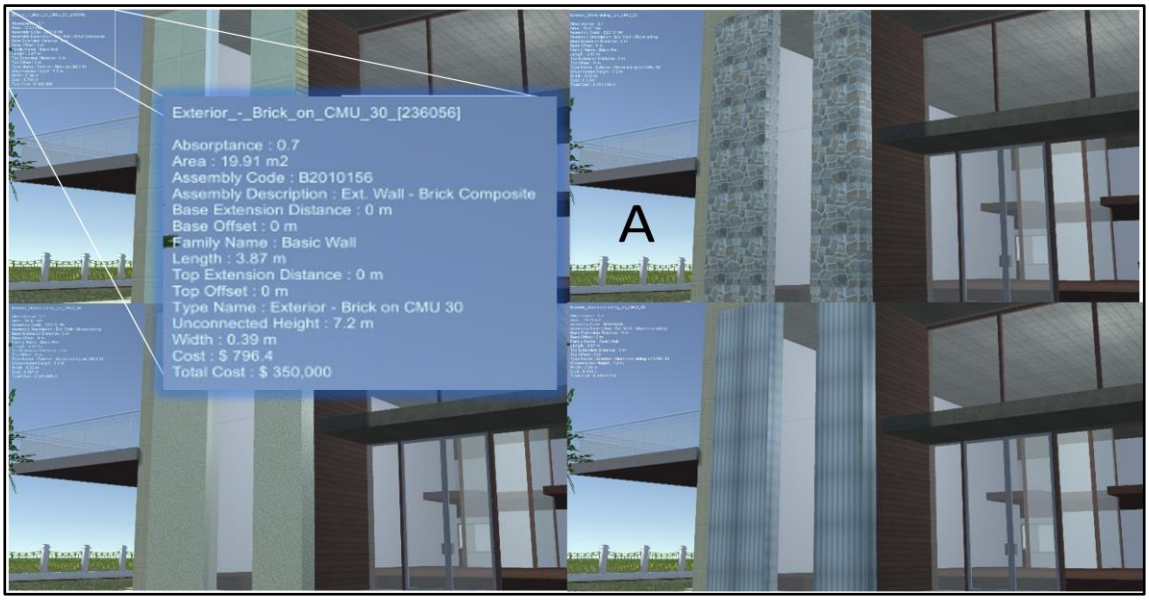

(a)

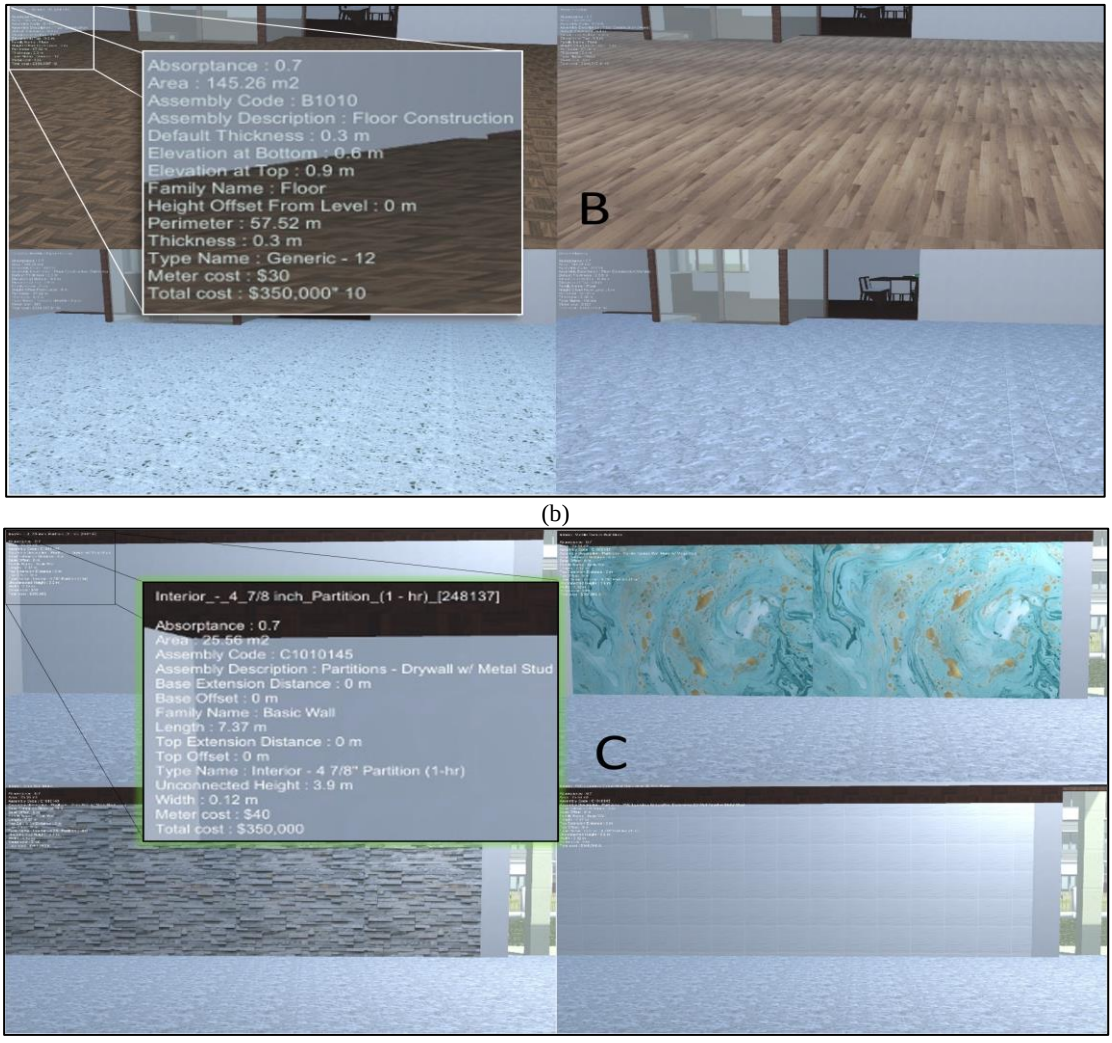

Figure 8. The third application shows (a) the four exterior wall alternatives (b) the four interior wall alternatives (c) the four-floor alternatives

The selections under each replacement are dining table type (i.e., Height, length, width, shape, number of Chairs, material, cost, and total cost), the properties (i.e., Height, radius, cost each, number, cost, and total cost) as shown in Figure 9.

Once the users are satisfied, they go to the finish button outside the project and click on it. The system tells them the location of the report on the computer, as shown in Figure 10. The users send the report to the designer or project manager to improve the project. The validation of this system is used by many users and they gave their notes about the system. The authors update the system according to the users' notes.

5. THE EVALUATION OF RESEARCH

The evaluation of any application is essential to give designer feedback. In this research, the evaluation questionnaire including five questions was created. The 5-point Likert scale ("5" Strongly Agreeing and "1" Strongly Disagreeing) was used to create the questions for the questionnaire. The BIM-VR-CE system was presented to the stakeholders. They were excited to experiment with the system. As a result, all participants finished the questionnaires. The participants who are complete the questionnaires are 85. Therefore, the size of the sample was 85 questionnaires. They used Oculus Rift headsets and Joystick devices individually to navigate the project before they responded to the survey questions, as shown in Figure 5.

The survey results were received, and all participants answer the questionnaires. the results of the analysis of the quantitative questionnaires are summarized in Table 1.

Before the analysis and discussion of the results of the evaluation, the chart of feedback results is created as shown in Figures 11 and 12.

Figure 9. The fourth application shows the four table alternatives

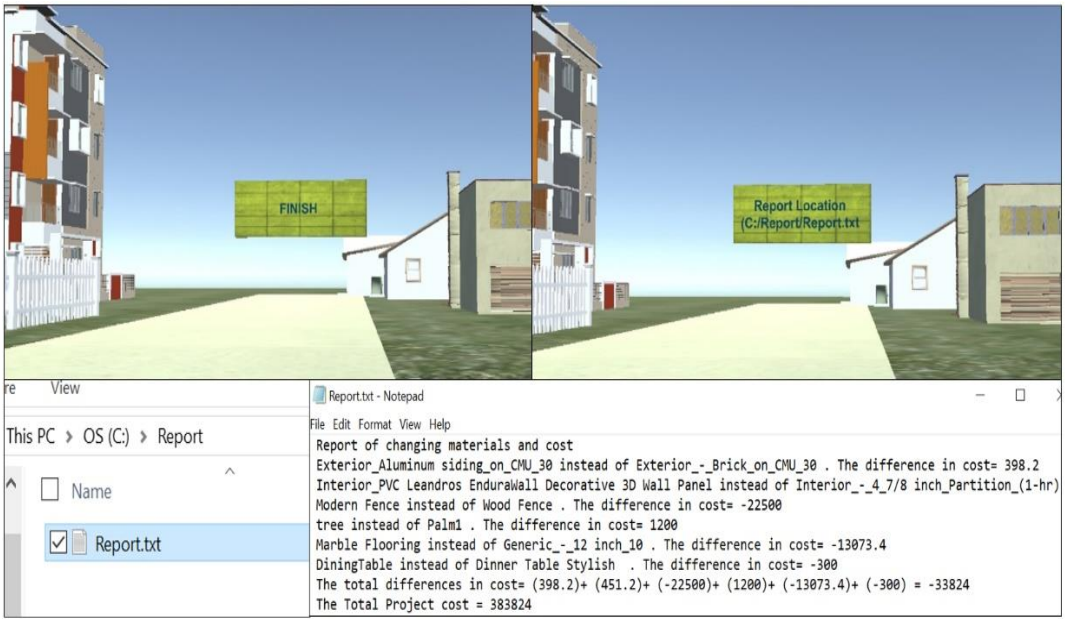

Figure 10. The final report process

TABLE 1. Results of quantitative questionnaires analysis

Question Description	Sample Size	Response Level (1 to 5) (%)					Average
		Strongly disagree	Disagree	Neutral	Agree	Strongly agree	
1- The simulation increased experience about estimating cost	85	0	0	12	36	37	4.29
2-The design of the simulation was easy to understand	85	0	0	3	18	64	4.72
3- The simulation reduced the change orders	85	0	0	6	23	56	4.59
4- The simulation enhanced my visualization experience about cost estimating	85	0	0	13	21	51	4.45
5- the simulation improved decision-making of cost estimates for future projects	85	0	0	16	35	34	4.21
Total	425	0	0	50	133	242	4.45

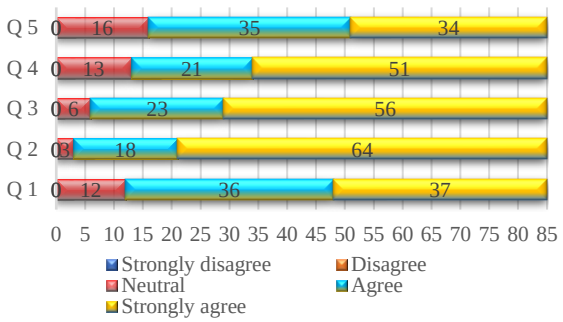

Figure 11. The feedback of the questionnaires

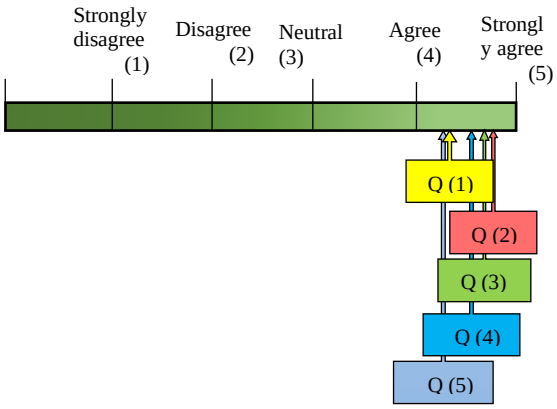

Figure 12. Questions Average

For question 1, the responses of participants were in a very good area, and the average of results is 4.29. That means the experience improved regarding cost estimates for participants. For question 2, responses showed an excellent result, and the average of results is 4.72. About 94% of the responses got positive feedback, indicating the simulation was easy to use and learn. Question 3 had a fantastic responses domain and the average of results is 4.59. This result indicts that if this system is used in any project, it will contribute to reducing the number of change orders. Question 4 as well as got an excellent value, and the average of results is 4.45. That means, the system enhanced the participants' realizing how the cost estimates for many element alternatives can affect their projects. Finally, question 5 had a very good evaluation, and the average result is 4.21. that indicts the shareholders improved their decision-making regarding cost estimates for future projects. All questions questionnaires got satisfaction, and the average is mean of 4.45, and the average result had a positive response of 89%.

6. DISCUSSION AND LIMITATION

The proposed BIM-VR system is found to be capable of assisting construction stakeholders to understand the art of cost estimation promptly and accurately. Also, it helps minimize costs through creates a 3D project model that can well be analyzed, and cost estimates made accurately. Through the participant evaluate the BIM-VR system, construction stakeholders found it easy to use. Moreover, the BIM-VR system is improved and enhanced their experience and decision-making regarding cost estimates, and it can be utilized to decrease the number of variation orders. The BIM-VR system can be applied to any project, building, or element in the building and it can give the owners satisfying element selection within a suitable cost. On the other hand, the BIM-VR system has limited alternatives for elements in the project. To solve this problem, we can use all possible alternatives for elements dependent on element important that can be defined by the owner.

7. CONCLUSION

1. In this research, the integration between BIM, VR, and CE was developed and presented. BIM, VR, and CE are working under the game engine to enhance visualization and educate students about project cost estimates.
2. The study provided the project's owner with a system that can interact with the real-time environment for cost estimating. creating a first-person view with a VR device, as well as street, land, and lighting were created to develop realistic surroundings.
3. The programming (i.e., C# scripts) was used to create a database that interfaces between project elements and the user, to change elements, properties, and cost estimates simultaneously. The programming is also used for creating the shaded element when the user looks at it and developing a report to inform the stockholder about the changes that occurred through using the system. The BIM-VR-CE system allows the integration of many components including building modeling information, virtual reality, cost estimating, navigation, and animation through using Autodesk software and Unity game engine.
4. The benefit of the BIM-VR-CE system has supported the decision-making of owners regarding cost estimating and minimized the variation order. Also, it is supported cost estimation education by implementing a platform that allows various cost estimates of projects to be evaluated through game playing.
5. A questionnaire was generated to evaluate the effectiveness of the BIM-VR-CE. The questionnaire result indicated that the BIM-VR-CE system could be used and understood easily. Also, the visualization and the knowledge regarding cost estimating are enhanced for participants. BIM-VR-CE system can be used to promote decision-making concerning cost estimates for future projects. additionally, the BIM-VR can be used

to reduce the number of variation orders. The overall BIM-VR system had excellent satisfaction from participants.

8. REFERENCES

1. Enshassi, A., Mohamed, S. and Modough, Z., "Contractors' selection criteria: Opinions of palestinian construction professionals", ***International Journal of Construction Management***, Vol. 13, No. 1, (2013), 19-37.
2. Shash, A.A. and Ibrahim, D., "Survey of procedures adopted by a/e firms in accounting for design variables in early cost estimates", ***Journal of King Saud University-Engineering Sciences***, Vol. 18, No. 1, (2005), 1-16.
3. Larson, E.W. and Gray, C.F., "Project management: The managerial process (special indian edition), Tata McGraw-Hill Education, (2006).
4. East, B. and Smith, D., "The united states national building information modeling standard: The first decade", in 33rd CIB W78 Information Technology for Construction Conference (CIB W78 2016), Brisbane, Australia., (2016).
5. Holness, G., "Bim gaining momentum.[article]", ***ASHRAE Journal***, Vol. 50, No. 6, (2008), 28-40.
6. Sunesson, K., Allwood, C.M., Paulin, D., Heldal, I., Roupé, M., Johansson, M. and Westerdahl, B., "Virtual reality as a new tool in the city planning process", ***Tsinghua Science and Technology***, Vol. 13, No. S1, (2008), 255-260. doi: 10.1016/S1007-0214(08)70158-5.
7. Eastman, C.M., Teicholz, P., Sacks, R. and Liston, K., "Bim handbook: A guide to building information modeling for owners, managers, designers, engineers and contractors, John Wiley & Sons, (2011).
8. Bouchlaghem, D., Shang, H., Whyte, J. and Ganah, A., "Visualisation in architecture, engineering and construction (AEC)", ***Automation in Construction***, Vol. 14, No. 3, (2005), 287-295.
9. Westerdahl, B., Suneson, K., Wernemyr, C., Roupé, M., Johansson, M. and Allwood, C.M., "Users' evaluation of a virtual reality architectural model compared with the experience of the completed building", ***Automation in Construction***, Vol. 15, No. 2, (2006), 150-165.
10. Mobach, M.P., "Do virtual worlds create better real worlds?", ***Virtual Reality***, Vol. 12, No. 3, (2008), 163-179. https://doi.org/10.1007/s10055-008-0081-2
11. Han, K.K. and Golparvar-Fard, M., "Appearance-based material classification for monitoring of operation-level construction progress using 4d bim and site photologs", ***Automation in Construction***, Vol. 53, (2015), 44-57.
12. Poussard, B., Loup, G., Christmann, O., Eynard, R., Pallot, M., Richir, S., Hernoux, F. and Loup-Escande, E., "Investigating the main characteristics of 3d real time tele-immersive environments through the example of a computer augmented golf platform", in Proceedings of the 2014 Virtual Reality International Conference., (2014), 1-8.
13. Sampaio, A. and Mota, C., "Bim model of structures used in construction planning", in Proceedings of the National Meeting of Structural Concrete. BE2016, Coimbra, Portugal., (2016), 2-4.
14. Charef, R., Alaka, H. and Emmitt, S., "Beyond the third dimension of bim: A systematic review of literature and assessment of professional views", ***Journal of Building Engineering***, Vol. 19, (2018), 242-257. http://dx.doi.org/10.1016/j.jobe.2018.04.028
15. McArthur, J., "A building information management (bim) framework and supporting case study for existing building operations, maintenance and sustainability", ***Procedia engineering***, Vol. 118, (2015), 1104-1111.
16. Goulding, J.S., Rahimian, F.P. and Wang, X., "Virtual reality-based cloud bim platform for integrated aec projects", ***Journal of Information Technology in Construction***, Vol. 19, (2014), 308-325.
17. Omaran, S.M., Alghamdi, A.A., Alharishawi, S.C. and Hains, D.B., Integrating bim and game engine for simulation interactive life cycle analysis visualization, in Computing in civil engineering 2019: Visualization, information modeling, and simulation. 2019, American Society of Civil Engineers Reston, VA.120-128.
18. Du, J., Shi, Y., Mei, C., Quarles, J. and Yan, W., "Communication by interaction: A multiplayer vr environment for building walkthroughs", in Construction Research Congress 2016., (2016), 2281-2290.
19. Rho, J. and Kim, J., "Cs10427: Virtual-augmented reality for construction, utilizing gear vr", ***Autodesk University***, (2015).
20. J., B., "Bim goes virtual: Oculus rift and virtual reality take architectural visualization to the next level.", (2014).
21. Sampaio, A.Z., "Enhancing bim methodology with vr technology", State of the Art Virtual Reality and Augmented Reality Knowhow, Vol. 59, (2018), 79.
22. Jiao, Y., Zhang, S., Li, Y., Wang, Y. and Yang, B., "Towards cloud augmented reality for construction application by bim and sns integration", ***Automation in Construction***, Vol. 33, (2013), 37-47.
23. Azhar, S., "Building information modeling (BIM): Trends, benefits, risks, and challenges for the aec industry", ***Leadership and Management in Engineering***, Vol. 11, No. 3, (2011), 241-252. https://doi.org/10.1061/(ASCE)LM.1943-5630.0000127
24. Aamran, S.M., "Establishing reform system for preparing bills of quantities", ***Engineering and Technology Journal***, Vol. 30, No. 15, (2012).
25. Al-Attar, T.S., Al-Zuheriy, A.S.J. and Hamza, S.M., "Optimum steel fiber content of high strength pozzolime concrete", ***Engineering and Technology Journal***, Vol. 39, No. 12, (2021), 1869-1874. http://doi.org/10.30684/etj.v39i12.2213
26. عمران, س.م., "Establishing total quality management application system for school building projects in iraq", ***Engineering and Technology Journal***, Vol. 28, No. 14, (2010).
27. AlizadehKharazi, B., Alvanchi, A. and Taghaddos, H., "A novel building information modeling-based method for improving cost and energy performance of the building envelope", ***International Journal of Engineering, Transactions B: Applications***, Vol. 33, No. 11, (2020), 2162-2173. doi: 10.5829/IJE.2020.33.11B.06.
28. Mollaei, H., Tavakkoli-Moghaddam, R. and Toloie-Eshlaghy, A., "A new multi-objective model for multi-mode project planning with risk", ***International Journal of Engineering, Transactions B: Applications***, Vol. 31, No. 5, (2018), 770-779. doi: 10.5829/ije.2018.31.05b.12.
29. Ghanem, S.Y., "Implementing virtual reality-building information modeling in the construction management curriculum", ***J. Inf. Technol. Constr.***, Vol. 27, (2022), 48-69. doi: 10.36680/j.itcon.2022.003.
30. Abbasnejad, B., Aranda-Mena, G., Nasirian, A., Wong, P.S. and Ahankoob, A., "Implementation of integrated bim-vr into construction management curriculum: Lessons learned and development of a decision support system", in IOP Conference Series: Earth and Environmental Science, IOP Publishing. Vol. 1101, (2022), 092029.
31. Kamari, A., Paari, A. and Torvund, H.Ø., "Bim-enabled virtual reality (vr) for sustainability life cycle and cost assessment", ***Sustainability***, Vol. 13, No. 1, (2020), 249. doi: 10.3390/su13010249.
32. Natephra, W., Motamedi, A., Fukuda, T. and Yabuki, N., "Integrating building information modeling and virtual reality development engines for building indoor lighting design", ***Visualization in Engineering***, Vol. 5, (2017), 1-21. https://doi.org/10.1186/s40327-017-0058-x

Persian Abstract

چکیده

منابع علمی و تحقیقات قبلی نشان داد که کاهش ترتیب تغییرات با انتخاب مواد مورد علاقه به صورت بصری توسط مالک پروژه در مرحله طراحی اخیراً در دسترس نیست. به عنوان یک مشکل، برآورد هزینه در زمان واقعی از تعاملات متوالی انتخاب اجزای ساختمانی چند جایگزین یک تهدید بالقوه برای موفقیت پروژه ها است، مگر اینکه یک سیستم تجسم وجود داشته باشد که به تصمیم گیری در مورد هزینه های اقلام مختلف ساختمان و مناسب بودن اقلام کمک کند. . این تحقیق ابزار قدرتمندی است که به صاحب پروژه اجازه می دهد تا با انتخاب بصری مواد مورد علاقه خود در مرحله طراحی، ترتیب تنوع را کاهش دهد. این کاربرد مدل سازی اطلاعات ساختمان (BIM)با واقعیت مجازی (VR)را برای بهبود برآورد هزینه (CE)و فرآیند انتخاب مصالح بیان می کند. محققین از فناوری BIM و واقعیت مجازی برای افزایش تجسم و پردازش برآورد هزینه پروژه در صنعت ساخت و ساز استفاده می کنند. در این مطالعه، هدف اولیه توسعه یک سیستم BIM-VR-CE است که به ذینفعان ساخت و ساز کمک می کند تا هزینه های اقلام مختلف ساختمان و مناسب بودن اقلام را تجسم کنند و به سرعت تصمیم بگیرند. بر این اساس، نویسندگان یک سیستم BIM-VR-CE را توسعه دادند که فناوری BIM و واقعیت مجازی را با استفاده از Unity 3D یکپارچه می کند. پیمایش محیط های ساختمانی به صورت بلادرنگ با قابلیت انتخاب هزینه و موارد مناسب برای عناصر پروژه، اکنون از طریق نمونه اولیه BIM-VR توسعه یافته در این مقاله در دسترس ذینفعان ساخت و ساز است. برای ارزیابی اثربخشی مدل اولیه پیشنهادی، پرسشنامه ای ایجاد شد و ۸۵ ارزیابی جمع آوری شد. یافته‌های این مقاله پتانسیل قابل‌توجهی را برای استفاده از مدل پیشنهادی در پروژه‌های ساختمانی برای مقابله با هزینه، کاهش سفارش‌های تغییرات و انتخاب عناصر مورد علاقه نشان می‌دهد.

International Journal of Engineering

Journal Homepage: www.ije.ir

Pupil Center Detection Using Radial Symmetry Transform to Measure Pupil Distance in the Eye

J. Utama*, V. R. L. Fitriani

Faculty of Engineering and Computer Science, Universitas Komputer Indonesia, Bandung, Indonesia

P A P E R I N F O

Paper history:
Received 10 December 2022
Received in revised form 30 January 2023
Accepted 14 Febuary 2023

Keywords:
Pupil Distance
Radial Symmetry Transform
Self Quotient Image
Euclidean Distance

A B S T R A C T

In patients with refractive errors or impaired vision, light rays received by the pupil do not fall directly onto the retina. This can be corrected by wearing monocled glasses. The focal point of the eyeglass lens needs to be adjusted to the center of the user's pupil. This can be known through the measured pupil distance (PD) value information. The measurement of the PD is very important to determine the center distance of the pupils in both eyes. where the eye does not experience the prism effect. This study aims to apply the radial symmetry transformation (RST) method combined with self-quotient (SQI) imagery to detect the pupillary center and measure PD. This algorithm combines to get more optimal results in detecting the center of the pupil in dark conditions or those exposed to shadow illumination. The program created using the MATLAB software simulates PD measurements for pupillary center detection in bright and dark images conditions. The test was carried out ten times, and the results showed that the system was able to measure PD on low-resolution images of 300 x 300 pixels at 72 dpi in bright image conditions; with measurement uncertainty values in each image of 0.60 mm. As for testing on dark images, the uncertainty values are 0.80 mm. In this case, the standard deviation value is obtained from the effect of the different dimensions of the face object on the tested image.

***doi**: 10.5829/ije.2023.36.05b.04*

1. INTRODUCTION

Glasses can help improve the quality of vision because they use lenses to regulate the light rays entering the eye. Light passing through the lens will be focused on one point and directed to the eyes via the pupil [1]. The light that enters the eye will be focused first at a point called the optical center (OC), which is located on the eyeglass lens so that the light that can be received by the pupil is right on the retina. The OC needs to be adjusted to the pupil distance, also called pupil distance (PD), to be comfortable when using glasses [2]. It is important to measure PD to determine the distance between the pupillary locations in both eyes so as not to experience prism effects or irregular focus shifts [3]. However, the PD measurement is still often skipped for time effectiveness in the examination because the measurement is still done manually by the examiner using the PD ruler or with tools such as the pupilometer [1]. The estimated time during the examination can be minimized by the presence of an automatic system for measuring pupil distance that utilizes image processing on photos or images of eye objects [4, 5].

Research conducted by Harto and Rahmani [6] utilized PD values for facial recognition systems. The system takes the face area to be converted from a color image into a grayscale image and then uses the Viola-Jones method, which focuses on cropping the eye area. The eye area image will go through several filter processes until the system can detect the pupil of the eye. The search for the centroid of the pupil of the eye is used to calculate the PD value by calculating the Euclidean distance, which will be displayed in pixels. This value will be used as a parameter by the system to recognize a person's face [6]. The pupil of the eye has the same shape as the iris, which is round. The existence of a characteristic pupil shape is used by some researchers as a way to detect it. Research conducted by Vázquez in

*Corresponding Author Institutional Email: jana.utama@email.unikom.ac.id (J. Utama)

Please cite this article as: J. Utama, V. R. L. Fitriani, Pupil Center Detection Using Radial Symmetry Transform to Measure Pupil Distance in the Eye, ***International Journal of Engineering, Transactions B: Applications***, Vol. 36, No. 05, (2023) 870-878

detecting the center of the pupil was carried out using four methods, namely the Circular Hough Transform (CHT), Ellipse Fitting (EF), Integro-Differential Operator (IDO), and Radial Symmetry Transform (RST). The result of the experiment in detecting the pupillary center is that the RST method is better in terms of accuracy and robustness than other types of methods. RST has the advantage of being robust when detecting the center of the pupil under disturbance conditions such as the presence of glasses, eyelashes, or the reflection of light in the eye image. This is because the disturbance is not affected by the radial shape which is ignored when the system is running compared to three other methods such as CHT which is still easily disturbed by objects around the eye and results in inaccurate detection results. EF relies on the use of a threshold which results in the detection process being disturbed by other objects around the eye area, especially objects with dark colors, and IDO utilizes the contours of objects. The presence of other elements that appear around the eye area causes the contours of the pupil object to be disrupted and has an impact on the inaccuracy of the prediction of the detected pupil center [7]. In low-resolution images [8], such as those produced by webcam cameras, the center of the pupil of the eye can be detected properly using the RST method [9, 10]; because this method works well in detecting the center point of an object. Lyasheva et al. [11] proved it through a comparison of the Hough method with the Fast Radial Symmetry Transform (FRST) in counting the number of objects, with the FRST method being able to detect the number of objects through the proximity level of the detected pupillary center. Similarly to that study, Ram and Rodríguez [12] tested FRST in detecting the number of nuclear cells by detecting the object's center. The research conducted by Zafari et al. [13] is FRST testing on overlapping objects that give good segmentation results through the detection of the center of the object.

However, the RST performance is less than optimal in dark-state images. The use of the self-quotient image (SQI) has the advantage of reducing the illumination or shadow in the image. SQI can remove shadows in dark areas of the image [14-16]. In addition, there are also Multi-Scale Retinex and Histogram Equalization [17] which are used for face illumination. Multi-Scale Retinex has an advantage for image improvement in terms of SNR (Signal to Noise Ratio), but the histogram distribution is not evenly distributed in improving images. Histogram Equalization can improve the illumination effect on dark images by equalizing the spread of the histogram to reduce the illumination effect on the image. SQI was used in the experiment because it does not destroy important information in low quality images such as edges. Once the pupil has been detected by the system, the next most important part is measuring the distance between the two pupils. This distance can be measured with Euclidean measurement, which is a calculation method for measuring the distance between two points in Euclidean space [18, 19].

2. METHOD

RST is one of the methods used to detect the center point of an object, especially objects that have circular characteristics. RST can work optimally on this object. The advantages of RST, which can optimally detect the center point of a circular object, are utilized in finding the center point of the pupil of the eye because of the characteristic circular shape of the pupil. The search area for the center of the pupil will focus on the negative area (p-ve), or the area with a low level of gray because the pupil has the darkest color of the rest of the eye.

At first, the pupillary area boundary is sought to determine the edge of the area around the pupil. This edge will follow the shape of the circle around the pupil, the iris. The known edge of the circle is then used as a place to consider the number of points that can be formed into a line of radius n. The magnitude of the radii value given to the system influences the radius n. The radii then meet and intersect at the center of the circle (p). The point of intersection at the center of the circle resulting from the radius n becomes a marker of the position of the center of the pupil that has been detected by RST, as illustrated in Figure 1. The range of n to be used is a minimum of 7 and a maximum of 11. The point of marking the center of the pupil can be confirmed by the large alpha value given to the system. The clarity of the point as a marker can be set by its thickness at the given standard factor value.

In dark images, the eye area on the face is often affected by the illumination of shadows. Information obtained in the pupillary area of the eye becomes difficult to obtain. This has an impact on the RST method when searching for a disturbed pupillary center due to the interference factor. SQI is a solution so that the detection of pupillary centers by RST can be carried out optimally, especially in dark images. SQI was used in the

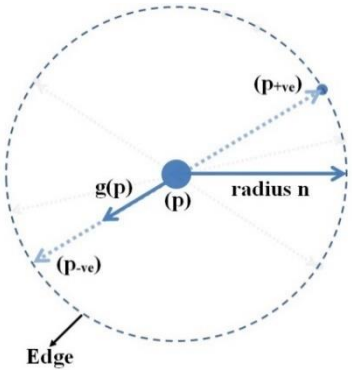

Figure 1. Center Point Detection on RST

experiment because it does not destroy important information in low quality images such as edges. The SQI method works to separate intrinsic elements as identity in images that are mixed with extrinsic elements such as shadow illumination in images. In accordance with system requirements because it tests cropping images of the eye with low image quality. As shown in Figure 2 for image enhancement using SQI, shadows in the area around the eyes are reduced and the image is created in a bright state. The histogram on SQI shows that the image tends towards a graylevel value of 255 (white in color) with brighter images compared to MSR and HE. The shadow effect on the image can be reduced through an image separation process based on extrinsic elements, namely the effect of shadow illumination, and an intrinsic element, namely the object in the image itself. The results of image improvement by SQI help RST detect the center of the pupil more accurately in dark images.

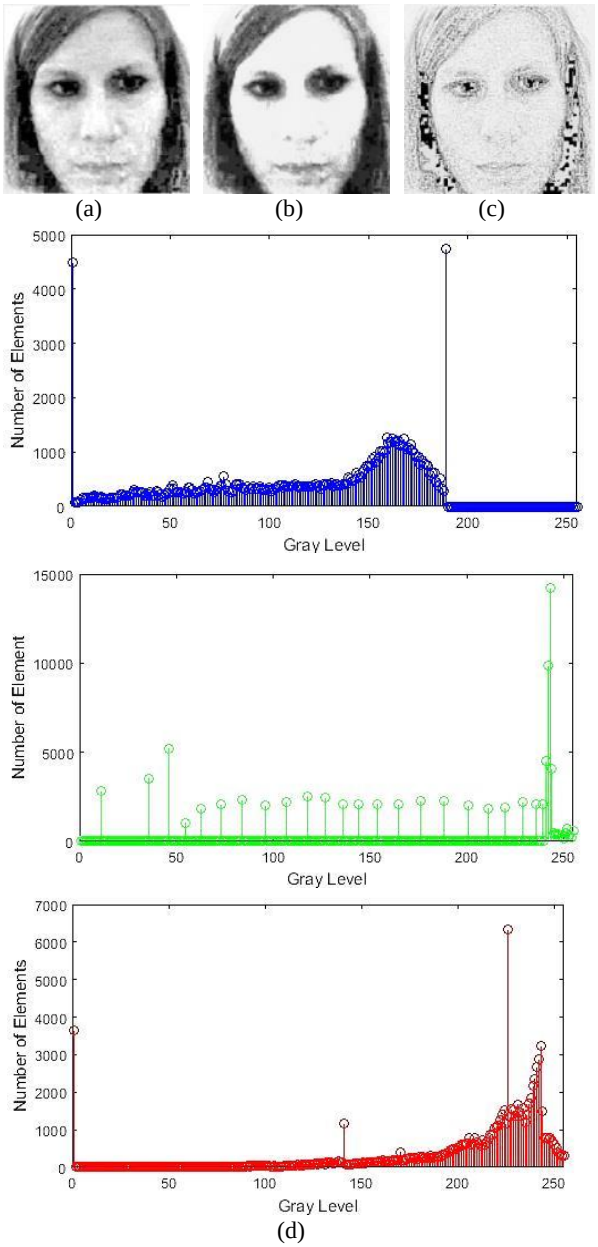

Figure 2. Comparison of (a) MSR, (b) HE, and (c) SQI in correcting dark images. Also presented are (d) histograms of each method; blue for MSR, green for HE, and red for SQI

2. 1. PD Measurement System Design The system created is a simulation that implements the RST method combined with SQI in detecting the center of the pupil to determine the size of the pupil distance (PD). Images with bright or dark conditions are used in the test. The image processing process can be seen in the block diagram in Figure 3.

Detects pupillary center distance, measured as the PD value, in images using datasets from MPIIGaze shown in Figure 4 and Real Self-Portraits in Figure 5. MPII Gaze are datasets containing face image data on 15 different models of people using their laptops daily for three months with a total of 213,659 images with an image resolution of 1280 x 720 pixels at 96 dpi. Real Self-Portrait datasets are a collection of real face images taken using a mobile phone camera on 2 different models of people with a total of 40 images. The use of different cameras makes the resolution of the image different for each model. The first model has a resolution of 2448 x 2448 pixels at 72 dpi and the second model has a resolution of 2576 x 1932 pixels at 72 dpi. The resolution for each dataset image will be changed and uniformed to a size of 300 x 300 pixels at 72 dpi to suit the system so it can work optimally. Done by processing the image to get information about the distance to the center of the pupil. The image used is an image that shows the face area with a straight head facing the camera. This system was built using Matlab 2015a software.

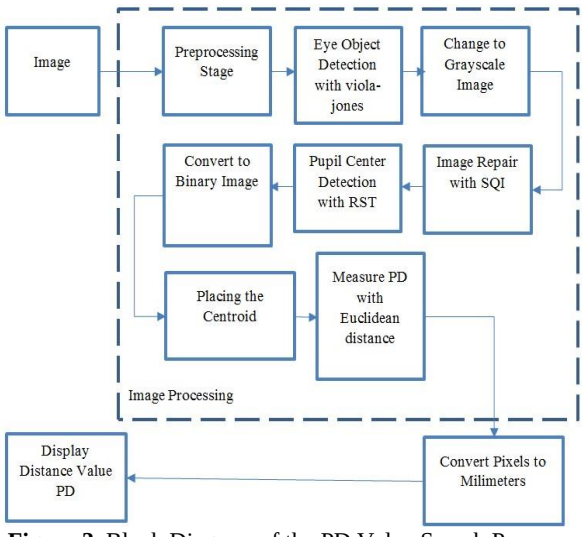

Figure 3. Block Diagram of the PD Value Search Process

Figure 4. Image of MPII Gaze Dataset

Figure 5. Image of Real Self-Photo Dataset

2. 1. 1. Eye Detection with Viola-Jones The object area in the image will be focused on the eye area. As shown in Figure 6, the system will automatically crop the eye area using the Viola-Jones method. The cropped image is used as an object that is focused on detecting the center of the pupil.

2. 1. 2. Converting RGB Image to Grayscale and Image Improvement with SQI Figure 7 shows the cropped area of the eye that is converted from an RGB image to a grayscale image. In the eye area that is disturbed by shadow illumination, the image is then corrected by SQI. This process is done to reduce the shadow effect that interferes with the system's ability to detect the center of the pupil.

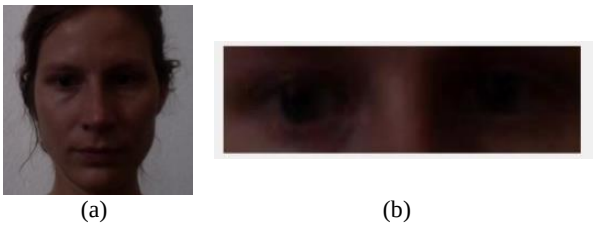

(a) (b)

Figure 6. Eye Area Cropping Process on (a) Original Image and (b) Cropping Results

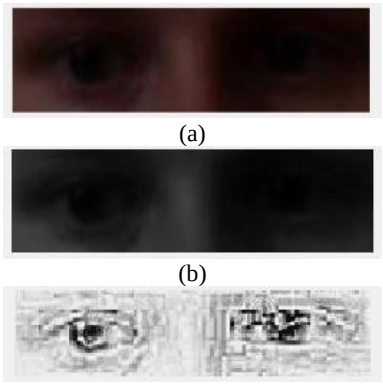

(a)

(b)

(c)

Figure 7. The Process of Changing Color and Image Quality with (a) RGB Image, (b) Grayscale Image, (c) Image Improvement Results with SQI

2. 1. 3. Detection of the Pupil Center with RST The corrected image generated by SQI is then used for the pupillary center detection process using RST, which is shown in Figure 8. The pupil center can be detected at the point of intersection of the n-radius line formed around the pupil. The magnitude of the given radii value determines the number of radii n.

2. 1. 4. Placement of Centroids to Measure PD Value The detected pupil center point in the form of a binary image is then marked using a centroid. The PD measurement results are obtained from the calculation of the distance between the first centroid (Point 1) and the second centroid (Point 2) as shown in Figure 9 using Equation (1) from the Euclidean method.

$$d(x.y) = \sqrt{\sum_{i=1}^{n}(x_i - y_i)^2} \quad (1)$$

The measurement results are then divided by a reference value of 1.325 pixels per millimeter so that the resulting PD value is in millimeter units.

2. 2. System Design with Simulation The system was tested on the image dataset that has been provided, namely Real Self-Portraits taken using a mobile phone camera and images from the MPII Gaze dataset. The PD

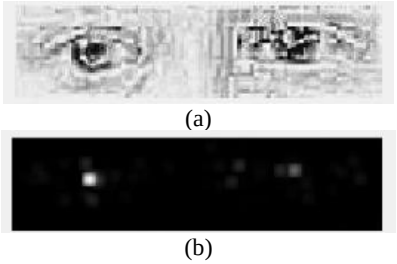

(a)

(b)

Figure 8. Pupil Center Detection Process with (a) SQI Corrected Image and (b) Pupil Center Detection Results by RST in Binary Image

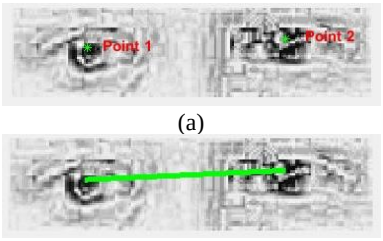

(a)

(b)

Figure 9. Measurement of PD by the system by (a) Marking the Pupil Center Point with Centroids and (b) Giving Illustration with Lines for PD Distance

measurement process is carried out by displaying the simulation through the MATLAB GUI as the interface. The system process in detecting the pupillary center using RST combined with SQI to measure the PD value which is shown Figure 10 by the flowchart.

3. RESULT AND DISCUSSION

The test was carried out using two datasets, namely the MPII gaze dataset and the Real Self-Photo dataset. The MPII Gaze dataset is used to test the system's ability to detect the center of the pupil in the image in bright or dark conditions as well as the success of the system in measuring PD distance. While the Real Self-Photo dataset is used for the comparison of PD values to know the accuracy of PD measurements made by the system.

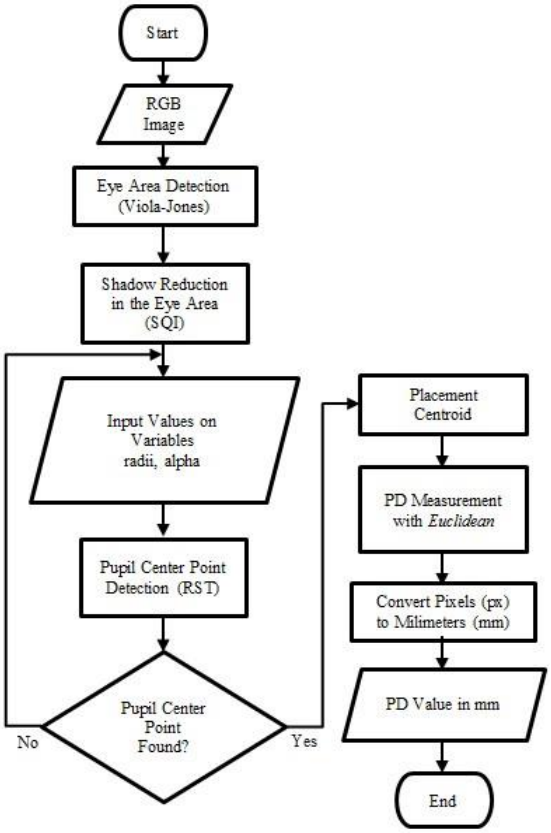

Figure 10. Flowchart of Automatic PD Measurement System

3. 1. Testing PD Measurements Tests in the form of simulations are carried out through the MATLAB GUI intermediary in displaying the pupil center detection process to measure the pupil distance (PD) in the eye. The test was carried out Real Self-Potraits and MPII Gaze dataset with various light conditions on objects of two different people. The test is done by using the image from the MPII Gaze dataset to detect the center of the pupil. There are two lighting conditions in the image, namely a bright state in Figure 11 and a dark state in Figure 12.

Figure 13 shows the PD measurements made by the system with size information in pixels (px) as well as millimeters (mm) using a low-resolution image of 300 x 300 pixels with 72 dpi, this resolution is the minimum limit for the system to work optimally and make the image at the lowest resolution. The test was carried out ten times on the same object model but there were various positions of the eye glances in each lighting state of the image shown in Figure 13. The experimental results were generated from 60 images from MPIIGaze and Real Self-Portraits like the example shown in Figure 14, consisting of 18 images with glasses and 42 without glasses.

3. 2. Evaluation Previously on Real Self-Potraits manual measurements had been carried out using the PD ruler as shown in Figure 15 with a PD range in general is

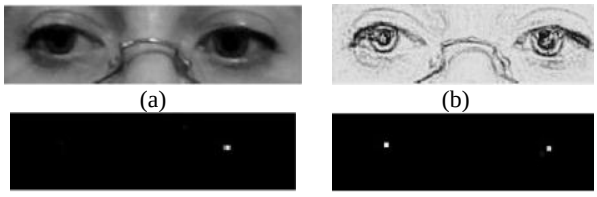

(a) (b)

(c) (d)

Figure 11. Detection of the Pupil Center on a Bright Image use radii n = 8 with (a) Grayscale Image, (b) Image Quality Improvement with SQI, (c) Pupil Center Detection with RST, and (d) Pupil Center Detection with RST Improve SQI

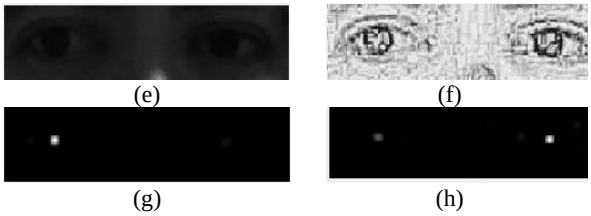

(e) (f)

(g) (h)

Figure 12. Detection of the Pupil Center in a Dark Image use radii n = 11 with (e) Grayscale Image, (f) Image Quality Improvement with SQI, (g) Pupil Center Detection with RST, and (h) Pupil Center Detection with RST Improve SQI

(a) (b)

Figure 13. Measurement of PD on Bright Image with Value (a) 63.1 mm and PD in Dark Image (b) 63.0 mm

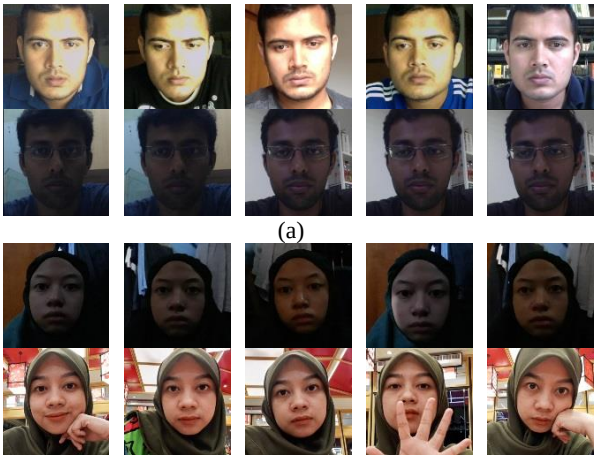

(a)

(b)

Figure 14. Bright State and Dark State Image from (a) MPIIGaze Dataset and (b) Real Self-Photograph Dataset

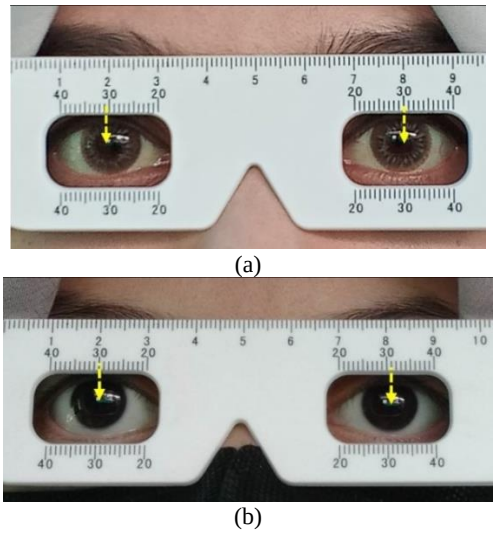

(a)

(b)

Figure 15. Manual Measurement Using PD Ruler with Image PD Value (a) 61 mm and (b) 61 mm

58-70 mm. The PD value data in Tables 1 and 2 will then be compared with the manual PD value to determine the percentage of system accuracy in measuring PD. Then, Tables 3 and 4 presents pure PD value data because MPIIGaze does not have a manual PD value. This data will be processed with a standard deviation to find out the value of the uncertainty in the PD measurement carried out by the system.

TABLE 1. Test Results on Real Self-Potraits with Bright Conditions

Image	PD (px)	PD (mm)	x_1^2
		x_1	
1	81.35	61.4	3769.96
2	80.67	60.9	3708.81
3	80.74	60.9	3708.81
4	79.59	60.1	3612.01
5	81.63	61.6	3794.56
6	81.53	61.5	3782.25
7	80.62	60.8	3696.64
8	82.06	61.9	3831.61
9	79.61	60.1	3612.01
10	80.66	60.9	3708.81
n = 10		$\sum x_1$ = 610.1	$\sum x_1^2$ = 37225.47

TABLE 2. Test Results on Real Self-Potraits with Dark Conditions

Image	PD (px)	PD (mm)	x_2^2
		x_2	
1	79.64	60.1	3612.01
2	77.09	58.2	3387.24
3	79.68	60.1	3612.01
4	79.55	60.0	3600.00
5	81.43	61.5	3782.25
6	79.55	60.0	3600.00
7	78.98	59.6	3552.16
8	79.61	60.1	3612.01
9	80.80	61.0	3721.00
10	80.33	60.6	3672.36
n = 10		$\sum x_2$ = 601.2	$\sum x_2^2$ = 36151.04

TABLE 3. Test Results on MPIIGaze with Bright Conditions

Image	PD (px)	PD (mm)	x_3^2
		x_3	
1	88.51	66.8	4462.24
2	89.06	67.2	4515.84
3	90.66	68.4	4678.56
4	88.51	66.8	4462.24
5	88.50	66.8	4462.24
6	88.29	66.6	4435.56
7	88.59	66.9	4475.61
8	90.27	68.1	4637.61
9	90.71	68.5	4692.25
10	88.91	67.1	4502.41
n = 10		$\sum x_3$ = 673.2	$\sum x_3^2$ = 45324.56

TABLE 4. Test Results on MPIIGaze with Dark Conditions

Image	PD (px)	PD (mm) x_4	x_4^2
1	87.25	65.8	4329.64
2	90.02	67.9	4610.41
3	88.39	66.7	4448.89
4	88.77	67.0	4489.00
5	89.59	67.6	4569.76
6	90,10	68.0	4624.00
7	88,81	67.0	4489.00
8	88,63	66.9	4475.61
9	88,79	67.0	4489.00
10	88,94	65.6	4303.36
n = 10		$\sum x_4$ = 669.5	$\sum x_4^2$ = 44828.67

In Real Self-Potraits was found that there are differences in the dimensions of the image object that can affect the value of the PD measurement processed by the system. The size of the object in question is the position of the face that is larger or smaller in the image.

A smaller face dimension will result in a smaller PD measurement value than the original value. This is influenced by the image quality of the eye object experiencing a decrease, which causes a burst effect and results in inaccurate pupil center detection. The results of the PD measurement are not the manual PD measurement values, which can be seen in Table 5. Therefore, it is necessary to pay attention to the dimensions of the image so that the measurement of the PD value on the system can match the PD value that has been measured manually.

From the test results, it can be seen that the value of the standard deviation (S) of measurement uncertainty is calculated using Equation (2).

TABLE 5. Differences in Face Object Dimensions Affecting PD Values on Real Self-Potraits

Correct Face Dimensions	PD (mm)	Incorrect Face Dimensions	PD (mm)
	60.1		24.7
	61.6		42.4
	60.1		53.4
	60.6		44.2

$$S = \sqrt{\frac{n\sum x_i^2 - (\sum x_i)^2}{n(n-1)}} \quad (2)$$

The uncertainty value for PD measurement on Real Self-Potraits is as follows:

$S_{bright} = \sqrt{\frac{10(37225.47) - (610.1)^2}{10(10-1)}} = \sqrt{0.36} = 0.60$ mm

$S_{dark} = \sqrt{\frac{10(36151.04) - (601,2)^2}{10(10-1)}} = \sqrt{0.77} = 0.88$ mm

The uncertainty value for PD measurement on MPIIGaze is as follows:

$S_{bright} = \sqrt{\frac{10(45324.56) - (673.2)^2}{10(10-1)}} = \sqrt{0.53} = 0.73$ mm

$S_{dark} = \sqrt{\frac{10(44828.67) - (669.5)^2}{10(10-1)}} = \sqrt{0.63} = 0.80$ mm

PD measurements made by the system have an average value of uncertainty less than 1 mm. From the known uncertainty values, it can be determined that the PD value of each object from Real Self-Potraits Dataset:

$PD_{bright} = \left(\frac{\sum x_1}{10}\right) \pm S_{Table\ 1}$
$= 61.01 \pm 0.60$ mm

$PD_{dark} = \left(\frac{\sum x_4}{10}\right) \pm S_{Table\ 2}$
$= 60.12 \pm 0.88$ mm

Meanwhile, PD value from MPIIGaze Dataset:

$PD_{bright} = \left(\frac{\sum x_3}{10}\right) \pm S_{Table\ 3}$
$= 67.32 \pm 0.73$ mm

$PD_{dark} = \left(\frac{\sum x_4}{10}\right) \pm S_{Table\ 4}$
$= 66.95 \pm 0.80$ mm

In the Real Self-Potraits dataset, it can be seen that the accuracy of the system in measuring PD by calculating the Mean Absolute Percentage Error (MAPE) using Equation (3).

$$MAPE = \frac{1}{n}\sum \left|\frac{Manual\ PD - Result\ PD\ Detection}{Manual\ PD}\right| \text{ x } 100\% \quad (3)$$

$MAPE_{bright} = \frac{1}{10}$ x |-0.16% | = 0.02%

$MAPE_{dark} = \frac{1}{10}$ x |14.42% | = 1.44%

From the results of the MAPE calculation, it is obtained that a percentage value ≤10 proves that the PD measurement carried out by the system has good accuracy in bright or dark images. This statement is in accordance with the interpretation of the MAPE value when the percentage value is less than 10, indicating that the prediction of the existing measurement value matches or approaches the actual measurement value.

In Figure 16, the measured PD in bright conditions is closer to the manual PD value than the PD in dark conditions from Real Self-Potraits datasets. Evidenced by the difference in the uncertainty value for bright conditions of 0.60 mm which is small compared to 0.88 mm for dark conditions.

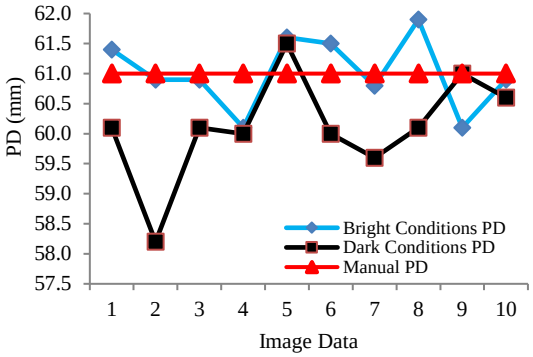

Figure 16. Graph of PD Value Proximity Measured by the System with Manual PD

4. CONCLUSION

PD measurements on the system were successfully carried out on test images from the MPIIGaze and Real Self-Potraits datasets with two varying lighting conditions. Test images that have a resolution of 300 x 300 pixels with 72 dpi provide optimal work for the system in measuring PD. The lighting in the image is divided into two conditions, namely bright conditions and dark conditions. The PD results measured on the system have an uncertainty value of less than 1 mm as in Real Self-Portrait which has an uncertainty value of 0.60 mm for bright conditions and 0.88 mm for dark conditions. MPIIGaze has an uncertainty value of 0.73 mm for bright conditions and 0.80 for dark conditions. The existence of this uncertainty value is influenced by the difference in the dimensions of the face object in the image being tested. The system for measuring PD has good accuracy as evidenced by the smallest MAPE value of 0.02% in bright images. However, the system is still constrained by dark image conditions with high shadow illumination when detecting the center of the pupil and the difference in image dimensions is also an obstacle to produce accurate PD measurements. For further research in measuring pupil distance (PD) through images, it is hoped that the system can detect the center of the pupil accurately and precisely in various image dimensions so that dimension changes are not done manually.

5. REFERENCES

1. Husna, H.N., Bambang, F., Sari, D.L. and JaNarta, A.R.O.L., "Penyimpangan titik pusat optik lensa (OC) dengan jarak pupil (PD) pemakai kacamata", ***Wahana Fisika***, Vol. 3, No. 2, (2018), 124-135.
2. Husna, H.N., Yulianti, A.M. and Milataka, I., "Efek prisma pada pemakai kacamata single vision", ***Jurnal Ilmu Fisika***, Vol. 12, No. 2, (2020), 98-104.
3. Toma, T., Abdillah, B.R. and Simarmata, M.M., "Pentingnya pengukuran pupil distance (PD) secara tepat untuk menjaga akurasi distance vitror (DV) kacamata", ***Jurnal Mata Optik***, Vol. 2, No. 2, (2021), 19-27.
4. Tegar, L.S. and Utama, J., *Rancang bangun sistem informasi lahan parkir kendaraan roda empat di unikom berbasis image processing designed build information system in unikom four-wheeled parking lot based on image processing*. 2016, Telekontran.
5. Sai Viswanathan, M. and Manoj Kumar, V., "Modelling of eyeball with pan/tilt mechanism and intelligent face recognition using local binary pattern operator", ***International Journal of Engineering, Transactions A: Basics***, Vol. 30, No. 7, (2017), 1098-1104. doi: 10.5829/ije.2017.30.07a.20.
6. Harto, D. and Rahmani, M.Z., "Sistem pengenalan wajah dengan metode eucliden distance", ***Elektrika Borneo***, Vol. 5, No. 2, (2019), 16-26.
7. Vázquez Romaguera, T., Vázquez Romaguera, L., Castro Piñol, D. and Vázquez Seisdedos, C.R., "Pupil center detection approaches: A comparative analysis", ***Computación y Sistemas***, Vol. 25, No. 1, (2021), 67-81. https://doi.org/10.13053/cys-25-1-3385
8. Utama, J. and Riki, D., "Implementasi sistem pendeteksi target berdasarkan pengenalan warna dan pola untuk robot pengikut bola", ***Telekontran: Jurnal Ilmiah Telekomunikasi, Kendali dan Elektronika Terapan***, Vol. 5, No. 2, (2017), 107-117.
9. Skodras, E. and Fakotakis, N., "An accurate eye center localization method for low resolution color imagery", in 2012 IEEE 24th International Conference on Tools with Artificial Intelligence, IEEE. Vol. 1, (2012), 994-997.
10. Loy, G. and Zelinsky, A., "A fast radial symmetry transform for detecting points of interest", in Computer Vision—ECCV 2002: 7th European Conference on Computer Vision Copenhagen, Denmark, May 28–31, 2002 Proceedings, Part I 7, Springer., (2002), 358-368.
11. Lyasheva, S., Shleymovich, M. and Shakirzyanov, R., "The image analysis using fast radial symmetry transform in control systems base on the computer vision", in 2019 International Multi-Conference on Industrial Engineering and Modern Technologies (FarEastCon), IEEE., (2019), 1-6.
12. Ram, S. and Rodriguez, J.J., "Size-invariant detection of cell nuclei in microscopy images", ***IEEE Transactions on Medical Imaging***, Vol. 35, No. 7, (2016), 1753-1764. doi: 10.1109/TMI.2016.2527740.
13. Zafari, S., Eerola, T., Sampo, J., Kälviäinen, H. and Haario, H., "Segmentation of overlapping elliptical objects in silhouette images", ***IEEE Transactions on Image Processing***, Vol. 24, No. 12, (2015), 5942-5952. doi: 10.1109/TIP.2015.2492828.

14. Wang, H., Li, S.Z., Wang, Y. and Zhang, J., "Self quotient image for face recognition", in 2004 International Conference on Image Processing, 2004. ICIP'04., IEEE. Vol. 2, (2004), 1397-1400.
15. Wang, H., Li, S.Z. and Wang, Y., "Face recognition under varying lighting conditions using self quotient image", in Sixth IEEE International Conference on Automatic Face and Gesture Recognition, 2004. Proceedings., IEEE., (2004), 819-824.
16. Arandjelović, O., "Making the most of the self-quotient image in face recognition", in 2013 10th IEEE International Conference and Workshops on Automatic Face and Gesture Recognition (FG), IEEE. (2013), 1-7.
17. Gunawan, A.A. and Setiadi, H., "Handling illumination variation in face recognition using multiscale retinex", in 2016 International Conference on Advanced Computer Science and Information Systems (ICACSIS), IEEE. (2016), 470-475.
18. Nishom, M., "Perbandingan akurasi euclidean distance, minkowski distance, dan manhattan distance pada algoritma k-means clustering berbasis chi-square", ***Jurnal Informatika***, Vol. 4, No. 01, (2019), 20-24.
19. Hassanpour, H. and Ghasemi, M., "A three-stage filtering approach for face recognition", ***International Journal of Engineering, Transactions B: Applications***, Vol. 34, No. 8, (2021), 1856-1864. doi: 10.5829/IJE.2021.34.08B.06.

Persian Abstract

چکیده

در بیماران مبتلا به عیوب انکساری یا اختلال بینایی، پرتوهای نور دریافتی مردمک به طور مستقیم روی شبکیه نمی‌افتد. این مشکل را می توان با استفاده از عینک های مونوکلد اصلاح کرد. نقطه کانونی عدسی عینک باید با مرکز مردمک چشم کاربر تنظیم شود. این را می توان از طریق اطلاعات مقدار فاصله مردمک اندازه گیری شده (PD) دانست. اندازه گیری PD برای تعیین فاصله مرکزی مردمک ها در هر دو چشم بسیار مهم است. جایی که چشم اثر منشور را تجربه نمی کند. این مطالعه با هدف استفاده از روش تبدیل تقارن شعاعی (RST) همراه با تصاویر خود بهره (SQI) برای تشخیص مرکز مردمک و اندازه گیری PD است. این الگوریتم ترکیب می شود تا نتایج بهینه تری در تشخیص مرکز مردمک در شرایط تاریک یا در معرض نور سایه بدست آورد. برنامه ایجاد شده با استفاده از نرم افزار متلب، اندازه گیری PD را برای تشخیص مرکز مردمک در شرایط تصاویر روشن و تاریک شبیه سازی می کند. آزمایش ده بار انجام شد و نتایج نشان داد که سیستم قادر به اندازه‌گیری PD بر روی تصاویر با وضوح پایین ۳۰۰ x 300 پیکسل در ۷۲ dpi در شرایط تصویر روشن است. با مقادیر عدم قطعیت اندازه گیری در هر تصویر ۰.۶۰ میلی متر. در مورد آزمایش روی تصاویر تاریک، مقادیر عدم قطعیت ۰.۸۰ میلی متر است. در این حالت، مقدار انحراف استاندارد از تأثیر ابعاد مختلف جسم صورت بر روی تصویر آزمایش شده به دست می آید.

International Journal of Engineering

Journal Homepage: www.ije.ir

Blockchain-based Traceability System for Indonesian Coffee Digital Business Ecosystem

I. G. M. T. Pradana*[a], T. Djatna[b], I. Hermadi[c], I. Yuliasih[b]

[a] *Post Graduate Program in Agroindustrial Engineering, IPB University, Bogor, Indonesia*
[b] *Department of Agroindustrial Technology, IPB University, Bogor, Indonesia*
[c] *Department of Computer Science, IPB University, Bogor, Indonesia*

PAPER INFO

Paper history:
Received 18 December 2022
Received in revised form 14 February 2023
Accepted 15 February 2023

Keywords:
Blockchain
Coffee
Digital Business Ecosystem Framework
Prototype
Smart Contract
Traceability

ABSTRACT

Coffee is a crucial agricultural commodity in developing nations like Indonesia; so it is important to implement a trustworthy traceability system for the product. However, there are no established guidelines for developing a blockchain-based traceability system that the coffee industry can adopt. Therefore, this study aims to present a Digital Business Ecosystem (DBE) framework and a blockchain-based traceability system prototype for Indonesian coffee. The study process involved a literature review, field observations, and the creation of the proposed frameworks and prototypes using an integrated rapid prototyping method. The proposed DBE framework has three layers: business, digital, and infrastructure, while the prototype has use case diagrams and a model of functional, technological, and transaction flows. The system was validated through deployment tests such as recording-tracking coffee data using Ethereum smart contracts and interplanetary file system. The interconnectivity was verified through a mobile-based user interface design that includes registration and login pages, a main page, a transaction confirmation page, and a traceability page. It was discovered that the proposed framework and prototype have a high potential for real-world implementation due to their ability to effectively address the challenges and promote a positive business community culture while being supported by the mapped DBE layers. Further study is recommended to test and enhance the proposed framework and prototypes and examine the relationship between system development and technology adoption. Moreover, managerial insights were provided to the coffee business community, policymakers, and developers for the successful development of Indonesian coffee DBE with the blockchain-based traceability system.

***doi**: 10.5829/ije.2023.36.05b.05*

1. INTRODUCTION

Coffee is one of the essential commodities traded internationally. It is also the second primary commodity with the highest export value after oil in developing countries [1]. The quantity of coffee production in Indonesia is continuously increasing; thereby, making the country the fourth largest producer in the world as indicated in Figure 1. Moreover, several factors such as the species and cultivars of coffee, the presence of defective seeds, storage conditions, geographical origin, processing method, as well as roasting technique, all play a crucial role in determining the quality and taste of coffee [2]. It is also important to note that there are also concerns regarding adulteration and food mixing despite the increasing popularity of coffee [3]. Previous studies showed that despite the ability of physical, chemical, and biological analytical methods to detect the presence of adulteration in roasted and ground coffee [4-7]; they are not practical for the use in transactions between different factors within the coffee supply chain. Therefore, several traceability systems have been developed to record production activities associated with coffee starting from the plantation stage (tracing) to the movement of the product during the transaction process (tracking) [8].

Centralized-based systems experienced a wave of loss of trust due to several problems and scandals [9] such as hacking and alteration of client data by server admins

*Corresponding Author Email: igmteddypradana@apps.ipb.ac.id
(I. G. M. T. Pradana)

Please cite this article as: I. G. M. T. Pradana, T. Djatna, I. Hermadi, I. Yuliasih, Blockchain-based Traceability System for Indonesian Coffee Digital Business Ecosystem, ***International Journal of Engineering, Transactions B: Applications***, Vol. 36, No. 05, (2023) 879-893

to benefit certain parties [10]. Therefore, blockchain was introduced as a decentralized and Distributed Ledger Technology (DLT) which brings an entirely new idea to challenge the existence of a centralized system [11]. In the early decades of its launch [12], most studies were focused on its utilization in financial technology [13, 14] but the introduction of the second-generation blockchain [15] such as smart contracts & Ethereum led to the massive development of blockchain-based projects. This further contributes to a broader range of sectors such as supply chain management, finance, logistics, and security [16]. Several pilot projects observed to have been developed include land registration systems management [17, 18] and voting [19, 20] apart from the traceability system [21]. An example showed the increasing need for a reliable traceability system in the health sector to re-register the distribution of vaccines and drugs during Covid-19 outbreak [22–24]. It was also reported in the agricultural sector that blockchain has the potential to improve food integrity and safety [21, 25] through immutable production records and steps as well as product monitoring [26]. Several blockchain-based traceability systems have been developed but developing countries were observed to be facing a critical risk due to their slow movement in exploiting and adopting blockchain technology [27]. This means there is a need for a system development framework and fundamental traceability system model to resolve certain specific problems.

Therefore, a development framework that does not only focus on technology but emphasizes the solution to the problems and challenges of the business community in the coffee agroindustry is proposed in this study. It is pertinent to note that ecosystem metaphors usually describe the interactions and symbiosis between digital species and businesses [28, 29] to create new business habitats [30]. This led to the proposal of a novel Digital Business Ecosystem (DBE) framework that reduces technological complexity, is collaborative and integrated, and has never been developed before as a catalyst for a blockchain-based traceability system in the Indonesian coffee industry.

This article has 8 sections which start with the introduction followed by a literature review on blockchain coffee projects, the study gaps to be filled, an explanation on the sequence of methods applied to obtain results, and the presentation of the proposed DBE framework and blockchain-based traceability system in Indonesian coffee. The key findings and limitations are discussed, conclusions and recommendations for possible future study are provided, and the last part focuses on the managerial insights of the business community, policymakers, and system developers.

2. BLOCKCHAIN-BASED PROJECTS IN COFFEE

A reliable record system to support product traceability is one of the projects most frequently developed to address food safety and integrity issues [31]. In parallel with scientific study, several private companies have claimed to implement blockchain technology in their operations. The collected data on several blockchain coffee projects based on the acclaimed successful implementation process was used to highlight the advantages. These projects are presented in the following Table 1 based on the year they were launched.

In terms of development goals, the projects are generally expected to create a more efficient and secure system to provide real-time transaction data traceability results. It is important to note that most blockchain-based coffee traceability projects focus on increasing the transparency of transactions between actors in the supply chain. However, some projects also focus on providing economic scale-up opportunities to farmers by providing access to new capital and improving the social-environmental conditions of the coffee-producing countries.

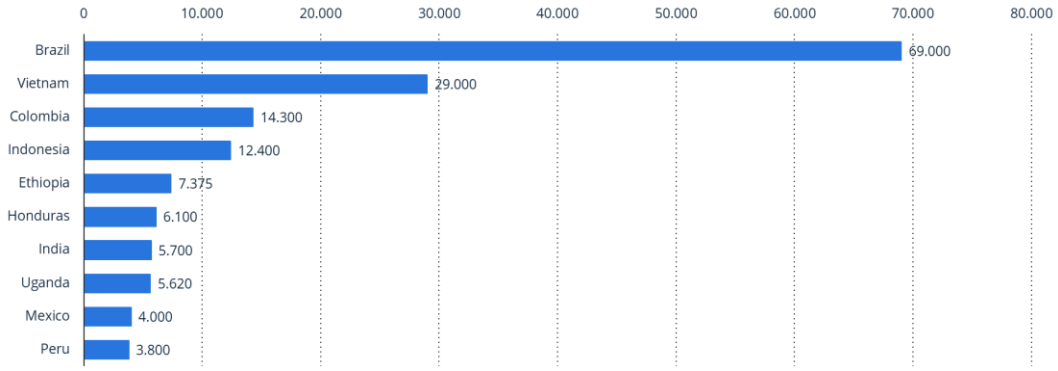

Figure 1. Coffee production worldwide in 2020 by leading country (in 1,000 60-kilogram bags)[1]

[1] www.statista.com/statistics/277137/world-coffee-production-by-leading-countries/

TABLE 1. Development Project of Coffee Traceability System Based on Blockchain Technology

Project and Initiator	Public Launched	Descriptions	Highlighted Features
Foodchain SpA[1] by *FoodChain*	2018	Provides the ultimate tool to follow the coffee product journey through the core engagement of the cooperative.	The company can choose the type of information to apply and share with users through a system of authorization and customized privacy.
Beyco[2] by *Progreso Foundation*	Oct 2018	Global independent coffee connection and trading platform on the blockchain. It uses a permissioned blockchain to verify the registration of all actors such as producers, exporters, importers, traders, and roasters playing a certain role in transporting coffee from the country of origin to the final consumer.	Signing smart contracts to provide connected access and chat with producers, traders, or roasters about their interests and public traceability as well as to apply for loans as a business continuity effort.
GrainChain[3] by *Medici Ventures*	May 2019	The platform includes a digital wallet enabling remote and unbanked farmers to apply for loans needed to improve their farming and crop standards. Smart contracts are used to improve traceability and logistics operations for vendors and buyers.	Product quality assurance is certified through sensors and stored using the Hyperledger-based blockchain. Payments use the dollar-backed stablecoin, GrainPay, to enable instant settlement of transactions between actors.
Yave[4] by *Yave*	May 2019	A coffee auction platform based on blockchain technology designed to remove intermediaries from the commodity or futures market and enable more transparent business between stakeholders in the coffee supply chain.	It uses Hyperledger to provide 5 excellent features which include digital ID, smart contract, direct payment, accessible record, and glass pipeline (transparency).
Farmer Connect[5], Thank My Farmer app by *IBM Blockchain*	Nov 2020	Food Trust Platform to enable a more efficient supply chain and create a better ecosystem for the global coffee farming community.	Ability to add taste profile (coffee type, acidity, sweetness, body, and intensity), filter based on taste characteristics and shareable reviews to product pages, and a fun Trivia quiz. The feature donates to local farming communities.
Angelique's Finest Goes Blockchain by *INA in Rwanda*	2020	Develop a transparent, open-source, and movable blockchain-based traceability solution that documents the path taken by coffee cherries from the planting stage to the finished product.	Development of an Open source blockchain solution to support Rwandan women farmers. Creating Digital IDs that can connect with markets and provide them with financial independence.
Emurgo Traceability Solution by *Emugo*	April 2021	Provide facilities to partner companies to track coffee products efficiently in a safe, transparent, and real-time manner. Display information such as source origin, processing date, shipping information, and other relevant data to each stakeholder at any time.	Provides a QR code for coffee products connected to the blockchain to ensure end customers have quick access to information about the origin of coffee by scanning with their smartphones.
FairChain Coffee[6] by *FairChain Foundation*	Nov 2021	It enables all stakeholders – growers, roasters, and consumers to access data across the supply chain and provides a fair-trading platform for coffee. Provide transparency to consumers regarding the origin and quality of the product.	Build a platform to radically improve the fair share of the deal, especially for farmers growing premium quality coffee, and to provide fair deals for their efforts.

From the regional perspective, it was discovered that most of these projects aim to solve the challenges in the coffee industries outside the Asian area. For example, the project initiated by Food-Chain[3] seeks to provide a recording system to secure the "distinctive ritual" of Italian espresso coffee. The blockchain-based system to support Rwandan women farmers created by INA project also focuses on encouraging Rwandan coffee production to meet the German market. Another point was that Rwandan coffee serves as a pilot project for the

[1] www.food-chain.it/public/case/san-Domenico
[2] www.beyco-nl.medium.com/the-different-forms-of-blockchain-284323b93ee2
[3] www.prnewswire.com/news-releases/grainchain-uses-blockchain-to-unite-honduras-coffee-industry-300923854.html
[4] www.gcrmag.com/yave-to-hold-worlds-first-blockchain-coffee-auction
[5] www.farmerconnect.com/traceability-solutions, www.ibm.com/thought-leadership/coffee
[6] www.fairchain.org/blockchain-info

traceability system designed by Starbucks in addition to the Colombian and Costa Rica coffee. Moreover, the pilot fair trade system was developed by FairChain for farmers of Moyee Coffee offering arabica beans from Ethiopia, Kenya, and Colombia. Emurgo also recently developed coffee traceability information services for Koerintji coffee in Southeast Asia but partnered with ALKO as an intermediate actor. This means the process required only passive input from the Koerintji coffee farmers and related communities.

Several companies have used platforms such as Food Trust designed by IBM which was applied directly by Sical[1] and Sucafina Specialty[2] to brand and provide added value to their products. However, it was discovered that there is no project designed to use a public blockchain-based traceability system for the coffee business community. There is also none developed to create and apply a DBE framework in the coffee industry. Therefore, this study seeks to fill this gap by providing alternative solutions while considering projects previously launched.

3. STUDY GAP

Taste, as a representation of coffee quality, is the most critical factor for consumers to make purchasing decisions [32]. This means improving the quality of Indonesian coffee can increase its global market but the process requires attention and good governance in collaboration with farmers [33]. Moreover, the integration of digitalization into the industry has a strong causal relationship with labor conditions, supply chain financing accessibility, and social responsibility [34]. This shows there is a need to adapt digital technology to the Indonesian coffee business community to solve environmental, economic, and social challenges [35].

Blockchain is an emerging technology with great potential to support sustainable agriculture and food security [36]. However, its implementation requires considering usability and flexibility before developing the applications in the business domain [37]. It has also been previously reported that integrity, decentralization, and tampering resistance are the characteristics of blockchain technology needed to meet the trust and transparency requirements of the system [25]. They serve as the principal features of applying blockchain technology as a reliable traceability system. Several studies have highlighted its great potential in the traceability of food and agricultural products but there is a need for the development of the system with due consideration for its properties, technology challenges, and specific case studies. Some of the properties requiring analysis before selection include the architecture, type, consensus, and platform [38]. Meanwhile, the technology challenges were related to the fundamental infrastructure, technical challenges, and data authenticity [39].

This study proposes a DBE framework for Indonesian coffee with a prototype of a blockchain-based traceability system as part of the digital layer. Previous studies have attempted to develop a coffee traceability system based on blockchain technology but none discussed the DBE framework encouraging the development of a blockchain-based traceability system with due consideration for the coffee business community. Therefore, this study is essential to describe the critical success factors to implement the proposed blockchain-based traceability system in the coffee industries through the framework and prototype proposed. The slices of the study gap discussed are presented in Figure 2.

4. METHOD

The first phase of this study focused on reviewing the literature on blockchain coffee projects, the condition of Indonesian coffee, and DBE development. Moreover, the problems of Indonesian coffee in the real world were explored through field observations and interviews conducted at the Kintamani coffee agroindustry in Bali. This was followed by the design of the proposed Indonesian coffee DBE framework based on work conducted by Nachira et al. [28], Corallo et al. [29] and the study gaps proposed by Senyo et al. [40].

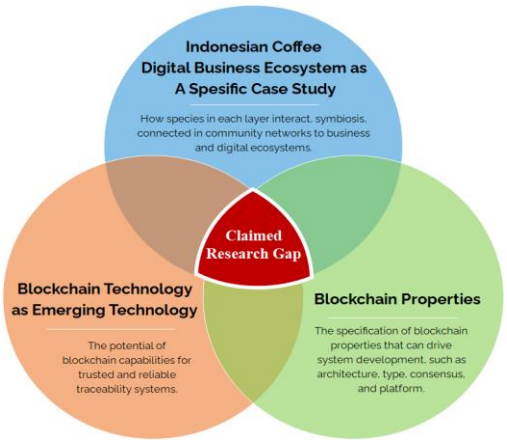

Figure 2. Claimed Study Gap

[1] www.esmmagazine.com/a-brands/sical-launches-limited-edition-coffee-with-blockchain-technology-225631, www.cointrust.com/market-news/sical-unveils-blockchain-certified-coffee-varieties

[2] www.sucafina.com/na/news/introducing-farmer-connect-coffee-transparency-through-blockchain-technology

The second phase was used to develop a prototype of a traceability system based on blockchain technology with due consideration for the blockchain coffee project previously analyzed. The proposed prototype was developed using the integrated rapid prototyping method [41, 42] including structuring system requirements [43] with the Unified Modeling Language (UML) [44], the development of the architectural layer and User Interface (UI) [45], and the consideration of the blockchain-traceability approach proposed by Betttin-Diaz et al. [46]. Finally, the prototype was validated through a deployment test process on the Ethereum network using two functions written into a smart contract and storing off-chain data on Interplanetary File System (IPFS).

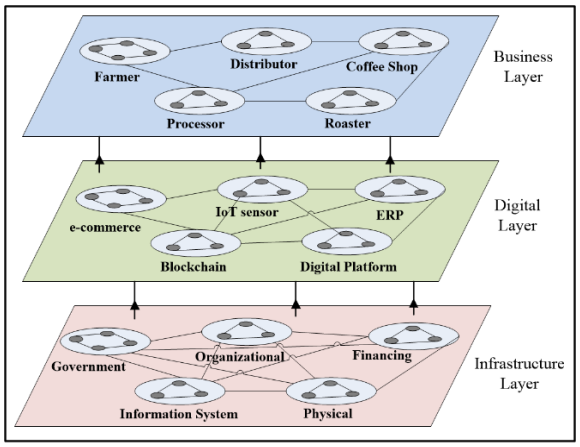

Figure 3. Proposed DBE for the Indonesian Coffee agroindustry

5. INDONESIAN COFFEE DBE

An in-depth analysis led to the proposition of a DBE framework for the Indonesian Coffee agroindustry with 3 main layers including business, digital, and architecture. At the business layer, the analysis showed that the Indonesian coffee industry currently has a good business ecosystem associated with production-consumption trends. The total coffee production over the past 5 years (2015-2019) in the country was observed to have an increasing linear trend [47] which strengthened its position as the fourth largest coffee-producing country after Columbia, Vietnam, and Brazil [48]. From the consumption perspective, Toffin [49] reported a threefold increase in coffee shops in Indonesia between 2016 and 2019. This was further confirmed by ICO data through the indication of a Compounded Annual Growth Rate (CAGR) value of 0.6% for coffee consumption which is higher than the average global value [50]. The increasing production and consumption (supply-demand) of coffee are good indicators of the development of the business ecosystem in Indonesia.

Key stakeholders in the Indonesian coffee agroindustry supply chain were also identified to form a business layer framework. The observation of the case study showed that the five main actors include the farmers, processors, distributors, roasters, and coffee shops with each playing specific roles in providing added value to coffee products followed by subsequent distribution to the next chain. At first, each actor is an individual species in the ecosystem but they come together to form a community interacting in the business ecosystem of the industry. The interactions are usually based on the principle of mutual benefit and adding value to the product. This business ecosystem is the top layer and this is the reason it is the most visible as indicated in Figure 3.

The second layer of the proposed Indonesian coffee DBE framework required mapping existing digital species and it was discovered several digital species are interacting in the industry such as blockchain, e-commerce, Internet of Things (IoT) technology devices, Enterprise Resource Planning (ERP) applications, and other digital platforms as presented in Figure 3. It is pertinent to note that the digital layer communities need to be developed using emerging technologies and encouraging interactions with other digital species to produce a trusted and reliable coffee traceability system. As a digital species, blockchain has excellent potential as the underlying technology for traceability systems. This is due to its ability to increase the flow of accurate information, reduce transaction costs, and encourage fair prices for all actors [51]. Moreover, the symbiosis between blockchain and other digital species existing in the Indonesian coffee industry was reported to have improved coffee market channels, reduced distribution intermediaries, assisted smallholder farmers to access the market, and provided new payment system options [52]. This means the blockchain-based traceability system needs to be developed within the Indonesian coffee DBE framework to address the challenges in the industry.

Finally, the identification results were used to propose an infrastructure layer that forms the basis for the two previous layers. This third layer consists of several main species including (1) the government and its regulations regarding coffee and traceability systems [53], (2) basic information systems such as population identity, (3) organizational structure and patterns of institutional development, (4) internet towers and other physical components, and (5) financing for the development of DBE as shown in Figure 3.

The Indonesian government issued regulations on Geographical Indication (GI) certification to guarantee the originality and quality of Indonesian coffee and strengthen its competitiveness. This certification shows the area of origin of an item or product which, due to geographical, environmental factors including natural, human, or a combination of the two, gives reputation,

quality, and unique characteristics to the goods or products produced[1]. There are at least 32 types of Indonesian coffee that have received GI certification, starting with Bali Kintamani Coffee[2] (2008). The coffee stakeholders initiated by the government have also formed an organization known as the Society for the Protection of Geographical Indications (abbreviated as MPIG). MPIG is tasked with the responsibility of setting boundaries and providing guidelines to maintain coffee GIs such as the establishment of a traceability system.

The observation also showed that other species of infrastructure layer have fulfilled the minimum requirements to develop Indonesian coffee DBE. This is indicated by the availability of an electronic identity system for Indonesian residents, 5G, and almost the coverage of 4G networks in every area of the coffee industry, as well as the finance provided for system development in the department of agriculture. Therefore, blockchain is considered an emerging technology which is feasible to be developed as the underlying traceability system as well as to support the realization of DBE for Indonesian coffee.

6. DEVELOPMENT OF A BLOCKCHAIN-BASED TRACEABILITY SYSTEM

6. 1. Requirement Engineering Stakeholders as users of the traceability system to be developed were successfully identified at the requirements determination stage. The information obtained was used to determine the interaction between the user and the proposed system as shown in the use case diagram presented in Figure 4. It is pertinent to note that each stakeholder in the coffee business community was identified as a user with the ability to log in (including register), confirm transactions, and track products. Moreover, the prototype used a permissioned system to ensure only the specified stakeholders can register as users by selecting the appropriate role during the process of accessing the system. The registration was also used to eliminate intermediary actors that usually disrupt the continuity of transactions between farmer-processors and processors-distributors.

Each actor is required to record the data related to its selected role. For example, the farmers are required to enter the data about cherry bean harvesting, information about the processing by the processor, packaging size and distribution route by the distributor, as well as the roasting and brewing data by the roasters and coffee shops. Finally, all the users and end customers can trace the coffee and store the data by entering the product ID code.

This study used three subsystems for the data recording and tracking process. First, the APIAuth subsystem processes each user's registration data to obtain an access code on the traceability system. Second, smart contracts are the core subsystem containing the agreement algorithms between users in the system and are applied to ensure a confirmation by the intended user before the transaction is successful and stored on the blockchain. Third, the IPFS subsystem was used for the distributed off-chain data storage.

The analysis also produced the minimum data required in addition to proposing system and user interactions as shown in Table 2. This was divided into internal and external records. The internal records include the activities of each user during a transaction

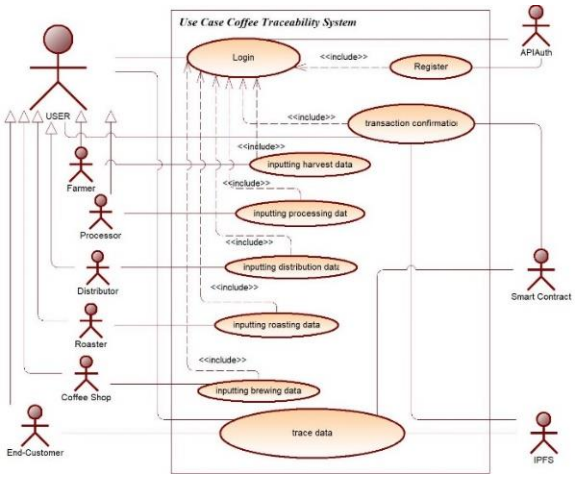

Figure 4. A proposed use case diagram

TABLE 2. Minimum data requirements

Variable	Contents
	Internal Record
Profile	Name, ID[+], Business Location, Business Properties
Process	Cultivation, Production, Processing, and other Business activities
Additional Documents	Product Photos, Activity Documentation, SOP[+], Standard compliance
	External Record
Origin	Varieties, Time, Timestamp, Location, Actor path
Link	The hyperlink to the shared additional document
Quality	GAP, GMP, GHP, SCAA, SNI[+]

[+]ID = Identity, SOP = Standar Operational Procedure, GAP = Good Agricultural Practices, GMP = Good Manufacturing Practices, GHP = Good Handling Practices,
SCAA = Specialty Coffee Association of America, SNI = Standar Nasional Indonesia (Indonesian National Standard)

[1] www.dgip.go.id/menu-utama/indikasi-geografis/pengenalan

[2] https://ig.dgip.go.id/

including the user profiles, product processing history according to their roles, and additional documents such as product photos and standardization documents. Meanwhile, the external records are data elicited from other sources such as seed variety certificates and quality standard documents as well as those recorded automatically by the system such as the timestamps and links to related documents.

6. 2. Modeling of The Proposed Prototype

6. 2. 1. Proposed Functional Model The system requirements analysis was used to propose a functional model of a traceability system with a focus on two main streams as presented in Figure 5 including (1) the flow of physical products and (2) the flow of information. These streams are required to be under the umbrella of the applicable regulations, certification, and food safety agreements set by the authority where the system is to be applied. Figure 5 shows the functional model proposed for the Indonesian coffee traceability system. It is important to note that each actor is expected to process coffee to ensure the products have added value in each of the streams. Moreover, the internal and external data recorded serve as a prerequisite for actors in the supply chain to make transactions. The transactions are subsequently stored on the blockchain network through a unique code embedded in each batch of products processed. The code for each product is formed into a QR code to make the tracking of the internal and external traceability processes easy.

6. 2. 2. Proposed Technological Architecture Model A model of technological architecture consisting of four layers was proposed to ensure the adequate development of the blockchain-based coffee traceability system. These include sensing, network, service, and application as shown in Figure 6. The QR code scanner has a sensor to obtain a unique code attached to coffee products for tracking purposes. Moreover, an internet connection and an Ethereum network are required at the network layer to perform transactions, record, and track. The interconnection between the blockchain network as a back-end and front-end display also requires services from the Web3 API. Furthermore, the data is large but there is a unified whole in transactions in the IPFS to ensure the blockchain stores the hash code of the file location. The application layer is the spearhead of the layer interacting with the user and this led to the application of a responsive web-based interface on mobile devices.

6. 2. 3. Proposed Transaction Flow Model This section was used to propose a transaction flow model consisting of 10 stages for one successful transaction cycle as shown in Figure 7. The transaction was designed to be initiated through the application UI when the registered user opens the system. The first transaction flow stores the large file in IFPS such as the product sample photo that can be used to check green bean defect standards. Furthermore, the hash address of IFPS can be obtained from the file stored and later displayed on the web application. The users are also allowed to enter the code containing the information on the coffee to be traded such as quantity and variety. The registered account is to be confirmed by the Ethereum or smart contract via the MetaMask wallet system. The response showing the account has connected to the network is then displayed to the user. It is also important to note that users are to receive notifications as a response from the system. Next, the system requests transactions to be stored on the blockchain network through a consensus algorithm on

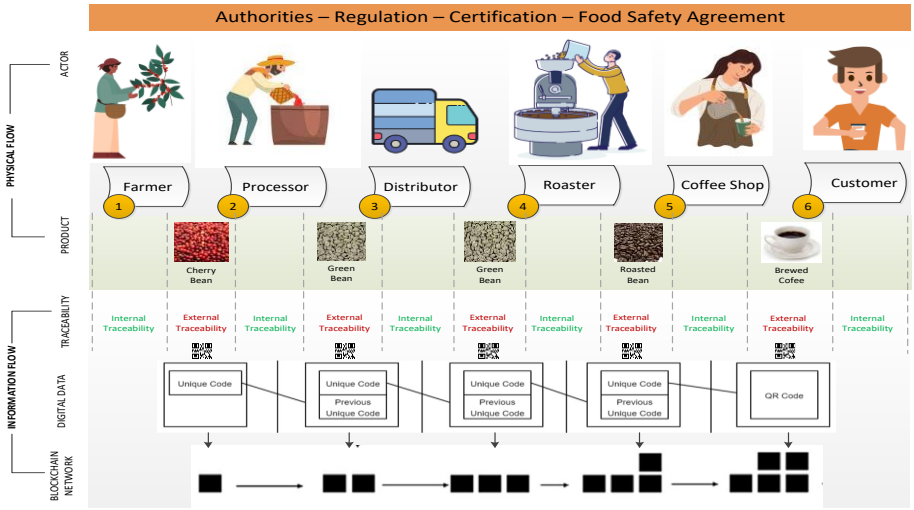

Figure 5. Proposed Functional Model of Indonesian Coffee Traceability System based on Blockchain Technology

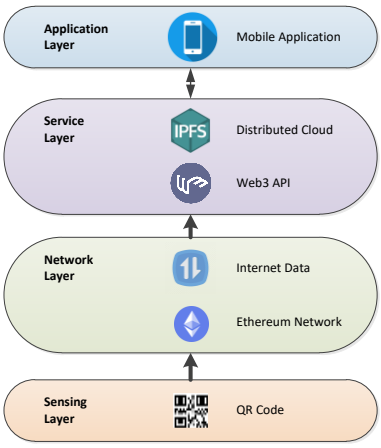

Figure 6. Proposed technological architecture model

the Ethereum network. In the end, the data stored in the traceability system is displayed as a successful transaction. The user gets a response as the final result of the transaction. The dotted line in Figure 7 separates the back-end and front-end environments of the proposed system, and the color differences indicate the different grouping of the system components.

6. 3. Verification and Validation of the Proposed System

6. 3. 1. Deployment Test The deployment test was used as the verification and validation step to provide a reliable blockchain-based coffee traceability system. It was discovered from the analysis conducted on the needs of the Indonesian coffee business community that at least 2 main functions are needed in the traceability system, and these include adding transactions to record data and tracing transactions to track coffee products. The deployment tests were performed using the sample solidity code shown in Figure 8 to represent the smart contract. The agreement shows each user is allowed to

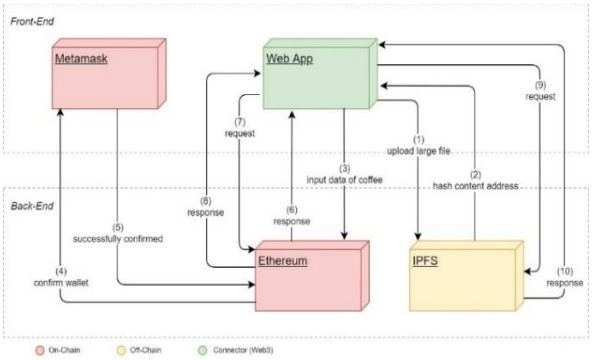

Figure 7. Proposed Transaction Flow Model of Blockchain-based Traceability System

```
pragma solidity 0.5.1;

contract traceability {
    uint256 public trxCount = 0;
    mapping(uint => transaction) public lihatTransaction;

    struct transaction{
        uint id;
        string varietas;
        int amount;

    }

    function addTransaction(string memory varietas, int amount) public {
        trxCount += 1;
        lihatTransaction[trxCount] = transaction(trxCount, varietas, amount);
    }
}
```

Figure 8. Example of solidity code for smart contract on Ethereum blockchain

enter the variety and quantity of each coffee product transacted. It is important to note that the application of different case studies can make smart contracts to be more complex and not limited to the management of multiple variables, functions, or data types. The deployment test validated that: (1) the addTransaction function stores variable and variable data on blocks on the Ethereum network and (2) lihatTransaction displays transactions made according to the hash record of the transaction.

In addition to testing the transaction process on the on-chain network (Ethereum), the off-chain data storage was also assessed in the form of green bean photos on the IPFS network. Figure 9(a) shows the process of inputting a file and the result of the hash address when submitted. It was discovered that the hash address used to identify the saved file is displayed in Figure 9(b) and later added as data stored in the on-chain. This test proves that additional files can be stored on IPFS and generate hash addresses as an alternative solution for the storage of large files when developing a proposed blockchain-based traceability system.

6. 3. 2. Designing UI A mobile-based UI prototype was designed to visualize the proposed

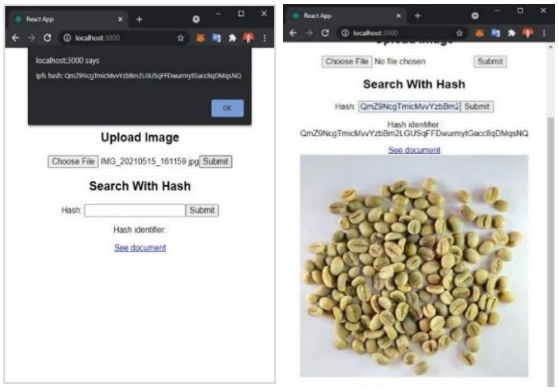

Figure 9. Deployment test on IPFS (a) Add green bean photos as an additional file (b) Result for the tracing of hash address

traceability system as shown in Figure 10. The four main components considered include the (a) login and register forms to select roles according to the use case of each actor in the supply chain, (b) the homepage which contains page information, profile information, action buttons to add and track transactions, as well as history and pending transaction information, (c) pages to confirm transactions, and (d) pages to trace the coffee products by end consumers. The register/login form validates the permissioned system requirements of each user while the addTransaction button and page to confirm transactions validate the user's need for reliable records. Finally, the traceability page verifies the success of the subsystem component and displays the time-based track of coffee products.

7. DISCUSSION AND CONCLUSION

7. 1. Blockchain-based Traceability System as Indonesia Coffee DBE Coupling This study focuses on DBE conceptualization and technical issues to address the challenges of developing DBE frameworks and models [40]. It has been generally proven that the development of a model providing all information related to agricultural production such as varieties, cultivation and treatment methods, as well as other information attracts customers [54]. Moreover, previous studies have proposed a DBE framework in the agricultural sector [55, 56] with case studies to develop a responsive supply chain system for pineapple and frozen shrimp traceability systems. These studies confirmed the business community's lack of knowledge, entrepreneurship, and technology adoption capabilities [29]. Therefore, this study focused on developing the DBE model further to provide affordable ICT solutions for upstream actors (farmers) and Micro Small Medium Enterprises (MSMEs) considered to be members of the business ecosystem. The aim was also to provide a prototype to serve as a fundamental guideline to develop a blockchain-based traceability system that can be replicated easily by the coffee business community. To achieve this goal, there was consideration for robust, inexpensive, and easy-to-apply technology components with significant impact on the ecosystem.

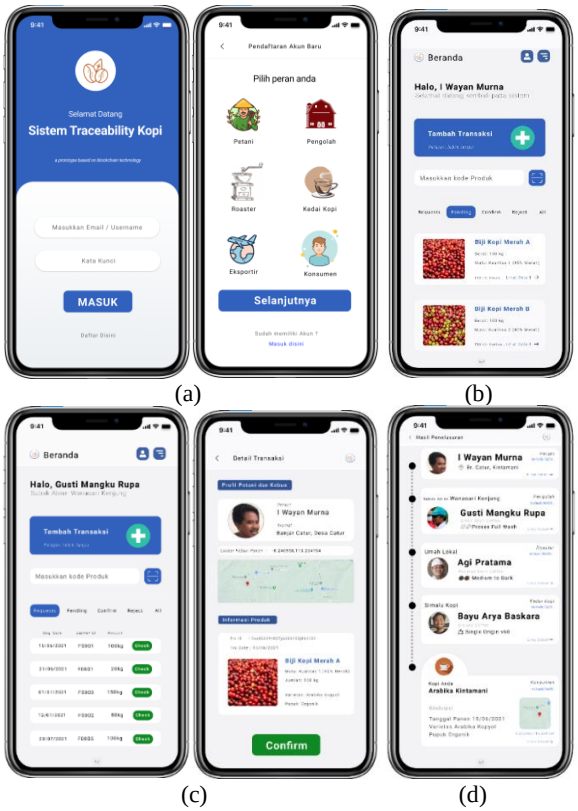

Figure 10. Proposed UI for (a) login and registration form, (b) homepage and addTransaction form, (c) transactions confirmation by the processor from farmers, and (d) time-based traceability page of coffee product

A blockchain-based coffee traceability system prototype was proposed using the configurations applied in several previous studies [57–60]. The process involved the application of Ethereum and IPFS networks with other supporting architectures and tools presented in Figure 6 to address the industry's usability, reliability, and scalability issues [37, 61–63]. It is pertinent to note that the IPFS is a technology enabler allowing a "decentralized database+blockchain" dual storage system structure through on-chain and off-chain mechanisms as indicated in Figure 7. It has been noted in previous studies that the proposed system has the ability to effectively reduce chain load pressure and realize efficient information queries [64, 65]. Moreover, the public-permissioned blockchain network was proposed by requiring a user registration process and transaction confirmation for each record made as indicated in Figure 4. This is to ensure privacy data security [66], a reduction in data entry errors, and a decrease in the risk of tampering [67], thereby, leading to an increase in the trust of the users in the system. It is pertinent to note that the public-permissioned network was selected because it is the most promising platform for a digital traceability system in the food industry [68]. Furthermore, a mechanism was designed to input and trace data by using QR Codes to mark each coffee product life cycle in the supply chain flows. The application of the QR Code is due to the convenience and simplicity provided for users in identifying products and inputting new data in subsequent transaction processes with minimal cost [69]. Lastly, several UIs were proposed to address the challenges associated with recording the data by supply chain actors and to provide immutable and traceable data benefits [70]. A time-based UI design was also proposed as indicated in Figure 10 due to the preference of the product origin traceability by end consumers [71].

A functional or operational system mechanism was also proposed as shown in Figure 5 to create internal and external traceability processes using the minimum input data presented in Table 2. Moreover, the standards of compliance with external data were proposed to include the components of local wisdom at each location of the Indonesian coffee GIs to encourage the sustainability of the coffee industry [72]. For example, there is an agricultural organization called Subak (a member of MPIG) in the Kintamani Coffee agroindustry, Bali with a philosophy of Tri Hita Karana (three causes of prosperity). This philosophy encourages a work culture in the business community such as good governance [73], adoption of innovation, farmer's welfare [74], sustainability [75], and fraud prevention [76]. It was discovered that the guidelines developed by Subak support food security programs, water distribution and allocation management, mobilization of resources for operations and maintenance, and facilitation of fund raising and conflict management [77]. This means the Tri Hita Karana philosophy set as the compliance standard for blockchain-based traceability systems influences the work culture of human resources in the Kintamani coffee supply chain. The phenomenon is ultimately expected to create a favorable ecosystem in the interconnection between coffee business species.

The proposed blockchain-based traceability system is expected to technically encourage digital layer interconnection with the supporting digital components integrated into immutable-decentralized storage. This means the proposed system is acting as a coupling to create the DBE of the Indonesian coffee industry. It was discovered to have a better sensitivity to real-world demands because it is based on capturing and analyzing the problems of the coffee business community at the business layer. Moreover, it provides an integrated digital platform and accommodates business processes. This simply means the proposed system has a higher success rate for implementation in the real world because it answers real challenges, encourages the good business community's culture, and is supported by a mapped infrastructure layer.

7. 2. Findings, Limitations, and Recommendations

This study has several significant findings. First, eight blockchain-coffee projects publicly launched were mapped with the core highlight features published in each considered in developing other coffee industry projects. Second, the DBE framework was developed for Indonesian coffee with three essential layers including business, digital, and infrastructure. Third, a prototype of a coffee traceability system was successfully proposed based on blockchain technology using properties that match the challenge and community needs in the Indonesian coffee industry. As an integral part of the proposed DBE framework, the prototype proved to have a better success rate for implementation and can be used as a basic model to develop traceability systems in several Indonesian coffee industrial areas.

The subjectivity of studies in translating observations and interviews is one of the weaknesses of this study and can affect the final results in several sections. Moreover, there is a need for a more in-depth verification and validation process to increase the reliability of the results. The proposed system configurations were based on the perspective of the authors that participated as users and this means there is a possibility of different decisions when a model is developed based on other views such as the government's perspective. Furthermore, the focus was only on one species at the digital layer, blockchain, which was argued to be an emerging core technology with the potential to serve as the underlying technology to design a traceability system in the DBE of the Indonesian coffee industry. The stages of field observation and case study interviews were also limited to the Kintamani coffee agroindustry in Bali and this reduces the generalizability of the findings.

The results can be used by scholars and practitioners to develop a blockchain-based traceability system for the Indonesian coffee agroindustry or coffee agroindustry in general. For academics, it is recommended that future studies are focused on (1) further development or testing of the model proposed with due consideration for the required novelty gaps in blockchain projects on coffee as described in section 2 and recommendations made by Senyo et al. [40] to fill DBE gaps in theories, methodologies, and themes. (2) The proposed DBE model requires a performance evaluation using the method proposed by Sadri et al. [78] based on the layer components or those considered to be sensitive to the system.

At the infrastructure layer, (3) it is recommended that the development of the physical architecture using Radio Frequency Identification (RFID) [69] has been studied for more efficient product detection and IoT integration [79, 80]. In the software development process, there is a need to (4) consider the Blockchain Development Life Cycle (BDLC) framework proposed by Takyar[1] and iFour[2] as the method to develop a coffee traceability system in the future. It is also necessary to add monitoring and evaluation stages to the application model generated using valid verification and validation methods. Another important suggestion is that (5) several technical developments need to be conducted on the digital layer of the Indonesian coffee ecosystem to increase the capability and automation of the blockchain-

[1] www.leewayhertz.com/guide-to-blockchain-development-process

[2] www.ifourtechnolab.com/blog/blockchain-project-development-life-cycle

based traceability system. Furthermore, studies on adding machine learning techniques to classify the quality and adulteration of coffee [81, 82] or clustering as an approach to detect product mixing [83] need to be conducted. Some essential features such as notifications on product demand forecasting to provide production plans [84] are also suggested to be added. Moreover, there is a need to consider a broader scope of technology such as artificial intelligence, IoT, and cyber-physical systems. (6) It is also important to develop a copy traceability system in the future using the Hyperledger platform due to the ever-evolving blockchain technology as well as to use smart contracts with due consideration for the usage cases and requirements of the business community [85–88].

It was assumed that the components outside the developed model ideally support the proposed Indonesian Coffee DBE. Therefore, the recommendation for future study is to (7) measure the requirements and readiness value of implementing the proposed model [89]. Moreover, previous studies have reported a lack of understanding and limited application of blockchain technology in MSMEs in Indonesia [90, 91]. This led to the need to evaluate the acceptance and adoption of blockchain technology, especially in the coffee agroindustry, in future studies [92]. Finally, (8) there is also the need to study the closed-loop supply chain domain of agroindustry [93, 94] to support a sustainable environment and circular economy [95, 96].

8. MANAGERIAL INSIGHT/ACUMEN

The results from the field analysis, literature, and model development were used to present a comprehensive reference for decision-making in relation to the development of Indonesian coffee DBE. Moreover, the increasing trend of system development based on blockchain technology, especially for coffee traceability, led to some insights recommended to be adopted by the community, policymakers, and developers.

- The coffee business community first needs to pay attention to the success of forming a business community network with positive and cooperative interactions or mutualism between the species. For example, some fundamental things need to be regulated and determined such as the interaction patterns, transaction rules, and boundaries between each community. Furthermore, the business community needs to agree on the properties of the digital technology used and encourage the development of fundamental infrastructure by relevant stakeholders. The digital properties agreed upon should become the guidelines and proposals to develop the digital ecosystem layer.
- Regulators and government can play a more active role in developing the DBE of the Indonesian coffee industry. This is due to the fact that infrastructure development is an enabler for the development of the digital and business layer and this means it requires the attention of policymakers. Regulations are also needed to ensure the availability of fundamental infrastructure to develop the DBE. Furthermore, the government needs to be open to input from the business community, consider digital layer development proposals, and conducted development analysis with developers. Using a third-person point of view, the government can also develop alternative models such as systems based on Hyperledger. However, the implementation of such development requires the government, as a system request, to define its authority in the system to avoid destabilizing the trusted decentralization database system.
- Developers also need to ensure the model is not limited to software development but involves hardware and human components of the business community. The use of physical components such as IoT sensors, RFID, and other needs to be considered to increase system efficiency and the effectiveness of interactions among the Indonesian coffee business community. Finally, this insight is not limited to the development of Indonesian coffee DBE but extended to similar business ecosystems with several configurations tailored to the specific case studies to be completed.

9. ACKNOWLEDGMENT

The authors appreciate all the practitioners that provided data and information to develop the models as well as the Ministry of Education, Culture, Research, and Technology, the Republic of Indonesia for supporting this study through the PMDSU schema under Grant 001/E5/PG.02.00PT/2022.

10. REFERENCES

1. Pendergrast, M. "Coffee second only to oil? Is coffee really the second largest commodity? Mark Pendergrast investigates and finds some startling results." ***The Free Library***. Retrieved June 10, (2022), https://www.thefreelibrary.com/Coffee+second+only+to+oil%3F+Is+coffee+really+the+second+largest...-a0198849799
2. Toledo, P. R. A. B., Pezza, L., Pezza, H. R., and Toci, A. T. "Relationship Between the Different Aspects Related to Coffee Quality and Their Volatile Compounds." ***Comprehensive Reviews in Food Science and Food Safety***, Vol. 15, No. 4, (2016), 705-719. https://doi.org/10.1111/1541-4337.12205
3. Sezer, B., Apaydin, H., Bilge, G., and Boyaci, I. H. "Coffee

arabica adulteration: Detection of wheat, corn and chickpea." ***Food Chemistry***, Vol. 264, (2018), 142-148. https://doi.org/10.1016/j.foodchem.2018.05.037

4. Toci, A. T., Farah, A., Pezza, H. R., and Pezza, L. "Coffee Adulteration: More than Two Decades of Research." ***Critical Reviews in Analytical Chemistry***, Vol. 46, No. 2, (2016), 83-92. https://doi.org/10.1080/10408347.2014.966185
5. Song, H. Y., Jang, H. W., Debnath, T., and Lee, K. G. "Analytical method to detect adulteration of ground roasted coffee." ***International Journal of Food Science and Technology***, Vol. 54, No. 1, (2019), 256-262. https://doi.org/10.1111/ijfs.13942
6. Cheah, W. L., and Fang, M. "HPLC-Based Chemometric Analysis for Coffee Adulteration." ***Foods***, Vol. 9, No. 7, (2020), 880. https://doi.org/10.3390/foods9070880
7. Wang, X., Lim, L. T., and Fu, Y. "Review of analytical methods to detect adulteration in coffee." ***Journal of AOAC International***, Vol. 103, No. 2, (2020), 295-305. https://doi.org/10.1093/JAOCINT/QSZ019
8. Espiñeira, M., and Santaclara, F. J. "Advances in Food Traceability Techniques and Technologies: Improving Quality Throughout the Food Chain" ***Advances in Food Traceability Techniques and Technologies: Improving Quality Throughout the Food Chain***. https://doi.org/10.1016/C2014-0-01963-6
9. Jaison, F., and Ramaiah, N. S. "A survey on traceability in food safety system using blockchain." ***Journal of Discrete Mathematical Sciences and Cryptography***, Vol. 25, No. 3, (2022), 793-799. https://doi.org/10.1080/09720529.2021.2016215
10. Wust, K., and Gervais, A. "Do you need a blockchain?" In 2018 Crypto Valley Conference on Blockchain Technology (CVCBT), 45-54. https://doi.org/10.1109/CVCBT.2018.00011
11. Gad, A. G., Mosa, D. T., Abualigah, L., and Abohany, A. A. "Emerging Trends in Blockchain Technology and Applications: A Review and Outlook." ***Journal of King Saud University - Computer and Information Sciences***, Vol. 34, No. 9, (2022), 6719-6742. https://doi.org/10.1016/j.jksuci.2022.03.007
12. Nakamoto, S. "Bitcoin: A Peer-to-Peer Electronic Cash System," (2008), 1-9. https://doi.org/10.1162/ARTL_a_00247
13. Derbentsev, V., Babenko, V., Khrustalev, K., Obruch, H., and Khrustalova, S. "Comparative performance of machine learning ensemble algorithms for forecasting cryptocurrency prices." ***International Journal of Engineering, Transactions A: Basics***, Vol. 34, No. 1, (2021), 140-148. https://doi.org/10.5829/IJE.2021.34.01A.16
14. Khedmati, M., Seifi, F., and Azizi, M. J. "Time series forecasting of bitcoin price based on autoregressive integrated moving average and machine learning approaches." ***International Journal of Engineering, Transactions A: Basics***, Vol. 33, No. 7, (2020), 1293-1303. https://doi.org/10.5829/ije.2020.33.07a.16
15. Buterin, V. "Ethereum : The Ultimate Smart Contract and Decentralized Application Platform (white paper), (2013)," (2013).
16. Moosavi, J., Naeni, L. M., Fathollahi-Fard, A. M., and Fiore, U. "Blockchain in supply chain management: a review, bibliometric, and network analysis." ***Environmental Science and Pollution Research***, (2021). https://doi.org/10.1007/s11356-021-13094-3
17. Shuaib, M., Hafizah Hassan, N., Usman, S., Alam, S., Bhatia, S., Koundal, D., Mashat, A., and Belay, A. "Identity Model for Blockchain-Based Land Registry System: A Comparison." ***Wireless Communications and Mobile Computing***, Vol. 2022, (2022). https://doi.org/10.1155/2022/5670714
18. Racetin, I., Kilić Pamuković, J., Zrinjski, M., and Peko, M. "Blockchain-Based Land Management for Sustainable Development." ***Sustainability (Switzerland)***, Vol. 14, No. 17, (2022). https://doi.org/10.3390/su141710649
19. Hassan Onik, M. M., Miraz, M. H., and Kim, C. S. "A recruitment and human resource management technique using blockchain technology for industry 4.0." In IET Conference Publications, Vol. 2018, 1-6. https://doi.org/10.1049/cp.2018.1371
20. Jafar, U., Ab Aziz, M. J., Shukur, Z., and Hussain, H. A. "A Systematic Literature Review and Meta-Analysis on Scalable Blockchain-Based Electronic Voting Systems." ***Sensors***, Vol. 22, No. 19, (2022). https://doi.org/10.3390/s22197585
21. González-Puetate, I., Marín-Tello, C., and Pineda, H. R. "Agri-food safety optimized by blockchain technology: review." ***Revista Facultad Nacional de Agronomia Medellin***, Vol. 75, No. 1, (2022), 9839-9851. https://doi.org/10.15446/RFNAM.V75N1.95760
22. Moosavi, J., Fathollahi-Fard, A. M., and Dulebenets, M. A. "Supply chain disruption during the COVID-19 pandemic: Recognizing potential disruption management strategies." ***International Journal of Disaster Risk Reduction***, Vol. 75, No. April, (2022), 102983. https://doi.org/10.1016/j.ijdrr.2022.102983
23. Cozzini, P., Agosta, F., Dolcetti, G., and Righi, G. "How a Blockchain Approach Can Improve Data Reliability in the COVID-19 Pandemic." ***ACS Medicinal Chemistry Letters***, Vol. 13, No. 4, (2022), 517-519. https://doi.org/10.1021/acsmedchemlett.2c00077
24. Dashtizadeh, M., Meskaran, F., and Tan, D. "A Secure Blockchain-based Pharmaceutical Supply Chain Management System: Traceability and Detection of Counterfeit Covid-19 Vaccines." In 2022 IEEE 2nd Mysore Sub Section International Conference (MysuruCon). IEEE. https://doi.org/10.1109/MysuruCon55714.2022.9972646
25. Krithika, L. B. S. "Survey on the Applications of Blockchain in Agriculture." ***Agriculture***, Vol. 12, No. 9, (2022), 1333. https://doi.org/10.47059/revistageintec.v11i4.2409
26. Sendros, A., Drosatos, G., Efraimidis, P. S., and Tsirliganis, N. C. "Blockchain Applications in Agriculture: A Scoping Review." ***Applied Sciences (Switzerland)***, Vol. 12, No. 16, (2022), 1-37. https://doi.org/10.3390/app12168061
27. Gillpatrick, T., Boğa, S., and Aldanmaz, O. "How Can Blockchain Contribute to Developing Country Economies? A Literature Review on Application Areas." ***Economics***, Vol. 10, No. 1, (2022), 105-128. https://doi.org/10.2478/eoik-2022-0009
28. Nachira, F., Nicolai, A., Dini, P., Louarn, M. Le, and Leon, L. R. Digital Business Ecosystems, Grouth Macro Economy Micro Economy Innovation Inclusion Efficiency Opportunities Social Science Socio-Cultural Layered Infrastructure-Adapts to Regions Cultural / Economi. Luxembourg: Office for Official Publications of the European Communities. Retrieved from http://www.digital-ecosystems.org/dbe-book-2007
29. Corallo, A., Passiante, G., and Prencipe, A. The digital business ecosystem. ***The Digital Business Ecosystem***. https://doi.org/10.4337/9781781009925
30. Herdon, M., Péntek, A., and Varallyai, L. "Digital business ecosystem prototyping for agri-food SMEs." ***CEUR Workshop Proceedings***, Vol. 1152, (2011), 273-285. https://doi.org/10.1108/13287261211279026
31. Galanakis, C. M. Food Technology Disruptions. ***Food Technology Disruptions***. Elsevier. https://doi.org/10.1016/B978-0-12-821470-1.01001-6
32. Pane, T. C., and Khaliqi, M. "Consumers' preferences for North Sumatera specialty coffees." IOP Conference Series: Earth and Environmental Science, Vol. 977, No. 1, (2022). https://doi.org/10.1088/1755-1315/977/1/012049
33. Dermoredjo, S. K., Pasaribu, S. M., Azahari, D. H., and Yusuf, E. S. "Indonesia's coffee and cocoa agribusiness opportunities in Regional Comprehensive Economic Partnership trade

cooperation." IOP Conference Series: Earth and Environmental Science, Vol. 892, No. 1, (2021). https://doi.org/10.1088/1755-1315/892/1/012071

34. Tseng, M.-L., Buia, T.-D., Lewi, S., Rizaldy, H., Lim, M. K., and Wu, K.-J. "Causality sustainable supply chain management practices in the Indonesian coffee industry using qualitative information: digitalization integration leads performance improvement." ***International Journal of Logistics Research and Applications***, (2022). https://doi.org/10.1080/13675567.2022.2155936
35. Sarvina, Y., June, T., Sutjahjo, S. H., Nurmalina, R., and Surmaini, E. "Why Should Climate Smart Agriculture Be Promoted In The Indonesian Coffee Production System?" ***Journal of Sustainability Science and Management***, Vol. 16, No. 7, (2021), 347-363. https://doi.org/10.46754/jssm.2021.10.024
36. Saha, A. S., Raut, R. D., Yadav, V. S., and Majumdar, A. "Blockchain Changing the Outlook of the Sustainable Food Supply Chain to Achieve Net Zero?" ***Sustainability (Switzerland)***, Vol. 14, No. 24, (2022). https://doi.org/10.3390/su142416916
37. Hameed, K., Barika, M., Garg, S., Amin, M. B., and Kang, B. "A taxonomy study on securing Blockchain-based Industrial applications: An overview, application perspectives, requirements, attacks, countermeasures, and open issues." ***Journal of Industrial Information Integration***, Vol. 26, (2022). https://doi.org/10.1016/j.jii.2021.100312
38. Altaf, A., Iqbal, F., Latif, R., Yakubu, B. M., Latif, S., and Samiullah, H. "A Survey of Blockchain Technology: Architecture, Applied Domains, Platforms, and Security Threats." ***Social Science Computer Review***, (2022), 1-22. https://doi.org/10.1177/08944393221110148
39. Zhou, Q., Zhang, H., and Wang, S. "Artificial intelligence, big data, and blockchain in food safety." ***International Journal of Food Engineering***, Vol. 18, No. 1, (2022), 1-14. https://doi.org/10.1515/ijfe-2021-0299
40. Senyo, P. K., Liu, K., and Effah, J. "Digital business ecosystem: Literature review and a framework for future research." ***International Journal of Information Management***, Vol. 47, No. June 2018, (2019), 52-64. https://doi.org/10.1016/j.ijinfomgt.2019.01.002
41. Kordon, F., and Luqi. "An introduction to rapid system prototyping." ***IEEE Transactions on Software Engineering***, Vol. 28, No. 9, (2002), 817-821. https://doi.org/10.1109/TSE.2002.1033222
42. Pressman, R. S., and Mixim, B. M. Software Engineering A Practitioners Approach (Ninth.). New York: McGraw-Hill Education.
43. Valacich, J. S., and George, J. F. Modern Systems Analysis and Design (Ninth Edit.). United Kingdom: Pearson Education Limited.
44. Booch, G., Rumbaugh, J., and Jacobson, I. The Unified Modeling Language Users Guide. ***Addison Wesley (2nd Edition)*** (Second.). Addison-Wesley.
45. Pearce, P., and Friedenthal, S. "A Practical Approach For Modelling Submarine Subsystem Architecture In SysML." In ***Submarine Institute of Australia Science, Technology & Engineering Conference*** (347-360).
46. Betttin-Diaz, R., Rojas, A. E., and Mejia-Moncayo, C. "Methodological Approach to the Definition of a Blockchain System Chain Traceability." In 18th International Conference on Computational Science and Its Applications, 19-33. Springer. https://doi.org/10.1007/978-3-319-95165-2
47. BPS-Statistics Indonesia. Statistik Kopi Indonesia (Indonesian Coffee Statistics) 2019 (2019th ed.). Jakarta: BPS-Statistics Indonesia.
48. ICO. *World Coffee Production 2021*. International Coffee Organization. https://doi.org/10.1079/9781845931292.0017
49. Toffin. *2020 BREWING IN INDONESIA: Insights for Successful Coffee Shop Business*. ***Toffin***. Retrieved from https://toffin.id/?page_id=2853
50. ICO. *World Coffee Consumption 2021*. Internacional Coffee Organization (Vol. January). Retrieved from http://www.ico.org/trade_statistics.asp?section=Statistics
51. Pradana, I. G. M. T., Djatna, T., and Hermadi, I. "Blockchain modeling for traceability information system in supply chain of coffee agroindustry." In 2020 International Conference on Advanced Computer Science and Information Systems, ICACSIS 2020, 217-224. https://doi.org/10.1109/ICACSIS51025.2020.9263214
52. Panggabean, Y. B. S., Arsyad, M., Mahyuddin, and Nasaruddin. "Coffee farming business development: E-commerce technology utilization." IOP Conference Series: Earth and Environmental Science, Vol. 807, No. 3, (2021), 0-7. https://doi.org/10.1088/1755-1315/807/3/032011
53. Tsatsou, P., Elaluf-Calderwood, S., and Liebenau, J. "Towards a taxonomy for regulatory issues in a digital business ecosystem in the EU." ***Journal of Information Technology***, Vol. 25, No. 3, (2010), 288-307. https://doi.org/10.1057/jit.2009.22
54. Burlacu, G., Cojocaru, L. E., Danila, C., Popescu, D., and Stanescu, A. M. "A digital business ecosystem integrated approach for farm management information system." 2013 2nd International Conference on Systems and Computer Science, ICSCS 2013, (2013), 80-85. https://doi.org/10.1109/IcConSCS.2013.6632027
55. Djatna, T., and Ginantaka, A. "An analysis and design of frozen shrimp traceability system based on digital business ecosystem." In Proceedings - ICACSIS 2014: 2014 International Conference on Advanced Computer Science and Information Systems, 157-163. https://doi.org/10.1109/ICACSIS.2014.7065876
56. Djatna, T., and Luthfiyanti, R. "An Analysis and Design of Responsive Supply Chain for Pineapple Multi Products SME Based on Digital Business Ecosystem (DBE)." ***Procedia Manufacturing***, Vol. 4, (2015), 155-162. https://doi.org/10.1016/j.promfg.2015.11.026
57. Matopoulos, A., Herdon, M., Várallyai, L., and Péntek, Á. "Digital business ecosystem prototyping for SMEs." ***Journal of Systems and Information Technology***, Vol. 14, No. 4, (2012), 286-301. https://doi.org/10.1108/13287261211279026
58. Chauhan, H., Gupta, D., Gupta, S., Nayak, S. R., Shankar, A., and Singh, P. "Framework for Enhancing the Traceability in Supply Chain Using Blockchain." ***Journal of Interconnection Networks***, Vol. 22, , (2022), 1-19. https://doi.org/10.1142/S0219265921440084
59. Garcia, A., Davila, J., and Wong, L. "Framework to Improve the Traceability of the Coffee Production Chain in Perú by Applying a Blockchain Architecture." Conference of Open Innovation Association, FRUCT, Vol. 2022-Novem, , (2022), 93-101. https://doi.org/10.23919/FRUCT56874.2022.9953846
60. Patro, P. K., Jayaraman, R., Salah, K., and Yaqoob, I. "Blockchain-Based Traceability for the Fishery Supply Chain." ***IEEE Access***, Vol. 10, No. August, (2022), 81134-81154. https://doi.org/10.1109/ACCESS.2022.3196162
61. Liu, P., Li, Q., Yuan, S., Liu, W., Yun, Z., Dai, Y., Duan, M., and Nian, Y. "Design and Implementation of Blockchain Based Food Quality and Safety Traceability Platform." In ACM International Conference Proceeding Series. https://doi.org/10.1145/3513142.3513210
62. Qiu, X., and Tian, Z. Blockchain-based cable supply chain traceability system. ACM International Conference Proceeding

Series (Vol. 1). Association for Computing Machinery. https://doi.org/10.1145/3569966.3569977

63. Pang, Y., Wang, D., Wang, X., Li, J., and Zhang, M. "Blockchain-Based Reliable Traceability System for Telecom Big Data Transactions." ***IEEE Internet of Things Journal***, Vol. 9, No. 14, (2022), 12799-12812. https://doi.org/10.1109/JIOT.2021.3138462
64. Yang, X., Li, M., Yu, H., Wang, M., Xu, D., and Sun, C. "A Trusted Blockchain-Based Traceability System for Fruit and Vegetable Agricultural Products." ***IEEE Access***, Vol. 9, , (2021), 36282-36293. https://doi.org/10.1109/ACCESS.2021.3062845
65. Yao, Q., and Zhang, H. "Improving Agricultural Product Traceability Using Blockchain." ***Sensors***, Vol. 22, No. 9, (2022). https://doi.org/10.3390/s22093388
66. Asadi Saeed Abad, F., and Hamidi, H. "An architecture for security and protection of big data." ***International Journal of Engineering, Transactions A: Basics***, Vol. 30, No. 10, (2017), 1479-1486. https://doi.org/10.5829/ije.2017.30.10a.08
67. Cocco, L., Mannaro, K., Tonelli, R., Mariani, L., Lodi, M. B., Melis, A., Simone, M., and Fanti, A. "A Blockchain-Based Traceability System in Agri-Food SME: Case Study of a Traditional Bakery." ***IEEE Access***, Vol. 9, (2021), 62899-62915. https://doi.org/10.1109/ACCESS.2021.3074874
68. Thume, M., Lange, J., Unkel, M., Prange, A., and Schürmeyer, M. "Blockchain-based traceability in the food industry: requirements analysis along the food supply chain." ***Technical Report***, Vol. 1466, (2021), 0-3. https://doi.org/10.31219/osf.io/uyb64
69. Wang, L., He, Y., and Wu, Z. "Design of a Blockchain-Enabled Traceability System Framework for Food Supply Chains." ***Foods***, Vol. 11, No. 5, (2022), 1-18. https://doi.org/10.3390/foods11050744
70. Tharatipyakul, A., and Pongnumkul, S. "User Interface of Blockchain-Based Agri-Food Traceability Applications: A Review." ***IEEE Access***, Vol. 9, (2021), 82909-82929. https://doi.org/10.1109/ACCESS.2021.3085982
71. Tharatipyakul, A., Pongnumkul, S., Riansumrit, N., Kingchan, S., and Pongnumkul, S. "Blockchain-Based Traceability System From the Users' Perspective: A Case Study of Thai Coffee Supply Chain." ***IEEE Access***, Vol. 10, (2022), 98783-98802. https://doi.org/10.1109/ACCESS.2022.3206860
72. Samper, L. F., and Quiñones-Ruiz, X. F. "Towards a balanced sustainability vision for the coffee industry." ***Resources***, Vol. 6, No. 2, (2017), 1-28. https://doi.org/10.3390/resources6020017
73. Ulupui, I. G. K. A., and Gurendrawati, E. "The role of local wisdom in the construction of good governance: An ethnography study in social organization in Bali Indonesia." In 32nd International Business Information Management Association (IBIMA) (454-466).
74. Suasih, N. N. R. S., Budhi, M. K. S., Yasa, I. N. M., and Saskara, I. A. N. "Implementation of Local Wisdom in Adoption of Innovation to Increase Traditional Farmer's Welfare in Bali." ***Journal of Comparative Asian Development***, Vol. 17, No. 1, (2018), 197-215.
75. Risna, R. A., Rustini, H. A., Herry, Buchori, D., and Pribadi, D. O. "Subak, a Nature-based Solutions Evidence from Indonesia." IOP Conference Series: Earth and Environmental Science, Vol. 959, No. 1, (2022). https://doi.org/10.1088/1755-1315/959/1/012030
76. Saputra, K. A. K., Mu'ah, Jurana, Korompis, C. W. M., and Manurung, D. T. H. "Fraud Prevention Determinants: A Balinese Cultural Overview." ***Australasian Accounting, Business and Finance Journal***, Vol. 16, No. 3, (2022), 167-181. https://doi.org/10.14453/aabfj.v16i3.11
77. Sedana, G., and Abdul, R. "Alternative Policies to Strengthen the Traditional Irrigation System for Supporting the Food Security Program:: Case of the Subaks' System in Bali, Indonesia." ***International Journal of Advanced Science and Technology***, Vol. 29, No. 7s, (2020), 973-984. Retrieved from http://sersc.org/journals/index.php/IJAST/article/view/10109
78. Sadri, E., Harsej, F., Hajiaghaei-Keshteli, M., and Siyahbalaii, J. "Evaluation of the components of intelligence and greenness in Iranian ports based on network data envelopment analysis (DEA) approach." ***Journal of Modelling in Management***, Vol. 17, No. 3, (2022), 1008-1027. https://doi.org/10.1108/JM2-03-2021-0071
79. Ferrández-Pastor, F. J., Mora-Pascual, J., and Díaz-Lajara, D. "Agricultural traceability model based on IoT and Blockchain: Application in industrial hemp production." ***Journal of Industrial Information Integration***, Vol. 29, No. May, (2022), 100381. https://doi.org/10.1016/j.jii.2022.100381
80. Zhang, Q. "Analysis of Agricultural Products Supply Chain Traceability System Based on Internet of Things and Blockchain." ***Mathematical Problems in Engineering***, Vol. 2022, (2022). https://doi.org/10.1155/2022/3162871
81. Mavaddati, S. "Rice classification and quality detection based on sparse coding technique." ***International Journal of Engineering, Transactions B: Applications***, Vol. 31, No. 11, (2018), 1910-1917. https://doi.org/10.5829/ije.2018.31.11b.15
82. de Morais, T. C. B., Rodrigues, D. R., de Carvalho Polari Souto, U. T., and Lemos, S. G. "A simple voltammetric electronic tongue for the analysis of coffee adulterations." ***Food Chemistry***, Vol. 273, (2019), 31-38. https://doi.org/10.1016/j.foodchem.2018.04.136
83. Pradana, I. G. M. T., and Djatna, T. "A design of traceability system in coffee supply chain based on hierarchical cluster analysis approach." In 2020 International Conference on Computer Science and Its Application in Agriculture, ICOSICA 2020. https://doi.org/10.1109/ICOSICA49951.2020.9243203
84. Al-Ani, B. R. K., and Erkan, E. T. "A Study of Load Demand Forecasting Models in Electricity Using Artificial Neural Networks and Fuzzy Logic Model." ***International Journal of Engineering Transactions C: Aspects***, Vol. 35, No. 6, (2022), 1111-1118. https://doi.org/10.5829/ije.2022.35.06c.02
85. Abebe, T. M., and Semegn, A. M. "Blockchain Based Green Coffee Supply Chain Management to Improve Traceability and Transparency (Case Study on Sidama Coffee) BT - Advances of Science and Technology." In M. A. Delele, M. A. Bitew, A. A. Beyene, S. W. Fanta, & A. N. Ali (Eds.), (Vol. 1, 304-318). Cham: Springer International Publishing. https://doi.org/10.1007/978-3-030-80621-7
86. Bettín-Díaz, R., Rojas, A. E., and Mejía-Moncayo, C. "Colombian Origin Coffee Supply Chain Traceability by a Blockchain Implementation." ***Operations Research Forum***, Vol. 3, No. 64, (2022), 64. https://doi.org/10.1007/s43069-022-00174-4
87. Valencia-Payan, C., Grass-Ramirez, J. F., Ramirez-Gonzalez, G., and Corrales, J. C. "A Smart Contract for Coffee Transport and Storage With Data Validation." ***IEEE Access***, Vol. 10, , (2022), 37857-37869. https://doi.org/10.1109/ACCESS.2022.3165087
88. Marchese, A., and Tomarchio, O. "A Blockchain-Based System for Agri-Food Supply Chain Traceability Management." ***SN Computer Science***, Vol. 3, No. 4, (2022). https://doi.org/10.1007/s42979-022-01148-3
89. Kampan, K., Tsusaka, T. W., and Anal, A. K. "Adoption of Blockchain Technology for Enhanced Traceability of Livestock-Based Products." ***Sustainability (Switzerland)***, Vol. 14, No. 20, (2022), 1-16. https://doi.org/10.3390/su142013148
90. Wahyuni, A. E., Juraida, A., and Anwar, A. "The Development of TRAM Model for Blockchain Use Readiness Among MSMEs in Indonesia BT - Proceedings of the Ninth International

Conference on Entrepreneurship and Business Management (ICEBM 2020)", 172-177. Atlantis Press. https://doi.org/https://doi.org/10.2991/aebmr.k.210507.026

91. Wahyuni, A. E., Juraida, A., and Anwar, A. "Readiness factor identification Bandung city MSMEs use blockchain technology." ***Jurnal Sistem dan Manajemen Industri***, Vol. 5, No. 2, (2021), 53-62. https://doi.org/10.30656/jsmi.v5i2.2787
92. Rijanto, A. "Business financing and blockchain technology adoption in agroindustry." ***Journal of Science and Technology Policy Management***, Vol. 12, No. 2, (2020), 215-235. https://doi.org/10.1108/JSTPM-03-2020-0065
93. Cheraghalipoura, A., Paydar, M. M., and Hajiaghaei-Keshtelia, M. "An Integrated Approach for Collection Center Selection in Reverse Logistics." ***International Journal of Engineering Transaction A: Basics***, Vol. 30, No. 7, (2017), 1005-1016. https://doi.org/10.5829/ije.2017.30.07a.10
94. Fasihi, M., Tavakkoli-Moghaddam, R., Najafi, S. E., and Hahiaghaei-Keshteli, M. "Developing a Bi-objective mathematical model to design the fish closed-loop supply chain." ***International Journal of Engineering, Transactions B: Applications***, Vol. 34, No. 5, (2021), 1257-1268. https://doi.org/10.5829/ije.2021.34.05b.19
95. Rejeb, A., Zailani, S., Rejeb, K., Treiblmaier, H., and Keogh, J. G. "Modeling enablers for blockchain adoption in the circular economy." ***Sustainable Futures***, Vol. 4, (2022), 100095. https://doi.org/10.1016/j.sftr.2022.100095
96. Pakseresht, A., Ahmadi Kaliji, S., and Xhakollari, V. "How Blockchain Facilitates the Transition toward Circular Economy in the Food Chain?" ***Sustainability (Switzerland)***, Vol. 14, No. 18, (2022), 1-22. https://doi.org/10.3390/su141811754

Persian Abstract

چکیده

قهوه یک کالای مهم کشاورزی در کشورهای در حال توسعه مانند اندونزی است. بنابراین اجرای یک سیستم قابل ردیابی قابل اعتماد برای محصول بسیار مهم است. با این حال، هیچ دستورالعمل مشخصی برای توسعه یک سیستم ردیابی مبتنی بر بلاک چین وجود ندارد که صنعت قهوه بتواند آن را اتخاذ کند. بنابراین، این مطالعه با هدف ارائه یک چارچوب اکوسیستم کسب و کار دیجیتال (DBE)و یک نمونه اولیه سیستم ردیابی مبتنی بر بلاک چین برای قهوه اندونزی است. فرآیند مطالعه شامل بررسی ادبیات، مشاهدات میدانی، و ایجاد چارچوب‌ها و نمونه‌های اولیه با استفاده از روش نمونه‌سازی سریع یکپارچه بود. چارچوب DBE پیشنهادی دارای سه لایه است: تجاری، دیجیتال و زیرساخت، در حالی که نمونه اولیه دارای نمودارهای مورد استفاده و مدلی از جریان های عملکردی، تکنولوژیکی و تراکنش است. این سیستم از طریق آزمایش‌های استقرار مانند ضبط و ردیابی داده‌های قهوه با استفاده از قراردادهای هوشمند اتریوم و سیستم فایل بین سیاره‌ای تأیید شد. اتصال متقابل از طریق طراحی رابط کاربری مبتنی بر تلفن همراه که شامل صفحات ثبت نام و ورود به سیستم، صفحه اصلی، صفحه تایید تراکنش و صفحه قابلیت ردیابی است، تأیید شد. مشخص شد که چارچوب و نمونه اولیه پیشنهادی به دلیل توانایی آنها در مقابله موثر با چالش‌ها و ترویج فرهنگ مثبت جامعه تجاری در حالی که توسط لایه‌های DBE نقشه‌برداری شده پشتیبانی می‌شوند، پتانسیل بالایی برای پیاده‌سازی در دنیای واقعی دارند. مطالعه بیشتر برای آزمایش و تقویت چارچوب و نمونه های اولیه پیشنهادی و بررسی رابطه بین توسعه سیستم و پذیرش فناوری توصیه می شود. علاوه بر این، بینش های مدیریتی برای توسعه موفقیت آمیز DBE قهوه اندونزی با سیستم ردیابی مبتنی بر بلاک چین به جامعه کسب و کار قهوه، سیاست گذاران و توسعه دهندگان ارائه شد.

International Journal of Engineering

Journal Homepage: www.ije.ir

Investigation and Optimization of Tribological Aspects of Babbitt-Ilmenite Composite using Weighted Grey Relation Analysis

A. S. Wadhwa*, A. Chauhan

University Institute of Engineering and Technology, Panjab University, Chandigarh, India

P A P E R I N F O

Paper history:
Received 21 December 2022
Received in revised form 01 February 2023
Accepted 19 February 2023

Keywords:
Morphological
Taguchi
Entropy
Analysis of Variance
Grey Relation Grade

A B S T R A C T

Babbitt-Ilmenite composite prepared via stir casting method with controllable parameters which include percentage weight of Ilmenite, stirring speed and aging time was investigated for its sliding wear characteristics and coefficient of friction (COF) with varying applied load, sliding velocity and sliding distance. Morphological tests were conducted for characterization of the composite and to ascertain the wear mechanism under mild and severe conditions. Taguchi philosophy with analysis of variance (ANOVA) statistical technique was used for multi-objective optimization of the tribological characteristics of the composite. The entropy based grey relation analysis (EGRA) performed for weighted multi-performance optimization of tribological aspects of the composite and hybrid Taguchi grey relation technique (TGRA) confirmed that the percentage weight of Ilmenite, applied load, sliding distance and stirring speed were the significant parameters with regard to multi - criteria optimization with contributions of 44.46%, 23.82%, 11.33%, and 5.66%, respectively. There is an overall improvement in wear resistance and COF at optimal TGRA conditions. Babbitt-Ilmenite composite can be used in steel slide bearing bushings for power, automobile and aerospace.

***doi**: 10.5829/ije.2023.36.05b.06*

1. INTRODUCTION

Metal matrix composites (MMCs) outperform monolithic materials in terms of strength, stiffness, wear resistance and weight reduction [1]. In MMCs a fibrous or particulate reinforcing phase is dispersed in a metallic matrix. The presence of hard phase in the metal matrix protects it from wear [2, 3]. Ceramic reinforced MMCs have higher sliding wear resistance resulting in improved tribological properties of the composite [4, 5]. The applied load is transmitted from the ductile matrix to the hard reinforcements during sliding wear resulting in higher wear resistance of the composite [6]. Solid lubricants like graphite forms protective layer between the counterpart and metal surface and lowers wear rate of the composite [7]. Secondary reinforcements like rice husk ash (RHA), fly ash, bamboo leaf ash (BLA) resulted in developing low-cost hybrid composite with good sliding wear characteristics comparable to single reinforced composite [8]. The addition of ceramic reinforcements decreases the wear rate of composite which remain constant with time and the wear performance of single ceramic reinforced composite is found to be better at elevated temperatures [9]. Wear rate is influenced the most with variation in load, sliding distance and speed conditions [10-12]. Sliding speed indirectly influence the worn morphology of the composite through temperature change leading to formation of mechanically mixed layer which affects the wear rate [13, 14]. Vortex stir casting is the most convenient and economical liquid state method to fabricate metal matrix composites [15-17] and the controllable parameters from the relevant literature survey which affect the tribological properties of the composite include percentage weight of reinforcement (W), stirring speed (S) and aging time (A) [18-23].

1. 1. Grey Relational Analysis (GRA) Several

*Corresponding Author Institutional Email: *aman_wadhwa77@rediffmail.com* (A. S. Wadhwa)

Please cite this article as: A. S. Wadhwa, A. Chauhan, Investigation and Optimization of Tribological Aspects of Babbitt-Ilmenite Composite using Weighted Grey Relation Analysis, ***International Journal of Engineering, Transactions B: Applications***, Vol. 36, No. 05, (2023) 894-903

scholars have utilized Grey relational analysis to optimize control parameters with more than one response by aggregating all performance attributes to a lone distinguishing characteristic called Grey relational grade to be optimized [24-27]. The procedure for grey relational analysis to optimize multi-performance characteristics is as:

1) Data Pre-processing: The responses are normalized from zero (0) to one (1) to reduce the scatter. The two most commonly used criteria for normalizing the sequence are larger is better and smaller is better. The expressions for the two criteria are:

For larger is better:

$$Yij = \frac{Zij - \min(Zij)}{\max(Zij) - \min(Zij)} \quad (1)$$

For smaller is better:

$$Yij = \frac{\max(Zij) - Zij}{\max(Zij) - \min(Zij)} \quad (2)$$

where, Yij refers to normalized value and Zij is the experimental response.

2) Determine Grey relation Coefficient

In order to establish the relationship between ideal and actual normalized response the factor called Grey relational coefficient (ξ) is calculated as:

$$\xi i = \frac{\Delta \min + \varsigma \Delta max}{\Delta i + \varsigma \Delta max} \quad (3)$$

where ς is the distinguish coefficient taken as 0.5 for better stability and moderate distinguish effects [28] and Δi is the difference between 1 and normalized value of i^{th} experiment treated as quality loss from target value. The values of Δ min and Δ max are 0 and 1, respectively.

3) Generation of Grey relation grade (GRG)

The Grey relation grade is then calculated as a weighted average of Grey relation coefficient for all the responses corresponding to one set of test parameters in an orthogonal array.

$$\alpha(i) = \sum_{k=1}^{n} w_k \xi_i(k) \quad (4)$$

where α(i) is the Grey relational grade corresponding to i^{th} experiment, w_k is the weight of k^{th} response, n are the number of performance attributes to be optimized such that $\sum_1^n w_k = 1$.

2. DEVELOPMENT OF BABBITT/ILMENITE COMPOSITE

2. 1. Materials In the process of composite fabrication, ASTM B-23 Grade 2 Babbitt alloy has been utilized as a matrix material. It is the bearing alloy used frequently for high speeds and large loads industrial applications. For the present investigation, it was obtained in form of ingots from Jain Metal Corporation in Ahmedabad, Gujarat. It has density of 7.39 g/cm^3 with melting and pouring temperature of 241°C and 424°C, respectively. Hardness, Tensile strength, Impact strength and fatigue strength of ASTM-23 Grade 2 Babbitt is 24.5 BHN, 77MPa, 3.4 J and 33 MPa, respectively. The 149-micron ball-milled Ilmenite procured from Integral Trading, Rajkot-360005 was utilized to reinforce Tin Babbitt composite. It is blackish grey, weakly magnetic, brittle, and has a high strength-to-weight ratio. It has specific gravity of 4.7 and hardness range of 5.5-6 MHN.

2. 2. Method Babbitt/Ilmenite composite was fabricated by vortex stir casting. The vortex produced by the impeller ensures uniform mixing at relatively low cost. Babbitt ingots were cut and stacked in the crucible. After weighing the alloy and reinforcement, the cut pieces were put in a muffle furnace maintained at 400 °C. Following the melting of the metal matrix, reinforcement was incorporated into the molten state at the desired speed, and the mixture was agitated for a period of five minutes. To ensure an even distribution of reinforcement, the molten material in the furnace was brought up to a temperature of 440°C and swirled again for few seconds. Then the molten material is put in the mold and the casting thus obtained after solidification was machined to proper size and form for tribological test. In order to refine the surface characteristics of the material, the samples were aged at 150 ° C for 2, 8, 24 and 48 hours and allowed to cool at ambient temperature.

3. TESTING

3. 1. Tribological Tests Wear test of the composite samples was performed using Tribometer (Model: TR-20LE-PHM-CHM- 400, Make: Ducom, Bangalore) in unlubricated conditions at temperature of 20 ± 2°C and relative humidity of 55± 5% (Figure 1). The ASTM G99-05 standard is used for testing the samples of 10 mm diameter and 30 mm length under varied experimental conditions according to designed orthogonal array. Steel disc of wear testing have hardness and surface roughness of 60 HRC and 1.6 Ra, respectively. The track diameter was kept constant at 100mm. The flat surface of the cylindrical pin is grounded manually with fine grained abrasive paper of 1200 grit size to achieve average surface roughness (Ra) of 100 nm. The counter weight mechanism has been provided with the tribo-meter to rigidly hold the grounded end of the pin against the steel disc for abrasive action and a digital microbalance with a least count of 1/10000 g was employed to weigh the specimen both before and after the wear test. The percentage weight of Ilmenite, stirring speed and aging time were selected as manufacturing test parameters whereas applied load, sliding distance and velocity were chosen as tribological test parameters based on extensive literature survey for L16 Taguchi array. The selected test parameters influence the sliding wear characteristics of the composite to the great extent and the weight loss due

Figure 1. Pin on disc wear testing machine

to wear was calculated as the difference between initial weight and final weight for each sample after wear test. Coefficient of friction.

(COF) is evaluated as the mean of steady state region from the graphs between coefficient of friction and time generated through WINDCOM software integrated with the tribo-tester (Table 1). An alternative way to find COF is to determine mean tangential force from the software and divide it by normal applied test load. The experiments were conducted with repeatability of two to minimize errors.

3. 2. Morphological Tests The microstructural analysis of the composite specimen was done using FESEM (Maker: Hitachi, Japan, Model: SU 8010 series) with resolution of 1nm at accelerating voltage of 1 kV after following the standard metallographic testing procedure. The specimen was initially polished with emery papers of different grit sizes ranging from 80 to 2000 and then polished on disc machine. After polishing the specimen were cleaned with acetone for clear image in microstructural analysis. The scanning electron micrograph and energy dispersive spectrum of ASTM B-23 Grade 2 Babbitt alloy are shown in Figures 2 and 3 respectively. Figure 4 shows the SEM micrograph of composite corresponding to Experiment No. 13 clearly indicating the presence of Ilmenite in the Babbitt alloy. The energy dispersive spectrum of Babbitt/8% Ilmenite composite shows the presence of peaks of Fe, Ti, Cl, Si, Mn, Mg, Na, Va, Al, Cu and Cr thereby ensuring successful amalgamation of Ilmenite in the metallic matrix (Figure 5). The element and atomic weight percentage for the EDS spectrum of Babbitt alloy and the

TABLE 1. Element and atomic wt% for the EDS spectrum of Babbitt alloy (Figure 3)

Element	wt%	Atomic wt%
Sn	89.9	88.68
Sb	7.39	7.11
Pb	0.62	0.35
Cu	2.09	3.86
Total	100	100

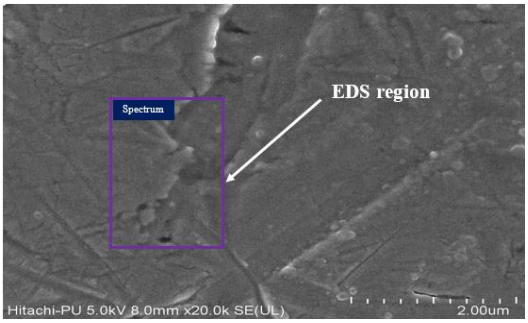

Figure 2. SEM image of Babbitt alloy at 20,000X magnification

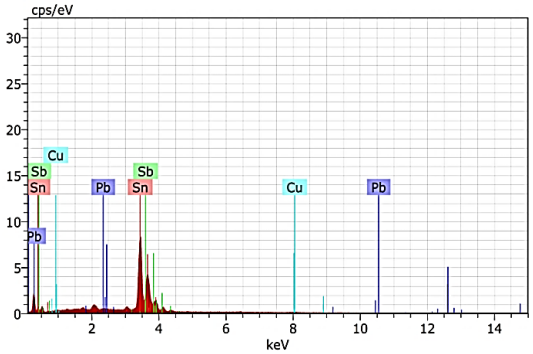

Figure 3. EDS spectrum of Babbitt alloy

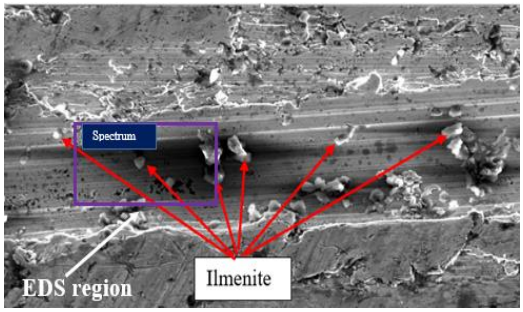

Figure 4. SEM image of composite sample (reinforcement 8wt%, stirring speed 250 rpm, aging time 48h) at 20,000X magnification

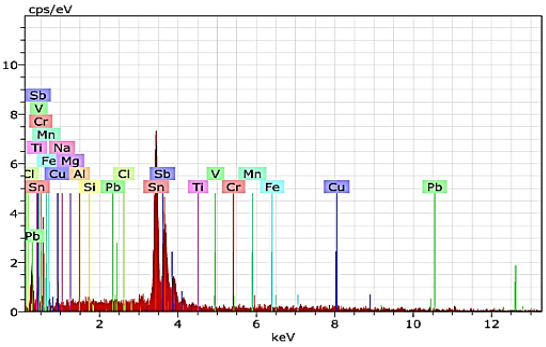

Figure 5. EDS spectrum of composite sample (reinforcement 8wt%, stirring speed 250 rpm, aging time 48h)

fabricated composite (reinforcement 8wt%, stirring speed 250 rpm, aging time 48h) are shown in Tables 1 and 2, respectively. The correct temperature and vortex conditions maintained throughout fabrication of composite resulted in homogeneous dispersion of Ilmenite particles in the Babbitt alloy thereby minimizing clustering for defect free castings.

The composite samples were fabricated at different levels of controllable parameters which include weight percentage of reinforcement, stirring speed and aging time according to L16 orthogonal array (Table 3). The SEM micrographs of the fabricated composites corresponding to set of controllable parameters are shown in Figures 6, 7 and 8 which confirmed the uniform distribution of Ilmenite in Babbitt matrix.

3. 2. 1. Wear Mechanism under Mild and Severe Conditions The composite's worn surface morphology was investigated for mild and severe wear conditions in order to establish a correlation between wear mechanism and test conditions. The transition of wear mechanism was observed with variation in applied load (10N - 40N) and sliding distance (2000m – 4000m). Under mild conditions (10N load and 2000m sliding distance) the wear is mostly abrasive with presence of wear scars due to micro ploughing by the hard counter-surface. Although some debris were formed due to micro-cutting and delamination but mild wear conditions were characterized with little material loss. With increase in load (40N) and sliding distance (4000m) the morphology of wear specimen shows deep long grooves that covers most of the area. Under severe conditions the cracks nucleate at highly strained sites and propagate to

TABLE 2. Element and atomic wt% for the EDS spectrum of the composite (reinforcement 8wt%, stirring speed 250 rpm, aging time 48h) (Extracted from Figure 5)

Element	wt%	Atomic wt%
Sn	83.51	76.75
Al	0.40	1.64
Mg	0.34	1.53
Mn	0.04	0.10
V	0.01	0.01
Pb	0.71	0.37
Si	0.38	1.47
Ti	0.75	1.73
Fe	0.02	0.02
Cu	4.30	7.45
Sb	9.31	8.30
Na	0.04	0.04
Cl	0.16	0.56
Cr	0.03	0.03
Total	100	100

TABLE 3. L16 orthogonal array with predicted and experimental responses

							Weight loss(g)		COF	
Exp. No.	W	S	A	L	SS	SD	Predicted	Observed	Predicted	Observed
1	2	250	2	1	0.5	2000	0.0586	0.0583	0.308	0.319
2	2	300	8	2	0.5	4000	0.0618	0.0621	0.347	0.336
3	2	350	24	3	1	2000	0.0427	0.0426	0.379	0.368
4	2	400	48	4	1	4000	0.0815	0.0812	0.384	0.395
5	4	250	8	3	1	4000	0.0565	0.0562	0.338	0.349
6	4	300	2	4	1	2000	0.0479	0.0482	0.453	0.442
7	4	350	48	1	0.5	4000	0.0361	0.0364	0.304	0.293
8	4	400	24	2	0.5	2000	0.0081	0.0078	0.285	0.296
9	6	250	24	4	0.5	4000	0.0754	0.0757	0.323	0.312
10	6	300	48	3	0.5	2000	0.0226	0.0223	0.341	0.353
11	6	350	2	2	1	4000	0.0348	0.0345	0.249	0.260
12	6	400	8	1	1	2000	0.0045	0.0048	0.193	0.182
13	8	250	48	2	1	2000	0.0033	0.0036	0.214	0.203
14	8	300	24	1	1	4000	0.0055	0.0052	0.187	0.198
15	8	350	8	4	0.5	2000	0.0228	0.0225	0.359	0.370
16	8	400	2	3	0.5	4000	0.0191	0.0194	0.235	0.224

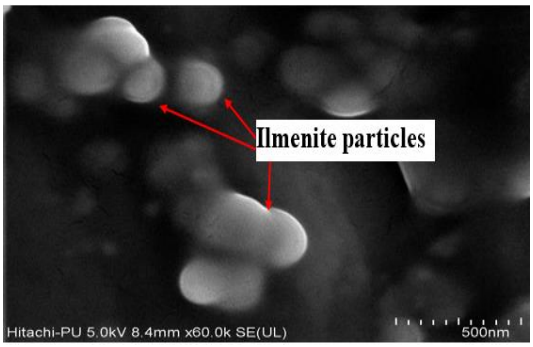

Figure 6. SEM image of composite sample (reinforcement 2wt%, stirring speed 250rpm, aging time 2h) at 60000X magnification

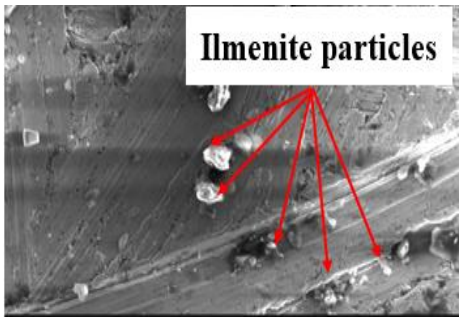

Figure 7. SEM image of composite sample (reinforcement 4wt%, stirring speed 350rpm, aging time 48) at 10000X magnification

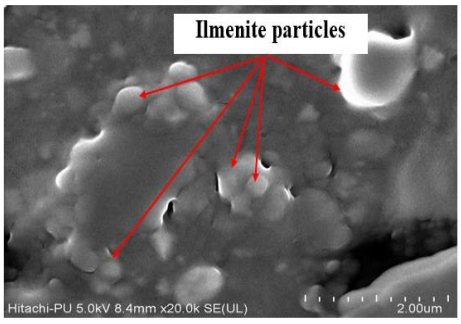

Figure 8. SEM image of composite sample (reinforcement 6wt%, stirring speed 400rpm, aging time 8h) at 20000X magnification

surface causing surface layer fracture. The fragmented wear debris formed at the surface due to tribo- chemical reaction at high load and sliding distance conditions in wear test fill the grooves leading to predominant adhesive wear. An increase in load and sliding distance generates local heating and a rise in temperature, resulting in the formation of a mechanically mixed layer that affects the wear mechanism which is in agreement with [13, 14]. Severe wear conditions were characterized with heavy material loss due to excessive delamination fracturing at the wear surface (Figure 9(a) and (b)).

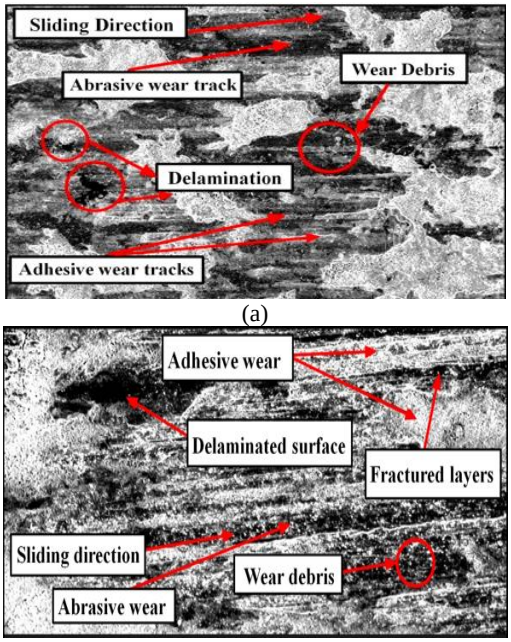

Figure 9. SEM micrographs of Babbitt/2 % Ilmenite under: (a) mild wear and (b) severe wear

4. MULTI-PERFORMANCE OPTIMIZATION

Entropy based grey relation analysis (EGRA) was used for multi objective optimization of the tribological characteristics of the composite. Objective weights of the responses were determined using entropy method [29, 30]. The procedure for calculating weights of the responses for multi criteria optimization is as:

1) Normalization of the performance characteristics:

$$p_{ij} = \frac{y_{ij}}{\sum_1^m y_{ij}} \quad (5)$$

where, p_{ij} is the project outcome of i^{th} experiment, y_{ij} is the experimental response of i^{th} experiment and m are the total number of trials.

2) Estimation of entropy measure of project outcome using the equation:

$$E_j = -c \sum_1^m p_{ij} \ln p_{ij} \quad (6)$$

where, c = 1/ln(m), m=16

3) Determining the objective weight based on entropy concept from the equation:

$$W_j = \frac{1-E_j}{\sum_{j=1}^m (1-E_j)} \quad (7)$$

The higher the value of Grey relational grade, the better are the multi-performance characteristics of the composite. Experiment No.13 has the highest grey relation grade with parameters setting of $A_4B_1C_4D_2E_2F_1$ corresponding to 8wt% Ilmenite, 250 rpm stirring speed, 48 hours of aging, 2kg_f applied load, 1m/s sliding

velocity and 2000 m sliding distance. The most influencing parameter towards multi criteria optimization from delta analysis was found to be percentage weight of reinforcement followed by applied load, stirring speed, sliding distance, aging time and sliding speed (Table 6).

TABLE 4. Determination of objective weights of the responses

Wear loss		COF	
p_{ij}	$p_{ij} \ln p_{ij}$	p_{ij}	$p_{ij} \ln p_{ij}$
0.100379	-0.23075	0.065102	-0.177846
0.106921	-0.23904	0.068571	-0.183763
0.073347	-0.19162	0.075102	-0.194432
0.139807	-0.27507	0.080612	-0.20299
0.096763	-0.22599	0.071224	-0.188169
0.082989	-0.20656	0.090204	-0.217002
0.062672	-0.17359	0.059796	-0.168434
0.01343	-0.05789	0.060408	-0.169543
0.130337	-0.26558	0.063673	-0.175356
0.038395	-0.12516	0.072041	-0.189505
0.059401	-0.16772	0.053061	-0.155804
0.008264	-0.03963	0.037143	-0.122311
0.006198	-0.03151	0.041429	-0.1319
0.008953	-0.04222	0.040408	-0.129659
0.03874	-0.12594	0.07551	-0.19508
0.033402	-0.11354	0.045714	-0.141044
	$\sum$ pij ln pij = -2.5118		$\sum$ pij ln pij = -2.7428
W_j= 0.897		W_j= 0.103	

TABLE 5. Generation of entropy based Grey relation Grade

	Normalization		Grey relation Coefficient		GRG
Experiment No.	**Wear**	**COF**	**Wear**	**COF**	
1	0.2951031	0.473077	0.414973	0.486891	0.422346
2	0.246134	0.407692	0.398767	0.457746	0.404813
3	0.4974227	0.284615	0.498715	0.411392	0.489763
4	0	0.180769	0.333333	0.379009	0.338016
5	0.3221649	0.357692	0.424508	0.43771	0.425861
6	0.4252577	0	0.465228	0.333333	0.451707
7	0.5773196	0.573077	0.541899	0.539419	0.541645
8	0.9458763	0.561538	0.902326	0.532787	0.864442
9	0.0708763	0.5	0.349865	0.5	0.365256
10	0.7590206	0.342308	0.674783	0.431894	0.649883
11	0.6018041	0.7	0.556671	0.625	0.563676
12	0.9845361	1	0.97	1	0.973075
13	1	0.919231	1	0.860927	0.985743
14	0.9793814	0.938462	0.960396	0.890411	0.953221
15	0.7564433	0.276923	0.672444	0.408805	0.645417
16	0.7963918	0.838462	0.710623	0.755814	0.715256

Complete experimental design is expensive and time-consuming. A factorial design reduces number of experiments and trial cost however it may not contain the best design point. Taguchi's design philosophy addresses this issue [31] using an orthogonal array to design low-cost, high-quality trials. ANOVA test applied on Grey relational grade as lone distinguishing response [24-27] confirmed percentage weight of Ilmenite, applied load, sliding distance and stirring speed to be the significant test parameters with regard to multi criteria optimization with contribution of 44.46 %, 23.82 %, 11.33% and 5.66%, respectively (Table 7). ANOVA statistical technique predicted the load, sliding distance and speed conditions to be significant which influence the sliding wear characteristics of the composite to great extent. The ANOVA results of the predicted model is in agreement with previous research [10-12]. Optimum level of controllable parameters from hybrid Taguchi Grey relation analysis (TGRA) was found to be $A_4B_4C_3D_1E_2F_1$ (Figure 10). The confirmation experiments validated hybrid Taguchi grey relation model with deviations of 2.4% and 2.7% for wear loss and COF respectively (Table 8). Based on ANOVA analysis Equation (8) is proposed for estimating multi-attribute performance of the composite (GRG):

$$GRG = 0.303 + 0.0650\,W + 0.000928\,S + 0.00159\,A - 0.0952\,L + 0.1430\,SS - 0.000073\,SD \quad (8)$$

The adequacy of the linear fit for GRG was verified from normal probability plot which clearly indicate that the points are close to the fitted line suggesting very good fit. Residual Vs fit plot shows randomly distributed residuals required for desirable constant variance (Figure 11(a) and (b)). There is an overall improvement in wear and COF at multi criteria optimized conditions by 38.6% and 44.2 %, respectively (Table 9). The results were similar to the

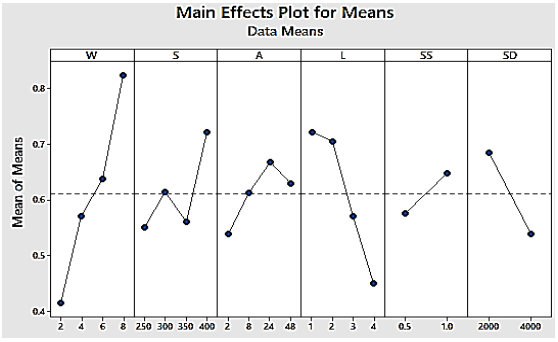

Figure 10. Means of GRG Vs test parameters

TABLE 6. Delta analysis for Grey relation grade

Level	W	S	A	L	SS	SD
1	0.4137	0.5498	0.5382	0.7226*	0.5761	0.6853*
2	0.5709	0.6149	0.6123	0.7047	0.6476*	0.5385
3	0.6380	0.5601	0.6682*	0.5702	-	-
4	0.8249*	0.7227*	0.6288	0.4501	-	-
Delta	0.4112	0.1729	0.1299	0.2725	0.0715	0.1468
Rank	1	3	5	2	6	4

Average Grey relational grade = 0.6118

TABLE 7. ANOVA test for multi-performance optimization

Source	DOF	Sum of squares	Mean Squares	F-statistic	p -statistic	% contribution
Regression	6	0.69072	0.11511	14.77	0.000	90.78%
% wt.	1	0.33830	0.33830	43.42	0.000	44.46%
Stirring speed	1	0.04304	0.04304	5.52	0.043	5.66%
Aging time	1	0.02147	0.02147	2.75	0.131	2.82%
Load	1	0.18122	0.18122	23.26	0.001	23.82%
Sliding speed	1	0.02045	0.02045	2.62	0.140	2.69%
Sliding distance	1	0.08624	0.08624	11.07	0.009	11.33%
Error	9	0.07013	0.0078			9.22%
Total	15	0.76084				100%

Model Summary: R-sq=89.65%; R-sq(adj)= 82.76%;R-sq(Pred)=70%

TABLE 8. Confirmation Test for hybrid Taguchi grey relation analysis

Optimum Conditions	Response	
$A_4B_4C_3D_1E_2F_1$	Wear loss	COF
Predicted	0.0207	0.149
Experimental	0.0212	0.145

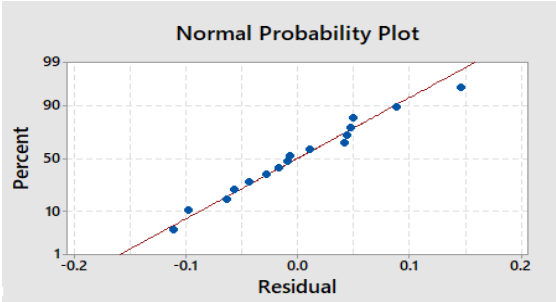

(a)

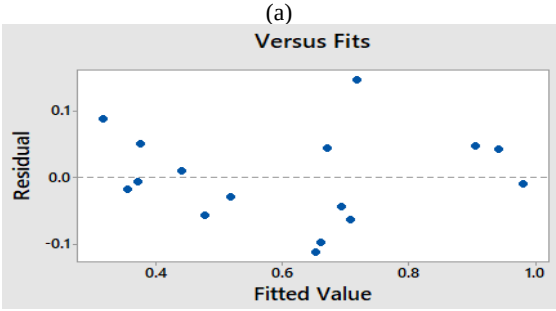

(b)

Figure 11 (a, b). Normal distribution and residual vs fit plot for GRG

TABLE 9. Improvement in multi-performance tribological aspects of composite

Condition	Wear loss	COF
Initial ($A_3B_3C_1D_2E_2F_2$)	0.0345	0.260
Optimal TGRA ($A_4B_4C_3D_1E_2F_1$)	0.0212	0.145
Improvement	38.6 %	44.2 %

*Initial condition is taken near the mean value of GRG

wear study conducted by Singhal and Pandey [32] on Ilmenite reinforced aluminum metal matrix composite which reported improvement in wear resistance and coefficient of friction by 57% and 47%, respectively at the optimum conditions. A similar study conducted by Priyadarshani et al. [33] observed improvement in wear resistance and coefficient of friction of AA 6061/Ilmenite composite which is in agreement with the current investigation. Ilmenite-reinforced composites showed similar tribological improvements [34, 35] in line with current study.

5. RESULTS AND DISCUSSION

There is an improvement in tribological aspects of the composite with increase in percentage weight of Ilmenite because of reduction in contact area of mating parts. The fluctuating trend of the tribological behavior of the composite with stirring speed was observed due to variation in dispersion of the reinforcement in the matrix. There is an improvement in the tribological behavior of the composite with increase in aging time up to certain optimum limit as a result of its strengthening due to dislocation pile up on grain boundaries. Over aging of the composites causes precipitates to coalesce and form big particles thereby weakening the dislocation barrier and promoting dislocation movement resulting in diminishing of the tribological characteristics of the composite. With increase in load from 10 N to 40 N, there is increase in counter surface penetration which causes increased abrasion of the composite resulting in the increase of wear loss and higher values of coefficient of friction. Increase in sliding velocity decreases area of contact and rubbing time of mating surfaces thereby improving tribological aspects of the composite. The increased temperature caused due to high sliding velocity leads to the formation of mechanically mixed layer. Wear loss increases as the sliding distance is increased from 2000 m to 4000 m due to weakening of the unstable tribo-layer. At greater sliding distances, the ilmenite particles are significantly fractured which interfere with the mechanically mixed layer on the composite surface and deteriorate the tribological properties of the composite.

6. CONCLUSIONS

In the current investigation Babbitt-Ilmenite composite developed via stir casting process was tested for wear loss and coefficient of friction with pin on disc tribometer. The effect of controllable parameters which include percentage weight of Ilmenite, stirring speed and aging time with varying applied load, sliding velocity and sliding distance on the tribological properties of the composite was studied. Morphological tests were conducted to ascertain the uniform distribution of Ilmenite in Tin-Babbitt and the type of wear mechanism. Weighted Grey relational analysis was performed for multi-objective optimization of the tribological attributes of the composite. The weights of the responses were determined objectively using entropy method. Hybrid Taguchi grey relation analysis determined the significant test parameters and their contribution for multi-performance optimization of tribological aspects of the composite. The following pertinent observations were made in the present study:

1. A morphological analysis conducted on the Babbitt-Ilmenite composite confirmed the uniform dispersal of Ilmenite in the Tin-Babbitt metal matrix.
2. The investigation of worn surface morphology under mild and severe conditions indicated predominant abrasive wear under mild condition characterized with scars on wear surface due to micro-ploughing and debris formed due to micro-cutting with little material loss. Under severe conditions the debris formed due to surface fracture are further fragmented as a result of tribo- chemical reactions and the wear is predominantly adhesive in nature with heavy material loss due to excessive delamination fracturing at wear surface.
3. The weights of the responses (wear and COF) were evaluated objectively using entropy method and grey relation analysis was applied to determine optimal parameter setting for multi-attribute optimization of the tribological aspects of composite. Experiment No.13 has the highest grey relation grade with parameters setting of $A_4B_1C_4D_2E_2F_1$ corresponding to 8% weight Ilmenite, 250 rpm stirring speed, 48 hours of aging, 2 kg_f applied load, 1m/s sliding velocity and 2000 m sliding distance.
4. The linear regression equation was proposed for estimating GRG and the confirmation tests validated the hybrid Taguchi grey relation model with deviations of 2.4% and 2.7% for wear loss and COF, respectively.
5. Optimum level of controllable parameters for hybrid Taguchi Grey relation analysis (TGRA) were found to be $A_4B_4C_3D_1E_2F_1$. The percentage weight of Ilmenite was the most influential test parameter with contribution of 44.46% followed by applied load, sliding distance and stirring speed with contribution of 23.82 %, 11.33% and 5.66%, respectively.
6. There is an overall improvement in wear and COF at optimal TGRA conditions by 38.6 % and 44.2 %, respectively.

7. REFERENCES

1. Chawla, K.K. and Chawla, K.K., "Metal matrix composites, Springer, (1998).
2. Deuis, R., Subramanian, C. and Yellup, J., "Dry sliding wear of aluminium composites—a review", ***Composites Science and Technology***, Vol. 57, No. 4, (1997), 415-435. https://doi.org/10.1016/S0266-3538(96)00167-4
3. Suresha, S. and Sridhara, B., "Effect of addition of graphite particulates on the wear behaviour in aluminium–silicon carbide–graphite composites", ***Materials & Design***, Vol. 31, No. 4, (2010), 1804-1812. https://doi.org/10.1016/j.matdes.2009.11.015
4. Sannino, A. and Rack, H., "Dry sliding wear of discontinuously reinforced aluminum composites: Review and discussion", ***Wear***, Vol. 189, No. 1-2, (1995), 1-19. https://doi.org/10.1016/0043-1648(95)06657-8
5. Sinclair, I. and Gregson, P., "Structural performance of discontinuous metal matrix composites", ***Materials Science and Technology***, Vol. 13, No. 9, (1997), 709-726. https://doi.org/10.1179/mst.1997.13.9.709
6. Chawla, N. and Shen, Y.L., "Mechanical behavior of particle reinforced metal matrix composites", ***Advanced Engineering Materials***, Vol. 3, No. 6, (2001), 357-370. https://doi.org/10.1002/1527-2648
7. Suresha, S. and Sridhara, B., "Wear characteristics of hybrid aluminium matrix composites reinforced with graphite and silicon carbide particulates", ***Composites Science and Technology***, Vol. 70, No. 11, (2010), 1652-1659. https://doi.org/10.1016/j.compscitech.2010.06.013
8. Singh, J. and Chauhan, A., "A review on sliding wear behaviour of aluminium matrix composites with hybrid reinforcements for automotive applications", ***Tribology Online***, Vol. 9, No. 3, (2014), 121-134. https://doi.org/10.2474/trol.9.121
9. Panwar, R.S. and Pandey, O., "Analysis of wear track and debris of stir cast lm13/zr composite at elevated temperatures", ***Materials Characterization***, Vol. 75, (2013), 200-213. doi. https://doi.org/10.1016/j.matchar.2012.11.003
10. Kumar, R. and Dhiman, S., "A study of sliding wear behaviors of al-7075 alloy and al-7075 hybrid composite by response surface methodology analysis", ***Materials & Design***, Vol. 50, (2013), 351-359. doi: j.matdes.2013.02.038.
11. Radhika, N., Subramanian, R. and Prasat, S.V., "Tribological behaviour of aluminium/alumina/graphite hybrid metal matrix composite using taguchi's techniques", ***Journal of Minerals and Materials Characterization and Engineering***, Vol. 10, No. 05, (2011), 427.
12. Chattoraj, P., Prabhakar, P., Koti, V., Natarajan, N.S., Lakshminarayana, M., Arul, K., Venkatachalapathy, M., Ahamed, M., Karnan, M. and Kumar, S.P., "Optimization on tribological behaviour of aa7178/nano titanium diboride hybrid composites employing taguchi techniques", ***Journal of Nanomaterials***, Vol. 2022, (2022). https://doi.org/10.1155/2022/1619923
13. Rajmohan, T., Palanikumar, K. and Ranganathan, S., "Evaluation of mechanical and wear properties of hybrid aluminium matrix composites", ***Transactions of nonferrous metals society of China***, Vol. 23, No. 9, (2013), 2509-2517. https://doi.org/10.1016/S1003-6326(13)62762-4
14. Alaneme, K.K. and Olubambi, P.A., "Corrosion and wear behaviour of rice husk ash—alumina reinforced al–mg–si alloy matrix hybrid composites", ***Journal of Materials Research and Technology***, Vol. 2, No. 2, (2013), 188-194. https://doi.org/10.1016/j.jmrt.2013.02.005
15. Mahesh, V., Nair, P.S., Rajan, T., Pai, B. and Hubli, R., "Processing of surface-treated boron carbide-reinforced aluminum matrix composites by liquid–metal stir-casting technique", ***Journal of Composite Materials***, Vol. 45, No. 23, (2011), 2371-2378. https://doi.org/10.1177/0021998311401086
16. Kuldeep, B., Ravikumar, K. and Pradeep, S., "Effect of hexagonal boron nitrate on microstructure and mechanical behavior of al7075 metal matrix composite producing by stir casting technique", ***International Journal of Engineering, Transactions A: Basics***, Vol. 32, No. 7, (2019), 1017-1022. https://doi.org/10.5829/ije.2019.32.07a.15
17. Mishra, S.K., Biswas, S. and Satapathy, A., "A study on processing, characterization and erosion wear behavior of silicon carbide particle filled za-27 metal matrix composites", ***Materials & Design***, Vol. 55, (2014), 958-965. https://doi.org/10.1016/j.matdes.2013.10.069
18. Kumar, D., Angra, S. and Singh, S., "Mechanical properties and wear behaviour of stir cast aluminum metal matrix composite: A review", ***International Journal of Engineering, Transactions A:***

Basics, Vol. 35, No. 4, (2022), 794-801. https://doi.org/10.5829/ije.2022.35.04A.19

19. Idusuyi, N. and Olayinka, J.I., "Dry sliding wear characteristics of aluminium metal matrix composites: A brief overview", ***Journal of Materials Research and Technology***, Vol. 8, No. 3, (2019), 3338-3346. https://doi.org/10.1016/j.jmrt.2019.04.017
20. Samal, P., Mandava, R.K. and Vundavilli, P.R., "Dry sliding wear behavior of al 6082 metal matrix composites reinforced with red mud particles", ***SN Applied Sciences***, Vol. 2, (2020), 1-11. https://doi.org/10.1007/s42452-020-2136-2
21. Singh, J. and Chauhan, A., "Investigations on dry sliding frictional and wear characteristics of sic and red mud reinforced Al2024 matrix hybrid composites using taguchi's approach", ***Proceedings of the Institution of Mechanical Engineers, Part L: Journal of Materials: Design and Applications***, Vol. 233, No. 9, (2019), 1923-1938. https://doi.org/10.1177/1464420718803126
22. Leszczyńska-Madej, B. and Madej, M., "The tribological properties and the microstructure investigations of tin babbit with pb addition after heat treatment", ***Archives of Metallurgy and Materials***, Vol. 61, No. 4, (2016), 1861-1868. http://dx.doi.org/10.1515%2Famm-2016-0300
23. Saindane, U., Soni, S. and Menghani, J., "Dry sliding behavior of carbon-based brake pad materials", ***International Journal of Engineering, Transactions B: Applications***, Vol. 34, No. 11, (2021), 2517-2524. https://doi.org/10.5829/IJE.2021.34.11B.14
24. Kumar, D. and Thakur, L., "A study of processing and parametric optimization of wear-resistant az91-tib2 composite fabricated by ultrasonic-assisted stir casting process", ***Surface Topography: Metrology and Properties***, Vol. 10, No. 2, (2022), 025024. https://doi.org/10.1088/2051-672X/ac7065
25. Kumar, S.S., Uthayakumar, M., Kumaran, S.T., Parameswaran, P., Mohandas, E., Kempulraj, G., Babu, B.R. and Natarajan, S., "Parametric optimization of wire electrical discharge machining on aluminium based composites through grey relational analysis", ***Journal of Manufacturing Processes***, Vol. 20, (2015), 33-39. https://doi.org/10.1016/j.jmapro.2015.09.011
26. Shivalingaiah, K., Nagarajaiah, V., Selvan, C.P., Kariappa, S.T., Chandrashekarappa, N.G., Lakshmikanthan, A., Chandrashekarappa, M.P.G. and Linul, E., "Stir casting process analysis and optimization for better properties in al-mwcnt-gr-based hybrid composites", ***Metals***, Vol. 12, No. 8, (2022), 1297. https://doi.org/10.3390/met12081297
27. Saindane, U., Soni, S. and Menghani, J., "Friction and wear performance of brake pad and optimization of manufacturing parameters using grey relational analysis", ***International Journal of Engineering***, Vol. 35, No. 3, (2022), 552-559. https://doi.org/10.5829/IJE.2022.35.03C.07
28. Ramu, I., Srinivas, P. and Vekatesh, K., "Taguchi based grey relational analysis for optimization of machining parameters of cnc turning steel 316", in IOP Conference Series: Materials Science and Engineering, IOP Publishing. Vol. 377, (2018), 012078.
29. Jangra, K., Grover, S. and Aggarwal, A., "Optimization of multi machining characteristics in wedm of wc-5.3% co composite using integrated approach of taguchi, gra and entropy method", ***Frontiers of Mechanical Engineering***, Vol. 7, (2012), 288-299. https://doi.org/10.1007/s11465-012-0333-4
30. Sharma, A., Belokar, R. and Kumar, S., "Multi-response optimization of al2024/red mud mmc using hybrid taguchi-gra-entropy optimization technique", ***Materials Today: Proceedings***, Vol. 5, No. 2, (2018), 4748-4760. https://doi.org/10.1016/j.matpr.2017.12.048
31. Maraki, M., Tagimalek, H., Azargoman, M., Khatami, H. and Mahmoodi, M., "Experimental investigation and statistical modeling of the effective parameters in charpy impact test on az31 magnesium alloy with v-shape groove using taguchi method", ***International Journal of Engineering, Transactions C: Aspects,*** Vol. 33, No. 12, (2020), 2521-2529. http://dx.doi.org/10.5829/ije.2020.33.12c.13
32. Singhal, V. and Pandey, O., "Influence of dual range particle size on wear and friction properties of ilmenite reinforced aluminium metal matrix composite", ***Silicon***, (2022), 1-16. https://doi.org/10.1007/s12633-022-01901-6
33. Morampudi, P., Ramana, V.V., Bhavani, K., Reddy, C.K. and Vikas, K.S.R., "Wear and corrosion behavior of aa6061 metal matrix composites with ilmenite as reinforcement", ***Materials Today: Proceedings***, Vol. 52, (2022), 1515-1520. https://doi.org/10.1007/s12633-022-01901-6
34. GUPTA, R., NANDA, T. and Pandey, O., "Comparison of wear behaviour of lm13 Al− Si alloy based composites reinforced with synthetic (B4C) and natural (ilmenite) ceramic particles", ***Transactions of Nonferrous Metals Society of China***, Vol. 31, No. 12, (2021), 3613-3625. https://doi.org/10.1016/S1003-6326(21)65752-7
35. Singhal, V. and Pandey, O., "Utilization of natural mineral ilmenite-reinforced composites for the dry sliding application", ***International Journal of Metalcasting***, (2021), 1-19. https://doi.org/10.1016/S1003-6326(21)65752-7

Persian Abstract

چکیده

کامپوزیت بابیت–ایلمنیت تهیه‌شده به روش ریخته‌گری هم‌زن با پارامترهای قابل کنترل که شامل درصد وزن ایلمنیت، سرعت همزدن و زمان پیری می‌شود، از نظر ویژگی‌های سایش لغزشی و ضریب اصطکاک (COF) با بار اعمالی متغیر، سرعت لغزش و فاصله لغزش مورد بررسی قرار گرفت. آزمایش‌های مورفولوژیکی برای شناسایی کامپوزیت و تعیین مکانیسم سایش در شرایط خفیف و شدید انجام شد. برای بهینه‌سازی چند هدفه ویژگی‌های تریبولوژیکی کامپوزیت، از فلسفه تاگوچی با تکنیک آماری آنالیز واریانس (ANOVA) استفاده شد. تجزیه و تحلیل رابطه خاکستری مبتنی بر آنتروپی (EGRA) که برای بهینه‌سازی وزنی چند عملکردی جنبه‌های تریبولوژیکی روش رابطه خاکستری ترکیبی و ترکیبی تاگوچی (TGRA) انجام شد، تأیید کرد که درصد وزن ایلمنیت، بار اعمال شده، فاصله لغزش و سرعت هم‌زدن معنی‌دار هستند. پارامترهای مربوط به بهینه سازی چند معیاره به ترتیب با سهم ٤٤.٤٦، ٢٣.٨٢، ١١.٣٣ و ٥.٦٦ درصد است. بهبود کلی در مقاومت به سایش و COF در شرایط بهینه TGRA وجود دارد. کامپوزیت Babbitt-Ilmenite را می توان در بوش های بلبرینگ فولادی برای برق، خودرو و هوافضا استفاده کرد.

IJE TRANSACTIONS B: Applications Vol. 36, No. 05, (May 2023) 904-913

International Journal of Engineering

Journal Homepage: www.ije.ir

Performance Studies on Glass Fiber Reinforced Recycled Aggregate Concrete

J. Sivamani*[a], M. P. Thiyaneswaran[b], K. S. Navaneethan[b]

[a] *Department of Civil Engineering, Sona College of Technology, Salem, Tamilnadu, India*
[b] *Department of Civil Engineering, Kongu School of Architecture, Perundurai, Tamilnadu, India*

PAPER INFO

Paper history:
Received 03 January 2023
Received in revised form 22 February 2023
Accepted 15 February 2023

Keywords:
Recycled Aggregate
Glass Fiber
Two-stage Mixing Approach
Strength
Paver Block

ABSTRACT

The utilization of fibers in the concrete reduces cracks, increases the energy absorption and concrete strength. The use of fine recycled aggregate (FRA) in concrete overcomes the scarcity of natural aggregates, however its deprived quality affects the concrete properties through development of cracks. This study investigates the effect of glass fiber (GF) utilization in reducing crack propagation using fine recycled aggregate (FRA) in the concreteThe coarse natural aggregate (CNA) was replaced with 10, 30, 50, 70, 90 and 100% of FRA and GF was added 0, 0.25, 0.5, 0.75, 1 and 1.5% by weight. The concrete mixtures with the optimal percentage of FRA and different percentages of GF were prepared by two-stage mixing approach (TSMA) and normal mixing approach (NMA) and tested for their fresh and hardened properties. The optimized mix was observed with 30% of FRA and 1% of GF prepared by TSMA, with a strength improvement of 11.3% compared to the control mix at 28 days. The study further investigated the practical suitability as a paver block for non-traffic and medium volume traffic applications as per IS 15658: 2006 and observed that minimum strength requirement of 40 MPa was achieved under both conditions with the optimized mix with an improvement of 17.4% compared to conventional paver block.

doi: *10.5829/ije.2023.36.05b.07*

1. INTRODUCTION

The generation of waste from construction industries has been increasing rapidly due to significant renovation in construction activities in recent decades. Various wastes from construction include concrete, steel, wood, metals etc., among which concrete fractions contribute to the higher volume. The production of construction waste is around 3 billion tons annually around the world [1]. Among the 3 billion tons, the maximum contribution ensued from developed countries due to its increased construction and rehabilitation activities. It is to be noted that only 40% of generated wastes were reutilized in the momentary application, and the remaining were dumped. Feasibly, the demand for natural aggregates was also increasing, prompting the use of sustainable waste materials as an alternative. The global construction aggregate market (GCAM) predicted an increase in the aggregate market to 6.8% from 2020 to 2030[1]. Statistics also ensure that the consumption of natural aggregate will rise from 43 to 63 billion tons[2], and the demand for natural aggregate will rise by 5.2% [2]. Thus, it could show a positive approach to use construction waste as a suitable replacement for natural aggregates.

Numerous studies were performed to explore the utilization of construction wastes as recycled aggregates in concrete. The recycled aggregates are the concrete proportions of the construction wastes consisting of natural aggregates with cement mortar smeared. Andal et al. [3] found that replacing CNA with 30% and 100% of coarse recycled aggregate (CRA) reduces the strength of recycled aggregate concrete (RAC) by 10.3% and 15.21%. The strength improvement was attributed to the increase in the pore size in CRA resulting from cement mortar on its surface. Koper et al. [4] used CRA obtained from mixes with various W/C ratios and observed that the CRA from higher W/C ratios exhibits inferior properties than those with lower W/C ratios.

*Corresponding Author Institutional Email: jagan.civil@sonatech.ac.in (J. sivamani)

[1] https://www.futuremarketinsights.com
[2] https://www.globenewswire.com/

Please cite this article as: J. Sivamani, M. P. Thiyaneswaran, K. S. Navaneethan, Performance Studies on Glass Fiber Reinforced Recycled Aggregate Concrete, ***International Journal of Engineering, Transactions B: Applications***, Vol. 36, No. 05, (2023) 904-913

Thomas et al. [5] used CRA in different volumetric fractions and observed that replacement of CRA beyond 25% increases the water absorption of RAC with a maximum of 29.41% at 100% replacement. Ozbakkaloglu et al. [6] observed that replacement of CRA beyond 25% reduces the strength by around 11% due to the increased perviousness of CRA ensuing from the adhered mortar on CRA. Similarly, Mi et al. [7] used CRA collected from a source with different concrete strength and observed that the strength of the source concrete is directly proportional to the quality of the CRA owing to the dense mortar adhered to the CRA. Lavado et al. [8] found that the slump loss in RAC increases with time due to the higher porosity characteristics of CRA. The study reported that a 6% slump loss at 30 minutes was increased to 63% at 90 minutes. It could be observed that the concrete properties with CRA were affected due to its inferior quality, which is mainly due to the recycling of construction wastes. The construction wastes are recycled into different fractions of varying sizes for their use as coarse or fine aggregates in concrete. During recycling, micro-cracks develop on the CRA, which expands with repeated recycling stages, resulting in higher water absorption and thus affecting the concrete [9-11]. The higher porous nature of CRA tends to absorb water from the concrete mix, which upon hardening, evaporates, resulting in void formation. Such higher porous concrete tends to exhibit minimum compressive and flexural strength. To counteract such reduced strength, adding fibers will be a viable option in addition to several pre-treatments methods.

Several fibers, such as steel, polypropylene (PP), glass etc., have been used in practice in recent times to improve the tensile property of concrete. Few researches have been developed using single and hybrid fibers in recycled aggregate concrete. Akca et al. [12] used 25 to 45% of CRA with 1% of optimized PP fibers and observed a 17% increase in strength with 1% of PP fibers and a 20% decrease in strength beyond 1.5% of PP fibers. Chan et al. [13] optimized 0.66% of polypropylene fiber with 100% of CRA and observed concrete mixes with CRA only tend to show lesser strength due to its higher perviousness; however, with PP fibers, significant improvement in flexural strength and elastic modulus was observed. Gao et al. [14] used steel fibers up to 2% with different percentages of CRA and found that with equivalent fiber content and compressive strength, replacement of CRA had a diminutive influence on the durability of the concrete. He et al. [15] used hybrid steel fibers and PP fibers and found that with 1.5% of hybrid steel fibers, the strength of the RAC was enhanced by 23%, but with 1.2% of PP fibers, the strength was reduced by 5.5%. Similarly Gao et al. [16] investigated different fibers such as steel, PP and basalt and FRA and observed a decrease in workability with an increase in fiber volume due to the higher surface area of fibers that occupies more mortar. The study also reported a higher strength of 6 MPa with 1.5% mild steel fibers, 3.15 MPa with 0.198% PP fibers, and 3.4 MPa with 0.15% of basalt fibers. Gyanendra Kumar et al. [17] reported that the use of optimized percentage of CRA (25%) and PP fibers (2%) improves the strength of RAC by 25.4% and shear strength by 30.8% due to the strong bond between the interface of cement paste and fibers. Juric et al. [18] observed that use of recycled GF polymer in the concrete increases the load bearing cpapcity of the member by 33% compared to conventional. Balamuralikrishnan et al. [19] used Alccofine (a high glass content reactive % material) as an alternative to cement and observed 17% strength improvement. Dadzie and Kaliluthin [20] used waste plastic bottles in the production of voided concrete slab and obsereved 13% reduction in the cost and subsequent CO_2 and embodied energy emissions. Sivamani et al. [21] used FRA and observed optimal replacement of 30% increases the strength by 7.85% and decreased by 23.5% with 100% replacement. Pawar et al. [22] analyzed the stress-strain behaviour of recycled aggregate concrete using stress-strain curve model and observed that the efficacy of model is similar in ascending and varying in descending portion for strength prediction.

The effectiveness of the research relies on its suitable practical applications. In such a case, Pederneiras et al. [23] used CRA obtained from the site and laboratory up to 60% and observed a strength of 40 MPa suitable for medium traffic conditions. However, Tam et al. [24] used both FRA and CRA and observed a 5% increase in water absorption, but with a prolonged curing period, the strength was found to be equivalent to the mix with CNA. It could be observed from the brief literature review that use of CRA in concrete creates voids due to higher porosity that weakens the concrete micro-structure. So, few fibers such as steel, PP and basalt fibers were commonly used with CRA in concrete. However, the effect of crimped GF with FRA and its practical suitability in traffic applications still needs to be reported. Thus, this study investigates the influence of 0.25, 0.5, 0.75, 1, and 1.5% crimped GF with 10, 30, 50, 70, 90 and 100% of FRA on the concrete properties and its suitability under different traffic volume conditions.

2. METHODOLOGY

2. 1 Materials This study used ordinary portland cement of 43 grades collected from the local vendor as per ASTM C150. Locally available river sand with a relative particle size of 1.18 mm~2.36 mm was used as fine natural aggregate (FNA). The concrete waste from

a demolished building in the institution with particle size equivalent to FNA was used as fine recycled aggregate (FRA). The huge boulders from the site were broken initially with a hammer and then crushed with a jaw crusher machine. It is then sieved with a mechanical sieve to obtain the particle size distribution equivalent to FNA. The FNA and FRA were pre-soaked separately for 24 hours and surface saturated for 3 hours before their use in the casting [11]. The photographic reflection of FNA and FRA is shown in Figure 1. The FNA was replaced with 10, 30, 50, 70, 90 and 100% of FRA by its volume. The coarse natural aggregate (CNA) was the river gravel with particle sizes ranging from 10 mm~20 mm. The gradation curves of FNA and FRA are shown in Figure 2. The glass fiber (GF) collected from the local vendor were chopped to an aspect ratio of 30 and was added in the weight fractions of 0.25, 0.5, 0.75, 1.0 and 1.5% in the concrete. The glass fiber is highly durable, do not corrode and has higher validity than other fibers. The visual and microscopic observation of fibers is shown in Figure 3. The properties of GF from the vendor are given in Table 1.

2. 2. Methodology The concrete mixtures are prepared as per IS 10262 (2009) to achieve a target strength of 30 MPa. Table 2 shows the mix proportions adopted with suitable material quantities. The concrete mixtures prepared with different aggregates were labelled as FRA-a-x-y, where 'a' represents the percentage of FRA, 'x' represents the percentage of fiber and 'y' represents the method of mixing adopted.

(a)

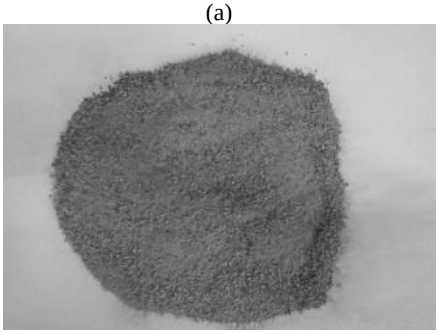

(b)

Figure 1. Visual Observation (a) FNA (b) FRA

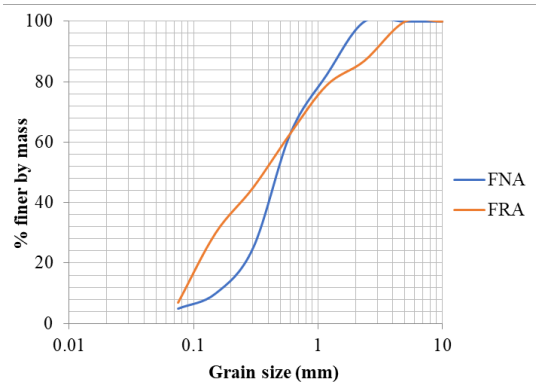

Figure 2. Gradation of fine aggregates

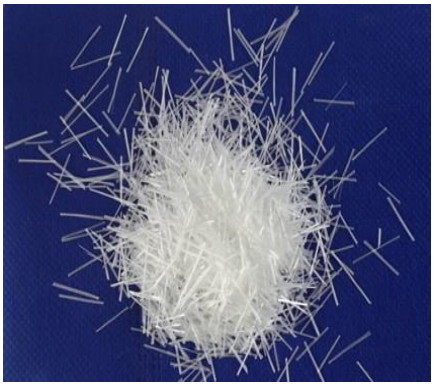

(a)

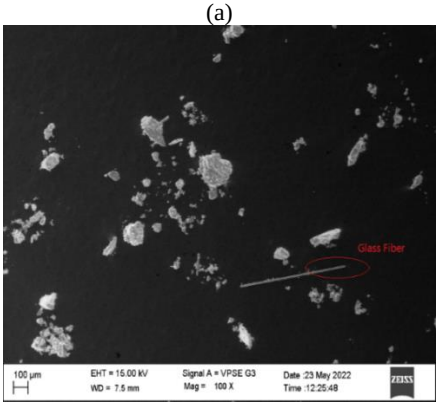

(b)

Figure 3. GF (a) Visual obervation (b) Microscopic observation

TABLE 1. Properties of GF

Fiber	Length (mm)	Aspect Ratio	Density (g/cm^3)	Elastic Modulus (GPa)
GF	18	30	0.84	70

For instance, the mix ID FRA-50-0.25-NMA indicates that the concrete mixture was prepared with 50% FRA and 0.25% GF by a normal mixing approach. In NMA, all the materials were added in suitable proportions and mixed well for 180 seconds to achieve uniform

TABLE 2. Concrete mix proportions (Optimized mixes)

Mix ID	(kg/m^3)				
	CEMEN	FNA	FRA	CNA	Water
FRA-0-0-NMA	413	799	0	1029	186
FRA-30-0-NMA	413	559.	239.	1029	186
FRA-100-0-NMA	413	0	799	1029	186
FRA-30-1-NMA	413	559.	239.	1029	186
FRA-100-1-NMA	413	0	799	1029	186
FRA-0-0-TSMA	413	799	0	1029	186
FRA-30-0-TSMA	413	559.	239.	1029	186
FRA-100-0-TSMA	413	0	799	1029	186
FRA-30-1-TSMA	413	559.	239.	1029	186
FRA-100-1-TSMA	413	0	799	1029	186

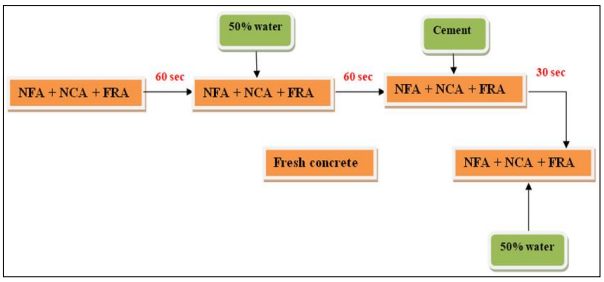

Figure 4. Schematic illustration of TSMA

blending. In TSMA, FNA, FRA, CNA and GF were added with half of the water and blended for 60 seconds. Following, cement was added and blended for 30 seconds, and the remaining 50% was added and mixed for 120 seconds [25]. The TSMA was uniquely adopted in the mixes with FRA as it tends to absorb excess water while mixing, affecting the workability of the concrete (Figure 4).

Initially, the concrete mixes were manufactured by NMA with different percentages of FRA to optimize the percentage of FRA, followed by the optimization of GF. The fresh concrete mixes prepared with optimized percentages of FRA and GF by both NMA and TSMA were tested for workability as per IS 1199 (1959). The fresh concrete was poured into moulds, vibrated and turned out into 150 mm cubes, 150 mm x 300 mm cylinders, and 500 mm x 100 mm x 100 mm prisms under laboratory conditions. The moulds were removed after 24 hours and tested for their hardened properties as per IS 516 (1959). The cubes were tested for compression, cylinders for tensile strength and elastic modulus and prism for flexural strength at 7, 14 and 28 days. The shear strength of the concrete was determined at 28 days [26]. All tests were conducted in trebles. It is essential for every research study to evaluate their suitability in real-time applications. In such perspective, the concrete mix with optimized FRA and GF was fabricated into hexagonal paver blocks (125 mm side area) and tested for non-traffic (60 mm thick) and medium volume (80 mm thick) traffic applications. For light volume non-traffic applications, the concrete mix was designed for M30 grade and for medium volume traffic applications, the concrete mix was designed for M40 grade. The paver blocks with varying thickness were tested for compressive strength at 28 days as per IS15658 (2006).

3. RESULTS AND DISCUSSIONS

3. 1. Characteristics of Aggregates Table 3 shows the properties of FNA, FRA and CRA used. The properties of aggregates were within the BIS limits (IS 383:2009). However, FRA's properties were inferior to FNA's due to its poor quality. The water absorption of FRA was 87% higher than FNA, and the density of FRA was 6.15% less compared to FNA. The higher porosity of FRA ensuing from the adhered mortar increases the water absorption and reduces the density [8, 10, 11]. Figure 5 shows the microstructure of FNA and FRA used in the study. The microstructure of FNA shows angular with flaky particles, whereas the microstructure of FRA, smearing of cement particles on the surface of it, causes an increase in porosity. Figure 6 shows the XRD patterns of FNA and FRA, and it is observed that the FNA shows higher silica and lesser calcite, whereas, in FRA, calcite is more than silica. The

TABLE 3. Properties of aggregates

AGGREGATE	G	W.A (%)	C.V (%)	I.V (%)	D (kg/m^3)
FNA	2.53	0.93	-	-	1526
FRA	2.41	7.12	-	-	1432
CNA	2.73	0.87	20.41	17.23	1978

G – specific gravity; W.A. – Water absorption; C.V – Crushing value; I.V – Impact value; D – Density

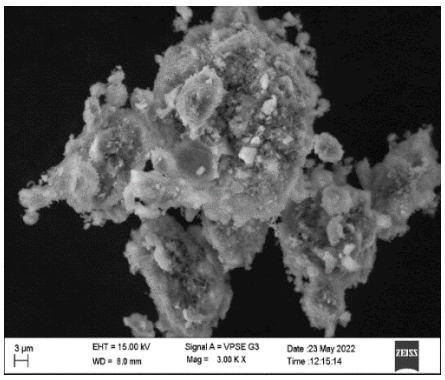

(a)

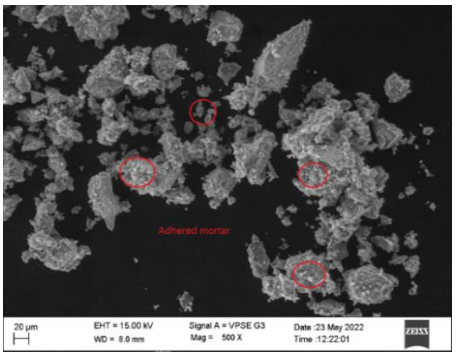

(b)

Figure 5. Microstructural images (a) FNA (b) FRA

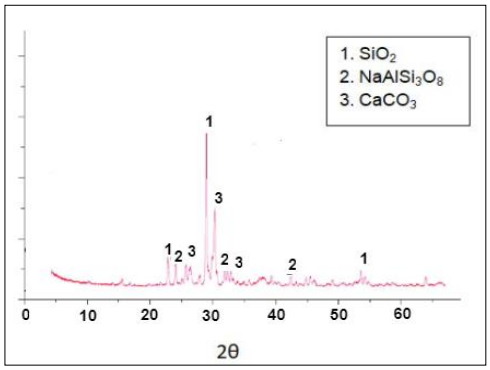

(a)

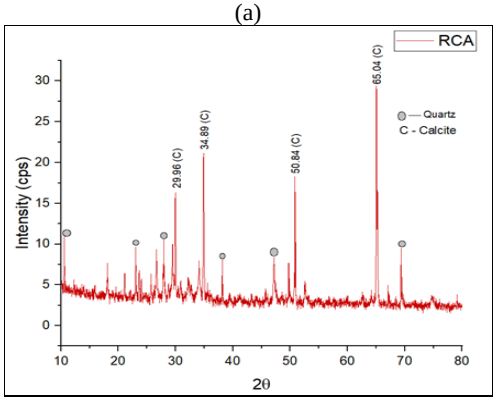

(b)

Figure 6. XRD images (a) FNA (b) FRA

former favors the C-S-H formation, while the latter is due to the smearance of cement mortar on recycled aggregates.

3. 2. Optimization of FRA and GF Figure 7(a) shows the variation in strength with the addition of GF. The optimum GF was 1%, with an increase in strength of 11.6% at 28 days. The strength of concrete with 0.25%, 0.5% and 0.75% of GF was increased by 4.9%, 11% and 11.32%. An increase in strength mainly depends on the percentage of GF. The crack-arresting property of GF increases the energy absorption of the concrete and improves its strength [27]. Conversely, with 1.5% of GF, the strength was reduced by 7.5% at 28 days. The reason may be the wrapping of aggregate by excess GF weakening the interlocking bond or uneven orientation/dispersion of GF in concrete [28].

Figure 7(b) shows the variation in strength with the addition of FRA at 28 days. The strength of concrete with 10% and 30% of FRA was increased by 1.1% and 3.8%. It is observed that only minimum improvement in the strength was observed which is due to the higher angularity of particles resulting from the crushing process [11, 29]. However, with 50%, 70%, 90% and 100% of FRA, the strength of concrete was reduced by 1.6%, 5.2%, 8.9% and 15.3%. The reduction in the strength of concrete was mainly influenced by increase in the porosity of FRA as a result of cement mortar smeared on it [10, 30]. Various other factors such as source, size, age, percentage of mortar etc. influence the strength of RAC. The production of FRA involves series of crushing to reduce the large boulder construction wastes to finer particles. During recycling, micro-cracks develop on recycled aggregates which prolongs with an increase in the crushing stages causing higher porosity in FRA and reducing the strength of the concrete.

3. 3. Properties of Concrete with Optimized Mixes It could be observed that 30% of FRA and 1% of GF tend to improve the strength of concrete individually.

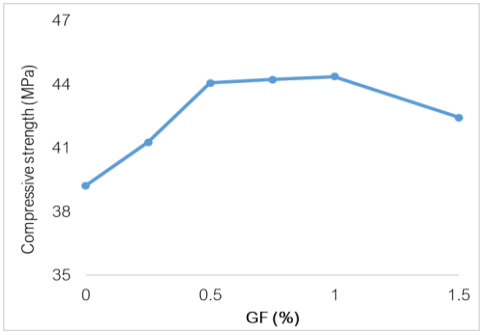

(a)

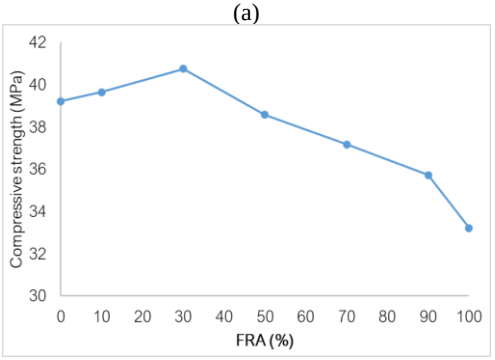

(b)

Figure 7. (a) Variation in strength with GF (b) Variation in strength with FRA

However, the effect of GF on the properties of the concrete with FRA by NMA and TSMA is the main intend of the research. Ten different mixes by NMA and TSMA with optimized percentage of FRA and GF was considered to investigate the concrete properties.

3. 3. 1. Workability The workability of optimized concrete mixes is shown in Figure 8. It is observed that the workability of mixes with FRA decreases; however, with TSMA, the workability improves. The slump of NAC was found to be 70 mm; however, with 30% of FRA, the slump was reduced by 14.3%. Similarly, with 100% of FRA, the slump of RAC prepared by NMA reduced by 71.4%. The higher porosity of FRA absorbs mixing water reducing the required water for a homogenous concrete mixture and reducing the workability of concrete [31, 32]. Through TSMA, the workability of NAC was found to be 75 mm, and the slump of the mix with 30% and 100% of FRA was reduced by only 10% and 64%. The mechanism of adding water in two stages in TSMA overcomes the negative effect of higher water absorption of FRA and insufficient water during concrete mixing [11, 20]. The addition of fibers further tends to reduce the slump of the concrete mixes, irrespective of aggregate replacement. The slump of FRA-30-1-NMA was reduced by 18.6%, and the slump of FRA-30-1-TSMA was reduced by 15.7%. Similarly, the slump of FRA-100-1-NMA was reduced by 74.3%, and the slump of FRA-100-1-TSMA was reduced by 67.2%. The higher surface area of GF requires more mortar to wrap and thus reduces the slump of the concrete [14]. Nevertheless, the mix with equivalent fiber content prepared by TSMA shows little higher slump values due to the addition of water in two-stages during concrete mixing. Similar other studies [10, 19] show improvement in the workability of RAC due to the influence of TSMA.

3. 3. 2. Compressive Strength The compressive strength of optimized mixes is shown in Figure 9. The

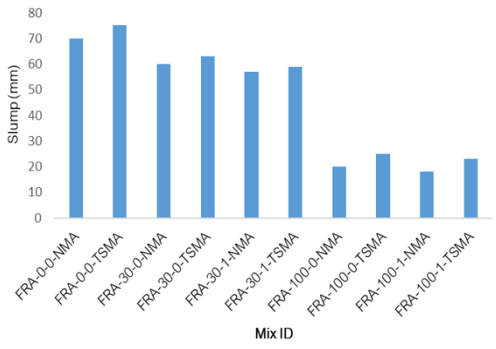

Figure 8. Workability of the mixes

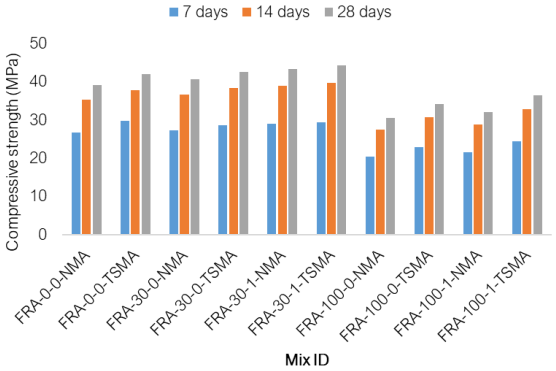

Figure 9. Compressive strength of the mixes

control mix FRA-0-0-NMA shows a strength of 39.2 MPa at 28 days, which meets the required target strength of M30 grade concrete. However, the strength of the control mix by TSMA was further enhanced by 6.5% due to the effectiveness of the mixing technique. When FNA is replaced by 30% of FRA, the strength is improved by only 1.9% at 7 days and 3.8% at 28 days. With TSMA, the strength was further improved by only 6.4% at 7 days and 8% at 28 days. However, with 100% FRA, the strength was reduced by 19.6% at 7 days and 18.1% at 28 days. The strength reduction with excess FRA particles is due to its poor-quality ensuing from the smearing of cement particles. A similar improvement in strength was observed in the TSMA mix, even with 100% of FRA. Upon the addition of fibers, the strength of RAC increases up to 1%, beyond which it decreases. The maximum compressive strength was achieved at 1% of GF with 30% of FRA as 44.23 MPa at 28 days. It could be observed that the strength improvement was 11.3% compared to control concrete, and only a 3.6% improvement was observed with the addition of GF. The variation with the addition of GF was observed to be minimum, as GF does not significantly impact the strength of RAC [33].

The higher angularity and aspect ratio of GF forms a grid that bridges within the matrix and arrests the crack propagation further upon loading. Nevertheless, adding a higher percentage of GF causes uneven distribution of fibers leading to the localization of fibers to specific regions. Such characteristics lead to void formation, and thus the reduction in strength was observed. In addition, a higher percentage of GF consumes excess mortar due to its increased surface area, affecting the workability and strength of the concrete. However, minor variations in strength were observed in optimized mixes, even with 100% of FRA and optimized GF. The strength of FRA-100-1-NMA was reduced by only 19.4% at 7 days and 18.1% at 28 days, and the strength of FRA-100-1-TSMA was reduced by 8.9% at 7 days and 7.2% at 28 days.

The addition of GF has shown only minimal improvement in the concrete strength. Few studies on fiber-reinforced RAC infer that the elastic modulus of fibers influences concrete strength. He et al. [15] reported that adding 1.5% of steel fiber with an elastic modulus of 210 GPa shows a 23.2% improvement in strength, whereas the GF with the elastic modulus of 35 GPa reduces the strength by 5.5%. Furthermore, Gao et al. [16] used hook-end steel fiber, micro steel fiber, PP and basalt fiber (BF) and inferred that PP and BF show reduced strength compared to steel fibers due to their lower elastic modulus. Compared with steel and PP fiber, the elastic modulus of GF was lesser, resulting in minor strength improvement in the concrete.

3. 3. 3. Split Tensile Strength The split tensile strength of the optimized mixes is shown in Figure 10. The variation in the trend of split tensile strength is similar to that of compressive strength for all optimized mixes. The tensile strength of control concrete with NMA and TSMA was 3.21 MPa and 3.47 MPa at 28 days. With 30% of FRA, the tensile strength was improved by only 4.5% for NMA mixes and 9.1% for TSMA mixes. However, with 100% FRA, the tensile strength was reduced by 22.7% for NMA mixes and 12.5% for TSMA mixes. The reason behind the variation in tensile strength with the addition of FRA and TSMA was equivalent to compressive strength.

Similar to compressive strength, the tensile strength of glass fiber-reinforced RAC tends to increase. The tensile strength of FRA-30-1-NMA and FRA-30-1-TSMA was improved by 11.32% and 12.5% at 28 days. However, with 100% FRA, the tensile strength was reduced by only 20.2% for NMA mixes and 11.2% for TSMA mixes. The addition of GF has a better influence on tensile strength than the compressive strength of RAC. When specimens are loaded for splitting, GF-oriented transverse to the longitudinal direction of the specimen acts as a link in effective load transfer carrying an additional load and thus improving the tensile strength of the concrete. In addition, localization of stress might occur in the mixes beyond the optimized percentage of GF, reducing the tensile strength of the concrete. Similar other study by Akca et al. [12] show influence of stress localization with the addition of excess fibers that affected the tensile strength of the concrete.

Besides the surface texture, dispersion, elastic modulus, and fiber orientation influence the concrete's strength. Figure 11(a) shows the effect of the orientation of GF on the concrete strength. It could be observed that fibers-oriented transverse to the direction of the applied load are subjected to tensile load. In contrast, those oriented along the applied load will compress rather than tension resulting in crumbling. This could reduce the strength as the fibers are strong in tension and weak

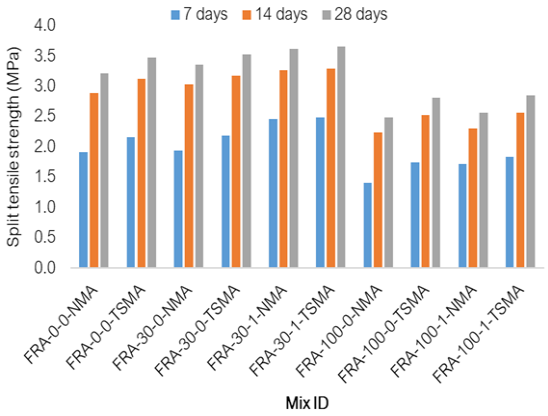

Figure 10. Split tensile strength of the mixes

in compression. Figure 11(b) shows the effect of excess GF on the concrete strength. The addition of excess GF causes uneven dispersion/accumulation of GF in a specific region leading to the localization of stress. This, in turn, causes void formation in that region resulting in a reduction in the concrete strength.

3. 3. 4. Flexural Strength The flexural strength of the optimized mixes is shown in Figure 12. The flexural strength of F-30-0-NMA and F-30-0-TSMA

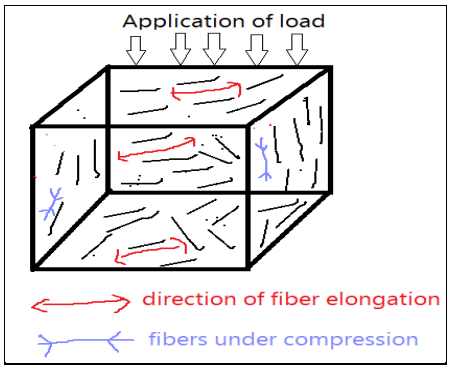

(a)

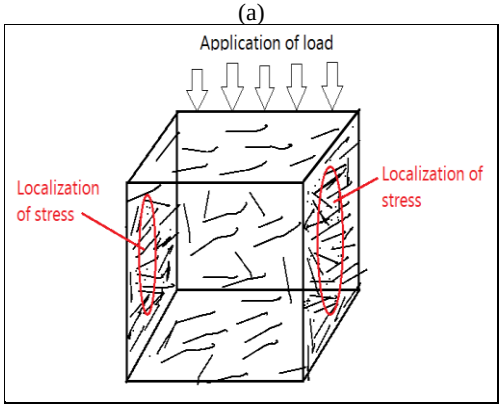

(b)

Figure 11. Schematic illustration (a) Orientation of GF (b) uneven dispersion of GF

was 2.3% and 4.9% more compared to the control concrete. With 100% of FRA, the flexural strength of the F-30-0-NMA and F-30-0-TSMA was reduced by 14.3% and 11.1%. After adding GF, the strength of F-30-1-NMA and F-30-1-TSMA was further improved by 16.2% and 17.8%. For the mix with 100% of FRA, adding 1% of GF reduced the strength by only 12.4% and 10.3%. The variation of flexural strength was observed to be in a similar compressive and tensile strength tendency.

3. 3. 5. Shear Strength The shear strength of the optimized mixes is shown in Figure 13. It could be observed that shear strength decreases with an increase in the FRA. The shear strength of the concrete with 30% FRA was improved by 2.5%, while with 100%, shear strength was reduced by 7.2%. The shear strength reduction with increased FRA is due to poor bonding characteristics between recycled aggregate and matrix resulting from adhered mortar [17]. After adding 1% of GF, the shear strength with 30% GF was increased by 3.6% and the shear strength with 100% of GF was reduced by only 2.2%. The addition of GF improves the bond characteristics by bridging the cement matrix firmly and improving the shear capacity of the concrete.

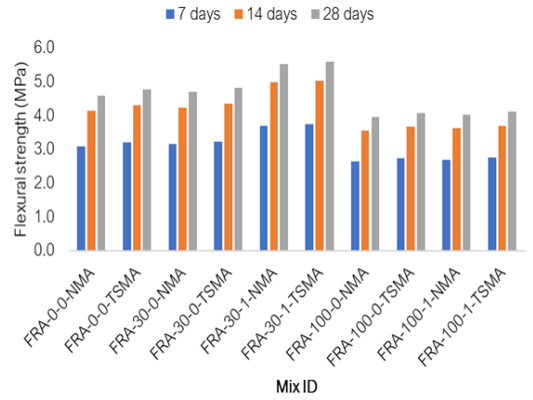

Figure 12. Flexural strength of mixes

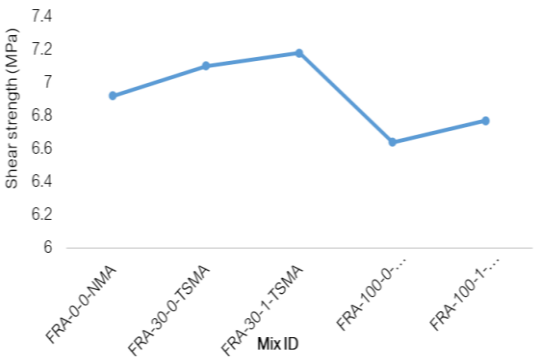

Figure 13. Shear strength of the mixes

3. 4. Effect of GF on the Performance of Paver Block The influence of GF on RAC was observed to yield positive results with the mix containing optimized FRA of 30% and GF of 1% prepared by TSMA. So, the study evaluates the performance of paver blocks with glass fiber-reinforced RAC. Figure 14 shows the compressive strength of the paver block at 28 days. For non-traffic applications, the strength of FRA-30-0-TSMA was increased by 1.2% and the strength of FRA-100-0-TSMA was reduced by 21.7%. However, the strength of FRA-30-1-TSMA was increased by 4.5% and the strength of FRA-100-1-TSMA was reduced by only 17.4%. Similarly, for medium traffic applications, the strength of FRA-30-0-TSMA was increased by 1.9% and the strength of FRA-100-0-TSMA was reduced by 20.38%. However, the strength of FRA-30-1-TSMA was increased by 5.4% and the strength of FRA-100-1-TSMA was reduced by only 15.8%. It could be observed that the addition of GF tends to increase the strength of the paver block. Furthermore, for medium traffic volume applications, with optimized GF and FRA, the strength of paver blocks reaches a maximum of 46 MPa at 28 days, which is suitable for medium volume traffic applications. Such improvement is due to the tensile property of GF, but eventually, the strength improvement was minimum compared to other fibers owing to its low elastic modulus.

4. CONCLUSIONS

The effect of glass fiber (GF) on the hardened properties of recycled aggregate concrete (RAC) was studied and their practical suitability were evaluated with paver blocks for non-traffic and medium volume traffic conditions. The following recommendations were made as folows:

1. The inferior quality of FRA increases the water absorption and optimizes the replacement to 30%.

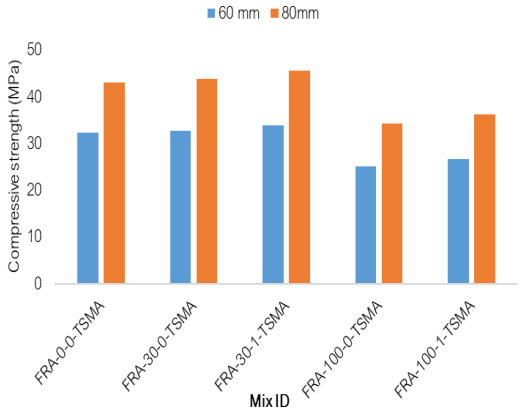

Figure 14. Compressive strength of paver block

2. The concrete mix prepared by two-stage mixing approach (TSMA) show 8% higher strength compared to normal mixing approach (NMA).
3. The concrete mix with 30% of FRA was increased by 8% while the mix with 100% of FRA was reduced by 7.1%.
4. The concrete mix with 1% of GF show 11.6% higher strength, beyond which it decreases due to pore formation resulting from the mortar covering the GF.
5. The concrete mix with optimized percentage of FRA and GF prepared by TSMA show 11.3% higher compressive strength, 12.5% higher tensile strength, 17.8% higher flexural strength and 3.6% increase in the shear strength of the concrete.
6. The paver block with optimized percentage of FRA and GF exhibit minimum strength of 33.9 MPa (non-traffic) and 45.6 MPa (medium traffic).

The research on the influence of GF on the recycled aggregate concrete tend to show better properties counteracting the negative effects of recycled aggregate concrete. However, the limitations are imposed on the utilization owing the glossy surface of GF and localization of stress leading to weaker bonding with recycled aggregate.

5. REFERENCES

1. Purchase, C.K., Al Zulayq, D.M., O'Brien, B.T., Kowalewski, M.J., Berenjian, A., Tarighaleslami, A.H. and Seifan, M., "Circular economy of construction and demolition waste: A literature review on lessons, challenges, and benefits", ***Materials***, Vol. 15, No. 1, (2022), 76. https://doi.org/10.3390/ma15010076
2. Garside, M., "Global cement production 1995–2020", ***Chem. Res***, (2021). https://www.statista.com/statistics/1087115/global-cement-production
3. Andal, J., Shehata, M. and Zacarias, P., "Properties of concrete containing recycled concrete aggregate of preserved quality", ***Construction and Building Materials***, Vol. 125, (2016), 842-855. https://doi.org/10.1016/j.conbuildmat.2016.08.110
4. Koper, A., Koper, W. and Koper, M., "Influence of raw concrete material quality on selected properties of recycled concrete aggregates", ***Procedia Engineering***, Vol. 172, (2017), 536-543. https://doi.org/10.1016/j.proeng.2017.02.063
5. Thomas, J., Thaickavil, N.N. and Wilson, P., "Strength and durability of concrete containing recycled concrete aggregates", ***Journal of Building Engineering***, Vol. 19, (2018), 349-365. https://doi.org/10.1016/j.jobe.2018.05.007
6. Ozbakkaloglu, T., Gholampour, A. and Xie, T., "Mechanical and durability properties of recycled aggregate concrete: Effect of recycled aggregate properties and content", ***Journal of Materials in Civil Engineering***, Vol. 30, No. 2, (2018), 04017275. https://doi.org/10.1061/(ASCE)MT.1943-5533.0002142
7. Mi, R., Pan, G., Liew, K. and Kuang, T., "Utilizing recycled aggregate concrete in sustainable construction for a required compressive strength ratio", ***Journal of Cleaner Production***, Vol. 276, (2020), 124249. https://doi.org/10.1016/j.jclepro.2020.124249
8. Lavado, J., Bogas, J., De Brito, J. and Hawreen, A., "Fresh properties of recycled aggregate concrete", ***Construction and Building Materials***, Vol. 233, (2020), 117322. https://doi.org/10.1016/j.conbuildmat.2019.117322
9. Jagan, S., Neelakantan, T., Reddy, L. and Kannan, R.G., "Characterization study on recycled coarse aggregate for its utilization in concrete-a review", in Journal of Physics: Conference Series, IOP Publishing. Vol. 1706, (2020), 012120.
10. Jagan, S., Neelakantan, T.R. and Saravanakumar, P., "Performance enhancement of recycled aggregate concrete–an experimental study", ***Applied Science and Engineering Progress***, Vol. 15, No. 1, (2022). https://doi.org/10.14416/j.asep.2021.07.003
11. Sivamani, J., Neelakantan, T., Saravana Kumar, P., Mugesh Kanna, C., Vignesh Harish, H. and Akash, M., "Efficient utilization of recycled concrete aggregates for structural applications—an experimental study", in Proceedings of SECON 2020: Structural Engineering and Construction Management 4, Springer., (2021), 567-579.
12. Akça, K.R., Çakır, Ö. and İpek, M., "Properties of polypropylene fiber reinforced concrete using recycled aggregates", ***Construction and Building Materials***, Vol. 98, (2015), 620-630. https://doi.org/10.1016/j.conbuildmat.2015.08.133
13. Chan, R., Santana, M.A., Oda, A.M., Paniguel, R.C., Vieira, L.B., Figueiredo, A.D. and Galobardes, I., "Analysis of potential use of fibre reinforced recycled aggregate concrete for sustainable pavements", ***Journal of Cleaner Production***, Vol. 218, (2019), 183-191. https://doi.org/10.1016/j.jclepro.2019.01.221
14. Gao, D., Zhang, L., Zhao, J. and You, P., "Durability of steel fibre-reinforced recycled coarse aggregate concrete", ***Construction and Building Materials***, Vol. 232, (2020), 117119. https://doi.org/10.1016/j.conbuildmat.2019.117119
15. He, W., Kong, X., Fu, Y., Zhou, C. and Zheng, Z., "Experimental investigation on the mechanical properties and microstructure of hybrid fiber reinforced recycled aggregate concrete", ***Construction and Building Materials***, Vol. 261, (2020), 120488. https://doi.org/10.1016/j.conbuildmat.2020.120488
16. Gao, D., Gu, Z., Pang, Y. and Yang, L., "Mechanical properties of recycled fine aggregate concrete incorporating different types of fibers", ***Construction and Building Materials***, Vol. 298, (2021), 123732. https://doi.org/10.1016/j.conbuildmat.2021.123732
17. Kumar, G., Shrivastava, S. and Gupta, R., "Paver blocks manufactured from construction & demolition waste", ***Materials Today: Proceedings***, Vol. 27, (2020), 311-317. https://doi.org/10.1016/j.matpr.2019.11.039
18. Jurić, A. and Štefić, T., "Experimental comparison of the bearing capacity of gfrp beams and 50% recycled gfrp beams", ***Civil Engineering Journal***, Vol. 8, No. 12, (2022), 3902-3911. https://doi.org/10.28991/CEJ-2022-08-12-017
19. Balamuralikrishnan, R. and Saravanan, J., "Effect of addition of alccofine on the compressive strength of cement mortar cubes", ***Emerging Science Journal***, Vol. 5, No. 2, (2021), 155-170. doi. https://doi.org/10.28991/esj-2021-01265
20. Dadzie, D.K. and Kaliluthin, A., "Sustainability performance of voided concrete slab using waste plastic bottles", ***Civil Engineering Journal***, Vol. 8, No. 11, (2022), 2490-2510. https://doi.org/10.28991/CEJ-2022-08-11-09
21. Sivamani, J., "Sustainable utilization of dumped concrete wastes as fine aggregates in concrete–an experimental study", ***International Journal of Engineering, Transactions C: Aspects***, Vol. 35, No. 9, (2022), 1795-1802. doi: 10.5829/IJE.2022.35.09C.16.

22. Pawar, A.J. and Suryawanshi, S., "Comprehensive analysis of stress-strain relationships for recycled aggregate concrete", ***International Journal of Engineering, Transactions B: Applications,***, Vol. 35, No. 11, (2022), 2102-2110. doi: 10.5829/IJE.2022.35.11B.05.
23. Pederneiras, C.M., Durante, M.D.P., Amorim, Ê.F. and Ferreira, R.L.d.S., "Incorporation of recycled aggregates from construction and demolition waste in paver blocks", ***Revista IBRACON de Estruturas e Materiais***, Vol. 13, (2020). https://doi.org/10.1590/S1983-41952020000400005
24. Tam, V.W., Tam, C.M. and Wang, Y., "Optimization on proportion for recycled aggregate in concrete using two-stage mixing approach", ***Construction and Building Materials***, Vol. 21, No. 10, (2007), 1928-1939. https://doi.org/10.1016/j.conbuildmat.2006.05.040
25. Hadi, M.N., Sajjad, U. and Sheikh, M.N., "Simple test method for determining shear strength of concrete", ***ACI Materials Journal***, Vol. 119, No. 1, (2022), 173-180. https://doi.org/10.14359/51732986
26. Hilles, M.M. and Ziara, M.M., "Mechanical behavior of high strength concrete reinforced with glass fiber", ***Engineering Science and Technology, an International Journal***, Vol. 22, No. 3, (2019), 920-928. https://doi.org/10.1016/j.jestch.2019.01.003
27. Jagan, S., Gokul Kannan, R. and Prasanth, S., "Effect of chopped glass fiber on the strength and durability of concrete", ***International Journal of Civil Engineering and Technology***, Vol. 8, No., (2017), 600-608.
28. Kirthika, S. and Singh, S., "Durability studies on recycled fine aggregate concrete", ***Construction and Building Materials***, Vol. 250, (2020), 118850. https://doi.org/10.1016/j.conbuildmat.2020.118850
29. Bai, G., Zhu, C., Liu, C. and Liu, B., "An evaluation of the recycled aggregate characteristics and the recycled aggregate concrete mechanical properties", ***Construction and Building Materials***, Vol. 240, (2020), 117978. https://doi.org/10.1016/j.conbuildmat.2019.117978
30. Leite, M. and Santana, V., "Evaluation of an experimental mix proportion study and production of concrete using fine recycled aggregate", ***Journal of Building Engineering***, Vol. 21, (2019), 243-253. https://doi.org/10.1016/j.jobe.2018.10.016
31. Khatib, J.M., "Properties of concrete incorporating fine recycled aggregate", ***Cement and Concrete Research***, Vol. 35, No. 4, (2005), 763-769. https://doi.org/10.1016/j.cemconres.2004.06.017
32. Das, C.S., Dey, T., Dandapat, R., Mukharjee, B.B. and Kumar, J., "Performance evaluation of polypropylene fibre reinforced recycled aggregate concrete", ***Construction and Building Materials***, Vol. 189, (2018), 649-659. https://doi.org/10.1016/j.conbuildmat.2018.09.036
33. Hanumesh, B., Harish, B. and Ramana, N.V., "Influence of polypropylene fibres on recycled aggregate concrete", ***Materials Today: Proceedings***, Vol. 5, No. 1, (2018), 1147-1155. https://doi.org/10.1016/j.matpr.2017.11.195

Persian Abstract

چکیده

استفاده از الیاف در بتن باعث کاهش ترک ها، افزایش جذب انرژی و مقاومت بتن می شود .استفاده از سنگدانه های بازیافتی ریز (FRA) در بتن بر کمبود سنگدانه های طبیعی غلبه می کند، اما کیفیت ضعیف آن از طریق ایجاد ترک بر خواص بتن تأثیر می گذارد .این مطالعه به بررسی اثر استفاده از الیاف شیشه (GF) در کاهش انتشار ترک با استفاده از سنگدانه بازیافتی ریز (FRA) در بتن می‌پردازد 0 GF، 0.25، 0.5، 0.75، 1 و 1.5 درصد وزنی اضافه شد .مخلوط‌های بتن با درصد بهینه FRA و درصدهای مختلف GF با روش اختلاط دو مرحله‌ای (TSMA) و روش اختلاط معمولی (NMA) تهیه و برای خواص تازه و سخت‌شده‌شان آزمایش شدند .مخلوط بهینه شده با FRA 30% و GF 1% تهیه شده توسط TSMA، با بهبود استحکام 11.3%در مقایسه با مخلوط شاهد در 28 روز مشاهده شد .این مطالعه بیشتر مناسب بودن عملی را به عنوان یک بلوک سنگفرش برای کاربردهای ترافیکی غیر ترافیکی و حجم متوسط طبق استاندارد IS 15658: 2006 بررسی کرد و در مقایسه با بلوک سنگفرش معمولی مشاهده کرد که حداقل مقاومت مورد نیاز 40 مگاپاسکال تحت هر دو شرایط با ترکیب بهینه با بهبود 17.4 درصد به دست آمد.

International Journal of Engineering

Journal Homepage: www.ije.ir

Effect of Surface Roughness on Brinell Hardness and Load-Displacement Curves using a Macro Indentation

A. Karbasian, M. Shirazi, A. H. Mahmoudi*

Mechanical Engineering Department, Bu-Ali Sina University, Hamedan, Iran

PAPER INFO

Paper history:
Received 06 February 2023
Received in revised form 03 March 2023
Accepted 04 March 2023

Keywords:
Macro Spherical Indentation
Roughness
Brinell Hardness
Load-displacement Curve
Finite Element Simulation

ABSTRACT

Surface roughness significantly affects the scattering of load-displacement curves and the measurement of mechanical properties by the macro-scale indentation. Many mechanical properties such as modulus of elasticity, yield stress, strain hardening exponent, and hardness can be determined using the indentation results, which are the information obtained from the load-displacement curve. Reliable parameters of the load-displacement (P-h) curve are employed to estimate the mechanical properties. The inaccurate P-h curve leads to a misestimation of material properties. Ignoring the surface roughness might be a source of error in the indentation results. In this paper, the effects of surface roughness on the P-h curve of macro spherical indentation and Brinell hardness number (BHN) were studied. The range of roughness with minimal effect on indentation results was obtained. The surface roughness of 2 and 12 microns was created on the experimental samples using the electrical discharge machining (EDM) process. The finite element simulations were performed with different surface roughnesses. The results showed that roughness affected both the P-h curve and hardness values in different indentation depths and various indenter sizes. It was observed that with increasing the Rq roughness, the P-h curve level and hardness value decreased and that with increasing the indentation depth, the effect of roughness on hardness decreased as well. The neumerical results showed a good agreement with the results of experiments.

doi: *10.5829/ije.2023.36.05b.08*

1. INTRODUCTION

The determination of material properties in engineering material has always been a subject of concern. Employing the indentation method is one of the non-destructive and effective methods to estimate the material properties; therefore, unreliable and inaccurate data of the indentation result is usually a source of error. Surface roughness is one of the important parameters which may cause uncertainties in indentation results, when is neglected. The indentation technique relies on the characterization of the P-h curve parameters. In general, surface roughness is determined using the peaks and valleys of the surface and their interval distribution along the surface [1]. In the indentation method, surface roughness can play an important role in the determination of mechanical properties. Studies showed that surface roughness can alter the P-h curves [2, 3]. However, it should be noted that most of the studies have been carried out on the nano and micro scales. Surface roughness in the low-depth indentations can be one of the primary sources of error in estimation of various mechanical properties. In the large indentation depth, the error at the contact point is reduced. It has been revealed that the error caused by the surface roughness is proportional to the indentation depth [4]. Surface roughness is effective when the dimensions of peaks and valleys are much smaller than dimension of the contact area [5]. Since the contact area of the indenter and the surface can be obtained indirectly from the indentation depth, surface roughness can cause errors in determination of the contact area between the indenter and the surface piece [1]. Bhaskara Rao and Beatrice Seventlin [6] developed a new technique based on the image processing to measure the surface roughness.

*Corresponding Author Email: a.h.mahmoudi@gmail.com, a.h.mahmoudi@basu.ac.ir (A. H. Mahmoudi)

Please cite this article as: A. Karbasian, M. Shirazi, A.H. Mahmoudi, Effect of Surface Roughness on Brinell Hardness and Load-Displacement Curves using a Macro Indentation, ***International Journal of Engineering, Transactions B: Applications***, Vol. 36, No. 05, (2023) 914-924

Walter et al. [7] assessed the effect of surface roughness on elastic modules using 2D and 3D FEM simulation on a Nano scale. They realized that for Ra>3 nm, the results varied considerably in both models [7]. Campbell et al. [8] investigated the effect of roughness on the reduced modulus (Er) in impact of two surfaces and presented a principle study using three-dimensional finite element modeling to implement the apparent modulus in a rough surface, which was measured by an atomic force microscope (AFM). Chen et al. [9] reported that when the applied forces are small, the surface roughness has a significant effect (due to the low level of indentation). However, this issue is not of importance in case of sharp indenters. They also developed a 3D roughness model using a Berkovich indenter in ABAQUS software [9]. Gao et al. [10] studied the effect of surface roughness on variables such as indentation force, contact area, and contact load in both loading and unloading. They modeled the roughness of different materials by mapping the experimental AFM data to a finite element model. Xia et al. [11] presented various quantitative models for estimating macro-hardness in studying the effect of roughness on hardness. the effect of non-reproducibility as an error of the Nano-indentation test was taken into consideration [11]. Bobji et al. [12] studied the effect of roughness on a macro scale with an average point height of 1 mm for different roughness shapes with a spherical indenter. They found that Young's modulus and hardness are sensitive to roughness. Furthermore, they studied the quasi-static indentation to determine the results of scatter due to the surface roughness parameters [12]. Bobji et al. [13] found that the hardness scatterings measured on a rough surface in Nano-indentation could be caused by geometric change of roughness during indentation, the effect of indenter geometry, and the material properties. In another case, they suggested that the hardness value is reliable when the indentation depth “h” is greater than or equal to four times the value of the Root Mean Square (RMS or Rq) of the profile height parameter [13]. Tang et al. [14] studied the influence of surface roughness on hardness measurement by using nano indentation tests and FE analysis. Xia [15] advised a method to accurately determine the mechanical properties, taking into account the calculation of the errors in the first contact point and also the effect of the surface roughness error. Using 2D Finite Element (FE) analysis of spherical indentation on a Nano scale, Walter et al. [16] observed that increasing the roughness decreased the contact area and, as a result, there was more scattering of the Young's modulus in an elastic deformation. They also stated that when the roughness value is much smaller than the contact surface, the geometric parameter of roughness has a significant effect on the results of the indentation process. In another case, they found that increasing the roughness led to more scattering of the P-h curve [16]. Nazemian et al. [17] showed that the surface roughness of thin films affects the Nanoindentation results, especially at low indentation depth. Mikowski et al. [18] determined the mechanical properties of the kaolinite material considering the effect of surface roughness in the Nano-indentation test on their samples. Bolesta and Fomin [19] found that the surface around the indentation area changed due to the surface roughness. In some cases, the accuracy of measuring the hardness and the P-h curve can be affected by these changes. Maslenikov et al. [20] resulted that the roughness deviates the hardness from its correct number. They corrected the hardness value by information of correlation function and height distribution. Jiang et al. [21] examined the effect of surface roughness on the nano hardness and elastic modulus of thin films. They used nano-indentation method to extract the material properties. They also showed that the micro hardness and elastic modulus decreased in rough samples in comparison with smooth ones.

Pham et al. [22] proposed a function from FE and regression analysis by using spherical indention to determine the plastic properties of materials. Goto et al. [23] obtained the stress - strain curve by employing an estimation technique based on the indentation method. Wagih [24] employed a sharp nano-indentation test and FE analysis to predict the hardness of composite and pure metal. Akahori et al. [25] also used the spherical indentation and numerical method to measure the yield stress and residual stresses.

In recent years, the indentation method, numerical inverse analysis, and FE simulations have been widely used to determine the material properties of various materials [26-28]. Bocciarelli and Maier [29] employed the imprint area and indentation test to estimate the residual stresses. Furthermore, studies have been performed for simultaneous determination of the material model and the residual stresses for different materials [30, 31].

As it was previously mentioned, many of the methods which have been proposed to estimate the material properties from the indentation approach, are based on the P-h curve parameters. Access to an accurate P-h curve is one of the complex challenges. An inaccurate P-h curve can lead to incorrect and scattered material properties. Different surface roughnesses can alter the P-h curves. It is one of the challenges to recognize the effect of roughness on the P-h curve and roughness range that does not affect the curves.

In this paper, the effect of surface roughness on the hardness value and P-h curve of the macro-spherical indentation was studied. The effects of the indenter size and the indentation depth were examined and compared for different rough surfaces. Most of the previous studies have been conducted for nano scale indentation and roughness. Finite Element Analysis with different surface roughness were performed to specify the effects

of roughness, indenter size, and indentation depth on both P-h curves and the Brinell hardness. The optimum roughness range within which the effect of micro roughness on the macro P-h curves results could be ignored, was obtained. The Finite Element (FE) results were also verified using several experimental tests.

2. 1. Roughness Simulation In this study, one of the challenges was modeling of the surface roughness. Despite many efforts, it was noticed that 3D modeling of the surface roughness in ABAQUS commercial code was complicated. For this purpose, a rough surface was first modeled in MATLAB coding commercial software and N×N points were created using a random statistical function. Then, by mapping the points from MATLAB to ABAQUS, the desired model with a specified Rq was modeled in ABAQUS [32-34].

The parameter Rq represents the distribution of the standard deviation in the surface point's height, which is an essential parameter for creating the surface roughness by statistical methods. This parameter represents the root mean square (RMS) of the profile height from the mean line and is more sensitive to the parameter Ra (arithmetic mean of the height of the points) in deviations of large surfaces from the mean line. Rq or RMS is defined by Equation (1) [35]:

$$R_q = \sqrt{\frac{1}{L}\int_0^L [Z(x)]^2 dx} \quad (1)$$

where in Equation (1), L is the sampling length and Z is the height of the points from the origin of the coordinate system .

The following smart and novel method was employed to model the rough surface. First, a rough surface with the desired Rq was created on the N×N point in MATLAB coding program. Then, all steps of the indentation simulation were performed in ABAQUS. The resulted rough surface was then mapped from the MATLAB to the indentation area in ABAQUS using the JAVA coding program. Figure 2 shows the created rough surface in MATLAB and Figure 3 illustrates the mapped surfaces to the FE model for different roughness values.

2. 2. Finite Element Method Finite element simulations were performed using ABAQUS commercial code. The indenter was modelled with a Young's modulus of 600 GPa, and a Poisson's ratio of 0.3 [36], which corresponds to the properties of tungsten carbide. The elastic regime was considered for the indenter material. Due to the symmetry in loading and geometry,

2. RESEARCH METHOD

The procedure of this research is described in the flowchart as shown in Figure 1.

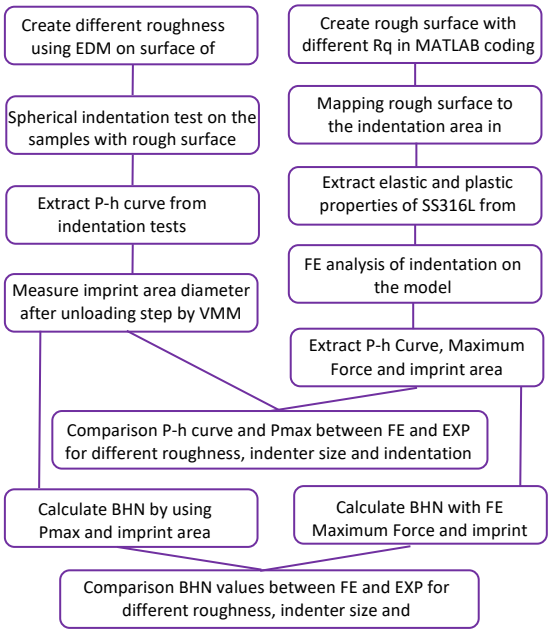

Figure 1. A Schematic presentation of the research flow diagram

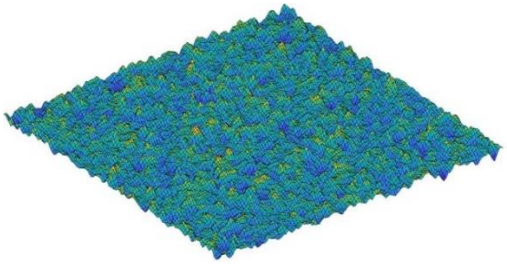

Figure 2. 3D rough surface schematic obtained from MATLAB software

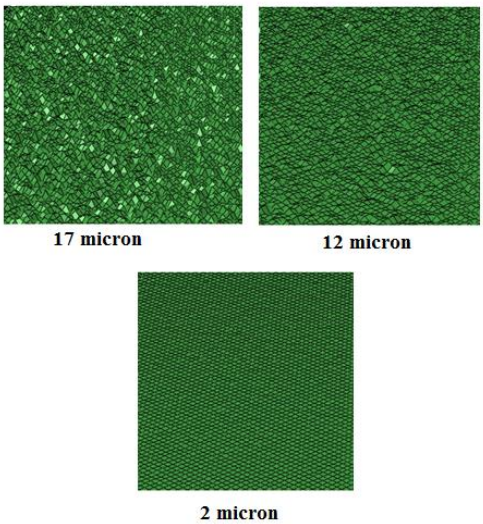

Figure 3. Roughness schematic created in ABAQUS

only a quarter of the sample was modelled for both the indenter and the specimen. The materials regime for the sample was considered to be elastic-plastic with a Young's modulus of 204 GPa, which was extracted from the uniaxial tensile test of stainless steel 316L, and the Poisson's ratio was considered to be 0.3 [37]. The plastic true strain-stress data extracted from the tensile test was used as the plastic properties. The type of the element used in the spherical indenter and specimen was C3D8R. The mesh size was 0.03 mm which was verified by a convergence checking. Figure 4 shows the P-h curve convergence. The total number of elements were 336,000. Spherical indenters with diameters of 1, 1.5, 2.5, and 4 mm and a block with dimensions of 3×4×4 mm^3 were modelled. Figure 5 illustrates the imprint area and deformation of the sample in the Y direction after the unloading step.

2. 3. Hardness Calculation Method The Brinell method is a two-stage indentation procedure to determine the hardness. In the first step, a hard indenter is pressed vertically into the surface of the sample under load. In the second step, the length of the indentation diameters is measured from at least two perpendicular directions. Equation (2) shows the Brinell's hardness equation [38, 39]. The Brinell hardness value is obtained by dividing the applied force by the area of the indented surface.

$$BHN = 0.102 \times \frac{2F}{\pi D\left(D-\sqrt{D^2-d^2}\right)} \quad (2)$$

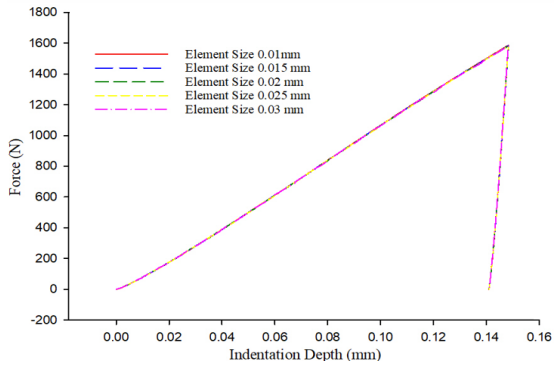

Figure 4. Convergence for the P-h curves

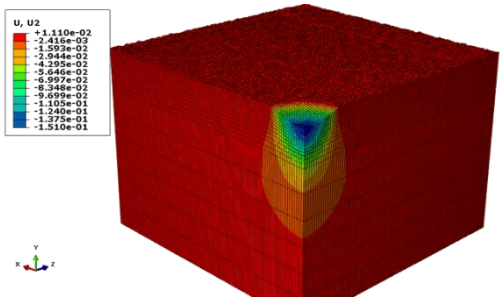

Figure 5. Deformed view of the FE model after unloading

In the above equation, BHN is the Brinell hardness value in (kg/mm^2), F is the force, D and d represent the diameter of the indenter and the diameter of the indentation imprint in (mm), respectively. In calculation of the hardness, the values of the force and the indentation imprint diameter were extracted from both numerical and experimental imprints. The force used in the hardness calculation was the maximum contact force (P_{max}) between the specimen and indenter. The P_{max} was extracted from the end of loading step of the P-h curve.

2. 4. Experimental Tests The material used in this study was stainless steel 316L. This grade of steel is widely used in marine structures, food devices, medical implants, and fasteners [40]. The samples for tensile tests were manufactured according to standard ASTM E 8M-04 [41]. In Figure 6 the true and engineering stress-strain curves of 316L are shown. The yield stress and elastic modulus of the specimen were 263Mpa and 204GPa, reespectively. Furthermore, the chemical compositions of 316L are appicted in Table 1.

The indentation tests were carried out using a universal tension-compression test device with a capacity of 5000 N. The indentation depth was measured by a linear variable differential transformer (LVDT) with accuracy of 0.1 micron. In Figure 7 the indentation test setup and its components are shown. Both load and indentation depth were recorded during the indentation tests.

An electric discharge machine (EDM) was used to create the required roughness on the block samples manufactured from stainless steel 316L. The EDM affects the morphology and roughness parameters of the material's surface [42]. The 2- and 12-micron roughness

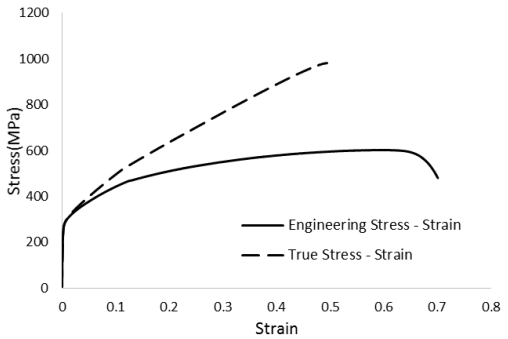

Figure 6. True and engineering stress - strain curves of 316L

TABLE 1. Chemical composition of experimented SS316L

Fe	C	Si	Mn	P	S	Cr	Mo
Base	0.024	0.41	1.79	0.020	0.013	16.95	2.034
Ni	Al	Co	Cu	Nb	Ti	V	W
10.06	0.004	0.41	0.41	0.008	0.002	0.053	0.077

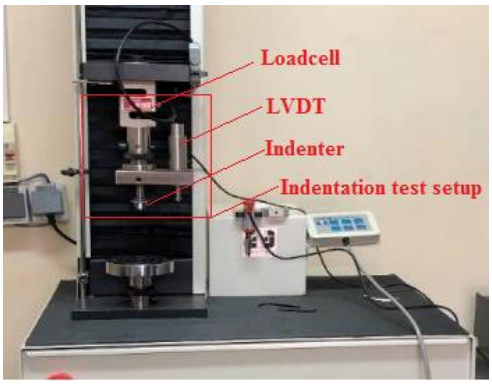

Figure 7. Macro spherical indentation test setup

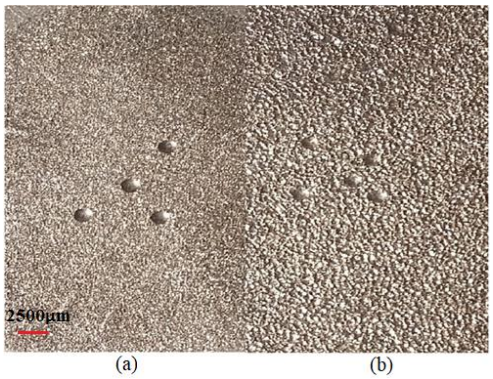

Figure 8. Two surfaces with different Rq roughness values (a) 2-microns (b) 12-microns

were achieved by changing the EDM input parameters, such as current intensity and the pulse time. Figure 8 shows two surfaces with different roughness values along with the imprints of the indentation remained after unloading. The advantage of having more diverse roughness values was provided by the application of the EDM to create the roughness. Although there are other techniques to create the roughness, the EDM process provided the requirement surface roughness with the least side effects.

Two indenters with diameters of 2.5 and 1.5 mm were employed in the experimental indentation test; therefore, the effect of the indenter size and the roughness could be observed simultaneously. Also, the indentation depths of 50, 90, and 150 microns were examined on the samples to investigate the effect of indentation depth of the rough surface on the spherical indentation. The diameters of the indentation imprint were measured using a vision measuring machine (VMM) in four different directions with high accuracy. The measurements were performed along different directions to achieve more accurate results. Then, the Brinell hardness was calculated using Equation (2). A surface profilometer was used to measure the roughness. Three important roughness parameters were obtained according to Table 2. Ra is the arithmetic mean of profile height, Rp is the maximum profile peak, and Rv is the maximum profile valley depth. In Table 2, the standard deviation (SD) of measured parameters are shown.

TABLE 2. Roughness parameters measured by surface profilometry device, (SD: Standard deviation)

Roughness (R_q)	R_a , µm (SD)	R_p , µm (SD)	R_v , µm (SD)
2-micron	1.56 (0.16)	4.66 (0.33)	5.1 (0.36)
12-micron	9.6 (0.59)	36.5 (4.84)	34 (3.45)

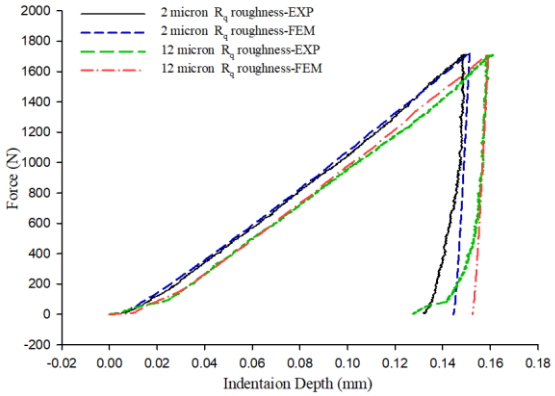

Figure 9. Comparison of P-h curves related to the 2.5 mm indenter in both 2 and 12-micron Rq roughness between FE results and experimental tests

3. RESULTS AND DISCUSSION

3. 1. Effect of Roughness on Load Displacement Curve Several finite element analyses with the Rq roughness values of 2, 7, 12, and 17-micron were performed. Figure 9 compares the P-h curves obtained from numerical simulations and experimental tests for 2 and 12-micron roughness using a 2.5-mm diameter indenter. The P-h curves for the 1.5-mm indenter with 2-micron roughness are shown in Figure 10 According to these figures, the P-h curves obtained from the finite element simulations illustrated a good agreement with the results from the experimental tests. In all figures the FEM, EXP and Dia are the abbreviations of finite element results, experimental results and diameter of indenter.

It is observed in Figure 9 that with the decrease in the surface roughness, the P-h curves were elevated in both the numerical and experimental results. This is mainly due to the less amount of load required for indentation in the case of 12-micron roughness. This is especially more observable in the beginning of the curves due to less

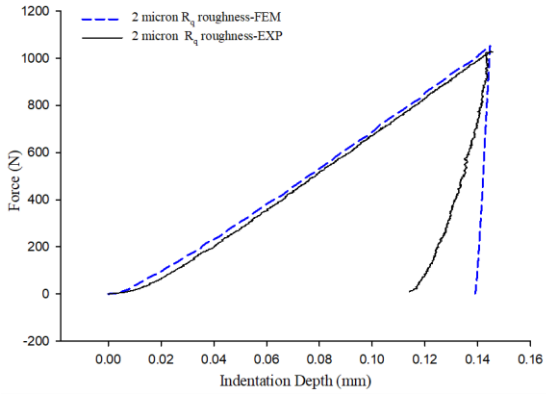

Figure 10. P-h curves, 1.5mm diameter indenter, 2-micron Rq roughness: A comparison between FE and experiments

materials constraint of a rough surface. The curve slops were also less at the beginning for the case of 12-micron roughness .

The experiment tests revealed that by increasing the surface roughness, the scattering of the P-h curves was increased. Little difference between the P-h curves relates to different points of surface for each roughness value was observed, but there was a meaningful difference between the indentation test results of various roughness.

Although the unloading step of the P-h curve was not the subject of this study, according to Figures 9 and 10, a considerable difference with FE was observed. This deviation was related to the indentation unloading test setup. However, no parameter has was extracted for this study from the unloading section of the curves and therefore this deviation did not affect the results. The loading part of the curves displayed a good agreement between the numerical and experimental results. Similar deviation was observed in other research [43].

In order to further clarify the effect of roughness on the P-h curves 7 and 17 micron roughness were also modeled. Figure 11 shows a comparison between their P-h curves and the 2 and 12-micron cases. Curves in Figure 11 also confirmed the above discussion.

3. 2. Effect of Indenter Diameter The diameters of the spherical indenters were selected in such a way that significant differences were observed in the results. Figures 12 and 13 illustrate the effects of 1, 1.5, 2.5, and 4 mm diameter indenters on the numerically obtained P-h curves resulting from the indentation on surfaces with 2 and 12 micron roughness. Trends of the curves were the same in both 2 and 12 micron roughness and the P-h curves were elevated with an increase in the indenter size. Table 3 shows the maximum force at 150-micron indentation depth for different conditions. The maximum deviation between forces of 2 and 12-micron roughness

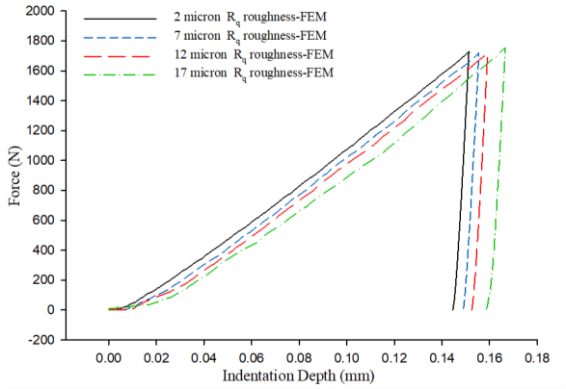

Figure 11. Effect of Rq roughness on the FE P-h curves

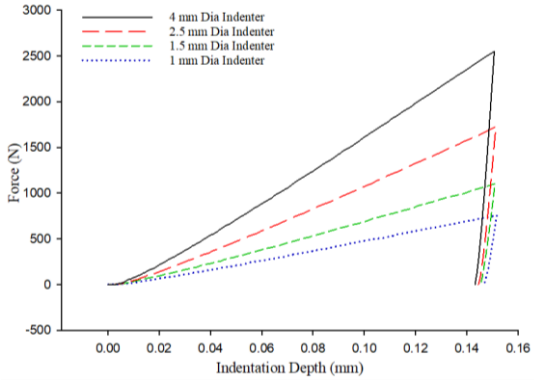

Figure 12. Comparison between FE P-h curves for different indenter sizes and 2-micron surface roughness

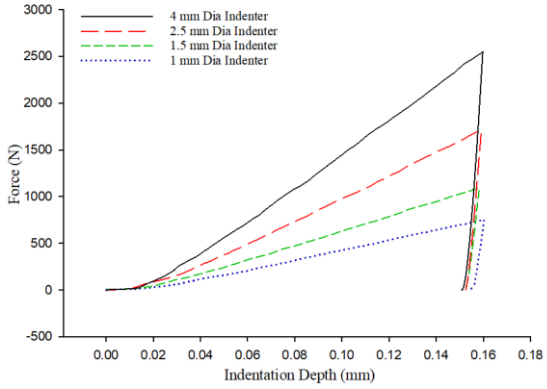

Figure 13. Comparison between FE P-h curves for different indenter sizes and 12-micron Rq roughness

was for the 1mm diameter indenter with a value of 7.07% and the minimum was related to the 4-mm-diameter indenter with a value of 6.18%. According to the presented results of Figures 12 and 13 and Table 3, it was concluded that the spherical indentations with larger indenter sizes were less affected by the surface

roughness. In the comparison of the experimental P-h curves between the 1.5 and 2.5mm indenters, a great reduction in the force of 1.5-mm-diameter indenter was observed (Figure 14).

3. 3. Optimum Roughness Range It was observed that the roughness of 2 micron and less was an appropriate range within which the effect of roughness on the P-h curves resulting from the 2.5-mm-diameter spherical indentation could be ignored. As shown in Figures 15 and 16, the P-h curves of 2-micron Rq roughness and the ideal surface (without roughness in the numerical model and polished surface in the experiment) indicated a good agreement. There are slight differences between the 3-micron roughness and the two other curves in the numerical results shown in Figure 15.

The deviation of 2 and 3-micron roughness P-h curves was related to the early loading stage of curves where the peaks and valleys of the surface have the maximum effect on the indentation force. It can be noted that a 2-micron roughness surface and less are a reliable range for spherical macro indentation.

TABLE 3. Maximum force values at the indentation depth of 150-microns caused by 1, 1.5, 2.5 and 4 mm diameter indenter in FE simulations

Indenter diameter (mm)	Rq Roughness (micron)	Force (N)	Deviation between forces (%)
1	2	748.7	7.07
	12	695.8	
1.5	2	1099	6.73
	12	1025	
2.5	2	1708.9	6.62
	12	1595.7	
4	2	2536.9	6.18
	12	2380.2	

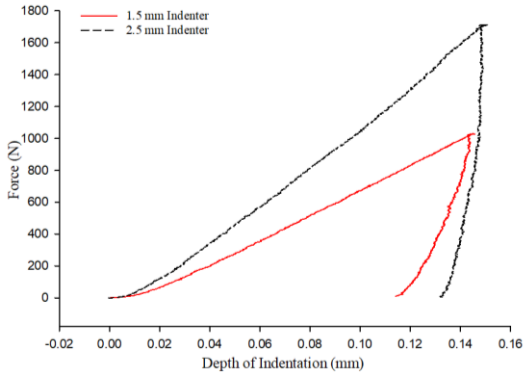

Figure 14. Comparison between experimental P-h curves with 1.5 and 2.5 mm indenter

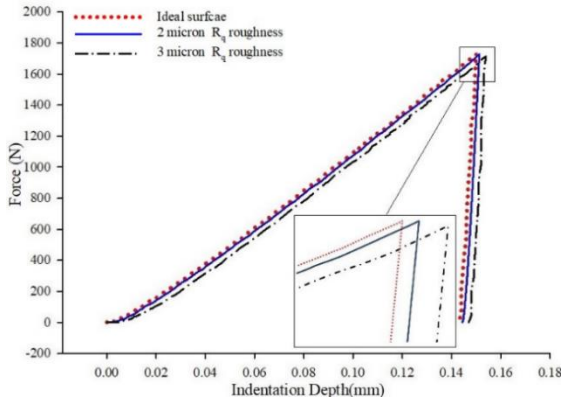

Figure 15. Comparison of the FE P-h curves between the 2- and 3-micron roughness and the ideal surface for the 2.5-mm indenter

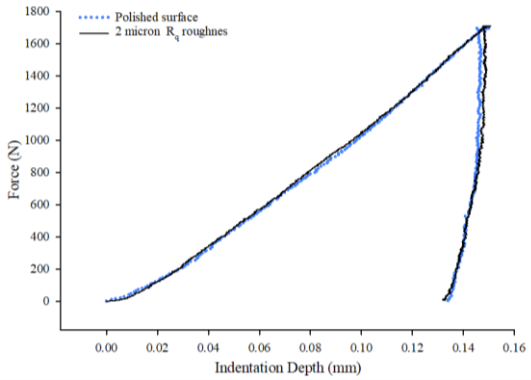

Figure 16. Comparison of the EXP P-h curves between the 2-micron Rq roughness and the polished surface for the 2.5-mm indenter

3. 4. Effect of Roughness on Hardness Figure 17 shows the Brinell hardness with a diameter of 2.5 mm for 2 and 12-micron roughness at 150, 90, and 50-micron indentation depths. The hardness values increased with a decrease in roughness for both numerical and experimental results. The slope of curves in the measured hardness based on the FE data was lower than the experimental hardness, indicating that the FE hardness values of 2 and 12 microns Rq roughness are closer to each other than the experimental values. The hardness values at 90 and 150-micron indentation depths were convergent, suggesting that the 50-micron indentation depth was not an appropriate depth considering the roughness values.

Indentation tests were performed at a depth of 150 microns with a 1.5-mm indenter on the 2 and 12-micron roughness to investigate the effect of the indenter size on the measured hardness. The FE simulations were also carried out using the same diameter and indentation depth and the corresponding hardness values were determined as shown in Figure 18. The trend of changes in the

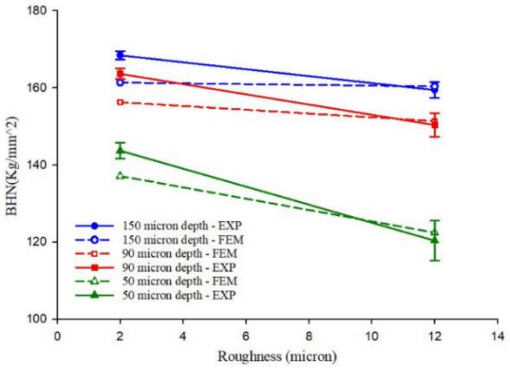

Figure 17. Comparison of the hardness for 2- and 12-micron Rq roughness and different indentation depths for both the FE and experimental results

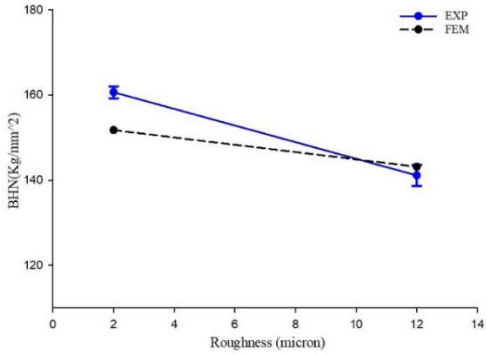

Figure 18. Effect of roughness on hardness values in FE and experimental results with the 1.5-mm-diameter indenter

TABLE 4. All hardness values with different indenter size, indentation depth and surface roughness

Indenter diameter (mm)	Indentation depth (μm)	FE/ EXP	Rq Roughness (μm)	BHN (kgf/mm^2)
2.5	50	EXP	2	143.7
			12	120.4
		FE	2	137.1
			12	122.4
2.5	90	EXP	2	163.6
			12	150.3
		FE	2	156.3
			12	151.4
2.5	150	EXP	2	168.4
			12	159.3
		FE	2	161.4
			12	160.3
1.5	150	EXP	2	160.3
			12	141.1
		FE	2	151.8
			12	143.2

hardness with the 1.5-mm diameter indenter was the same as previous results shown in Figure 17. All calculated values of hardness are depicted in Table 4.

The influence of both the indentation depth and surface roughness on the measurement of hardness in shown in Figure 19. The figure contains the measured hardness values of both numerical and experimental results. It can be noted that the hardness values of the surface with 2 micron roughness were higher than the 12-micron roughness and this is mainly due to the higher values of force in the indention with 2-micron roughness. The measured values of hardness became closer together with an increase in the indentation depth. Therefore, it can be concluded that with an increase in the indention depth, the effect of roughness on the hardness decreased.

Based on the standard deviation values of Figures 17 and 19, it can be concluded by increasing the roughness, the BHN scattering increased. The reason based on Table 2, is the higher standard deviation of 12-micron roughness compared to 2-micron roughness. Figure 19 Shows that by increasing indentation depth, the hardness values deviations decreased in both 2 and 12-micron roughnesses. There are two reasons for this subject: first the difficulties and errors of measuring the imprint area in the low-depth indentation due to the presence of roughness and second the better repeatability of maximum force in deeper indentation.

Finally, the numerical results showing the effects of wider range of surface roughness on the hardness values are shown in Figure 20. In this figure the hardness values for different roughness of 2, 7, 12, and 17-microns with a 150-micron indentation depth were compared. The results also confirmed the previous discussion.

The results of this study had a good agreement with other research. Chen et al. [9] by employing sharp nano-indentation, concluded roughness in the nano scale affects the P-h curve and hardness. They resulted in that by decreasing the surface roughness from 20 nm to 2 nm

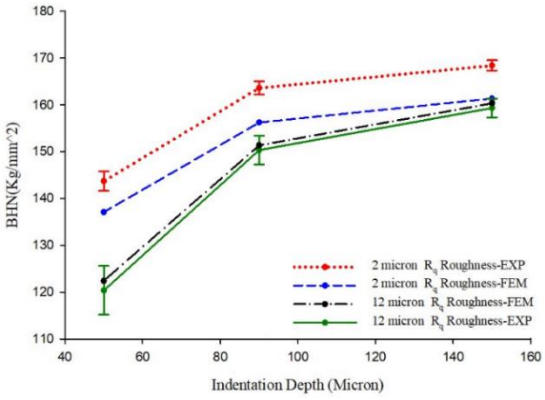

Figure 19. Comparison between the curves of experimental and numerical hardness for the 2.5-mm-indenter with 2- and 12-micron Rq roughness and indentation depths of 50, 90, and 150 microns

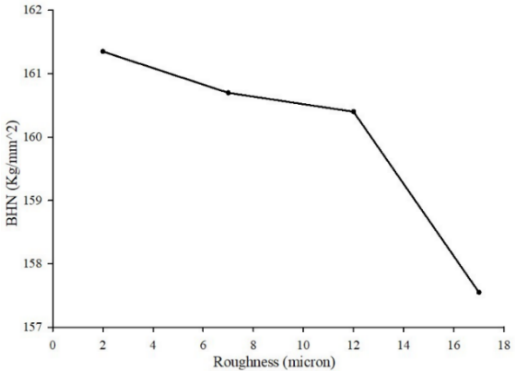

Figure 20. Comparison of hardness in 2, 7, 12, and 17-micron Rq roughness

in 362 nm indentation depth, the P-h curve elevated. The scattering of P-h curves and hardness numbers were minimum in 2 nm roughness. In the current study, similar results were obtained from macro spherical indentation on the rough surfaces.

4. CONCLUSIONS

In this study, the effect of surface roughness on the P-h curves and hardness of macro spherical indentation was investigated. In this regard, a rough surface was modeled and several FE simulations and experimental tests with different surface roughness, indentation depths, and indenter sizes were performed. Findings of this work can be concisely expressed below:

- With decreasing the Rq roughness, the P-h curves elevated and the hardness values increased.
- With increasing the indenter diameter for indentation on the rough surfaces, the effect of Rq roughness on the P-h curves and hardness decreased .
- An increase in depth of indention played a significant role in decreasing the effect of Rq roughness in both the P-h curves and the hardness values. The values of hardness were closer with increasing the indentation depth for different values of roughness.
- The Rq roughness of 2 microns and less was a range within which the effect of roughness on the P-h curves for the 2.5-mm-diameter indenter and 150-micron indentation depth could be ignored.
- By increasing the roughness, the scattering in measured hardness increased.

5. REFERENCES

1. Fischer-Cripps, A.C. and Nicholson, D., "Nanoindentation. Mechanical engineering series", ***Applied Mechanics Reviews***, Vol. 57, No. 2, (2004), B12-B12.
2. Marteau, J., Jourani, A. and Bigerelle, M., "Determination of an objective criterion for the assessment of the feasibility of an instrumented indentation test on rough surfaces", ***Materials***, Vol. 13, No. 7, (2020), 1589. https://doi.org/10.3390/ma13071589
3. Marteau, J. and Bigerelle, M., "Toward an understanding of the effect of surface roughness on instrumented indentation results", ***Journal of Materials Science***, Vol. 52, (2017), 7239-7255. https://doi.org/10.1007/s10853-017-0961-5
4. Standardization, I.O.f., "Metallic materials: Instrumented indentation test for hardness and materials parameters. Test method, ISO, (2015).
5. Johnson, K.L. and Johnson, K.L., "Contact mechanics, Cambridge university press, (1987).
6. Bhaskara Rao, J. and Beatrice Seventline, J., "Estimation of roughness parameters of a surface using different image enhancement techniques", ***International Journal of Engineering, Transactions B: Applications***, Vol. 30, No. 5, (2017), 652-658. doi: 10.5829/idosi.ije.2017.30.05b.04.
7. Walter, C. and Mitterer, C., "3d versus 2d finite element simulation of the effect of surface roughness on nanoindentation of hard coatings", ***Surface and Coatings Technology***, Vol. 203, No. 20-21, (2009), 3286-3290. https://doi.org/10.1016/j.surfcoat.2009.04.006
8. Campbell, A.C., Buršíková, V., Martinek, J. and Klapetek, P., "Modeling the influence of roughness on nanoindentation data using finite element analysis", ***International Journal of Mechanical Sciences***, Vol. 161, (2019), 105015. https://doi.org/10.1016/j.ijmecsci.2019.105015
9. Chen, L., Ahadi, A., Zhou, J. and Ståhl, J.-E., "Modeling effect of surface roughness on nanoindentation tests", ***Procedia CIRP***, Vol. 8, (2013), 334-339. doi: 10.1016/j.procir.2013.06.112.
10. Gao, C., Proudhon, H. and Liu, M., "Three-dimensional finite element analysis of shallow indentation of rough strain-hardening surface", ***Friction***, Vol. 7, (2019), 587-602. https://doi.org/10.1007/s40544-018-0245-3
11. Xia, Y., Bigerelle, M., Marteau, J., Mazeran, P.E., Bouvier, S. and Iost, A., "Effect of surface roughness in the determination of the mechanical properties of material using nanoindentation test", ***Scanning: The Journal of Scanning Microscopies***, Vol. 36, No. 1, (2014), 134-149. doi: 10.1002/sca.21111.
12. Bobji, M., Shivakumar, K., Alehossein, H., Venkateshwarlu, V. and Biswas, S., "Influence of surface roughness on the scatter in hardness measurements—a numerical study", ***International Journal of Rock Mechanics and Mining Sciences***, Vol. 36, No. 3, (1999), 399-404. http://dx.doi.org/10.1016/S0148-9062(99)00009-1
13. Bobji, M. and Biswas, S., "Deconvolution of hardness from data obtained from nanoindentation of rough surfaces", ***Journal of Materials Research***, Vol. 14, No. 6, (1999), 2259-2268. https://doi.org/10.1557/JMR.1999.0302
14. Tang, D., Zhao, L., Wang, H., Li, D., Peng, Y. and Wu, P., "The role of rough surface in the size-dependent behavior upon nano-indentation", ***Mechanics of Materials***, Vol. 157, (2021), 103836. https://doi.org/10.1016/j.mechmat.2021.103836
15. Xia, Y., "A robust statistical method for determining material properties and indentation size effect using instrumented indentation testing", Université de Technologie de Compiègne, (2014),
16. Walter, C., Antretter, T., Daniel, R. and Mitterer, C., "Finite element simulation of the effect of surface roughness on nanoindentation of thin films with spherical indenters", ***Surface and Coatings Technology***, Vol. 202, No. 4-7, (2007), 1103-1107. doi: 10.1016/j.surfcoat.2007.07.038.
17. Nazemian, M., Chamani, M. and Baghani, M., "A combined experimental and numerical study of the effect of surface roughness on nanoindentation", ***International Journal of Applied Mechanics***, Vol. 11, No. 07, (2019), 1950070. https://doi.org/10.1142/S1758825119500704

18. Mikowski, A., Soares, P., Wypych, F., Gardolinski, J. and Lepienski, C., "Mechanical properties of kaolinite 'macro-crystals'", ***Philosophical Magazine***, Vol. 87, No. 29, (2007), 4445-4459. doi: 10.1080/14786430701550394.
19. Bolesta, A. and Fomin, V., "Molecular dynamics simulation of sphere indentation in a thin copper film", ***Physical Mesomechanics***, Vol. 12, No. 3-4, (2009), 117-123. https://doi.org/10.1016/j.physme.2009.07.003
20. Maslenikov, I., Useinov, A., Birykov, A. and Reshetov, V., "Reducing the influence of the surface roughness on the hardness measurement using instrumented indentation test", in IOP Conference Series: Materials Science and Engineering, IOP Publishing. Vol. 256, (2017), 012003.
21. Jiang, W.-G., Su, J.-J. and Feng, X.-Q., "Effect of surface roughness on nanoindentation test of thin films", ***Engineering Fracture Mechanics***, Vol. 75, No. 17, (2008), 4965-4972. doi: 10.1016/j.engfracmech.2008.06.016.
22. Pham, T.-H., Phan, Q.-M. and Kim, S.-E., "Identification of the plastic properties of structural steel using spherical indentation", ***Materials Science and Engineering: A***, Vol. 711, (2018), 44-61. https://doi.org/10.1016/j.msea.2017.10.097
23. Goto, K., Watanabe, I. and Ohmura, T., "Determining suitable parameters for inverse estimation of plastic properties based on indentation marks", ***International Journal of Plasticity***, Vol. 116, (2019), 81-90. doi: 10.1016/j.ijplas.2018.12.007.
24. Wagih, A., "Experimental and finite element simulation of nano-indentation on metal matrix composites: Hardness prediction", ***International Journal of Engineering, Transactions A: Basics***, Vol. 29, No. 1, (2016), 78-86. doi: 10.5829/idosi.ije.2016.29.01a.11.
25. Akahori, T., Nagakura, T., Fushimi, S. and Yonezu, A., "An indentation method for evaluating the residual stress of polymeric materials: Equi-biaxial and non-equi-biaxial residual stress states", ***Polymer Testing***, Vol. 70, (2018), 378-388. doi: 10.1016/j.polymertesting.2018.07.024.
26. Hosseinzadeh, A. and Mahmoudi, A., "Determination of mechanical properties using sharp macro-indentation method and genetic algorithm", ***Mechanics of Materials***, Vol. 114, (2017), 57-68. doi: 10.1016/j.mechmat.2017.07.004.
27. Xia, J., Won, C., Kim, H., Lee, W. and Yoon, J., "Artificial neural networks for predicting plastic anisotropy of sheet metals based on indentation test", ***Materials***, Vol. 15, No. 5, (2022), 1714. https://doi.org/10.3390/ma15051714
28. Luo, C. and Yuan, H., "Determination of elastoplastic properties in anisotropic materials with cubic symmetry by instrumented indentation", ***Mechanics of Materials***, Vol. 174, (2022), 104461. https://doi.org/10.1016/j.mechmat.2022.104461
29. Bocciarelli, M. and Maier, G., "Indentation and imprint mapping method for identification of residual stresses", ***Computational Materials Science***, Vol. 39, No. 2, (2007), 381-392. https://doi.org/10.1016/j.commatsci.2006.07.001
30. Salmani Ghanbari, S. and Mahmoudi, A., "An improvement in data interpretation to estimate residual stresses and mechanical properties using instrumented indentation: A comparison between machine learning and kriging model", ***Engineering Applications of Artificial Intelligence***, Vol. 114, (2022). https://doi.org/10.1016/j.engappai.2022.105186
31. Wang, Z., Deng, L. and Zhao, J., "A novel method to extract the equi-biaxial residual stress and mechanical properties of metal materials by continuous spherical indentation test", ***Materials Research Express***, Vol. 6, No. 3, (2018), 036512. doi: 10.1088/2053-1591/aaeca6.
32. Gascón, F. and Salazar, F., "Simulation of rough surfaces and analysis of roughness by matlab", MATLAB—A Ubiquitous Tool for the Practical Engineer, InTech, Rijeka, (2011), 391-420. doi: 10.5772/22534.
33. Wu, J.-J., "Simulation of rough surfaces with fft", ***Tribology International***, Vol. 33, No. 1, (2000), 47-58. http://dx.doi.org/10.1016/S0301-679X(00)00016-5
34. Garcia, N. and Stoll, E., "Monte carlo calculation for electromagnetic-wave scattering from random rough surfaces", ***Physical Review Letters***, Vol. 52, No. 20, (1984), 1798. https://doi.org/10.1103/PhysRevLett.52.1798
35. Luo, Y., Wang, Y., Guo, H., Liu, X., Luo, Y. and Liu, Y., "Relationship between joint roughness coefficient and statistical roughness parameters and its sensitivity to sampling interval", ***Sustainability***, Vol. 14, No. 20, (2022), 13597. https://doi.org/10.3390/su142013597
36. Mahmoudi, A., Ghanbari-Matloob, M. and Nourbakhsh, S., "A novel method to determine material properties and residual stresses simultaneously using spherical indentation", ***Journal of Testing and Evaluation***, Vol. 43, (2015), 87-95. doi: 10.1520/JTE20130236.
37. Zhong, T., He, K., Li, H. and Yang, L., "Mechanical properties of lightweight 316l stainless steel lattice structures fabricated by selective laser melting", ***Materials & Design***, Vol. 181, (2019), 108076. doi: 10.1016/j.matdes.2019.108076.
38. Kim, S.-H., Jeon, E.-c. and Kwon, D., "Determining brinell hardness from analysis of indentation load-depth curve without optical measurement", ***Journal of Engineering Materials and Technology***, Vol. 127, No. 1, (2005), 154-158. https://doi.org/10.1115/1.1839213
39. International, A., "Standard test method for brinell hardness of metallic materials, ASTM International, (2012).
40. Jooya, M., Hosseinzadeh, A.R. and Mahmoudi, A., "Plasticity effect on residual stresses measurement using contour method", ***International Journal of Engineering, Transactions A: Basics***, Vol. 26, No. 10, (2013), 1203-1212. doi: 10.5829/idosi.ije.2013.26.10a.10.
41. ASTM, E., "Standard test methods for tension testing of metallic materials", ***Annual Book of ASTM Standards. ASTM***, Vol., No., (2001).
42. Phan, N., Dong, P., Muthuramalingam, T., Thien, N., Dung, H., Hung, T., Duc, N. and Ly, N., "Experimental investigation of uncoated electrode and pvd alcrni coating on surface roughness in electrical discharge machining of ti-6al-4v", ***International Journal of Engineering, Transactions A: Basics***, Vol. 34, No. 4, (2021), 928-934. doi: 10.5829/ije.2021.34.04a.19.
43. Yonezu, A., Yoneda, K., Hirakata, H., Sakihara, M. and Minoshima, K., "A simple method to evaluate anisotropic plastic properties based on dimensionless function of single spherical indentation–application to sic whisker-reinforced aluminum alloy", ***Materials Science and Engineering: A***, Vol. 527, No. 29-30, (2010), 7646-7657. doi: 10.1016/j.msea.2010.08.014.

Persian Abstract

چکیده

زبری سطح به طور قابل توجهی بر پراکندگی منحنی های بار–جابجایی و اندازه گیری خواص مکانیکی توسط نفوذ در مقیاس ماکرو تأثیر می‌گذارد. بسیاری از خواص مکانیکی مانند مدول الاستیسیته، تنش تسلیم، توان کرنش سختی و سختی را می توان با استفاده از نتایج نفوذ، که اطلاعات به دست آمده از منحنی بار–جابجایی است، تخمین زد. پارامترهای قابل اعتماد منحنی بار–جابجایی (P-h) برای تخمین خواص مکانیکی استفاده می شود. منحنی P-h غیر دقیق، منجر به تخمین نادرست خواص مواد می‌شود. نادیده گرفتن زبری سطح ممکن است یک منبع خطا در نتایج نفوذ باشد. در این مقاله، اثرات زبری سطح بر روی منحنی نیرو – عمق نفوذ و عدد سختی برینل (BHN) مورد بررسی قرار گرفت. محدوده زبری با کمترین تأثیر بر روی نتایج نفوذ کروی به دست آمد. زبری سطح ۲ و ۱۲ میکرون بر روی نمونه های آزمایشی با استفاده از فرآیند ماشینکاری تخلیه الکتریکی (EDM) ایجاد شد. شبیه‌سازی اجزای محدود با زبری‌های سطحی مختلف انجام شد. نتایج نشان داد که زبری بر منحنی P-h و مقادیر سختی در عمق نفوذهای مختلف با نفوذگرهای با سایزهای مختلف، تأثیر می‌گذارد. مشاهده شد که با افزایش زبری Rq، سطح منحنی P-h و مقدار سختی کاهش یافت و با افزایش عمق فرورفتگی، تأثیر زبری بر سختی نیز کاهش یافت. نتایج تطابق خوبی بین شبیه‌سازی FE و آزمون تجربی نشان داد.

International Journal of Engineering

Journal Homepage: www.ije.ir

Security and Data Privacy of Medical Information in Blockchain Using Lightweight Cryptographic System

R. P. Puneeth*[a,b], G. Parthasarathy[b]

[a] *Department of Computer Science and Engineering, NMAM Institute of Technology-Affiliated to NITTE (Deemed to be University), India*
[b] *School of Computing and Information Technology, REVA University, Karnataka, India*

PAPER INFO

Paper history:
Received 21 September 2022
Received in revised form 10 January 2023
Accepted 01 March 2023

Keywords:
Data Security
Blockchain
Lightweight Cryptographic System
Intuitionistic Derivative Symmetrical Encryption Algorithm
Differential Hashing Pattern
Decentralization
Electronic Health Records

ABSTRACT

In the healthcare system and hospital environment, the data security and the data connectivity are the major factors to consider for patient data management system. For that, there are several techniques are used to preserve and arrange the patient data with enhanced security system. In that, Blockchain structure of data management improves the secure data storage and transmission process. In the data security system, the quality measure can be validate by means of the size of key that are used for the encryption process. Combined with the blockchain, the encryption model is to be improved for the solve the problem in data security system. This also needs to focus on the size reduction of data storage due to the large key size of encrypted data. In the proposed work, Intuitionistic Derivative Symmetrical Encryption (IDSE) Algorithm based security algorithm along with blockchain function was integrated to form the authorized data storage and transmission process. For the key pattern generation, Differential Hashing Pattern (DHP) based key pattern extraction model was used for high speed data transmission and to reduce the size of data that are encrypted. The features that are considered for the appropriate security system are the data transmission pattern with respect to the time and the hashing model of key generation. In the result analysis, the performance of the IDSE-DHP are validated with the parameters of data transmission and loss rate in the Blockchain and with the throughput related features.

***doi**: 10.5829/ije.2023.36.05b.09*

1. INTRODUCTION

One of the emerging technologies, blockchain offers a number of intriguing features that can undoubtedly address current problems in real-time applications. Blockchain encourages decentralization, more openness, better traceability, and safe architecture as opposed to centralized approach, secretive, exclusive, and modifiable alternatives. The adoption of blockchain in the healthcare industry offers a number of interesting alternatives for enabling safe stakeholder communications and an effective method of clinical report distribution. The use of blockchain along with cloud environment [1] and the other database management system, the data security and the transmission rate are mainly considered. Similarly, with the combination of cloud data retrieval process, the intermediate needs to act the perfect data management for fast data transmission process. To achieve this, the block computing was introduced for the analyzing of parameters from blocks with enhanced model of data transmission between the blocks and cloud storage system. This forms the edge of hash-key connectivity with secured communication model. It performs the functionalities of data computing, storage utilizes, and the related structure of services that are in the networking system and its management. The blockchains are used with these arrangements for fast computing and the data transmission between the cloud and the end device. The basic structure of Blockchain connectivity to the clod based on the block computing is shown in Figure 1.

In this figure, the architecture of the blockchain model was sub-classified into three stages such as, cloud environment, block computing and the end-user of patient blocks. The blocks are connected to the data link unit to retrieve data from the cloud to local system while

*Corresponding Author Institutional Email: puneeth.reval313@gmail.com (R. P. Puneeth)

Please cite this article as: R. P. Puneeth, G. Parthasarathy, Security and Data Privacy of Medical Information in Blockchain Using Lightweight Cryptographic System, ***International Journal of Engineering, Transactions B: Applications***, Vol. 36, No. 05, (2023) 925-933

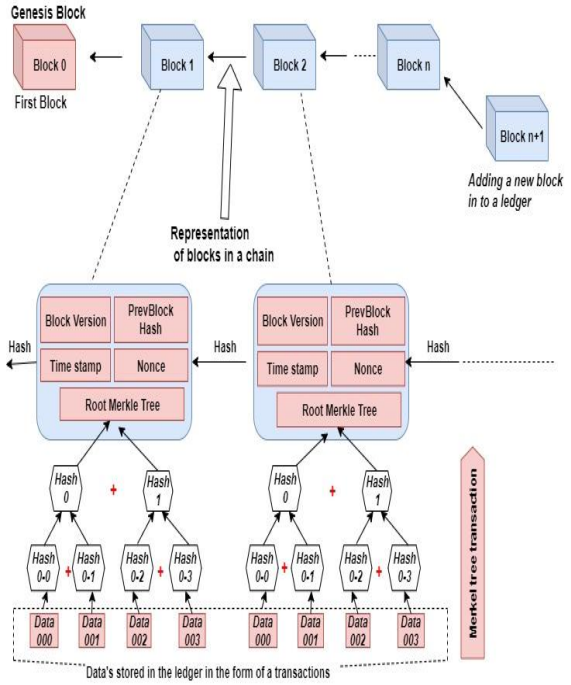

Figure 1. Basic architecture of blockchain

at the dynamic hash-key structure. The block computing and the other controllers are done in the data link unit that controls the flow of data transmission to the blocks and cloud storage. Here, the data security can also process under the controlling unit which forms the secure hash-key combination. The data link placement and the structure are referred to route the patient blocks based on the index and coverage size. In that, some of the algorithm that are used for security model such as Adaptive Data Dissemination Protocol (AddP) [2], intelligent forwarding method [3], Random Fire-Fly [4], map-based relaying algorithm (MBR) [5], adaptive beacon generation rate (ABGR) [6], etc. are implementing the appropriate feature selection for security block identification with the hash-key security problem.

From these arrangements, to achieve the better transmission rate and to increase the throughput parameters in the hash-key formation, the security block selection needs to select with the best appropriate block that is to achieve the best matching with the parameters that are related to the data transmission. This can also combine with the Block computing technique to enhance the security experience and enhance the high speed data transmission. This was enhanced in the proposed technique based on the batching process of data security algorithm to achieve the parameters range. The hash-key security in the proposed architecture can be achieved by using the light-weight key generation model and the hashing key pattern to enhance the speed of performance and the secure data transmission rate.

The objective of the proposed model of appropriate security and the Blockchain security can be listed as follows:

- To estimate the hash-key properties and the block characteristics based on the pattern extraction and security system in blockchain.
- To perform the appropriate selection of best security block by using the Intuitionist Derivative Symmetrical Encryption (IDSE) Algorithm that validates the data size and the identification of block index.
- To estimate the relevant features attributes that are to find the best selection of parameters that are can be used for data arrangement in the blockchain with the proper link structure.
- To enhance the hash-key security model in the blockchain architecture based on the key pattern extraction and the combination of block computing technique.
- To implement the Differential Hashing Pattern method of encryption model for the secure data transmission with light-weighted architecture for high speed data transmission model.

The full description about the proposed architecture and the algorithm descriptions are explained in the following sections. According to that, the survey of various types of hash-key security system and the security algorithms are explained with its merits and demerits in section I. the IDSE and the DHP based secure appropriate security algorithm are explained in the section II. The simulation parameters and the performance validation of the proposed model with the comparison chart and the table results are described in the section III. Finally, the conclusion of proposed model was justified and the future works are presented in section IV.

1. 1. Related Works The brief surveys of related works for the proposed algorithms are reviewed and find the merits and demerits of those existing algorithms in this section. This was also to analyze the limitations of existing algorithms that are identified for the different types of existing data security model. In this, the survey is divided as the two categories such as for the appropriate security system and hash-key security system in the dynamic blockchain architecture.

Ismail et al. [7] proposed the novel model of Adaptive Byte Hybrid Automatic Repeat reQuest (AB-HARQ) based intelligent communication system for the blockchain in the application of road safety system which can avoid the accidents. To overcome the problem of non-line of sight (NLOS) blocks by introducing broadcasting storm and channel congestion during data dissemination. For this weighted inertia-based dynamic virtual bat algorithm (WIDVBA) [8] based appropriate security algorithm. Bhattacharya et al. [9] proposed a

novel model of forwarding scheme to deliver data based security algorithm for time management in data transmission. A survey of different blockchain communication algorithm was presented in literature [10, 11].

In high dynamic topology, Saif et al. [12] proposed GHN model that works on the selective block security to prevent unwanted data flooding. Batch technique and the certificate-less ring signature (CL-RS) for data validation were performed by Wang et al. [13]. This paper focused on the data security and privacy issue in the blockchain communication. Similarly, the challenges in the data security such as time-consuming certificate revocation list (CRL) checking, computation overhead and identity revocation problem are validated by Abdul Rahoof et al. [14]. To overcome the flooding problem in Blockchain architecture, Optimized Link State Allocation Protocol (OLSR) performs the multipoint relay scheme (MPR) which is to manage the data congestion in the hash-key. Pandey and Ratnesh [15], Puneeth and Parthasarathy [16] proposed a cyber-security system in the blockchain hash-key. These implements the set of NIST tests based on the self-checking process to identify the DOS attack and protect the data from attackers. Farouk et al. [17] proposed the comprehensive identity authentication scheme (CIAS) based an encryption model which is worked as the asymmetrical model. This provides the security and privacy to the blockchain communication system. A blockchain based mobile edge computing was performed by Puneeth and Parthasarathy [18]. This provides the trusted central entities that are in the single point failure cases. Similarly, while facing the challenges in the security model of blockchain hash-key. Saha et al. [19] proposed intelligent transportation system (ITS) for secure data transmission to overcome the issues in the hash-key environment. Also, Zaabar et al. [20] presented an overview of blockchain security system and the privacy design of algorithm. For reliable data acquisition in the blockchain. Yaqoob et al. [21] proposed a dynamic entity-centric trust model of blockchain security system. Similarly, to manage the DDOS attack. El-Rahman and Ala-Saleh [22] proposed Trust-based Framework for Reliable Data Delivery and DoS defense (TFDD) for the blockchain architecture for the development of intrusion detection module. Li et al. [23] implemented the Massive Open Online Courses (MOOCs) based on the blockchain model. In that, the system requires more learning records to perform the secure data storage process. For that, Electronic Learning Records (ELRs) was used in the MOOCs to perform efficient conditional anonymity, secure storage, and sharing without the need for sophisticated cryptographic calculations. Ajao et al. [24], Liu et al. [25] Kumar and Rakesh [26] Jafar [27], Jyoti and. Chauhan [28] proposed a crypto-hashing technique to secure the data by the encryption process and the data privacy detection system.

2. MATERIALS & METHODS

The methodology structure and the algorithm details are explained briefly in this section. Figure 2 shows the flow diagram of proposed work model for the appropriate security and secure transmission system. In this security system, the patient details are preserved by generating an efficient key pattern for the indexing of data blocks to represent the private key for individual patients. The blocks are considered for the overall hospital management system. This it contains the details of doctor and the patient information in the overall hospital database. The link information about the patient and doctor details are preserved by the proposed Intuitionist Derivative Symmetrical Encryption (IDSE) algorithm. The combination of the proposed key pattern and the encryption model increased the data security system compare to traditional encryption model.

The symmetrical encryption system has the advantage of data storage of larger data size and the less time complexity. And in the medical field the patient's data such as MRI, CT-SCAN, X-Ray and other information's are of higher size. Also, the random key generation helps to improve the secure data storage in a model. For that, the hashing technique enhances the random key pattern and provides better security parameters for the huge amount of data storage in the blockchain environment.

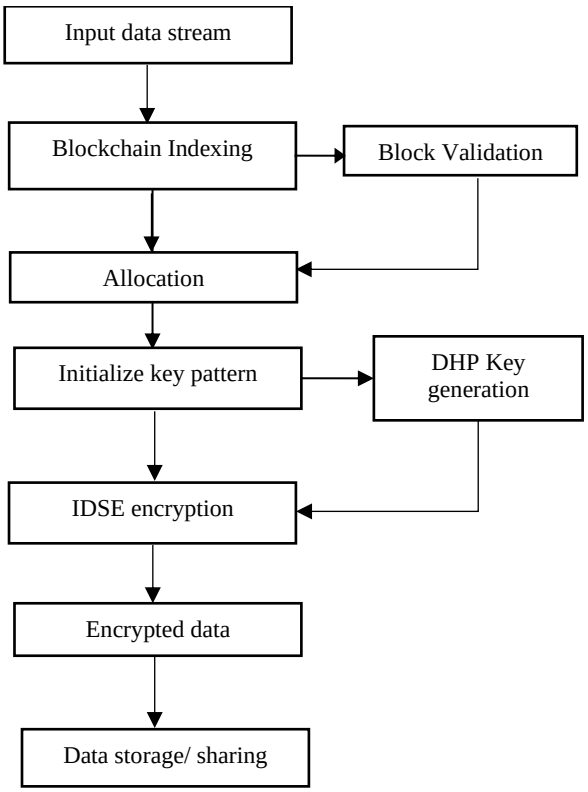

Figure 2. Overall flow of the proposed system

Similarly, the hash-key generation system achieved the high throughput of random key generation for the secure data transmission model and also for the data management process. Since, the encryption time is depending on the amount of data and the size of key formation. This can be reduced by the implementation of DHP based data encryption model that achieved the light-weight encryption model. This can be achieved the high speed transmission rate than by using other state-of-art methods. The proposed work is segmented as two major class that are listed as follows.

A. Intuitionistic Derivative Symmetrical Encryption,
B. Differential Hashing Pattern.

2. 1. Intuitionistic Derivative Symmetrical Encryption The main intension of this data security algorithm is to optimize the data size with high security model. For this process, the light-weight encryption model was integrated to achieve the high security model with reduced size of data bits. This overall encryption model is depending on the hash key pattern generation block to retrieve the encoded data from the bit stream of data. The architecture of the encryption and the decryption model is shown in Figure 3. In that the encoder was divided as two individual blocks to represent the generation of random address and the random key value for the data encoding process. This it refers the generation of private and public key pattern generation for the overall encryption model. The step-by-step procedure with the equation model of IDSE algorithm is presented in Algorithm 1.

Algorithm 1. IDSE based Data Security algorithm

Input: Data samples (D_i)
Output: Encrypted Data (E_D)
Select the random key size as 64-bit chipper (R_b).
Split the data samples into 16-bit block size. This can be represent as the function block f_k.
Construct the data blocks.
Retrieve the $R_{a_i}f_k$ by extracting the 16-bit blocks from Equation (1).
Construct M1, M2, M3, M4 matrix from Equations (2) to (5) based on the block function 'f'.
Estimate the keys as K1, K2, K3, K4 from Equations (6) to (9).
Estimate the key K5 from Equation (10).
Perform the XOR operation to extract the bitwise character '$Y_{o_{i,j}}$' and concatenate encrypted bit sequence from Equation (11).

Let the message can be segment as the blocks which can be represent as in Equation (1).

$$Ra_if_k = f(Rb_if_k) \quad (1)$$

where,

$$Rb_if_k = \left\| \left(R_{b_{4(j-1)+i}} \right)_{j=1}^{4} \right.$$

To estimate the encryption key pattern, the transformation can be estimate by the random table value that are from the Hexa-decimal value. The table can be represented by the matrixes M1, M2, M3 and M4, respectively. This can be followed by the Equations (2) to (6).

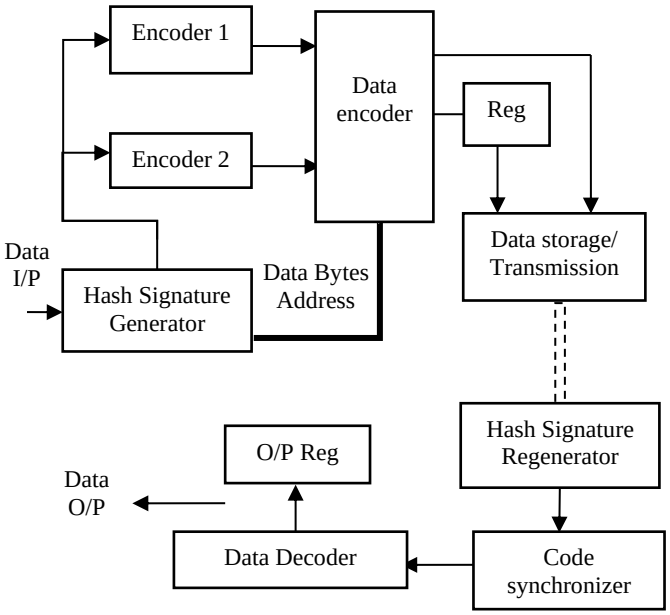

Figure 3. Architecture Diagram of Proposed Data Storage/ Transmission System

$$M1 = \begin{bmatrix} Ra_1f_1 & \dots & Ra_1f_4 \\ \dots & \dots & \dots \\ Ra_1f_{13} & \dots & Ra_1f_{16} \end{bmatrix} \quad (2)$$

$$M2 = \begin{bmatrix} Ra_2f_1 & \dots & Ra_2f_4 \\ \dots & \dots & \dots \\ Ra_2f_{13} & \dots & Ra_2f_{16} \end{bmatrix} \quad (3)$$

$$M3 = \begin{bmatrix} Ra_3f_1 & \dots & Ra_3f_4 \\ \dots & \dots & \dots \\ Ra_3f_{13} & \dots & Ra_3f_{16} \end{bmatrix} \quad (4)$$

$$M4 = \begin{bmatrix} Ra_4f_1 & \dots & Ra_4f_4 \\ \dots & \dots & \dots \\ Ra_4f_{13} & \dots & Ra_4f_{16} \end{bmatrix} \quad (5)$$

The key pattern can be represented by concatenating the bit sequences that are for each block which can be estimated by Equations (6) to (10).

$$K1 = \{\{a_4, \dots a_1\}, \{a_5 \dots a_8\}, \{a_{12} \dots a_9\}, \{a_{13} \dots a_{16}\}\} \quad (6)$$

$$K2 = \{\{b_4, \dots b_1\}, \{b_5 \dots b_8\}, \{b_{12} \dots b_9\}, \{b_{13} \dots b_{16}\}\} \quad (7)$$

$$K3 = \{\{c_4, \dots c_1\}, \{c_5 \dots c_8\}, \{c_{12} \dots c_9\}, \{c_{13} \dots c_{16}\}\} \quad (8)$$

$$K4 = \{\{d_4, \dots d_1\}, \{d_5 \dots d_8\}, \{d_{12} \dots d_9\}, \{d_{13} \dots d_{16}\}\} \quad (9)$$

$$K5 = \bigoplus_{i=1}^{4} K_i \quad (10)$$

From this the ciphered data can be represented as in Equation (11).

$$E_D = \{R_{51}, R_{52}, R_{53}, R_{54}\} \quad (11)$$

where,

$$R_{o_{i,j}} = \begin{cases} Y_{x_{i,j}} \odot K_i \quad ; \quad j = \{1, 4\} \\ Y_{x_{i,j+1}} \oplus K_i; \quad j = 2 \\ Y_{x_{i,j-1}} \oplus K_i; \quad j = 3 \end{cases}$$

2. 2. Hashkey Generation using DHP From the cryptographic system, the data security can be defined by the bit size of random key that are initialized for encryption process**.** The more the size of key size can increase the security level in traditional cryptographic system. This will lead to increasing the data size for storage and transmission process. This may also lead to reduce the throughput of overall system. To overcome, the key pattern are needs to improve and to reduce the size of key with the rate of high security level. This can be achieved by using the light-weight cryptographic system. Compare to the traditional model such as AES, DES, ECC and other types of encryption techniques, the key size was managed and the size was appropriately used according to the properties of data streams that are to transmit over the hash-key structure.

The detailed steps for the DHP based data encryption model was described in Algorithm 2.

Algorithm 2. Differential Hashing Pattern (DHP)

Input: Data input, D_r
Output: Hash key patternE_T.

For$i = 1\ to\ n$loop// 'n' is the size of data,T_i in meta-blocks M_v
For$j = 1\ to\ m$loop all resources // Loop running for all the selected resources R_j
Calculate the pattern of key formation, $C_{ij} = D_{ij} + R_j$
Where, R_j – Random weight value for the related parameters of data structure. Ranges from 0->1.
While Key_Bins in Mv do
Find the bins of data structure for each data samples with respect to time.

$$T_k = sort(C_i(t))$$

Find the respective key bits to encrypt the data from T_k.

$$Y = min(T_k)$$

Estimate binaries for$Y$ to the random sequenceR_j
Make zero's in$T_k$that are irrelevant to the pattern fromM_v
End while
Update R_j
Update C_{ij} for all i
End loop 'j'
Perform XOR operation to represent the hash key result of overall bit size$E_T(i)$
End loop 'i'.

3. RESULTS AND DISCUSSION

In this section, the simulation results and the testing analysis of the proposed model of blockchain security system. The performance of the proposed work was validated by the comparison of data delivery ratio with the delay rate and other related parameters from existing security algorithm and the hash-key system. Here, the overall design work was implemented in the PYTHON tool for the version of 3.8. the comparison parameters are considered for the traditional security system and for proposed blockchain based data security model. The environmental setup for the result analysis are referred by Li et al [23] and Ajao et al. [24]. In this, the comparison results are validated for the amount of data packets that are considered for data transmission and the storage system from the traditional model and by the blockchain model. The size of data packets was varied according to the size what are specified by Li et al. [23]. To estimate the performance of data security, the comparison is taking in the part of number of packets that are considered for the transmission and amount of time taken to transmit it. The testing results are calculated from the data transmission structure of blockchain architecture to

represent the QoS in a hash-key. The parameters that are considered for the comparison are can be listed as follows:

1. Data Delivery Ratio % (DDR),
2. Data Confidentiality Ratio % (DCR),
3. Data Integrity Ratio % (DIR),
4. Privacy Preserving Ratio % (PPR) and
5. Time Consumption (Sec)

3. 1. Data Delivery Ratio The Data Delivery Rati (DDR) in the unit of percentage is referred to estimate the amount of data that are successively transmitted to the destination with minimum amount of loss. This can be calculated by the ratio of amount of data that are received at the destination block to the total number of data that are transmitted by the source. This can be represented as in Equation (12). This can be multiplied by 100 to get the value in terms of percentage.

$$DDR = \frac{Total\ No.\ of\ data\ samples\ received}{Total\ No.\ of\ data\ sent} \quad (12)$$

The line graph in Figure 4 shows the comparison result of proposed model with the other existing models of blockchain security system introduced by Ajao et al. [24].

3. 2. Data Confidentiality Ratio (%) The IDSE-DHP based appropriate security system achieved the better DCR rate by referring the data loss ratio. This parameter is to calculate the amount of data that are not able to reach the destination which may fail to data loss. This can be represented as in Equation (13).

$$DCR = \frac{(No.of\ Sensitive\ Patient\ Data)}{Total\ No.of\ Data\ samples} \quad (13)$$

3. 3. Data Integrity Ratio (%) The Data Integrity Ratio refers the ratio of number of user data at the receiver without changes (N_{UD}) to the total number of data samples (T_D). This was represented in Equation (14). Figure 5 shows the comparison chart of the DIR (%).

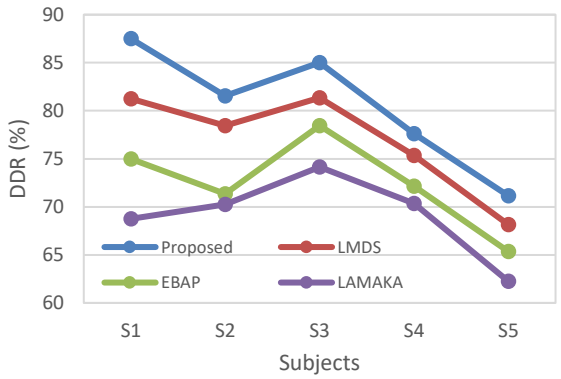

Figure 4. DDR analysis by Ajao et al. [24]

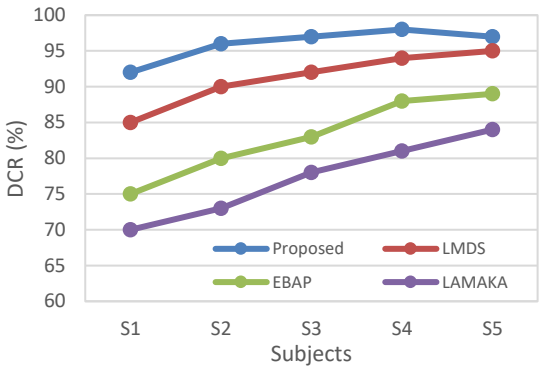

Figure 5. Data Confidentiality Ratio analysis by Ajao et al. [24]

$$DIR = \frac{N_{UD}}{T_D} \times 100 \quad (14)$$

3. 4. Privacy Preserving Rate The privacy preserving rate refers the ratio of number of user data that are in the encrypted form and was secured (N_{SD}) to the total number of available data samples (T_D). This was represented in Equation (15). Figure 6 shows the comparison chart of the PPR.

$$PPR = \frac{N_{SD}}{T_D} \quad (15)$$

The proposed encryption model in the blockchain system was analyzed with the traditional encryption system such as RES, DES and AES techniques for the parameters of Encryption and decryption time referred by El-Rahman and Ala-Saleh [22] in Figures 7 and 8, respectively. The execution time of the encryption system in the blockchain system refers the time consumption for the execution of encryption and the total transmission time. Figure 9 shows the total transmission time in (s) that are compared from the existing IoMT [23] model of data security in blockchain system.

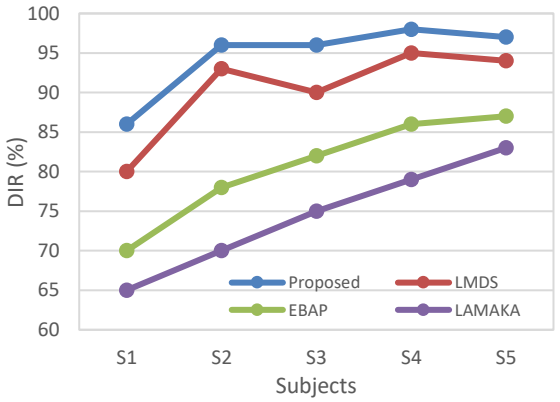

Figure 6. Data Integrity Ratio analysis by Ajao et al. [24]

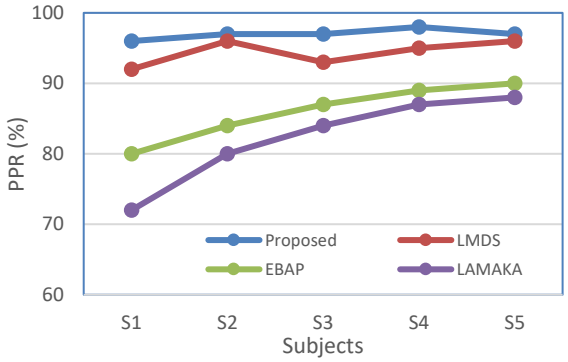

Figure 7. Privacy Preserving Rate by Ajao et al. [24]

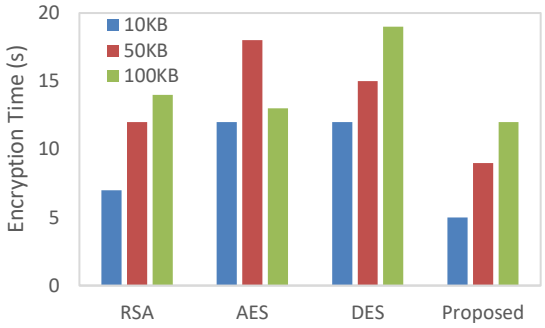

Figure 8. Encryption Time (s) [21]

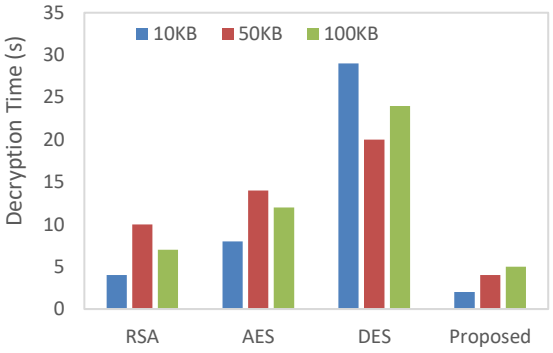

Figure 9. Decryption Time (s) [22]

3. 5. Storage Size Consumption The data storage size was depending on the encryption size and the selective key size for the data security model. This was estimated for the data size in the range of (kB). Figure 10 shows the storage consumption of proposed model compare to other existing systems [23]. This was also evaluated for the different transmission process that are represented in Figure 11 referred to Ajao et al. [24].

The Table 1 and Figure 12, shows the comparison result of proposed encryption time with other existing methods of encryption system. Here the parameters are validated based on the size of file to be encrypted and the number of users that are initialized for the encryption process respectively.

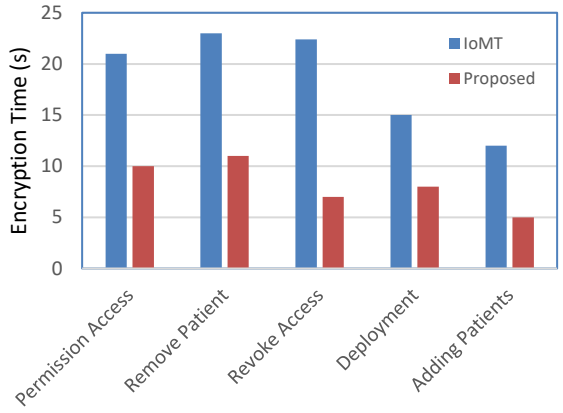

Figure 10. Execution time (s) [23]

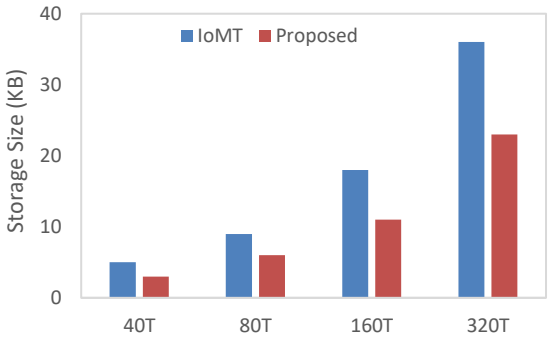

Figure 11. Storage Size (KB) [23]

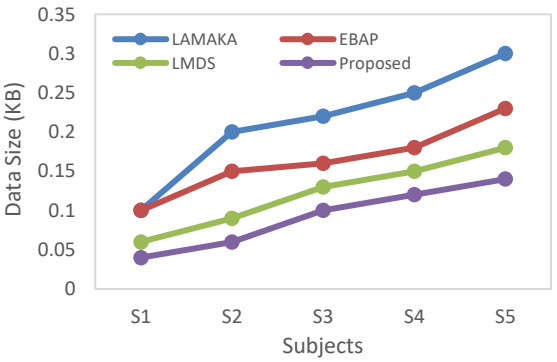

Figure 12. Storage Size (KB) [24]

TABLE 1. Comparison result of encryption time (s) [27]

File Size	Encryption Time (s)				
	BHA	ISA	CGA	BSCDP	Proposed
128	7.6	7.4	3.6	1	0.87
256	12	8.5	5.1	2.7	1.75
512	31	20	8.7	3.5	2.65
768	37.5	24	10	5	4.75
1024	47.8	37.8	12	8.7	7.2

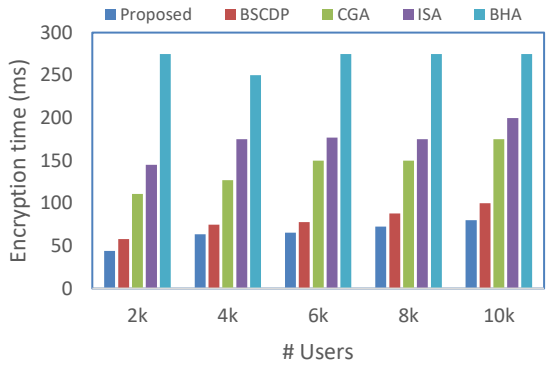

Figure 13. Execution time (ms) [28]

4. CONCLUSION

The security of medical data can be increased through encryption; however encryption and decryption both demand a lot of processing resources. The need for high security, low computational-power encryption techniques is critical. This paper proposed a novel model of blockchain security system with appropriate hash-key security algorithm to achieve high speed data transmission rate. The Intuitionistic Derivative Symmetrical Encryption (IDSE) based data encryption model presented lightweight cryptographic system to reduce the key size based on the hashing technique to generate the random key. This type of data security system along with the blockchain improves the prediction rate and the better security model to achieve the retrieval rate from cloud environment. Similarly, the Differential Hashing Pattern (DHP) based encryption model makes the overall system as light-weighted encryption model for enhanced transmission rate and the improved value of throughput. The analytical results show the performance of proposed design that represents the proposed method gives the less value of delay rate in millisecond and the improved value of data loss ratio at different number of patient blocks. The overall process of this paper was validated for the environment of hospital data management system for patient blocks.

In future, the appropriate security and security system in the blockchain architecture are can be improved by an enhanced model of machine learning technique with data security function in block computing. The hash-key security can be focused on the space complexity by the design of key management.

5. REFERENCES

1. Jameii S. M. and Khanzadi K., "A Latency Reduction Method for Cloud-fog Gaming based on Reinforcement Learning", ***International Journal of Engineering, Transactions C: Aspects,*** Vol. 35, No. 09, (2022) 1674-1681. https://doi.org/10.5829/ije.2022.35.09c.01
2. Fan, K., Wang, S., Ren, Y., Li, H. and Yang, Y., "Medblock: Efficient and secure medical data sharing via blockchain." ***Journal of Medical Systems,*** Vol. 42, No. 8, (2018), 1-11. https://doi.org/10.1007/s10916-018-0993-7
3. Kim, M. G., Lee, A. R., Kwon, H. J., Kim, J. W. and Kim, I. K., "Sharing Medical Questionnaries based on Blockchain," IEEE International Conference on Bioinformatics and Biomedicine (2018), 2767-2769. https://doi.org/10.1109/BIBM.2018.8621154
4. Hussein, A., F., ArunKumar, N., Gonzalez, G., R., Abdulhay, E., Manuel, R., S., J., Tavares. and Hugo C. V., "A medical records managing and securing blockchain based system supported by a Genetic Algorithm and Discrete Wavelet Transform", ***Cognitive Systems Research***. Vol. 52, (2018), 1-11. https://doi.org/10.1016/j.cogsys.2018.05.004
5. Ramani, V., Kumar, T., Bracken, A., Liyanage, M. and Ylianttila, M., "Secure and Efficient Data Accessibility in Blockchain Based Healthcare Systems," IEEE Global Communications Conference (GLOBECOM). (2018), 206-212. https://doi.org/10.1109/GLOCOM.2018.8647221
6. Zhu, L., Wu, Y., Gai, K. and Choo, K-K, R., "Controllable and trustworthy blockchain-based cloud data management" ***Future Generation Computer Systems,*** Vol 91, (2019), 527-535. https://doi.org/10.1016/j.future.2018.09.019
7. Ismail, L., Materwala H. and Zeadally, S., "Lightweight Blockchain for Healthcare," ***IEEE Access***, Vol. 7, (2019), 149935-149951. https://doi.org/10.1109/ACCESS.2019.2947613.
8. Chen, Y., Ding, S., Xu, Z., Zheng, H. and Yang S. "Blockchain-Based Medical Records Secure Storage and Medical Service Framework" ***Journal of Medical System,*** Vol. 43, No. 1, (2019), 1-9. https://doi.org/10.1007/s10916-018-1121-4
9. Bhattacharya, P., Tanwar, S., Bodkhe, U., Tyagi, S. and Kumar, N. "BinDaaS: Blockchain-Based Deep-Learning as-a-Service in Healthcare 4.0 Applications," ***IEEE Transactions on Network Science and Engineering,*** Vol. 8, No. 2, (2021), 1242-1255. https://doi.org/10.1109/TNSE.2019.2961932
10. Zhou, T., Li, X. and Zhao, H., "Med-PPPHIS: Blockchain-Based Personal Healthcare Information System for National Physique Monitoring and Scientific Exercise Guiding" ***Journal of Medical System,*** Vol 43, No 9, (2019), 1-23. https://doi.org/10.1007/s10916-019-1430-2
11. Xu, J., Xue, K., Li, S., Tian, H., Hong, J., Hong, P. and Yu, N., "Healthchain: A Blockchain-Based Privacy Preserving Scheme for Large-Scale Health Data" ***IEEE Internet of Things Journal***, Vol. 6, No. 5, (2019), 8770-8781. https://doi.org/10.1109/JIOT.2019.2923525
12. Saif, S., Biswas, S. and Chattopadhyay, S. "Intelligent, Secure Big Health Data Management Using Deep Learning and Blockchain Technology: An Overview" ***Deep Learning Techniques for Biomedical and Health Informatics***, Springer, Vol 68. (2020), 187-209. https://doi.org/10.1007/978-3-030-33966-1_10
13. Wang, Z., Luo, N. and Zhou, P. "GuardHealth: Blockchain empowered secure data management and Graph Convolutional Network enabled anomaly detection in smart healthcare", ***Journal of Parallel and Distributed Computing,*** Vol. 142, (2020), 1-12, https://doi.org/10.1016/j.jpdc.2020.03.004
14. Abdul- Rahoof T.P. and Deepthi V.R. "Health Chain: A Secure Scalable Health Care Data Management System Using Blockchain" ***Proceedings Springer***, (2020), 380-391. https://doi.org/10.1007/978-3-030-36987-3_25
15. Pandey, P. and Litoriya, R. "Securing and authenticating healthcare records through blockchain technology" ***Cryptologia***, Vol. 44, No. 4, (2020), 341-356. https://doi.org/10.1080/01611194.2019.1706060
16. Puneeth, R.P. and Parthasarathy, G. "A Survey on Security and Interoperability of Electronic Health Records Sharing Using

Blockchain Technology" ***Acta Informatica Pragensia,*** Vol. 12, No. 1, https://doi.org/10.18267/j.aip.187

17. Farouk, A., Alahmadi, A., Ghose, S. and Mashatan, A. "Blockchain platform for industrial healthcare: Vision and futureopportunities" ***Computer Communications***, Vol. 154, (2020), 223-235. https://doi.org/10.1016/j.comcom.2020.02.058
18. Puneeth, R.P. and Parthasarathy, G. "A Comprehensive Survey on Privacy-Security and Scalability Solutions for Blockchain Technology", ***Smart Intelligent Computing and Communication Technology IOS Press.*** (2021), 173-178, https://doi.org/10.3233/APC210031
19. Saha, S., Majumder, A., Bhowmik, T., Basu, A. and Choudhury, A. "A Healthcare Data Management System on Blockchain Framework" ***Communication and Networking,*** (2021), 1-5. https://doi.org/10.1109/SMARTGENCON51891.2021.9645890
20. Zaabar, B., Cheikhrouhou, O., Jamil, F., Ammi, M. and Abid, M. "HealthBlock: A secure blockchain-based healthcare data management system", ***Computer Networks,*** Vol 200, (2021). https://doi.org/10.1016/j.comnet.2021.108500
21. Yaqoob, I., Salah, K., Jayaraman, R. and Al-Hammadi, Y. "Blockchain for healthcare data management: opportunities, challenges, and future recommendations" ***Neural Computing and Applications,*** Vol. 34, No. 14, (2021), 1-16. https://doi.org/10.1007/s00521-020-05519-w
22. ElRahman, S.A. and Alluhaidan, A.S. "Blockchain technology and IoT-edge framework for sharing healthcare services." ***Soft Computing***, Vol. 25, No. 21, (2021), 13753-13777. https://doi.org/10.1007/s00500-021-06041-4
23. Li, D., Han D., Zheng Z., Weng, T., H., Li H., Liu H., Castiglione A. and Li K.-C., "MOOCsChain: A blockchain-based secure storage and sharing scheme for MOOCs learning." ***Computer Standard and Interface- Elsevier***, Vol. 81, (2022). https://doi.org/10.1016/j.csi.2021.103597
24. Ajao, L.A., Umar, B.U., Olajide, D.O. and Misra, S. "Application of Crypto-Blockchain Technology for Securing Electronic Voting Systems" ***Springer Innovations in Communication and Computing. Springer,*** (2022). https://doi.org/10.1007/978-3-030-89546-4_5
25. Liu, J., Zhao, J., Huang, H. and Xu, G. "A novel logistics data privacy protection method based on blockchain" ***Multimed Tools and Applications***, Vol. 81, (2022), 23867-23887. https://doi.org/10.1007/s11042-022-12836-w
26. Kumar, R. and Tripathi, R. "Towards design and implementation of security and privacy framework for Internet of Medical Things (IoMT) by leveraging blockchain and IPFS technology" ***Journal of Supercomputing,*** Vol. 77, (2021), 7916-7955. https://doi.org/10.1007/s11227-020-03570-x
27. Jafar, A. A. "Blockchain-based Lamport Merkle digital signature: authentication tool in IoT healthcare" ***Computer Communications***, Vol. 170 (2021), 200-208. https://doi.org/10.1016/j.comcom.2021.02.002.
28. Jyoti A. and Chauhan, R., K. "A blockchain and smart contract-based data provenance collection and storing in cloud environment" ***Wireless Networks,*** Vol. 28, No. 4, (2022), 1541-1562. https://doi.org/10.1007/s11276-022-02924-y

Persian Abstract

چکیده

زمینه و هدف: در سیستم مراقبت های بهداشتی و محیط بیمارستان، امنیت داده ها و اتصال داده ها از عوامل اصلی برای سیستم مدیریت داده های بیمار است. برای آن، چندین تکنیک برای حفظ و مرتب کردن داده های بیمار با سیستم امنیتی پیشرفته استفاده می شود. به این ترتیب، ساختار بلاک چین مدیریت داده، فرآیند ذخیره سازی و انتقال ایمن داده را بهبود می بخشد. اهداف: در سیستم امنیت داده، معیار کیفیت را می توان با استفاده از اندازه کلیدی که برای فرآیند رمزگذاری استفاده می شود، تایید کرد. در ترکیب با بلاک چین، مدل رمزگذاری برای حل مشکل در سیستم امنیت داده ها بهبود می یابد. این همچنین باید بر کاهش اندازه ذخیره سازی داده ها به دلیل اندازه کلید بزرگ داده های رمزگذاری شده تمرکز کند. روش‌ها: در کار پیشنهادی، الگوریتم امنیتی مبتنی بر الگوریتم رمزگذاری متقارن مشتق شهودی (IDSE)همراه با عملکرد بلاک چین برای تشکیل فرآیند ذخیره‌سازی و انتقال داده مجاز یکپارچه شد. برای تولید الگوی کلید، مدل استخراج الگوی کلید مبتنی بر الگوی درهم‌سازی دیفرانسیل (DHP)برای انتقال داده‌ها با سرعت بالا و کاهش اندازه داده‌هایی که رمزگذاری شده‌اند، استفاده شد. ویژگی هایی که برای سیستم امنیتی مناسب در نظر گرفته می شود، الگوی انتقال داده ها با توجه به زمان و مدل هش سازی تولید کلید است. نتایج: در تجزیه و تحلیل نتایج، عملکرد IDSE-DHP با پارامترهای انتقال داده و نرخ تلفات در بلاک چین و با ویژگی‌های مربوط به توان عملیاتی تایید می‌شود.

International Journal of Engineering

Journal Homepage: www.ije.ir

Full Characterization of Sarcheshmeh and Khatoon-Abad Copper Anode Slimes: Characterization Impact on the Decopperization Operation

M. Alaviyan, S. Shakibania, M. Mokmeli*, S. Sheibani

School of Metallurgy and Materials Engineering, College of Engineering, University of Tehran, Tehran, Iran

P A P E R I N F O

Paper history:
Received 25 September 2022
Received in revised form 07 February 2023
Accepted 04 March 2023

Keywords:
Characterization
Sarcheshmeh Copper Complex
Khatoon-Abad Copper Complex
Bottom-cell Slime
Adherent Slime

A B S T R A C T

Copper anode slime, a valuable by-product generated during the electrorefining process, is an important secondary resource for the recovery of metals, such as gold, silver, selenium, tellurium, PGMs and copper. A full characterization of the anode slime is an essential part of the efficient recovery of these valuable metals. In this research, the refinery slimes of the Sarcheshmeh and Khatoon-Abad copper complexes, were fully characterized and compared using inductively coupled plasma (ICP), X-ray diffraction (XRD), X-ray fluorescence (XRF), scanning electron microscopy (SEM), energy dispersive spectroscopy (EDS), thermogravimetric analysis (TGA), differential thermal analysis (DTA), and particle size analysis. Besides the bottom cell slime characterization, properties of the Sarcheshmeh's adherent slime was also analyzed and correlated. Sarcheshmeh copper slime particle size was found much smaller than the Khatoon-Abad slime. For both slimes though, the major part the gold and tellurium are located in larger than 38-micron particles. The main difference in thermal analysis of the two slime samples was originated from their selenium content difference. This has caused the higher concentration of non-selenide copper compounds at Khatoon-Abad slime, resulted in its easier copper recovery. Decopperization of both bottom-cell slimes were investigated and a significant difference in copper dissolution behaviors of the two slimes were observed due to their characteristic difference including the copper-selenide phases and capsulated copper in the barium sulfate agglomerates. Copper dissolution from Khatoon-Abad slime was observed to reach 90% comparing to 40% for Sarcheshmeh slime using atmospheric leaching.

***doi**: 10.5829/ije.2023.36.05b.10*

1. INTRODUCTION

In the copper electrorefining process, the impure anode electrochemically dissolves and deposit as a pure metal on the cathode surface. During this process, a solid by-product of the anode slime is generated. The slime generally contains Cu, Ag, Au, Se, Te, Pb, Ni, Sb, As, and elements from platinum group metals [1, 2]. The composition of the slime depends on the input concentrate and the extraction method [3, 4]. Therefore, the slime analysis and its properties vary from one refinery plant to another. Moreover, the mineralogy and the composition of the slime may also drastically change within the same plant due to the fluctuation of the feed material and the process disturbances [4]. Copper anode slime is a dark-colored, fine-grained powder with the particle size often less than 50 microns with the spherical, semicircular, and elongated plate shapes [5-12]. Slime production usually varies from 2 to 28 kg per ton of copper cathode with an average value of 5 kg/ton at Sarcheshmeh and Khatoon-Abad [13]. The precious metal content of the anode is concentrated over the electrorefining process and collected in the slime. The small particle size of the slime makes some of the operating cost contributors, such as crushing and grinding a virtue out of necessity. Comprehensive studies were done by Chen and Dutrizac [5-12, 14, 15] on the characterization of copper anode slime, which shows that precious metals are mainly present in the oxide complexes and selenide phases. Anode slime constituents

*Corresponding Author Institutional Email: mokmeli@ut.ac.ir
(M. Mokmeli)

Please cite this article as: M. Alaviyan, S. Shakibania, M. Mokmeli, S. Sheibani, Full Characterization of Sarcheshmeh and Khatoon-Abad Copper Anode Slimes: Characterization Impact on the Decopperization Operation, ***International Journal of Engineering, Transactions B: Applications***, Vol. 36, No. 05, (2023) 934-945

are often transferred from the anode to the slime in various ways. During the copper electrorefining process, elements with less reduction potentials than the copper dissolve from the copper anode, whereas elements with higher reduction potential than copper are deposited at the bottom of the electrolyte cell [16].

Anode slime is classified into two main groups: the primitive slime, which is mainly collected at the bottom of the electrorefining cells, and the secondary slime, which mainly forms on the anode surface or suspended in the electrolyte [17]. The slime is continuously formed during the electrorefining process. Wang et al. [18] represented the classification of anode slimes, according to Figure 1.

Primitive slime contains metals nobler than copper, such as gold, and other insoluble compounds, such as selenides, telluride, or other complex refractory oxides. The components of this slime are directly released from the slime and mostly fall to the bottom of the electrolyte cell. A portion of this slime can also coat the surface of the copper anode as a porous layer. Secondary slime includes compounds precipitated in the interface of the anolyte region (generates by the 1st reaction) where other phases formed from the electrolyte (2nd reaction). For example, lead sulfate is a 1st reaction slime component formed by the reaction of Pb^{2+} (dissolved from the copper anode) and sulfate. Elements such as Ni, As, Sb, Bi, and Ag are partially soluble in the electrolyte; therefore, they can be found in both slime and electrolyte. Compounds of these elements mainly belong to the 2nd reaction slimes. Insoluble compounds of these elements, such as Kuferglimmer, can report to the primitive slime. However, gel-like phases containing these elements are named floating slime and are usually suspend in electrolyte. In copper refinery plants, barium sulfate is added to prevent the adhesion of the cast anodes to the mold. Excessive use of $BaSO_4$ could result in contamination of the anode and, consequently, the primitive slime. The presence of barium in the slime can adversely affect the extraction efficiency of the precious metal.

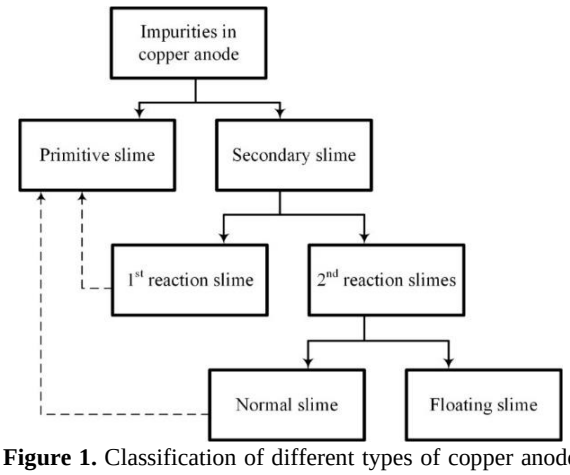

Figure 1. Classification of different types of copper anode slime [18]

Sarcheshmeh copper complex and Khatoon-Abad copper complex as the two largest copper producers of the country are producing about a total of 250,000 tons/year copper cathode [19]. A considerable number of studies have been conducted on the recovery of the metallic content of the Iranian copper anode slimes, mostly from Sarcheshmeh copper complex due to its earlier operation history. The authors of this work have found about 40 research works on the recovery of the Sarcheshmeh copper slime mostly written in Farsi. None of the studies were suggested a comprehensive plan for the recovery of all recoverable constituents of the slime, including copper, selenium, tellurium, silver, gold, and PGMs. Few studies were focused on the recovery of the two or, at most, three of the elements. For instance, Dehghanpoor et al. [20] investigated the extraction of Au and Cu from Sarcheshmeh bottom-cell slime. The result showed that by using a multi-stage leaching process in sulfuric acid, nitric acid, and aqua regia, more than 90% of the Cu and 80% of the Au could be dissolved from the slime. Similarly, Khanlarian et al. [21] used a sulfation-roasting process for recovering Cu, Ag, and Se content of the Sarcheshmeh bottom-cell slime. At their optimum experimental conditions, (sulfation at T=250°C, and acid to solid ratio of 1.95 followed by leaching in water), more than 90% of the stated metals were observed to be recovered. Saeedi et al. [22] studied the dissolution behavior of the Au from Sarcheshmeh bottom-cell slime by acidic chloride leaching at elevated temperature. Under the optimum conditions, the recovery of more than 90% of gold was shown to be obtained. Few more examples of the published researches on the recovery of the metallic content of the copper anode slime mostly from Sarcheshmeh Copper Complex are listed in literature [23-29]. Despite the extensive research have conducted on the recovery of the metallic content of the refinery slimes, none has made a comprehensive study in characterization of different types of slimes. Moreover, the main part of the available work on characterization of the copper anode slimes, date back to at least twenty years ago. Accordingly, recent variations in copper ores and the changes applied in the copper production processes, that can potentially alter the anode slime characterization, has been another impetus to conduct this study. In this research, various analysis techniques have been used to characterize and compare various types of the Sarcheshmeh and Khatoon-Abad anode slimes

The aim of this research is to provide a vision on the recovery plan of the various types of slime based on their characteristics. To recover the valuable content of the slime and to propose a comprehensive recovery flow diagram, the elemental analysis, morphology and microstructure, phase analysis, particle size, and thermal

analysis of the slime should be determined. These characteristics can strongly influence the selection of the proper method of recovery for valuable content of the slime. For better illustration of the importance of the characterization, decopperization of the bottom-cell slimes of Sarcheshmeh and Khatoon-Abad, considering the characterization results were investigated and described. Several procedures were suggested in removal of copper from the copper anode slime, including atmospheric sulfuric acid leaching, sulfuric acid roasting, atmospheric oxidation acid leaching with air and oxygen and pressure oxidative sulfuric acid leaching [30, 31].

The pressure oxidative sulfuric acid leaching is a simple and fast process that generates very high copper recovery of copper, but high reactor corrosion alongside low leaching efficiency of selenium and tellurium [32, 33]. In atmospheric oxidative sulfuric acid leaching, copper is oxidized to copper sulfate in a dilute sulfuric acid solution using O_2 gas. This is an easy, cheap and simple process with low consumption of H_2SO_4. The main drawback is the partial oxidation of cuprous sulfide and selenide that causes typical recovery of copper blow 80%. The aim of this research, apart from the full characterization, was to deliver a vision on differences of various types of slime and its impact on the recovery of the constituent metals.

2. EXPERIMENTAL PROCEDURE

Two different types of anode slime were characterized in this research. The first type of slime was gathered from the anode surface, which is known as the adherent slime. The second type of slime was gathered from the bottom of the electrorefining cells, which is known as bottom-cell slime. Both Sarcheshmeh bottom-cell and adherent slimes were characterized; however, in the case of Khatoon-Abad, only bottom-cell slime was characterized. The chemical compositions of the slimes were determined using the fire assay analysis (for gold and silver), inductively coupled plasma optical emission spectroscopy (ICP-OES, Varian735), inductively coupled plasma mass spectrometry (ICP-MS, HP4500), and X-ray fluorescence (XRF, ARL8410). The particle size distribution of the bottom-cell slime was determined by screen analysis. X-ray diffraction (XRD, Philips PW 3040/60) was used for phase detection. The microstructure of the samples was studied using an electron microscopy (SEM, FEI Quanta 450) equipped with an energy dispersive spectroscopy (EDS, Brunker Xflash 6L10). Simultaneous thermogravimetric analysis (STA, PerkinElmer STA6000) with a heating rate of 10°C/min from 30 to 800°C, was used for thermal characterization of the bottom-cell slimes. The chemical composition of the Sarcheshmeh electrolyte was also determined using ICP-OES technique. A scheme of the methodology used in this study is shown in Figure 2. Finally, decopperization of Sarcheshmeh and Khatoon-Abad bottom-cell slimes were studied based on the obtained results of the characterization section. Leaching experiments for the recovery of copper were conducted at T=85°C, sulfuric acid concentration of 160 g/L, solid to liquid ratio of 1:5 g:ml and in presence of air and pure oxygen.

3. RESULTS AND DISCUSSION

3. 1. Chemical Composition Results The chemical compositions of Sarcheshmeh bottom-cell slime (SBS), Sarcheshmeh adherent slime (SAS), Sarcheshmeh electrolyte, and Khatoon-Abad bottom-cell slime (KBS) are shown in Table 1. As evident, notable differences can be observed between various types of slime within a refinery plant (Sarcheshmeh). Also, there are distinct differences between the slimes of different copper refinery plants.

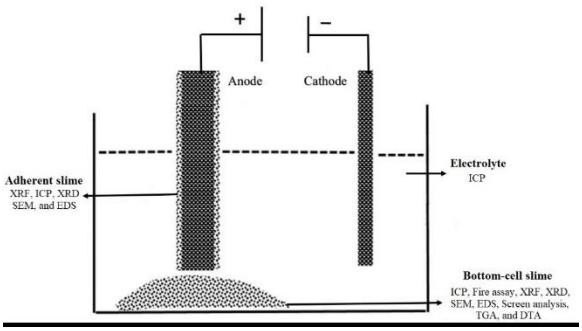

Figure 2. Scheme of the methodology used for characterizing the samples

TABLE 1. Chemical composition of SBS, SAS, Sarcheshmeh electrolyte and KBS

Elements	SBS (wt.%)	SAS (wt.%)	Sarcheshmeh Electrolyte (ppm)	KBS (wt.%)
Cu	8.18	34.74	40110	23.47
Ag*	6.5	7.78	0.005	2.11
As	1.03	4.37	3068	3.10
Au	0.15	-	-	0.11
Ba*	20.90	0.41	0.09	6.71
Ni	0.02	0.01	812	0.04
Pb	9.02	11.93	5.4	2.00
Sb	0.70	0.72	236	0.87
Se	14.09	16.29	0.7	7.73
Te	0.15	0.85	0.01	0.59

* Measured by XRF

Regarding Sarcheshmeh slime, copper concentration is considerably higher in the adherent slime in comparison to the bottom-cell slime. The adherent slime forms on the surface of the copper anode, which is mainly constituent of the metallic copper, copper oxide, and copper sulfate. Moreover, the main portion of the copper constituent of the bottom-cell slime is dissolved, whether during the electrorefining process by the electrolyte turbulence or through the collection of the slime process, which could result in a lower copper concentration. The Sarcheshmeh bottom slime was collected after the slime was water washed at the electrolysis cell and passed over through the collection tanks, thickeners, and the filter press. It should be noted that, most of the copper finds its way to the bottom-cell slime. Accordingly, despite the higher copper concentration of the adherent slime, a higher fraction of the total copper is presented in the bottom-cell slime. The Khatoon-Abad slime is, however, collected right after the electrolysis cell. The Khatoon-Abad slime wash with 80°C deionized water at S/L ratio of 1/4 g/mL over 2 hours was proven the weight loss of about 30%. The prior wash and after wash analysis of the Khatoon-Abad slime is shown in Table 2. The solubility of a few constituents of slime such as arsenates and entrapped copper sulfate are much easier in hot water than the sulfuric acid, copper sulfate solution medium.

Another significant difference between the adherent slime and the bottom slime is the barium concentration. Most of the barium is dropped down to the bottom cell due to its larger particle size and higher density. The barium concentration in the Sarcheshmeh adherent slime is negligible compared to its concentration in the Sarcheshmeh bottom-cell slime. Some elements, such as As, Sb, Se, and Ni, have been found in both of the slimes, as well as, in the electrolyte. These are the partially soluble elements that are expected to be found in the slimes and the electrolyte. The concentrations of the partial soluble elements are a little higher in the Sarcheshmeh adherent slime. This is possibly due to the dissolution of a fraction of these elements during their transformation to the Sarcheshmeh bottom-cell slime. Pb is found in both Sarcheshmeh bottom-cell slime and Sarcheshmeh adherent slime in an almost similar concentration. For the lead, non-soluble or low-soluble species of the element is formed in the sulfuric acid medium. This is, however, after the lead is being dissolved in a cationic form from the anode. The dissolved lead is rapidly reacting with the sulfate content of the solution and forms the lead sulfate layer on top of the anode. This layer is partly dropped to the cell bottom but continuously generates on the anode surface. The Pb behavior is different from the barium as the barium sulfate particles are non-soluble and originate from the barium sulfate slurry added through the casting process. The barium sulfate particles are adherent to the anode surface, and by the dissolution of the copper content of the anode is dropped form the anode surface to the cell bottom. The adherent slime was found free of the barium sulfate as the barium may just appear at the beginning of the dissolution process due to its presence on top of the anode surface .

TABLE 2. Chemical composition of Khatoon-Abad bottom-cell slime before and after washing with 80°C water

Element	Concentration before washing (%)	Concentration after washing (%)	Recovery (%)
Cu	21.47	24.56	19.94
Ag	2.11	3.01	-*
As	3.10	3.42	22.84
Au	0.11	0.16	-
Ba	6.71	9.59	-
Ni	0.04	0.04	33.96
Pb	2.00	2.86	0.05
Sb	0.87	1.24	0.14
Se	7.73	11.04	0.04

* Negligible

As stated earlier, the copper concentrate input and the extraction process can profoundly affect the composition and properties of the copper anode slime. Accordingly, a comparison has been made between the bottom-cell slimes of the two different refinery plants, Sarcheshmeh bottom-cell slime, and Khatoon-Abad bottom-cell slime. Significant differences in the chemical composition of these two slimes can be observed. The copper and arsenic concentration difference between the Sarcheshmeh bottom-cell slime and the Khatoon-Abad bottom-cell slime is attributed to the dissolution of the water-soluble constituent of the Sarcheshmeh bottom-cell slime. The concentration is about 2-3 times lower in Khatoon-Abad bottom-cell slime. On the contrary, barium, lead, silver, and selenium content of the Sarcheshmeh bottom-cell slime is about 2-3 times higher than the Khatoon-Abad bottom-cell slime. The significantly higher selenium content (higher ratio of selenium to copper concentration) of the Sarcheshmeh slime is important due to the fact that refractory selenide phases of various elements, such as copper and silver can be formed and affect dissolution process. The concentration of the insoluble content of the slime such as barium, lead, silver, and selenium are concentrated 2-3 times when the initial slime lost its copper and arsenic content. In contrast with sliver, the gold content of the Sarcheshmeh bottom-cell slime was not increased following the 2-3 times increment in the concentration ratio. The difference is most probably due to the lower gold content of the Sarcheshmeh feed concentrate than the Khatoon-Abad feed concentrate. The chemical composition of the Sarcheshmeh and Khatoon-Abad copper concentrates are

shown in Table 3. These significant differences can profoundly affect the slimes responses to various treatments.

3. 3. XRD Results The XRD pattern with phase composition of Sarcheshmeh bottom-cell slime, Sarcheshmeh adherent slime, and Khatoon-Abad bottom-cell slime is shown in Figure 3. According to this figure, Sarcheshmeh adherent slime mainly consists of lead sulfate, copper selenide, and mixed compounds of copper, silver, and selenium. In Sarcheshmeh bottom-cell slime, however, $BaSO_4$, $PbSO_4$, $Cu_{1.8}Se$, $Cu_4As_2Se_5$, CuSe, and Ag_2Se were detected as the main phases. There are noticeable differences between the phase composition of Sarcheshmeh adherent slime and Sarcheshmeh bottom-cell slime. $PbSO_4$ and copper selenide are the only common compounds found in both of these two slimes. In the Sarcheshmeh bottom-cell slime, various compounds of selenium are observed. This is due to the different chemical composition of the slimes. In the XRD pattern of the Khatoon-Abad bottom-cell slime, dominant peaks of barium sulfate and silver selenide were observed. In addition of these two compounds, two mixed compounds of Cu, Ag and Se were also detected. Due to expressively different chemical compositions, different major phases were observed in Sarcheshmeh and Khatoon-Abad bottom-cell slimes. Sarcheshmeh bottom-cell slime contains significantly higher amounts of selenium. Accordingly, most of the elements were found in close association with Se. Selenium presented in all of the detected phases in the XRD pattern, except lead sulfate. On the other hand, among the detected compounds at Khatoon-Abad bottom-cell slime, only two of them has contained selenium.

TABLE 3. Chemical composition of Sarcheshmeh and Khatoon-Abad copper concentrate

Element	Sarcheshmeh concentrate	Khatoon-Abad concentrate
Cu	26-30 %	30-35 %
Fe	25-26	21-22 %
As	0.02 %	0.03 %
Sb	0.03 %	0.01 %
Pb	0.23 %	0.01 %
Ag	50 ppm	40 ppm
Au	1.3 ppm	1.4 ppm
Bi	160 ppm	96 ppm
Se	140 ppm	80 ppm
Te	42 ppm	34 ppm

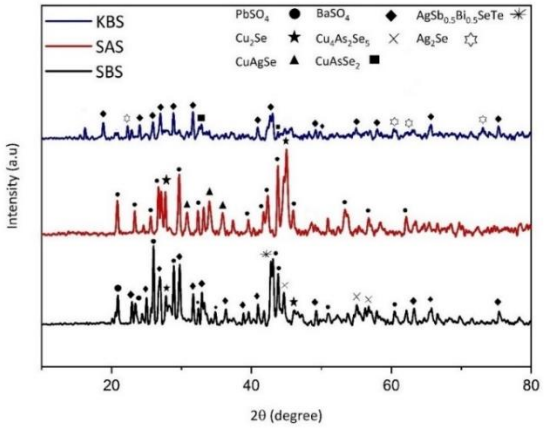

Figure 3. XRD patterns and phase detection of Sarcheshmeh adherent slime (SAS), Sarcheshmeh bottom-cell slime (SBS), and Khatoon-Abad bottom-cell slime (KBS)

3. 3. SEM Results The morphology and the chemical composition of various phases in the slimes were studied using SEM-EDS analysis. The results are shown in Figure 4. SEM image of Sarcheshmeh adherent slime is shown in Figure 4(c). Various phase compositions with a particle size below 10 μm are apparent in this figure. For phase detection, EDS analysis was performed for three different points on the SEM image. Oxide matrix phases consisting of Cu, Ag, Se, Pb, and as were identified in all of the three plotted points. However, the concentration of these elements varied with the morphology of the phases. At point 1, a spherical phase with high silver content was observed. Point 2 had a similar chemical composition to point 1; however, its sulfur content was relatively higher. The morphology of the detected phase at point 2 was different from the one found at point 1. Phase morphology at point 2 was more like drawn-out plates. A multifaceted phase with high copper and selenium content was identified at point 3. Tellurium and selenium content at point 3 was much higher in comparison to point 1 and 2, which indicates that Te is probably associated with the selenide phases.

The SEM result of Sarcheshmeh bottom-cell slime and EDS map of Cu, Se, Te, Ag, and Sb are shown in Figure 4(a). The chemical composition of the phases with different morphologies was studied using EDS analysis. Particles of this slime seemed to be agglomerated in some areas. Four different points on the SEM image of the Sarcheshmeh bottom-cell slime with various morphologies and color tones were selected for EDS analysis. At point 1, Sb, Te, and oxygen are presented with the highest concentration, which indicates the formation of oxide complex phases of these elements. Point 2 seems to be a representation of lead sulfate, which is also in a lighter color (compounds with higher masses are observed in lighter colors in SEM backscattered images). Points 3 and 4 consists of Ag, Se, and Cu with minor amounts of Te. Another finding regarding points 3 and 4, in which the highest copper concentrations were

observed, is that the Ba concentration at these points are relatively high (18 to 25%). Accordingly, copper recovery can be affected by its association with barium sulfate and the possible agglomerated Ba-Cu particles. Barium sulfate does not dissolve in acidic medium. The distribution of the Cu, Se, Te, Ag, and Sb are also shown in the same figure. It can be seen that some elements have a similar distribution pattern. Cu is presented within the same area of Se, which suggests the presence of copper selenide compounds. Te and Sb have similar distribution patterns. Te and Sb zones are surrounded by Cu-Se areas. Accordingly, Te and Sb are majorly present at the core distribution of copper selenide compounds. The SEM image of Khatoon-Abad bottom-cell slime is shown in Figure 4(b). In this figure, phases with spherical, semicircular, elliptical, and drawn-plate shapes were observed. In total, seven points on the SEM image with different morphologies were analyzed using EDS. Point 1 was determined to be barium sulfate with the morphology of spherical-shape. The particle size of this compound was found to be larger in comparison to other phases. Unlike Sarcheshmeh bottom cell slime, barium particles were only found in larger particle size and were not in association with other elements. The other six remaining points were copper selenide phases carrying different elements, such as silver, arsenic, and tellurium. According to the previous studies, these phases could be Cu_2Se, Ag_2Se, AgCuSe, AgCu(Se,Te), and $(Cu,Ag)_2Se$. These phases are visible in spherical and semicircular, elliptical, and drawn-out plate shapes. The EDS map of Khatoon-Abad bottom-cell slime is also shown in this figure. According to this figure, copper can be seen to have a uniform distribution throughout the studied area. Similar to Sarcheshmeh bottom-cell slime, tellurium was found to be in close association with Sb and Se. Ag particles were also found in association with corresponding selenium compounds.

By comparing the SEM results of Sarcheshmeh bottom-cell slime and Khatoon-Abad bottom-cell slime, it can be seen that the phase morphologies were almost similar in both slimes. Phases with the spherical, drawn-out plate, and semicircular shapes were majorly observed in both cases. However, the chemical compositions of the minor phases were different. Because of the high copper content of the Khatoon-Abad bottom-cell slime, most of the phases were detected in association with copper. In the case of Sarcheshmeh bottom-cell slime, a similar case was observed for selenium.

3. 4. Particle Size Results Screen analysis was performed to determine the particle size of the Sarcheshmeh bottom-cell slime and Khatoon-Abad bottom-cell slime, and also, to determine the distribution of precious metals at different particle sizes within these slimes. The cumulative particle size distribution of both slimes is shown in Figure 5. According to this figure, the particle size of Sarcheshmeh bottom-cell slime is relatively smaller than Khatoon-Abad bottom-cell slime. The reason for the particle size difference could be the difference of the injected barium sulfate particle size during casting, the agglomeration of the particles, and the difference in the anode solidification time. The longer the solidification time, the larger the particle size. 80% passing particle size of the Sarcheshmeh bottom-cell slime was below 38 microns, whereas the P80 for the Khatoon-Abad slime was measured around 106 microns.

It has been shown that barium particles are mostly agglomerated at particle sizes above 17 microns. Accordingly, the possibility of the physical separation of the barium sulfate particles from the rest of the slime using the hydrocyclone or the sieve was investigated. As

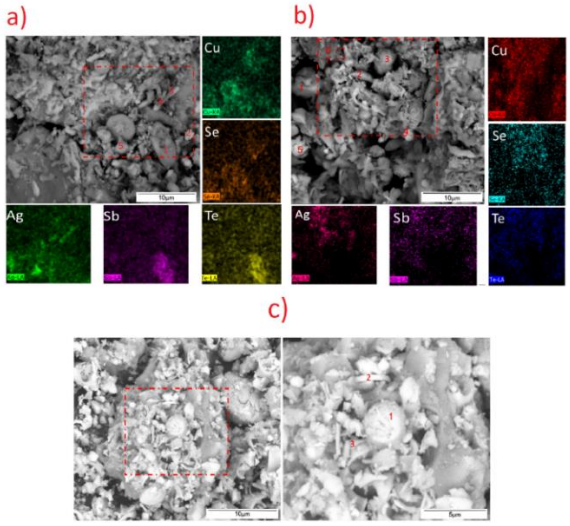

Figure 4. SEM image of (a) Sarcheshmeh bottom-cell slime (SBS), (b) Khatoon-Abad bottom-cell slime (KBS) and (c) Sarcheshmeh adherent slime (SAS)

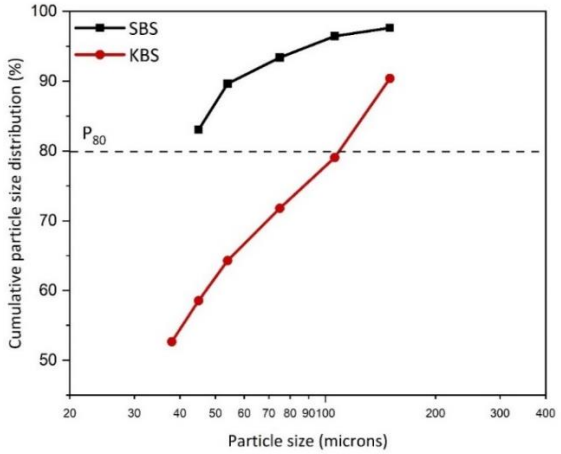

Figure 5. Particle distribution of Sarcheshmeh bottom-cell slime (SBS) and Khatoon-Abad bottom-cell slime (KBS)

stated earlier, the presence of barium can impose challenges in recovery of precious metals. The high abrasion of the barium sulfate can cause the decopperrizing tank to get corroded very fast. A shaking screen can help to separate the unwanted particles from the rest of the slime. The chemical composition of the slimes, with particle size above 38 microns, was determined using the ICP-MS. The results are summarized in Table 4. According to this table, due to the presence of a significant fraction of precious metals in particles above 38 microns, physical separation of barium through sieve analysis does not seem practical.

3. 5. STA Results Simultaneous thermal analysis of TGA and DTA was carried out to determine the interaction of the Sarcheshmeh bottom-cell slime and Khatoon-Abad bottom-cell slime compounds with temperature. Among the known recycling process, a pyrometallurgical pretreatment of the slime is popular. Oxidative roasting, sulfation roasting, and soda roasting are the industrial examples of the few pretreatment processes. As a result, the TGA and DTA results are essential in the design of the slime recovery processes. The results are shown in Figure 6. According to this figure, the TG curve of the Sarcheshmeh bottom-cell slime (Figure 6(a)) can be divided into three main parts: First is the initial mass loss, that happens at temperatures below 400˚C, second is the simultaneous mass loss and mass gain that happens from 400ºC to around 600ºC, and third is the final mass loss which happened at temperatures above 600ºC. Sarcheshmeh bottom-cell slime contains considerable amount of Se. Accordingly, most of the thermal interactions are based on selenium bearing compounds.

The initial mass loss at temperatures below 400ºC originates from removing moisture, chemically bonded water, and evaporation of volatile compounds. The free

TABLE 4. Distribution of Sarcheshmeh bottom-cell slime and Khatoon-Abad bottom-cell slime components in particle sizes above 38 microns

Sarcheshmeh bottom-cell slime			Khatoon-Abad bottom-cell slime	
Element	**Wt. % in fraction >38 microns**	**Fraction presented at >38 microns**	**Wt. % in fraction >38 microns**	**Fraction presented at >38 microns**
Ba	30.17	23.39	9.34	47.70
Cu	4.36	8.79	25.88	57.02
Au	0.08	8.22	0.118	58.95
Ag	3.28	8.15	5.32	5.23
Se	8.19	3.98	11.80	42.65
Te	0.21	51.93	0.56	86.76

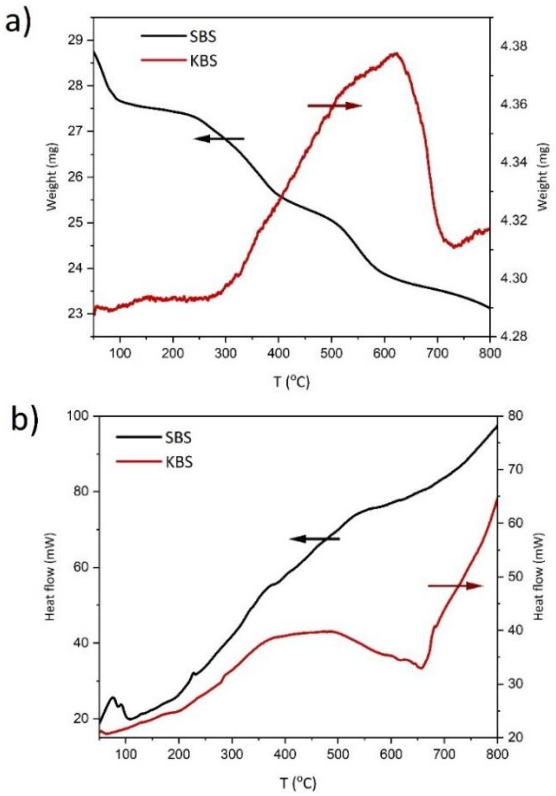

Figure 6. Thermal analysis results of Sarcheshmeh bottom-cell slime (SBS) and Khatoon-Abad bottom-cell slime (KBS) a) TGA results b) DTA results

selenium and silver selenide are the main volatile compounds. Evaporation of selenium compounds may occur as following [18]:

$$Se_{(s)} = Se_{(g)} \qquad 227.5<\Delta H\ (kJ)<229.9 \qquad (1)$$

$$Se_{(s)} + O_{2(g)} = SeO_{2(g)} \qquad -128.8<\Delta H\ (kJ)<-118.9 \qquad (2)$$

$$Ag_2Se_{(s)} = 2Ag_{(s)} + Se_{(g)} \qquad 260.0<\Delta H\ (kJ)<269.3 \qquad (3)$$

$$Ag_2Se_{(s)} + O_{2(g)} = 2Ag_{(s)} + SeO_{2(g)} \qquad -81.6<\Delta H\ (kJ)<-79.9 \qquad (4)$$

The standard Gibb's free energy of these reactions are shown in Figure 7. Some of the above-stated reactions have positive standard Gibb's free energy, which imputes that they cannot occur in thermodynamic standard condition. They can however occur in non-standard conditions. Three endothermic peaks have been observed in the temperature range of 100 to 400°C (Figure 6(b)). The first two endothermic peaks have occurred at temperatures below 100ºC, which is related to the evaporation of the sample's moisture. Another endothermic peak is visible at around 200ºC, which is probably for the evaporation of the elemental selenium and molecular water.

After 300°C, a mass gain happens by the reactions between anode slime components, the gas products, and the oxidizing atmosphere. The formation of silver selenite can happen according to the following reaction:

$$Ag_2Se_{(s)} + 1.5O_{2(g)} = Ag_2SeO_{3(s)} \quad -288.2<\Delta H\ (kJ)<-239.2 \quad (5)$$

Moreover, copper compounds, such as Cu_2Se and Cu_2O, can also react with oxygen and sulfur dioxide to form solids with higher weights [19]:

$$Cu_2Se_{(s)} + 2O_{2(g)} = Cu_2SeO_{4(s)} \quad -288.2<\Delta H\ (kJ)<-239.2 \quad (6)$$

$$Cu_2O_{(s)} + 2SO_2 + 1.5O_{2(g)} = CuSO_{4(s)} \quad -288.2<\Delta H\ (kJ)<-239.2 \quad (7)$$

Based on reaction 7, for the conversion of copper oxide to copper sulfate, the presence of sulfur dioxide gas is essential. Considering a low concentration of elemental sulfur in slime, the sulfur dioxide can be provided from decomposition of other sulfide compounds. Due to the high selenium content of the Sarcheshmeh slime, the two above reactions possibly happen at lesser quantities in comparison to selenium compounds reactions. The formation of these compounds could result in a slight mass gain of the slime. As the temperature increases, the previous mass loss reaction, due to the endothermic nature of the reactions, happens at higher rates. In the case of Sarcheshmeh bottom-cell slime, the mass loss reactions have overcome mass gain reactions, which eventually resulted in an overall mass loss. Finally, the mass losses at temperatures above 600°C can represent the decomposition of silver selenide and sulfated compounds, such as $BaSO_4$, $PbSO_4$, and $CuSO_4$ through the following reactions [19-22]:

$$Ag_2SeO_{3(s)} + SO_{3(g)} = Ag_2SO_{4(s)} + SeO_{2(g)} \quad -106.1<\Delta H\ (kJ)<-99.5 \quad (8)$$

$$PbSO_{4(s)} = PbO_{(s)} + SO_{3(g)} \quad 292.0<\Delta H\ (kJ)<299.9 \quad (9)$$

$$BaSO_{4(s)} = BaO_{(s)} + SO_{2(g)} + 0.5O_{2(g)} \quad 562.2<\Delta H\ (kJ)<603.3 \quad (10)$$

$$CuSO_{4(s)} = CuO_{(s)} + SO_{2(g)} + 0.5O_{2(g)} \quad 303.7<\Delta H\ (kJ)<308.9 \quad (11)$$

A significantly different behavior was observed in Khatoon-Abad bottom-cell slime thermal peaks comparing to the Sarcheshmeh bottom-cell slime. Khatoon-Abad bottom-cell slime was dried previously at 90°C for 24 hours. Accordingly, no weight loss or endothermic peaks were observed pre-100°C. The Khatoon-Abad bottom-cell slime contains a significant amount of copper; therefore, most of the interaction can be attributed to the copper-containing compounds. Till 300°C, no significant interaction is evident in the thermograph. However, after 300°C, up to around 600°C, a considerable mass gain was observed in the TGA graph (Figure 6(a)). The mass gain can be attributed to the oxidation of different copper compounds. The mass loss reaction may also occur similar to the reactions previously discussed. Their effect, however, could be potentially masked by mass gain reactions. A mass gain as the result of oxidation of copper selenide and cuprous oxide is viable according to reactions 6 and 7. Another possible reaction involving copper that could result in increased weight of the sample is as follows:

$$Cu_2S_{(s)} + 7.5O_{2(g)} = 2CuSO_{4(s)} + 3Cu_2O + 2SO_2 \quad -288.2<\Delta H\ (kJ)<-239.2 \quad (12)$$

The combination of reaction 12 with reactions 6 and 7 can cause an exothermic peak at around 600°C. After 600°C, due to the decomposition of sulfates of different elements, such as copper, barium, and lead, a mass loss has happened. Due to the differences in the chemical composition, especially in copper and selenium concentrations, distinct behaviors were observed in the interaction of these slimes with temperature. A consistent mass loss was observed in the TGA result of Sarcheshmeh bottom-cell slime with increasing temperature as a result of high selenium content. An opposite result was observed in the Khatoon-Abad bottom-cell slime TGA graph. A consistent mass gain trend was observed up to temperatures around 600°C, due to the oxidation of copper-containing compounds.

As stated earlier, pyrometallurgical pretreatments are common in copper anode slime processing. Accordingly, besides the above explanations, a brief thermodynamic assessment of the discussed reactions are presented below. Since the thermal interactions in the studied slimes (Sarcheshmeh and Khatoon-Abad bottom-cell slimes) were mostly found in association with Cu-Se-Ag compounds, oxidative roasting in the systems of Ag-Se-O and Cu-Se-O has been studied.

In Figures 7 and 8 the standard Gibbs free energy (ΔG^0) of Ag-Se-O and Cu-Se-O system and their dominant species at various temperature and oxygen pressure are illustrated. The thermodynamic data was obtained from HSC software database (Version 6, Outokumpu research). It should be noted that the data presented in these figures are ΔG^0 not ΔG. Accordingly, although some reactions have positive ΔG^0, they could still thermodynamically happen if their ΔG becomes negative in a non-standard condition. Oxidizing roasting is mostly applied to convert elements, such as copper, nickel, and tellurium into soluble compounds in sulfuric acid solution and also evaporate the selenium. According to Figure 7, evaporation of selenium is mostly happening by conversion of Se-containing compounds to $SeO_{2\,(g)}$. The process of Se removal involves the formation of

intermediate selenite species. As discussed in the previous section, in bottom-cell copper anode slimes, selenium can present as silver selenide (Ag_2Se). At lower temperatures (around <400ºC), due to relatively lower ΔG^0, the transformation of Ag_2Se to either intermediate species, such as Ag_2SeO_3 or directly to SeO_2 happens. Intermediate species of silver and selenium tend to become less stable with increasing temperature, which leads to the evaporation of selenium as SeO_2. This is also evident in the speciation diagram of Ag-Se-O (Figure 7(b)). At temperatures above 300ºC and oxygen partial pressure of 10^{-5}, SeO_2 is mostly stable.

Similar to Ag-Se-O system, the same graphs were plotted for Cu-Se-O system. The presence of copper selenide is possible in bottom-cell anode slimes. The process of selenium removal and transformation of copper selenide to soluble copper species is evident in Figure 8. At temperatures below 600ºC, the transformation of Cu_2Se to copper selenate happens spontaneously. By increasing temperature, the Gibbs free energy of the decomposition reaction of copper selenate to CuO and SeO_2 becomes less negative. Accordingly, the thermodynamic driving force for the copper selenate decomposition becomes larger. As a result of this process, selenium can be removed from the slime as SeO_2, and also copper transforms to non-sulfide/soluble species, such as $CuSO_4$ and CuO.

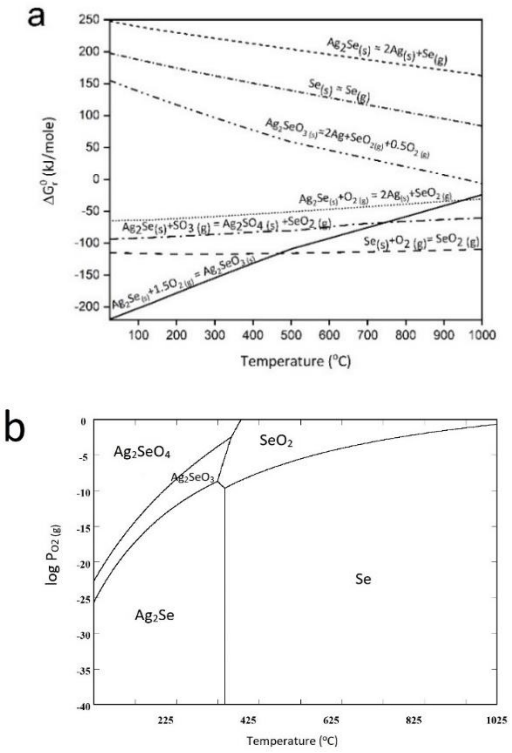

Figure 7. Oxidative roasting in Ag-Se-O system a) Standard Gibbs free energy of reaction as the function of temperature b) Effect oxygen partial pressure and temperature on Ag-Se-O species

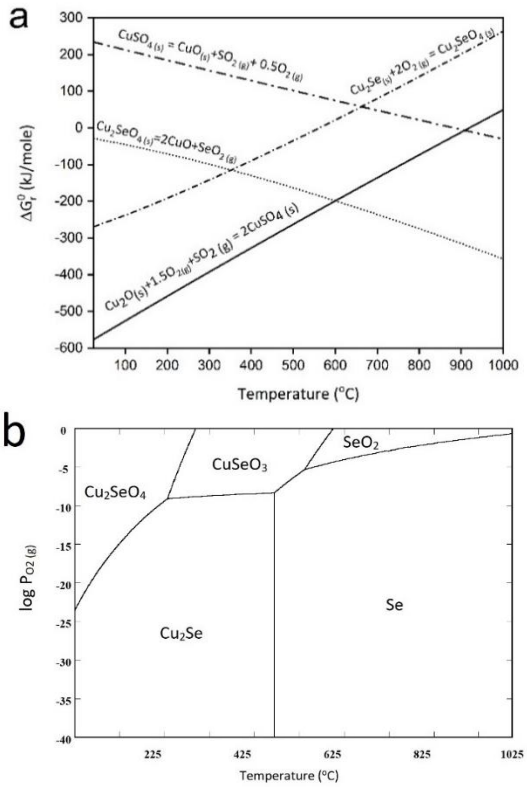

Figure 8. Oxidative roasting in Cu-Se-O system a) Standard Gibbs free energy of reaction as the function of temperature b) Effect oxygen partial pressure and temperature on Cu-Se-O species

3. 6. Decopperization The proper characterization can strongly influence the selection of the proper method in recovery of the valuable content of the slime. In this section, as an example, a hydrometallurgical recovery of copper from Sarcheshmeh and Khatoon-Abad bottom-cell slimes, considering the characterization results, are investigated. In hydrometallurgical recovery of copper anode slime components, the first step is often the decopperization process .

Chemical analysis showed that copper concentration in Khatoon-Abad slime was considerably higher than Sarcheshmeh slime. However, a significant fraction of copper in Khatoon-Abad slime was in a form of water-soluble copper compounds. Phase composition analysis of both slimes revealed that copper was mostly associated with selenium, which necessities using of the oxidants for efficient copper recovery. However, the ratio of selenium to copper in Sarcheshmeh slime was significantly higher than that of it in Khatoon-Abad slime, which imputes that copper concentration of non-selenide compounds are potentially higher at Khatoon-Abad slime. This could result in easier copper dissolution. Moreover, copper selenide in Sarcheshmeh slime was agglomerated within barium sulfate, which could negatively affect the copper dissolution, especially in sulfuric acid medium.

Considering the small particle size of the Sarcheshmeh slime, further grinding may not be feasible in liberating of the copper particles from barium sulfate. Accordingly, conventional leaching may not be a suitable solution for the full copper recovery of Sarcheshmeh slime and therefore more severe conditions in terms of temperature and pressure may be essential. Therefore, copper recovery from Sarcheshmeh and Khatoon-Abad bottom-cell slimes using sulfuric acid in a concentration similar to copper electrolyte (160 g/L) in the presence of air and oxygen as an oxidant were investigated. The copper recovery results are shown in Figure 9.

As it is evident, for recovering copper from both slimes, the presence of oxidant is required. Copper recovery was improved by substituting air with oxygen. However, considering different characteristics of the slimes, significantly different copper dissolution behavior was observed. After 12 hours, copper dissolution from Khatoon-Abad slime reached around 90% recovery, while copper recovery from Sarcheshmeh slime was limited to around 40%. As stated earlier, one possible reason for low copper dissolution of Sarcheshmeh slime can be attributed to higher selenium to copper ratio and agglomeration of copper particles in barium sulfate. Therefore, higher copper dissolution at the elevated pressures and temperatures is predicted. Accordingly, another experiment in autoclave was conducted over the Sarcheshmeh slime. The temperature and pressure in this experiment were 120°C and 8 bars, respectively. The pressure was adjusted by oxygen gas. The obtained results are shown in Figure 10.

As it is evident, copper recovery was significantly improved by increasing temperature and pressure. Increasing pressure increases the dissolved oxygen content of the leachate and increasing temperature helps the dissolution reaction to occur faster; both resulted in higher copper dissolution. Obviously, a difference in the phase composition of the slimes has caused different decopperization results. For Khatoon-Abad slime, an atmospheric leaching was efficient; whereas for Sarcheshmeh slime, leaching in autoclave was requiered.

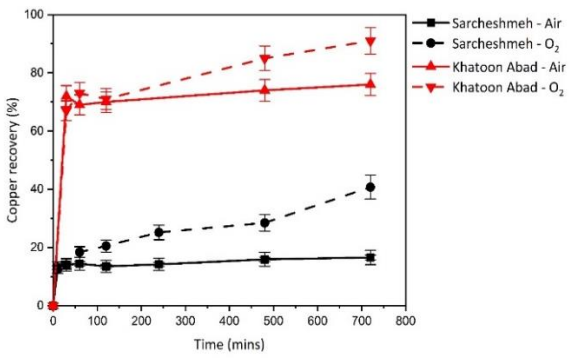

Figure 9. Copper dissolution behavior from Sarcheshmeh and Khatoon-Abad bottom-cell slimes

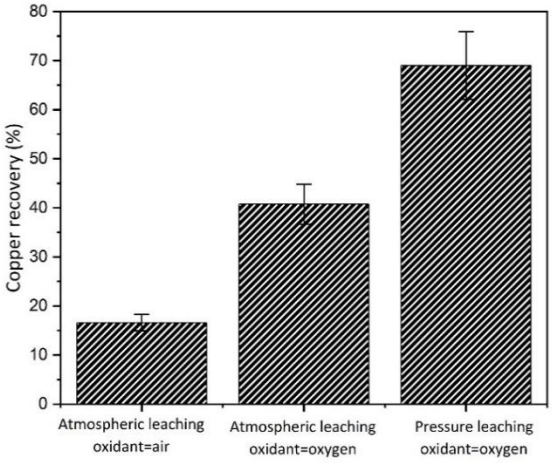

Figure 10. Effect of leaching method on copper dissolution from Sarcheshmeh bottom-cell slime

This difference will also extend to the recovery of other constituent elements of the slime such as tellurium and selenium .

4. CONCLUSION

In this research, two different types of slimes from Sarcheshmeh copper complex and Khatoon-Abad copper complex were characterized and compared. The results showed that characteristic properties of the slime could significantly vary from one refinery plant to another due to the differences in feed material and smelting production processes. Chemical composition of the slimes can result in profound differences in the major phase constituents, the minor phases, particle size, and interaction of slimes with temperature. Sarcheshmeh bottom-cell slime contained high amounts of selenium; therefore, most of the other slime components were observed in association with this element. Khatoon-Abad bottom-cell slime, however, contained significant amounts of copper. Accordingly, other components were closely linked to copper. These distinctions resulted in significant differences in TGA-DTA results. Since Sarcheshmeh bottom-cell slime contained a high amount of selenium, most of thermal interactions were with Se-containing compounds. In the case of Khatoon-Abad bottom-cell slime, however, due to high copper content, most of thermal interactions were attributed to the Cu-containing compounds. Adherent slime of Sarcheshmeh refinery plant was also characterized and compared to Sarcheshmeh bottom-cell slime. The adherent slime was found free of barium sulfate. The variance in characteristic properties of the slimes have resulted in significant differences in copper dissolution behavior of slime. Due to the association of copper with selenium and barium in the Sarcheshmeh slime, copper content of the

slime was only effectively dissolved at elevated temperature and pressure, while high copper recovery from Khatoon-Abad slime was obtained at moderate conditions.

5. CONFLICT OF INTEREST

On behalf of all authors, the corresponding author states that there is no conflict of interest.

6. ACKNOWLEDGMENTS

The authors would like to acknowledge the support of Iran National Science Foundation Grant No. 97013338. The authors are also thankful to Sarcheshmeh Copper Complex and Khatoon-Abad copper complex for providing the copper anode slimes' of their company.

7. REFERENCES

1. Xiao, L., Wang, Y.L., Yu, Y., Fu, G.Y., Han, P.W., Sun, Z.H.I., and Ye, S.F., "An Environmentally Friendly Process to Selectively Recover Silver from Copper Anode Slime." ***Journal of Cleaner Production***, Vol. 187, No. 20, (2018), 708-716, doi: 10.1016/j.jclepro.2018.03.203.
2. Liu, W., Yang, T., Zhang, D., Chen, L., and Liu, Y., "Pretreatment of Copper Anode Slime with Alkaline Pressure Oxidative Leaching." ***International Journal of Mineral Processing***, Vol. 128, No. 10, (2014), 48-54, doi: 10.1016/j.minpro.2014.03.002.
3. Bäckström, J., "Copper, Nickel and Tellurium Yields during Leaching of Anode Slime." Master Thesis, ***Lulea University of Technology***, (2010).
4. Mahmoudi, A., Shakibania, S., Mokmeli, M., and Rashchi, F, "Tellurium, from Copper Anode Slime to High Purity Product: A Review Paper." ***Metallurgical and Materials Transactions B***, Vol. 51, No. 6, (2020), 2555-2575, doi: 10.1007/s11663-020-01974-x.
5. Chen, T.T., and Dutrizac, J.E., "Mineralogical Characterization of Anode Slimes-IV. Copper-Nickel-Antimony Oxide ("Kupferglimmer") in CCR Anodes and Anode Slimes." ***Canadian Metallurgical Quarterly***, Vol. 28, No. 23, (1989), 127-134, doi: 10.1179/cmq.1989.28.2.127.
6. Chen, T.T., and Dutrizac, J.E., "The Mineralogy of Copper Electrorefining." ***The Journal of the Minerals, Metals & Materials Society***, Vol. 42, No. 32, (1990), 39-44 doi: 10.1007/BF03221053.
7. Chen, T.T., and Dutrizac, J.E., "Mineralogical Characterization of Anode Slimes: Part 7-Copper Anodes and Anode Slimes from the Chuquicamata Division of Codelco-Chile." ***Canadian Metallurgical Quarterly***, Vol. 30, No. 12, (1991), 95-106 doi: 10.1179/cmq.1991.30.2.95.
8. Chen, T.T., and Dutrizac, J.E. "A Mineralogical Study of the Deportment and Reaction of Silver during Copper Electrorefining." ***Metallurgical and Materials Transactions B,*** Vol. 20, No. 11, (1989), 345-361, doi: 10.1007/BF02696987.
9. Chen, T. T., and Dutrizac, J.E., "Mineralogical Characterization of Anode Slimes: Part V-Nickel-Rich Copper Anodes from the CCR Division of Noranda Minerals Inc." ***Canadian Metallurgical Quarterly***, Vol. 29, No. 8, (1990), 27-37, doi: 10.1179/cmq.1990.29.1.27.
10. Chen, T.T., and Dutrizac, J.E., Mineralogical Characterization of Anode Slimes: Part 10. Tellurium in Raw Anode Slimes. ***Canadian Metallurgical Quarterly***, Vol. 35, No. 54, (1996), 337-351, doi: 10.1179/cmq.1996.35.4.337.
11. Chen, T.T., and Dutrizac, J.E., "Mineralogical Characterization of Anode Slimes: Part 8-Silica in Copper Anodes and Anode Slimes." ***Canadian Metallurgical Quarterly***, Vol. 30, No. 7, (1991), 173-185, doi: 10.1179/cmq.1991.30.3.173.
12. Chen, T.T., and Dutrizac, J.E. "Mineralogical Characterization of a Copper Anode and the Anode Slimes from the La Caridad Copper Refinery of Mexicana De Cobre." ***Metallurgical and Materials Transactions B,*** Vol. 36, No. 41, (2005), 229-240 doi: 10.1007/s11663-005-0024-1.
13. Habashi, F., A Textbook of Hydrometallurgy. Metallurgie Extractive: Quebec, 1999.
14. Chen, T.T., and Dutrizac, J.E., "The Mineralogical Characterization of Tellurium in Copper Anodes." ***Metallurgical and Materials Transactions B,*** Vo. 24, No. 11, (1993), 997-1007, doi: 10.1007/BF02660991.
15. Chen, T.T., and Dutrizac, J.E., "Mineralogical Characterization of Anode Slimes-I. Anode Copper from Inca's Copper Cliff Copper Refinery." ***Canadian Metallurgical Quarterly***, Vol. 27, No. 8, (1988), 91-96, doi: 10.1179/cmq.1988.27.2.91.
16. Schlesinger, M.E., Sole, K.C., and Davenport, W.G., Extractive Metallurgy of Copper. Oxford: Elsevier Science, 2011.
17. Kiviluoma, M., Aaltonen, M., Aromaa, J., Lundström, and M., Forsén, O., "Development of Characterization Methods for Adherent Anode Slimes in Copper Electrorefining.", ***Physicochemical Problems of Mineral Processing***, Vol. 52, No. 1, (2016), 295-302, doi: 10.5277/ppmp160125
18. Wang, X., Chen, Q., Yin, Z., Wang, M., and Zhang, F., "Homogeneous Precipitation of As, Sb and Bi Impurities in Copper Electrolyte During Electrorefining." ***Hydrometallurgy***, Vol. 105, No. 12, (2011), 355-358, doi: 10.1016/j.hydromet.2010.10.004.
19. Mokmeli, M., "Pre-feasibility Study in Hydrometallurgical Treatment of Low-Grade Chalcopyrite Ores from Sarcheshmeh Copper Mine." ***Hydrometallurgy***, Vol. 191, No. 105215, (2020), doi: 10.1016/j.hydromet.2019.105215.
20. Dehghanpoor, M.H., Zivdar, M., and Torabi, M., "Extraction of Copper and Gold from Anode Slime of Sarcheshmeh Copper Complex." ***Journal of the Southern African Institute of Mining and Metallurgy***, Vol. 116, No. 17, (2016), 1153-1157, doi: 10.17159/2411-9717/2016/v116n12a9.
21. Khanlarian, M., Rashchi, F, and Saba, M., "A Modified Sulfation-Roasting-Leaching Process for Recovering Se, Cu, and Ag from Copper Anode Slimes at a Lower Temperature." ***Journal of Environmental Management***, Vol. 235, No. 45, (2019), 303-309, doi: 10.1016/j.jenvman.2019.01.079.
22. Saeedi, M., Alamdari, E.K., Darvishi, D., and Alamdari, A.K., "Chlorine Leaching of Au from Copper Anode Slimes using the Response Surface Method in an Agitated Reactor.' ***Mineral Processing and Extractive Metallurgy,*** Vol. 124, No. 8, (2015), 9-15, doi: 10.1179/1743285514Y.0000000071.
23. Abdollahy, M., Shafaei, S.Z. "Optimized Leaching Conditions for Selenium from Sar-Cheshmeh Copper Anode Slimes." ***Iranian Journal of Chemistry and Chemical Engineering***, Vol. 23, No. 11, (2004), 101-108, doi: 10.30492/ijcce.2004.8144
24. Ranjbar, R., Naderi, M., Omidvar, H., and Amoabediny, G. "Gold Recovery from Copper Anode Slime by Means of Magnetite Nanoparticles (MNPs)." ***Hydrometallurgy***, Vol. 143, No. 12, (2014), 54-59, Vol: 10.1016/j.hydromet.2014.01.007.

25. Zahedi, H., Mollahosseini, A., and Noroozian, E. "Synthesis Silver Nanoparticles by Recovery Silver from Anode Slime of Kerman Sarcheshmeh Cooper Complex." ***International Journal of Bio-Inorganic Hybrid Nanomaterials***, Vol. 4, No. 1, (2015), 15-19.

26. Ranjbar, R., Naderi, M., and Ghazitabar, A. "Hydrochemically Separation of Gold from Copper Anode Slime by Means of Thiourea Solution." ***Journal of Advanced Materials and Processing,*** Vol. 5, No. 2, (2017), 22-31.

27. Javanshir, S., Abdollahy, M., and Abolghasemi, H. "Drop Size Distribution in A Mixer-Settler Reactor for the Gold Chloride/Dbc System." ***Chemical Engineering Research and Design,*** Vol. 90, No. 8, (2012), 1680-1686 doi: 10.1016/j.cherd.2012.01.011

28. Shojaei, M.R., Khayati, G.R., Assadat Yaghubi, N., Bagheri Sharebabaki, F., and Khorasan, S.M.J., "Removing of Sb and As from Electrolyte in Copper Electrorefining Process: A Green Approach." ***International Journal of Engineering, Transactions C: Aspects***, Vol. 34, No. 3, (2021), 700-705. doi: 10.5829/ije.2021.34.03c.14.

29. Khazaei Feizabad, M.H., Khayati, G.R., Kafi Hernashki, R., Khorasani, and S.M.J., "Modeling and Optimization of Charge Materials Ranges in Converter Furnace with Enhanced Passivation Time in Copper Electrorefining Process: A Mixture Design Approach." ***International Journal of Engineering, Transactions A: Basics***, Vol. 34, No. 4, (2021), 966-975. doi: 10.5829/ije.2021.34.04a.23.

30. Kilic, Y., Kartal, G., and Timur, S., "An Investigation of Copper and Selenium Recovery from Copper Anode Slimes." ***International Journal of Mineral Processing***, Vol. 124, No. 10, (2013), 75-82, doi: 10.1016/j.minpro.2013.04.006.

31. Dönmez, B., Celik, C., Colak, S., and Yartaşi, A., "Dissolution Optimization of Copper from Anode Slime in H_2SO_4 Solutions." ***Industrial & Engineering Chemistry Research***, Vol. 37, No. 8, (1998), 3382-3387, doi: 10.1021/ie9800290.

32. Seisko, S., Aromaa, J., Latostenmaa, P., Forsen, O., and Lundstrom, M., "Effect of Process Variables on Oxidative Pressurized Acid Leaching of Copper Electrorefining Anode Slimes." In E3S Web of Conferences, Vol. 8, 01006, (2016), EDP Science.

33. Seisko, S., Aromaa, J., Latostenmaa, P., Forsen, O., Wilson, B., and Lundström, M. "Pressure Leaching of Decopperized Copper Electrorefining Anode Slimes in Strong Acid Solution.' ***Physicochemical Problems of Mineral Processing***, Vol. 53, No. 1, (2017), 465-474, doi: doi.org/10.5277/ppmp170136

Persian Abstract

چکیده

لجن آندی مس، محصول جانبی با ارزشی است که در طول فرایند تصفیه الکتریکی مس تولید می شود و یکی از مهمترین منابع ثانویه بازیابی فلزات طلا، نقره، سلنیوم، تلوریوم، مس و فلزات گروه پلاتین می باشد. مشخصه یابی کامل لجن آندی پیش نیاز بازیابی مطلوب این فلزات می باشد. در این تحقیق، مشخصه یابی کامل لجن آندی مجتمع مس سرچشمه و مجتمع مس خاتون آباد با استفاده از روشهای ICP، XRD، XRF، SEM، EDS، TGA، DTA و تعیین اندازه دانه صورت پذیرفت. علاوه بر لجن جمع آوری شده در کف سلول، مشخصات لجن چسبنده به سطح آند در مجتمع مس سرچشمه نیز مورد بررسی و مقایسه قرار گرفت. مشاهدات نشانگر اندازه بسیار کوچکتر لجن سرچشمه نسبت به لجن خاتون آباد می باشد. در عین حال، قسمت عمده طلا و تلوریوم در هر دو لجن، در ذرات درشت تر از ۳۸ میکرون تجمع یافته است. تفاوت عمده در مشخصات حرارتی دو لجن نیز متاثر از میزان سلنیوم محتوی دو لجن می باشد. در لجن خاتون آباد، غلظتهای بالاتر ترکیبات مس دار غیر سلنیدی، انحلال بالاتر مس محتوی لجن را به همراه داشته است. اختلاف چشمگیر در انحلال مس محتوی این دو لجن بواسطه حضور فازهای سلنیدی مس و محصور شدن مس در ذرات کلوخه ای سولفات باریم است. با توجه به تفاوتهای فوق، انحلال اتمسفری محتوی مس لجن خاتون آباد برابر ۹۰ درصد و در لجن سرچشمه برابر ۴۰ درصد مشاهده گردید.

International Journal of Engineering

Journal Homepage: www.ije.ir

A Baseline Free Method for Multiple Damage Identification and Localization using the Roving Mode Shape Response

B. Patel*, U. K. Dewangan

Department of Civil Engineering, National Institute of Technology, Raipur, India

P A P E R I N F O

Paper history:
Received 05 January 2023
Received in revised form 24 February 2023
Accepted 27 February 2023

Keywords:
Damage Detection
Structural Health Monitoring
Dynamic Response
Inverse System Identification

A B S T R A C T

The identification of structural systems with unknown vibration signature response is still a challenging issue which has been addressed by many reviewers. The current sensor technology states that the sensor position should be very close to the damaged element in order to identify and localize the damage. The primary goal of this research is to present a baseline-free method using the roving mode shape response based, multiple damage localization in a cantilever beam. Consequently, the damage location indicator is based on the roving mode shape approach (DLRA). The theoretical development is carried out on a cantilever beam, a finite element model. The different cases for multiple damages i.e. 2 elements damage, 3 elements damage and 5 elements to be damage, at a time, have been modelled on the structural member. The system response, for the healthy and damaged structural systems, has been determined using the roving mode shape approach. Further, the algorithm has been developed for multiple damage identification and localization using MATLAB software. The combined mass and stiffness damage, as well as only the mass change damage, both cases were considered. From the results, it was found that the proposed method can reliably identify the damage and its position. The method will also be helpful while keeping the sensor's position very close to the damage. The novelty of this method is that it uses the response which is basically a field output and no prior assumptions have been made at the damaged element's location.

***doi**: 10.5829/ije.2023.36.05b.11*

NOMENCLATURE

M	Distributed mass matrix (N)	**Greek Symbols**	
C	Damping coefficient matrix	ω	Modal frequency (Hz)
K	Stiffness matrix (N/mm)	$\Delta\phi$	Modal amplitude perturbation matrix
t	Time period (s)	ϕ_d	Modal amplitude of the damaged structure
$u(t)$	Structural response matrix in terms of displacement (mm)	ϕ_u	Modal amplitude of the undamaged structure
$\dot{u}(t)$	Structural response matrix in terms of velocity (mm/s)	α	Coefficient of proportionality
$\ddot{u}(t)$	Structural response matrix in terms of acceleration (mm/s^2)	**Subscripts**	
A	Column matrix of modal amplitude (mm)	d	Damage case
N	Total number of elements in the Finite Element model	u	Undamage case
		i	Natural number

1. INTRODUCTION

Vibration is a motion that repeatedly revolves about its mean position while being constrained between two clearly defined boundaries (known as extreme positions) on each side of the mean position. The vibration shows the build-up of energy in the system. The various techniques for free vibration analysis of beams on elastic foundations has been given by Ozturk and Coskun [1-3]. Various researchers have found that damage alters the system's dynamic response such as Natural Frequency and Mode shape [4]. Also, these responses can be evaluated by vibration analysis, hence, this property has been used by researchers for structural system

*Corresponding Author Institutional Email: bpatel.phd2018.ce@nitrr.ac.in (B. Patel)

Please cite this article as: B. Patel, U. K. Dewangan, A Baseline Free Method for Multiple Damage Identification and Localization using the Roving Mode Shape Response, ***International Journal of Engineering, Transactions B: Applications***, Vol. 36, No. 05, (2023) 946-954

identification [5-7]. Various structural system identification techniques particularly in the beam have been developed to date. Still, complete system identification using in-field data is a challenging issue [8]. The damage-tolerant and fail-safe design of civil structures necessitates extensive inspection and defect monitoring at regular intervals, and due to this, a lot of structural health monitoring research is going on [9]. Intelligent real-time monitoring is essential, to provide safe and affordable buildings since the danger of failure and the expense of scheduled but unnecessary maintenance are both rising. The sensor-based technologies are frequently used for this. The actuators and sensors are integrated into the structures or can be used instantly. With the advancement in sensor technology, the researchers found that the appropriate positioning of the sensor is very important in order to find out the damaged element [10]. The same algorithm may provide misleading data when the sensors are away from damaged members. The sensor position should be very close to the damage location in order to find out the damage in the structural systems [11-14]. Patel and Dewangan [15] have also found that the sensor if placed in the purview of the damage will only be able to detect the damage accurately.

Aydin et al. [16-17] provided the information on support optimization. The different beam vibrations will cause different distributions of elastic supports. Internal forces can occasionally exceed yield limits, which is significant for damage. This could be a guess for the damage existence. The mode shapes are more vulnerable to local damage since they carry local information [18]. Also, they are less sensitive to the temperature effect than the natural frequency [19]. Huang et al. [20] developed a baseline-free method for system identification based on the node displacement of structural mode shapes. It has been found that the natural frequency is significantly influenced by both temperature and damage. Consequently, using a frequency-based technique to identify the damage separately is challenging. The monitored region may be split into larger and smaller areas to improve the damage location resolution. With additional sensors, this technique might provide more accurate detection. Malekinejad and Rahgozar [21] presented a mathematical model of the cantilever beam \ for each tube through the structure's height. The free vibration analysis case has been considered. The mode shape has been calculated by simplifying the mathematical equation using Hamilton's principle and the assumptions. Various mode shape based techniques have been used by the researchers for damage identification [22-31]. Nahvi and Jabbari [32] used the experiment modal data and the natural frequency to identify the damage in the form of a crack in a cantilever beam. It can be inferred that the variations in the frequencies of higher modes rely on the distance between the crack position and the appropriate mode shape's nodes. As a result, for a crack located at the nodal points of the corresponding mode shape, the natural frequency of the cracked beam remains unchanged. Since early 1979 the introduction of the digital FFT spectrum analyzer and various other equipment has grown in popularity for determining the mode shape. However, since these types of equipment are highly expensive, they cannot be easily affordable. An effort has been made by Chandra and Samal [33] to use experimental roving impact tests to identify a beam's mode shapes without using these expensive types of equipment. The experimental modal analysis has been performed in the cantilever beam by Prashant et al. [34] and Zhang et al. [35].

Until now, there has been no reported literature on baseline free structural damage identification and localization by DLRA for multiple damages using the infield data. Hence, the primary goal of this research is to present a baseline free method using the roving mode shape response based, multiple damage identification and localization in a cantilever beam. The combined mass and stiffness damage, as well as only the mass change damage, both cases were considered. Finding the ideal position for the sensor during on-site structure health monitoring is another goal of this paper. Further, for the single damage case, many research works have been published. In order to identify the structural system with multiple damages, the sensor can be located in advance using the DLRA.

2. THEORETICAL DEVELOPMENT

The general form of the equation of motion of the linear structural system in structural dynamics is given by Equation (1):

$$M\ddot{u}(t) + C\dot{u}(t) + Ku(t) = 0 \quad (1)$$

Hence, the distributed mass and stiffness matrix is given by Equations (2) and (3), respectively.

$$M = \begin{bmatrix} 156 & 22l & 54 & -13l \\ 22l & 4l^2 & 13l & 3l^2 \\ 54 & 13l & 156 & -22l \\ -13l & 3l^2 & -22l & 4l^2 \end{bmatrix} \quad (2)$$

$$K = \begin{bmatrix} k_1 + k_2 & -k_2 & & \\ -k_2 & \cdots & & \\ & & k_{i-1} + k_i & -k_i \\ & & & k_i \end{bmatrix} \quad (3)$$

For the multiple degree of freedom system, the solution to the problem is reduced to the solution of Equation (4), which is given below:

$$([K] - \omega^2[M])\{A\} = 0 \tag{4}$$

Equation (4) represents the general form of the modal characteristic equation. The above equation is rank deficient since the rank of the matrix is less than the number of rows. Hence the mode shape and the natural frequency of the system can only be determined using the above equation. The modal amplitude perturbation matrix should be introduced as the difference between the modal amplitude of the damage structure and the undamage structure, for the i^{th} mode and $(i+1)^{th}$ mode, it is given by Equations (5) and (6), respectively.

$$(\Delta\phi)_i = (\phi_d)_i - (\phi_u)_i \tag{5}$$

$$(\Delta\phi)_{(i+1)} = (\phi_d)_{(i+1)} - (\phi_u)_{(i+1)} \tag{6}$$

Damage to the structure leads to a change in the modal amplitude. At the position of damage, it is assumed that the damage modal amplitude will change by say α times the undamage modal amplitude, hence it can be given by the below expression:

$$\phi_d = \alpha \times \phi_u \tag{7}$$

On subtracting Equation (6) from Equation (5) and substituting the value from Equation (7) into the resulted equation will be given as follows:

$$(\Delta\phi)_i - (\Delta\phi)_{(i+1)} = (1-\alpha)((\phi_d)_i - (\phi_d)_{(i+1)}) \tag{8}$$

It can be noted that the expression on the right-hand side of Equation (8) contains only the damage response along with the constant term. This damage response only, will be useful for obtaining the baseline free equation. But, the expression is not sufficient, hence further pre and post multiply Equation (8) by $(\sum_{i=1}^{N}((\phi_d)_{(i)} - (\phi_d)_{(i+1)}))/N$ on both sides and further simplifying, it can be rewritten as follows:

$$\frac{1}{1-\alpha} = X \times \frac{((\phi_d)_{(i)} - (\phi_d)_{(N)})/N}{(\Delta\phi)_i - (\Delta\phi)_{(i+1)}} \tag{9}$$

The value of X is represented by Equation (10). It has been observed that the expression contains only the damage structure responses hence the expression could be used as the damage detection and localization indicator. The proposed equation is formulated by the small amount of available structural information.

Although the above equation provides only, some general information regarding the existence of the damage, it cannot precisely detect the position of the damage. It has also been observed that the damage in its early stages could not be directly detected using the damage index given by Equation (10).

$$X = \frac{((\phi_d)_{(i)} - (\phi_d)_{(i+1)})}{(\sum_{i=1}^{N}((\phi_d)_{(i)} - (\phi_d)_{(i+1)}))/N} \tag{10}$$

This is due to the fact that differences are directly averaged over all measurement points. Further, when these data are directly plotted, the damage can not be clearly identified and located. Hence Equation (10) is further modified and given by the expression below:

$$DLRA = \frac{Abs((\phi_d)_{(i)}) - Abs((\phi_d)_{(i+1)})}{(\sum_{i=1}^{N}(Abs(\phi_d)_i - Abs(\phi_d)_{i+1}))/N} \tag{11}$$

In the above expression, the response from the roving mode shape technique will be employed to determine the value of DLRA. Consequently, Equation (11) will be used as the damage position indicator based on the roving mode shape approach. The combined mass and stiffness damage, as well as only the mass change damage, both cases could be applicable for determining the DLRA using the above expression.

3. EXPERIMENTAL ROVING TEST APPROACH

In this section, the experimental roving test approach described by Chandra and Samal [33] has been applied to estimate the modal amplitude of the cantilever beam. Aluminum was used as the beam specimen, and its material characteristics and dimensions are listed in Table 1. As shown in Figure 1(a), the 200 mm long beam was discretized into 20 elements. As a result, 10 mm was found to be the distance between the two nodes. Various damages, with varying degrees and locations of damage, were introduced. For this purpose, eleven locations were randomly chosen on the cantilever beam at a distance of 30 mm, 40 mm, 60 mm, 70 mm, 90 mm, 100 mm, 120 mm, 130 mm, 150 mm, 160 mm and 170 mm. Further, the details of the damage considered are shown in Figure 1. D1, D2, D3, D4, D5, D6, D7, D8, D9, D10 and D11

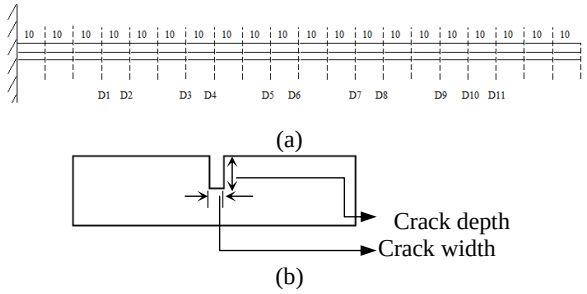

Figure 1. (a) Damage location in cantilever beam (b) Vertical section of the crack damage region

TABLE 1. Specimen details

Details	Value
Young's modulus (E)	69.1 N/mm^2
Poisson's ratio (t)	0.334
Density (q)	2668.32 x 10^{-10} N/mm^3
Dimension	(200 x 9 x 50) mm

represent the crack position, the depth of crack was taken in terms of percentage reduction in depth as 30 %, 50 % and 60 % reduction and the width of the crack is considered negligible. Table 2 provides a summary of these cases' specifics.

TABLE 2. Damage induced in the cantilever beam

Damage case	Crack location	Damage induced	
		Depth reduction (%)	Mass reduction (%)
Two elements damage cases			
Case 1	D2, D6	0.3	-
Case 2	D2, D7	0.3	-
Case 3	D4, D8	0.3	-
Case 4	D4, D9	0.3	-
Case 5	D5, D9	0.3	-
Case 6	D5, D10	0.3	-
Case 7	D2, D6	0.6	0.6
Case 8	D2, D7	0.6	0.6
Case 9	D4, D8	0.6	0.6
Case 10	D4, D9	0.6	0.6
Case 11	D5, D9	0.6	0.6
Case 12	D5, D10	0.6	0.6
Three elements damage cases			
Case 13	D2, D6, D9	0.5	-
Case 14	D2, D7, D11	0.5	-
Case 15	D4, D6, D9	0.5	-
Case 16	D4, D7, D11	0.5	-
Case 17	D5, D7, D9	0.5	-
Case 18	D5, D8, D11	0.5	-
Case 19	D2, D6, D9	0.6	0.6
Case 20	D2, D7, D11	0.6	0.6
Case 21	D4, D6, D9	0.6	0.6
Case 22	D4, D7, D11	0.6	0.6
Case 23	D5, D7, D9	0.6	0.6
Case 24	D5, D8, D11	0.6	0.6
Five elements damage cases			
Case 25	D1, D3, D5, D7, D9	0.3	-
Case 26	D1, D3, D5, D7, D11	0.3	-
Case 27	D2, D3, D5, D7, D9	0.3	-
Case 28	D2, D3, D5, D7, D11	0.3	-
Case 29	D2, D4, D6, D8, D10	0.3	-
Case 30	D2, D4, D6, D8, D11	0.3	-
Case 31	D1, D3, D5, D7, D9	0.6	0.6
Case 32	D1, D3, D5, D7, D11	0.6	0.6
Case 33	D2, D3, D5, D7, D9	0.6	0.6
Case 34	D2, D3, D5, D7, D11	0.6	0.6
Case 35	D2, D4, D6, D8, D10	0.6	0.6
Case 36	D2, D4, D6, D8, D11	0.6	0.6

Free vibration has been introduced by applying initial displacement at the free end of the beam. Signals from the accelerometers were analyzed in order to determine the natural frequencies and the amplitudes correspondingly. It has been observed that the system response for the healthy and damaged structural system has been determined using the roving mode shape approach. Damage in its early stages could not be detected using these data directly. This is due to the fact that differences are averaged over all measurement points when determining the mode shape.

Further, when these data are directly plotted, the damage could not be clearly identified and located. Hence further analysis is required, which has been addressed in section 4. The algorithm has been developed for multiple damage identification and localization using MATLAB software. It should also be noted that the proposed damage detection method inevitably and essentially depends on determining the displacement modal amplitude. It is extremely important to note that inaccurate assessments of the structure's original physical characteristics result in inaccurate damage detection.

4. STRUCTURAL MODELLING AND IDENTIFICATION

The theoretical development is carried out on a cantilever beam, using the finite element method. The two noded linear elements are used for meshing, as shown in Figure 2(a). The degree of freedom considered is vertical deflection u1 and u3 and rotation about the z-axis is u2 and u4. The finite element model is shown in Figure 2(b).

The physical properties and dimensions of the beam are mentioned in Table 1. In order to determine the effectiveness of suggested damage localization technique, several damage scenarios are taken into consideration. Table 2 provides a summary of these cases' specifics. The damages result in a sudden fluctuation in amplitude as well as adverse vibrational performances. These generated damages cause the structure to behave dynamically inadequate. The suggested DLRA using the data gathered, such as the modal parameters of the structure after the occurrence of damage, is used to identify the existence and then the position of induced damage.

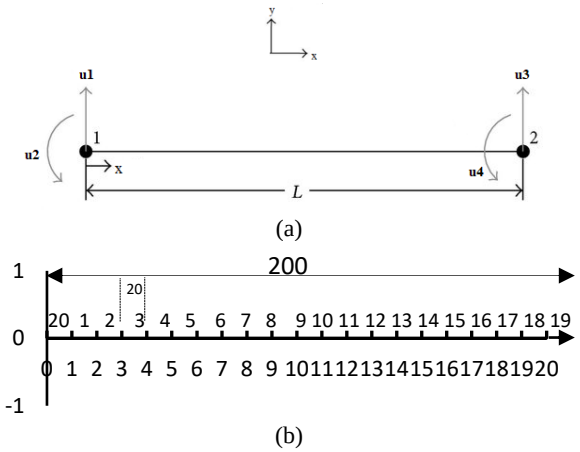

Figure 2. (a) Beam element with 2 degrees of freedom at each node. (b) Finite element model of a cantilever beam

5. RESULTS AND DISCUSSIONS

The damage localization by 'DLRA' has been plotted for various damage cases. It could predict the damage existance and locations for that particular structure very clearly. Figures 3 to 5 illustrate all the cases for, the damage without considering the mass variation. Figures 6 to 8 illustrate all the cases for the damage, by considering the mass variation. The technique provides a clear indication of DLRA for that element with multiple damages at a time, with a significance change in the numerical value, as well as it is very clear form Tables 3 to 8. For each of the damage cases, it has been observed that there are variations in the DLRA value of damage and undamaged condition of the structure at particular locations, which denotes the presence and location of the damage. This variation is approximately between 11% to 16% as stated in Table 3, the sudden fluctuation in the graph, at the damaged location, is for this reason.

The drastic shift in the amplitude of the DLRA points out the damage location. Hence, in Figure 3, that the damage position is the 4th and 10th element for damage Case 1. The DLRA is easier to calculate than the other methods due to the mass matrix's simplicity and associated damage index. Along with this, the multiple damages have been taken for up to 5 damages at a time in the present study, and the proposed algorithm is able to identify and localize the damage. These results can be clearly observed in Figures 3 to 8. Further, this algorithm will be effective for even more than 5 damages at a time. This result will also be helpful in finding the position of the sensor placement in advance. The proposed method is based on the roving mode shape response. Hence, the algorithm is useful for computer automation, which provides the self-generated technique by element automation, which could predict the damage location in terms of DLRA value element by element.

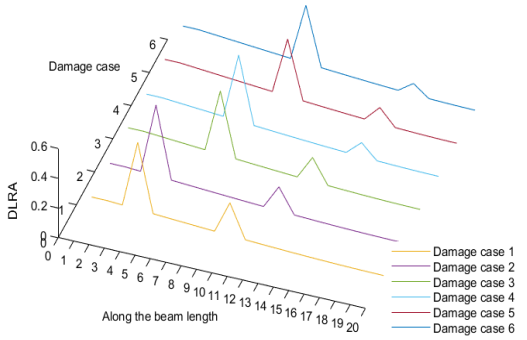

Figure 3. Plot for DLRA, for 2 elements damage

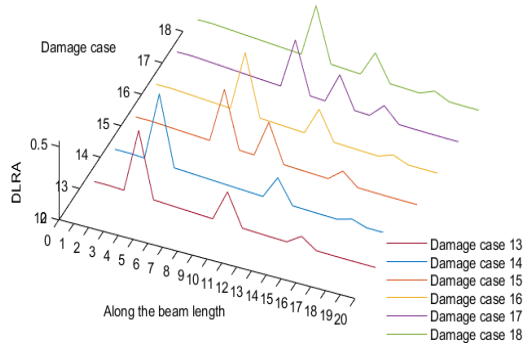

Figure 4. Plot for DLRA, for 3 elements damage

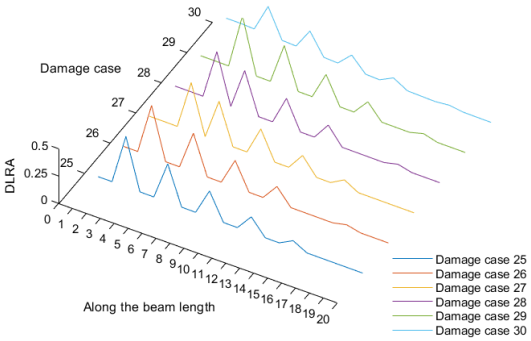

Figure 5. Plot for DLRA, for 5 elements damage

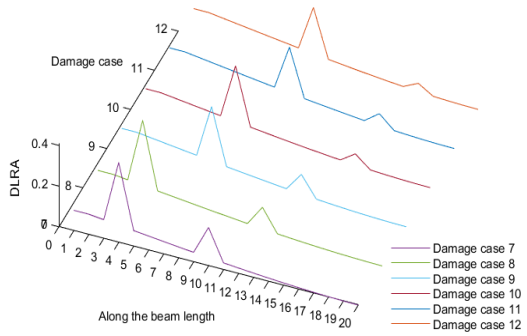

Figure 6. Plot for DLRA, for 2 elements damage

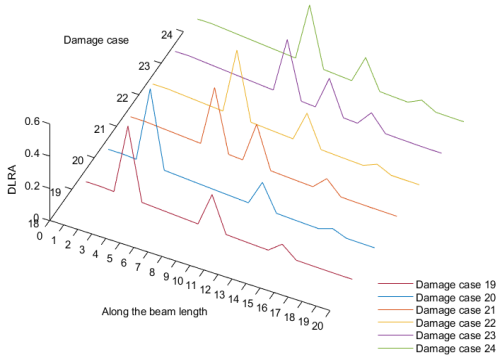

Figure 7. Plot for DLRA, for 3 elements damage

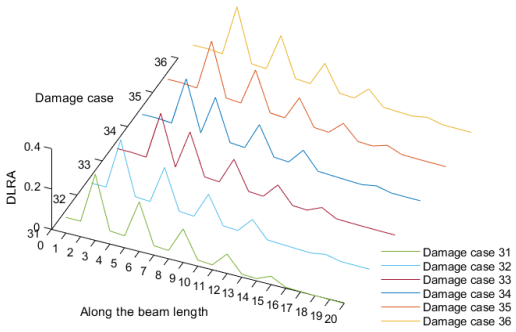

Figure 8. Plot for DLRA, for 5 elements damage

TABLE 3. The numerical result of values of DLRA

	Crack Location	Undamage DLRA	Damage DLRA	% Variation in DLRA
Case 1	D2	0.06	0.51	11.76
	D6	0.03	0.25	12.00
Case 3	D4	0.06	0.49	12.24
	D8	0.03	0.18	11.11
Case 5	D5	0.05	0.44	11.36
	D9	0.02	0.12	16.67

TABLE 4. The numerical result of values of DLRA

	Crack Location	Undamage DLRA	Damage DLRA	% Variation in DLRA
Case 13	D2	0.06	0.50	12.00
	D6	0.03	0.25	12.00
	D9	0.01	0.08	12.50
Case 15	D4	0.05	0.43	11.62
	D6	0.03	0.29	10.34
	D9	0.01	0.09	11.11
Case 17	D5	0.05	0.40	12.50
	D7	0.03	0.24	12.50
	D9	0.02	0.11	18.18

TABLE 5. The numerical result of values of DLRA

	Crack Location	Undamage DLRA	Damage DLRA	% Variation in DLRA
Case 25	D1	0.012	0.475	2.53
	D3	0.010	0.360	2.78
	D5	0.007	0.249	2.81
	D7	0.004	0.149	2.68
	D9	0.002	0.068	2.94
Case 27	D2	0.013	0.460	2.82
	D3	0.011	0.381	2.89
	D5	0.007	0.265	2.64
	D7	0.004	0.159	2.52
	D9	0.002	0.073	2.74
Case 29	D2	0.015	0.515	2.91
	D4	0.011	0.382	2.88
	D6	0.007	0.256	2.73
	D8	0.004	0.143	2.80
	D10	0.001	0.057	1.75

TABLE 6. The numerical result of values of DLRA

	Crack Location	Undamage DLRA	Damage DLRA	% Variation in DLRA
Case 7	D2	0.08	0.39	20.51
	D6	0.04	0.19	21.05
Case 9	D4	0.07	0.34	20.59
	D8	0.03	0.12	25.00
Case 11	D5	0.06	0.29	20.69
	D9	0.02	0.08	25.00

TABLE 7. The numerical result of values of DLRA

	Crack Location	Undamage DLRA	Damage DLRA	% Variation in DLRA
Case 19	D2	0.08	0.39	20.51
	D6	0.04	0.19	21.05
	D9	0.01	0.06	16.67
Case 21	D4	0.06	0.32	18.75
	D6	0.04	0.21	19.05
	D9	0.01	0.06	16.67
Case 23	D5	0.07	0.27	25.93
	D7	0.04	0.16	25
	D9	0.02	0.07	28.57

TABLE 8. The numerical result of values of DLRA

	Crack Location	Undamage DLRA	Damage DLRA	% Variation in DLRA
Case 31	D1	0.077	0.328	23.48
	D3	0.059	0.246	23.98
	D5	0.040	0.168	23.81
	D7	0.023	0.098	23.47
	D9	0.010	0.043	23.26
Case 33	D2	0.073	0.310	23.55
	D3	0.060	0.254	23.62
	D5	0.040	0.173	23.12
	D7	0.024	0.101	23.76
	D9	0.011	0.045	24.44
Case 35	D2	0.077	0.329	23.40
	D4	0.057	0.241	23.65
	D6	0.037	0.158	23.42
	D8	0.020	0.086	23.26
	D10	0.007	0.032	21.88

TABLE 9. Comparative study of DLRA with similar methods, for the Damage Case 31

S. No.	Method	Multiple Damage location (5 damages at a time)		Percentage variance (%)	Average Percentage variance (%)
		Actual damage location (mm)	Identified damage location (mm)		
1.	Approximate curvature method [36]	30	33	10	9.4
		60	65	8.3	
		90	99	10	
		120	131	9.2	
		150	164	9.3	
2.	Mode shape damage index method (MSDI) [37]	30	31	3.3	3.3
		60	62	3.3	
		90	92	2.2	
		120	125	4.2	
		150	155	3.3	
3.	Mode shape based damage detection (MBDD) [38]	30	31	3.3	1.5
		60	61	1.7	
		90	89	-1.1	
		120	122	1.7	
		150	153	2.0	
4.	DLRA	30	30	0	0.1
		60	60	0	
		90	90	0	
		120	120	0	
		150	151	0.7	

6. FINAL REMARKS

In this study, a new method for damage identification has been proposed for assessing the structural multiple damages at a time, in the cantilever beam. Further for the single damage case, many research works have been published, and the multiple damages have been taken for up to 4 damages at a time. This algorithm will be effective for even more than 5 damages at a time. In the first stage of this method, the existence and position of damaged elements are identified by considering the damage with no mass variation. Subsequently, the effect of mass variation is considered. In order to assess the proposed method, the experimental roving test approach described has been applied to estimate the modal amplitude of the cantilever beam. The extracted modal data from experimental modal testing are usually complex values. For identifying the damage positions, further analysis is required, which has been addressed in section 2, where the algorithm is described to form a damage location indicator. The location indicator is defined by the DLRA. It should be noted that the results of DLRA depend on the correct determination of the structural model's initial information. It has been found that the DLRA was able to capture and localize the damage accurately which is clear from Figures 3 to 8. The proposed methodology will also be helpful while keeping the sensor positions very close to the damaged location. The algorithm is useful for computer automation, which provides the self-generated technique by element automation, which could predict the damage location in terms of DLRA value element by element.

7. REFERENCES

1. Ozturk, B. and Coskun, S. B., "Analytical Solution for Free Vibration Analysis of Beam on Elastic Foundation with Different Support Conditions", ***Mathematical Problems in Engineering***, Vol. 2013, (2013), doi: 10.1155/2013/470927
2. Ozturk, B., "Free Vibration Analysis of Beam on Elastic Foundation by the Variational Iteration Method", ***International Journal of Nonlinear Sciences and Numerical Simulation***, Vol. 10, No. 10, (2009), 1255-1262. doi: 10.1515/IJNSNS.2009.10.10.1255
3. Ozturk, B. and Coskun, S. B., "The Homotopy Perturbation Method for free vibration analysis of beam on elastic foundation", ***Structural Engineering and Mechanics***, Vol. 37, No. 4, (2011) 415-425. doi: 10.12989/sem.2011.37.4.415
4. Fan, W., Qiao, P., "Vibration-based damage identification methods: a review and comparative study." ***Structural Health Monitoring***, Vol. 10, No. 1, (2011), 83-111. doi: 10.1177/1475921710365419
5. Jayasundara, N., Thambiratnam, D., Chan, T., Nguyen, A., "Vibration-based dual-criteria approach for damage detection in arch bridges." ***Structural Health Monitoring*** Vol. 18, (2019). doi: 10.1177/1475921718810011
6. Weijtjens, W., Verbelen, T., Capello, E., Devriendt, C., "Vibration based structural health monitoring of the substructures

of five offshore wind turbines." ***Procedia Engineering,*** 199, (2017), 2294-2299. doi: 10.1016/j.proeng.2017.09.187

7. Ubertini, F., Comanducci, G., Cavalagli, N., "Vibration-based structural health monitoring of a historic bell-tower using output-only measurements and multivariate statistical analysis." ***Structural Health Monitoring,*** Vol. 15, No. 4, (2016), 15:438–57. doi: 10.1177/147592171664394
8. Patel, B., Dewangan, U. K., "Damage Detection Techniques to Identify the Unknown Damage Parameters from the Structural Response Data in Beam: A Review." Pathak, K.K., Bandara, J.M.S.J., Agrawal, R. (eds) ***Recent Trends in Civil Engineering. LNCE***, Springer, Singapore. Vol 77. (2021) 175-183. doi: 10.1007/978-981-15-5195-6_13
9. Banerjee, S., Ricci, F., Monaco, E., Ajit, Ma., "A wave propagation and vibration-based approach for damage identification in structural components." ***Journal of Sound and Vibration***, Vol. 322, (2009), 167-183. doi: 10.1016/j.jsv.2008.11.010
10. Alamatian, J., Rezaeepazhand, J., "A simple approach for determination of actuator and sensor locations in smart structures subjected to the dynamic loads." ***International Journal of Engineering, Transactions A: Basics***, Vol. 24, No. 4, (2011). doi: 10.5829/idosi.ije.2011.24.04a.03
11. Bruant, I., Coffignal, G., Lene, F. and Verge, M., "A methodology for determination of piezoelectric actuator and sensor location on beam structures." ***Journal of Sound and Vibration,*** Vol. 243, No. 5, (2001), 861- 882. doi: 10.1006/jsvi.2000.3448
12. Hac, A. and Liu, L., "Sensor and actuator location in motion control of flexible structures", ***Journal of Sound and Vibration,*** Vol. 167, (1993), 239-261. DOI: 10.1006/jsvi.1993.1333
13. Kondoh, S., Yatomi, C. and Inoue, K., "The positioning of sensors and actuators in the vibration control of flexible systems", ***JSME International Journal***, Vol. 33, No. 3, (1992), 145-152. doi: 10.1299/jsmec1988.33.145
14. Arbel, A., "Controllability measures and actuator placement in oscillatory systems", ***International Journal of Control***, 33, (1981), 565-574. doi: 10.1080/00207178108922941
15. Patel, B., Dewangan, U. K., "The Behaviour of Wave Propagation for Structural System Identification: A Comparative Study" ***International Journal of Engineering, Transactions C: Aspects,*** Vol. 35, No. 12, (2022) 2305-2312. doi: 10.5829/ije.2022.35.12c.05
16. Aydin, E., Dutkiewicz, M., Ozturk, B. and Sonmez, M., "Optimization of elastic spring supports for cantilever beams", ***Structural and Multidisciplinary Optimization***, Vol. 62, No. 1, (2020), 55-81. doi: 10.1007/s00158-019-02469-3. 5.
17. Aydın, E., Ozturk, B. and Dutkiewicz, M., "Determination of optimal elastic springs for cantilever beams supported by elastic foundation", ***Proceedings of 24th International Conference Engineering Mechanics*** 2018 (Svratka, Czech Republic, 2018), (2018), 33-36, doi: 10.21495/91-8-33. 6.
18. Caddemi, S., Morassi, A., "Multi-cracked Euler-Bernoulli beams: mathematical modeling and solutions." ***International Journal of Solids and Structures,*** Vol. 50, No. 6, (2013), 944-956. doi: 10.1016/j.ijsolstr.2012.11.018
19. Dilena, M., Morassi, A., Perin, M., "Dynamic identification of a reinforced concrete damaged bridge." ***Mechanical Systems and Signal Processing***, Vol. 25, No. 8, (2009), 2990-3009. doi: 10.1016/j.ymssp.2011.05.016
20. Huang, T., Chaves-Vargas, M., Yang, J., Schröder, K. U., "A baseline-free structural damage indicator based on node displacement of structural mode shapes." ***Journal of Sound and Vibration,*** Vol. 433, (2018), 366-384. doi: 10.1016/j.jsv.2018.07.001
21. Malekinejad, M., Rahgozar, R., "A closed form solution for free vibration analysis of tube-in-tube systems in tall buildings" ***International Journal of Engineering, Transactions A: Basics,*** Vol. 25, No. 2, (2012). doi: 10.5829/idosi.ije.2012.25.02a.01
22. Hassan Ghasemi, M., Mofid Nakhaei, A., & Dardel, M., "A Simple Method for Modeling Open Cracked Beam." ***International Journal of Engineering, Transactions B: Applications,*** Vol. 28, No. 2, (2015), 321-329. doi: 10.5829/idosi.ije.2015.28.02b.20
23. Ismail, Z., Razak H. A., Rahman A. G. A.., "Determination of damage location in RC beams using mode shape derivatives." ***Engineering Structures,*** Vol. 28, No. 11, (2006), 1566-1573. doi: 10.1016/j.engstruct.2006.02.010
24. Pandey, A. K., Biswas, M., Samman, M. M., "Damage detection from changes in curvature mode shapes." ***Journal of Sound and Vibration***, Vol. 145, No. 2, (1991), 321-332. DOI: 10.1016/0022-460X(91)90595-B
25. Hansen, J. B., Brincker, R., López-Aenlle, M., Overgaard, C. F., Kloborg K., "A new scenario-based approach to damage detection using operational modal parameter estimates." ***Mechanical Systems and Signal Processing***, Vol. 94, No. 15, (2017), 359-373. doi: 10.1016/j.ymssp.2017.03.007
26. Abdel Wahab MM, De Roeck G., "Damage detection in bridges using modal curvatures: application to a real damage scenario." ***Journal of Sound and Vibration,*** Vol. 226, No. 2, (1999), 217-235. doi: 10.1006/jsvi.1999.2295
27. Roy, K., Ray-Chaudhuri, S., "Fundamental mode shape and its derivatives in structural damage localization." ***Journal of Sound and Vibration,*** Vol. 332, No. 21, (2013), 5584-5593. doi: 10.1016/j.jsv.2013.05.003
28. Yazdanpanah, O., Seyedpoor, S. M., Bengar, H. A., "A new damage detection indicator for beams based on mode shape data." ***Structural Engineering & Mechanics,*** Vol. 53, No. 4, (2015), 725-744. doi: 10.12989/sem.2015.53.4.725
29. Ratcliffe, C. P., "Damage detection using a modified laplacian operator on mode shape data." ***Journal of Sound and Vibration***, Vol. 204, No. 3, (1997), 505-517. doi: 10.1006/jsvi.1997.0961
30. Talaei, S., Beitollahi, A., Moshirabadi, S., Fallahian, M., "Vibration-based structural damage detection using Twin Gaussian Process (TGP)." ***Structures,*** Vol. 16, (2018) 10-19. doi: 10.1016/j.istruc.2018.08.006
31. Chance, J., Tomlinson, G. R., Worden, K., "A simplified approach to the numerical and experimental modeling of the dynamics of a cracked beam." ***In Proceedings-SPIE the International Society for Optical Engineering,*** (1994), 778-785.
32. Nahvi, H., Jabbari, M., "Crack detection in beams using experimental modal data and finite element model." ***International Journal of Mechanical Sciences,*** Vol. 47, No. 10, (2005) 147771497. doi: 10.1016/j.ijmecsci.2005.06.008
33. Chandra, C. A., Samal, P. K., "Experimental determination of mode shapes of beams by roving impact test." ***Materials Today: Proceedings,*** Vol. 46, No. 19, (2021) 9159-9163. doi: 10.1016/j.matpr.2020.01.119
34. Prashant, S. W., Chougule, V. N., Mitra, A. C., "Investigation on modal parameters of rectangular cantilever beam using experimental modal analysis." ***Materials Today: Proceedings,*** (2015), 2121-2130, doi: 10.1016/j.matpr.2015.07.214
35. Zhang, Y., Guo, J., Jia, T., Cheng, H., "Experimental research on frequency-based damage identification of beams with free boundary condition." ***Ocean Engineering***, Vol. 266, No. 2, (2022), 112901. doi: 10.1016/j.oceaneng.2022.112901
36. Duong, T. H., "On the use of mode shape curvature for multi-crack detection in beam like structures." ***International Journal of Civil Engineering and Technology***, Vol. 10, No. 6, (2019), 54-65. doi: 10.34218/IJCIET.10.6.2019.006

37. Duvnjak, I., Damjanovic, D., Bartolac, M., Skender, A., "Mode Shape-Based Damage Detection Method (MSDI): Experimental Validation." ***Applied Sciences***, Vol. 11, No. 10, (2021), 4589. doi: 10.3390/app11104589

38. Kim, J. T., Ryu, Y. S., Cho, H. M., Stubbs, N., "Damage identification in beam-type structures: frequency-based method versus mode-shape-based method." ***Engineering Structures***, Vol. 25, No. 1, (2003), 57-67. doi: 10.1016/s0141-0296(02)00118-9

Persian Abstract

چکیده

شناسایی سیستم‌های سازه‌ای با پاسخ امضای ارتعاش ناشناخته هنوز یک موضوع چالش برانگیز است که توسط بسیاری از بازبین‌ها مورد توجه قرار گرفته است .فناوری حسگر فعلی بیان می‌کند که موقعیت سنسور باید بسیار نزدیک به عنصر آسیب‌دیده باشد تا آسیب را شناسایی و محلی‌سازی کند .هدف اصلی این تحقیق ارائه یک روش بدون خط مبنا با استفاده از پاسخ شکل حالت چرخشی مبتنی بر مکان‌یابی آسیب چندگانه در یک تیر کنسول است .در نتیجه، نشانگر مکان آسیب بر اساس رویکرد شکل حالت چرخشی (DLRA) است .توسعه نظری بر روی یک تیر کنسول، یک مدل المان محدود انجام شده است .موارد مختلف برای آسیب های متعدد یعنی آسیب ۲ المان، آسیب ۳ عنصر و۵ المان آسیب در یک زمان بر روی عضو سازه مدل شده است .پاسخ سیستم، برای سیستم های ساختاری سالم و آسیب دیده، با استفاده از رویکرد شکل حالت چرخشی تعیین شده است .علاوه بر این، الگوریتم برای شناسایی آسیب های متعدد و محلی سازی با استفاده از نرم افزار MATLAB توسعه یافته است .آسیب ترکیبی جرم و سفتی، و همچنین تنها آسیب تغییر جرم، هر دو مورد در نظر گرفته شد .از نتایج، مشخص شد که روش پیشنهادی می‌تواند آسیب و موقعیت آن را با اطمینان شناسایی کند .این روش همچنین در حالی که موقعیت سنسور را بسیار نزدیک به آسیب نگه می دارد مفید خواهد بود .تازگی این روش این است که از پاسخی استفاده می کند که اساساً یک خروجی میدانی است و هیچ فرض قبلی در محل عنصر آسیب دیده انجام نشده است.

International Journal of Engineering

Journal Homepage: www.ije.ir

Utilization of Steel Micro-fiber and Carbon Nanotubes in Self-compacting Lightweight Concrete

Y. Mohammadi*[a], M. Bagheripour Asil[b]

[a] *Department of Civil Engineering, University of Mohaghegh Ardabili, Ardabil, Iran*
[b] *Department of Civil Engineering, University of Guilan, Rasht, Iran*

PAPER INFO

Paper history:
Received date 09 February 2023
Received in revised form 03 March 2023
Accepted 11 March 2023

Keywords:
Carbon Nanotubes
Steel Micro-fibers
Self-compacting Lightweight Concrete
Mechanical Characteristics
Durability Characteristics

ABSTRACT

In this research, the engineering characteristics of self-compacting lightweight concrete (SCLWC) containing carbon nanotubes and steel micro-fiber were evaluated. The variables included the amount of carbon nanotubes (0, 0.02, 0.04, and 0.06% by weight of cement) and steel micro-fiber (0, 0.5, and 1% by volume). Lightweight expanded clay aggregate was used as lightweight aggregates. The experimental tests were self-compacting tests, compressive, splitting tensile, and flexural strengths, ultrasonic pulse velocity, electrical resistivity, water penetration depth, and scanning electron microscope. Adding 0.02 to 0.06 percent of carbon nanotubes to SCLWC reinforced with steel micro-fiber increases the compressive strength by about 33 to 64 percent. The use of 0.06% carbon nanotubes and 1% steel micro-fiber increased the splitting tensile strength by 36%. The use of carbon nanotubes and steel micro-fiber has the effect of influencing the filling of empty spaces and reducing concrete porosity. This can be attributed to the growing process of cement paste hydration and the filling of pores and capillary pores with the products of cement reactions, resulting in concrete compaction. Adding 0.02% carbon nanotubes to SCLWC samples containing 0.5% and 1% steel micro fibers increased the 28-day compressive strength by 36%, 34% and 33%, respectively.

doi: *10.5829/ije.2023.36.05b.12*

1. INTRODUCTION

The use of old materials and traditional construction methods no longer meets the desired speed and design needs. Therefore, the use of new and effective materials along with new techniques in construction is inevitable [1-3]. Researchers are trying to produce desirable structures by reducing the weight of concrete structures, easing their construction, using high-strength materials, and increasing durability in destructive environments. Lightweight concrete (LWC) has attracted the attention of researchers as a suitable option for building concrete structures [4-7]. Fiber concrete with high strength has many structural applications [8]. The strength of fiber concrete under static and dynamic loads is increased and the propagation of cracks and crushing is reduced [9, 10]. In recent years, extensive research has been done for the advancement and innovation in the use of micron fibers and nanoparticles to improve the mechanical behavior of cement and concrete compounds [11, 12]. According to these micron-scale research studies, it is very important to pay attention to nanoparticles with the help of knowledge and nanotechnology and study their effects on concrete properties.

Afzali and Mazloum [13] investigated the fresh and hardened properties of LWC-containing nano-silica. The results showed that the combined use of silica fume and nano-silica had a more effective role in improving the characteristics of LWC.

Abd Elrahman et al. [14] investigated the effect of silica nanoparticles on the characteristics, durability, and microstructure of LWC. Silica nanoparticles modified the structure of fine pores and thus improved the transfer characteristics. Wu et al. [15] investigated LWC reinforced with steel and carbon fibers. The water-to-cement ratio and the characteristics of the aggregates can

* Corresponding Author Email: Yaghoubm@uma.ac.ir
(Y. Mohammadi)

Please cite this article as: Y. Mohammadi, M. Bagheripour Asil, Utilization of Steel Micro-fiber and Carbon Nanotubes in Self-compacting Lightweight Concrete, ***International Journal of Engineering, Transactions B: Applications***, Vol. 36, No. 05, (2023) 955-964

have a role in influencing the results. Badogiannis et al. [16] evaluated LWC reinforced with steel and polypropylene fibers. For this purpose, pumice was used as a filler. The use of fibers improves the mechanical properties of LWC and significantly increases the compressive and flexural strengths. It was also shown that the use of fibers improves the cracking resistance of concrete. Yeganeh et al. [17] investigated the characteristics of fiber LWC. For this purpose, three types of high-density polyethylene fibers, rubber crumbs, and polyvinyl alcohol were used. The fibers decreased the crack width in the failure stage. Lan et al. [18] investigated carbon nanotube-modified concrete. They showed that carbon nanotubes improved the characteristics of concrete by improving crack resistance. Liu et al. [19] evaluated the effect of carbon nanotubes on reactive powder concrete performance in a sulfate dry-wet cycling environment. Carbon nanotubes limited concrete cracks.

Considering the advantages mentioned about the use of steel fibers, and carbon nanotubes, in the present study, self-compacting lightweight concrete (SCLWC) containing different volume ratios of steel micro-fiber and carbon nanotubes was investigated. Finally, an optimal combination of the mentioned additives was determined.

2. MATERIAL CHARACTERISTICS AND METHODS

2. 1. Material The materials used in the present laboratory study included sand, lightweight expanded clay aggregate (LECA), cement, water, superplasticizer, carbon nanotubes, and steel micro-fiber. The sand used was natural sand. According to ASTM-C33 [20], the grading curve of the used sand is illustrated in Figure 1. Natural sands are river sands that are extracted from riverbeds. The characteristics of these sands are their rounded corners. The sand was obtained from the Joben Rudbar mine located in Gilan province, Iran. This sand was free of harmful particles and dust. The specific gravity, fineness Modulus, and water absorption of the sand used were 2627 kg/m^3, 2.89 and 3%, respectively.

The specific weight of the used LECA is 660 kg/m^3 (Figure 2(a)). The LECA granulation curve is presented in Figure 1. The LECA granulation curve is within the permissible range of ASTMC33 [21] standard.

The specifications of the carbon nanotubes are listed in Table 1. They were prepared by the Iranian oil industry research institute and have a specific surface area of 3200 g/cm^3 and a density of 15.3 g/cm^3. Carbon nanotubes are cylinders of carbon whose wall diameter is about nanometers. These tubes are seamless and made of one or more carbon layers. They are available in single-walled (SWCNT) and multi-walled (MWCNT) forms. In these tubes, carbon atoms with a hexagonal and hollow

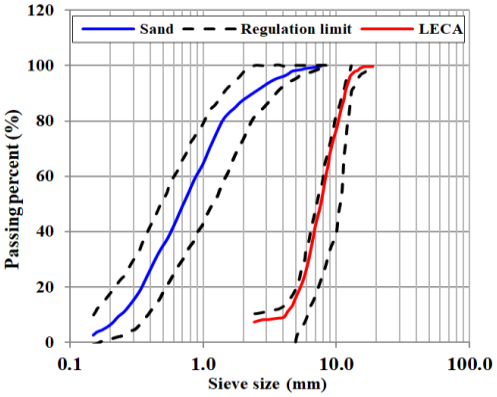

Figure 1. The grading curve of the sand and LECA

(a) (b)

Figure 2. Material used (a) LECA (b) Carbon nanotubes

TABLE 1. The properties of carbon nanotubes

Characteristic	Quantity
External diameter (nm)	20-30
Length (mm)	10
Ash percentage (%)	0.2
Purity (%)	95
Specific surface (m^2/gr)	250-280
Amorphous carbon (%)	3

ring structure were placed together, giving a cylindrical shape to the structure (Figure 2(b)).

The fibers used in this research were of the straight type and had micro dimensions (diameter 0.15 and length 14 mm). (Table 2). Despite the advantages of microfibers, some considerations should be made to distribute the fibers uniformly prevent separation or the phenomenon of lumping and create an effective mixture for concreting, densification, and polishing of concrete, sieving is one of these methods.

The pH of the water is about 7.5. The Polycarboxylate superplasticizer was used in order to achieve the desired workability.

2. 2. Experimental Methods The tests related to fresh concrete according to EFNAC [21] method included V-funnel, T50, L-box, and slump flow tests.

TABLE 2. The properties of steel micro-fiber

Characteristic	Quantity
Length (mm)	20-30
Diameter (mm)	10
Tensile strength (MPa)	0.2

Self-compacting concrete measurement parameters were used to measure the workability of self-compacting concrete containing carbon nanotubes and steel micro-fiber.

The compressive strength (CSt) test was performed in accordance with ASTM C39 [22]. The tensile strength of concrete was determined using the split tensile strength (SPTSt) test according to ASTM C496 [23].

The ultrasonic pulse velocity was measured using a non-destructive ultrasonic device according to ASTM C597 [24]. This test is proposed based on the theory of ultrasound transmission inside the material, which is generally used to obtain information about concrete porosity [25, 26].

Electrical resistivity (ER) is considered an indicator of communication between holes. This index determines the resistance of concrete against the penetration of liquid or gas through the concrete surface which is in contact with the outside environment. This parameter is considered one of the most key parameters related to the durability of concrete. Electrical resistance is one of the intrinsic properties of materials, which mainly depends on the nature and topography of the cavity structure, humidity conditions, temperature, and concentration of dissolved ions in the environment [27-29]. In order to perform this test, an electrical resistance measuring device with a variable frequency of 10 to 10000 Hz was used. ER was calculated using Equation (1).

$$\rho = \frac{R.A}{L} \quad (1)$$

In this regard, ρ is specific ER, R is Electrical resistance, A is the surface area of the concrete in square meters and L is the distance between the positive and negative poles.

Estimating the probability of corrosion of reinforcements buried in concrete based on ER is presented in Table 3.

The water penetration depth (WPD) in the SCLWC samples was determined according to DIN 1048-5. According to this test underwater pressure at a certain time, the WPD in concrete is determined. The cubic samples were taken out of the water pool for 28 days and kept inside the oven for 20 hours at a temperature of 111°C to dry completely. For one day (24 hours), the samples were placed in the device for determining the WPD, and under a pressure equal to 10 bars after the test, they were split in half using a cutting device and divided into two halves, and the WPD was measured [30].

2. 3. Mixed Design The specifications of the mixing plant and the amounts of each of the consumables are presented in Table 4. The desired mixing design was

TABLE 3. Estimating the probability of corrosion of reinforcements buried in concrete based on ER [31, 32]

ER (kΩ-m)	Possibility of corrosion
50<	Very high
50-100	High
100-200	Moderate
200>	Very low

TABLE 4. Mixture design

Mix code	W/B	Cement (kg/m^3)	CN	SMF	W	Sand	LECA	SP
CNTs0SF0	0.4	405	0	0	180	950	393	1.15
CNTs0SF0.5	0.4	405	0	0.5	180	950	393	1.20
CNTs0SF1	0.4	405	0	1	180	950	393	1.25
CNTs0.02SF0	0.4	396.9	8.1	0	180	950	393	1.17
CNTs0.02SF0.5	0.4	396.9	8.1	0.5	180	950	393	1.23
CNTs0.02SF1	0.4	396.9	8.1	1	180	950	393	1.30
CNTs0.04SF0	0.4	388.8	16.2	0	180	950	393	1.21
CNTs0.04SF0.5	0.4	388.8	16.2	0.5	180	950	393	1.27
CNTs0.04SF1	0.4	388.8	16.2	1	180	950	393	1.35
CNTs0.06SF0	0.4	380.7	24.3	0	180	950	393	1.26
CNTs0.06SF0.5	0.4	380.7	24.3	0.5	180	950	393	1.34
CNTs0.06SF1	0.4	380.7	24.3	1	180	950	393	1.40

W: Water B: Binder CN: Carbon nanotubes MSF: Steel micro-fiber
LECA: Light Expanded Clay Aggregate SP: Superplasticizer

obtained using past experimental studies and by trial and error in accordance with ACI [30]. The variables include carbon nanoparticles (0, 0.5, 1, 1.5, and 2% by weight of cement) and steel micro-fiber (0, 0.5, and 1% by volume of concrete), respectively. After making and molding, the samples were kept in the mold for 24 hours. Then, it was taken out of the mold and subjected to moisture treatment until the tests were performed.

3. EXPERIMENTAL RESULTS

3. 1. Examining the Properties of Fresh Concrete

The concrete should be workable but not excessively bleeding. Concrete bleeding is the movement of water toward the surface of freshly poured concrete, which is caused by the settling of solid materials including cement, sand, and gravel inside the concrete mass. The settling of solid particles is the result of the sum of the effects of shaking and the weight of the particles [33]. Figure 3 shows the values of concrete slump flow in seconds and the formation time of 500 mm diameter in seconds (T50). The slump flow of the control sample was found to be 782 mm. The use of 0.5% and 1% steel micro-fiber caused the slump flow to be 768 and 756 mm, respectively; that is, the addition of 0.5% and 1% steel micro-fiber reduced the slump flow of LWC by about 1.8% and 3.3%.

Also, the slump flow of LWC samples without fibers and containing 0.02, 0.04, and 0.06 % of carbon nanotubes are 751, 752, and 691 mm, respectively. Adding 0.02, 0.04 and 0.06 % of carbon nanotubes reduced the slump flow by 4, 3.8, and 11.6 %, respectively. Also, the combined use of carbon nanotubes and steel micro-fiber reduced the slump flow. For example, the combined use of 0.06% of carbon nanotubes and 1% of steel micro-fiber reduced the slump flow of SCLWC by about 15%.

The slump flow range is by the EFNARC standard in the range of 650 to 800 mm. All SCLWC samples are in this range. Although the addition of steel micro-fiber and carbon nanotubes reduces the slump flow of LWC, it is possible to overcome this problem by using a superplasticizer and achieve concrete with permissible slump flow. Of course, excessive use of polycarboxylate-based superplasticizers leads to an increase in concrete aeration and affects the mechanical and reliability characteristics of concrete.

By increasing the percentage of carbon nanotubes, the amount of slump current also increases. The reason for this can be attributed to the roughness of the mixture and its tendency to flow. Concretes with carbon nanotubes and steel micro-fiber have the lowest amount of slump flow.

In Figure 3 in addition to the slump current, T50 values are also compared with each other. The use of both types of proposed materials has increased the T50 time and reduced the fluidity of concrete. So that the T50 time of the control sample is equal to 1.4 seconds and the T50 time of the sample containing 0.06% carbon nanotubes and 0.5% steel micro-fiber is 4.9 seconds. Also, the allowed range introduced for T50 is between 2 and 5 seconds, and all the samples made are in this range.

Figure 4 compares the concrete discharge time from the V-shaped funnel and the blockage ratio in the L-box test. The results of the V-funnel and L-box tests are in agreement with the slump flow and T50 tests; because in these two experiments, the addition of steel micro-fiber and carbon nanotubes affected the workability of concrete and led to a decrease in the flowability of LWC samples.

According to the EFNARC recommendation, the time for concrete discharge from the V-funnel is between 6 and 12 seconds. As it is known, the time related to the emptying of the witness concrete from the V-shaped funnel is equal to 2.8 seconds. Meanwhile, the time for emptying the concrete containing 0.06% carbon nanotubes and 1% steel micro-fiber is equal to 10.9 seconds. On the other hand, the diagram related to the blocking ratio of the L box test in Figure 4 is descending.

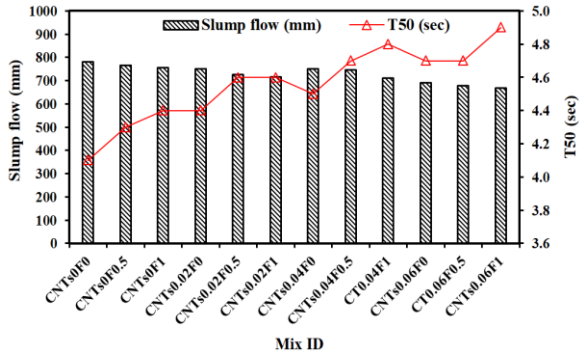

Figure 3. Comparison of slump flow values and T50 times of SCLWC samples

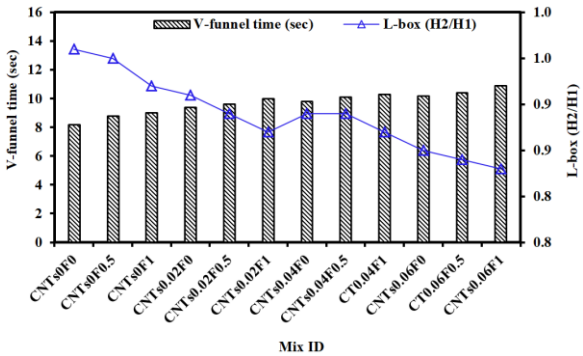

Figure 4. Comparison of the concrete discharge time from the V funnel and the blockage ratio in the L box test

Steel micro-fiber reduces the flow of concrete by creating friction in LWCs containing LECA and carbon nanotubes. To overcome this problem, you can use super lubricant within the allowed range. The allowed occlusion ratio introduced by EFNARC is between 0.8 and 1. All the samples made are in this range.

3. 2. Mechanical Characteristics

3. 2. 1. CSt Figures 5 and 6 compare the CSt of 7 and 28 days of SCLWC samples, respectively. The use of carbon nanotubes has a role in increasing the CSt of SCLWC samples with and without steel micro-fibers. In SCLWC samples without steel micro-fibers, the addition of 0.02, 0.04, and 0.06% of carbon nanotubes has increased the 7-day CSt by 35, 57, and 62%, respectively. In SCLWC samples containing 0.5% of steel micro-fibers, the addition of 0.02%, 0.04%, and 0.06% of carbon nanotubes increased the 7-day CSt by 34%, 58%, and 64%, respectively. Also, in SCLWC samples containing 1% steel micro-fibers, the addition of 0.02%, 0.04%, and 0.06% carbon nanotubes has increased the 7-day CSt by 32%, 53%, and 62%, respectively. Therefore, it can be stated that the addition of 0.02 to 0.06 carbon nanotubes to SCLWC reinforced with steel micro-fibers increases the 7-day CSt by about 32 to 64%, depending on the amount of microfibers.

Figure 4 compares the 28-day CSt of SCLWC samples. The addition of carbon nanotubes to all samples has led to an increase in the 28-day CSt.

The 28-day CSt of SCLWC samples containing 0, 0.5, and 1% of steel micro-fibers, in which without carbon nanotubes were 22.2, 22.5, and 22.9 MPa, respectively. The addition of 0.02 to SCLWC samples containing 0, 0.5, and 1% steel microfibers has increased the 28-day CSt by 36, 34, and 33%, respectively. Adding 0.04 to SCLWC samples containing 0, 0.5, and 1% steel microfibers increased the 28-day CSt by 58, 59, and 54%, respectively. Also, the addition of 0.06 to SCLWC samples containing 0, 0.5, and 1% steel microfibers increased the 28-day CSt by 63, 64, and 63%, respectively.

3. 2. 2. SPTSt The addition of 0.02, 0.04 and 0.06% of carbon nanotubes increased the SPTSt by 13, 20 and 27%, respectively (Figure 7). Also, the addition of 0.5% and 1% steel micro-fibers increased the SPTSt by 15% and 19%. The combined use of 0.06% of carbon nanotubes and 1% of steel fibers increased the SPTSt by 36%. Therefore, it can be stated that the use of carbon nanotubes and steel micro-fibers together has a more effective role compared to the single use of each of them.

ACI 318-99 [34] and EN 1992-1 [35] regulations introduce a range for tensile strength based on cylindrical CSt. These ranges are presented in Figure 8.

Since these relationships are between cylindrical CSt and tensile strength, and the strength results of the upcoming study were obtained on cubic samples based on the test results, first, the CSt results obtained from the cubic sample were converted to cylindrical CSt. Figure 8 shows the relationship between the tensile and CSts values of the upcoming study and the aforementioned regulations, as well as the studies of Coquillat [36] and Berg [37]. The results of the present study are very close to the experimental curves introduced by ACI318-99 [34].

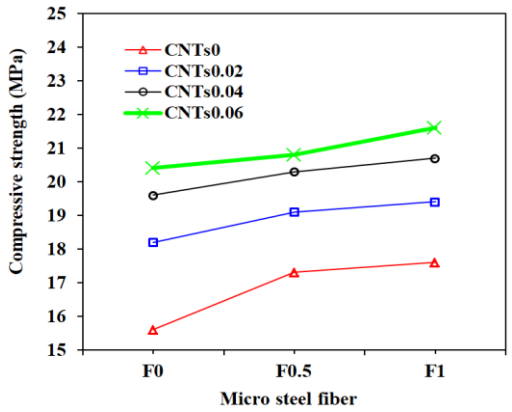

Figure 5. Comparison of 7-day CSt of SCLWC samples

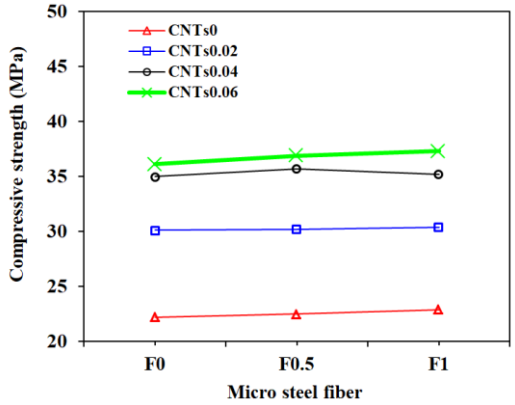

Figure 6. Comparing the 28-day CSt of SCLWC

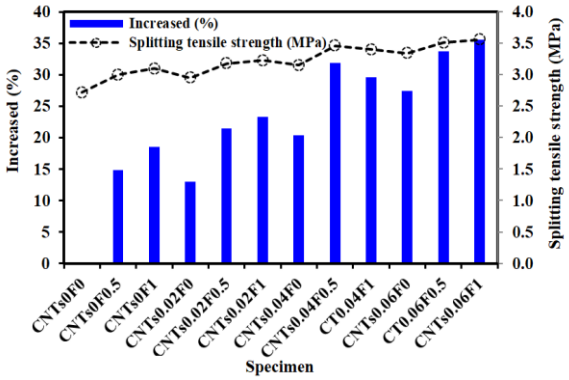

Figure 7. SPTSt and percentage increase

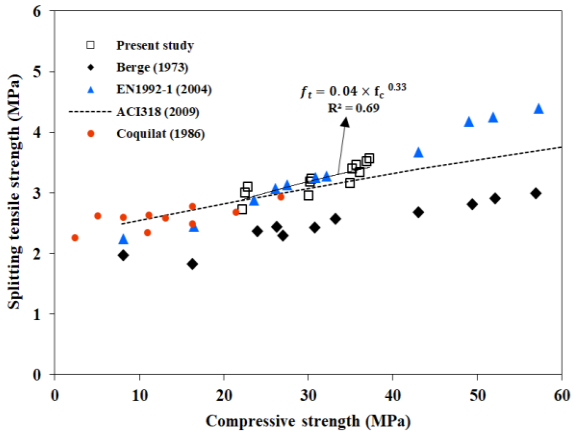

Figure 8. The relationship between the CSt and SPTSt of SCLWC containing steel micro-fibers and carbon nanotubes

Based on Figure 8, Equation (3) presented.

$$f_t = 0.4 \times (f_c)^{0.33} \quad (3)$$

3. 2. 3. Ultrasonic Pulse Velocity This test can be done at a low cost and quickly, which confirms its suitability from every point of view for evaluation. In this research, the trend of changes in the ultrasonic pulse velocity was investigated in different designs at the age of 28 days for 10×10×10 cm samples. In Figure 9 the results of ultrasonic pulse velocity against the CSt of cubic concrete samples are presented. Whitehurst [37] classified concrete into five categories based on the speed of ultrasonic waves: excellent (greater than 4500 m/s), good (3500 to 4500 m/s), questionable (3000 to 3500 m/s), poor (2000 to 3000 m/s) and very weak (less than 2000 m/s). According to this classification, all designs are in the "good" range. More porosity results in a lower pulse velocity.

The use of carbon nanotubes and steel micro-fibers together leads to an improvement in concrete density. The carbon nanotubes fill the fine pores of the cement, and the steel micro-fibers prevent the development of micro cracks. The rate of increase in ultrasonic pulse velocity was observed to be slower than the compressive resistance. The steel micro-fibers increased the ultrasonic pulse velocity.

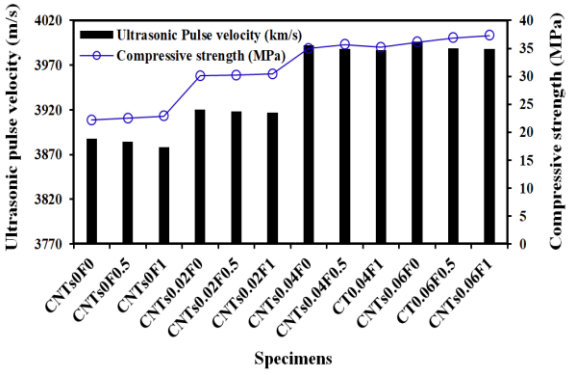

Figure 9. CSt and ultrasonic pulse velocity

3. 2. 4. Microstructure of the Concrete Samples Four samples were selected to represent the manufactured samples and their SEM images were prepared (Figure 10). These samples include CNTs0F0, CNTs0F1, CNTs0.04F0 and CNTs0.04F1, respectively.

The purpose of choosing these SCLWC samples was to evaluate the effect of steel micro-fibers and carbon nanotubes individually and in combination on the microstructure of SCLWC. The use of carbon nanotubes in combination with steel micro-fibers is effective in making SCCLWC contain LECA. The steel micro-fibers prevent the crack from spreading and the carbon nanotubes fill the holes created by the microfibers. Also, carbon nanotubes lead to improvements in the mechanical properties and durability of concrete by filling the very small holes in the cement.

3. 3. Durability Characteristics

3. 3. 1. ER In Figure 11, the ER of the SCLWC samples at 90 days of age is compared with each other.

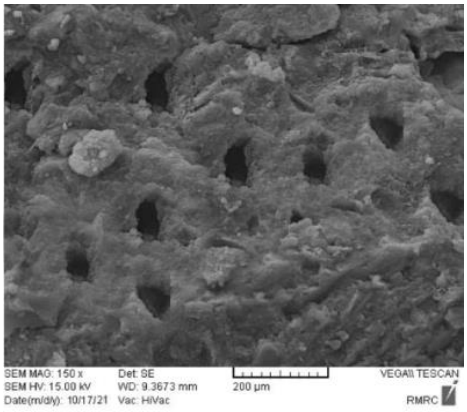

CNTs0F0

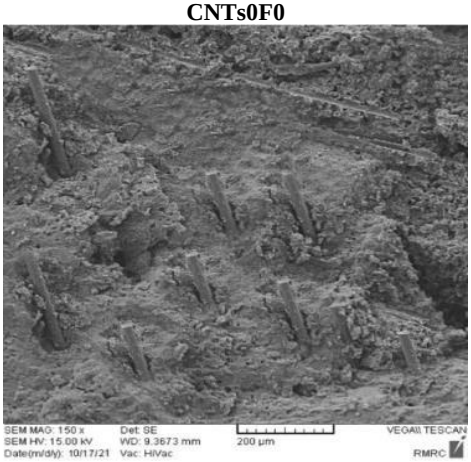

CNTs0F1

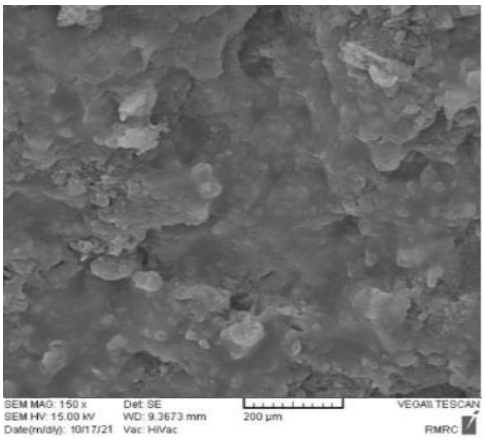

CNTs0.04F0

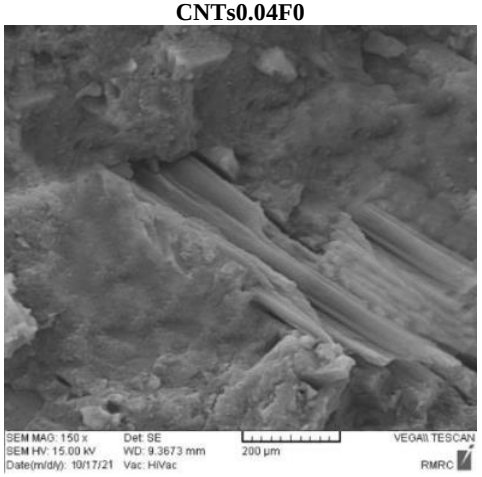

CNTs0.04F1

Figure 10. Microstructure examination of concrete samples

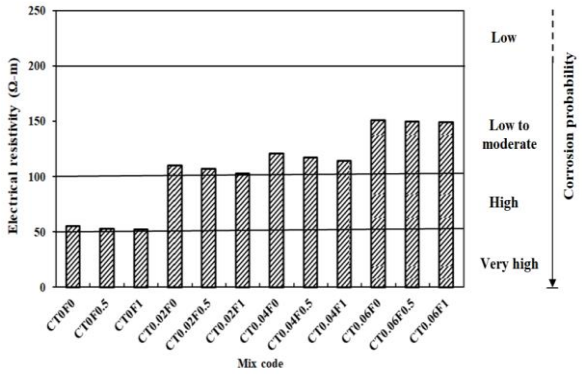

Figure 11. ER of samples in different states

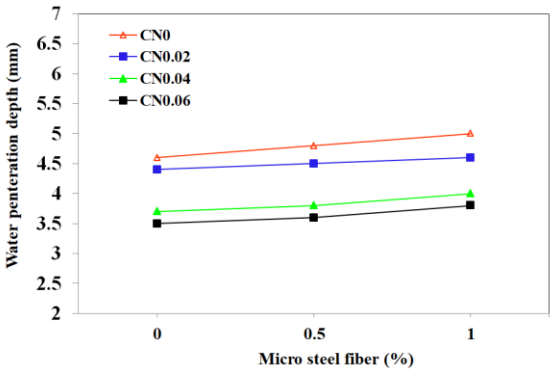

Figure 12. The WPD of samples in different modes

The higher the electrical resistance, the more durable and desirable concrete will be, and its corrosion will be less. Song and Saraswathy [29] and Alki and Selevold [30] divide concrete into four categories in terms of corrosion probability. Adding carbon nanotubes to SCLWC samples containing steel micro-fibers has been effective and has increased the electrical resistance by 87-173% compared to the control sample. As a result, concrete corrosion is reduced. In other words, the resistance of concrete against corrosion increases. The electrical resistance of all samples with fibers is lower than the control sample. This issue is due to the fact that the presence of fibers in concrete increases the air content of the concrete, and in this way, the electrical resistance decreases in samples reinforced with fibers.

3. 3. 2. Water Penetration Depth (WPD) The addition of carbon nanotubes to SCLWC samples containing steel micro-fibers significantly reduced the WPD (Figure 12). Adding 0.02, 0.04 and 0.06 percent of carbon nanotubes to samples without steel micro-fibers reduced the WPD by 4, 19 and 24 percent, respectively. Adding 0.02%, 0.04% and 0.06% of carbon nanotubes to the SCLWC samples containing 0.5% steel micro-fibers reduced the WPD by 6%, 21% and 25%, respectively. Also, adding 0.02, 0.04, and 0.06 percent of carbon nanotubes to the SCLWC samples containing 1 percent of steel micro-fibers reduced the WPD by 8, 20, and 24 percent, respectively. The powder effect and pozzolanic reaction speed of the used carbon nanotubes are among the reasons for the reduction of water infiltration inside the investigated SCLWC samples.

4. CONCLUSIONS

In this study, the rheological, mechanical, durability, and microstructure characteristics of concretes containing steel micro-fibers and carbon nanotubes by performing slump flow, T50, L box, and V funnel tests, CSt, SPTSt strength, speed of ultrasonic waves, electrical resistance, water absorption, determination of water penetration depth and microscopic photography were evaluated.

- Although the addition of steel micro-fibers and carbon nanotubes reduces the slump flow of LWC; it is possible to overcome this problem by using superplasticizer and achieve concrete with permissible slump flow. Of course, excessive use of polycarboxylate-based superplasticizers leads to an

increase in concrete aeration and affects the mechanical and reliability characteristics of concrete.
- By increasing the amount of carbon nanotubes, the amount of slump current increases. The reason for this can be attributed to the roughness of the mixture and its lower tendency to flow. Concretes with carbon nanotubes and steel micro-fibers have the lowest amount of slump flow.
- The addition of steel micro-fibers and carbon nanotubes affected the workability of concrete and led to a decrease in the flowability of SCLWC samples.
- Steel micro-fibers reduced the flow of concrete by creating friction in LWC containing LECA and carbon nanotubes. To overcome this problem, a superplasticizer within the allowed range can be used.
- Adding carbon nanotubes from 0.02 to 0.06 to LWC reinforced with steel micro-fibers increases the 7-day CSt by about 32 to 64%, depending on the amount of steel microfibers.
- Adding 0.02% carbon nanotubes to SCLWC samples containing 0.5% and 1% steel microfibers has increased the 28-day CSt by 36%, 34%, and 33%, respectively.
- Adding 0.04 percent of carbon nanotubes to SCLWC samples containing 0, 0.5, and 1 percent of steel micro fibers has increased the 28-day CSt by 58, 59, and 54 percent, respectively.
- The addition of 0.06 percent of carbon nanotubes to SCLWC samples containing 0, 0.5, and 1 percent of steel micro-fibers has increased the 28-day CSt by 63, 64, and 63 percent, respectively.
- The addition of 0.02, 0.04, and 0.06 carbon nanotubes has increased the SPTSt by 13, 20, and 27%, respectively. Also, the addition of 0.5% and 1% steel micro-fibers has increased the SPTSt by 15% and 19%, respectively. The combined use of 0.06% of carbon nanotubes and 1% of steel fibers has increased the SPTSt by 36%. Therefore, it can be stated that the combined use of carbon nanotubes and steel micro-fibers has a more effective role compared to the single use of each of them.
- The combined use of carbon nanotubes and steel micro-fibers has the effect of influencing the filling of empty spaces and reducing concrete porosity. This can be attributed to the growing process of cement paste hydration and the filling of pores and capillary pores with the products of cement reactions, resulting in concrete compaction.
- The addition of carbon nanotubes to the SCLWC samples with and without steel micro-fibers causes a great increase in electrical resistance. The resistance of concrete against corrosion increases. The electrical resistance of all SCLWC samples with fibers is lower than the control sample. The resistance decreases due to the presence of metal particles.
- Adding 0.02, 0.04, and 0.06 percent of carbon nanotubes to SCLWC samples without steel micro-fibers reduced the WPD by 4, 19, and 24 percent, respectively. Adding 0.02%, 0.04%, and 0.06% of carbon nanotubes to the SCLWC samples containing 0.5% steel micro-fibers has reduced the water penetration depth by 6%, 21%, and 25%, respectively. Also, adding 0.02, 0.04, and 0.06 percent of carbon nanotubes to the samples containing 1 percent of steel micro-fibers has reduced the depth of water penetration by 8, 20, and 24 percent, respectively.

5. REFERENCES

1. Faez, A., Sayari, A. and Manie, S., "Mechanical and rheological properties of self-compacting concrete containing al 2 o 3 nanoparticles and silica fume", ***Iranian Journal of Science and Technology, Transactions of Civil Engineering***, Vol. 44, No., (2020), 217-227. doi: 10.1007/s40996-019-00339-y.
2. Heidarzad Moghaddam, H., Lotfollahi-Yaghin, M. and Maleki, A., "Durability and mechanical properties of self-compacting concretes with combined use of aluminium oxide nanoparticles and glass fiber", ***International Journal of Engineering, Transactions A: Basics***, Vol. 34, No. 1, (2021), 26-38. doi: 10.5829/ije.2021.34.01a.04.
3. Ghanbari, M., Kohnehpooshi, O. and Tohidi, M., "Retrofitting of reinforced concrete beams using lightweight rc jacket containing silica nano particles and glass fiber", ***International Journal of Engineering, Transactions B: Applications***, Vol. 35, No. 11, (2022), 2164-2175. doi: 10.5829/ije.2022.35.11b.11.
4. Zhang, S., Liu, L., Tan, K., Zhang, L. and Tang, K., "Influence of burning temperature and cooling methods on strength of high carbon ferrochrome slag lightweight aggregate", ***Construction and Building Materials***, Vol. 93, No., (2015), 1180-1187. doi: 10.1016/j.conbuildmat.2015.04.045.
5. Ghanbari, M., Kohnehpooshi, O. and Tohidi, M., "Experimental study of the combined use of fiber and nano silica particles on the properties of lightweight self compacting concrete", ***International Journal of Engineering, Transactions B: Applications***, Vol. 33, No. 8, (2020), 1499-1511. doi: 10.5829/ije.2020.33.08b.08.
6. Asil, M.B. and Ranjbar, M.M., "Hybrid effect of carbon nanotubes and basalt fibers on mechanical, durability, and microstructure properties of lightweight geopolymer concretes", ***Construction and Building Materials***, Vol. 357, No., (2022), 129352. doi: 10.1016/j.conbuildmat.2022.129352.
7. Perez-Garcia, A., Víllora, A.G. and Pérez, G.G., "Building's eco-efficiency improvements based on reinforced concrete multilayer structural panels", ***Energy and buildings***, Vol. 85, No., (2014), 1-11. doi: 10.1016/j.enbuild.2014.08.018.
8. Zhao, C., Wang, Z., Zhu, Z., Guo, Q., Wu, X. and Zhao, R., "Research on different types of fiber reinforced concrete in recent years: An overview", ***Construction and Building Materials***, Vol. 365, No., (2023), 130075. doi: 10.1016/j.conbuildmat.2022.130075.
9. Wu, H., Shen, A., Ren, G., Ma, Q., Wang, Z., Cheng, Q. and Li, Y., "Dynamic mechanical properties of fiber-reinforced concrete: A review", ***Construction and Building Materials***, Vol. 366, No., (2023), 130145. doi: 10.1016/j.conbuildmat.2022.130145.
10. Hasan, R., Sobuz, M.H.R., Akid, A.S.M., Awall, M.R., Houda, M., Saha, A., Meraz, M.M., Islam, M.S. and Sutan, N.M., "Eco-

friendly self-consolidating concrete production with reinforcing jute fiber", ***Journal of Building Engineering***, Vol. 63, (2023), 105519. doi: 10.1016/j.jobe.2022.105519.

11. Coşkun, S. and Öztürk, B., "Analysis of longitudinal vibration of nanorods via homotopy perturbation method", 5th International Conference on Advances in Mechanical Engineering (ICAME 2019), December 2019, Istanbul, Turkey.
12. Coşkun, S. and Öztürk, B., "Stability of nanobeams via homotopy perturbation method", 5th International Conference on Advances in Mechanical Engineering (ICAME 2019), Istanbul, Turkey.
13. Afzali-Naniz, O. and Mazloom, M., "Assessment of the influence of micro-and nano-silica on the behavior of self-compacting lightweight concrete using full factorial design", ***Asian Journal of Civil Engineering***, Vol. 20, (2019), 57-70. doi: 10.1007/s42107-018-0088-2.
14. Abd Elrahman, M., Chung, S.-Y., Sikora, P., Rucinska, T. and Stephan, D., "Influence of nanosilica on mechanical properties, sorptivity, and microstructure of lightweight concrete", ***Materials***, Vol. 12, No. 19, (2019), 3078. doi: 10.3390/ma12193078.
15. Wu, T., Yang, X., Wei, H. and Liu, X., "Mechanical properties and microstructure of lightweight aggregate concrete with and without fibers", ***Construction and Building Materials***, Vol. 199, (2019), 526-539. doi: 10.3390/ma12193078.
16. Badogiannis, E., Christidis, K. and Tzanetatos, G., "Evaluation of the mechanical behavior of pumice lightweight concrete reinforced with steel and polypropylene fibers", ***Construction and Building Materials***, Vol. 196, (2019), 443-456. doi: 10.1016/j.conbuildmat.2018.11.109.
17. Ehsani Yeganeh, A., Kouroshnezhad, F., Dadsetan, S., Hossain, K.M. and Lachemi, M., "Experimental investigation on mechanical properties of fiber reinforced lightweight self-consolidating concrete", in Rheology and Processing of Construction Materials: RheoCon2 & SCC9 2, Springer. (2020), 536-543.
18. Lan, Y., Zheng, B., Shi, T., Ma, C., Liu, Y. and Zhao, Z., "Crack resistance properties of carbon nanotube-modified concrete", ***Magazine of Concrete Research***, Vol. 74, No. 22, (2022), 1165-1175. doi: 10.1680/jmacr.21.00227.
19. Liu, G., Kan, D., Cao, S.C., Chen, Z. and Lyu, Q., "Effect of multi-walled carbon nanotube on reactive powder concrete (rpc) performance in sulfate dry-wet cycling environment", ***Construction and Building Materials***, Vol. 342, (2022), 128075. doi: 10.1016/j.conbuildmat.2022.128075.
20. Standard, A., "C33/c33m-18", Standard specification for concrete aggregates. ASTM International, West Conshohocken PA, (2018).
21. EFNARC, F., "Specification and guidelines for self-compacting concrete", European federation of specialist construction chemicals and concrete system, (2002).
22. Concrete, A.I.C.C.o. and Aggregates, C., "Standard test method for compressive strength of cylindrical concrete specimens, ASTM international, (2014).
23. Concrete, A.I.C.C.o. and Aggregates, C., "Standard test method for splitting tensile strength of cylindrical concrete specimens1, ASTM international, (2017).
24. Astm, C., "597, standard test method for pulse velocity through concrete", ASTM International, West Conshohocken, PA, (2009).
25. Vasconcelos, G., Lourenço, P.B., Alves, C. and Pamplona, J., "Ultrasonic evaluation of the physical and mechanical properties of granites", ***Ultrasonics***, Vol. 48, No. 5, (2008), 453-466. doi: 10.1016/j.ultras.2008.03.008.
26. Sayyadi, A., Mohammadi, Y. and Adlparvar, M.R., "Mechanical, durability, and gamma ray shielding characteristics of heavyweight concrete containing serpentine aggregates and lead waste slag", ***Advances in Civil Engineering***, Vol. 2023, (2023). doi: 10.1155/2023/7873637.
27. Ramezanianpour, A.A., Pilvar, A., Mahdikhani, M. and Moodi, F., "Practical evaluation of relationship between concrete resistivity, water penetration, rapid chloride penetration and compressive strength", ***Construction and Building Materials***, Vol. 25, No. 5, (2011), 2472-2479. doi: 10.1016/j.conbuildmat.2010.11.069.
28. Sengul, O. and Gjørv, O.E., "Electrical resistivity measurements for quality control during concrete construction", ***ACI Materials Journal***, Vol. 105, No. 6, (2008), 541.
29. Song, H.-W. and Saraswathy, V., "Corrosion monitoring of reinforced concrete structures-a", ***International Journal of Electrochemical Science***, Vol. 2, No. 1, (2007), 1-28.
30. Akers, D.J., Gruber, R.D., Ramme, B.W., Boyle, M.J., Grygar, J.G., Rowe, S.K., Bremner, T.W., Kluckowski, E.S., Sheetz, S.R. and Burg, R.G., "Guide for structural lightweight-aggregate concrete", ACI 213R-03. American Concrete Institute (ACI), Michigan, (2003).
31. Elkey, W. and Sellevold, E.J., "Electrical resistivity of concrete", Norwegian Road Research Laboratory, Oslo, Norway, (1995).
32. En, B., "12390-8," depth of penetration of water under pressure", ***British Standards Institution***, (2000).
33. Bartos, P., "Fresh concrete: Properties and tests, Elsevier, Vol. 38, (2013).
34. Concrete, S.-C., "American concrete institute; farmington hills, mi, USA: 2007", ACI 237R-07.[Google Scholar].
35. Code, P., "Eurocode 2: Design of concrete structures-part 1–1: General rules and rules for buildings", British Standard Institution, London, (2005).
36. Coquillat, G., "Influence des caractéristiques physiques et mécaniques des granulats légers sur les propriétés des bétons legers de structure", Arnould, M.; M. Virlogeux, M.(eds.) Granulats et betons legers-Bilan de dix ans de recherches, (1986), 255-298.
37. Berge, O., "Reinforced structures in lightweight concrete", PhDThesis, Stockholm, Publ, No. 47, (1973).

Persian Abstract

چکیده

در این تحقیق، ویژگی‌های مهندسی بتن سبک خود متراکم (SCLWC)حاوی نانولوله‌های کربنی و میکروالیاف فولادی مورد ارزیابی قرار گرفت. متغیرها شامل مقدار نانولوله کربنی (۰، ۰.۰۲، ۰.۰٤ و ۰.۰٦ درصد وزنی سیمان) و میکروالیاف فولادی (۰، ۰.۵ و ۱ درصد حجمی) بودند. از سنگدانه های رس منبسط شده سبک وزن به عنوان سنگدانه های سبک استفاده شد. آزمون های خود تراکم، مقاومت فشاری، شکاف کششی و خمشی، سرعت پالس اولتراسونیک، مقاومت الکتریکی، عمق نفوذ آب و میکروسکوپ الکترونی روبشی بودند. افزودن ۰.۰۲ تا ۰.۰٦ درصد نانولوله های کربنی به SCLWC تقویت شده با میکروالیاف فولادی، مقاومت فشاری را حدود ۳۳ تا ٦٤ درصد افزایش می دهد. استفاده از نانولوله های کربنی ۰.۰٦ درصد و میکروالیاف فولادی ۱ درصد استحکام کششی شکافتگی را تا ۳٦ درصد افزایش داد. استفاده از نانولوله های کربنی و میکروالیاف فولادی بر پر شدن فضاهای خالی و کاهش تخلخل بتن تأثیر می گذارد. این را می توان به روند رو به رشد هیدراتاسیون خمیر سیمان و پر شدن منافذ و منافذ مویرگی با محصولات واکنش سیمان و در نتیجه تراکم بتن نسبت داد. افزودن ۰.۰۲ درصد نانولوله های کربنی به نمونه های SCLWC حاوی ۰.۵ درصد و ۱ درصد الیاف میکرو فولاد، مقاومت فشاری ۲۸ روزه را به ترتیب ۳٦، ۳٤ و ۳۳ درصد افزایش داد.

IJE TRANSACTIONS B: Applications Vol. 36, No. 05, (May 2023) 965-978

International Journal of Engineering

Journal Homepage: www.ije.ir

Comparative Environmental Impact Assessment of Battery Electric Vehicles and Conventional Vehicles: A Case Study of India

A. P. Bhosale*, S. A. Mastud

Department of Mechanical Engineering, Veermata Jijabai Technological Institute (VJTI), Mumbai, India

PAPER INFO

Paper history:
Received 17 February 2023
Received in revised form 26 February 2023
Accepted 27 February 2023

Keywords:
Life Cycle Analysis
Electric Vehicles
Battery Electric Vehicles
Environmental Analysis

ABSTRACT

The battery electric vehicle (BEV) adaptation is at an accelerated pace due to its zero tail-pipe emissions and estimated environmental benefits. However, when considering an electric vehicle's entire life cycle, the environmental benefit could be a deception. It should be reckoned whether electric vehicles are really environmentally friendly and if they are, then under which conditions? According to the literature, the carbon footprint of electric mobility varies by geographic location as well as by the regional energy mix and the environmental impacts might exacerbate by introducing a plethora of electric vehicle. Since very less research has been carried out in the Indian context; this paper contemplates the environmental impacts of BEV and compares it with conventional vehicles performing a life cycle assessment.The paramount purpose of the study is to unveil weather BEVs are low carbon transport mode in India and where do they stand compared globaly. The results reveal that out of 18 impact categories considered under mid-point analysis, BEV outperformed IC Engine vehicles for 10 categories. The green house gases emissions from a BEV is 242 g CO_2eq/km at mid-point level and the single score at end-point level is 0.58 kpt compared to that of ICEV which has 2.1 kpt. Further, separate impacts from the production and the use-to-end life phase were derived to pinpoint the major emission contribution phase. At the ReCePi end-point analysis BEV favors being more environmentally friendly, however, switching to cleaner energy will further alleviate the environmental impacts.

***doi**: 10.5829/ije.2023.36.05b.13*

1. INTRODUCTION

The development of electric vehicles has become a global endeavour in the hope of electrifying road transportation which is techno-economic-environmentally better than conventional vehicles. Because of this, a large number of alternative fuel vehicles (Electric & Hybrid) may be witnessed in the near future. Elucidating the mode shift from conventional vehicles to electric vehicles attributes to mitigation of emissions, omitting high fuel prices, and resolving the national energy security issue. Observing these benefits, BEVs are considered as a potential substitute to promote sustainable transportation. Hauschild et al. [1] stated that: cost, customer satisfaction and performance are the backbones of the automotive market. The same applies for Electric Vehicle's (EV's) successful deployment in the existing vehicle fleet. Environmental impact plays a significant role in public opinion and market acceptance which is closely associated with customer satisfaction.

Although electric vehicle technology is at a nascent stage in India, comparatively, the EV's deployment pace is much slower. Additionally, for the Financial Year 2022, the adoption of electric four-wheelers is much behind that of electric three- and two-wheeled vehicles[1]. This may be attributed to the high initial cost, lack of credible infrastructures such as charging stations, environmental concerns, range anxiety and low awareness [2-4]. The statistics for electric vehicles sold in India for the past three financial years is illustrated in Figure 1. Murugan and Marisamynathan [5] have stressed to focus on range anxiety (travel distance) and high initial cost as governing parameters to promote electric two-wheelers. High initial cost is depicted as a

*Corresponding Author Email: apbhosale_p18@me.vjti.ac.in (A. P. Bhosale)

[1] https://www.statista.com/statistics/1234761/india-electric-vehicle-sales-by-type/

Please cite this article as: A. P. Bhosale, S. A. Mastud, Comparative Environmental Impact Assessment of Battery Electric Vehicles and Conventional Vehicles: A Case Study of India, ***International Journal of Engineering, Transactions B: Applications***, Vol. 36, No. 05, (2023) 965-978

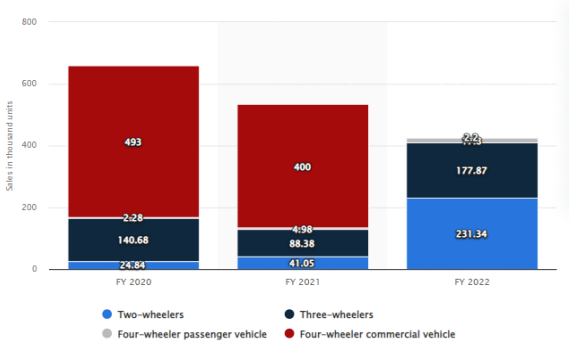

Figure 1. Electric vehicles sold in India for last three financial years [2]

significant barrier by conducting a Total Cost of Ownership (TCO) analysis for electric four wheeled vehicles Gilmore and Patwardhan [6], Bhosale et al. [7]; moreover, charging facilities are found to be another significant barrier for customers in India Murugan and Marisamynathan [8]. The high initial cost, infrastructure and range anxiety are tangible factors and can be mitigated with the help of means such as: providing incentives and special exemptions for EV (for high initial cost), proper policies such as government-private collaborations (for infrastructure) and developing research (for better battery technology). However, from an environmental perspective, which is an intangible factor, more efforts are required unless until which the basic purpose for mode changing to e-transport and the electric vehicle's bandwagon will remain incoherent.

The low EV uptake in India have encompassed many researchers to contemplate about its causes and encouraged to find the remedies Goel et al. [2], Singh et al. [9], Kumar et al. [10], Shrimali [11]. Further, Chaturvedi et al. [13] has expressed a complex interplay between various stakeholders in Indian EV industry and has suggested the possible remedies. In this prospect the government of India have also implemented imperative tools by introducing National Electric Mobility Mission Plan-2020 (NEMMP-2020) [12]. Observing the slower adoption of electric vehicles, the government also extended the promulgation by incentivising the EVs through policy titled as "Faster Adoption and Manufacturing of (hybrid &) Electric vehicles in India (FAME I & II)"[1]. The NEMMP 2020 and FAME I & II schemes were accepted with alacrity and the government prognosticated the replacement of all passenger and light weight vehicles with electric vehicles[2]. However, observing the discrepancy between the acceptance and implementation due to various barriers, the government re-quoted the announcement to replace only 30% total fleet by electric vehicles[3].

One of the major concerns for India related to the national energy security is the umpteen crude oil import bills. India is third largest oil importer in the world and more than 81% of the crude oil requirement relies on import rather than indigenous sources[4]. Additionally, the cost of importing crude oil doubled from the previous year to roughly $120 billion for FY 2022[5]. The second concern which is closely related to energy security is the alarming pollution. The transport category ranks third in CO_2 emissions where as road transport contributed the most in total transport category[6]. These much vexed questions of national energy security and environmental concerns avenues the need for electric vehicles which are found to be a potential substitute. The necessity of the article is to prevent the further exabaration of the already saddled environmental issues in India. The BEVs play a complex interplay with the environmental concerns which when intruded at a greater pace in India, can make the situation more worse than that in present. The article/study is necessary to find out the intensity of the environmental impacts arrising from a BEV which will further help to frame the forthcomming policies in order to fight this major concern. Further, to the best of our knowledge the emissions estimation comparison from both vehicles is rarel done in India. This article uses a innvoative implementation of LCA software named OpenLCA which is based on ReCePi 2016 methodology with using realistic data rather than relying on generic data which defends the novelty of the study. As discussed earlier, the environmental aspect regarding electric vehicles, which is an intangible factor, needs to be meticulously contemplated. This article unveils the environmental effects of BEVs in comparison to traditional ICEVs with regard to the Indian context. The structure of the acticle is as follows: 1. Introduction: Gives the current status and statistics of electric vehicles in India, the major concerns, the need to approach this study and a brief light on the innovativeness of the article. 2. Literature Review: Highlights the current barriers for electric vehicles, approching the dicussion of the environmental concerns around the globe including all

[1] https://fame2.heavyindustries.gov.in/content/english/15_1_FAMEI.aspx, https://fame2.heavyindustries.gov.in/content/english/13_1_brief.aspx

[2] http://lithiumionbattery.org/industry-updates/news/india-aiming-for-all-electric-car-fleet-by-2030-petrol-and-diesel-to-be-tanked#:~:text=India%20is%20looking%20at%20having,vehicles%20self%2D%20sufficient%20like%20UJALA.

[3] https://asia.nikkei.com/Economy/India-starts-argument-over-realistic-EV-targets-for-2030 accessed 06/11/2022

[4] https://www.newindianexpress.com/business/2022/jul/14/indias-crude-imports-from-russia-up-72-timesin-april-may-2022-2476374.html#:~:text=India%20is%20the%20world's%20third,and%2014%25%20from%20the%20US

[5] https://economictimes.indiatimes.com/industry/energy/oil-gas/indias-oil-import-bill-doubles-to-usd-119-bn-in-fy22/articleshow/91049349.cms accessed 07/11/2022

[6] https://pib.gov.in/PressReleasePage.aspx?PRID=1748514#:~:text=India%20has%20a%20massive%20and,of%20the%20total%20CO2%20emissions

the impact categorie. 3. Drivers, Method and Objective: Explains the motivation for the study and the prime objective. Further the methodology used to approach the study. 4. Results and Discussion: Illustrated the findings of the study and interpreats the outcomes. 5. Conclusion: Gives briefly the major findings and the attributed causes and resole approach.

2. LITERATURE REVIEW

The transportation system is completely built around the ICEVs which have high impact on the environment [13-15]. Additionally, emissions from IC Engine Vehicles have always been notorious of all the emission sources [16, 17]. Moreover, it unveiled that IC Engine vehicles will dominate the global vehicle market till 2040 due to complex interplay of demand-supply, energy policy and technology trends reported by Kalghatgi [18]. Therefore, when more vehicles are added to the global number, the environmental impact will exacerbate. The BEVs are looked upon as a potential alternative to ICEVs due to their zero tailpipe emissions. Considering this benefit, many governments around the globe are aggressively introducing electric vehicles with the help of various tools under the rubrics of sustainability reported by Yong and Park [19], Heidrich et al. [20] Lieven et al. [21] Mohanty et al. [22]. The overall effects and techno-economic-environmental aspect of deployment of electric vehicles are reckoned by Bharathidasan et al. [23] along with the environmental concern. Additionally, it is observed the greenhouse gases emissions from lifecycle of an electric vehicle relies on manufacturing technique and the energy mixture used to recharge electric cars [10, 24, 25]. Nevertheless, using the electric vehicles without de-carbonizing the source of electricity will simply hamstring the electric vehicle's environmental benefits (zero tailpipe emissions). The environmental impact include emissions of gaseous pollutions such as CO, CO_2, NO_x, VOC, SO_2, metal particulates such as mercury and lead, other organic pollutants and particulate matter. The secondary concern with these umpteen conventional vehicles is the noise level/pollution. The limit noise level above which it is found to be unfit for humans is 55 dB Lden (European Agency). As depicted in acoustics study and noise map determination, shifting to electric vehicles has considerably mitigated the urban noise pollution[1], however the environmental concern is still not addressed from a sustainability point of view.

The emissions from electric vehicles mainly come from two phases know as pre-use and use phase. In the pre-use phase, also known as manufacturing phase, most of the emissions come from extraction of the materials/ resources then the transportation and refinement. In case of use phase, the energy mix used to charge the e-vehicles play a significant role as reported by Oliveira et al. [26]. The emissions also rely on the geographical region, system boundaries and the assessment method. The literature also justifies variation in the emission estimation by using various impact assessment methods such as IPCC, CML, CED, Ecopoints97, ReCePi reported by Parvez Mahmud et al. [27]. The assessment discrepancies may also be observed by using different assessment tool/software such as GaBi, SimaPro, GEMIS, Mobius, Open LCA, CMLCA and also using different data inventories [23]. Focusing to the pinpoint, the material extraction and manufacturing of the battery used in an electric vehicle has the GHG emissions and the energy utilization twice as compared to conventional IC Engine Vehicle. If the batteries are to be considered, mostly in modern vehicles, Li-Ion batteries are used. However, in a choice between lead-acid batteries and maintenance free batteries for automobile application, global warming and acidification are the major contributing impact categories. Premrudee et al. [28] suggested the use of maintenance-free batteries which can bring down these effects by 28% for an automobile application. Wang et al. [29] analyzed lead-acid and Li-ion batteries using the ReCiPe model, highlighting that a lithium iron phosphate battery's (LIPB) production phase contributes the least impact. Moreover, Tin and Lead are the major metals causing emissions for Lead-acid batteries. It is also found that out of the total contribution, the battery production contribution is 15% in which the extraction of copper and aluminum are major emission sources rather than the extraction of lithium. From the study of Peters et al. [30], it is reckoned that on an average 110 gCO_2eq of GHG emissions are made by Li-Ion batteries for 1 kWh of energy production. In a similar study, Ambrose [31] highlighted that total CO_2 emissions are in a range of 200-500 Kg CO_2 equivalent for Li-Ion batteries with different chemistries for an automobile application.

The assessment conducted by Finkbeiner [32] with the aid of the GaBi programme emphasizes the impact categories for acidification potential (AP) and global warming potential (GWP) as key contributors. Further, the battery production phase is the major contributor for both categories as compared to conventional vehicles where the impact categories have 2 times and up to 4 times higher emissions of GWP and AP respectively. In Belgium, electric vehicles are found to be more environmental friendly (limited to GWP) with the current Belgium energy mix. The battery electric vehicles have an emission of 50 g/km CO_2eq compared to diesel (above 200 g/km CO_2eq) and petrol (above 250 g/km CO_2eq) vehicles. Additionally, CO_2 emissions per kWh were 190 g/kWh for the Belgium energy mix which further fall down to 11 g/kWh using wind energy as reported by

[1] http://noise.eea.europa.eu/

Mierlo [33]. This justifies the significance of the type of energy source used to power the BEVs. In Brazil, Souza et al. [34] conducted the environmental assessment comparisons of BEVs with conventional ICEV & also ICEVs with ethanol were also considered. Still the overall environmental benefit stands in the favor of the BEV followed by ICEV with ethanol blended fuel. However, BEVs with lithium ion batteries have highest impact on human toxicity category whereas ICEVs with ethanol doesn't prove to be environmentally benefited in acidification, eutrophication and photochemical oxidation categories. In the GWP category ICEVs with ethanol has less impact (97.2 g/km CO_2eq) compared to BEVs (151 g/km CO_2eq). In China, Shi et al. [35] justified the savings in the petroleum by about 98% with the use of battery electric vehicles. Additionally, the BEVs stand advantageous in CO, CO_2, VOCs, NO_x and PM2.5 emissions but perform abysmal in PM10 category. Relatively the BEVs emit up to 318 g/km CO_2eq which is observed to be at bit higher side as compared to other literatures in the same timeline. Nevertheless these CO_2 emissions will be further reduced by 11% to 28% by 2030. The literature reviewed by Shi et al. [35] is limited to single province (Hebei province) whereas Zhou et al. [36] presented the statistics for different power grid zone across China. In this work average CO_2 eq. emission of whole country is 206.13 g/km CO_2eq and the total range of all the grid zones is in the range of 158 to 247 g/km CO_2eq. In an another parallel study in China by Qiao et al. [37], it has revealed that GHG impacts are 18% less than conventional ICEV and the major contributing phase is emissions from well-to-wheel (WTW) phase. To alleviate the life cycle GHG emissions of BEVs in future, Qiao et al. [37] suggested enhancing the recycling of battery electric vehicles and switch to much cleaner power grid. It is estimated that the GHG emission will reduce by approximately 50% with the use of the above tools.

As discussed earlier in literature, the environmental impact may vary with different boundary conditions. The relationship between an electric vehicle's environmental impact and its travel range is emphasized by Hawkins et al. [14]. The production impact of manufacturing a battery electric vehicles are more with respect to the use phase when compared to an ICEV. Hence, as the number of kilometer travelled or annual kilometer travelled (AKT) is more, the global warming potential (GWP) decreases for BEVs. With the current electricity mix in Europe, the electric vehicle's GWP is about 10 to 24 % less compared to the ICEV (diesel) for 150 K (AKT), 27 to 29 % less for 200 K AKT and 9 to 14% less for 100 K AKT. Further, to reduce the overall emissions, impacts from the manufacturing supply chain must be addressed in conjunction with electricity source with cleaner production. Peng et al. [38] conducted study in 6 countries and observed geographical difference causing variations in GHG emissions. The GHG emission reductions are prominently observed in geographical regions where low-carbon electricity is produced. The European Union with comparatively cleaner energy generation has least GHG emissions, about 55.51 gCO_2 eq. /km and about 170.15 gCO_{2e}/km for China. Burchart-Korol [39] unveiled the environmental burdens of using BEVs in Poland and the Czech Republic with respect to current and future time-line. Interestingly, the results show the environmental impacts for current and future will be lower than comparable ICEV. Comparatively, the impacts are relatively more for Poland than Czech Republic. The GHG emissions for BEV in Poland were 2.72% lower than ICEV and 24.67 % lower for Czech Republic. Further, an intuitive observation shows that switching to renewable energy sources will reinforce the GHG emission reduction by 2050. A bit out of the way approach, Othman et al. [40] came up with using BEVs with Autonomous Driving (ADV) to reduce the emissions. In this observations, ADV using platooning and optimum traffic management by the ADV significantly reduces the travel distance and eventually the fuel used and the emissions. Similarly, Tahmasseby et al. [41] emphasized use of electric and automated vehicles along with Intelligent Transportation Systems (ITS) to cope up with stringent emissions norms.

The reviewed literature can be used to identify the following literature gaps: 1. Majority of Environmental Life Cycle Analysis are carried out in developed countries, however, limited studies are available for developing countries. In developing countries like India, although the electric vehicles uptake is at a verge of a revolution and in coming decades, very high proportion of EVs will be witnessed. Intruding the Electric vehicles without contemplating its actual environmental hazards is counterproductive and this stands a need to investigate the environmental impacts in India. 2. Nevertheless, Environmental Life Cycle Analysis (ELCA) carried out in many developed countries is for limited number of impact categories. The BEVs may be favorable in one impacts category but might not be performing good in other. Hence, to get a panoramic idea of the BEV's environmental impact, the analysis needs to be leveraged with an extensive ELCA including all impact categories. 3. The environmental analysis with more realistic data must be carried out instead of relying on generic data. Most of the countries do not have indigenous sources of materials such as lithium battery pack materials and needs to be imported. The emissions from the transport/ import of the materials need to be accounted instead of considering the start point as material available on site. 4. The study of the emissions from vehciles can be further enhanced with the use of travel mode option/ transport preference opted especially in metropolis. Influence of various parameters such as the infrastructure and accecibility opinion for travel mode preference as

highlighted by literatures such as Lukina et al. [42] can further help the emission studies needs to be implemented.

3. RESEARCH DRIVERS, METHOD AND OBJECTIVE

3. 1. Life Cycle Analysis (LCA) The fundamental objective of LCA is to evaluate the environmental effects in development, usage, and disposal (LCA) phases of a product. Typically, a product undergoes a "full LCA," often known as a cradle-to-grave examination. However, considering the end-user of the study, different types of LCA, such as cradle-to-gate (raw material-factory) and cradle-to-cradle (a closed-loop LCA that includes recycling of part products), are also occasionally evaluated. The LCA flowchart is displayed in Figure 2.

3. 2. Objectives and Research Drivers This article's primary objective is to ascertain which power train (BEV or ICEV) has less impact on the environment in the context of India. In addition, it's important to evaluate the environmental impact while taking different life phases into account. Finally, we'll talk about the Cumulative Impact (endpoint Recepi 2016 assessment).

One of India's main worries about electric automobiles is the environment. As a result, our inquiry is motivated by the "RRR" (Reduced, Revival, and Renewable) pattern. Where, Reduction: lowers the cost of imports, Revive: reduce the amount of hazardous emissions by transitioning to electric vehicles with better battery chemistry, Renewable Energy: By converting to green transportation and utilising an energy mix that supports renewable energy, you can lower your GHG emissions. Thus, upholding strict environmental standards and sticking to them is what motivates this study and justifies the societal contribution.

3. 3. Methodology

3. 3. 1. System Boundaries and Scope of Study The methodology follows the guidelines and advice provided by the European standards series: ISO 14040 and ISO 14044, quantifying the emissions from a product or procedure over the course of its use period. This study evaluates the environmental impacts by using battery electric vehicles and diesel ICEV with reference to India as a geographical region. The emissions produced during the gathering and processing of materials, transportation, manufacturing and use of both the vehicles are taken into account from the birth to end-life of the product. However, omissions regarding recycling of the product (vehicle in this case) are considered owing to India's lack of reliable recycling infrastructure. This life cycle analysis falls under cradle-to-grave assessment and illustrates the various flows, processes, product systems and the project involved in this cradle-to-grave analysis shown in Figure 3. This analysis's objective is to compare the life cycle emissions of ICEVs with BEVs (diesel), considering a functional unit of 1 p*km. The emissions accounted include the direct tail-pipe emissions (for the diesel ICEV) and emissions from electricity generation sources. Additionally emissions from the vehicle and battery manufacturing, fuel (extraction and refinement), indirect emissions from brake and tyre wear are also taken into account. This research assumes that the vehicle is used for 100,000 km for an average lifetime of 10 years.

3. 3. 2. Data Inventory Analysis This study uses OpenLCA software to perform the impact assessment within the geographical region of India. The inventory makes use of the configurable Ecoinvent-3 database with other database, in case if data needs to be imported from other database. The simulation includes various product flows such as product or elementary flow which eventually builds up a process. Different processes combine together to form a product system separately for BEV and ICEV which are later compared in a Project including system boundaries and impact assessment method. The process involved in building a product system for a BEV is illustrated in a model graph shown in Figure 4.

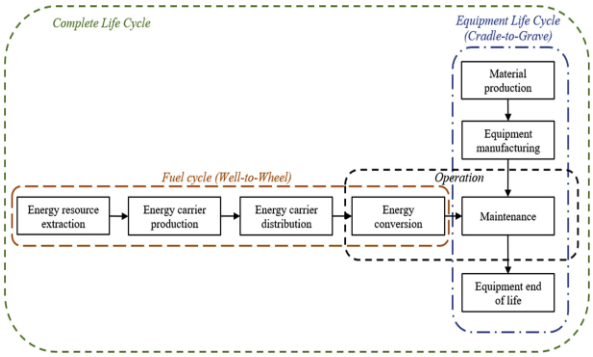

Figure 2. Material and Fuel line LCA for a typical automobile analysis [54]

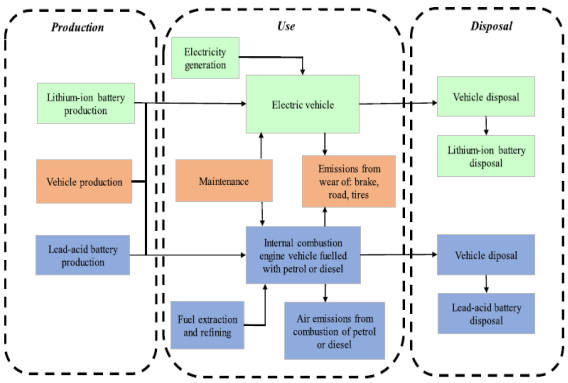

Figure 3. Flow diagram of life cycle analysis

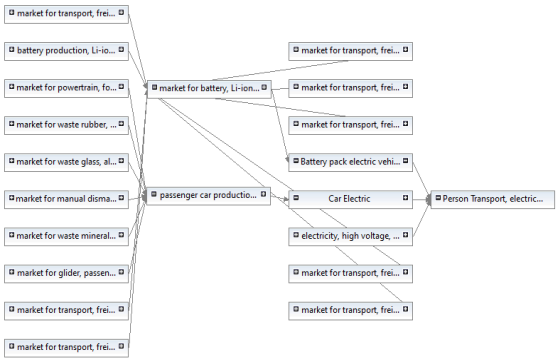

Figure 4. Model graph of battery electric vehicle product system

The weights of the vehicles are 1500 kg (ICEV) and 1250 kg (BEV without battery), weight of the Li-ion battery pack is 326 kg. The battery considered is of 23 kWh and the energy density is 70 Wh/kg. The total cruising range of the battery is 200,000 km, however for the vehicle used in this analysis required amount of battery is for 100,000 kilometres. BEVs use 17.11 kWh of electricity per 100 kilometres and the ICEV consumes 17 km per litre diesel. The energy required to assemble the final Li-ion battery pack is 3.47 kWh [43]. The electricity-mix considered is Indian energy-mix (2022) which has almost 60% energy generated from conventional fossil fuels. The necessary transport needs right from raw materials to manufacturing unit (some items of battery pack manufacturing are imported) and from manufacturing to customers through assembly unit are also considered.

3. 3. 3. Impact Assessment and Interpretation

As highlighted by Parvez Mahmud et al. [27], the impacts assessment method significantly affects the LCA assessment. To perform the impact assessment, we have considered ReCePi 2016 method based on what majority of the literature have considered and suitable for the automobile application. Both ReCePi 2016 mid-point and end-point are accounted to analyze the individual and cumulative effects of all the impact categories. The major impact categories considered in this case are global warming, ionizing radiation, human toxicity (both carcinogenic and non-carcinogenic), fossil and mineral depletion. In addition to these categories, other impact categories of interest are water and land use, ozone formation, ecotoxicity and eutrophication under the ReCePi mid-point. To precisely measure them, the effect categories in the end-point are classified into a small number of categories. The grouped impact categories in end-point analysis include resource scarcity, human health and ecosystem quality. The cost of extracting minerals and fossil fuels, represented in US dollars ($), is what is meant by resource scarcity. Human health demonstrated loss of years due to disability from the environmental impact and is expressed in DALY (disability adjusted life years) whereas as ecosystem quality gives the loss for the species in various ecosystem expressed as species.year unit. Finally, the relative results for both the vehicles are presented to cogitate the individual and relative effect for various impact categories. The Methodology Flow Chart is shown in Figure 5.

4. RESULTS AND DISCUSSION

Figure 6 (a-g) shows the environmental effects of BEV and ICEV in India for various important impact categories such global warming, fine particulate matter, ionising radiation, human toxicity (both carcinogenic and non-carcinogenic), and fossil and mineral depletion. Additionally, it depicts the spitted impact in production and use-end life phase for panoramic emission assessment.

The impact from global warming is shown in Figure 6(a). ICEV account the highest in climate change category which is 282 g CO_2eq/km whereas for BEV it is 242 g CO_2eq/km. As observed in earlier literatures, the obtained results are in-line with these studies where the ICEVs have the greatest impact [33, 39, 44-46]. Comparatively, the GHG emissions observed for BEV in production phase are less as compared to use phase. The higher impacts for BEV come from ‘use phase’ which is closely associated to the energy-mix. The current energy mix of India has about 60% energy generation from convention fuel such as coal which signifies switching to electricity generation from renewable sources will surely alleviate global warming category.

Although the BEV emit less GHG emissions, the gap between BEV and ICEV in climate change is less than 15%. Moreover the climate change emissions in global warming category are more prominent in use phase

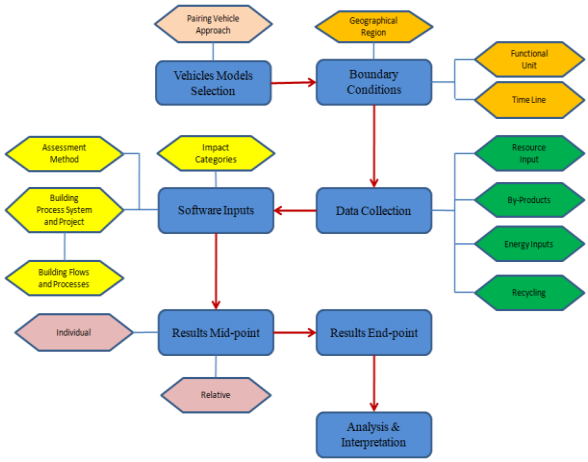

Figure 5. Flow Chart for Methodology of LCA Analysis

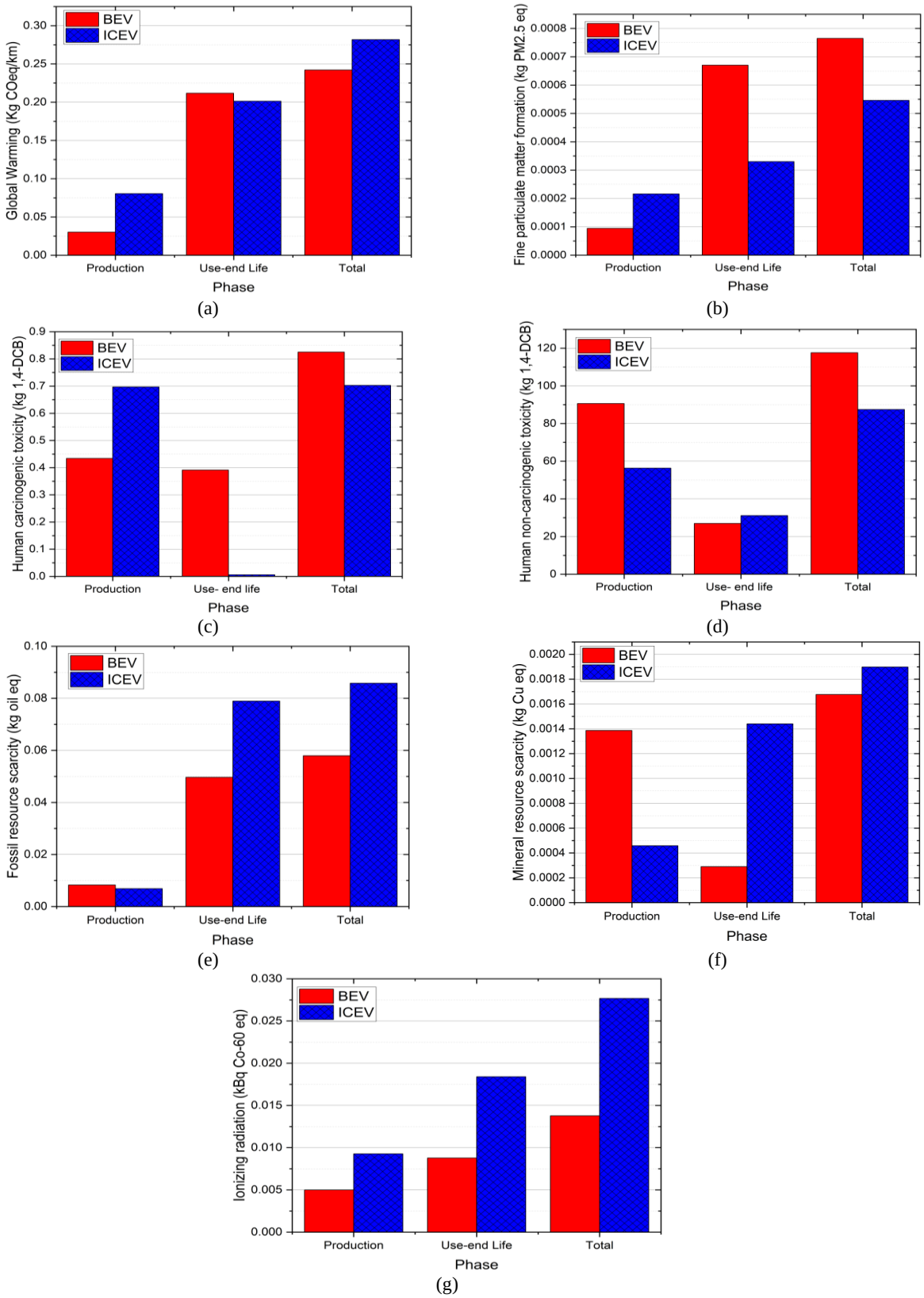

Figure 6. Impact assessment of BEV in comparison to ICEV for a) Global warming b) fine particulate matter c) human toxicity (carcinogenic) d) human toxicity (non-carcinogenic) e) Fossil resource scarcity f) Mineral resource scarcity g) Ionizing radiation

which clearly indicate that the energy source use to charge the BEVs should be shifted to much cleaner mode. Currently India mostly relies on the conventional coal powered plants to cater it most of the electricity needs. This causes to shoot up the emissions with more demand for electricity as the number of BEV goes up. The government on one hand is promulgating the BEV aggressively but it should also make provisions for this other side of the coin.

On the Contrary, for fine particulate matter category, the battery electric vehicle fair poor, the total emissions have almost 40% more impact as compare to ICEV. Impact of ICEV and BEV on particulate matter category is shown in Figure 6(b). Almost 88% of the total emissions come from use phase which attributes to umpteen combustion of fossil fuel for energy generation.

The impact burden for this category for BEV is 7.65E-04 kg PM2.5 eq and the ICEV contribute 5.46E-04 kg PM2.5 eq. It can be justified that less combustion of fossils for energy generation and advanced manufacturing techniques can reinforce the impact reductions as mentioned by Shi et al. [35].

The emissions for human toxicity (carcinogenic & non-carcinogenic) are illustrated in Figure 6(c) & (d). When the total emissions are taken into account, battery electric vehicles fair substantially worse. In case of different use phases, for carcinogenic impact category, the emissions from ICEV are only 1.5% than that from BEV in use-end life phase. However, for use-end life phase and in non-carcinogenic category, the ICEV has more emissions than BEV, albeit with smaller margin. Nevertheless, the total impact for BEV in both categories is at higher side and is the result of the interaction between the production of batteries and cars, as well as the energy-mix.; these results are identical as observed by Burchart-Korol et al. [39].

In case of resource scarcity (fossil and mineral) the impact from ICEV outnumbers BEV in both fossil and metal resource scarcity. The resource scarcity results are demonstrated in Figures 6(e) & (f). The fossil resource scarcity for BEV is 5.79E-02 kg oil eq and 8.58E-02 kg oil eq for ICEV. Whereas, the mineral resource scarcity for BEV is 1.68E-03 kg Cu eq and ICEV is 1.90E-03 kg Cu eq. For the production phase, the resource scarcity impact for BEV is more as compared to ICEV, specifically for mineral resource scarcity. This is due to the heavy requirement of minerals for the battery and allied components such as battery management system and motor windings production. The BEV have high impact in production phase compare to ICEV, however, the low impact benefit for ICEV in production phase is simply offset by the high impacts in use phase , thus catapulting the total impact for ICEV.

Battery electric vehicles are found to be advantageous from an ionizing radiation impact category point. The ionizing radiation for BEV is 1.38E-02kbq CO-60 eq in comparison to ICEV which is 2.77E-02kbq CO-60 eq. According to Tahmasseby [41], the ionising impact of a BEV is almost half that of an ICEV. BEV's ionizing impact is less for both production and use phase significantly as compared to ICEV. Impacts from ionizing radiations are shown in Figure 6(g).

In order to observe the results of the current study and compare it with the other studies in the literature, comparative results are presented in Table 1. Although the battery electric vehicles are emitting less emissions in India context compare to the ICEV for climate change category, the overall emissions magnitude are considerably higher compared to the global values in the near about same timeline. This demonstrates the significance of the power source and how clean is the energy generation. Failing to achieve the energy from cleaner source, BEV use will be just shifting the emissions from the vehicle's tail pipe to the energy generation site. Additionally the Human Toxicity value compared to the global values are also much higher in this case study. The human toxicity arises from the mining of materials which are used to manufacture the vehicle parts. Moreover the extraction of the battery pack materials further worsens the emission levels in can of BEV. Attributing to this the overall human toxicity levels are considerably higher for this case study.

The impacts for various the impact categories other than mentioned above and not much widely discussed in many of the literatures but are illustrated in Table 2 (software generated table image). The result from table depict that for the impact categories namely Freshwater ecotoxicity, Marine eutrophication, Ozone formationHuman health, Ozone formation, Terrestrial ecosystems, Stratospheric ozone depletion, Terrestrial acidification BEV becomes advantageous and having low impact burden as compared to ICEV. In most of the above impact categories BEV have 25% less impact than ICEV.

For panoramic outlook of all the impact categories, the relative results for the ReCePi mid-point assessment are displayed in Figure 7. Out of 18 impact categories considered, battery electric vehicle fair good in 10 impact categories in comparison with ICEV. The highest variation is found in freshwater eutrophication where ICEV has just 27% impact as that of battery electric vehicle. The lease variation is observed for terrestrial acidification category where BEV has just 6% impact gap compared to ICEV. We found that for land and water use impact category, the ICEV is almost 40% more advantageous than the BEV. Focusing on the global warming category, interestingly a positive point is to be highlighted that the g CO_2eq/km gap between BEV and ICEV is less as compared to other literature [16, 17, 47]. Moreover, switching to cleaner energy BEV can bridge

TABLE 1. Comparative emissions with other literatures for climate change and human toxicity

	Country/ Region	Timeline	Climate change, g CO2 eq/km	Human toxicity, kg 1,4-DB eq/km
			GRAMS	
This article	India	2022	BEV: 242 ICEV: 281	BEV: 0.82 ICEV: 0.7
Bauer et al. [46]	Switzerland	2012	BEV: 220 ICEV: 260	BEV: 1.0 ICEV: 0.3
		2030	BEV : 90 ICEV: 210	BEV: 0.27 ICEV: 0.25
Van Merilo et al. [33]	Belgium	2017	BEV: 50 ICEV: 212	BEV: 0.040 ICEV: 0.026
Bickert et al. [48]	Germany	2015	BEV: 204 ICEV: 262	
		2020	BEV: 196 ICEV: 212	
Souza et al. [34]	Brazil	2018	BEV: 151 ICEV: 97.2	BEV: 0.035 ICEV: 0.012
Del Pero et al. [49]	Italy	2018	BEV: 129 ICEV: 203	
Onat et al. [50]	United States	2015	BEV: 180 ICEV: 260	
Bicer and Dincer [47]	Canada	2018	BEV: 160 ICEV: 230	BEV: 0.26 ICEV: 0.04
Qiao et al. [37]	China	2015	BEV: 273 ICEV: 333	
		2020	BEV: 227	
Burchart-Korol et al. [39]	Poland	2015	BEV: 276 ICEV: 284	BEV: 0.331 ICE: 0.085
		2050	BEV: 172	BEV: 0.234
Burchart-Korol et al. [39]	Czech Republic	2018	BEV: 214 ICEV: 284	BEV: 0.306 ICEV: 0.085
		2050	BEV: 145	BEV: 0.234
Petrauskiene et al. [43]	Lithuania	2020	BEV: 142 ICEV: 76	BEV: 0.077 ICEV:0.0073
		2050	BEV 78	BEV: 0.073
Zhou et al. [36]	China	2009	BEV 206 ICEV 249	

TABLE 2. ReCePi mid-point results of BEV and ICEV (software generated table image)

Indicator	BEV	ICEV	Unit
Fine particulate matter formation	7.64982e-4	5.46229e-4	kg PM2.5 eq
Fossil resource scarcity	5.79452e-2	8.57900e-2	kg oil eq
Freshwater ecotoxicity	1.48779e-2	2.47261e-2	kg 1,4-DCB
Freshwater eutrophication	1.42334e-4	3.81529e-5	kg P eq

Global warming	2.42092e-1	2.81770e-1	kg CO2 eq
Human carcinogenic toxicity	8.25258e-1	7.02699e-1	kg 1,4-DCB
Human non-carcinogenic toxicity	1.17596e+2	8.74670e+1	kg 1,4-DCB
Ionizing radiation	1.37743e-2	2.76725e-2	kBq Co-60 eq
Land use	3.33749e-3	2.00561e-3	m2a crop eq
Marine ecotoxicity	1.41523e+2	1.02429e+2	kg 1,4-DCB
Marine eutrophication	2.35348e-5	3.29772e-5	kg N eq
Mineral resource scarcity	1.67656e-3	1.89831e-3	kg Cu eq
Ozone formation, Human health	6.85209e-4	9.27953e-4	kg NOx eq
Ozone formation, Terrestrial ecosystems	6.91598e-4	9.49920e-4	kg NOx eq
Stratospheric ozone depletion	9.49468e-8	1.19844e-7	kg CFC11 eq
Terrestrial acidification	1.52559e-3	1.62241e-3	kg SO2 eq
Terrestrial ecotoxicity	9.36751e-1	4.11475e-1	kg 1,4-DCB
Water consumption	1.53252e-3	9.80542e-4	m3

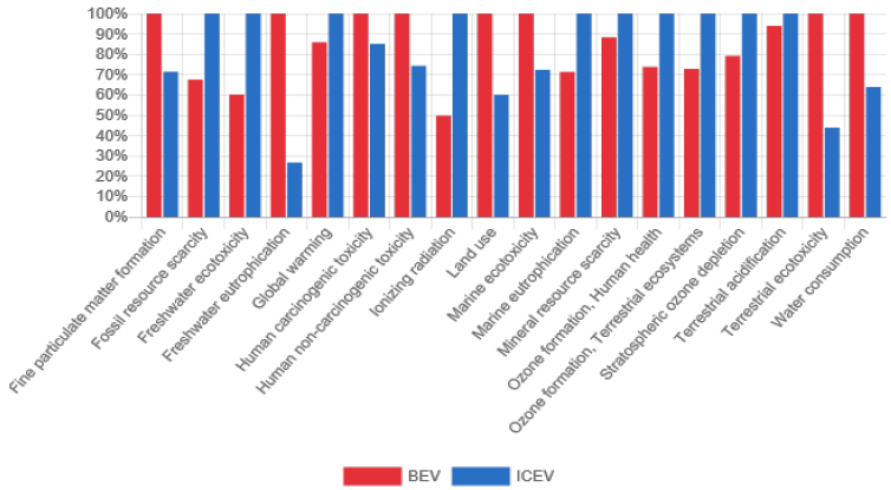

Figure 7. Relative results of LCA

the gap or even can deliver less impact than ICEV in all phases in the near future. Additionally, mining/extracting and manufacturing the resources from the indigenous sources instead of importing may save the transport emissions which eventually be advantageous for effect categories like ionising radiation, fine particulate pollution, and global warming.

Further, the results for ReCePi end-point analysis are illustrated in Table 3 (software generated table image). The end point results are derived by grouping and mapping the impact categories mainly in three groups as mentioned in impact analysis section. Further, a single point score is determined to compare BEV with ICEV and assess the impact magnitude. The end-point

TABLE 3. ReCePi end-point results of BEV and ICEV (software generated table image)

Indicator	BEV	ICEV	Unit
Fine particulate matter formation	4.80660e-7	3.43069e-7	DALY
Fossil resource scarcity	8.82989e-3	3.60161e-2	USD2013
Freshwater ecotoxicity	1.02783e-11	1.70967e-11	species.yr
Freshwater eutrophication	9.53209e-11	2.55511e-11	species.yr

Global warming, Freshwater ecosystems	2.04244e-14	2.43820e-14	species.yr
Global warming, Human health	2.47796e-7	2.95840e-7	DALY
Global warming, Terrestrial ecosystems	7.47822e-10	8.92548e-10	species.yr
Human carcinogenic toxicity	3.90473e-8	3.42167e-8	DALY
Human non-carcinogenic toxicity	8.85132e-8	9.35561e-8	DALY
Ionizing radiation	8.23619 e-11	7.61240e-11	DALY
Land use	2.96106e-11	1.77933e-11	species.yr
Marine ecotoxicity	2.14079e-12	3.30650e-12	species.yr
Marine eutrophication	3.99890e-14	5.60576e-14	species.yr
Mineral resource scarcity	3.86860e-4	4.38672e-4	USD2013
Ozone formation, Human health	6.23551e-10	8.44464e-10	DALY
Ozone formation, Terrestrial ecosystems	8.92156e-11	1.22539e-10	species.yr
Stratospheric ozone depletion	3.36976e-11	4.88163e-11	DALY
Terrestrial acidification	3.23416e-10	3.43937e-10	species.yr
Terrestrial ecotoxicity	9.94784e-12	4.36638e-12	species.yr
Water consumption, Aquatic ecosystems	9.25639e-16	5.92248e-16	species.yr
Water consumption, Human health	3.40218e-9	2.17680e-9	DALY
Water consumption, Terrestrial ecosystem	2.06890e-11	1.32373e-11	species.yr

assessment reveals that the major contributor when cumulative effect of all the impact categories are considered, the primary influencing factor for both vehicles is resource scarcity, which includes both fossil and mineral resources.. Relatively the total single point score (out of 3 kpt) for BEV is 0.58 kpt and for ICEV it is 2.1 kpt. This justifies that the BEV is environmentally advantageous than ICEV at end-point level.

5. CONCLUSION

The performed Environmental Life Cycle analysis of BEV and ICEV leads to an epiphany that for all impact categories, the battery-electric car did not perform worst. The results substantiate that out of 18 impact categories considered for mid-point assessment, BEV fair good in 10 impact categories in comparison with ICEV. The end-point results show that, on an overall single point scale, BEV is still environmentally beneficial as compared to ICEV with a greater margin.

Resource scarcity is the major contributor for both vehicles when studied on a single point scale. When a slpited analysis (use phase and end-life phase) is observed in all the categories for BEVs, with the exception of human toxicity and fossil resource categories, usage phase is the dominant impact contributor. This use phase is closely associated with the energy mix which needs to be eventually shifted to renewable sources with sustainability angle of approach.

The global warming g-CO_2eq/ km for both vehicles are quite compatible with not much gap in the impact. Better manufacturing techniques and use of cleaner energy will help to amplify this gap in near future. Continuing the current energy mix will simply exacerbate the environmental issue in future when more number of BEVs will be introduced to the total vehicle fleet.

This article contributes towards the societal application by making aware the emissions from both the vehicle propulsion types which in turn helps in strengthening the public opinion about the environmental benefits of using BEVs. Further, it provides guidance to the policy drafter's fraternity for alleviating the saddled environmental issues in India. This surely provides guidelines for the BEV's manufacturing ecosystem to implement the optimized manufacturing techniques, the precautions in material extraction-processing-refinement & transport to build a compatible infrastructure encompassing the low carbon transportation. This article further acts as a nexus between government perseverance for BEV's uptake and perceiving the customers towards BEV; which inturn helps in achieving national energy security, reduce the oil import bills and combating environmental issues.

The limitations of the study is the access to convincing recycling of the end-life BEV and to be more specifically the Li-Ion batteries. Unavailability of the reliable BEV's recycling facilities in India may deviate the emissions estimation and if proper recycling infra is

used the impacts might come down which is also reckoned by various literatures. India being a colossal country, the factory to vendor or end user distance may vary considerably, further changing the amount of emissions which depend on the local transport mode of semi-knocked part or the finished vehicle. Variation emissions observation in all regions of India also comes under the limitation rubrics.

Significantly the emission estimates made in this study are derived from near to realistic data. The emission impacts from both the vehicles for all 18 impact categories at mid-point and end-point level of ReCePi Methodology for the Indian context justifies the scientific and technological top-up. Moreover, the study can be extended as future scope by accounting the regional/ statewise energy-mix which has a substantial influence on the total emissions. At present the no indigenous sources are available in India which includes greater travel distance for it's import. However, if a local source obtained then the updated material travel distances needs to be updated and can be accounted as future study. Additionally, as the technology advances, different and a better battery technology/ chemistry may be introduced. Estimating emissions with these batteries can be done as a extended study.

The electric vehicle bandwagon is saddled with various hurdles; meticulously overcoming these barriers will prove BEV as an epitome of the future transport. Retrospection of BEVs for environmental impact; cleaner energy mix, efficient manufacturing and recycling may prove to be an elixir for BEV to be a ubiquity in the near future.

6. REFERENCES

1. Hauschild, M.Z., Rosenbaum, R.K. and Olsen, S.I., "Life cycle assessment, Springer, (2018).
2. Goel, S., Sharma, R. and Rathore, A.K., "A review on barrier and challenges of electric vehicle in india and vehicle to grid optimisation", ***Transportation Engineering***, Vol. 4, (2021), 100057. doi: 10.1016/j.treng.2021.100057.
3. Bhosale, A.P., Gholap, A., Mastud, S. and Bhosale, D., "A research on market status and purchasing decision influencing parameters for electric vehicles: Indian context", ***International Journal of Recent Technology and Engineering***, Vol. 8, (2019), 2700-2706. https://doi.org/10.35940/ijrte.B1331.0982S1119
4. Tarei, P.K., Chand, P. and Gupta, H., "Barriers to the adoption of electric vehicles: Evidence from india", ***Journal of Cleaner Production***, Vol. 291, (2021), 125847. https://10.1016/j.jclepro.2021.125847
5. Murugan, M. and Marisamynathan, S., "Mode shift behaviour and user willingness to adopt the electric two-wheeler: A study based on indian road user preferences", ***International Journal of Transportation Science and Technology***, (2022). https://doi.org/10.1016/j.ijtst.2022.03.008
6. Gilmore, E.A. and Patwardhan, A., "Passenger vehicles that minimize the costs of ownership and environmental damages in the indian market", ***Applied Energy***, Vol. 184, (2016), 863-872. https://doi.org/10.1016/j.apenergy.2016.09.096
7. Bhosale, A.P., Sharma, S. and Mastud, S., "Characterizing the economic competitiveness of battery electric vehicles in india", ***Asian Transport Studies***, Vol. 8, (2022), 100069. https://doi.org/10.1016/j.eastsj.2022.100069
8. Murugan, M. and Marisamynathan, S., "Elucidating the indian customers requirements for electric vehicle adoption: An integrated analytical hierarchy process–quality function deployment approach", ***Case Studies on Transport Policy***, Vol. 10, No. 2, (2022), 1045-1057. https://doi.org/10.1016/j.cstp.2022.03.017
9. Singh, V., Singh, V. and Vaibhav, S., "Analysis of electric vehicle trends, development and policies in india", ***Case Studies on Transport Policy***, Vol. 9, No. 3, (2021), 1180-1197. doi: 10.1016/j.cstp.2021.06.006.
10. Kumar, R., Lamba, K. and Raman, A., "Role of zero emission vehicles in sustainable transformation of the indian automobile industry", ***Research in Transportation Economics***, Vol. 90, No., (2021), 101064. https://doi.org/10.1016/j.retrec.2021.101064
11. Shrimali, G., "Getting to india's electric vehicle targets cost-effectively: To subsidize or not, and how?", ***Energy Policy***, Vol. 156, (2021), 112384. doi: 10.1016/j.enpol.2021.112384.
12. Gulati, V., "National electric mobility mission plan 2020", ***Department of Heavy Industry, Ministry of Heavy Industries & Public Enterprises, Government of India***, (2012). https://heavyindustries.gov.in/writereaddata/Content/NEMMP2020.pdf
13. Ma, H., Balthasar, F., Tait, N., Riera-Palou, X. and Harrison, A., "A new comparison between the life cycle greenhouse gas emissions of battery electric vehicles and internal combustion vehicles", ***Energy Policy***, Vol. 44, (2012), 160-173. https://heavyindustries.gov.in/writereaddata/Content/NEMMP2020.pdf
14. Hawkins, T.R., Singh, B., Majeau-Bettez, G. and Strømman, A.H., "Comparative environmental life cycle assessment of conventional and electric vehicles", ***Journal of Industrial Ecology***, Vol. 17, No. 1, (2013), 53-64. https://doi.org/10.1111/j.1530-9290.2012.00532.x
15. Lucas, A., Silva, C.A. and Neto, R.C., "Life cycle analysis of energy supply infrastructure for conventional and electric vehicles", ***Energy Policy***, Vol. 41, (2012), 537-547. https://doi.org/10.1016/j.enpol.2011.11.015
16. Omidi Kashani, B. and Pirouzpanah, V., "Development of a mathematical model for prediction of pollutants emission in di diesel engines", ***International Journal of Engineering***, Vol. 11, No. 1, (1998), 37-42.
17. Nemati, A., Jafarmadar, S., Khalil Arya, S. and Mardi Kolur, M., "Hydrogen and ethanol as potential alternative fuels compared to gasoline under improved exhaust gas recirculation", ***International Journal of Engineering***, ***Transactions C: Aspects,*** Vol. 27, No. 3, (2014), 449-456. doi: 10.5829/idosi.ije.2014.27.03c.13.
18. Kalghatgi, G., "Is it really the end of internal combustion engines and petroleum in transport?", ***Applied energy***, Vol. 225, No., (2018), 965-974. doi: 10.1016/j.apenergy.2018.05.076.
19. Yong, T. and Park, C., "A qualitative comparative analysis on factors affecting the deployment of electric vehicles", ***Energy Procedia***, Vol. 128, (2017), 497-503. doi: 10.1016/j.egypro.2017.09.066.
20. Heidrich, O., Hill, G.A., Neaimeh, M., Huebner, Y., Blythe, P.T. and Dawson, R.J., "How do cities support electric vehicles and what difference does it make?", ***Technological Forecasting and Social Change***, Vol. 123, (2017), 17-23. doi: 10.1016/j.techfore.2017.05.026.
21. Lieven, T., Mühlmeier, S., Henkel, S. and Waller, J.F., "Who will buy electric cars? An empirical study in germany",

Transportation Research Part D: Transport and Environment, Vol. 16, No. 3, (2011), 236-243. doi: 10.1016/j.trd.2010.12.001.

22. Mohanty, P. and Kotak, Y., Electric vehicles: Status and roadmap for india, in Electric vehicles: Prospects and challenges. 2017, Elsevier.387-414.
23. Bharathidasan, M., Indragandhi, V., Suresh, V., Jasiński, M. and Leonowicz, Z., "A review on electric vehicle: Technologies, energy trading, and cyber security", ***Energy Reports***, Vol. 8, (2022), 9662-9685. doi: 10.1016/j.egyr.2022.07.145.
24. Verma, S., Dwivedi, G. and Verma, P., "Life cycle assessment of electric vehicles in comparison to combustion engine vehicles: A review", ***Materials Today: Proceedings***, Vol. 49, (2022), 217-222. doi: 10.1016/j.matpr.2021.01.666.
25. Holland, S.P., Mansur, E.T., Muller, N.Z. and Yates, A.J., *Environmental benefits from driving electric vehicles?* 2015, National Bureau of Economic Research.
26. Oliveira, L., Messagie, M., Rangaraju, S., Sanfelix, J., Rivas, M.H. and Van Mierlo, J., "Key issues of lithium-ion batteries–from resource depletion to environmental performance indicators", ***Journal of Cleaner Production***, Vol. 108, (2015), 354-362. https://doi.org/10.1016/j.jclepro.2015.06.021
27. Mahmud, M.P., Huda, N., Farjana, S.H. and Lang, C., "Comparative life cycle environmental impact analysis of lithium-ion (LIIO) and nickel-metal hydride (NIMH) batteries", ***Batteries***, Vol. 5, No. 1, (2019), 22. https://doi.org/10.3390/batteries5010022
28. Premrudee, K., Jantima, U., Kittinan, A., Naruetep, L., Kittiwan, K. and Sudkla, B., "Life cycle assessment of lead acid battery. Case study for thailand", ***Environment Protection Engineering***, Vol. 39, No. 1, (2013), 101-114. https://doi.org/10.5277/EPE130108
29. Wang, Q., Liu, W., Yuan, X., Tang, H., Tang, Y., Wang, M., Zuo, J., Song, Z. and Sun, J., "Environmental impact analysis and process optimization of batteries based on life cycle assessment", ***Journal of Cleaner Production***, Vol. 174, (2018), 1262-1273. https://doi.org/10.1016/j.jclepro.2017.11.059
30. Peters, J.F., Baumann, M., Zimmermann, B., Braun, J. and Weil, M., "The environmental impact of li-ion batteries and the role of key parameters–a review", ***Renewable and Sustainable Energy Reviews***, Vol. 67, (2017), 491-506. https://doi.org/10.1016/j.rser.2016.08.039
31. Ambrose, H. and Kendall, A., "Effects of battery chemistry and performance on the life cycle greenhouse gas intensity of electric mobility", ***Transportation Research Part D: Transport and Environment***, Vol. 47, (2016), 182-194. https://doi.org/10.1016/j.trd.2016.05.009
32. Finkbeiner, M., "Towards life cycle sustainability management, Springer Science & Business Media, (2011).
33. Van Mierlo, J., Messagie, M. and Rangaraju, S., "Comparative environmental assessment of alternative fueled vehicles using a life cycle assessment", ***Transportation Research Procedia***, Vol. 25, (2017), 3435-3445. doi: 10.1016/j.trpro.2017.05.244.
34. De Souza, L.L.P., Lora, E.E.S., Palacio, J.C.E., Rocha, M.H., Renó, M.L.G. and Venturini, O.J., "Comparative environmental life cycle assessment of conventional vehicles with different fuel options, plug-in hybrid and electric vehicles for a sustainable transportation system in brazil", ***Journal of Cleaner Production***, Vol. 203, (2018), 444-468. doi: 10.1016/j.jclepro.2018.08.236.
35. Shi, S., Zhang, H., Yang, W., Zhang, Q. and Wang, X., "A life-cycle assessment of battery electric and internal combustion engine vehicles: A case in hebei province, china", ***Journal of Cleaner Production***, Vol. 228, (2019), 606-618. doi: 10.1016/j.jclepro.2019.04.301.
36. Zhou, G., Ou, X. and Zhang, X., "Development of electric vehicles use in china: A study from the perspective of life-cycle energy consumption and greenhouse gas emissions", ***Energy Policy***, Vol. 59, (2013), 875-884. doi: 10.1016/j.enpol.2013.04.057.
37. Qiao, Q., Zhao, F., Liu, Z., Jiang, S. and Hao, H., "Cradle-to-gate greenhouse gas emissions of battery electric and internal combustion engine vehicles in china", ***Applied Energy***, Vol. 204, (2017), 1399-1411.
38. Peng, T., Ou, X. and Yan, X., "Development and application of an electric vehicles life-cycle energy consumption and greenhouse gas emissions analysis model", ***Chemical Engineering Research and Design***, Vol. 131, (2018), 699-708. doi: 10.1016/j.cherd.2017.12.018.
39. Burchart-Korol, D., Jursova, S., Folęga, P., Korol, J., Pustejovska, P. and Blaut, A., "Environmental life cycle assessment of electric vehicles in poland and the czech republic", ***Journal of Cleaner Production***, Vol. 202, (2018), 476-487. doi: 10.1016/j.jclepro.2018.08.145.
40. Othman, K., "Multidimension analysis of autonomous vehicles: The future of mobility", ***Civil Engineering Journal***, Vol. 7, (2022), 71-93. doi: 10.28991/CEJ-SP2021-07-06.
41. Tahmasseby, S., "The implementation of smart mobility for smart cities: A case study in qatar", ***Civil Engineering Journal***, Vol. 8, No. 10, (2022), 2154-2171. doi: 10.28991/CEJ-2022-08-10-09.
42. Lukina, A.V., Sidorchuk, R.R., Mkhitaryan, S.V., Stukalova, A.A. and Skorobogatykh, I.I., "Study of perceived accessibility in daily travel within the metropolis", ***Emerging Science Journal***, Vol. 5, No. 6, (2021), 868-883. doi: 10.28991/esj-2021-01316.
43. Petrauskienė, K., Skvarnavičiūtė, M. and Dvarionienė, J., "Comparative environmental life cycle assessment of electric and conventional vehicles in lithuania", ***Journal of Cleaner Production***, Vol. 246, (2020), 119042. doi: 10.1016/j.jclepro.2019.119042.
44. Schüller, M., Tewiele, S., Bruckmann, T. and Schramm, D., "Evaluation of alternative drive systems based on driving patterns comparing germany, china and malaysia", ***International Journal of Automotive and Mechanical Engineering***, Vol. 14, No. 1, (2017), 3985-3997. https://doi.org/10.15282/ijame.14.1.2017.13.0323
45. Wu, L., Liu, S., Liu, D., Fang, Z. and Xu, H., "Modelling and forecasting CO_2 emissions in the brics (brazil, russia, india, china, and south africa) countries using a novel multi-variable grey model", ***Energy***, Vol. 79, (2015), 489-495. https://doi.org/10.1016/j.energy.2014.11.052
46. Bauer, C., Hofer, J., Althaus, H.-J., Del Duce, A. and Simons, A., "The environmental performance of current and future passenger vehicles: Life cycle assessment based on a novel scenario analysis framework", ***Applied Energy***, Vol. 157, (2015), 871-883. https://doi.org/10.1016/j.apenergy.2015.01.019
47. Bicer, Y. and Dincer, I., "Life cycle environmental impact assessments and comparisons of alternative fuels for clean vehicles", ***Resources, Conservation and Recycling***, Vol. 132, (2018), 141-157. https://doi.org/10.1016/j.resconrec.2018.01.036
48. Bickert, S., Kampker, A. and Greger, D., "Developments of co2-emissions and costs for small electric and combustion engine vehicles in germany", ***Transportation Research Part D: Transport and Environment***, Vol. 36, No., (2015), 138-151. doi: 10.1016/j.trd.2015.02.004.
49. Del Pero, F., Delogu, M. and Pierini, M., "Life cycle assessment in the automotive sector: A comparative case study of internal combustion engine (ICE) and electric car", ***Procedia Structural Integrity***, Vol. 12, (2018), 521-537. https://doi.org/10.1016/j.prostr.2018.11.066
50. Onat, N.C., Kucukvar, M. and Tatari, O., "Conventional, hybrid, plug-in hybrid or electric vehicles? State-based comparative carbon and energy footprint analysis in the united states", ***Applied Energy***, Vol. 150, (2015), 36-49. https://doi.org/10.1016/j.apenergy.2015.04.001

Persian Abstract

چکیده

انطباق وسیله نقلیه الکتریکی باتری (BEV) به دلیل انتشار گازهای خروجی صفر و مزایای زیست‌محیطی تخمین زده شده با سرعتی سریع انجام می‌شود. با این حال، وقتی کل چرخه عمر یک وسیله نقلیه الکتریکی را در نظر می گیریم، مزایای زیست محیطی می تواند یک فریب باشد. باید در نظر گرفت که آیا خودروهای برقی واقعاً دوستدار محیط زیست هستند و اگر هستند، پس در چه شرایطی؟ با توجه به ادبیات، ردپای کربن تحرک الکتریکی بسته به موقعیت جغرافیایی و همچنین با ترکیب انرژی منطقه‌ای متفاوت است و اثرات زیست‌محیطی ممکن است با معرفی انبوهی از وسایل نقلیه الکتریکی تشدید شود. از آنجایی که تحقیقات بسیار کمتری در زمینه هند انجام شده است. این مقاله تأثیرات زیست‌محیطی BEV را در نظر می‌گیرد و آن را با وسایل نقلیه معمولی که ارزیابی چرخه زندگی را انجام می‌دهند مقایسه می‌کند. هدف اصلی این مطالعه، پرده‌برداری از آب‌وهوای BEVهایی است که حالت انتقال کربن کم در هند دارند و در مقایسه با سطح جهانی در کجا قرار دارند. نتایج نشان می دهد که از ۱۸ دسته ضربه در نظر گرفته شده در تجزیه و تحلیل نقطه میانی، BEV از خودروهای موتور IC برای ۱۰ دسته بهتر عمل کرد. انتشار گازهای گلخانه ای از BEV 242 گرم CO_2eq/km در سطح نقطه میانی است و امتیاز واحد در سطح نقطه پایانی ۰.۵۸ kpt است در مقایسه با ICEV که ۲.۱ kpt است. علاوه بر این، اثرات جداگانه از تولید و مرحله استفاده تا پایان عمر برای مشخص کردن فاز مشارکت عمده انتشار به دست آمد. در تجزیه و تحلیل نقطه پایانی ReCePi، BEV دوستدار محیط زیست بیشتر است، با این حال، روی آوردن به انرژی پاک تر اثرات زیست محیطی را کاهش می دهد.

International Journal of Engineering

Journal Homepage: www.ije.ir

Seismic and Economic Optimization of Water Distribution Networks Using Entropy and Ant Colony Algorithm

S. A. Mousavi. M., F. Nateghi*

International Institute of Earthquake Engineering and Seismology (IIEES), Tehran, Iran

P A P E R I N F O

Paper history:
Received 07 April 2022
Received in revised form 27 November 2022
Accepted 18 February 2023

Keywords:
Network Reliability
Wwater Distribution Network
Mechanical Properties
Entropy
Metaheuristic Methods

A B S T R A C T

Extensive research have been conducted to optimize the water distribution networks, but none has simultaneously considered the economic-mechanical and hydraulic properties of the networks. Moreover, the entropy difference in the various networks has not been exactly calculated. Therefore, the present study suggests a modified entropy function for computing the information entropy of the water distribution networks to calculate the demand nods and entropy difference amongst the various networks considering the mechanical and hydraulic properties of the network. This modification is carried out by defining a coefficient in entropy function as the output amount in every node by the exponent of all the power wasted in the network. Furthermore, the most optimum diameter and the most economic state are obtained simultaneously using the ant colony algorithm (ACO). Thus, considering all the three mechanical, hydraulic, and economic properties of the network while keeping simplicity, a more realistic method will be offered using these two metaheuristic methods. The efficiency of the proposed method was evaluated in some of the sample water networks using the modified function

***doi**: 10.5829/ije.2023.36.05b.14*

1. INTRODUCTION

Water distribution system is a network of source nods, links, demand notes, and other hydraulic components like pumps, pipes, and tanks. Water distribution systems substantially serve the water supply on the surface and a sufficient amount of water pressure to all the users and fire extinction purposes. Quantifying the reliability of the water distribution networks, as a vital system [1, 2], also, repair and maintenance of water system [3]. In recent decades, the basis of reliability of water distribution networks has been defined based on receiving a sufficient source of demand and pressure required by the consumer [4]. Various researchers have proposed in several scales of reliability for water distribution networks, and some of them include an alternative scale.

Some reseaerchers have suggested that entropy as a general performance index is possible for the water distribution systems [5]. This method possesses several advantages in contrast to the other performance indices and reliability; as an example, its calculation is very fast and simpler than the other scales; it needs the least amount of data, and it can be directly embedded in the designs' optimization frameworks [6]. and it can be a scale for system redundancy [7].

The redundancy of water distribution networks is especially important because when links fail to provide the required services, additional links will be replaced [7]. Closely interrelated with reliability, redundancy is a mostly neglected aspect of the system's general performance. Past earthquakes show that a redundancy index can dramatically increase network reliability. In other words, networks with more redundancies are more reliable against failure [8]. Therefore, redundancy can be considered an alternative scale for calculating the reliability of the water distribution networks.

It seems that Awumah et al. [5, 7] were the first researchers who suggested using Shannon's entropy [9]. As an alternative scale for computing the reliability of the water distribution networks. Later on, Tanyimobh and Templeman [10] used a multiple probability space model and conditional probability. Khinchin, [11] proposed a

* Corresponding Author Institutional Email: nateghi@iiees.ac.ir
(F. Nateghi)

Please cite this article as: S. A. Mousavi. M., F. Nateghi, Seismic and Economic Optimization of Water Distribution Networks Using Entropy and Ant Colony Algorithm, ***International Journal of Engineering, Transactions B: Applications***, Vol. 36, No. 05, (2023) 979-990

more appropriate definition of entropy function for water distribution networks. They, also, created a non-repetitive algorithm for finding the maximum entropy of the current distribution in the single-source networks. In their study, the network's topology, current direction in every link, and supply-demand in every node were considered; while, some of the other parameters like length, diameter, and coarseness of the link were ignored. A nearly extreme number of current distributions is possible unless the network is found in the tree branch type. This non-repetitive algorithm was formulated using the path entropy concept [12]. Using the concept of the super-source, they also endeavored to expand the single-source algorithm for covering multi-source networks, and it has been proved not to be consistent with the research conducted by Walters [13]. In another study, Yasin-Kassab et al. [14] presented a non-iterative algorithm based on a single source algorithm to calculate the current distribution entropy in multi-source networks. Later, the relationship between entropy and reliability of water distribution networks was investigated by Tanyimboh and Templeman [6]. Their study showed that the higher the entropy of water distribution networks, the greater the reliability.

Hosseini and Emamjomeh [15] used a simple water distribution network to examine the meaning of network entropy. Their research examined the relationship between the total power wasted by the water distribution network and the numerical value of the entropy of the network. Ang and Jowitt [16] used a simple ring network with its link diameter ranging from zero to infinite and endeavored to calculate entropy. The related network entropy and the wasted energy for the water distribution network were investigated in other work [5]. Also, Hosseini and Emamjomeh [17] in 2014 were able to obtain acceptable results by modifying some of the hydraulic and mechanical parameters. They offered an alternative method for calculating the entropy of the water distribution systems, and expressed this new concept of network entropy. The path entropy method (PEM) provided a simpler concept of network entropy and maximum water distribution network entropy. PEM's formula was presented based on the various paths for a water molecule's movement from an extraordinary source towards a super sink. Further explanations about PEM will be given herein later on. Ang and Jowitt [18] discussed about observations on energy loss and network entropy in water distribution networks.

In defining the entropy function, Templeman and Tanyimboh [19] defined the networks with an amount of redundancy can have an alot can considerably increase the reliability of the system disregarded the differences between the branching-tree networks featuring different plans as well as the number of the identical demand-supply nodes, all of which with identical PEM diagrams. Hosseini and Emamjomeh [17] proposed a new weight ratio based on each penalty number equal to the amount of damage in case of failure in order to overcome the problem. The order of the demand nodes in the network was considered in entropy calculations by considering a new coefficient in the entropy function.

The highest redundancy indices for water distribution networks are based on hydraulic or mechanical characteristics of the network, meaning that none of them considers both of the properties in its calculations. However, the network risk is intensively influenced by both of these properties. Thus, the present study aims at investigating the deficiencies of the prior definitions of water distribution network's entropy and suggesting a novel scale based on weighted entropy for the evaluation of the reliability of water distribution networks in terms of the system's mechanical and hydraulic properties Finally, economic optimization is performed using the method of meta-exploration algorithm of the ant community.

2. ENTROPY FUNCTION FOR WATER DISTRIBUTION NETWORKS

The formulation of the entropy function relies more on Shannon's [9] uncertainty scale, and this is a fundamental principle in information theory. Tanyimboh and Templeman [10] were the first one to develop a suitable entropy function using the multiple probability and conditional probability space model [11]. Flow direction has a significant effect on maximum entropy, which has not been considered in previous studies. In addition, the length, diameter and coarseness of the joints are not directly applied in their formulation. There will be a large number of possible current patterns except in branch networks. The entropy function of the network developed by Tanyimboh and Templeman [10] is calculated according to the following formula:

$$\frac{S}{K} = S = S_0 + \sum_{n=1}^{N} P_n S_n \quad (1)$$

S is the entropy, k is Boltzmann constant, is assumed to be 1, N is the total number of nodes, and S_0 is the entropy of the external input current.

$$S_0 = -\sum P_{0i} \ln P_{0i} \quad (2)$$

In this relationship, I is the system of all the source nodes, and P0i is calculated according to the following relation:

$$\frac{q_{01}}{T_0} = P_{01} \quad (3)$$

where, q_{01} is the external current flowing into the i-th source node, and T_0 is the amount of the total supply or total demand.

The second term in the entropy function is composed of the weighted entropy sum for each of the nodes (S_n), and the weight of each (P_n) is defined in the form of the ratio of the total inflowing current for every node to the

total inflowing current for the entire network as shown beneath:

$$\frac{T_n}{T_0} = P_n \quad (4)$$

where, T_n is the total current flowing out of node n. The important point in the definition of the out-flowing current is that the outflow incorporates all the needs in the related node. The weighted entropy of each of the nodes (S_n) is calculated from the following relation:
Where, T_n is the total outflow from the node n. Another important point in defining the outflow is that it encompasses any demand in the node. In Equation (1), the entropy of the outflow from every node (S_n) is given according to the following relation:

$$S_n = -\sum_{n\epsilon ND_m} P_{nj}\, In\, P_{nj} \quad (5)$$

where, NDn is a system of all the currents flowing out of the node n:

$$P_{nj} = \frac{q_{nj}}{T_n} \quad (6)$$

where, q_{nj} is the current flowing from node n to node j. The entropy function in Equation (1) displays that the entropy of a water distribution network is comprised of two parts. The entropy of the externally inflowing current (S_0), as the first component, is uncertain. Figure 1 shows a sample network with two sources and four demand nodes as well as details of entropy calculations.

3. PATH ENTROPY METHOD FOR CALCULATING THE ENTROPY OF WATER DISTRIBUTION NETWORK

As stated in the theoretical foundations of entropy section, Information entropy measures the degree of uncertainty in a situation or system. That is, the entropy of a water distribution network should be defined according to the number of paths available for a water molecule to move from the source point to the point of consumption. Based on this perspective, there is offered another alternative method by Ang and Jowitt [16] for calculating the entropy of a network, and it is called the entropy method.

The PEM diagram in the first step involves determining the number of paths of the source node according to the paths of the consumption node and drawing a PEM diagram with all its nodes and links. In the second step, the flow through each link by examining the flow rate in all network links.

Calculating the entropy of a PEM network is relatively simpler compared to the network entropy equation proposed by Tanyimboh and Templeman [12]. The true power of PEM is its ability to provide new insights into the meanings of network entropy, such as the entropy of branched tree networks and the maximum current entropy of a single-source network with a specified flow direction (Figure 2). Figure 3 shows the sample network PEM shown in Figure 4 as well as its entropy calculations.

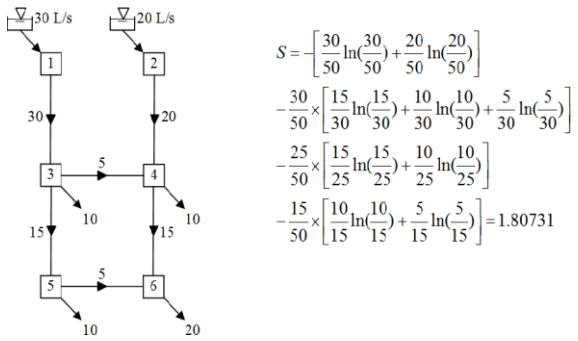

Figure 1. A sample network with two sources and four demand nodes as well as the entropy calculations' details [19]

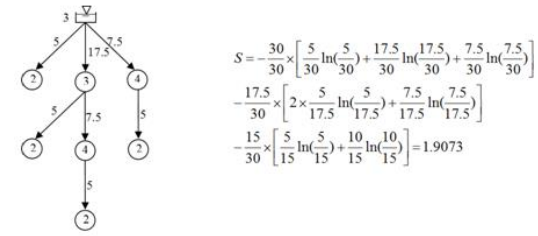

Figure 2. Tree diagram of the sample network shown in Figure 4 with entropy calculations [18]

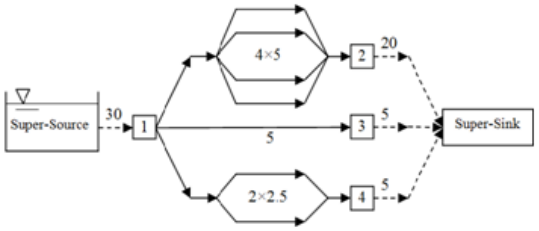

Figure 3. PEM diagram of the sample network shown in Figure 4 along with entropy computations [17]

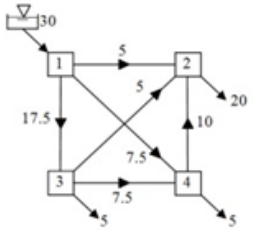

Figure 4. A fully connected sample network with maximum network entropy [16]

4. DISCUSSION ABOUT THE PRIOR DEFINITIONS

OF ENTROPY FUNCTION

As mentioned by Walters [13], all of the branching-tree networks at least have identical entropy values. Ang and Jowitt [16] showed this reality using the path entropy method. Figure 5 shows all of the various plans of the branching-tree networks related to the sample network displayed in Figure 4.

As shown in Figure 5, there is only one path from the source node to the demand node in all cases. Therefore, from the perspective of information, all of them essentially have identical entropies.

For the tree sample network in Figure 6, it has been shown that various diagrams can be applied for displaying each PEM plans. However, in the definition by Templeman and Tanyimboh [10], there is no difference between the tree networks featuring different configurations.

Examining the networks shown in Figure 5, it is clear that some of them are more sensitive to damage to one of their links. For example, if the 3-1 link in networks (d), (c) and (e) in Figure 5 is damaged due to earthquake hazards, the loss rates will be 30, 10 and 5 liters per second, respectively. Therefore, the amount of service losses in a network, in addition to the series or parallel mode of the network, also depends on the connection of different consumption nodes to the source node.

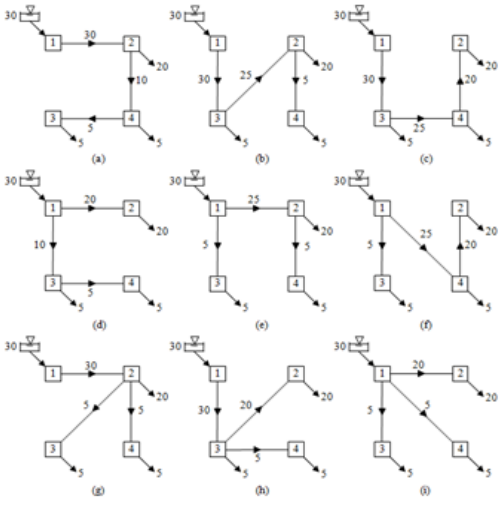

Figure 5. Various branching-tree network diagrams

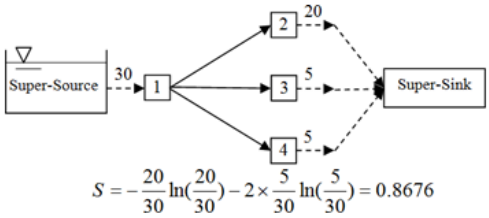

Figure 6. PEM diagram of the branching-tree network

Various states of the demand-supply connections in the branching-tree networks are shown in Figure 6 [16, 17] As shown in Figure 7, according to the four modes shown, the fourth pattern has the most redundancy because each demand node has a separate path to the source and the failure of each link does not affect the other nodes. Conversely, the first model is the most vulnerable water distribution network because each sphere depends on the previous node.

Hosseini and Emamjomeh [17] defined a penalty value (TP) for every link in order to add the effects of the connection states and orders that actually determine the sensitivity of a network. Based on these penalty values, the new weight ratio (P′n) was introduced, as explained in the following words. They defined the amount of every link's penalty as being equal to the amount of damage imposed onto the network in case of cessation in repairing (7).

Where the numerator is the outflow discharge rate, and the denominator is the penalty functions for all of the network's links.

Where TP is the sum of the penalty factors for all of the network's links, they used this weight ratio instead of the prior ratio, i.e., P′n, in Equation (1).

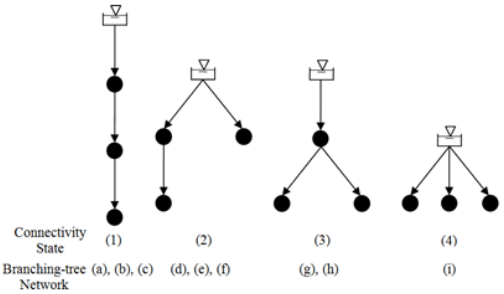

Figure 7. PEM diagram of branching-tree networks shown in Figure 6

TABLE 1. Amount of entropy (S') for the branching-tree networks in Figure 5 based on the modifications proposed by Hosseini and Emamjomeh [15]

Network	a	b	c	d	e	f	g	h	i
Amount of entropy based on the function proposed [15]	0.5784	0.4338	0.3470	0.7436	0.7436	0.5206	0.6507	0.4732	0.8676

The amount of entropy (S') for all of the branching-tree networks shown in Figure 5 based on the modifications by Hosseini and Emamjomeh [15] can be seen in Table 1, according to which only network (i) has an entropy value similar to what has been suggested by Tanyimboh and Templeman [10] because each demand node in this network is separately connected to the source. The amount of entropy in the networks featuring more node connections to the source is notably reduced with the new weight ratio. Therefore, Hosseini and Emamjomeh [15] could define a new weight index (P′n) in entropy function to modify the effect of the order of connection in the network's demand nodes as well as the difference between the various branching-tree networks. Considering the results shown in Table 1, in the case of using the entropy functions modified by Hosseini and Emamjomeh [15], the same entropy amount is calculated for branching-tree networks (d) and (e). However, it can be observed through a more exact analysis of these two networks that in case of the detachment in link 2-1 in network (d), the amount of the scattered water would be 20 l/s. Therefore, the needs of the second consumer would not be met. If the same link fails in a network (e), the amount of the scattered water would be 25 l/s. Therefore, the needs of the second and the fourth consumers would not be satisfied. Thus, network (d), in contrast to a network (e), features higher reliability and, in case of considering entropy as the reliability scale, it has to be larger in a network (d) as compared to a network (e). Resultantly, the modifications by Hosseini and Emamjomeh [17] cannot determine the real differences in the reliability rates of various networks with the identical mechanical specifications, to wit length, diameter and coarseness coefficient. In addition, the reliability of the various networks with diverse mechanical properties cannot be measured with this modified version. As a specimen, if the length, diameter, or substance is changed in one of the branching-tree networks, the effect of this change on the entropy amount cannot be measured using this entropy function. In the next section, a new ratio will be offered in entropy functions so as to be able to consider both the mechanical specifications and hydraulic properties of the network in entropy calculations. Additionally, the connection order of the network's demand nodes and the differences in the various networks will be investigated with more precision.

5. IDENTIFICATION OF THE FLAWS IN THE PREVIOUS DEFINITIONS OF ENTROPY FUNCTION AND OFFERING A NEW FUNCTION

As it was concluded in the previous section, the entropy function offered by Tanimboh and Templeman [19] has two substantial flaws even with all the changes that have been brought about therein. Firstly, not both the mechanical and hydraulic properties of the network have been considered in this function; especially, only the rate of the flow through the links has been taken into account in entropy calculations. Besides, the mechanical parameters like length, diameter, and coarseness of the link have been ignored in entropy calculations, whereas it is evident that the above mentioned parameters have many effects on the amount of entropy as a scale of the network's reliability. Secondly, considering all the changes made in the entropy function, they could not show the numerical difference between the branching-tree networks of different types with identical numbers of sources and demand nodes. In the current research paper, the wasted power has been utilized for considering the mechanical characteristics of the network, such as length, diameter, and coarseness of the links, along with the hydraulic specifications. Moreover, after linking to EPANET Software, the best diameter and the best entropy were obtained with the result being the most optimum economic state, and based on the amount of the wasted power calculated for each link, a new P″n ratio was defined for every network node. The equation took the following form:

$$P_n^{"} = \frac{T_n}{\sum_{i=1}^{np} P_{wi}} \quad (8)$$

In the above relation, Tn, like the relation proposed by Tanimboh and Templeman [19] is equal to the amount of water that flows out of node n, and Tpw is the total power wasted in the network, and it is equal to the sum of power wasted in all of the network's pipes, and it is expressed in the following form:

$$T_{pw} = \sum_{i=1}^{nl} P_{wi} \quad (9)$$

Pwi is the power wasted in every pipe, and nl is the total number of the network's pipes. The power wasted in every pipe is calculated from the following relation.

$$P_{wi} = \rho g h_i Q_i \quad (10)$$

In the above relation, ρ is the water density in kg/m^3, g is the earth gravity's acceleration in m/s^2, hi is the amount of head loss in every pipe in m, and Qi is the flow rate in the i-th pipe in m^3/s. Amongst the relations offered for the calculation of the loss rate, such as the formula by Hazen Williams and the formula by Darcey Weisbach, and the formula by Chesey-Manning, the first is most suitable for water distribution networks. Darcey-Weisbach's formula is usable for stratified currents and fluids other than water, and Chesey-Manning's formula is mainly applicable to the flows in open channels.

Hazen William's formula is defined in the following form for the calculation of head loss in every pipe:

$$h_i = \frac{6.78L_i}{D_i^{1.165}} = \left(\frac{V_i}{C_i}\right)^{1.85} = \frac{10.6L_i}{D_i^{4.865}C_i^{1.85}} Q_i^{1.85} = K_i Q_i^{1.85} \quad (11)$$

where Li is the length of the i-th pipe in m; Di is the diameter of the pipe i-th in m; Ci is the coarseness coefficient of the i-th pipe, and Ki is the resistance coefficient of i-th pipe in s/m^2. Replacing the relation

(11) in relation (10) gives the amount of the power wasted in i-th pipe in watts (w) as shown underneath:

$$P_{wi} = \rho g k_i Q_i^{2.85} \quad (12)$$

Following the calculation of the new weight coefficient ($P"_n$) for every node, it was substituted for the previous weight coefficient (P_n) in the entropy proposed by Tanimboh and Templeman [19]. With the new coefficient, the modified entropy function takes the following form:

$$\frac{S}{K} = S = S_0 + \sum_{n=1}^{N} P"_n S_n \quad (13)$$

If, in the relation (12), the amount of $\rho g k_i$ is set equal to a, P_{wi} can be written in the following form:

$$P_{wi} = a Q_i^{2.85} \quad (14)$$

In fact, the denominator of the new weight coefficient's fraction is in the form of $\sum_{i=1}^{n1} a\, Q_i^{2.85}$while the denominator of the coefficient's fraction defined by Hosseini and Emamjomeh [17] is in the form of $\sum_{i=1}^{n1} Q_1$. It means that the denominator of the new coefficient's fraction is a nonlinear function of the discharge rate.

The other notable point about the proposed coefficient is the amount of diameter for the calculation of the power wasted in every link. The diameter influences the amount of current passing through the links. Put differently, the amount of current passing through the links changes with the change in diameter, and this creates new conditions in terms of the network's hydraulic status, which necessitates any specific entropy state. Due to the same reason, in the various states of the current in a network, the diameters of all the links are assumed to be fixed for the calculation of the power wasted in the links. As for the diameter of the networks' links, this number can be the diameter of the network's links or the largest diameter in the network or even unity. Thus, in the forthcoming sections that try investigating the reliability of a network in various flow states, a fixed value would be considered for the diameter.

The amount of entropy in tree networks shown in Figure 5 has been offered in Table 2 based on the modification made by Hosseini and Emamjomeh (s') [17] and the modification made herein ($\bar{S}$). In the calculation of the wasted power, the length of the peripheral pipes is equal to 1000m, the diameter of all the pipes is equal to 400mm, and the coarseness coefficient of all the pipes is equal to 130. For instance, the details of calculating the entropy of branching-tree networks (b) shown in Figures 3 and 4 are as explained below:

$$L_{1-3}, L_{2-4} = 1000\text{m}, L_{3-2} = 1414.21\text{m}$$
$$P_{w(1-3)} = 50.34W, P_{w(3-2)} = 42.34W, P_{w(2-4)} = 0.305W$$
$$\sum_{i=1}^{3} P_{wi} = 92.985W \quad (15)$$
$$\bar{S} = -\frac{30}{92.985} \times \left[\frac{5}{30} In\left(\frac{5}{30}\right) + \frac{25}{30} In\left(\frac{25}{30}\right)\right] - \frac{25}{92.985} \times \left[\frac{20}{25} In\left(\frac{20}{25}\right) + \frac{5}{25} In\left(\frac{2}{25}\right)\right] = 0.2799$$

Considering Table 2, it is observed that the amount of entropy is larger in the network (d) in comparison to the amount of entropy in the network (e) with the modifications made in this research, and this is consistent with what was expected.

6. INVESTIGATING THE BEHAVIOR OF THE ENTROPY FUNCTION PROPOSED IN PARALLEL NETWORK

A parallel network with two links, as shown in Figure 8, has been used for the investigation of the behavior of the function proposed for the parallel networks. In this network, the inflow rate, the lengths of the links, the diameters of the links, and the coarseness coefficient of the links are respectively 30 l/s, 1000m, 400mm, and 130. If the flow speed of the first link is set at x, the speed of the second link's flow would be x-30. Based on the function proposed herein, the changes in the entropy of the parallel network in regard to x have been shown in Figure 9, and, as seen therein, the amount of entropy is larger for the two closer links. Specifically, the maximum entropy occurs when the amounts of flows through two links are exactly identical. Put another way, the maximum amount of entropy would be equal to x=15, and the entropy function's diagram would be symmetrical in regard to this amount. These changes are exactly based on our expectations about the entropy's behavior.

7. INVESTIGATING THE BEHAVIOR OF THE ENTROPY FUNCTION SUGGESTED FOR THE RING NETWORK

A network with one supply node and three demand nodes, as shown in Figure 10, will be used for the

TABLE 2. Amounts of entropy in the branching-tree networks shown in Figure 5 based on the modifications made by Hossein and Emamjomeh (**S'**) [17] and modifications made herein ($\bar{S}$)

Network	a	b	c	d	e	f	g	h	i
S'	0.5784	0.4338	0.3470	0.7436	0.7436	0.5206	0.6507	0.4732	0.8676
$\bar{S}$	0.4957	0.2799	0.2707	1.4181	0.8519	0.4449	0.5096	0.3562	1.5812

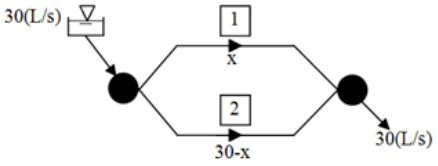

Figure 8. A parallel network with two links

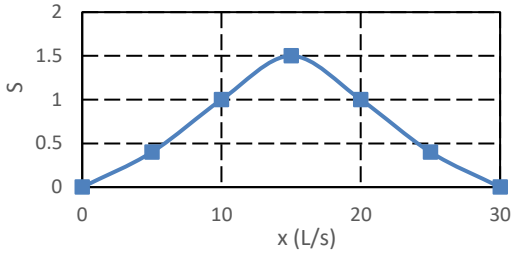

Figure 9. Entropy changes in parallel network versus the various amounts of flow passing through the first link (x) using the entropy function proposed in this study

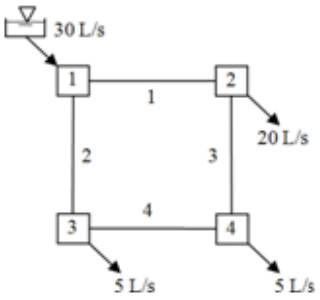

Figure 10. The sample ring network with a source node and three demand nodes [20]

evaluation of the entropy function. In order to evaluate the entropy function suggested by Ang and Jowitt [18], this network was used in the ring networks used by Tanimboh and Templeman [19].

The heights of the source node and demand nodes were respectively 100m and 99m. The length, diameter, and coarseness coefficient of all the links are identical, i.e., equal to 890m, 400mm, and 130. Figure 11 shows three various states of flow directions. Table 3 displays the entropy amounts calculated using Taniymboh and Templeman's method (s) and Hosseini and Emamjomeh's [15] modified method (S') and the entropy method proposed in this research (S''). Considering Figure 11, it can be concluded that the reliability of network (a) is larger than the network (b) and reliability of network (b) is larger than that of the network (c). in fact, the breakage in link 2-1 in networks (a), (b) and (c) respectively causes wastage of water for 10, 22.5 and27.5 liters per second. Moreover, the maximum difference between the flow rates in the network's links

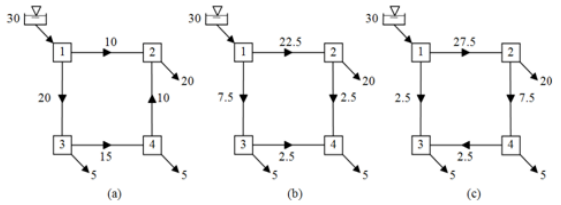

Figure 11. Three different possible current directions for the network shown in Figure (10) [20]

TABLE 3. The entropy amounts for the networks shown in Figure 11 using three discussed functions

Network	2	12	42	63
R	0.998933	0.998777	0.998872	0.998485
S	3.0201	2.6424	2.8640	2.6362
$\overline{S}$	0.009483	0.008845	0.006732	0.00578

in the state (a) is 10 l/s, while this difference in (b) and (c) states is respectively 20 l/s and 25 l/s. Based on these two realities, the network is expected to have a larger entropy in the state (a) as compared to the state (b), and it is also expected to be larger in the state (b) than in state (c). However, table (3) shows that although the amount of entropy in the network (a) is larger than the amount of entropy in networks (b) and (c), the amounts of entropy in networks (b) and (c) are identical using the first method. And based on the modified function proposed by Hosseini and Emamjomeh [17], the amount of entropy in the network (b) is larger than the amount of entropy in the network (c), and the amount of entropy in a network (c) is larger than the amount of entropy in the network (a). In the end, it is worth mentioning that the amounts of entropy calculated by the method proposed herein, as seen in Table 3, are consistent with our expectations. In other words, the amount of entropy in the network (a) is larger than the amount of entropy in the network (b), and the amount of entropy in the network (b) is larger than the amount of entropy in the network (c).

8. OPTIMIZATION OF RELIABILITY AND ECONOMIC OPTIMIZATION OF THE SAMPLE NETWORK USING THE ANT COLONY METHOD AND THIS STUDY'S PROPOSED ENTROPY FUNCTION

One of the most important issues about the entropy of the water distribution networks is the relationship between the amount of entropy and the reliability of the network. In the study performed by Tanyimboh and Templeman [6], use was made of various hydraulic networks with different numbers of links and various rings, and it was proved that this relationship is strong. Resultantly, they concluded that the networks with higher entropy feature higher reliability. In this section, the relationship between

the proposed entropy function and the network's reliability as well as the controlling of the network's parameters in hydraulic, mechanical, and economic matters will be investigated via linking to MATLAB program and EPANET Software. In this study, the following network was used for the same purpose; it has also been used by Tanyimboh and Templeman [6] for comparing their own entropy function with others in this network.

The configurations presented in Figure 12 have been divided in terms of their links to five groups, including a network with 17 links and configurations with 13, 14, 15, and 16 links. In this section, the goal is to find a network with the minimum cost, maximum entropy, and lowest loss. Thus, after hydraulic analysis of the 64 states in EPANET Software for every network, the rate of the flow passing through the links, the flow speed in the links, and the amount of the head loss in every link was extracted and, using this information, the wasted power of each link and the total wasted power of the network was calculated. Having this information and clarifying the direction of the flow in the links, the entropy can be calculated for every network with three investigated functions (the entropy function proposed by Tanimboh and Templeman [19] the one modified by Hosseini and Emamjomeh [17], and the one modified in this research paper). The entropy function has been calculated for 64 states and, using the comprehensive ant algorithm prepared in MATLAB Software and linked to EPANET software; the lowest diameter was set in such a way that the hydraulic specifications of the network are satisfied.

The amounts of the input information for every network and the amount of the entropy were investigated based on the three discussed methods of S, S' and S" as well as by the utilization of the comprehensive ant colony algorithm which was presented herein; resultantly, the best network states were obtained in economic terms and in regard of the network parameters' satisfaction.

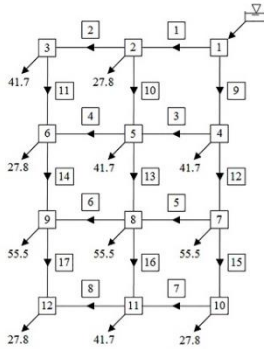

Figure 12. Sample water distribution network with one source node and 11 demand nodes [6]

After the specification of the amounts of the networks' entropy, finding the optimum network becomes feasible. In this section and in the first stage and from amongst each group of the networks and considering the number of the links, the network the entropy of which is largest according to the entropy function modified herein with its total head loss being the lowest in that network is introduced as the optimum network. To do so, the networks with an identical number of links are organized firstly based on the maximum loss in the network; then, the loss and entropy amounts are normalized to the maximum amount, and the loss and networks' entropy diagrams are delineated in a system. Based on these diagrams, the network with the lowest loss and highest entropy is selected as the best network.

The reliability of the network's general structure has been displayed in Figure 12. As it is seen, this network has one source node and 11 demand nodes with various demand rates. The lengths of all the links and their coarseness coefficients are respectively 1000m and 130. The heights of the source node and demand nodes are respectively 100m and zero. Diverse plans can be designed for this network. As it is shown in Figure 13, use was made of six various plans in this research. Using the entropy function proposed by Tanimboh and Templeman [19], these networks have been designed in such a way that the rate of flow discharge in various links should have maximum entropy with the least cost. Table 4 gives the related diameters and the speed rates of the links for the patterns shown in Figure 13 [6]. One of the formulations for the calculation of the network's reliability is the function proposed by Tanyimboh and Templeman [6], Therefore, the final formula of the single-source water distribution network can be expressed as follows:

$$R = \frac{1}{T}\Big[P(0)T(0) = \sum_{m=1}^{M} P(m)T(M) + \sum_{\substack{m=1 \\ \forall n \neq m}}^{M} P(m,n)T(m,n) + \cdots\Big] + \frac{1}{2}\Big[1 - P(0) - \sum_{m=1}^{M} P(m) - \sum_{\substack{m=1 \\ \forall n \neq m}}^{M} P(m,n) - \cdots\Big] \quad (17)$$

In the above formula, R is the network's reliability, P(0) is the possibility of having no access to the link, P(m) is the possibility of having no access to the only link m, and P(m, n) is the probability with which m and n might be inaccessible. Similarly, T(0), T(m), and T(m, n) are the total flows that are available in enough pressure and without any link with only link m being unavailable and with m and n links being respectively unavailable. In the end, M is the abbreviation for the number of links, whereas T indicates the total demand [6]. The reliability rates of the plans shown for four superior designs as specified in the optimizing software along with their entropy amounts have been presented in Table 5 based on the entropy function proposed by Tanyimboh and Templeman [6] (S) and the function proposed herein ($\bar{S}$).

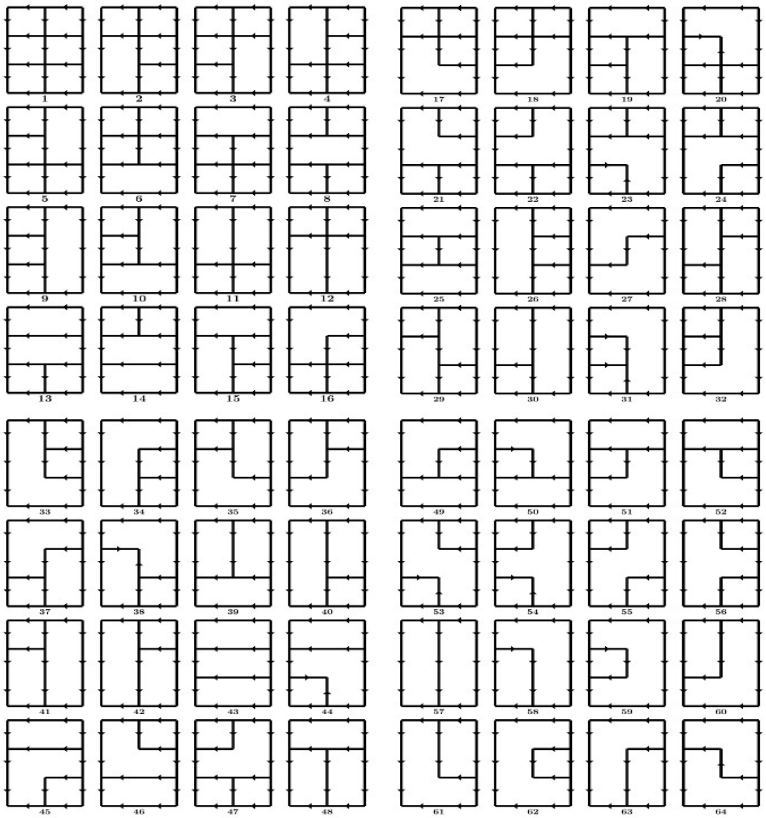

Figure 13. Various configurations of the water distribution network with 11 consumption nodes

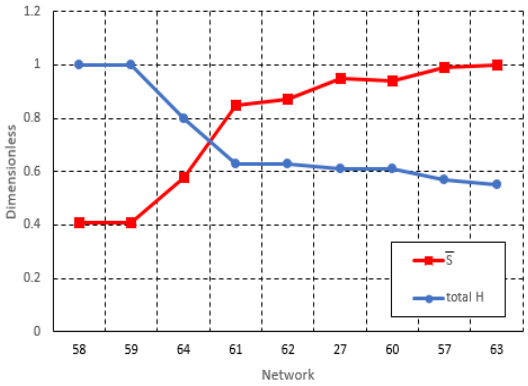

Figure 14. The diagram of the loss and entropy for a number of sample networks in this study

As it is seen, the decrease in the reliability rates of various arrangements causes reductions in the amounts of the network's entropy in general based on the entropy function proposed by Tanimboh and Templeman [19] and the function proposed in this research paper. Therefore, the entropy function proposed herein is exactly directly associated like in the entropy function proposed by Tanimboh and Templeman [19] with the network's reliability, but, in addition to the advantages of the function proposed by Tanimboh and Templeman [19], the entropy function proposed herein and written simultaneously in MATLAB and EPANET and enabling the optimization of the diameters by ACO algorithm can consider both the best mechanical and the hydraulic states of the network, and this leads to the most optimum economic state.

TABLE 4. Optimum network of each group based on the number of links along with the specifications of the network's configuration

Group of networks based on the number of links	Network with 16 links	Network with 15 links	Network with 14 links	Network with 13 links
Number of the optimum network	2	12	42	63
∑L(m)	16000	15000	14000	13000
∑H	143.3	145.64	163.18	174.38
$\bar{S}$	0.009483	0.008845	0.006732	0.005643

Network's shape	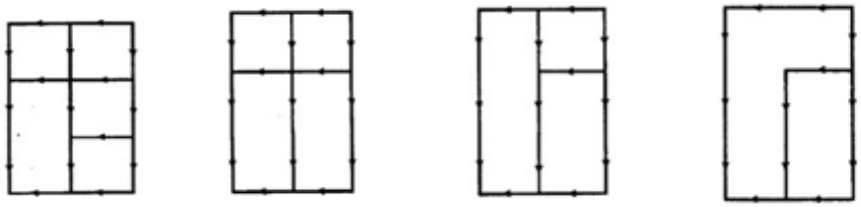

TABLE 5. Reliability and entropy amoungs based on function proposed by Tanyimboh and Templeman (S) [6] and the function proposed herein for the best of the obtained states

Network	2	12	42	63
R	0.998933	0.998777	0.998872	0.998485
S	3.0201	2.6424	2.8640	2.6362
$\bar{S}$	0.009483	0.008845	0.006732	0.00578

9. COMPREHENSIVE ANT COLONY SYSTEM (ACS) USED IN THIS STUDY

In order to provide a higher possibility of more control over the creation of a balance between the explorations and productions, Dorigo and Gambardella suggested a comprehensive ant colony system by Bulm and Roli [20].

$$\text{Q<q}_0,\quad P_{ij}(k,t)=\begin{cases}\dfrac{[\tau_{ij}(t)]^{\alpha}}{\sum_{j=1}^{J}[\tau_{ij}(t)]^{\alpha}[\tau_{ij}]^{\beta}} \\ I_{\arg\max([\tau_{ij}(t)]^{\alpha}[\tau_{ij}]^{\beta}}\end{cases}\text{, o.w} \qquad (18)$$

In the above formula, q is a value within the range of (0, 1). q0 is the factor of the exploration's productivity ($0 \le q_0 \le 1$).

If $q>q_0$, the defined probability function would be in match with the probability function defined for AS. And, if $q>q_0$, the path with the highest amount of $[\tau_{ij}(t)]^{\alpha} \times [\eta_{ij}]^{\beta}$, would be chosen with a probability of unity and the probability of choosing the other paths in the branched routes in the decision point i would be zero, or it can be stated in summary that the path with the maximum amount of $[\tau_{ij}(t)]^{\alpha} \times [\eta_{ij}]^{\beta}$, will be chosen in every decision point i. As it is observed in the above relation, exploration and production are both included in both of the cases. If $q>q_0$, the exploration phenomenon would be included and if $q>q_0$, the production phenomenon would be included.

In this algorithm, the commands' synchronization is carried out in both online and offline forms. Online synchronization in this method is in such a way that the commands of this path are immediately synchronized when an answer is constructed in a single iteration, and this iteration would be applied for the next ants. This is conducted in the form of the following formula:

$$\tau_{ij}(t)=\rho\tau_{ij}(t)+(1-\rho)\tau_{ij} \qquad (19)$$

Furthermore, offline synchronization is also carried out in this method in addition to online synchronization, as well. For offline commands' synchronization, we will have the following according to the formula given below:

It means that when all of the ants constructed their answers in one iteration, the best answer constructed in this iteration would be applied for the synchronization of the paths' commands in the next iteration.

$$\tau_{ij}(t+1)=\rho\tau_{ij}(t)+(1-\rho)\Delta\tau_{ij}^{gb} \qquad (20)$$

$\Delta\tau_{ij}^{gb}$ is calculated according to the following formula:

$$\Delta\tau_{ij}^{gb}(t)=\frac{\varphi}{f(S^{gb}(t))}I_{S^{gb(t)}}\{(i,j)\} \qquad (21)$$

In the above formula, $= S^{gb}(t)$is the best local optimum answer in t-th iteration; $= f(S^{gb}(t))$is the cost of the best local optimum answer in t-th iteration; $= \emptyset$ is a quantity depending on the amount of the commands and it is termed the factor of the command's value and $I_{S^{gb(t)}}\{(i,j)\}$is calculated according to the relation given in the previous section.

Table 6 shows that for 10-link network, after 10 runs, the most optimal economic state (minimum diameter) is created, which 13-link network has the most optimal entropy in its group. Therefore, both in terms of reliability and economics, acceptable results were obtained. Figure 15 shows that the greater the number of iterations, the lower the value of the objective function, which is the diameter.

TABLE 6. the results obtained using the ACO method in 10 executions for the optimization of the economic state

	Diameter									
Link	**Run 1**	**Run 2**	**Run 3**	**Run 4**	**Run 5**	**Run 6**	**Run 7**	**Run 8**	**Run 9**	**Run 0**
1	120	120	120	100	140	100	140	100	100	0
2	120	0	100	100	100	120	120	140	140	100
3	0	120	100	100	120	100	0	0	100	0

4	0	0	100	100	0	100	0	100	100	120
5	80	100	80	80	80	0	120	0	0	0
6	0	80	100	100	0	0	100	100	80	100
7	100	100	0	0	100	100	0	0	80	120
8	100	100	80	80	140	120	120	80	100	120
9	120	120	120	120	100	100	100	100	100	0
10	100	100	100	80	0	80	0	80	0	140
11	160	120	140	140	120	160	140	180	160	140
12	160	120	140	140	120	1+60	140	180	160	140
13	140	160	140	160	160	140	140	120	140	140
Cost ($)	41900	44100	42600	42900	42900	43300	39900	41400	41600	39400

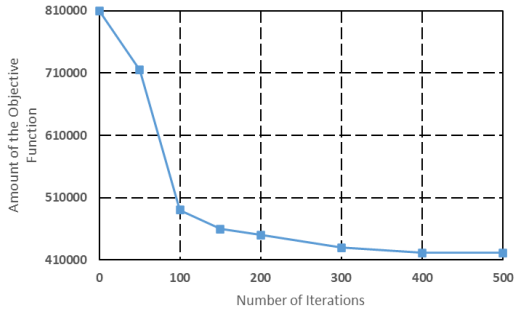

Figure 15. The mean values of the objective function for the sample ring network after ten runs of the ACO algorithm

10. CONCLUSION

Considering the various water distribution networks studied herein and the numerical results offered in this study, it can be concluded that the metaheuristic method is a good scale for analyzing the reliability according to the mechanical, hydraulic, and economic aspects of the water distribution networks. The entropy in the water distribution networks can be a proper scale for evaluating the reliability of the networks exposed to natural or artificial dangers. The more the number of the network's specifications for calculating the entropy, the more real the scale for the calculation of the reliability. After investigating the extant methods suggested by several researchers for the calculation of the entropy of water distribution networks and their modification by various researchers, it was figured out there are two essential flaws.

Firstly, all of them have just considered the flow rate of the links, whereas they have fallen short of considering the network's mechanical specifications like length and coarseness coefficient of the links. Secondly, despite the changes recommended for these functions, they cannot show the numerical difference between the various tree networks having the identical number of source and demand nodes as well as the different kinds of flow directions in a given network. In order to overcome these two flaws and improve the evaluation of the reliability in these networks, the present study made some modifications to the proposed entropy function. This modification enabled the evaluation of the water distribution network's reliability via considering the mechanical specifications (the head loss in the network) for a number of the networks, and it was made clear that the proposed function, though being simple, can take into account the order of the connection between the source and demand nodes as well as the difference between the various water distribution networks and also the effects of the both

Numerical results show that in each network group, according to the number of links, the most optimal design has the highest entropy, and using the optimizer program (ACO), the most optimal diameter can be obtained as shown in Table 7. Brought. In this study, the most optimal entropy state is simultaneously placed in the optimizer software designed by the Ant Society Algorithm (ACO) and at the same time all hydraulic, mechanical and economic characteristics are controlled and the most optimal state is extracted, so we can answer. It is more economical and reliable to use entropy exploration methods and comprehensive ant algorithm in water distribution networks. In general, the goal is to optimize both in terms of reliability and at the same time to be economically viable design, which in this study using two meta-exploration methods (entropy and ant community algorithm) this has been achieved.

11. REFERENCES

1. Moghtaderi-Zadeh, M. and Kiureghian, A., "Reliability upgrading of lifeline networks for post-earthquake serviceability", ***Earthquake Engineering and Structural Dynamics***, Vol. 11, (1983), 557-566. https://doi.org/10.1002/eqe.4290110408
2. Selçuk, R.D.A.S. and Yücemen, M.S., "Reliability of lifeline networks under seismic hazard", ***Reliability Engineering and***

System Safety, Vol. 65, (1999), 213-227. https://doi.org/10.1016/S0951-8320(98)00098-2

3. Quimpo, R.G. and Shamsi, U.M., "Reliability-based distribution system maintenance", ***Journal of Water Resources Planning and Manage, ASCE***, Vol. 117, (1991), 321-339. https://doi.org/10.1061/(ASCE)0733-9496(1991)117:3(321)
4. Tanyimboh, T., Burd, R., Burrows, R. and Tabesh, M., "Modelling and reliability analysis of water distribution systems", ***Water Science and Technology***, Vol. 39, No. 4, (1999), 249-255. https://doi.org/10.1016/S0273-1223(99)00078-5
5. Awumah, K., Goulter, I. and Bhatt, S., "Assessment of reliability in water distribution networks using entropy based measures", ***Stochastic Hydrology and Hydraulics***, Vol. 4, (1990), 309-320. https://doi.org/10.1007/BF01544084
6. Tanyimboh, T.T. and Templeman, A.B., "A quantified assessment of the relationship between the reliability and entropy of water distribution systems", ***Engineering Optimization***, Vol. 33, No. 2, (2000), 179-199. https://doi.org/10.1080/03052150008940916
7. Awumah, K., Goulter, I. and Bhatt, S.K., "Entropy-based redundancy measures in water-distribution networks", ***Journal of Hydraulic Engineering***, Vol. 117, No. 5, (1991), 595-614. https://doi.org/10.1061/(ASCE)0733-9429(1991)117:5(595)
8. Javanbarg, M.B., Takada, S. and Kuwata, Y., "Seismic vulnerability evaluation of water delivery system", The 12th Japan Earthquake Engineering Symposium, Tokyo, Japan, (2006).
9. Shannon, C., "A mathematical theory of communication", ***The Bell System Technical Journal,*** Vol. 27, No. 3, (1948), 379-423. DOI: 10.1002/j.1538-7305.1948.tb01338.x
10. Tanyimboh, T. and Templeman, A., "Calculating maximum entropy flows in networks", ***Journal of the Operational Research Society***, Vol. 44, No. 4, (1993), 383-396. https://doi.org/10.1057/jors.1993.68
11. Khinchin, A.I., "The entropy concept in probability theory", Courier Corporation, (2013).
12. Tanyimboh, T. and Templeman, A., "Maximum entropy flows for single-source networks", ***Engineering Optimization***, Vol. 22, No. 1, (1993), 49-63. https://doi.org/10.1080/03052159308941325
13. Walters, G., "Discussion on: Maximum entropy flows in single source networks3", ***Engineering Optimization+ A35***, Vol. 25, No. 2, (1995), 155-163. https://doi.org/10.1080/03052159508941260
14. Yassin-Kassab, A., Templeman, A. and Tanyimboh, T., "Calculating maximum entropy flows in multi-source, multi-demand networks", ***Engineering Optimization***, Vol. 31, No. 6, (1999), 695-729. https://doi.org/10.1080/03052159908941393
15. Hosseini, M. and Emamjomeh, H., "A method for assessmentof water distribution networks' redundancyby using informational entropy", in 4th International Conference from Scientific Computing to Computational Engineering 4th IC-SCCE, Athens., (2010 of Conference).
16. Ang, W.K. and Jowitt, P.W., "Some new insights on informational entropy for water distribution networks", ***Engineering Optimization***, Vol. 37, No. 3, (2005), 277-289. https://doi.org/10.1080/03052151233132825 9
17. Hosseini, M. and Emamjomeh, H., "Entropy-based serviceability assessment of water distribution networks subjected to natural and man-made hazards", ***International Journal Engineering, Transactions B: applications***, Vol. 27, No. 5, (2014), 675-688. DOI: 10.5829/idosi.ije.2014.27.05b.02
18. Ang, W.K. and Jowitt, P., "Some observations on energy loss and network entropy in water distribution networks", ***Engineering Optimization***, Vol. 37, (2003), 375-389. https://doi.org/10.1080/0305215031000154668
19. Tanyimboh, T.T. and Templeman, A.B. "Calculating the reliability of single-source networks by the source head method", ***Advances in Engineering. Software***., Vol 29, (1998), 499-505. https://doi.org/10.1016/S0965-9978(98)00016-7
20. Bulm, C. and Roli, A., "Metaheuristics in combinatorial optimization overview and conceptual comparison", ***ACM Computing Surveys*** Vol. 35, (2003), 268-308. https://doi.org/10.1145/937503.937505

Persian Abstract

چکیده

مطالعات زیادی برای بهینه سازی شبکه‌های توزیع آب انجام شده است، اما هیچ کدام از آنها همزمان ویژگی‌های مکانیکی اقتصادی و هم هیدرولیکی شبکه‌ها را در نظر نگرفته‌اند. همچنین تفاوت آنتروپی در شبکه‌های مختلف دقیقاً محاسبه نشده است. بنابراین، این مطالعه یک تابع آنتروپی اصلاح‌شده را برای محاسبه آنتروپی اطلاعاتی شبکه‌های توزیع آب پیشنهاد می‌کند تا ترتیب گره‌های تقاضا و اختلاف آنتروپی در بین شبکه‌های مختلف با در نظر گرفتن ویژگی‌های مکانیکی و هیدرولیکی شبکه محاسبه شود. این اصلاح از طریق تعریف یک ضریب در تابع آنتروپی به عنوان مقدار خروجی در هر گره به تمام توان تلف شده در شبکه انجام می‌شود. و همچنین همزمان از طریق الگوریتم جامعه مورچگان (ACO) بهینه‌ترین قطر و در نتیجه بهینه‌ترین حالت اقتصادی حاصل می‌شود از این رو، با در نظر گرفتن هر سه ویژگی مکانیکی و هیدرولیکی و اقتصادی شبکه با حفظ سادگی، روش واقعی‌تری با استفاده از این دو روش فرا کاوشی ارائه شده است. کارایی روش پیشنهادی برخی از شبکه‌های آب نمونه با استفاده از تابع اصلاح شده ارزیابی شد.

International Journal of Engineering

Journal Homepage: www.ije.ir

Finite Element Modelling of Laboratory Tests on Reinforced Concrete Beams Containing Recycled Aggregate Concrete

A. J. Pawar*, M. Patel, S. R. Suryawanshi

Department of Civil Engineering, S. V. National Institute of Technology, Surat, India

P A P E R I N F O

Paper history:
Received 21 January 2023
Received in revised form 28 February 2023
Accepted 02 March 2023

Keywords:
Recycled Concrete Aggregate
Normal Strength Concrete Beam
Flexural Behavior
Numerical Simulation

A B S T R A C T

The predictive accuracy of the finite element (FE) based packages are broadly based on the compatibility of adopted non-linear numerical procedures and incorporated material models. However, the routine way to define concrete material is not applicable to the concretes containing substitute materials in place of conventional concrete ingredients. Therefore, in this work, appropriate definition of materials in terms of stress-strain relations have been utilized to simulate the experimental work of RC beams containing coarser fractions of recycled concrete aggregates (RCA). The entire work has been carried out into two phases; an experimental work and the simulation of experimental work using FEA package, ABAQUS. In the experimental part, three number of full-scaled beam specimens were tested to failure through four-point monotonous loading. The replacement level of natural coarse aggregates was taken as 0.0, 50 and 100% by direct substitution. In the simulation phase, in addition to laboratory evaluated properties like compressive stress, tensile stress and elastic modulus, the measured stress-strain relationship for reinforcing steel and constitutive relationship for recycled aggregate concrete (RAC) reported in the literature have been considered as an input. The stress-strain relationships of RAC selected from the literature has been treated as user defined model. Besides the strength, serviceability in terms of deflections, crack patterns and load deformation characteristics of simulated beams have been investigated and compared with those of laboratory tested beam specimens.

***doi**: 10.5829/ije.2023.36.05b.15*

NOMENCLATURE

FEA	Finite element analysis	NA	Natural aggregate
RC	Reinforced concrete	NAC	Natural aggregate concrete
RCC	Reinforced cement concrete	LVDT	Linear variable differential transformer

1. INTRODUCTION

A good number of FEA packages have been developed to evaluate the response of RCC structural forms during last few decades. The performance in terms of accuracy of these packages are broadly based on the adopted non-linear numerical procedures and incorporated material models [1]. These models mainly categorised into two classes such as empirical models and continuum mechanics-based models [2]. Initially continuum mechanics-based models were confined to isotropic and homogeneous materials. However, with an advancement in technology and broadened requirement, these theories have been extended to heterogeneous materials like concrete [3]. On the other hand, in the construction industry, sustainability become an urgent necessity of an hour, and to that end, utilization of waste products as a substitute material for concrete ingredients become evident [4]. Eventually, the use of recycled aggregates in concrete making and structural applications of such concrete is started gaining momentum [5, 6]. However, the analysis of such structural elements containing RAC requires special attention as the concrete models available in these softwares are not compatible with the modified properties and stress-strain relationships of RAC. Because RAC beams exhibit higher strains and deflection and lower or similar cracking moments than

*Corresponding Author Email: akshay4592@gmail.com (A. J. Pawar)

Please cite this article as: A. J. Pawar, M. Patel, S. R. Suryawanshi, Finite Element Modelling of Laboratory Tests on Reinforced Concrete Beams Containing Recycled Aggregate Concrete, ***International Journal of Engineering, Transactions B: Applications***, Vol. 36, No. 05, (2023) 991-999

conventional ones [7, 8]. Nevertheless, some packages offer freedom to the users to use laboratory evaluated index properties and measured stress-strain relationships. ABAQUS is one of such softwares which offers freedom to users to use user-defined material-models with ease.

As discussed in the preceding paragraph, the use of FEA packages has become the essential component of the modern analysis and design procedures pertaining to civil engineering structures [9]. With the rapid growth of FE techniques and material constitutive models in the last decade, the numerical methods have become more significant, since they can successfully simulate difficult or even complicated cases [10]. An important part of numerical analysis has been the development of a numerical method that works well with measured uniaxial stress-strain relationships [11]. Computer programs like LS-Dyna, ABAQUS and ANSYS are being extensively used [12]. On the contrary, some analysis software's have the limitations regarding the simulation of appropriate support conditions. For instance, to establish the line contact in order to simulate the steel rollers as point loads and supports to carry out the analysis of four-point bending test of RCC beam specimens. The software is programmed in such a way that only finite dimensions can create the support and load contacts. Therefore, in some studies [13, 14] steel plates (finite dimensions) in place of steel rollers were considered to define and simulate the support condition (as no alternative left to simulate rollers) even though the companion laboratory tests on RCC beams consist of steel rollers. Besides this, the input parameters assigned prior to simulation of structural components or structure as a whole plays very crucial role especially when alternate materials for concrete ingredients are to be used aiming sustainable development [15, 16]. It should be noted that the routine way to define concrete material is not applicable to the concretes containing substitute materials in place of conventional ingredients. In such a scenario, it becomes inevitable to carry out the simulation in the way the user manual administers. Few software offer liberty to the users to describe material behaviours employing measured stress-strain relationships as an input.

Typically, a FEA package is deemed to be competent in producing reasonable predictions when the variation between the anticipated and the experimentally measured values of certain structural attributes is less than 20% of the measured values, such structural characteristics typically include the load vs. displacement profiles, the load-carrying capacity, etc. and the qualitative behaviour pattern matches, such as the crack patterns at various load stages are also considered. Furthermore, FEA software is called objective and generic when it can accurately estimate structural behaviour for any structural concrete setup without recalibrating the constitutive model or parameters [3].

In this work, ABAQUS was employed to simulate numerically the experimental work of RC beams of concrete containing coarse RCA, subjected to pure flexure failure. To ascertain the efficacy of the FE model, the typical constitutive model for RCA-concrete available in literature was examined with the corresponding experimental results of the beam specimens. Moreover, the flexural behaviour of beams obtained from the numerical-analysis was compared with the measured results in terms of the flexure strength, load deflection behaviour and crack patterns.

2. EXPERIMENTAL INVESTIGATION

In this experimental investigation, total three number of beam specimens were cast and tested to the failure in order to assess the structural behaviour of RCA-concrete beams. All the beam specimens were 2100 mm long and designed for a cross-section of 125 mm width and 250 mm depth according to Indian Standards IS 456 [17], and were tested over 1800 mm simply supported span with 150 mm overhangs on each side. For all the beams, the shear-span of 600 mm was considered. The four-point loading was applied to the beam specimens in order to get no shear force in the region of constant moment. The region of constant moment was defined 600 mm, which was equal to the one-third of effective span. The nominal top reinforcement was curtailed in the region of constant moment to eliminate the effect of it on pure flexure failure, as the beam section was desired to be singly reinforced. Thermo-Mechanically Treated (TMT) steel rebars conforming to IS 1786 [18] were used to form cages. The measured yield strength of Fe500 grade rebar was 500 MPa. The reinforcement details of the beam specimens are depicted in Figure 1.

The concrete containing RCA extracted from the debris of demolished RCC structures was used to cast test specimens. The control concrete mixture containing natural coarse aggregates was designed by absolute volume method, conforming IS 10262 [19] whereas the mix for RAC was designed by the direct weight replacement method (DWRM). In the DWRM, the natural coarse aggregates were replaced with an equivalent weight of recycled coarse aggregate particles. The weight proportion of recycled coarse aggregates in

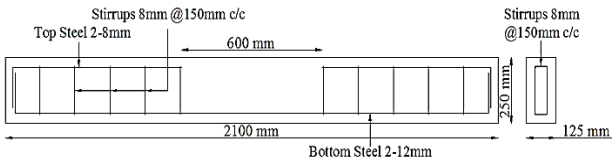

Figure 1. Typical reinforcement detail

TABLE 1. Mixture composition (in terms of ratios by weight) and measured properties of the NAC and the RCA-concretes

Mix Id	RCA replacement level	Cement	Mixing Water	Fine aggregates	Coarse NA (4.75-20 mm)	Coarse RCA (4.75-20 mm)	HRWRA (% by weight of cement)	Compressive strength (MPa)
R0	0	1.0	0.45	1.92	2.82	0.00	1.0	30.00
R50	50	1.0	0.45	1.92	1.41	1.41	1.0	28.50
R100	100	1.0	0.45	1.92	0.00	2.82	1.0	26.50

TABLE 2. Simmary of test and simulation results

Beam Id	Replacement ratio (%)	Measured ultimate load (kN)	Ultimate load predicted by ABAQUS (kN)	Measured displacement at ultimate load (mm)	Displacement at ultimate load predicted by ABAQUS (mm)
R0	0	84.00	87.72	14.10	14.41
R50	50	80.50	84.37	12.96	13.70
R100	100	78.00	81.65	12.01	12.40

the total coarse aggregates of the concrete mix is specified as the recycled coarse aggregate replacement percentage. The replacement level of natural coarse aggregates with RCA in percentage was as follows: 0.0, 50 and 100%. Control concretes are identified in this investigation by the generic name of NAC whereas the concretes containing full fractions of the recycled coarse aggregates are identified by the generic name of RCA-concrete. Except for substitution of the natural coarse aggregate particles with the recycled coarse aggregate, the other constituents in these two concrete types were nominally the same. The mixture composition and concrete compressive strength using 150 x 300 mm cylindrical specimens of the NAC and the RCA-concrete used in the experimental programme are given in Table 1.

The first placeholder in the nomenclature of the beam represents replacement of natural coarse aggregate in concrete. The second placeholder (digits) indicates the level of replacement in percentage. For example, in the beam specimen R100 indicate 100% replacement of natural coarse aggregate.

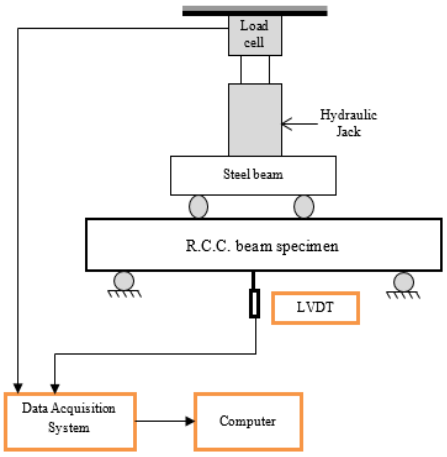

Figure 2. Schematic test set-up for beam tests

After 24 hours of casting, the formwork was removed, and all the beam specimens were kept in a normal environment condition, enclosed with wet jute gunny bags until they were tested at 28 days of age. The beam specimens were surface dried after 28 days of curing, followed by application of a single layer of white wash to facilitate detection of crack formation and growth. The test setup for a typical beam in four-point loading across a simply supported span of 1800 mm is illustrated in Figure 2. On the side faces of the beams, an orthogonal grid of lines spaced 50 mm vertically and 100 mm horizontally was marked to aid with crack tracing. Each specimen was tested in a load frame of capacity 2000 kN in order to evaluate load carrying capacity of the beam specimens. The monotonically increased load was applied on the top face of the beams with the help of a 1000 kN capacity hydraulic jack until the beam failed. Before the actual loading, preloading was performed to ensure that the load cell and LVDT sensor function normally. The applied load was measured with the load cell. At the load point, two rollers were used to transfer equal applied load to each support through the steel beam arrangement as seen in Figure 2. Hinge and roller supports are illustrated in Figure 2 and the deflections at the load-point were measured using LVDT.

3. THE FINITE ELEMENT MODELLING

A FEA package is known for realistic predictions of the behaviour of structural forms in terms of structural characteristics. Load carrying capacity, load-deformation, moment-curvature relations and pattern matches like the crack patterns corresponding to different load stages and failure modes are some of them. Moreover, it should be capable of predicting the realistic behaviour of any structural form without recalibration. The main requirements of FEA modelling are as follows: 1) to adopt a constitutive relationship to

describe the material nonlinearity of concrete, steel rebars and their mutual interactions; 2) to incorporate a nonlinear numerical procedure that is effectively capable of implementing internal stresses redistribution forced by material nonlinearity against imposed external loadings plus a numerical description on cracking process.

Though the peak stress value is assumed to be implicit due to the gradual degradation of the stiffness related to residual material strength after a peak stress yet the numerical procedural scheme adopted by most of the softwares were developed independent of material models. The majority of FEA packages employed an iterative procedures based on numerical techniques like Newton-Raphson method. The iterative procedure is to account for the checks for redistribution of stresses during crack openings and crack closure, besides the simultaneous checks on convergence in each iteration. The iterations are repeated till the convergence criterion met resulting into attainment of predefined minimum value of residual forces estimated from the use of equilibrium equations.

3. 1. Geometry Definition There are several approaches available to create geometry of an element in ABAQUS out of which the simple objects method has been used. The 3D geometry of the element is created in create part tab by taking modelling space and element type. The cross section (125 mm thick and 250 mm deep) of the concrete beam was created and the beam was extruded in the direction of length. By adopting the prescribed procedure to create elements, geometrical model of beam specimens created in ABAQUS is depicted in Figure 3 (a). For the simplicity of assembling the elements, datum planes were created using create partition cell tool.

The steel reinforcement (both main steel and stirrups) was modelled as wire elements in ABAQUS as per the experimental reinforcement detailing. Elements of reinforcement i.e., tension bar, top bar and stirrups were created individually under the create part section and assigned a cross section area of these wire elements as a truss element. These elements were assembled and rearranged using translate, rotate and linear pattern instance tool in the assembly section by providing required spacing, effective covers and other details according to reinforcement assembly. The 8 mm diameter bar was used as web reinforcement and top bars in the beams whereas the 12 mm diameter bar was used as a main steel provided at the bottom. The nominal top reinforcement in the compression zone was curtailed in order to achieve the effect of singly reinforced section in predefined region of pure bending as described earlier. The reinforcement cage similar to actually used in the beam is modelled which is shown in Figure 3(b).

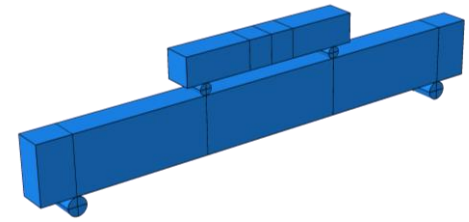

(a) Geometrical modelling of beams and supports

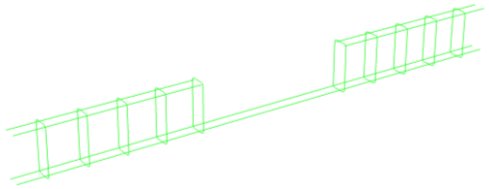

(b) Configuration of reinforcement

Figure 3. Geometry of the beam specimen created in ABAQUS

3. 2. Material Definition In the FE analysis part, the brittle-cracking model available in ABAQUS is employed as a material model. This yields better results when the behaviour of concrete material is governed by tensile cracking. The behaviour in compression is also idealised to be linear before cracking. In order to detect the crack initiation and propagation, a simple Rankine yield criterion has been utilised. According to Rankine yield criterion, the material starts cracking when resultant principal stress crosses the concrete tensile-strength. It is obvious that the crack surface is perpendicular to the major principal tensile stress. Subsequently other developed cracks are normal to the existing crack at the same location. Unlike other models, in this model, crack closing and reopening is allowed. Crack gets bridged as soon as the resultant principal stress becomes compressive after redistribution of stress. Moreover, it uses smeared crack model philosophy to characterize the non-ductile response of concrete.

The Brittle-cracking model includes two modes of failures as follows: 1) Mode-I based on tension-stiffening and Mode-II is on the basis of shear-retention. In strain-softening the stress linearly goes on decreasing to zero. As per the model, in the post-peak region, the strain is 10 times that of failure strain when the stress resumes to zero value. The crack initiation is controlled by Mode-I while the post-peak cracks are governed by both the modes. To model shear-behaviour, the post-cracking shear-modulus is defined in terms of the fractions of non-cracked shear-modulus. The model treats shear-retention in terms post-cracking shear-stiffness which is defined in terms of opening strain normal to crack.

3. 2. 1. Concrete ABAQUS offers freedom to user to define the material of practical relevance. It defines the concrete behaviour in terms of Concrete

Damage Plasticity (CDP) model. The other input parameters should be evaluated in the laboratory or idealised values reported in the literature may be used in absence of data. However, the real values are expected to use as an input in order to get accurate analysis.

The stress-strain relation of concrete used in the numerical-analysis should to be determined by testing the specimen in the laboratory. Figure 4 depicts the window to enter user defined material definition in the form of compression test stress-strain data and damage parameter on the basis of inelastic strain. Likewise, tensile test stress-strain data and damage parameter of the material model can be fed up to define the CDP model for concrete.

In this investigation, typical constitutive model for RAC was proposed by Suryawanshi et al. [11] which is used to define the concrete behaviour as follows:

$$\bar{\sigma} = a(\bar{\varepsilon}) + b(\bar{\varepsilon})^2 + c(\bar{\varepsilon})^3 + d(\bar{\varepsilon})^4 \quad (1)$$

where, $\bar{\sigma}$ is the normalized stress, $\bar{\varepsilon}$ is the normalized strain. Constants a, b, c and d were determined by regression analysis of test data. Constant a has definite meaning and may be defined in terms of percentage replacement of NA. Other coefficients b, c and d were expressed in relation of a.

3. 2. 2. Steel Reinforcement As discussed in the preceding sections, ABAQUS allow users to enter the stress-strain relationship of steel as input data so that the software can effectively simulate the behaviour of reinforcement steel. Figure 5 shows the appearance of dialogue box after entering the measured stress-strain values. It should be noted that, the ABAQUS accepts only inelastic strain values and corresponding stress values. The value of inelastic strain is determined as a difference of total strain and elastic strain.

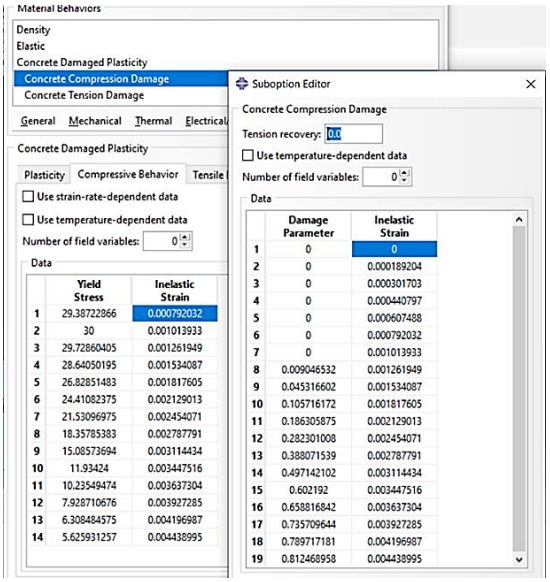

Figure 4. Details of stress-strain relations for concrete as an input parameter

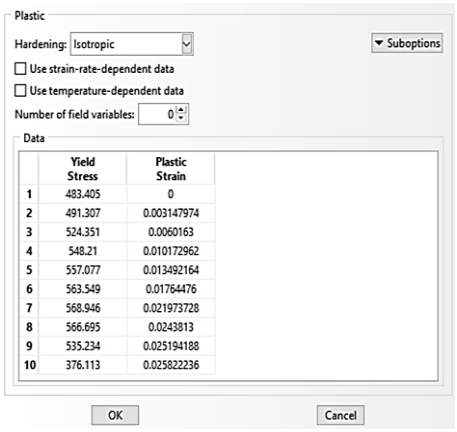

Figure 5. Details of measured stress-strain relations for reinforcement as an input parameter

3. 3. Modeling of Support and Load Points Unlike few FEA packages, ABAQUS allows to model and simulate curved elements like steel rollers used at loading points and supporting points through perfect contact as illustrated in Figure 6. The force was applied to beam by displacement controlled strategy as per prescribed deformation rate at the centre-point of the top surface of the spreader beam. The supports, in the form of two steel rollers used in experiments were modelled by appropriate boundary conditions on a line of contact. The supports were assumed as a rigid body and restricted to a predefined point as a reference. The movement reference point in vertical direction was restrained. Similarly, the steel rollers were modelled beneath the spreader beam used to apply load on the RC beam. The monitoring point to record the magnitude of applied load was placed at the centre-point of top surface of spreader beam. The position of the deflection monitors was the point where the LVDT was mounted in the prototype test.

For the structured meshes, the ABAQUS solver allows the usage of first-order hexahedral components; however, for unstructured meshes it permits the use of both first and second-order tetrahedral elements. 8-noded 3D hexahedral elements in the form of bricks (C3D8I) were employed in this investigation. The behaviour of traditional 8-noded elements is prohibited from being over rigid in bending by internally incompatible deformation modes, besides the normal degrees of freedom for displacement. The mesh being utilised for the concrete has an impact on how these components are implemented in the FE model. This work made use of the 3D linear truss (T3D2) element type with a mesh size of 10 mm. The geometry of a simulated beam with produced mesh elements is shown in Figure 6.

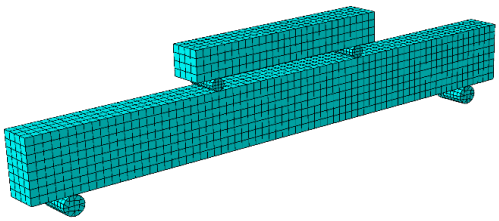

Figure 6. Finite element mesh of assembly

4. RESULT AND DISCUSSION

4. 1. Load Deflection Behavior The results of beam tests are compiled in Table 2 for reference and compared against results obtained from the ABAQUS analysis. It is clearly seen that the load carrying capacity of the beam when analysed by ABAQUS software is found in the close range to that of experimentally obtained results. It has been observed that the load carrying capacity of the RAC-beam is marginally lesser and slightly higher deflections than that of the NAC-beam. The ABAQUS analysis also indicate similar trend of reduction in load carrying capacity and increased deflections on higher replacement levels. Recent literature review on experimental flexure tests performed by Seara-Paz et al. [20] and Pradhan et al. [8] also agree that load carrying capacity of RAC-beam is lesser and shows higher deflection compared to NAC-beam. This may be attributed to the reduction of modulus of elasticity of concrete corresponding to a higher degree of replacement of NA [21].

The comparison of experimentally obtained load-deflection curves for beam specimens R00, R50 and R100 respectively are shown in Figure 7(a). A side-by-side comparison of ABAQUS analysis load-deflection curves for each beam is also presented in Figure 7(b). The trends of load-deformation characteristics in both the analysis are similar. The RAC beams had a lesser cracking load than the NAC beams due to the presence of two types of interfacial transition zones (ITZ) [22]. The ITZ between residual mortar and virgin aggregate in and the ITZ between new mortar and residual mortar. On the contrary, the NAC has one ITZ (between fresh mortar and virgin aggregate). Moreover, the RAC beams exhibited lower stiffness after the cracking load, which may be attributed to the RCA-concrete having comparatively lower modulus of elasticity to that of the NAC [23].

Figure 8(a), (b) and (c) reveals load-deflection relationships of tested beam specimens correspond to different RCA replacement levels, 0.0, 50 and 100%. The load-deflection relationships generated by ABAQUS software are also shown in Figure 8(a), (b) and (c). After cracking, each specimen behaved almost linearly until the tension bar began to yield. Each specimen thereafter

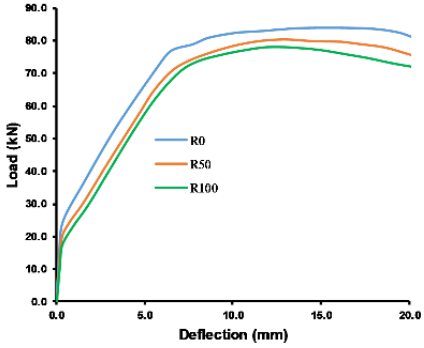

(a) Measured load-deflection relationship

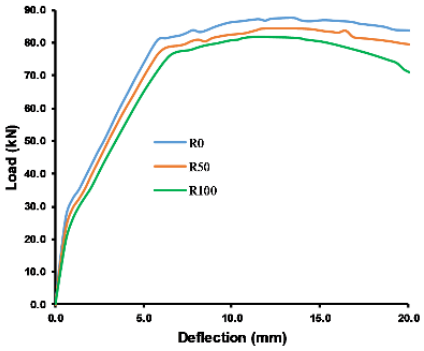

(b) Predicted load-deflection relationship

Figure 7. Comprehensive comparison of trends of measured and predicted load-deflection relationships

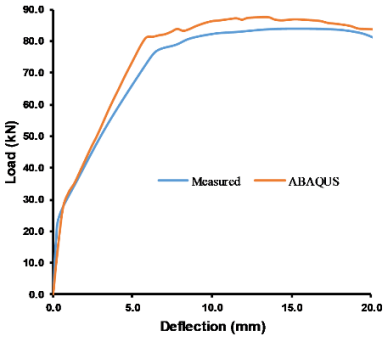

(a) Beam R00

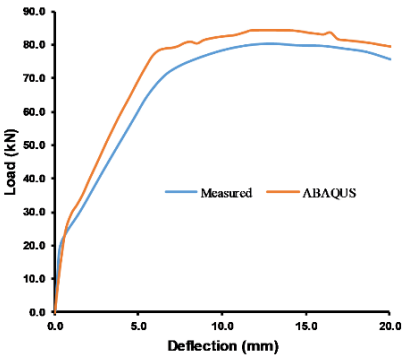

(b) Beam R50

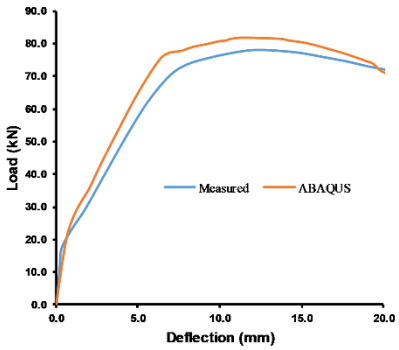

(c) Beam R100

Figure 8. Comparison of measured and predicted load-deflection relationships of various beams

exhibited nonlinear behavior until it reached its failure load. The beams then reached a ductile plateau which is typical behaviour of RCC flexural member. After enough rotation of the developed plastic-hinge, extreme stresses are developed in the compression zone of the specimens, culminating in crushing failure.

4. 2. Cracking Behavior of RCA-Concrete Beam

The cracking behavior of the beams in terms of the number, the orientation, and the extent of the cracks, was monitored throughout the loading history. The first crack started forming from the soffit of beam in the mid-span region, the region of maximum bending moment. The first crack occurred at 25 kN in R00-beam whereas the FEA simulation revealed it at 27.32 kN. Similarly, the first crack formed at 17.21 kN in R100-beam and at 25.78 kN in simulated beam. All beam specimens containing RCA-concrete showed the tendency of first crack formation comparatively at lower load to that of beam containing NAC. With increase in applied load, additional flexural cracks were formed between the loading point and the support points. All these cracks propagated towards the compression zone revealed the typical crack-pattern of inclined flexure-shear cracks. It is clearly seen that the R00-beams has the least number but prominent cracks (Figure 9), whereas the R100-beam comparatively has a greater number of minor cracks. The findings of this investigation were in good agreement with observations of past study [8], in which the cracks in the RCA beams were closely spaced than in the NA beams. This might be due to the weakened interfacial transition zone of RCA between the new mortar and the old attached mortar. Besides the experientially observed cracking patterns, the bands of principal tensile strains revealed in ABAQUS analysis also presented in Figure 9.

On the contrary, it generates the bands of principal tensile strains [24]. The formation of tensile strain bands with specific colour to represent certain magnitude of

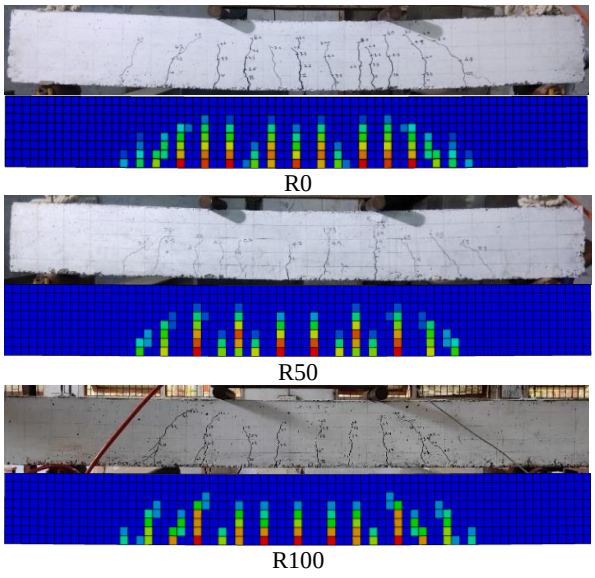

Figure 9. Comparison of observed creack patterns with ABAQUS simulated principal tensile strain profiles

strains can be compared with the actual crack patterns observed during experiments. The comparison of crack patterns of beams with different replacement levels of RCA is shown in Figure 9. along with the principal tensile strain patterns generated by ABAQUS. The trend of the principal tensile strain patterns generated by ABAQUS is comparable with the experimentally observed crack patterns.

5. CONCLUSIONS

In this comparative study, the flexural member was numerically investigated and compared with the results of experimental study. Based on the experimental findings and results of numerical analysis, the following conclusions have been drawn.

1. The comparison of ABAQUS results and experimental observations revealed no major differences in the load carrying capacities of the beams. The trend of reduction in load carrying capacity and increasing mid-point deflections with increased replacement level in both the investigations are similar.
2. The load deformation characteristics revealed by ABAQUS simulation is significantly in match with that of experimentally measured load-deformation relationships. Thus indicating the importance of well define material definitions in terms of measured stress-strain relations on yield of numerical simulations.
3. Unlike other FEA packages, ABAQUS does not generate crack patterns. However, the crack patterns observed during experiments can be correlated with

the principal tensile strain profiles generated through numerical simulation. The cracking patterns and principal tensile strain profiles are found comparable.

4. Besides, correct material definitions, other input parameters in terms of index properties of materials has a control on the quality of simulation.
5. Geometric definition, well defined support conditions and appropriate selections of finite elements are the major factor influencing the outcomes of FEA analysis.

6. REFERENCES

1. Buyukozturk, O. and Shareef, S.S., "Constitutive modeling of concrete in finite element analysis", ***Computers & structures***, Vol. 21, No. 3, (1985), 581-610. https://doi.org/https://doi.org/10.1016/0045-7949(85)90135-X
2. Pawar, A.J. and Suryawanshi, S., "Comprehensive analysis of stress-strain relationships for recycled aggregate concrete", ***International Journal of Engineering, Transactions B: Applications***, Vol. 35, No. 11, (2022), 2102-2110. https://doi.org/10.5829/ije.2022.35.11b.05
3. Cotsovos, D.M., Zeris, C.A. and Abbas, A.A., "Finite element modeling of structural concrete", in Proceedings of the 2nd International Conference on Computational Methods in Structural Dynamics & Earthquake Engineering., (2009).
4. Yasin Mousavi, S., Tavakkoli, A., Jahanshahi, M. and Dankoub, A., "Performance of high-strength concrete made with recycled ceramic aggregates (research note)", ***International Journal of Engineering, Transactions C: Aspects***, Vol. 33, No. 6, (2020), 1085-1093. https://doi.org/10.5829/ije.2020.33.06c.05
5. Silva, R., De Brito, J. and Dhir, R., "Use of recycled aggregates arising from construction and demolition waste in new construction applications", ***Journal of Cleaner Production***, Vol. 236, (2019), 117629. https://doi.org/https://doi.org/10.1016/j.jclepro.2019.117629
6. Masne, N. and Suryawanshi, S., "Effect of replacement ratio on torsional behaviour of recycled aggregate concrete beams", ***International Journal of Engineering, Transactions A: Basics***, Vol. 36, No. 4, (2023), 659-668. doi: 10.5829/ije.2023.36.04a.07.
7. Kang, T.H.-K., Kim, W., Kwak, Y.-K. and Hong, S.-G., "Flexural testing of reinforced concrete beams with recycled concrete aggregates", ***ACI Structural Journal***, Vol. 111, No. 3, (2014). https://doi.org/10.14359/51686622
8. Pradhan, S., Kumar, S. and Barai, S.V., "Performance of reinforced recycled aggregate concrete beams in flexure: Experimental and critical comparative analysis", ***Materials and Structures***, Vol. 51, (2018), 1-17. https://doi.org/10.1617/s11527-018-1185-0
9. Cotsovos, D.M. and Kotsovos, M.D., "Constitutive modelling of concrete behaviour: Need for reappraisal", ***Computational Methods in Earthquake Engineering***, Vol. 21, (2011), 147-175. https://doi.org/10.1007/978-94-007-0053-6_7
10. Raveendra, B.R., Benipal, G.S. and Singh, A.K., "Constitutive modelling of concrete: An overview", (2005).
11. Suryawanshi, S., Singh, B. and Bhargava, P., "Equation for stress–strain relationship of recycled aggregate concrete in axial compression", ***Magazine of Concrete Research***, Vol. 70, No. 4, (2018), 163-171. https://doi.org/10.1680/jmacr.16.00108
12. Masne, N. and Suryawanshi, S., "Analytical and experimental investigation of recycled aggregate concrete beams subjected to pure torsion", ***International Journal of Engineering, Transactions A: Basics***, Vol. 35, No. 10, (2022), 1959-1966. https://doi.org/10.5829/ije.2022.35.10a.14
13. Yuan, S., Liu, Z., Tong, T. and Fu, C.C., "A pilot study on structural responses of normal concrete-uhpc composite bridge decks w/wo rebars through an experimental-numerical approach", ***Advances in Civil Engineering***, Vol. 2020, (2020), 1-21. https://doi.org/10.1155/2020/8816337
14. Tambusay, A. and Suprobo, P., "Predicting the flexural response of a reinforced concrete beam using the fracture-plastic model", ***Journal of Civil Engineering***, Vol. 34, No. 2, (2019), 61-67. https://doi.org/10.12962/j20861206.v34i2.6470
15. Bouzaiene, A. and Massicotte, B., "Hypoelastic tridimensional model for nonproportional loading of plain concrete", ***Journal of Engineering Mechanics***, Vol. 123, No. 11, (1997), 1111-1120. https://doi.org/10.1061/(ASCE)0733-9399(1997)123:11(1111)
16. Chen, W., "Plasticity in reinforced concrete, mcgraw-hill", New York, NY, USA, (1982).
17. IS456, I.S.C., "Plain and reinforced concrete—code of practice (fourth revision)", ***Bureau of Indian Standards, Manak Bhavan***, Vol. 9, (2000).
18. BIS, I., "Indian standard for high strength deformed steel bars and wires for concrete reinforcement", ***Bureau of Indian Standards, New Delhi***, (2008).
19. 10262:, I., *Concrete mix proportioning–guidelines (second revision)*. 2019, IS: 10262, Bureau of Indian Standards New Delhi, India.
20. Seara-Paz, S., González-Fonteboa, B., Martínez-Abella, F. and Eiras-López, J., "Flexural performance of reinforced concrete beams made with recycled concrete coarse aggregate", ***Engineering Structures***, Vol. 156, (2018), 32-45. https://doi.org/10.1016/j.engstruct.2017.11.015
21. Chen, X., Zhang, Z., Xu, Z., Wu, Q., Fan, J. and Zhao, X., "Experimental analysis of recycled aggregate concrete beams and correction formulas for the crack resistance calculation", ***Advances in Materials Science and Engineering***, Vol. 2022, (2022). https://doi.org/10.1155/2022/1466501
22. Deng, Z., Sheng, J. and Wang, Y., "Strength and constitutive model of recycled concrete under biaxial compression", ***KSCE Journal of Civil Engineering***, Vol. 23, (2019), 699-710. https://doi.org/10.1007/s12205-018-0575-8
23. Arezoumandi, M., Smith, A., Volz, J.S. and Khayat, K.H., "An experimental study on flexural strength of reinforced concrete beams with 100% recycled concrete aggregate", ***Engineering Structures***, Vol. 88, (2015), 154-162. https://doi.org/10.1016/j.engstruct.2015.01.043
24. Earij, A., Alfano, G., Cashell, K. and Zhou, X., "Nonlinear three–dimensional finite–element modelling of reinforced–concrete beams: Computational challenges and experimental validation", ***Engineering Failure Analysis***, Vol. 82, (2017), 92-115. https://doi.org/https://doi.org/10.1016/j.engfailanal.2017.08.025

Persian Abstract

چکیده

دقت پیش‌بینی بسته‌های مبتنی بر المان محدود (FE) به طور گسترده بر اساس سازگاری رویه‌های عددی غیرخطی اتخاذ شده و مدل‌های مواد گنجانده شده است. با این حال، روش معمول برای تعریف مواد بتن برای بتن های حاوی مواد جایگزین به جای مواد بتن معمولی قابل اجرا نیست. بنابراین، در این کار، از تعریف مناسب مواد از نظر روابط تنش-کرنش برای شبیه‌سازی کار تجربی تیرهای RC حاوی بخش‌های درشت‌تر از سنگدانه‌های بتن بازیافتی (RCA) استفاده شده است. کل کار در دو مرحله انجام شده است. یک کار آزمایشی و شبیه سازی کار آزمایشی با استفاده از بسته FEA، ABAQUS. در بخش آزمایشی، سه نمونه تیر با مقیاس کامل از طریق بارگذاری یکنواخت چهار نقطه‌ای برای شکست مورد آزمایش قرار گرفتند. سطح جایگزینی سنگدانه های درشت طبیعی با جایگزینی مستقیم ۰.۰، ۵۰ و ۱۰۰ درصد در نظر گرفته شد. در مرحله شبیه سازی، علاوه بر خواص آزمایشگاهی ارزیابی شده مانند تنش فشاری، تنش کششی و مدول الاستیک، رابطه تنش-کرنش اندازه گیری شده برای فولاد تقویت کننده و رابطه سازنده برای بتن سنگدانه های بازیافتی (RAC) گزارش شده در ادبیات به عنوان ورودی در نظر گرفته شده است. . روابط تنش-کرنش RAC انتخاب شده از ادبیات به عنوان مدل تعریف شده توسط کاربر در نظر گرفته شده است. علاوه بر استحکام، قابلیت سرویس از نظر انحراف، الگوهای ترک و ویژگی‌های تغییر شکل بار تیرهای شبیه‌سازی شده بررسی و با نمونه‌های تیر آزمایش‌شده آزمایشگاهی مقایسه شده است.

IJE TRANSACTIONS B: Applications Vol. 36, No. 05, (May 2023) 1000-1011

International Journal of Engineering

Journal Homepage: www.ije.ir

Seismic Vulnerability Assessment of Existing RC Moment Frames using a New Stiffness Based Damage Index

M. Mazloom*, N. Fallah

Department of Civil Engineering, University of Guilan, Rasht, Iran

P A P E R I N F O

Paper history:
Received 25 January 2023
Received in revised form 18 March 2023
Accepted 19 March 2023

Keywords:
Damage
Stiffness Based Damage Index
Pushover Analysis
Capacity Curve
RC Frame

A B S T R A C T

Earthquakes cause a lot of damage to structures. A quantitative estimate of the amount of damage to the structure always seems quite necessary after an earthquake. For this purpose, seismic damage indices have been introduced as dimensionless quantities that can report the extent of damage using various criteria. This quantitative assessment can help make decisions about the process of improving, repairing, and strengthening structures. This paper presented a new stiffness-based damage index with simple formulation by performing pushover analysis on existing concrete models and applying the results. Using the capacity curve obtained from the pushover analysis output, this index can provide a quantitative estimate of the amount of damage to the entire structure. To validate the results, damage estimation was also performed using several reliable models such as the Park-Ang model and then compared with the proposed index results. Then, a series of theoretical suggestions were presented to address the existing weaknesses, which were implemented, and new results were obtained. Finally, the implemented reform proposals led to an improvement in the performance of the proposed index, resulting in excellent accuracy due to the simple computational process compared to the complex implementation of the Park & Ang index.

***doi**: 10.5829/ije.2023.36.05b.16*

1. INTRODUCTION

Different structures are made to last for long periods. However, they may suffer some damage during their service life as a result of changes in loading patterns and random excitations such as earthquakes. Predicting the extent of damage to the structure over its service life is a probabilistic issuem. Nevertheless, many researchers have proposed several equations to quantify damage by applying various engineering parameters, such as curvature, rotation, strength, stiffness, and dissipated energy [1]. The performance-based structural design method allows designers to purposefully control the amount of damage to the structure as a result of mild to severe earthquakes. One of the most effective tools to handle the results about the damage performance of the structure is the damage index (DI) together with the damage states, which are used to correlate the damage indices with the damage that occurred in the actual structures [2]. Damage indices use different initial parameters to estimate the amount of damage, and therefore, the degree of complexity in how they are used varies. Given the importance of detecting seismic damage, several studies have been performed on the seismic performance of reinforced concrete frames based on seismic indices. These studies aimed to investigate the condition of a reinforced concrete building following an earthquake and estimate the amount of damage according to seismic demands. Another goal was to study the relationship between structural damage level and the important characteristics of the input earthquake. Wen and Loh [3] attempted to determine the relationship between design level and performance level. The project investigated the relationship between the annual probability of exceeding the seismic hazard level and the performance of a building subjected to a certain intensity of earthquake loading. The Park-Ang index was used as a damage criterion to quantitatively introduce the

*Corresponding Author Email: Meisam_mazloom@yahoo.com (M. mazloom)

Please cite this article as: M. Mazloom, N. Fallah, Seismic Vulnerability Assessment of Existing RC Moment Frames using a New Stiffness Based Damage Index, ***International Journal of Engineering, Transactions B: Applications***, Vol. 36, No. 05, (2023) 1000-1011

performance level. Also, the relationship between the components of earthquakes in Iran region and the amount of damage to concrete frames was investigated in a research project [4]. De Domenico and Hajirasouliha [5] investigated the steel frames criteria and the damage index in the performance-based design method of reinforced concrete buildings. They also studied the relationship between damage to components and the values of the above criteria. In another study, researchers investigated the relationship between the proposed levels of FEMA and different damage indices. In this research project, several models of steel frames were analyzed, and the time history and damage index curves were plotted against different performance levels [6]. In addition, the correlation assessment between the damage criteria obtained from the results of a pushover analysis at different performance levels of a 2D bending moment frame was performed in another research work [7]. Some researchers conducted a laboratory study on the seismic response of concrete foundations of existing bridges. They attempted to build a model of a multi-column concrete foundation in the laboratory and measure the behavior of the structure at different performance levels under the effect of cyclic loading [8]. Tasnimi [9] investigated the Park index at the seismic performance levels of reinforced concrete frames using the results of nonlinear dynamic analysis. The vulnerability of concrete frames was examined in another study. They performed nonlinear dynamic analysis on multi-story concrete frames. They also examined the characteristics of the incoming earthquake and used the Park & Ang damage index to assess damage in numerical models [10]. Also, some researchers attempted to quantify the damage level of Shear Wall RC Frames based on nonlinear static and dynamic analysis results. They used the Park & Ang damage index as benchmark, examined other indices such as drift percent and finally introduced some practical relations [11]. Aghagholizadeh and Massumi [12] assessed the seismic vulnerability of concrete moment frames by nonlinear dynamic analysis. In their study, the relationship between changes in structural vibration period and damage index was investigated and finally a new relationship was proposed to estimate the damage [12]. Habibi and Asadi [13] developed drift-based index to estimate damage to reinforced concrete moment frames with vertical irregularity setback. They used inelastic dynamic time-history analysis on several frames with different types of setbacks and their damage is computed by the Park & Ang damage index [13]. Rastegarian and Sharifi [14] evaluated dependency of structural performance level on its corresponding inter-story drift in RC moment frames. They used pushover analysis and finally proposed equations to predict drift percent at performance levels. Hait et al. [15] studied the damage in RC buildings using an analytical method, presented a new damage index based on a combination of different structural response criteria which provided accurate results compared to the Park & Ang damage index. Ozturk et al. [16] evaluated precast industrial concrete buildings by using dynamic analysis and fragility curves that were designed and built according to the building codes of Turkey. Other researchers have performed static and dynamic analyses on a number of concrete frames [17]. Kassem et al. [18] presented by performing nonlinear static and dynamic analysis and by classifying damage levels, a simple and practical method to assess damage in reinforced concrete buildings based on the results of vulnerability damage index. In another paper, based on the suggested method of damage assessment using the vulnerability index, they examined the damage in a school building. With the help of the results of this research, it is possible to provide a proper assessment of the structural damages without the need for expert observations [19]. The evaluation of the effect of ductile details in reinforced concrete structures was investigated in another study. In this research, two ductile and non-ductile frames were modeled and using the results of pushover analysis, the effect of using ductile details on the safety, stability and economy of the models was investigated [20]. In another paper, Mibang and Choudhury [21] investigated seismic damage in reinforced concrete frames with shear walls. In this research, the Park & Ang damage index was used to calculate the amount of damage. The research results showed that in these structures, the most damage occurred on the ground story [21]. In another work, Nair et al. [22] evaluated the seismic vulnerability of high-rise concrete frames in the United Arab Emirates with the help of fragility curves. Zameeruddin and Sangle [7] proposed a damage index based on stiffness changes in order to estimate the structural global damage, and calculated its value at the proposed performance levels of FEMA-273. The history of using damage indexes in estimating post-earthquake damage was examined, indicating that most of the research was performed using the nonlinear dynamic analysis method. Limited research has been conducted on the relationship between pushover analysis and damage assessment, including. Also, some seismic instructions such as FEMA-273 [23] and ATC-40 [24] have stated the amount of damage to the structure based on the relative lateral displacement values resulting from pushover analysis.

The present paper presents a damage index based on pushover analysis output, which was performed on several concrete frames. The amount of damage can be measured based on the cumulative degradation of the stiffness. Then, to validate the results compared to the values of valid indices, the amount of damage was also calculated and classified based on the Park & Ang model and relative lateral displacement, followed by

comparing the values of the presented index with its results. Several theoretical modifications were made to improve the performance of the introduced index and the results; the results were re-examined. As a result of the improvements made, the results improved compared to the original model and became more coherent with the Park index. The amount of damage to the whole structure can be properly estimated by performing a series of simple calculations away from the complexity of the Park index by using this index that only uses the information of the capacity curve of the structure.

2. DAMAGE INDEX

The main purpose of assessing the damage to the structure is to find a set of reliable quantities to determine the amount of damage to the structure. Over the years, a significant body of research has focused on developing such methods. An appropriate damage index has the following characteristics:

A) General usability: Damage indices should be able to be applied to different systems under different loads.

B) Easy evaluation: Damage indices should be usable in practice, and their introduced parameters can be understood, observed, and measured.

C) Physical interpretation capability: Damage indices should be able to express the physical meaning of the damage to the structure. Damage indices are generally defined either in terms of parameters related to economic conditions or in terms of resistance-safety considerations. Economic damage indices are usually defined in terms of the parameters representing the cost of replacing and repairing the necessary structural elements. Specific and complete information is required in this regard, and determining repair and replacement costs is relatively difficult. Resistance-safety damage indices are related to the amount of reduction in structural strength. The damage index is generally a normalized quantity with numerical values between 0 and 1, with 0 meaning no damage and 1 meaning collapse.

2. 1. Relative Lateral Displacement Based Damage Index The criterion of " Story relative lateral displacement " can be used as a simple and popular tool to assess the total damage to the structure. Performance based design instructions such as FEMA-356 and ATC-40 detemine the structural performance level by setting four limit values for this index. This index can be calculated based on the results of pushover analysis using Equation (1) [25]:

$$DI_{drift} = \frac{\Delta_m}{H} \quad (1)$$

In this regard, Δ_m is the target displacement at the performance level and H is the height of the structure studied. In Table 1, the limit state values of this index are presented for each performance level.

2. 2. Park&Ang Damage Index Extensive research has been conducted in recent years to develop an accurate model for assessing the extent of damage to structures. The Park and Ang model [26] is one of the most common damage indices used to analyze damage to members and, on a larger scale, structures. Three types of damage indices can be calculated using this model: member damage index (e.g., column, beam, and shear wall), floor damage index, and total structure damage index. The Park & Ang damage index was initially a combination of maximal non-cumulative deformation and hysteretic energy. Reinhorn et al. [27] modified the Park & Ang damage model based on Equation (2):

$$DI_{Park\,\&Ang} = \frac{\theta_m - \theta_y}{\theta_u - \theta_y} + \frac{\beta}{M_y \theta_u} \int dE \quad (2)$$

where θ_y , θ_m and θ_u are the yield rotation, maximum rotation, and maximum rotation capacity of the member section, respectively, under uniform incremental loading. This model is currently used in IDARC-**2**D software to analyze the damage to reinforced concrete structures. This damage index is proportional to the observed damage classified, as shown in Table 1 [28]. The value of this index is calibrated in the range [0, 1], reporting the absence of damage and complete damage and destruction of the member (or structure), respectively. Other performance levels, such as immediate occupancy, life safety, etc., will fall within these limits. Operational, immediate occupancy, life safety, and collapse prevention performance levels correspond to minor, low, moderate, and severe damage (Table 1 and references ATC-40 and FEMA-273).

TABLE 1. Classification of Structural Damage According to Park & Ang Index values and drift percent

Performance levels	Degree of damage	Park&Ang damage index value	Drift damage index(%)
Operational	Slight	$DI < 0.10$	$DI_{drift} < 0.70$
Immediate occupancy	Minor	$0.10 < DI < 0.25$	$0.70 < DI_{drift} < 1$
Life safety	Moderate	$0.25 < DI < 0.40$	$1 < DI_{drift} < 2$
Collapse prevention	Severe	$0.40 < DI < 1$	$2 < DI_{drift} < 4$
Collapse	Collapse	$DI > 1$	$DI_{drift} > 4$

2. 3. Stiffness-Based Damage Index The amount of damage can be calculated according to the slope of the structural capacity curve obtained from pushover analysis at different levels. Saleemuddin and Sangle [1], presented a stiffness-based damage index to the original form of Equation (3), derived from the following expression [29]:

$$DI_C = 1 - \frac{K_C}{K_O} \tag{3}$$

In Equation (3), DI_C is the damage index at the moment of collapse of the structure. Also, K_C and K_O are the structural stiffness at the collapse level and the service level, both derived from the capacity curve, respectively. From the above equation, it can be concluded that the amount of damage is estimated based on the occurrence of the first yield in the structure. To solve the challenge of not considering the cumulative effects of structural damage, a new equation was presented and used as follows [1]:

$$(1 - DI_C)K_O = K_C \tag{4}$$

$$(1 - DI_C)K_0 d_p = V_p \tag{5}$$

According to Equations (4) and (5), stiffness can be replaced by base shear and displacement at the collapse level. According to the incremental steps of pushover analysis, Equations (6)-(9) can be written according to the capacity curve:

$$K_o d_1 = V_1 \tag{6}$$

$$K_1(d_2 - d_1) = V_2 \tag{7}$$

$$K_2(d_3 - d_2) = V_3 \tag{8}$$

$$K_n(d_p - d_n) = V_p \tag{9}$$

In the above equation, K_o is the structural stiffness at the full-service level, d_p is the displacement of the structure at the calculated level, and V_p is the shear force of the structure at the same level, obtained from the capacity curve. Also, d_n is the displacement at any desired point n and K_n is the structural stiffness at the desired point,

which must be read from the curve. For each step of pushover analysis, according to Equations (6)-(9) and Figure 1, the left-hand side of Equation (9) can be rewritten as a sum of several terms as Equation (10):

$$\sum_{i=0}^{n=l} K_o d_1 + K_1(d_2 - d_1) + K_2(d_3 - d_2) + K_n(d_p - d_n) = V_p \tag{10}$$

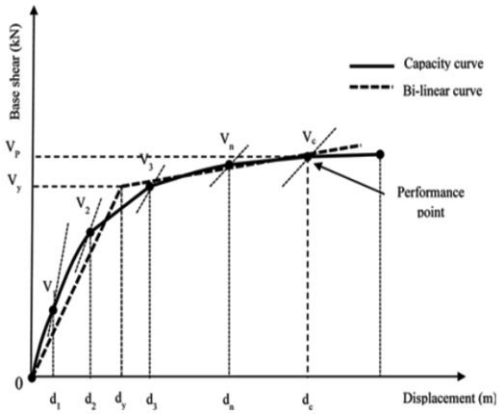

Figure 1. Display parameters on the pushover curve [1]

$$DI_C = 1 - \frac{V_p}{K_0 d_p} = 1 - \frac{\sum_{i=0}^{n=l} K_o d_1 + K_1(d_2 - d_1) + K_2(d_3 - d_2) + \ldots + K_n(d_p - d_n)}{K_o d_p} \tag{11}$$

The above equation represents the value of the damage index at any desired level, which can also consider the reduced cumulative stiffness [1]. Therefore, the damage index values for the performance levels based on FEMA273, i.e., IO, LS, and CP were written as follows (Equations (12)-(14)):

$$DI_{IO} = 1 - \frac{\sum_{i=0}^{n=l} K_o d_1 + K_1(d_2 - d_1) + K_2(d_3 - d_2) + \ldots + K_{IO}(d_{IO} - d_n)}{K_o d_p} \tag{12}$$

$$DI_{LS} = 1 - \frac{\sum_{i=0}^{n=l} K_o d_1 + K_1(d_2 - d_1) + K_2(d_3 - d_2) + \ldots + K_{LS}(d_{LS} - d_n)}{K_o d_p} \tag{13}$$

$$DI_{CP} = 1 - \frac{\sum_{i=0}^{n=l} K_o d_1 + K_1(d_2 - d_1) + K_2(d_3 - d_2) + \ldots + K_{CP}(d_{CP} - d_n)}{K_o d_p} \tag{14}$$

The damage index calculates the total damage to the structure at different performance levels based on the above model.

3. THE RESEARCH PROCESS

3. 1. Description of Study Models Three concrete frame models were selected based on the specifications in the research conducted by Reinhorn et al. [27] and Ferracuti et al. [30]; modeled in the IDARC 2D Version 7.0 program [18]. In these frames, the number of floors is 3, 4, and 6, respectively, and the number of frame spans is 2, 3, and 2, respectively (Figure 2). The height of the floors in the first frame,

taken from a frame with laboratory dimensions [18], is 1.5 meters, and the length of each span is 3 meters. In the second (three-span) and third (two-span) models, the height of the first floor was equal to 3.5 meters, and the height of the other floors was equal to 3 meters. Also, in the second model, the length of each span was equal to 5 m, and in the third model, it was equal to 5.5 and 5 m [30]. The concrete used in the first frame has a compressive strength of 40.2 MPa, and the steel used has a yield strength of 400 MPa. In the second and third models, the concrete used had a compressive strength of 30 MPa, and the steel used was considered to have yield strength of 414 MPa [27, 30].

3. 2. Numerical Modeling in the Program and Performing Nonlinear Analysis The models introduced in the preceding section were generated in IDARC-2D V7.0. As a set with the ability to consider various aspects of concrete element behavior, the IDARC program was introduced in 1987, to study the nonlinear response of reinforced concrete structures [27]. This program is capable of doing nonlinear static and dynamic analyses and provides various information according to the user's request such as displacement status, stress ratio in elements, plastic hinge formation process, the amount of damage in the structure, and modal information of the structure in different steps during progress. In the mentioned program, columnar elements are considered as macro models with inelastic flexural deformations and elastic shear and axial deformations, and in the beam elements, inelastic flexural deformations are considered with elastic shear deformations [27]. Nonlinear static analysis is done on numerical models of the present paper.

To consider the nonlinear behavior of beams and columns, a concentrated plasticity model was used at both ends of the element (Figure 3). The IDARC-2D program uses a modified model in which the program considers two nonlinear rotational springs at both ends of the element while considering the element as elastic. As a result, the plasticity behavior of the element will be

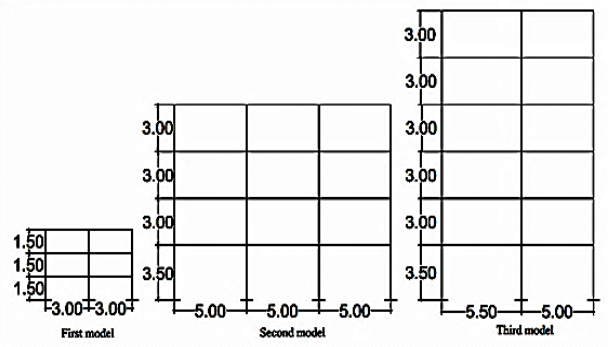

Figure 2. Geometric view of the numerical models

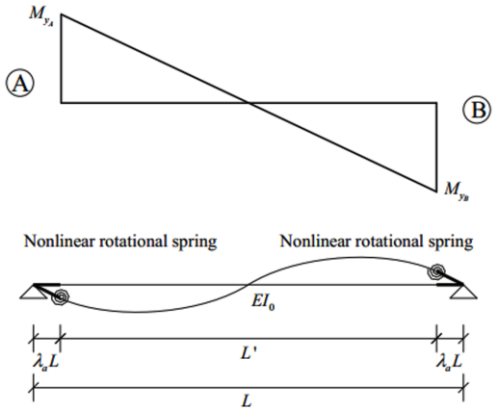

Figure 3. Concentrated plasticity model [28]

active only at both ends of the beams and columns. This model also includes rigid end zones [27]. Since the lengths of the beams and columns introduced to the program are center-to-center, the rigid end zones that must be defined by the user for both ends of the elements are the joint area where the elements connect to each other and to the ground, which is considered rigid in the element of the beam or column. In addition, to model, the behavior of beams and columns, a multi-linear hysteretic model was used. The selected cycle parameters for the elements were introduced as ductile sections with appropriate details. It must be mentioned that the IDARC program considers hysteretic behavior for both ends of the element. To introduce hysteretic behavior to the program, regarding the program guide, the user must specify the HC, HBD, HBE, and HS values. These values are determined based on the definitions provided in Table 2.

Generally, increasing the amount of HC delays the amount of stiffness degradation. In addition, increasing HBD and HBE will increase the resistance degradation rate, and increasing HS will reduce the slip value. Consequently, the HC value was considered equal to the default value of 200, which is the maximum value proposed for the introduction of behavior without stiffness degradation. To introduce the strength deterioration parameter, the values of HBD and HBE were equal to 0.01 to introduce the mode without strength deterioration and the value of HS was equal to one for bond slipping (Pinching) [27]. Regarding the program guide, the model intended for the rotational behavior of elements was introduced in Figure 4. Also, nonlinear geometric effects (P-Δ) were considered. The uniform vertical load applied to the floor beams was equal to 20 kN/m.

The IDARC program can perform pushover analysis in the form of displacement control and force control. In this study, pushover analysis was performed based on force control.

TABLE 2. Details of typical parameters and default values to introduce hysteretic behavior in members [27]

Parameter	Meaning	Value	Effect
HC	Stiffness degradation parameter	4	Severe degradation
		10	Moderate degradation
		15	Mild degradation
		200	No degradation (Default)
HBD	Strength degradation parameter (ductility-based)	0.60	Severe degradation
		0.30	Moderate degradation
		0.15	Mild degradation
		0.01	No degradation (Default)
HBE	Strength degradation parameter (energy-controlled)	0.60	Severe deterioration
		0.15	Moderate deterioration
		0.08	Mild deterioration
		0.01	No deterioration (Default)
HS	Slip or Crack-closing parameter	0.05	Severe pinched loops
		0.25	Moderate pinching
		0.40	Mild pinching
		1	No pinching (Default)

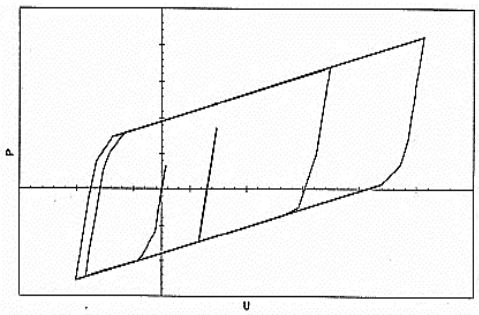

Figure 4. Multi-linear hysteretic model [28]

a) In the first model, the lateral load distribution was considered an inverse triangle. This distribution is often suggested by building codes, which assume that the building is subject to a linear acceleration distribution along its height (Figure 5(a)). Therefore, the incremental lateral force at each step is calculated for story i based on Equation (15):

$$\Delta F_i = \frac{W_i h_i}{\sum_{i=1}^{n} W_i h_i} \Delta V_b \quad (15)$$

b) In the second and third models, the lateral load distribution was assumed to be uniform. This distribution assumes a constant distribution of lateral load at the height of the building, regardless of floor weight .(Figure 5(b)). The increased lateral force in each step for story i is equal to:

$$\Delta F_i = \frac{\Delta V_b}{N} \quad (16)$$

where N is the number of floors of the building. After the analysis of pushover, a comparison was made between the initial results of the analysis to validate the modeling method and tools used, which included the vibration period of the first three modes and the structural capacity curve.

Briefly, information about the second model, the 4-story frame, is provided above. Based on the comparison of the first three modes of vibration, it was found that the model developed in the current paper has a mass and stiffness distribution almost similar to that was reported by Reinhorn et al. [27]. In addition, by pushover analysis, it was found that the observed trend in the obtained capacity curve is similar to the results presented in the reference article (Table 3 and Figure 6).

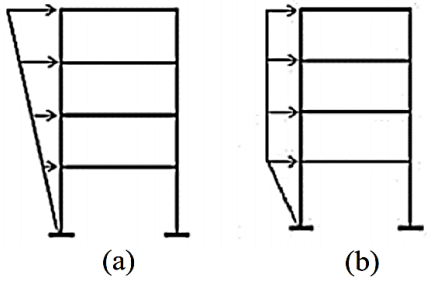

Figure 5. Lateral load distribution types (a: inverse triangle, b: uniform)

TABLE 3. Comparison between the results of the current study and Ferracuti et al. [30]

Results	Mode1	Mode 2	Mode 3
Ferracuti et al. [30]	0.50	0.17	0.11
Current Paper	0.51	0.175	0.104
Difference %	1.4	2.94	5.45

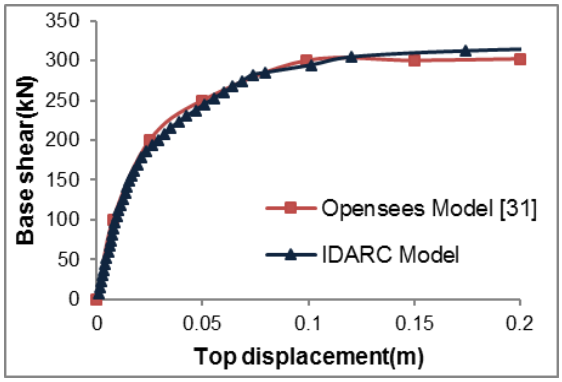

Figure 6. Comparison between the results of the current study and Ferracuti et al. [30]

4. DAMAGE ASSESSMENT BASED ON PARK-ANG MODEL AND STIFFNESS BASED MODEL

In the previous sections, the stifness based damage index was introduced which had previously been provided by the researchers for the performance levels of immediate occupancy (IO), life safety (LS), and collapse prevention (CP). Introducing this index at performance levels alone cannot validate the results. This index has not been calibrated based on valid numerical models, and its results have not been compared with those of other indices. Therefore, the present study calculated the stiffness damage index based on the results of the pushover analysis and compared it with the results of the Park-Ang model. The IDARC program can calculate Park-Ang index values at the same time as pushover analysis and present the results when requested by the user at different levels of analysis. Based on the description given above, numerical calculations were presented in a series of separate tables for each of the above three models. The first four columns of each table contain the results of the nonlinear static analysis performed on the model and the value of the global Park&Ang damage index, which are obtained from the program output.

The amount of stiffness was calculated using the data presented in these columns, followed by calculating the cumulative stiffness reduction ratio and, finally, the amount of damage index based on the stiffness model at different displacement levels. Tables 4 to 6 are related to the first, second, and third frames. Columns 3-6 from the left are related to stiffness-based damage index calculations. To cover the levels of "low to severe" damage according to the Park-Ang criterion, the domain of the index value varies from 0 (without damage) to 1 (structural collapse).

According to the results, the stiffness-based damage index was higher than that calculated based on the Park-Ang model. Accordingly, the following is a review of changes in stiffness-based damage index values with Park & Ang index values as well as drift levels for each model, separately (Figures 7 to 9). Based on analysis results mentioned above, the present study's findings indicated a limited range of changes in the stiffness-based damage index. In other words, at low damage levels where the value of the Park & Ang damage index is less than 0.10, the value of this index indicates a 50-60% damage.

In the literature of damage indices, this value does not mean the amount of damage is small and insignificant, which can be guessed based on the steep slope of the change curve. On the other hand, with a change in Park & Ang damage index value in the range of 20-60%, the value of the stiffness-based index has changed only about 15%. This is not a reliable criteria for determining the post-earthquake performance level of the structure in question. In summary, this index has shown the trend of rapid and slow changes at low and high damage levels, respectively.

TABLE 4. Damage index calculations for the first model

Drift%	$DI_{P\&A}$	Stiffness kN/m	$K_o d_p$	$\sum V_i$	DI
0	0	0	0	0	0.00
0.22	0.01	17305.79	168.13	168.13	0.00
1.66	0.13	3212.59	1291.19	376.61	0.71
1.72	0.13	3106.87	1337.91	385.00	0.71
1.78	0.14	3007.94	1384.79	393.15	0.72
2.02	0.16	2670.03	1573.02	423.50	0.73
2.26	0.18	2402.55	1762.57	450.86	0.74
2.32	0.18	2344.18	1810.15	457.30	0.75
2.53	0.20	2169.50	1970.26	477.93	0.76
3.70	0.30	1539.97	2881.41	559.01	0.81
6.04	0.50	1009.64	4703.71	665.33	0.86
7.22	0.60	871.73	5622.65	711.62	0.87

TABLE 5. Damage index calculations for the Second model

Drift%	$DI_{P\&A}$	Stiffness kN/m	$K_o d_p$	$\sum V_i$	DI
0	0	0	0	0	0
0.29	0.01	6167.58	215.52	215.52	0.00
0.42	0.02	4813.19	314.18	299.55	0.05
0.50	0.02	4346.57	369.02	339.16	0.08
0.54	0.03	4160.54	396.48	357.68	0.10
0.61	0.03	3835.62	453.84	394.05	0.13
0.66	0.04	3579.14	490.99	415.61	0.15
0.85	0.05	2903.58	625.61	478.99	0.23
1.00	0.06	2527.78	743.22	527.19	0.29
1.45	0.10	1793.16	1073.45	623.20	0.42
2.32	0.17	1149.27	1714.54	742.66	0.57
3.16	0.24	860.72	2342.30	830.27	0.65

TABLE 6. Damage index calculations for the third model

Drift%	$DI_{P\&A}$	Stiffness kN/m	$K_o d_p$	$\sum V_i$	DI
0	0	0	0	0	0.00
0.04	0.00	6126.33	50.10	50.10	0
0.12	0.01	5440.24	136.57	126.89	0.07
0.26	0.01	4109.30	289.01	229.14	0.21
0.45	0.03	2537.53	513.87	322.27	0.37
0.74	0.06	1600.39	835.29	406.24	0.51
1.10	0.10	1092.18	1241.61	478.68	0.61
2.19	0.22	569.16	2484.12	594.11	0.76

2.45	0.25	513.34	2782.09	619.08	0.78
3.60	0.36	364.20	4080.02	696.24	0.83
4.63	0.45	291.56	5248.42	751.84	0.86
4.76	0.46	284.72	5394.51	758.63	0.86
5.60	0.53	247.71	6344.61	797.05	0.87

To reduce these weaknesses, this paper proposes two models. Following the proposed changes, the results are represented in the form of a series of comparison charts between the models and then compared with the initial state of the proposed index.

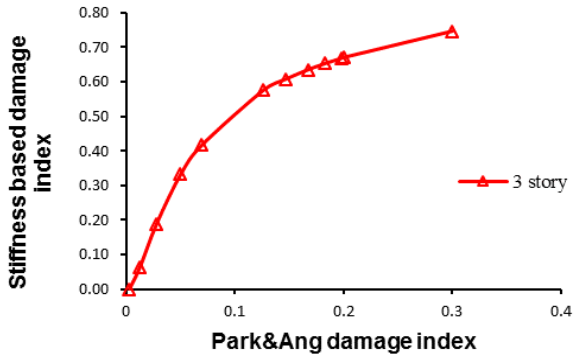

(a)

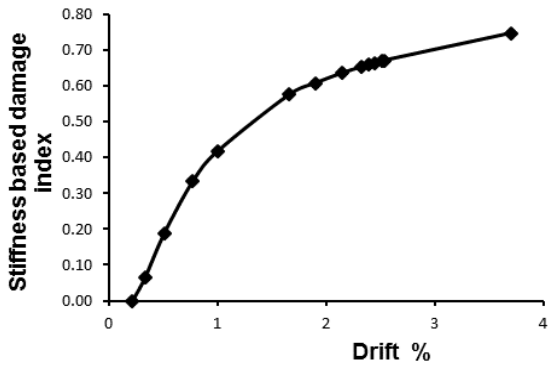

(b)

Figure 7. Relationship between Stiffness based damage index and (a) Park-Ang damage index and (b) Drift index for the 3 story frame

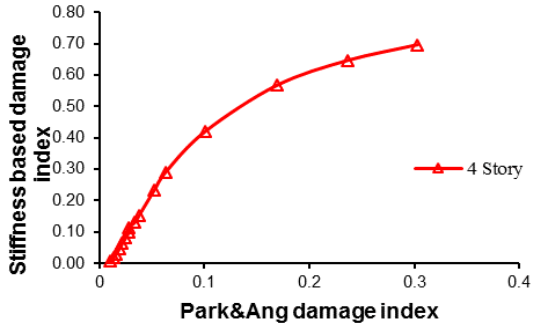

(a)

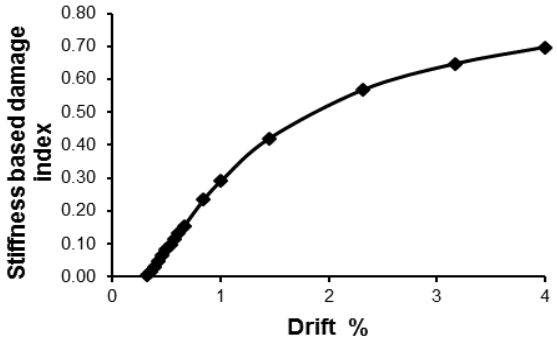

(b)

Figure 8. Relationship between Stiffness based damage index and (a) Park-Ang damage index and (b) Drift index for the 4 story frame

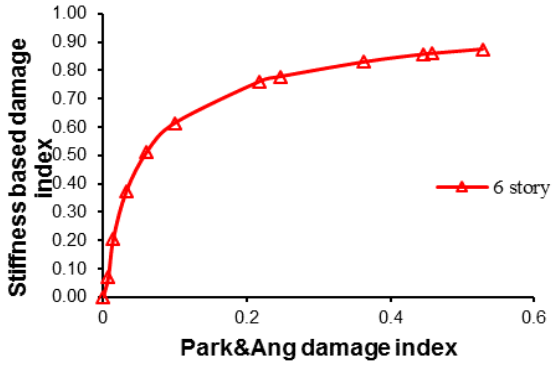

(a)

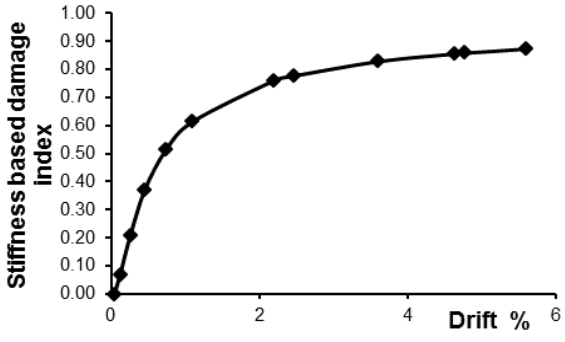

(b)

Figure 9. Relationship between Stiffness based damage index and (a) Park-Ang damage index and (b) Drift index for the 6 story frame

5. PROPOSED MODELS TO IMPROVE STIFFNESS-BASED INDEX RESULTS

According to previous results from the study of the stiffness-based damage index, the following weaknesses can be mentioned:
A) Weakness in determining the amount of damage to the structure at low damage levels, which can be used to repair the structure if possible after the earthquake.
B) According to the basic definitions, the damage index is defined in the range between 0 and 1. However, the cumulative stiffness index has reported values above 0.5, even at low damage levels based on the Park index.
Accordingly, the present research work sought to provide new definitions according to which the mentioned weaknesses could be reduced.

5. 1. First Proposed Model (E1) According to the definition provided in section 2, the damage index introduced can be expressed on another basis. As a result, several corrections were defined as follows, based on which the results of previous calculations will be represented:

$$DI_c = 1 - \frac{\Sigma V_n}{K_o d_p} \tag{17}$$

$$V_o = K_o d_1 \tag{18}$$

$$V_1 = K_o (d_2 - d_1) \tag{19}$$

$$V_2 = K_1 (d_3 - d_2) \tag{20}$$

$$V_3 = K_2 (d_4 - d_3) \tag{21}$$

In the above equations, the values d_1 to d_p are the displacements read from the pushover analysis and the value of ΣV_n is the sum of the shear forces calculated according to Equations (18)-(21) to the desired performance level, respectively. The value of the damage index is between 0 and 1.

5. 2. Second Proposed Model (E2) Based on the changes that will occur in the fundamental period of vibration of a structure after damage, the softening index [31] was defined as Equation (22):

$$DI = 1 - \frac{T_o}{T_i} \tag{22}$$

where T_i and T_o are the fundamental period of vibration of the structure in position i after damage and o without damage, respectively. Given the relationship between period of vibration and stiffness, the period of vibration can be related to the stiffness of the condition i of the structure as follows, assuming that structural mass remains constant after damage:

$$T_i \propto \frac{1}{\sqrt{K_i}} \tag{23}$$

Therefore, the damage index changes according to the new form as follows:

$$DI = 1 - \sqrt{\frac{K_i}{K_o}} = 1 - \sqrt{\frac{K_i d_p}{K_o d_p}} = 1 - \sqrt{\frac{\Sigma V_i}{V_o}} \tag{24}$$

d_p represents the displacement of the node control of the structure in the performance level being calculated. To calculate ΣV_i , we must use the relations (25) to (29):

$$V_0 = K_o d_1 \tag{25}$$

$$V_1 = K_1 (d_2 - d_1) \tag{26}$$

$$V_2 = K_2 (d_3 - d_2) \tag{27}$$

$$V_n = K_n (d_c - d_n) \tag{28}$$

$$\Sigma_{i=0}^{i=n} V_i = V_0 + V_1 + V_2 + V_3 + \ldots + V_n \tag{29}$$

5. 3. Reviewing the Results of the Proposed Amendments According to the corrections presented in this study, the results should be evaluated in comparison with the first case. The following is a presentation of changes in the stiffness-based index versus changes in the Park index after applying (E1) and (E2) in a series of diagrams. Based on the results, it is clear that the results of the proposed index have improved compared to their initial state. (Figures 10 to 12) It is also clear that the second proposition has yielded better results than the first. At damage rates of up to 10% based on the Park & Ang model, the difference in results can be reduced to 25% by applying a second proposition. Also, there is little difference between the values of the two indices at high damage levels.

In light of the foregoing, a quantitative comparison can be made between the damage index results and the Park index values by averaging the results. Table 7 is based on the initial classification of damage status based on Park index values. Drift damage index values were also obtained from the results corresponding to the values of this index. The results of the stiffness-based damage index before and after the correction are presented below. Based on the obtained values:

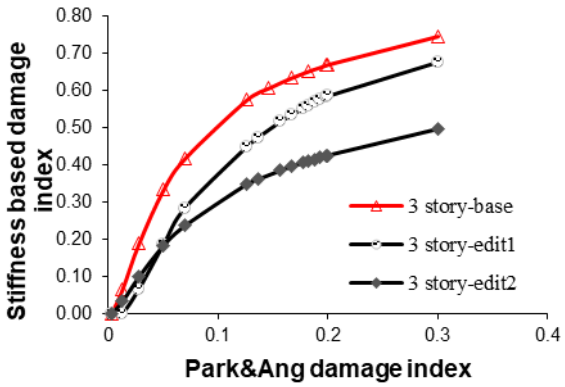

Figure 10. Comparison of changes in damage index results before and after corrections, 3story frame

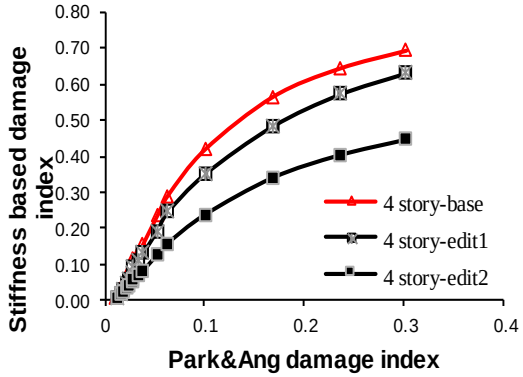

Figure 11. Comparison of changes in damage index results before and after corrections, 4story frame

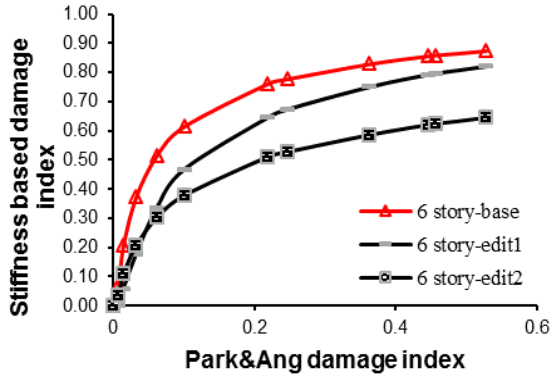

Figure 12. Comparison of changes in damage index results before and after corrections, 6story frame

A: Drift limit values corresponding to the performance levels of IO, LS, and CP were 1.24, 2.96, and 4.68%, respectively (Table 7). However, the recommended values for the FEMA guidelines are 1, 2, and 4%, respectively.

B: The stiffness-based yield index showed better results following improvements in its configuration. It is also clear from the results of Table 7 that the second proposed model introduced in this paper has succeeded in offering both a larger range of changes and more realistic values despite its relatively low computational complexity compared to the valid Park-Ang model.

TABLE 7. Comparison of the results of the indices in the studied models

$DI_{P\&A}$	**Drift index (%)**	**Initial Stiffness based damage index**	**Stiffness based damage index after first correction (e1)**	**Stiffness based damage index after Second correction (e2)**
$DI < 0.10$	Less than 1.24 %	Less than 0.56	Less than 0.42	Less than 0.31
$0.10 \le DI < 0.25$	Between 1.24-2.96 %	Between 0.56-0.74	Between 0.42-0.66	Between 0.31-0.49
$0.25 \le DI < 0.40$	Between 2.96-4.68 %	Between 0.74-0.81	Between 0.66-0.74	Between 0.49-0.57
$DI \ge 0.40$	More than 4.68%	More than 0.81	More than 0.74	More than 0.57

6. CONCLUSIONS

Given the importance of the issue of damage and vulnerability and the need for quantitative post-earthquake estimation of the damaged structure, this study introduced a new stiffness-based index. Thanks to its low computational complexity, this index can conveniently estimate the total damage of the structure based on the output of pushover analysis, i.e., the capacity curve. Three numerical models were developed to evaluate the performance of the index, and the results were compared with those of the valid Park-Ang damage index as well as the drift damage index. By comparison, the initial stiffness-based damage index model states that the results are somewhat higher than the actual values, based on the damage index technical literature. In other words, this index was not very sensitive at low damage levels. Two correction models were proposed to improve the results, and their performance on numerical models was re-examined. The results showed the ability of the modified models to quantify the damage a little better.

In other words, the scope of this index was also expanded to include low breakdown ranges after modifying the damage calculation algorithm. Also, changes in the results of stiffness-based damage index were presented in comparison with Park-Ang indices and relative lateral displacement index. Two main goals of this research were achieved:

1) Provide a new damage index with a low

computational complexity that can consider the cumulative effects of damage and reliably assess overall damage.

2) Calibration of the results of this damage index based on valid damage indices using correction suggestions.

Given the importance of evaluating structures after seismic damage, it is necessary to develop and provide a set of damage indices with acceptable accuracy due to their low computational complexity. This study analyzed concrete flexural frames. However, the performance of the stiffness-based damage index should also be examined in a series of separate studies on other systems due to the diversity of structural systems used in buildings. It is also suggested to conduct a study on the effects of various cyclical behavioral models for nonlinear modeling of structures and their effect on the progress of damage. The effect of lateral load distribution patterns on the damage process should also be considered.

7. REFERENCES

1. Saleemuddin, M.Z.M. and Sangle, K.K., "Seismic damage assessment of reinforced concrete structure using non-linear static analyses", ***KSCE Journal of Civil Engineering***, Vol. 21, (2017), 1319-1330. doi: 10.1007/s12205-016-0541-2.
2. Makhloof, D., Ibrahim, A. and Ren, X., "Damage assessment of reinforced concrete structures through damage indices: A state-of-the-art review", ***Cmes-Computer Modeling In Engineering & Sciences***, Vol. 128, No. 3, (2021), 849-874. doi: 10.32604/cmes.2021.016882.
3. Wen, T.H. and Loh, C.H., "Establishing the relationship between damage measure, seismic hazard, structural ductility and period for pbsd", ***Journal of the Chinese Institute of Engineers***, Vol. 28, No. 4, (2005), 617-626. doi: 10.1080/02533839.2005.9671030.
4. Soleymani, A., "Investigation of correlations between seismic parameters and damage indices for earthquakes of iran region", ***International Journal of Engineering, Transactions B: Applications,***, Vol. 27, No. 2, (2014), 283-292. doi: 10.5829/idosi.ije.2014.27.02b.12.
5. De Domenico, D. and Hajirasouliha, I., "Multi-level performance-based design optimisation of steel frames with nonlinear viscous dampers", ***Bulletin of Earthquake Engineering***, Vol. 19, No. 12, (2021), 5015-5049. https://doi.org/10.1007/s10518-021-01152-7
6. Estekanchi, H., Vafai, A. and Arjomandi, K., "Correlation between structural performance levels and damage indexes in steel frames subjected to earthquakes", ***Scientia Iranica***, Vol. 16, No. 2, (2009).
7. Zameeruddin, M. and Sangle, K.K., "Performance-based seismic assessment of reinforced concrete moment resisting frame", ***Journal of King Saud University-Engineering Sciences***, Vol. 33, No. 3, (2021), 153-165. https://doi.org/10.1016/j.jksues.2020.04.005
8. Bahrani, M., Vasseghi, A., Esmaeily, A. and Soltani, M., "Experimental study on seismic behavior of conventional concrete bridge bents", ***Journal of Seismology and Earthquake Engineering***, Vol. 12, No. 3, (2010), 107-118.
9. Tasnimi, A., "Assessment of the park-ang damage index for performance levels of rc moment resisting frames", ***Modares Civil Engineering journal***, Vol. 17, No. 1, (2017), 43-53.
10. Mazloom, M., "Studying the park-ang damage index of reinforced concrete structures based on equivalent sinusoidal waves", ***Structural Engineering and Mechanics, An Int'l Journal***, Vol. 72, No. 1, (2019), 83-97. doi: 10.12989/sem.2019.72.1.083.
11. Habibi, A., Saffari, H. and Izadpanah, M., "Optimal lateral load pattern for pushover analysis of building structures", ***Steel Compos Struct***, Vol. 32, No. 1, (2019), 67-77. doi: 10.12989/scs.2019.32.1.067.
12. Aghagholizadeh, M. and Massumi, A., "A new method to assess damage to rcmrfs from period elongation and park–ang damage index using ida", ***International Journal of Advanced Structural Engineering***, Vol. 8, (2016), 243-252. https://doi.org/10.1007/s40091-016-0127-8
13. Habibi, A. and Asadi, K., "Development of drift-based damage index for reinforced concrete moment resisting frames with setback", ***International Journal of Civil Engineering***, Vol. 15, (2017), 487-498. doi: 10.1007/s40999-016-0085-3.
14. Rastegarian, S. and Sharifi, A., "An investigation on the correlation of inter-story drift and performance objectives in conventional rc frames", ***Emerging Science Journal***, Vol. 2, No. 3, (2018), 140-147. doi: 10.28991/esj-2018-01137.
15. Hait, P., Sil, A. and Choudhury, S., "Damage assessment of reinforced concrete buildings considering irregularities (research note)", ***International Journal of Engineering, Transactions A: Basics***, Vol. 32, No. 10, (2019), 1388-1394. doi: 10.5829/ije.2019.32.10a.08.
16. Ozturk, B., Sahin, H.E. and Yildiz, C., "Seismic performance assessment of industrial structures in turkey using the fragility curves", in 15th World Conference on Earthquake Engineering, Lisbon, Portugal., (2012), 1-7.
17. Somwanshi, R.B., Pawar, A., Singh, A., Kadukar, N. and Kharade, R., "Evaluation of seismic damage index of reinforced concrete moment resisting frames using nonlinear static procedure", (2020).
18. Kassem, M.M., Nazri, F.M. and Farsangi, E.N., "Development of seismic vulnerability index methodology for reinforced concrete buildings based on nonlinear parametric analyses", ***MethodsX***, Vol. 6, (2019), 199-211. https://doi.org/10.1016/j.mex.2019.01.006
19. Kassem, M.M., Nazri, F.M., Farsangi, E.N. and Ozturk, B., "Improved vulnerability index methodology to quantify seismic risk and loss assessment in reinforced concrete buildings", ***Journal of Earthquake Engineering***, Vol. 26, No. 12, (2022), 6172-6207.
20. Chiluka, S. and Oggu, P., "Performance assessment of ductile detailing code-based reinforced concrete special moment resisting frames", ***International Journal of Engineering, Transactions C: Aspects***, Vol. 36, No. 3, (2023), 457-464. doi: 10.5829/ije.2023.36.03c.04.
21. Mibang, D. and Choudhury, S., "Modified damage index calculation method for frame-shear wall building considering multiple demand parameters", ***International Journal of Engineering, Transactions A: Basics***, Vol. 34, No. 10, (2021), 2294-2301. doi: 10.5829/ije.2021.34.10a.10.
22. Nair, S., Hemalatha, G. and Stephen, E., "Seismic vulnerability studies of a g+ 17 storey building in abu dhabi-uae using fragility curves", ***International Journal of Engineering, Transactions B: Applications,***, Vol. 34, No. 5, (2021), 1167-1175. doi: 10.5829/ije.2021.34.05b.10.
23. Seminar, C., "Nehrp guidelines for the seismic rehabilitation of buildings (fema 273)", Building Seismic Safety Council: Washington, DC, USA, (1997).
24. Council, A.T., "Seismic evaluation and retrofit of concrete buildings", Report No. SSC 96-01: ATC-40, Vol. 1, (1996).
25. DiPasquale, E. and Cakmak, A., "Seismic damage assessment using linear models", ***Soil Dynamics and Earthquake***

Engineering, Vol. 9, No. 4, (1990), 194-215. doi: 10.1016/S0267-7261(05)80010-7.

26. Park, Y.-J. and Ang, A.H.-S., "Mechanistic seismic damage model for reinforced concrete", ***Journal of Structural Engineering***, Vol. 111, No. 4, (1985), 722-739. https://doi.org/10.1061/(ASCE)07339445(1985)111:4(722)
27. Reinhorn, A., Roh, H., Sivaselvan, M., Kunnath, S., Valles, R., Madan, A., Li, C., Lobo, R. and Park, Y., "Idarc2d version 7.0: A program for the inelastic damage analysis of structures (mceer-09-0006)", Multidisciplinary center for earthquake engineering research (MCEER…, (2009).
28. Ang, A.-S., "Seismic damage assessment and basis for damage-limiting design", ***Probabilistic Engineering Mechanics***, Vol. 3, No. 3, (1988), 146-150. doi: 10.1016/0266-8920(88)90026-4.
29. Ghobarah, A., Abou-Elfath, H. and Biddah, A., "Response-based damage assessment of structures", ***Earthquake Engineering & Structural Dynamics***, Vol. 28, No. 1, (1999), 79-104. https://doi.org/10.1002/(SICI)1096-9845(199901)
30. Ferracuti, B., Pinho, R., Savoia, M. and Francia, R., "Verification of displacement-based adaptive pushover through multi-ground motion incremental dynamic analyses", ***Engineering Structures***, Vol. 31, No. 8, (2009), 1789-1799. doi: 10.1016/ j.engstruct.2009.02.035.
31. Habibi, A., Izadpanah, M. and Yazdani, A., "Inelastic damage analysis of rcmrfs using pushover method", ***Iranian Journal of Science and Technology-Transactions of Civil Engineering***, Vol. 37, No. c2, (2013). doi: 10.22099/ijstc.2013.1623.

Persian Abstract

چکیده

در هنگام وقوع زلزله‌ها، سازه‌ها خسارات مختلفی را تجربه می‌کنند و همواره پس از وقوع زلزله تخمین کمی میزان خسارت وارد بر سازه امری بسیار ضروری به نظر می‌رسد. برای تخمین میزان خسارات در سازه‌ها، شاخص‌های خسارت لرزه‌ای به عنوان کمیت‌های بدون بعد معرفی شده‌اند که قادرند با استفاده از معیارهای مختلف، میزانی از خرابی را گزارش دهند. به کمک این ارزیابی کمی می‌توان در خصوص فرایند بهسازی و ترمیم و تقویت سازه‌ها تصمیم‌گیری کرد. در این مقاله با انجام تحلیل بارافزون بر روی مدل‌های بتنی موجود و استفاده از نتایج این تحلیل، شاخص خسارت جدیدی بر مبنای سختی و با فرمول‌بندی ساده ارائه شده است. این شاخص با استفاده از منحنی ظرفیت حاصل از خروجی تحلیل بارافزون، قادر است تا تخمینی کمی از میزان خسارت کل سازه را ارائه دهد. برای اعتبارسنجی نتایج، تخمین خسارت به کمک مدل‌های معتبری چون مدل پارک و انگ نیز انجام شده و سپس با نتایج شاخص پیشنهادی مقایسه شده است. سپس جهت رفع ضعف‌های موجود پیشنهاداتی تئوریک ارائه شده و این پیشنهادات به اجرا در آمده و نتایج جدید حاصل گردید. در پایان مشخص شد که با لحاظ‌کردن پیشنهادات اصلاحی، عملکرد شاخص پیشنهادی بهبود یافته بطوریکه با روند محاسباتی ساده که پیچیدگی پیاده‌سازی شاخص پارک را ندارد، به دقت بسیار مناسبی دست یافت.

International Journal of Engineering

Journal Homepage: www.ije.ir

A Framework for Analysis of Predictors of Mobile-marketing Use by Expanding Unified Theory of Acceptance and Use of Technology and Artificial Neural Networks

N. Safaie*, H. Hamidi, M. Vali

Faculty of Industrial Engineering, K. N. Toosi University of Technology, Tehran, Iran

PAPER INFO

Paper history:
Received 14 February 2022
Received in revised form 22 March 2023
Accepted 23 March 2023

Keywords:
Mobile Marketing
Technology Acceptance
Partial Least Squares
Artificial Neural Networks
Unified Theory of Acceptance
Use Technology

ABSTRACT

This study developed unified theory of acceptance and use technology (UTAUT) to examine the predictive factors of mobile marketing adoption. Variables such as personal innovativeness, hedonic motivations, performance expectancy, mobility, and social influence were studied for mobile marketing acceptance. The predicted artificial neural networks (ANN) approach was applied to evaluate the data, and the results of the data were used for comparison with path analysis. The ANN model was derailed by the linear statistical model and was able to show the importance of all predictors that could not be identified by the path analysis model. The results show that personal innovativeness is the most effective factor in mobile marketing acceptance. Subsequently, the hedonic motivations, performance expectancy, mobility, social influence, trust, and facilitating conditions play a vital role. Furthermore, the results illustrate that price value, perceived risk, and effort expectancy were not effective.

doi: *10.5829/ije.2023.36.05b.17*

1. INTRODUCTION

Over time, mobile marketing and mobile services businesses have grown rapidly to expand customer networks. Importantly, more than half of the world's population is online today [1]. Nowadays, many smartphone users are doing more sophisticated activities such as electronic payments, shopping, marketing services with their mobile devices, using voice services, etc. In 2022, Google's advertising revenue is estimated to be $ 224 billion[1]. These figures show evidence of the enormous growth and influence of mobile marketing. Therefore, developing countries such as Iran, with its high number of subscribers (123.7 million mobile subscribers) [2-4], as well as the potential and profits that are growing in this industry, need to be present seriously in this industry and commerce. Although China currently has the largest mobile payment market, developing countries such as India and Iran are being recognized as the future of mobile marketing owing to the rapid growth of their market and their large number of mobile users [5-8]. Figure 1 illustrated the average changes in media consumption in 2019 vs. 2011.

The benefits of mobile marketing include its ubiquitous availability, customization based on the time, place, and individual characteristics of users [9]. By reducing search costs for users, increased diversity of products offered, lower prices for both users and retailers, empowering consumers to make better choices, enhancing brand [10, 11] relationship after purchase. Mobile marketing also differentiates itself usefully from other marketing media such as television, radio, and newspapers as well as the website (due to its fully interactive nature). However, there are some challenges in mobile marketing, such as the concern of the lack of explicit written law to protect consumer rights in mobile marketing and advertising. Government agencies can help by taking steps to ensure the privacy of consumers, for example, the confidentiality of personal information and requesting permission to post ads before making extensive use of this tool [12].

The goals that we want to achieve in this research are:

*Corresponding Author Institutional Email: *nsafaie@kntu.ac.ir* (N. Safaie)

[1] https://www.statista.com/statistics/266249/advertising-revenue-of-google/

Please cite this article as: N. Safaie, H. Hamidi, M. Vali, A Framework for Analysis of Predictors of Mobile-marketing Use by Expanding Unified Theory of Acceptance and Use of Technology and Artificial Neural Networks, ***International Journal of Engineering, Transactions B: Applications***, Vol. 36, No. 05, (2023) 1012-1022

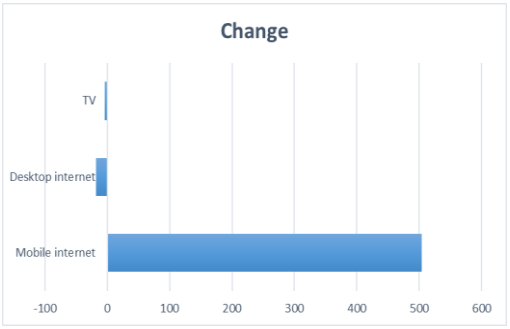

Figure 1. Average Changes in Media Consumption in 2019 vs. 2011

1. This study aims to explore the use of mobile marketing in Iranian consumer market, which is one of the fastest-growing mobile marketing markets. This is also the first study to examine mobile marketing for consumers in Iran.
2. This study aims to identify the important factors that can predict the use of mobile marketing based on the extended UTAUT model. This study adds variables of mobility, personal innovativeness, trust and perceived risk to the UTAUT model by using previous studies.
3. In this study, a more detailed analysis was performed using artificial neural networks. This approach provides a better prediction of conventional linear models for predicting mobile marketing acceptance by considering the nonlinear decision model. To this end, the results of the neural network have been compared with the analysis of linear statistical methods to determine which techniques can improve mobile marketing acceptance. It also responds to the call to apply analytical forecasting techniques to information systems research.

2. LITERATURE REVIEW

As mentioned in the previous section, the internet plays an important role in people's activities today. In examining the determinants of technology acceptance, researchers often consider behavior or approach as an important part of understanding actual behavior [13, 14]. Users often accept applying technologies suggested by their social and business partners. Therefore, the advice of users to other people can be extremely important in increasing the influence and development of mobile marketing in Iran. In addition to the recommendation, the study also explored a proposal to expand UTAUT2, taking into account the degree of risk and trust considered as a factor [15]. Since mobile marketing and its technology adoption in developing countries is a valuable topic, the proposed model is presented in Figure 2.

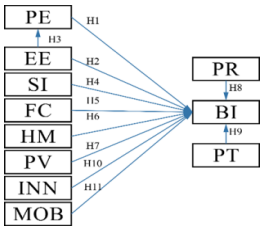

Figure 2. The proposed model

2. 1. Performance Expectancy The performance expectancy is a set of different features of information systems that can explain the benefits to users and is quite similar to the perceived usefulness of TAM technology adoption. It is generally agreed that people are more inclined to use new technology that they think will be useful [16-18]. In the context of mobile marketing, the performance expectancy means that the consumer realizes that using mobile marketing can be beneficial and optimal for completing business transactions. However, since the expected performance goes beyond being useful, it also includes aspects of relative advantage and extrinsic motivation [19]. The following hypothesis is proposed:

H 1: Performance expectancy positively affects the behavioral intention of mobile marketing acceptance.

2. 2. Effort Expectancy Effort expectancy is defined as "the degree of easy to interact with technology for users" [20, 21]. This topic is similar to the discussion of the perceived ease of use and users' understanding of the application in TAM, which illustrates how comfortable the users are with the application. In the context of mobile marketing, the degree of effort and performance can be described as the ability to complete a mobile marketing transaction with minimal effort. In such a situation, consumers can easily make mobile marketing deals within these applications. However, recent studies on the adoption of other mobile technologies have found no direct and significant relationship between effort expectancy and behavioral intention [22-28]. Instead, it is expected that it has an indirect effect on behavioral intention on acceptance through its positive effect on performance expectancy [29-31]. Since ease of use is considered to have a great impact on mobile marketing, the following hypothesis is proposed:

H 2: Effort expectancy positively influences behavioral intention on mobile marketing acceptance.

H 3: Effort expectancy has a positive effect on performance expectancy.

2. 3. Social Influence Social influence is significant to the extent that it can be said that users are strongly influenced by their family [32]. When other users' feedbacks are positive, they are encouraged to use that technology and, in turn, misuse the other people's feedbacks. Previous studies have shown that social influence has a significant impact on consumers'

acceptance of mobile marketing solutions [33, 34]. For this reason, this study assumes that:

H 4: Social influence positively influences behavioral intention on mobile marketing acceptance.

2. 4. Facilitating Conditions In other words, facilitation conditions can be perceived by consumers about environmental barriers or available resources that make it easy to use mobile marketing solutions. The early concept of UTAUT examined facilitating conditions only as a predictor of behavior. However, Imtiaz [35] in UTAUT2 showed that facilitating conditions is also a behavioral approach for technology adoption. However, the generalization of this relationship is controversial, as some studies have shown significant conditions[1]. While others have found no significant association of facilitation conditions. Do not have a behavioral approach [36]. Despite these contradictory results, this study examines facilitation conditions according to studies conducted by Kalinic and Marinkovic [37], they stated facilitating conditions significantly influence the behavioral intention to accept using a technology. Facilitating conditions have a significant impact on mobile Internet use[2], which can have had a great impact on mobile marketing adoption because mobile internet is a vital part of mobile marketing transactions. So, this research assumes that:

H 5: Conditions of facilitation positively influence behavioral intention on mobile marketing acceptance.

2. 5. Hedonic Motivations Hedonic motivation is the pleasure that is given to the consumer through the use of technology. In fact, users are increasingly concerned about the overall experience of using precision technology. So, whether it enjoys it or not or in other words, whether communicating with technology or not for users can change the way technology is used. Even if support for the relationship between hedonic motivations and behavioral approach has not been fully elucidated, many other studies confirm the significant role of this factor in proving and explaining hedonic motivations for predicting goals have been argued in different technologies adoption [38, 39]. As such, this research assumes that:

H 6: Hedonic motivations for positively influences on behavioral intention to mobile marketing acceptance.

2. 6. Price Value In the context of mobile marketing, this factor can be considered as the advantage of using business applications that are more valuable than the financial costs of conducting similar transactions in an in-person transaction or other types of transactions. Given the potential benefits of using different mobile marketing applications as introduced in UTAUT2. However, there are also studies that have found that financial value is not significant in predicting behavioral approach [40]. Therefore, this study shows that:

H 7: Price value has a positive effect on behavioral intention on mobile marketing acceptance.

2.7. Extended UTAUT2

2. 7. 1. Perceived Risk Perceived risk refers to individual conclusions about the risks and negative consequences of using technology. researches shows that the risks posed by users' use of Internet technologies have a significant negative impact on their decision to use electronic systems [40]. Researches have shown that building trust between consumers and vendors and providing a degree of control over the disclosure of personal information online can alleviate privacy risk concerns [38]. Because privacy issues in online settings affect the attitudes and goals of website use [39], risk-taking increases the amount of mobile activity associated with providing information to companies, and the content will be accessed. Therefore, this study shows that:

H 8: Perceived risk has a significant negative impact on behavioral intention on m-marketing acceptance.

2. 7. 2. Perceived Trust When a significant amount of trust is provided and guaranteed for an application, the user is more likely to use that application and system and is then persuaded to provide personally identifiable information and other sensitive information to the m-marketing service provider. As such, this research assumes that:

H 9: Perceived trust has a significant positive effect on behavioral intention on m-marketing acceptance.

2. 7. 3. Personal Innovativeness and Mobility Consumer innovativeness has been used to study the acceptance behavior of new products and services [40]. The level of personal innovativeness is often referred to as a personality structure, which has been used to predict innovative consumer tendencies to embrace different types of technological innovations. To accurately conceptualize the structure of "innovativeness" some scholars separate the concepts of "inherent innovativeness" and "real innovativeness" [37]. The following hypothesis is developed on this basis:

H 10: Consumer's personal innovativeness positively influences behavioral intention on mobile marketing acceptance.

H 11: Mobility has a significant and positive effect on behavioral intention to accept m-marketing. Table 1 also presents summarizes of previous studies as reported in literature.

[1] https://www.itu.int/en/ITU-D/Statistics/Documents/publications/misr2018/MISR-2018-Vol-1-E.pdf

[2] https://wearesocial.com/blog/2019/01/digital-2019-global-internet-use-accelerates

TABLE 1. Summarizes of previous studies

Source	Base model	Factors	Findings
Duarte and Pinho [21]	UTAUT2	Performance Expectancy, Effort Expectancy, Social Influence, Facilitating Conditions, Personal Interests, Price value, Risk, Trust	• The positive impact of perceived risk, perceived trust, and personal attachment • In the context of the environment, the key factors for the adoption of e-commerce in Cameroon are the social influence and facilitating conditions
Chong [12]	UTAUT	Trust, Performance Expectancy, Effort Expectancy, Perceived Value, Perceived Enjoyment, Personal Innovation, Facilitating Conditions, Social Influence, Perceived Ease of Use, Demographic Factors	Based on ANN analysis, perceived value is the most important predictor of mobile commerce usage, followed by performance expectancy, social influence, trust, perceived ease of use, age, perceived enjoyment, education level, personal innovativeness, facilitating conditions and gender.
Dai and Palvia [17]	TAM	Perceived Usefulness, Perceived Ease of Use, Perceived Privacy, Perceived Cost, Compatibility, Perceived Enjoyment, and Perceived Added Value	In the Chinese model, innovation, perceived usefulness, perceived ease of use, perceived cost, and subjective norms significantly influence consumers' intentions to use mobile commerce.
Alalwan [3]	TAM	Perceived usefulness, perceived ease of use, trust, innovation, perceived enjoyment	Perceived enjoyment is the strongest predictor of consumers' decisions. Perceived enjoyment also has a significant impact on the perceived usefulness of Saudi customers in the conceptual model. This means that as long as the customers feel that it is enjoyable to use mobile internet, they will positively perceive mobile internet as productive and useful.
Benbasat and Barki [7]	TAM	Perceived Usefulness, Perceived Ease of Use, Trust, Mobility, Customization, Customer engagement	The results show that customization and customer engagement are the strongest predictors of behavioral intention to use mobile commerce.
Herrero et al. [27]	UTAUT2	Perceived Value, Personal Innovativeness, Performance Expectancy, Perceived Privacy, Perceived Personal Risk, Perceived Transaction Risk,	Perceived value replaces price value to represent the value of an IT product that does not have direct costs associated with it, as a compromise between privacy concerns and performance expectations.
Faqih and Jaradat [23]	TAM	Perceived Usefulness of Mobile Online Stores for Searching Information, Perceived Usefulness of Mobile Online Stores for Shopping,	This study aims to examine the processes of understanding consumer concepts by examining the processes of online shopping in Europe.
Carlsson et al. [10]	UTAUT	Performance Expectancy, Effort Expectancy, Social Influence, Facilitating Conditions, Perceived Enjoyment, Perceived Risk, Personal Innovativeness in Accepting Different E-Commerce Categories.	Performance expectancy includes improvements in performance, productivity, greater convenience through the use of e-commerce applications.
Gao et al. [24]	TAM	Risk acceptance, personal dependence instead of the perceived ease of use of the old model,	Providing information and content availability in both the US and Pakistan have a positive impact on mobile marketing acceptance.

This study developed UTAUT to examine the predictive factors of mobile marketing adoption. Variables such as personal innovativeness, hedonic motivations, performance expectancy, mobility, and social influence were studied for mobile marketing acceptance.

3. METHODOLOGY

UTAUT2 is a validated model and comprises a comprehensive structure of diverse findings in various contexts [26, 27]. For this reason, it is important to continually review and refine UTAUT2 to enhance its generalizability, and it is particularly important in mobile marketing since different studies show similar results for similar variables [11, 29].

This information was collected in the spring of 2019. In this article, a convenient tool for student information gathering was applied using a questionnaire. As well as, participation in this questionnaire was completely optional. Table 2 summarized the details of demographic characteristics.

The results of the questionnaire analysis are shown in Figure 3. This figure shows the percentage of respondents in each factor separation based on the Likert scale. As shown in the Figure 3, most participants believe that the use of mobile marketing will be useful in everyday life in general. They also find it easy to learn how to use mobile marketing. More than half of users believe that facilitating conditions such as the resources and knowledge they need, helping others, or adapting to other technologies make it possible for them to use mobile marketing. Moreover, more than 80 percent of users believe that they are interested in using new technologies, and among their peers, they usually use technology earlier than others.

TABLE 2. The details of demographic characteristics

Characteristics		Number	Percentage
Gender	Male	154	44%
	Female	196	56%
Age	18-20	65	19%
	21-30	245	70%
	31-40	26	7%
	>40	14	4%
Marriage	Single	241	68%
	Married	33	9%
Education level	Diploma	63	18%
	Bachelor	154	44%
	Master	113	32%
	Ph.D. and higher	20	5%

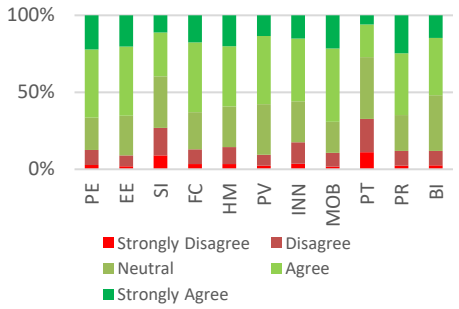

Figure 3. Distribution of responses

3. 1. Survey Development The survey questions in this study were designed using the opinions of experts and previous studies. Questions for the main variables of UTAUT2 including PE, EE, SI, FC, HM, and PV come from [26], and have been privatized by the technology used in the study of mobile marketing acceptance. Other questions come from [11, 13, 26] in the context of mobile marketing has been extracted.

3. 2. Data Analysis SEM is a technique that estimates the relationships between variables [36]. SEM can be implemented using two methods: covariance-based method (such as EQS, AMOS, and LISREL) and variance-based PLS. According to literature [13, 26], partial least squares techniques are less restrictive than structural equation modeling, capable of simultaneously analyzing structural model and evaluation, and are more suitable for small-scale research and predictive purposes. The PLS method is principally used to analyze models that contain several different dimensions and the number of pathways is small [35]. Based on the conditions of this study (statistical population of 350 people and not using mobile marketing in Iran), the PLS method is preferred to SEM. According to Hamidi and Chavoshi [26], methods such as PLS and SEM consider complex human decisions so simple, including the tendency to use new technologies. Therefore, there exists a need to apply new artificial intelligence approaches such as ANNs for solving this problem. The partial least squares method is also not capable of analyzing nonlinear relationships. In fact, using the combination of artificial neural networks and partial least squares (PLS-ANN) makes the advantages of both methods better for data analysis. Therefore, in this study, this approach was implemented using SPSS and Smart PLS. The details of the data analysis and the steps to do this are schematically shown in Figure 4.

3. 3. Outer Model: Validity and Reliability The outer model is used to assess the validity and reliability of the questionnaire. Validity determines that the questions in the questionnaire measure the same concept as that of the researchers, and for its evaluation, convergent and discriminant validity must be tested [26]. Validity is meant to show the degree of reasonableness of the survey questions for the relevant factor, and reliability indicates that the questions related to each factor measure precisely and yield similar results at different times and conditions [30].

According to Chavoshi and Hamidi [11], to measure reliability, factor loadings of all indices must be greater than 0.5, and the corresponding t-statistic should be greater than ±1.96% and composite reliability (CR) greater than 0.7. Also, calculating internal consistency reliability is critical. For this purpose, the Cronbach's alpha correlation coefficient should be calculated, the closer this value shows a higher degree of internal consistency reliability. Table 3 shows the values of factor loadings, alpha correlation coefficient and composite reliability for this study. Accordingly, the reliability of the questionnaire is confirmed.

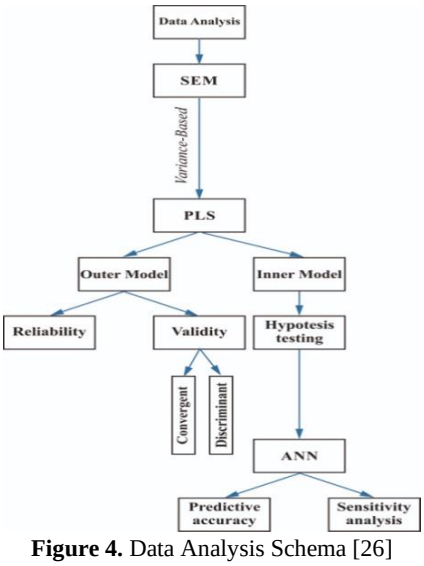

Figure 4. Data Analysis Schema [26]

TABLE 3. Outer Model

Construct	Indicator	Factor Loading	t-statistics	Cronbach's alpha	CR	AVE
Performance Expectancy	PE1	0.849	41.776	0.830	0.887	0.663
	PE2	0.847	45.259			
	PE3	0.796	25.509			
	PE4	0.764	29.054			
Effort Expectancy	EE1	0.819	32.519	0.847	0.897	0.686
	EE2	0.847	37.886			
	EE3	0.833	34.790			
	EE4	0.812	31.244			
Social Influence	SI1	0.798	23.916	0.734	0.849	0.653
	SI2	0.743	21.258			
	SI3	0.879	57.612			
Facilitating Conditions	FC1	0.767	26.171	0.702	0.834	0.626
	FC2	0.779	25.462			
	FC3	0.827	32.878			
Hedonic Motivations	HM1	0.834	36.594	0.727	0.847	0.650
	HM2	0.881	58.987			
	HM3	0.693	14.268			
Price Value	PV1	0.790	23.482	0.761	0.861	0.674
	PV2	0.868	47.883			
	PV3	0.804	19.946			
Perceived Risk	PR1	0.856	2.996	0.704	0.870	0.771
	PR2	0.899	3.379			
Perceived Trust	PT1	0.808	34.225	0.842	0.894	0.678
	PT2	0.831	29.741			
	PT3	0.846	39.745			
	PT4	0.809	35.794			
Personal Innovativeness	INN1	0.754	24.885	0.777	0.856	0.599
	INN2	0.693	17.830			
	INN3	0.811	34.502			
	INN4	0.830	41.015			
Mobility	MOB1	0.866	48.459	0.846	0.897	0.686
	MOB2	0.874	39.756			
	MOB3	0.840	16.999			
	MOB4	0.725	41.776			
Behavioral intention	BI1	0.880	62.348	0.891	0.925	0.754
	BI2	0.860	53.058			
	BI3	0.905	77.499			
	BI$	0.827	34.520			

The convergent validity is used to measure the amount of explanation of a hidden variable by its observable variables [26].

Discriminant validity means that the factors are not statistically correlated with each other [25]. Table 4 shows the mentioned comparisons. The bold numbers represent the square root of AVE for each factor. According to the presented results in this table, the discriminant validity of this study is also confirmed.

3. 4. Inner Model To evaluate the internal model, we need to calculate the beta, the corresponding t-statistic, R^2, f^2, and Q^2 [11, 26]. For this purpose, the Bootstrap procedure is applied with 5000 replicates. To test the hypotheses, the correlation coefficients of the path (beta) with the corresponding t-statistic should be checked. To support any of the hypotheses, the t-statistic is required to be higher than ±1.96 [11]. Obviously, hypotheses with statistics below this threshold value are rejected. As shown in Table 5, hypotheses 2 (EE -> BI), 7 (PV -> BI) and 8 (PR -> BI) are rejected.

According to Figure 5, the values of R^2 for the dependent factors behavioral intention to use and the performance expectancy is 0.631 and 0.168, respectively. In fact, about 63% of the variance associated with the behavioral intention to use m-marketing is attributable to performance expectancy factors, personal innovativeness, mobility, and perceived trust. Also, about 17% of the variance of performance expectancy depends on the effort expectancy.

According to Chavoshi and Hamidi [11], the values of R^2 equal to 0.25, 0.5 and 0.75 indicate that the model is weak, moderate and robust, respectively. Finally, given the value of R^2 for the tendency to use mobile marketing which is equal to 0.631, it can be concluded that the model presented in this study is robust and acceptable.

TABLE 4. Discriminant validates

	BI	EE	FC	HM	INN	MOB	PE	PR	PT	PV	SI
BI	**0.868**										
EE	0.388	**0.828**									
FC	0.547	0.585	**0.791**								
HM	0.588	0.315	0.395	**0.807**							
INN	0.679	0.422	0.531	0.538	**0.774**						
MOB	0.483	0.368	0.440	0.376	0.383	**0.828**					
PE	0.613	0.410	0.560	0.575	0.548	0.415	**0.815**				
PR	0.033	0.092	0.110	0.078	0.060	0.143	0.174	**0.878**			
PT	0.509	0.247	0.333	0.401	0.449	0.355	0.414	-0.066	**0.824**		
PV	0.446	0.391	0.443	0.410	0.458	0.356	0.473	0.100	0.342	**0.821**	
SI	0.599	0.416	0.549	0.518	0.522	0.327	0.581	0.093	0.484	0.462	**0.808**

TABLE 5. Inner model's hypotheses

Hypothesis	Path Coefficients	Standard deviations	t-statistics	Supported
PE -> BI	0.141	0.053	2.692	Yes
EE -> BI	0.021	0.043	0.482	No
EE -> PE	0.410	0.042	9.644	Yes
SI -> BI	0.153	0.048	3.194	Yes
FC -> BI	0.091	0.044	2.060	Yes
HM -> BI	0.143	0.047	3.066	Yes
PV -> BI	-0.000	0.037	0.013	No
PR -> BI	-0.057	0.047	1.220	No
PT -> BI	0.101	0.040	2.496	Yes
INN -> BI	0.314	0.047	6.613	Yes
MOB-> BI	0.147	0.039	3.791	Yes

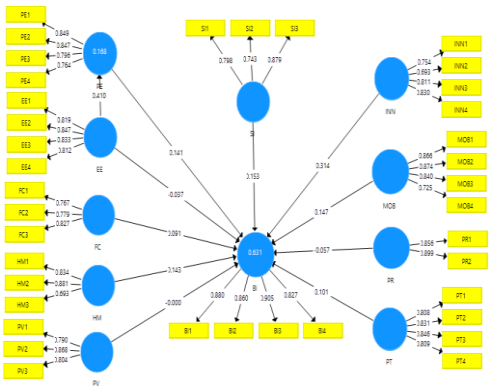

Figure 5. Obtained values of path correlations and R^2 through Smart PLS

Since the p-index is not a suitable criterion for measuring the impact of the independent variable on the dependent variable, a better index, f^2, should be used [29]. Given the values are shown in Table 6, perceived trust and facilitating conditions have low impact, performance expectancy, hedonic motivations, personal innovativeness, mobility, and social influence size have a moderate effect on behavioral intention to use, as well as, the effort expectancy has a significant impact on the performance expectancy.

Then we need to calculate the predictive relationship. For this purpose, the value of Q^2 must be calculated through the Blindfolding procedure. According to Hamidi and Chavoshi [26], for values above zero, the model has a predictive relationship, and if this value is 0.02, 0.15 and 0.35, it indicates a weak, moderate predictive relationship, respectively. The results of Table 7 show that the predictive relevance of the model presented in this study is a robust mobile marketing acceptance model.

3. 5. ANN Analysis The artificial neural network is "a machine that has been devised to model brain function for a specific task" [31]. In fact, the artificial neural network is a modeling of the human nervous system that enables the learning process to be simulated by the human brain. Due to the ANN's learning capability, this technique can improve its performance through learning process [39, 40].

TABLE 6. Effect size of independent variables

Independent variable	Dependent variable: Behavioral intention	Dependent variable: Performance Expectancy
Performance Expectancy	0.025	-
Effort Expectancy	0.002	0.202
Social Influence	0.031	-
Facilitating Conditions	0.010	-
Hedonic Motivations	0.031	-
Price Value	0.000	-
Perceived Risk	0.008	-
Perceived Trust	0.018	-
Personal Innovativeness	0.139	-
Mobility	0.040	-

TABLE 7. Indicator of model's predictive relevance

Dependent Variable	Construct cross-validated redundancy
Performance Expectancy	0.102
Behavioral intention	0.433

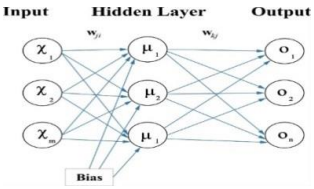

Figure 6. ANN Different Layers [12]

As noted in previous studies by Hamidi and Chavoshi [26], to evaluate the size of relative significance of independent variables for dependent variables the most common artificial neural network model, namely multi-layer perceptron, has been used. To this end, the confirmed factors in PLS analysis are given as input to the neural network. The proposed model of this study transformed into two artificial neural network models due to its two paths, which are shown in detail in Figure 7.

To avoid over-fitting, a 10-fold cross-validation procedure is used in which 90% of the data is considered as training data, and 10% is considered as test data [26]. The activation function in both the hidden and the output layers was sigmoid. The number of hidden layers and their associated neurons is also automatically calculated by the software to obtain the optimal state. Table 8 shows the Root Mean Square Errors (RMSE) values to measure model prediction for all 10 networks for both the training and the test modes.

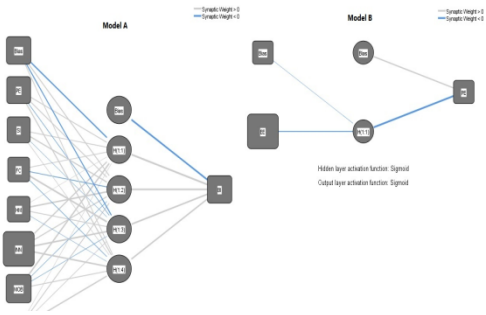

Figure 7. ANN Models

TABLE 8. RMSE values of ANN

Network	Model A Inputs: PE, SI, FC, HM, INN, MOB, and PT Output: BI		Model B Input: EE	
	Training	Test	Training	Test
1	0.0933	0.1019	0.1402	0.1091
2	0.0937	0.1	0.1440	0.1381
3	0.0869	0.0959	0.1404	0.906
4	0.0908	0.0570	0.1417	0.1136
5	0.0931	0.0764	0.1407	0.1255
6	0.0916	0.0915	0.1404	0.1328

7	0.0916	0.0820	0.1337	0.1687
8	0.0928	0.0665	0.1410	0.1340
9	0.0945	0.0748	0.1383	0.1445
10	0.0906	0.0885	0.1471	0.1217
Mean	0.0919	0.0834	0.1408	0.1278
Standard deviation	0.0020	0.0140	0.0032	0.0202

Sensitivity analysis is used to measure the sensitivity of the independent factors for the dependent factor. For this purpose, relative importance is shown by how much the predicted output value for the dependent factor varies with different inputs. Table 9 shows these values for both models.

Comparing the results of this table with Table 7, it can be concluded that there is a little difference in the order of importance of the factors influencing the adoption of

TABLE 9. ANN sensitivity analysis

Network	**Model A**							**Model B**
	PE	**SI**	**FC**	**HM**	**INN**	**MOB**	**PT**	**EE**
1	0.103	0.182	0.129	0.179	0.184	0.101	0.121	1.000
2	0.195	0.173	0.081	0.124	0.230	0.067	0.130	1.000
3	0.152	0.152	0.079	0.140	0.244	0.135	0.098	1.000
4	0.110	0.130	0.087	0.122	0.303	0.150	0.097	1.000
5	0.136	0.089	0.132	0.184	0.219	0.110	0.129	1.000
6	0.160	0.095	0.017	0.113	0.307	0.182	0.126	1.000
7	0.129	0.126	0.023	0.124	0.310	0.160	0.128	1.000
8	0.100	0.125	0.091	0.151	0.330	0.105	0.097	1.000
9	0.086	0.047	0.154	0.194	0.286	0.098	0.136	1.000
10	0.131	0.111	0.085	0.104	0.285	0.156	0.129	1.000
Average importance	0.130	0.123	0.088	0.144	0.270	0.126	0.119	1.000
Normalized importance (%)	48	45.5	32.5	53	100	47	44	100

mobile marketing use. For example, sensitivity analysis results indicate that the second most important factor is hedonic motivations, while effect size analysis results (f^2) believe that the second important factor is the mobility factor. This difference is due to varieties in the method of better analysis in artificial neural networks that detect nonlinear relationships in the model.

4. CONCLUSION

The variables of this study include factors such as UTAUT2 technology adoption, perceived risk and trust and mobility were used to extend this model. These factors have been tested by some hypotheses. This test is performed by SEM, PLS, and ANN. The data required for this study were collected electronically and by paper. Here's a look at each of the UTAUT2 factors and the factors that extend it. Despite many efforts, this study is not without limitations. The first limitation of this study is that in academic research the statistical population is relatively small and has only studied the student population of a university in Iran. Although online polls were posted on popular social media websites among students of K. N. Toosi University of Technology, Iran, responses were very slow and resulted in a small sample size. Future studies could consider distributing this survey to consumers about specific products in the consumer community of a product for its mobile marketing. Secondly, the information collected here is from Iranian consumers and has not been considered by the international communities. Future studies could examine the acceptance of mobile marketing in two societies, a developed and one developing country.

5. REFERENCES

1. Al-Louzi, B. and Iss, B., "Factors influencing customer acceptance of m-commerce services in jordan", ***Journal of Communication and Computer***, Vol. 9, No. 1, (2011), 1424-1436.
2. Al-Shihi, H., Sharma, S.K. and Sarrab, M., "Neural network approach to predict mobile learning acceptance", ***Education and Information Technologies***, Vol. 23, (2018), 1805-1824. https://doi.org/10.1007/s10639-018-9691-9
3. Alalwan, A.A., Baabdullah, A.M., Rana, N.P., Tamilmani, K. and Dwivedi, Y.K., "Examining adoption of mobile internet in saudi arabia: Extending tam with perceived enjoyment, innovativeness

and trust", ***Technology in Society***, Vol. 55, (2018), 100-110. https://doi.org/10.1016/j.techsoc.2018.06.007

4. Alalwan, A.A., Dwivedi, Y.K. and Rana, N.P., "Factors influencing adoption of mobile banking by jordanian bank customers: Extending UTAUT2 with trust", ***International Journal of Information Management***, Vol. 37, No. 3, (2017), 99-110. https://doi.org/10.1016/j.tele.2017.05.008
5. Alalwan, A.A., Rana, N.P., Dwivedi, Y.K. and Algharabat, R., "Social media in marketing: A review and analysis of the existing literature. ", ***Telematics and Informatics***, Vol. 34, (2017), 1177-1190. https://doi.org/10.1016/j.tele.2017.05.008
6. Alharbi, S. and Drew, S., "The role of self-efficacy in technology acceptance", in Proceedings of the Future Technologies Conference (FTC) 2018: Volume 1, Springer. (2019), 1142-1150.
7. Benbasat, I. and Barki, H., "Quo vadis tam?", ***Journal of the Association for Information Systems***, Vol. 8, No. 4, (2007), 7. https://doi.org/10.17705/1jais.00126
8. Brasel, S.A. and Gips, J., "Tablets, touchscreens, and touchpads: How varying touch interfaces trigger psychological ownership and endowment", ***Journal of Consumer Psychology***, Vol. 24, No. 2, (2014), 226-233.
9. Budiono, F., Lau, S. and Tibben, W., "Cloud computing adoption for e-commerce in developing countries: Contributing factors and its implication for indonesia", (2018).
10. Carlsson, C., Carlsson, J., Hyvonen, K., Puhakainen, J. and Walden, P., "Adoption of mobile devices/services-searching for answers with the utaut", in Proceedings of the 39th annual Hawaii international conference on system sciences (HICSS'06), IEEE. Vol. 6, (2006), 132a-132a.
11. Chavoshi, A. and Hamidi, H., "Social, individual, technological and pedagogical factors influencing mobile learning acceptance in higher education: A case from iran", ***Telematics and Informatics***, Vol. 38, (2019), 133-165. https://doi.org/10.1016/j.tele.2018.09.007
12. Chong, A.Y.-L., "Predicting m-commerce adoption determinants: A neural network approach", ***Expert Systems with Applications***, Vol. 40, No. 2, (2013), 523-530. https://doi.org/10.1016/j.eswa.2012.07.068
13. Chong, A.Y.-L., Chan, F.T. and Ooi, K.-B., "Predicting consumer decisions to adopt mobile commerce: Cross country empirical examination between china and malaysia", ***Decision Support Systems***, Vol. 53, No. 1, (2012), 34-43. https://doi.org/10.1016/j.dss.2011.12.001
14. Chong, A.Y.-L., Darmawan, N., Ooi, K.-B. and Lin, B., "Adoption of 3g services among malaysian consumers: An empirical analysis", ***International Journal of Mobile Communications***, Vol. 8, No. 2, (2010), 129-149. https://doi.org/10.1504/IJMC.2010.031444
15. Hamidi, H. and Seyed Lotfali, S., "Analysis of role of cloud computing in providing internet banking services: Case study bank melli iran", ***International Journal of Engineering, Transactions B: Applications***, Vol. 35, No. 5, (2022), 1082-1088. doi: 10.5829/ije.2022.35.05b.23.
16. Cohen, J., *Statistical power analysis for the behavioral sciences (revised ed.)*. 1977, New York: Academic Press.
17. Dai, H. and Palvi, P.C., "Mobile commerce adoption in china and the united states: A cross-cultural study", ACM SIGMIS Database: the DATABASE for Advances in Information Systems, Vol. 40, No. 4, (2009), 43-61. https://doi.org/10.1145/1644953.1644958
18. Davis, F.D., "Perceived usefulness, perceived ease of use, and user acceptance of information technology", ***MIS Quarterly***, (1989), 319-340. https://doi.org/10.2307/249008
19. Davis, R., "Conceptualising fun in mobile commerce environments", ***International Journal of Mobile Communications***, Vol. 8, No. 1, (2010), 21-40. https://doi.org/10.1504/IJMC.2010.030518
20. Torabi, A., Hamidi, H. and Safaie, N., "Effect of sensory experience on customer word-of-mouth intention, considering the roles of customer emotions, satisfaction, and loyalty", ***International Journal of Engineering, Transactions C: Aspects***, Vol. 34, No. 3, (2021), 682-699. doi: 10.5829/ije.2021.34.03c.13.
21. Duarte, P. and Pinho, J.C., "A mixed methods UTAUT2-based approach to assess mobile health adoption", ***Journal of Business Research***, Vol. 102, (2019), 140-150. https://doi.org/10.1016/j.jbusres.2019.05.022
22. Dwivedi, Y.K., Shareef, M.A., Simintiras, A.C., Lal, B. and Weerakkody, V., "A generalised adoption model for services: A cross-country comparison of mobile health (m-health)", ***Government Information Quarterly***, Vol. 33, No. 1, (2016), 174-187. https://doi.org/10.1016/j.giq.2015.06.003
23. Faqih, K.M. and Jaradat, M.-I.R.M., "Assessing the moderating effect of gender differences and individualism-collectivism at individual-level on the adoption of mobile commerce technology: Tam3 perspective", ***Journal of Retailing and Consumer Services***, Vol. 22, (2015), 37-52. https://doi.org/10.1016/j.jretconser.2014.09.006
24. Gao, T.T., Rohm, A.J., Sultan, F. and Pagani, M., "Consumers un-tethered: A three-market empirical study of consumers' mobile marketing acceptance", ***Journal of Business Research***, Vol. 66, No. 12, (2013), 2536-2544. https://doi.org/10.1016/j.jbusres.2013.05.046
25. Guo, X., Zhao, Y., Jin, Y. and Zhang, N., "Two-sided adoption of mobile marketing platforms: Towards an integrated conceptual model", in 2010 Ninth International Conference on Mobile Business and 2010 Ninth Global Mobility Roundtable (ICMB-GMR), IEEE., (2010), 474-480.
26. Hamidi, H. and Chavoshi, A., "Analysis of the essential factors for the adoption of mobile learning in higher education: A case study of students of the university of technology", ***Telematics and Informatics***, Vol. 35, No. 4, (2018), 1053-1070. https://doi.org/10.1016/j.tele.2017.09.016
27. Herrero, Á. and San Martín, H., "Explaining the adoption of social networks sites for sharing user-generated content: A revision of the UTAUT2", ***Computers in Human Behavior***, Vol. 71, (2017), 209-217. https://doi.org/10.1016/j.chb.2017.02.007
28. Hew, J.-J., Badaruddin, M.N.B.A. and Moorthy, M.K., "Crafting a smartphone repurchase decision making process: Do brand attachment and gender matter?", ***Telematics and Informatics***, Vol. 34, No. 4, (2017), 34-56. https://doi.org/10.1016/j.tele.2016.12.009
29. Hew, T.-S., Leong, L.-Y., Ooi, K.-B. and Chong, A.Y.-L., "Predicting drivers of mobile entertainment adoption: A two-stage sem-artificial-neural-network analysis", ***Journal of Computer Information Systems***, Vol. 56, No. 4, (2016), 352-370. https://doi.org/10.1080/08874417.2016.1164497
30. Hirschman, E.C., "Innovativeness, novelty seeking, and consumer creativity", ***Journal of Consumer Research***, Vol. 7, No. 3, (1980), 283-295. https://doi.org/10.1086/208816
31. Hsu, C.-I., Shih, M.-L., Huang, B.-W., Lin, B.-Y. and Lin, C.-N., "Predicting tourism loyalty using an integrated bayesian network mechanism", ***Expert Systems with Applications***, Vol. 36, No. 9, (2009), 11760-11763. https://doi.org/10.1016/j.eswa.2009.04.010
32. Huang, L., Mou, J., See-To, E.W. and Kim, J., "Consumer perceived value preferences for mobile marketing in china: A mixed method approach", ***Journal of Retailing and Consumer Services***, Vol. 48, (2019), 70-86. https://doi.org/10.1016/j.jretconser.2019.02.007
33. Huang, T.-L. and Liao, S.-L., "Creating e-shopping multisensory flow experience through augmented-reality interactive

technology", ***Internet Research***, (2017). https://doi.org/10.1108/IntR-11-2015-0321

34. Im, S., Bayus, B.L. and Mason, C.H., "An empirical study of innate consumer innovativeness, personal characteristics, and new-product adoption behavior", ***Journal of the Academy of Marketing Science***, Vol. 31, No. 1, (2003), 61-73. https://doi.org/10.1177/0092070302238602
35. Imtiaz, S., "The studies of unified theory of acceptance and use of technology (utaut) in m-commerce context", ***International Journal of Information Communication Technology and Digital Convergence***, Vol. 3, No. 1, (2018), 42-56.
36. Jaradat, M.-I.R.M. and Faqih, K.M., "Investigating the moderating effects of gender and self-efficacy in the context of mobile payment adoption: A developing country perspective", ***International Journal of Business and Management***, Vol. 9, No. 11, (2014), 147. https://doi.org/10.5539/ijbm.v9n11p147
37. Kalinic, Z. and Marinkovic, V., "Determinants of users' intention to adopt m-commerce: An empirical analysis", ***Information Systems and e-Business Management***, Vol. 14, (2016), 367-387. https://doi.org/10.1007/s10257-015-0287-2
38. Khalifa, M. and Ning Shen, K., "Explaining the adoption of transactional B2C mobile commerce", ***Journal of enterprise Information Management***, Vol. 21, No. 2, (2008), 110-124. https://doi.org/10.1108/17410390810851372
39. Kim, C., Mirusmonov, M. and Lee, I., "An empirical examination of factors influencing the intention to use mobile payment", ***Computers in Human Behavior***, Vol. 26, No. 3, (2010), 310-322. https://doi.org/10.1016/j.chb.2009.10.013
40. Kim, H.-W., Chan, H.C. and Gupta, S., "Value-based adoption of mobile internet: An empirical investigation", ***Decision Support Systems***, Vol. 43, No. 1, (2007), 111-126. https://doi.org/10.1016/j.dss.2005.05.009

Persian Abstract

چکیده

این مطالعه تئوری یکپارچه پذیرش و استفاده از فناوری (UTAUT) را برای بررسی عوامل پیش‌بینی کننده پذیرش بازاریابی تلفن همراه توسعه داد. متغیرهایی مانند نوآوری شخصی، انگیزه های لذت جویانه، انتظار عملکرد، تحرک و نفوذ اجتماعی برای پذیرش بازاریابی تلفن همراه مورد مطالعه قرار گرفتند. برای ارزیابی داده‌ها از رویکرد شبکه‌های عصبی مصنوعی پیش‌بینی‌شده (ANN) استفاده شد و از نتایج داده‌ها برای مقایسه با تحلیل مسیر استفاده شد. مدل ANN توسط مدل آماری خطی از ریل خارج شد و توانست اهمیت همه پیش‌بینی‌کننده‌هایی را که با مدل تحلیل مسیر قابل شناسایی نبود، نشان دهد. نتایج نشان می‌دهد که نوآوری شخصی مؤثرترین عامل در پذیرش بازاریابی تلفن همراه است. پس از آن، انگیزه های لذت جویانه، انتظار عملکرد، تحرک، نفوذ اجتماعی، اعتماد و شرایط تسهیل کننده نقش حیاتی ایفا می کنند. علاوه بر این، نتایج نشان می‌دهد که ارزش قیمت، ریسک درک شده و انتظار تلاش موثر نبودند.

International Journal of Engineering

Journal Homepage: www.ije.ir

Mixed-mode Multiphase Sinusoidal Oscillators using Differential Voltage Current Conveyor Transconductance Amplifiers and Only Grounded Passives Components

T. Phianpranthong[a], A. Suksawad[b], A. Jantakun*[a]

[a] *Electronics and Telecommunication Engineering Department, Faculty of Engineering, Rajamangala University of Technology Isan, Khon Kaen Campus, Khon Kaen, Thailand*
[b] *Computer Engineering Department, Faculty of Engineering, Rajamangala University of Technology Isan, Khon Kaen Campus, Khon Kaen, Thailand*

PAPER INFO

Paper history:
Received 31 October 2022
Received in revised form 10 December 2022
Accepted 10 December 2022

Keywords:
Mixed-mode
Multiphase Sinusoidal Oscillators
Grounded Passive Component
Gain-controllable
Low-pass Filter
High Impedance

ABSTRACT

This article is about mixed-mode multiphase sinusoidal oscillators that are made up of differential voltage current conveyor transconductance amplifier (DVCCTA) and use all the grounded passive components. The proposed multiphase sinusoidal oscillators provide a single DVCCTA, a single grounded resistor and a capacitor for each phase which is suitable for integrated circuit implementation. In addition, the sinusoidal outputs generate currents and voltages simultaneously. The current signals from the outputs have high impedances, which make it easier to connect them directly to the next circuit or stage. The proposed circuits can generate multiphase sinusoidal signals that are both equally phased and in amplitude. The oscillation can be adjusted simultaneously of the frequency of oscillation by the electronic method. A simulation with the PSPICE program and an experiment with commercially available ICs (AD830, AD844, and LM13700N) demonstrated. The results show the efficiency of the circuit is completely consistent with the theory.

***doi**: 10.5829/ije.2023.36.05b.18*

1. INTRODUCTION

The multiphase sinusoidal oscillator (MSO) has come to be part of electrical and electronic engineering; which makes it an important component. MSO is widely used in many fields, such as communications, where it is used in phase modulators, quadrature mixers, and single-sideband generators [1, 2], in power electronics systems for work related to a three-phase induction motor drive [3], and in measurement systems, where it is used for the selective voltmeters and vector generators [4]. From research and reviews of the literature, many researchers and publishers have suggested different ways to design the MSO, such as by using a low-pass filter, high-pass filter, and all-pass filter, which used active building 1blocks at high performance in development [5-24]. Table 1 summarized the various MSOs have different advantages: a single active building block is used per phase of [7-11, 13-24], which makes it easy to assemble for simulation and experimentation, the passive elements that have been used in minimal numbers in the literture [5-12, 14, 16, 19-24]. MSOs are all grounded, where a grounded capacitor is attractive for integrated circuit implementation. The design techniques of MSOs in literture [5, 6, 9, 10, 13, 15, 17-24] do not require additional amplifier circuit for sinusoidal oscillation. The condition of oscillation (CO) can easily be adjusted electronically by a microcontroller or microcomputer [25, 26]. In addition, some research has shown the results of experiments with commercially available integrated circuits (ICs) [5, 7-9, 15, 18]. However, in various MSOs, it was also found that there were various weaknesses as follow. Jaikla et al. [5], Thongdit et al. [6] and Tangsrirat et al. [12] reported that more than one active building block is used per phase. Skotis and Psychalinos [8], Wu et al. [9] Jaikla et al. [13], Klahan et al. [15], Pandey et

*Corresponding Author Institutional Email: Adirek.ja@rmuti.ac.th
(A. Jantakun)

Please cite this article as: T. Phianpranthong, A. Suksawad, A. Jantakun, Mixed-mode Multiphase Sinusoidal Oscillators using Differential Voltage Current Conveyor Transconductance Amplifiers and Only Grounded Passives Components, ***International Journal of Engineering, Transactions B: Applications***, Vol. 36, No. 05, (2023) 1023-1033

TABLE 1. Comparison between various MSOs

Ref.	(a)	(b)	(c)	(d)	(e)	(f)	(g)	(h)	(i)	(j)
Jaikla et al. [5]	OTA	2	High-pass filter	Yes	1+1	No	Yes	Voltage	-	Yes
Thongdit et al. [6]	OTA	2	High-pass filter	Yes	0+1	No	Yes	Current	Yes	No
Prommee and Dejhan [7]	OTA	1	Low-pass filter	Yes	0+1	Yes	Yes	Voltage	-	Yes
Skotis and Psychalinos [8]	CCII	1	Low-pass filter	Yes	2+1	Yes	No	Voltage	-	Yes
Wu et al. [9]	CCII	1	Low-pass filter	Yes	2+1	No	No	Voltage	-	Yes
Abuelma'atti and Al-Qahtani [10]	CCCII	1	Low-pass filter	Yes	0+2	No	Yes	Current	Yes	No
Loescharataramdee et al. [11]	CCCII	1	Low-pass filter	Yes	0+1	Yes	Yes	Current	Yes	No
Tangsrirat et al. [12]	CDTA	2	All-pass filter	No	0+1	Yes	Yes	Current	Yes	No
Jaikla et al. [13]	CDTA	1	All-pass filter	No	2+1	No	Yes	Current	Yes	No
Tangsrirat and Tanjaroen [14]	CDTA	1	Low-pass filter	Yes	0+1	Yes	Yes	Current	Yes	No
Klahan et al. [15]	CDBA	1	Low-pass filter	No	2+1	No	No	Voltage	-	Yes
Sagbas et al. [16]	CBTA	1	Low-pass filter	Yes	0+1	Yes	Yes	Voltage	-	No
Pandey et al. [17]	OTRA	1	All-pass filter	No	3+1	No	No	Voltage	-	No
Pandey and Bothra [18]	OTRA	1	Low-pass filter	No	2+1	No	No	Voltage	-	Yes
Jaikla and Prommee [19]	CCCDTA	1	All-pass filter	Yes	1+1	No	Yes	Current	Yes	No
Kumngern [20]	CCCDTA	1	Low-pass filter	Yes	0+1	No	Yes	Current	Yes	No
Kumngern [21]	CCCDTA	1	High-pass filter	Yes	0+1	No	Yes	Current	Yes	No
Uttaphut et al. [22]	CCCCTA	1	All-pass filter	Yes	0+1	No	Yes	Current	Yes	No
Gupta and Pandey [23]	DO-VDBA	1	All-pass filter	No	0+1	No	Yes	Voltage	-	No
Pitaksuttayaprot et al. [٢٤]	VDCC	١	Low-pass filter	Yes	٢+١	No	Yes	Current	Yes	Yes
This work MSOs	DVCCTA	1	Low-pass filter	Yes	1+1	No	Yes	Current/Voltage	Yes	Yes

Remarks: (a) Active element (b) No. of active element per phase (c) Design technique (d) All grounded passive elements
(e) No. of R+C per phase (f) Additional amplifier (g) Electronic tune CO (h) Output type
(i) High output impedance for current-mode (j) Experimental results

al. [17], Pandey and Bothra [18] reported a large number of resistors and capacitors are used, making the area of the integrated circuit (IC) larger. A floating capacitor has been used in literature [12-13, 17-18, 23], which are unsuitable for fabrication in an integrated circuit. The circuits reported in litertaure [7-8, 11-12, 14, 16] required additional amplifiers for sinusoidal oscillation. The stated conditions of oscillation in litertaure [8-9, 15, 17-18] cannot be adjusted electronically.

The aim of this paper is to propose the use of three MSOs using a single differential voltage current conveyor transconductance amplifier (DVCCTA), a single resistor, and a single capacitor per phase, and to make use of all the grounded passive components. The current outputs have a high impedance and are directly connected to loads. The proposed circuits provide multiphase signals that are equally spaced in phase and of equal amplitude. It does not need additional amplifiers for oscillation as it can be adjusted electronically. In addition, the proposed MSOs show that the simulation results with the PSPICE program and experimental results with commercially available ICs agree well with the theoretical analysis.

2. PRINCIPLE OF OPERATION

This topic presents the electrical characteristics of the differential voltage current conveyor transconductance amplifier as an active building block. It was used as the basis for the design of the proposed MSOs. Next is analysis of the various working operations of MSOs, and last is a non-ideal case analysis of the proposed circuits.

2. 1. Differential Voltage Current Conveyer Transconductance Amplifier The differential voltage current conveyor transconductance amplifier (DVCCTA) was used in the synthesis of the proposed MSOs. The DVCCTA was published by Jantakun et al. [27]. It shows the details of the electrical symbols and equivalent circuits in Figure 1, which has various terminals as follow: terminals (Y_1 and Y_2) are input

voltages, the voltage (V_X) at the X terminal is the difference between the input voltages V_{Y1} and V_{Y2}, the current (I_Z) at the Z terminal is obtained by mirroring the current (I_X) which is of equal amplitude, the output current (I_O) at the O terminal is caused by multiplying the transconductance (g_m) and the voltage (V_Z). In addition, these terminals have high impedance except for the X terminal. The characteristics equation of DVCCTA can be written by the relative voltage and current as follows:

$$\begin{pmatrix} I_{Y1} \\ I_{Y2} \\ V_X \\ I_Z \\ I_O \end{pmatrix} = \begin{pmatrix} 0 & 0 & 0 & 0 & 0 \\ 0 & 0 & 0 & 0 & 0 \\ 0 & 1 & -1 & 0 & 0 \\ 1 & 0 & 0 & 0 & 0 \\ 0 & 0 & 0 & \pm g_m & 0 \end{pmatrix} \begin{pmatrix} I_X \\ V_{Y1} \\ V_{Y2} \\ V_Z \\ V_O \end{pmatrix}. \quad (1)$$

The DVCCTA of the proposed circuit is implemented by BJT technology. The transconductance (g_m) can be written as follows:

$$g_m = \frac{I_B}{2V_T}. \quad (2)$$

From Equation (2), the transconductance (g_m) can be adjusted electronically with the DC bias current (I_B). The thermal voltage (V_T) is equal to 26 mV at room temperature.

2. 2. DVCCTA-based Gain-controllable Low-pass Filter The gain-controllable lossy integrator, which is also known as the gain-controllable low-pass filter is shown here since the proposed MSOs are based-on these integrators. The DVCCTA-based gain controlled low-pass filters are shown in Figure 2. The current transfer function of Figures 2(a), 2(b), and 2(c) can be found in Table 2, which can be derived from the DVCCTA features. The current output can be constructed to work with non-inverting or inverting signals, as the current transfer function can act as either non-inverting or inverting gain-controllable low-pass filter.

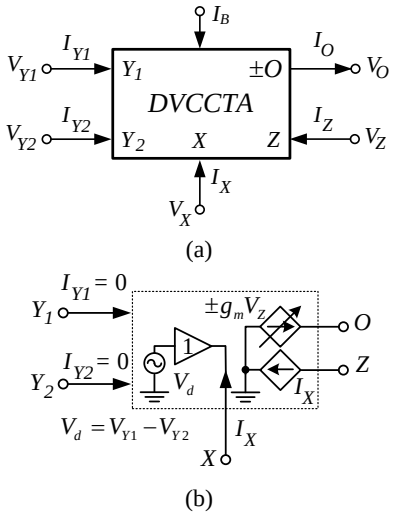

Figure 1. DVCCTA (a) electrical symbol (b) equivalent circuit

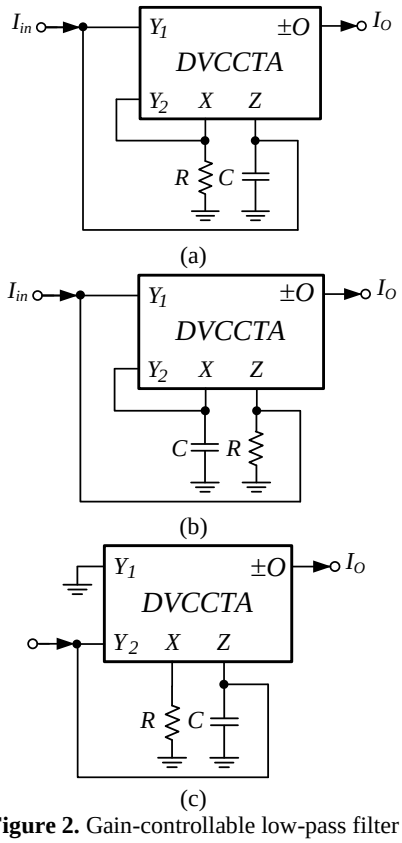

Figure 2. Gain-controllable low-pass filter

TABLE 2. The current transfer function of Figure 2

Figure	Transfer function
2 (a)	$\frac{I_O(s)}{I_{in}(s)} = \pm\frac{2g_mR}{2sRC+1}$
2 (b)	$\frac{I_O(s)}{I_{in}(s)} = \pm\frac{g_mR}{sRC/2+1}$
2 (c)	$\frac{I_O(s)}{I_{in}(s)} = \pm\frac{g_mR}{sRC+1}$

It is clear that all three circuits of the gain-controllable low-pass filters have the same capability. This capability is that the circuit consists of one DVCCTA, one grounded resistor, and one grounded capacitor. Additionally, the circuit can be electronically tuned by adjusting the transconductance gain g_m of the DVCCTA, making it appropriate for IC implementation [28-30]. Furthermore, it has high output impedances, allowing for simple cascading in current-mode configurations.

2. 3. The Proposed Mixed-mode Multiphase Sinusoidal Oscillator The proposed three mixed-mode multiphase sinusoidal oscillators, which are odd-phase MSO, in Figures 3(a), 3(b), and 3(c) are implemented. They are cascading the N identical stages (N ≥ 3, 5, 7….) of the DVCCTA-based inverting gain-controllable low-pass filters for each phase. The sinusoidal signals are simultaneously generated for both the current and the voltage-mode. The sinusoidal current outputs are high impedance that can be cascaded directly to load or the next stage without any additional current amplifiers. However, the voltage outputs must be used with voltage buffers to make it connect to the next stage. Also, the even-phase MSO can be constructed by cascading non-inverting and inverting gain-controllable low-pass filters, as explained and reported in literature [31]. The transconductance and passive components in MSOs satisfy the equality conditions g_m, C, and R. The parameters of MSOs can be then analyzed, and the results are summarized in Table 3. They provide the loop gain of the system, the characteristic equation, the CO and FO, and the phase relationship. When the CO and FO are set up, the steady-state magnitude ratios of the sinusoidal signals for voltages and currents show the same magnitude, as presented in Table 4. The output amplitude level of each gain-controllable low-pass filter may be easily stabilized using an optocoupler and photoresistor that is described in literature [32].

It is clearly seen that the three mixed-mode MSOs have the same ability, which is the CO can be tuned electronically/simultaneously of the FO by adjusting the DC bias current of DVCCTAs. Furthermore, when the CO and FO are archived, the ratio of output signals are close to unity. Consequently, the output signals are equally in amplitude and spaced in phase with respect to all oscillation frequencies.

2. 4. Non-ideal Case Analysis of The Proposed Circuits The non-ideal analysis of the proposed circuits is important to take the non-idealities of

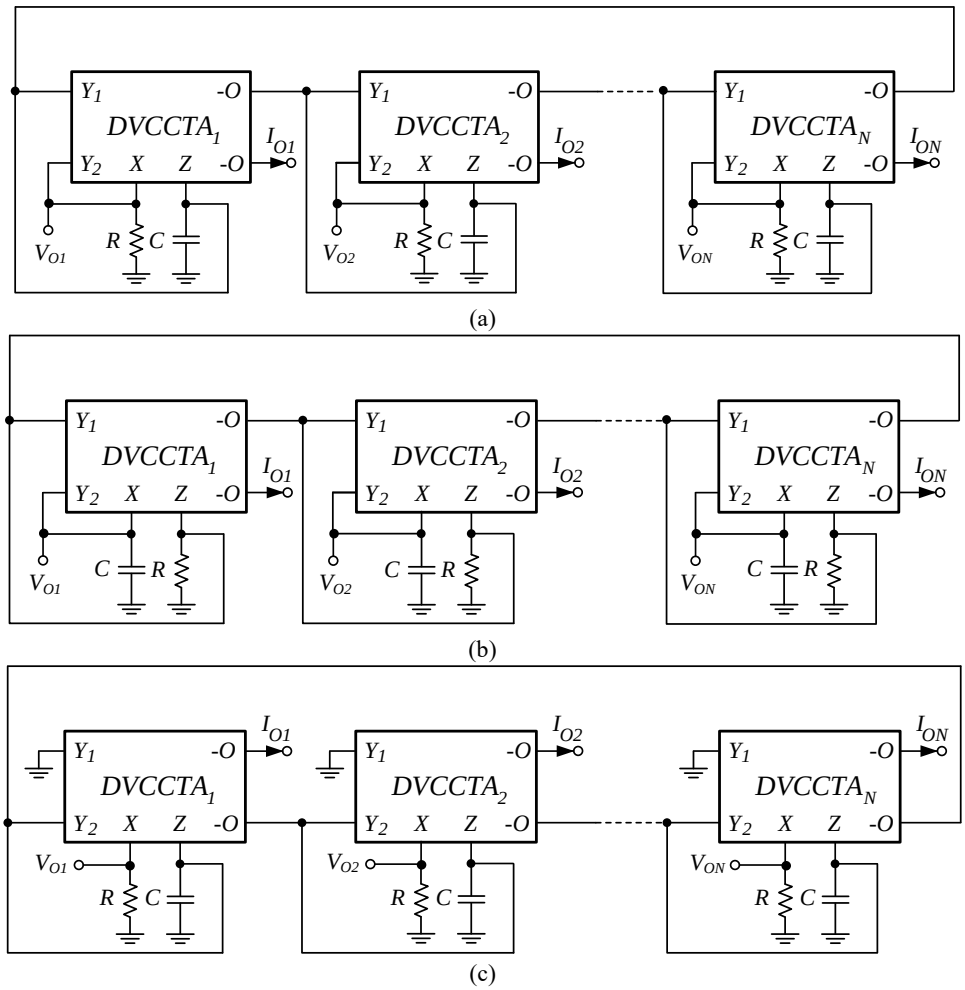

Figure 3. The proposed MSOs

TABLE 3. The MSOs parameters

Figure	(a)	(b)	(c)	(d)	(e)
3 (a)	$\left[\frac{-2g_mR}{2RCs+1}\right]^N=1$	$\left(j\omega_{osc}2RC+1\right)^N+(-1)^{N+1}\left(2g_mR\right)^N=0$	$2g_mR\geq\sqrt{1+\tan^2\frac{\pi}{N}}$	$\omega_{osc}=\frac{1}{2RC}\tan\frac{\pi}{N}$	$\phi=\frac{2\pi}{N}$
3 (b)	$\left[\frac{-g_mR}{s\frac{RC}{2}+1}\right]^N=1$	$\left(j\omega_{osc}\frac{RC}{2}+1\right)^N+(-1)^{N+1}\left(g_mR\right)^N=0$	$g_mR\geq\sqrt{1+\tan^2\frac{\pi}{N}}$	$\omega_{osc}=\frac{2}{RC}\tan\frac{\pi}{N}$	$\phi=\frac{2\pi}{N}$
3 (c)	$\left[\frac{-g_mR}{sRC+1}\right]^N=1$	$\left(j\omega_{osc}RC+1\right)^N+(-1)^{N+1}\left(g_mR\right)^N=0$	$g_mR\geq\sqrt{1+\tan^2\frac{\pi}{N}}$	$\omega_{osc}=\frac{1}{RC}\tan\frac{\pi}{N}$	$\phi=\frac{2\pi}{N}$

Remarks: (a) The system loop gain (LG) of the MSO circuits. (b) The frequency of oscillation $\omega_{osc}=2\pi f_{osc}$, the Barkhausen's condition. (c) The condition of oscillation (CO) .(d) The frequency of oscillation (FO) for *N*=3, 5, 7, …(e) The phase relations of output sinusoidal signals.

TABLE 4. The ratio between the output sinusoidal signals

Figure	The ratio of outputs
3 (a)	$\left\|\frac{I_{O2}(j\omega_{osc})}{I_{O1}(j\omega_{osc})}\right\|=\left\|\frac{I_{ON}(j\omega_{osc})}{I_{O2}(j\omega_{osc})}\right\|=\left\|\frac{I_{O1}(j\omega_{osc})}{I_{ON}(j\omega_{osc})}\right\|=\left\|\frac{V_{O2}(j\omega_{osc})}{V_{O1}(j\omega_{osc})}\right\|=\left\|\frac{V_{ON}(j\omega_{osc})}{V_{O2}(j\omega_{osc})}\right\|=\left\|\frac{V_{O1}(j\omega_{osc})}{V_{ON}(j\omega_{osc})}\right\|=\left\|\frac{2g_mR}{2RC\omega_{osc}+1}\right\|=1$
3 (b)	$\left\|\frac{I_{O2}(j\omega_{osc})}{I_{O1}(j\omega_{osc})}\right\|=\left\|\frac{I_{ON}(j\omega_{osc})}{I_{O2}(j\omega_{osc})}\right\|=\left\|\frac{I_{O1}(j\omega_{osc})}{I_{ON}(j\omega_{osc})}\right\|=\left\|\frac{V_{O2}(j\omega_{osc})}{V_{O1}(j\omega_{osc})}\right\|=\left\|\frac{V_{ON}(j\omega_{osc})}{V_{O2}(j\omega_{osc})}\right\|=\left\|\frac{V_{O1}(j\omega_{osc})}{V_{ON}(j\omega_{osc})}\right\|=\left\|\frac{g_mR}{\frac{RC\omega_{osc}}{2}+1}\right\|=1$
3 (c)	$\left\|\frac{I_{O2}(j\omega_{osc})}{I_{O1}(j\omega_{osc})}\right\|=\left\|\frac{I_{ON}(j\omega_{osc})}{I_{O2}(j\omega_{osc})}\right\|=\left\|\frac{I_{O1}(j\omega_{osc})}{I_{ON}(j\omega_{osc})}\right\|=\left\|\frac{V_{O2}(j\omega_{osc})}{V_{O1}(j\omega_{osc})}\right\|=\left\|\frac{V_{ON}(j\omega_{osc})}{V_{O2}(j\omega_{osc})}\right\|=\left\|\frac{V_{O1}(j\omega_{osc})}{V_{ON}(j\omega_{osc})}\right\|=\left\|\frac{g_mR}{RC\omega_{osc}+1}\right\|=1$

DVCCTA, which consist of the voltage and current tracking errors and the effects of the parasitic conponents, with details as follows:

2. 4. 1. The Voltage and Current Tracking Errors The voltage and current tracking errors of DVCCTA must be occurred by the mismatch of internal BJT which can be written with the characteristics equation as follows:

$$\begin{pmatrix} I_{Y1} \\ I_{Y2} \\ V_X \\ I_Z \\ I_O \end{pmatrix} = \begin{pmatrix} 0 & 0 & 0 & 0 & 0 \\ 0 & 0 & 0 & 0 & 0 \\ 0 & \gamma_1 & -\gamma_2 & 0 & 0 \\ \alpha & 0 & 0 & 0 & 0 \\ 0 & 0 & 0 & \pm\beta g_m & 0 \end{pmatrix} \begin{pmatrix} I_X \\ V_{Y1} \\ V_{Y2} \\ V_Z \\ V_O \end{pmatrix} \quad (3)$$

where the voltage tracking errors from Y_1 and Y_2 terminals to the *X* terminal are the γ_1 and γ_2. The current tracking error from *X* terminal to *Z* terminal is the α, and the voltage tracking error from *Z* terminal for transfer to *O* terminal is the β. The ideally values of α, β, and γ parameters are equal to unity. However, the influence of the voltage and current tracking errors can be examined for the proposed MSOs, as stated in Table 5.

2. 4. 2. The Effects of Parasitic Conponents The parasitic resistances and capacitances of DVCCTA are presented in Figure 4. The parasitic elements are connected to the ground at terminals Y_1, Y_2, Z, and O due to the presence of high impedances composed by parasitic resistances (R_{Y1}, R_{Y2}, R_Z, and R_O) and parasitic

TABLE 5. The CO and FO of MSOs by tracking errors effected

Figure	CO	FO
3 (a)	$2\gamma_2\beta gmR\geq\sqrt{1+\tan^2\frac{\pi}{N}}$	$\omega_{osc}=\frac{\gamma_2}{2\gamma_1RC}\tan\frac{\pi}{N}$
3 (b)	$\gamma_2\beta gmR\geq\sqrt{1+\tan^2\frac{\pi}{N}}$	$\omega_{osc}=\frac{2\gamma_2}{\gamma_1RC}\tan\frac{\pi}{N}$
3 (c)	$\beta g_mR\geq\sqrt{1+\tan^2\frac{\pi}{N}}$	$\omega_{osc}=\frac{\gamma_2}{RC}\tan\frac{\pi}{N}$

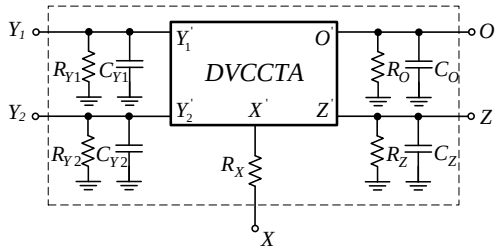

Figure 4. Non-ideal DVCCTA model

capacitances (C_{Y1}, C_{Y2}, C_Z, and C_O). Simultaneously, the X terminal has low impedance and has parasitic resistance (R_X) connected in series. In Table 6, the effects of parasitic resistances and capacitances on the performance of the proposed MSOs are evaluated and explained in detail. It can be observed that both the CO and FO have been influenced by parasitic elements. It is clear that these parasitic elements have downgraded the performance of the proposed MSOs.

TABLE 6. The CO and FO of MSOs by the parasitic elements effected

Figure	CO	FO	Settings of parasitic elements
3 (a)	$2g_m / Y_{T2}$	$\omega_{osc} = \frac{1}{2Y_{T1}/Y_{T2}}\tan\frac{\pi}{N}$	$G_Z = \frac{1}{R_Z}, G_R = \frac{1}{R}, G_{Y1} = \frac{1}{R_{Y1}}, G_{Y2} = \frac{1}{R_{Y2}},$ $G_{T1} = G_Z + G_{Y1}, G_{T2} = G_R + G_{Y2}, sC_T = s(C_Z + C_{Y1} + C),$ $Y_{T1} = G_{T1} + sC_T, Y_{T2} = G_{T2} + sC_{Y2}$
3 (b)	g_m / Y_{T1}	$\omega_{osc} = \frac{2Y_{T1}}{Y_{T2}}\tan\frac{\pi}{N}$	$G_Z = \frac{1}{R_Z}, G_R = \frac{1}{R}, G_{Y1} = \frac{1}{R_{Y1}}, G_{Y2} = \frac{1}{R_{Y2}},$ $G_{T1} = G_Z + G_{Y1} + G_R, sC_{T1} = s(C_Z + C_{Y1}), sC_{T2} = s(C + C_{Y2}),$ $Y_{T1} = G_{T1} + sC_{T1}, Y_{T2} = G_{Y2} + sC_{T2}$
3 (c)	g_m / G_R	$\omega_{osc} = \frac{1}{Y_{T1}/G_R}\tan\frac{\pi}{N}$	$G_Z = \frac{1}{R_Z}, G_R = \frac{1}{R}, G_{Y2} = \frac{1}{R_{Y2}},$ $G_{T1} = G_Z + G_{Y2}, sC_T = s(C_Z + C_{Y2} + C),$ $Y_{T1} = G_{T1} + sC_T$

3. RESULTS OF SIMULATION AND EXPERIMENTAL

To prove the validity of the theoretical analysis, the proposed mixed-mode MSO circuit in Figure 3(c) was chosen as a simulation example. For example, $N = 3$ or three phase sinusoidal oscillators have been simulated through the PSPICE program. Figure 5 shows the internal construction of DVCCTA which is created by the PNP and NPN transistors using the parameters of the PR200N and NR200N bipolar transistors of the ALA400 transistor array from AT &T [32]. The setting of the condition of oscillation must have a value about of 2. In this arrangement, the resistors in the circuit have a standard value of $R = 2$ kΩ and DC bias current of $I_A = 50$ μA and $I_B = 50$ μA has been specified. The capacitor chooses a standard value of $C = 1$ nF and the power supply voltage

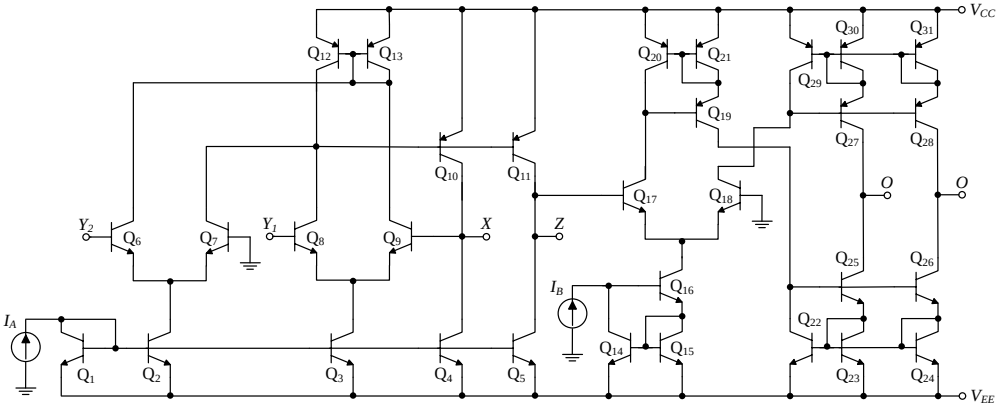

Figure 5. The internal construction of DVCCTA

is set at ±1.5 V. The proposed MSO waveforms of I_{O1}, I_{O2}, and I_{O3} have been simulated and plotted with two states, including: the transient-state at 0 to 1000 µs of time simulation, as shown in Figure 6, and the steady-state, as shown in Figure 7. The frequency spectrums of the sinusoidal signals which have a frequency of 137 kHz are presented in Figure 8. When compared to the theoretically determined frequency of 137.83 kHz, the sinusoidal signals have a frequency error of 0.60 % which may have been caused by a voltage and current tracking error, as well as by the parasitic components described in the previous section. The total harmonic distortions (THD) of sinusoidal signals I_{O1}, I_{O2}, and I_{O3} have values of 0.793%, 0.726%, and 0.799%, respectively. The Lissajous patterns in Figure 9 show the phase relationships between output signals I_{O1} - I_{O2}, I_{O2} - I_{O3}, and I_{O3} - I_{O1}.

In addition, the sinusoidal waveforms of voltage outputs are depicted in Figures 10 and 11, which are transient and steady state, respectively. Figure 12 depicts the THD and spectrum frequencies of the sinusoidal signals, where THD is defined as 0.343 %, 0.324 %, and 0.298 % of V_{O1}, V_{O2}, and V_{O3}, respectively.

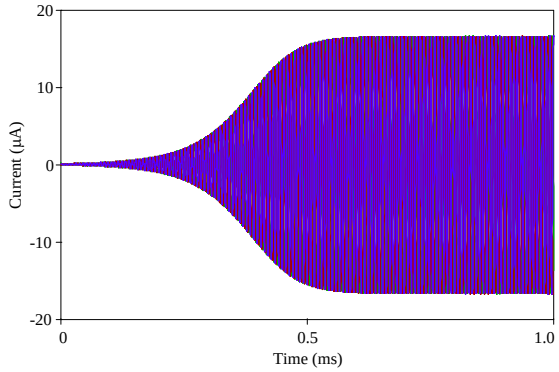

Figure 6. The current waveforms of proposed MSO during transient-state

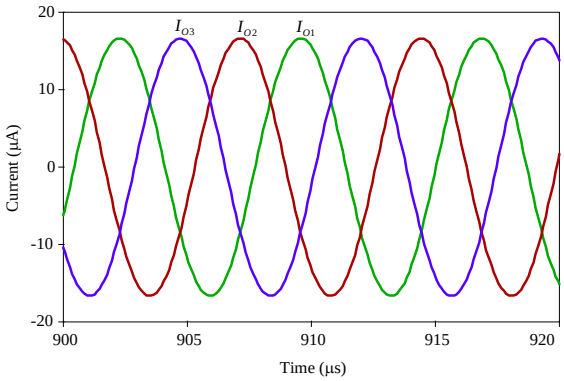

Figure 7. The current waveforms of proposed MSO during steady-state

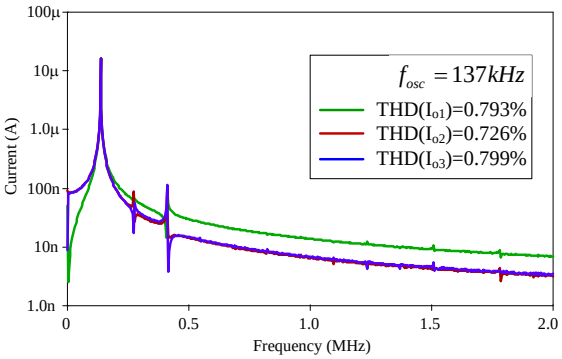

Figure 8. Frequency spectrum of I_{O1}, I_{O2} and I_{O3}

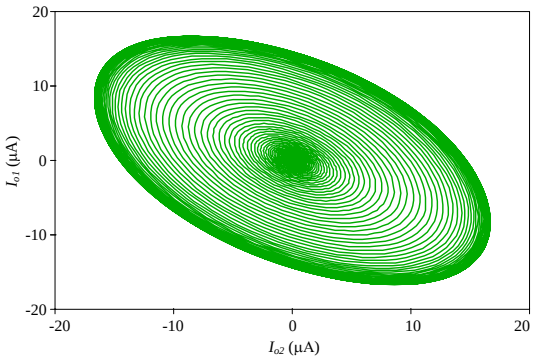

(a)

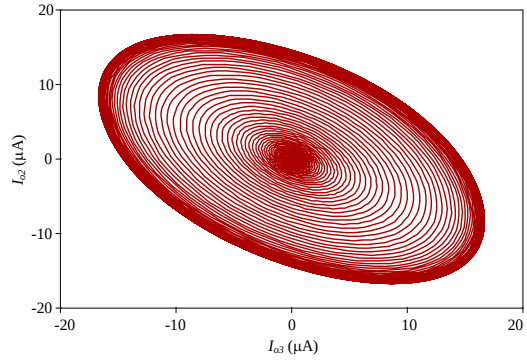

(b)

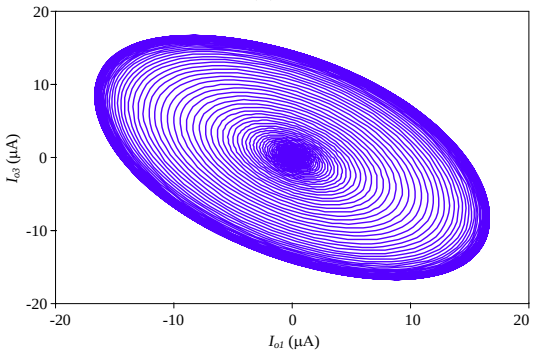

(c)

Figure 9. The Lissajous patterns (a) I_{O1}-I_{O2}, (b) I_{O2}-I_{O3}, and (c) I_{O3} – I_{O1}

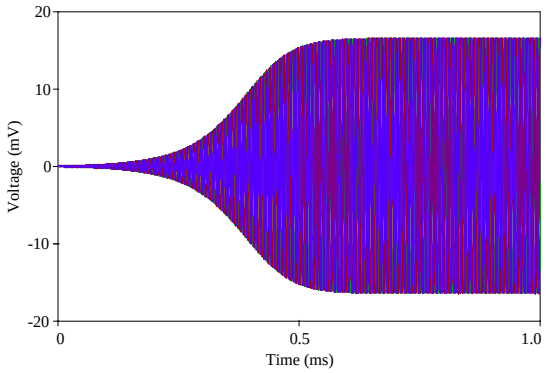

Figure 10. The voltage waveforms of proposed MSO during transient state

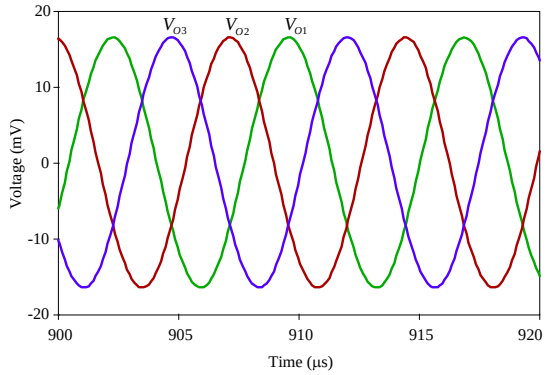

Figure 11. The current waveforms of proposed MSO during steady-state

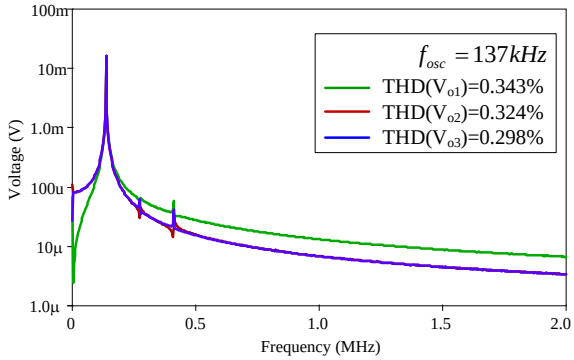

Figure 12. Frequency spectrum of V_{O1}, V_{O2} and V_{O3}

The phase relation of V_{O1} - V_{O2}, V_{O2} - V_{O3}, and V_{O3} - V_{O1} are plotted in Figure 13. As demonstrated in Figure 14, the simulation results and theoretical calculation of the oscillation frequency can be plotted by adjusting the resistor values between 400Ω and 2kΩ while keeping the ratio of resistor-to-DC bias constant. The simulation frequencies range between 137 kHz and 612 kHz, which are close to the theoretical calculation.

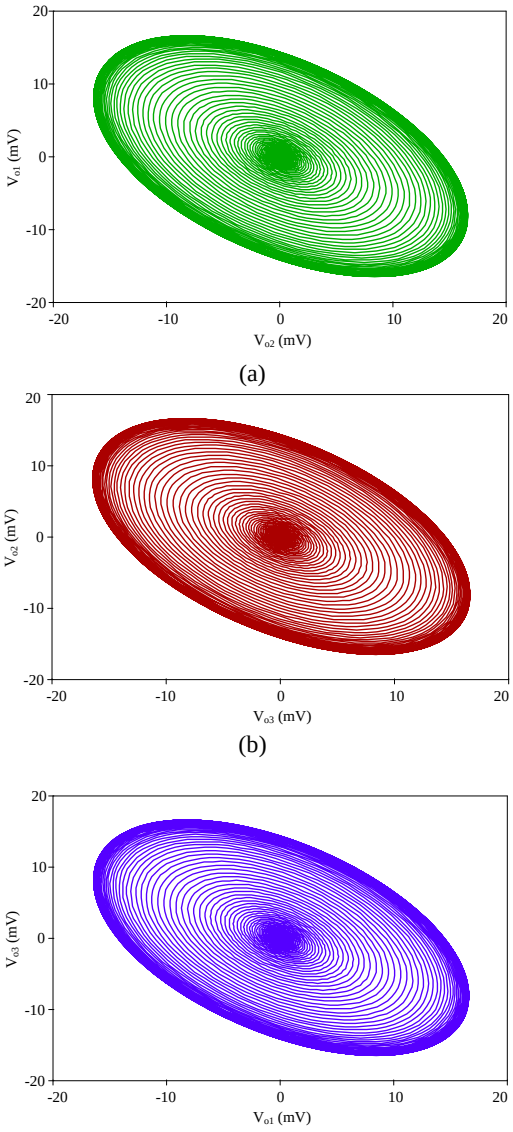

Figure 13. The Lissajous pattern (a) V_{O1}-V_{O2}, (b) V_{O2}-V_{O3}, and (c) V_{O3}- V_{O1}

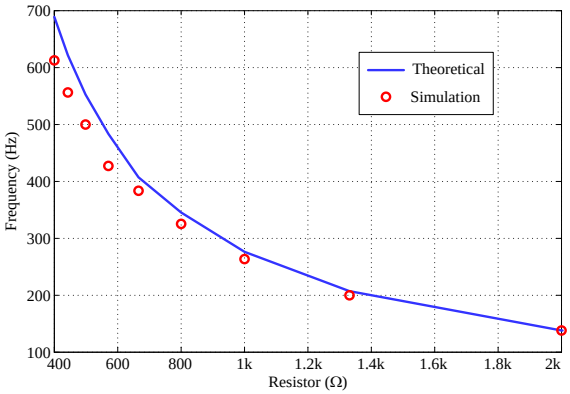

Figure 14. The oscillation frequency adjustment

However, in practice, the tolerance errors of passive conponents affect the performance of proposed MSO circuits. These tolerance errors can be analyzed by using the Monte Carlo Analysis. The Gaussian probability distributions were set with 100 trials, which had a 1% tolerance error for each resistors and a 10% tolerance error for each capacitors. The simulation result can be plotted on the histogram of spread space FO as shown in Figure 15. The minimum and maximum of FO are 121.558 kHz and 157.007 kHz, respectively. The mean and median of FO are 136.054 kHz and ١٣٥.789 kHz, respectively.

To confirm the performance of the proposed MSO so that it conforms to the theory and the simulation, the circuit in Figure 3(c) is chosen as an experimental example for N = 3. The DVCCTA has been constructed using commercial ICs: AD830, AD844, and LM13700N as shown in Figure 16. The setting for the CO was set by a value of g_mR greater than 2 which is set by configuring a value of R = 2 kΩ and bias currents are about I_B = 50 µA. The capacitors are chosen with a value of C = 1 nF. The input bias currents were tested with a Keysight 34461A and using a Siglent SPD3303C power supply was used to power the circuit by ±5 V. The Keysight DSOX3024T oscilloscope is used to display and measure sinusoidal waveforms parameters. The experimental is set up by the hardware used in Figure 17. The experimental results in Figure 18 are show the sinusoidal output waveforms of V_{O1}, V_{O2}, and V_{O3} which can generate a frequency of oscillation at 131.24 kHz. The calculated FO yields 137.83 kHz, while the FO of experimental had a 4.78% error frequency. The phase relationships between V_{O1} - V_{O2}, V_{O2} -V_{O3}, and V_{O3} - V_{O1} are 118.36°, 121.46°, and 120.24°, respectively, which is in accord with the theory proposed. The frequency spectrum of V_{O1}, V_{O2}, and V_{O3} are displayed in Figure 19 and the total harmonic distortions were measured at 0.56%, 0.44%, and 0.78%, respectively. In addition, the experimental results in Figures 19(a), 19(b) and 19(c) show the the magnitude of the first harmonic was higher

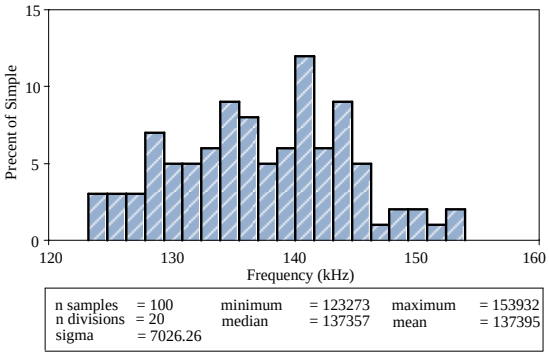

Figure 15. The histograms of the possible spread of FO

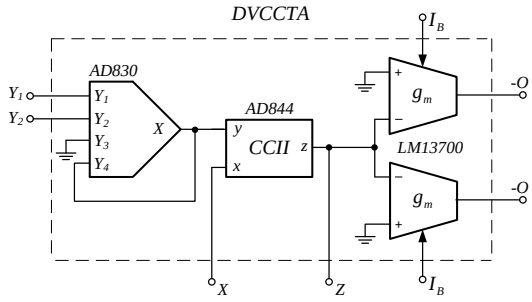

Figure 16. The DVCCTA for experimental test

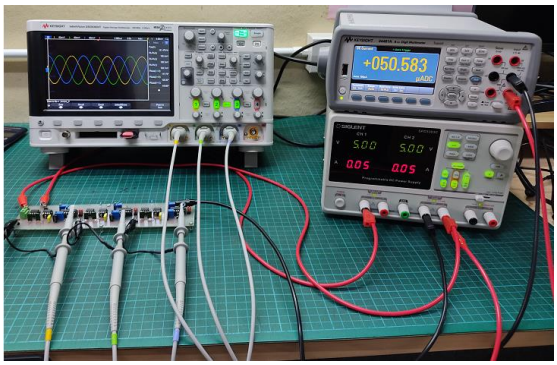

Figure 17. The experimental setup

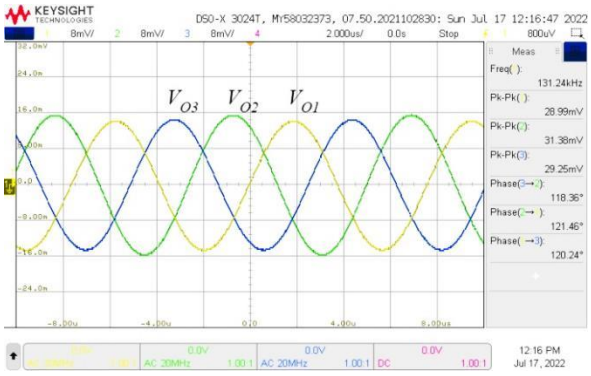

Figure 18. The output waveforms of the MSO

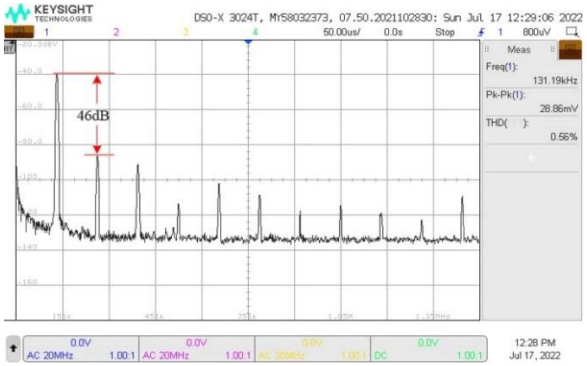

(a)

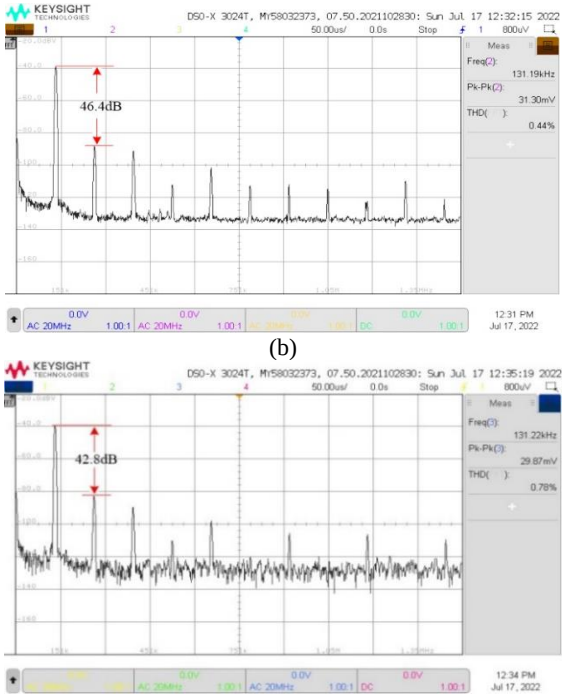

Figure 19. Spectrums frequencies of the MSO (a) V_{O1}, (b) V_{O2}, and (c) V_{O3}

than the second harmonic by about 46 dB, 46.4 dB and 42.8 dB, respectively. It is pleasing that simulation and experiment results correspond well with theoretical analysis.

4. CONCLUSION

The three circuits of mixed-mode MSO using DVCCTA have been presented. They consist of a single DVCCTA, a single grounded resistor, and a single grounded capacitor for each phase. The proposed MSOs are both equally phased and of equal amplitude, which do not require additional amplifier for sinusoidal oscillation. Moreover, high impedance output currents are cascaded to the load without current buffers. Also, the oscillation can be adjusted simultaneously by the oscillation frequency using the electronic method. Finally, to confirm the validity of the proposed MSOs theory, it has been simulated with the PSPICE program and experimentally with commercially available ICs. The simulated and experimental results are completely consistent with the theory.

5. ACKNOWLEDGEMENT

This research was supported by a grant from the Faculty of Engineering, Rajamangala University of Technology, Isan, Khon Kaen Campus, Khon Kaen, Thailand.

6. REFERENCES

1. Dunlop, J., "Telecommunications engineering, Routledge, (2017).
2. Tomasi, W., "Electronic communications system: Fundamentals through advanced, 5/e, Pearson Education India, (2009).
3. Kazmierkowski, M.P. and Silva, F.A., "Power electronics handbook, (rashid, mh; 2011)[book news]", ***IEEE Industrial Electronics Magazine***, Vol. 2, No. 5, (2011), 54-55.
4. Senani, R., Bhaskar, D., Singh, V.K. and Sharma, R., "Sinusoidal oscillators and waveform generators using modern electronic circuit building blocks, Springer, Vol. 622, (2016).
5. Jaikla, W., Talabthong, P., Siripongdee, S., Supavarasuwat, P., Suwanjan, P. and Chaichana, A., "Electronically controlled voltage mode first order multifunction filter using low-voltage low-power bulk-driven otas", ***Microelectronics Journal***, Vol. 91, (2019), 22-35. https://doi.org/10.1016/j.mejo.2019.07.009
6. Thongdit, P., Kunto, T. and Prommee, P., "Ota high pass filter-based multiphase sinusoidal oscillator", in 2015 38th International Conference on Telecommunications and Signal Processing (TSP), IEEE., (2015), 1-5.
7. Prommee, P. and Dejhan, K., "An integrable electronic-controlled quadrature sinusoidal oscillator using cmos operational transconductance amplifier", ***International Journal of Electronics***, Vol. 89, No. 5, (2002), 365-379. doi: 10.1080/713810385.
8. Skotis, G. and Psychalinos, C., "Multiphase sinusoidal oscillators using second generation current conveyors", ***AEU-international Journal of Electronics and Communications***, Vol. 64, No. 12, (2010), 1178-1181. https://doi.org/10.1016/j.aeue.2009.11.013
9. Wu, D.-S., Liu, S.-I., Hwang, Y.-S. and Wu, Y.-P., "Multiphase sinusoidal oscillator using second-generation current conveyors", ***International Journal of Electronics***, Vol. 78, No. 4, (1995), 645-651. doi: 10.1080/00207219508926198.
10. Abuelmaatti, M.T. and Al-Qahtani, M.A., "A new current-controlled multiphase sinusoidal oscillator using translinear current conveyors", ***IEEE Transactions on Circuits and Systems II: Analog and Digital Signal Processing***, Vol. 45, No. 7, (1998), 881-885. doi: 10.1109/82.700937.
11. Loescharataramdee, C., Kiranon, W., Sangpisit, W. and Yadum, W., "Multiphase sinusoidal oscillators using translinear current conveyors and only grounded passive components", in Proceedings of the 33rd Southeastern Symposium on System Theory (Cat. No. 01EX460), IEEE., (2001), 59-63.
12. Tangsrirat, W., Tanjaroen, W. and Pukkalanun, T., "Current-mode multiphase sinusoidal oscillator using cdta-based allpass sections", ***AEU-international Journal of Electronics and Communications***, Vol. 63, No. 7, (2009), 616-622. https://doi.org/10.1016/j.aeue.2008.05.001
13. Jaikla, W., Siripruchyanun, M., Biolek, D. and Biolkova, V., "High-output-impedance current-mode multiphase sinusoidal oscillator employing current differencing transconductance amplifier-based allpass filters", ***International Journal of Electronics***, Vol. 97, No. 7, (2010), 811-826. doi: 10.1080/00207211003733288.
14. Tangsrirat, W. and Tanjaroen, W., "Current-mode multiphase sinusoidal oscillator using current differencing transconductance amplifiers", ***Circuits, Systems & Signal Processing***, Vol. 27, (2008), 81-93. doi: 10.1007/s00034-007-9010-y.
15. Klahan, K., Tangsrirat, W. and Surakampontorn, W., "Realization of multiphase sinusoidal oscillator using cdbas", in The 2004 IEEE Asia-Pacific Conference on Circuits and Systems, 2004. Proceedings., IEEE. Vol. 2, (2004), 725-728.
16. Sagbas, M., Ayten, U.E., Herencsar, N. and Minaei, S., "Voltage-mode multiphase sinusoidal oscillators using cbtas", in 2012 35th

International Conference on Telecommunications and Signal Processing (TSP), IEEE., (2012), 421-425.

17. Pandey, R., Pandey, N., Mullick, R., Yadav, S. and Anurag, R., "All pass network based mso using otra", ***Advances in Electronics***, Vol. 2015, (2015). https://doi.org/10.1155/2015/382360
18. Pandey, R. and Bothra, M., "Multiphase sinusoidal oscillators using operational trans-resistance amplifier", in 2009 IEEE Symposium on Industrial Electronics & Applications, IEEE. Vol. 1, (2009), 371-376.
19. Jaikla, W. and Prommee, P., "Electronically tunable current-mode multiphase sinusoidal oscillator employing cccdta-based allpass filters with only grounded passive elements", ***Radioengineering***, Vol. 20, No. 3, (2011), 594-599.
20. Kumngern, M., "Current-mode multiphase sinusoidal oscillator using current-controlled current differencing transconductance amplifiers", in 2010 IEEE Asia Pacific Conference on Circuits and Systems, IEEE., (2010), 728-731.
21. Kumngern, M., "Current-controlled current-mode multiphase oscillator using cccdtas", in 2011 IEEE Symposium on Computers & Informatics, IEEE., (2011), 188-191.
22. Uttaphut, P., Mekhum, W. and Jaikla, W., "Current-mode multiphase sinusoidal oscillator using cccctas and grounded elements", in 2011 IEEE 9th International New Circuits and systems conference, IEEE., (2011), 345-349.
23. Gupta, P. and Pandey, R., "Dual output voltage differencing buffered amplifier based active-c multiphase sinusoidal oscillator", ***International Journal of Engineering, Transactions C: Aspects***, Vol. 34, No. 6, (2021), 1438-1444.
24. Pitaksuttayaprot, K., Phanrattanachai, K. and Jaikla, W., "Electronically adjustable multiphase sinusoidal oscillator with high-output impedance at output current nodes using vdccs", ***Electronics***, Vol. 11, No. 19, (2022), 3227. doi: 10.3390/electronics11193227.
25. Jaikla, W., Khateb, F., Kulej, T. and Pitaksuttayaprot, K., "Universal filter based on compact cmos structure of vddda", ***Sensors***, Vol. 21, No. 5, (2021), 1683. doi: 10.3390/s21051683.
26. Jaikla, W., Khateb, F., Kumngern, M., Kulej, T., Ranjan, R.K. and Suwanjan, P., "0.5 v fully differential universal filter based on multiple input otas", ***IEEE Access***, Vol. 8, (2020), 187832-187839. doi: 10.1109/ACCESS.2020.3030239.
27. Jantakun, A., Pisutthipong, N. and Siripruchyanun, M., "A synthesis of temperature insensitive/electronically controllable floating simulators based on dv-cctas", in 2009 6th International Conference on Electrical Engineering/Electronics, Computer, Telecommunications and Information Technology, IEEE. Vol. 1, (2009), 560-563.
28. Bhushan, M. and Newcomb, R., "Grounding of capacitors in integrated circuits", ***Electronics Letters***, Vol. 3, No. 4, (1967), 148-149.
29. Chauhan, D.S., Tomar, R. and Singh, S., "A new trans-admittance-mode biquad filter suitable for low voltage operation", ***International Journal of Engineering, Transactions B: Applications,*** Vol. 28, No. 12, (2015), 1738-1745. doi: 10.5829/idosi.ije.2015.28.12c.06.
30. Keramatzadeh, A. and Farshidi, E., "A new approach for low voltage cmos based on current-controlled conveyors", ***International Journal of Engineering, Transactions B: Applications***, Vol. 27, No. 5, (2014), 723-730. doi: 10.5829/idosi.ije.2014.27.05b.07.
31. Frey, D., "Log-domain filtering: An approach to current-mode filtering", ***IEE Proceedings G (Circuits, Devices and Systems)***, Vol. 140, No. 6, (1993), 406-416.
32. Bajer, J., Lahiri, A. and Biolek, D., "Current-mode ccii+ based oscillator circuits using a conventional and a modified wien-bridge with all capacitors grounded", ***Radioengineering***, Vol. 20, No. 1, (2011), 245-250. https://www.radioeng.cz/fulltexts/2011/11_01_245_251.pdf

Persian Abstract

چکیده

این مقاله در مورد نوسان سازهای سینوسی چند فازی است که از تقویت کننده ترانس رسانایی انتقال جریان ولتاژ دیفرانسیل (DVCCTA) ساخته شده اند و از تمام اجزای غیرفعال زمین شده استفاده می کنند. اسیلاتورهای سینوسی چند فازی پیشنهادی یک DVCCTA، یک مقاومت زمینی تک و یک خازن برای هر فاز ارائه می‌کنند که برای اجرای مدار مجتمع مناسب است. علاوه بر این، خروجی های سینوسی به طور همزمان جریان و ولتاژ تولید می کنند. سیگنال های جریان خروجی دارای امپدانس های بالایی هستند که اتصال مستقیم آنها را به مدار یا مرحله بعدی آسان تر می کند. مدارهای پیشنهادی می‌توانند سیگنال‌های سینوسی چند فازی تولید کنند که هم فاز و هم در دامنه هستند. نوسان را می توان به طور همزمان فرکانس نوسان را با روش الکترونیکی تنظیم کرد. شبیه‌سازی با برنامه PSPICE و آزمایشی با آی‌سی‌های تجاری موجود (AD830، AD844 و LM13700N) نشان داد. نتایج نشان می دهد که کارایی مدار کاملاً با تئوری مطابقت دارد.

AIMS AND SCOPE

The objective of the International Journal of Engineering is to provide a forum for communication of information among the world's scientific and technological community and Iranian scientists and engineers. This journal intends to be of interest and utility to researchers and practitioners in the academic, industrial and governmental sectors. All original research contributions of significant value focused on basics, applications and aspects areas of engineering discipline are welcome.

This journal is published in three quarterly transactions: Transactions A (Basics) deal with the engineering fundamentals, Transactions B (Applications) are concerned with the application of the engineering knowledge in the daily life of the human being and Transactions C (Aspects) - starting from January 2012 - emphasize on the main engineering aspects whose elaboration can yield knowledge and expertise that can equally serve all branches of engineering discipline.

This journal will publish authoritative papers on theoretical and experimental researches and advanced applications embodying the results of extensive field, plant, laboratory or theoretical investigation or new interpretations of existing problems. It may also feature - when appropriate - research notes, technical notes, state-of-the-art survey type papers, short communications, letters to the editor, meeting schedules and conference announcements. The language of publication is English. Each paper should contain an abstract both in English and in Persian. However, for the authors who are not familiar with Persian, the publisher will prepare the latter. The abstracts should not exceed 250 words.

All manuscripts will be peer-reviewed by qualified reviewers. The material should be presented clearly and concisely:

- *Full papers* must be based on completed original works of significant novelty. The papers are not strictly limited in length. However, lengthy contributions may be delayed due to limited space. It is advised to keep papers limited to 7500 words.
- *Research* notes are considered as short items that include theoretical or experimental results of immediate current interest.
- *Technical notes* are also considered as short items of enough technical acceptability with more rapid publication appeal. The length of a research or technical note is recommended not to exceed 2500 words or 4 journal pages (including figures and tables).

Review papers are only considered from highly qualified well-known authors generally assigned by the editorial board or editor in chief. Short communications and letters to the editor should contain a text of about 1000 words and whatever figures and tables that may be required to support the text. They include discussion of full papers and short items and should contribute to the original article by providing confirmation or additional interpretation. Discussion of papers will be referred to author(s) for reply and will concurrently be published with reply of author(s).

INSTRUCTIONS FOR AUTHORS

Submission of a manuscript represents that it has neither been published nor submitted for publication elsewhere and is result of research carried out by author(s). Presentation in a conference and appearance in a symposium proceeding is not considered prior publication.

Authors are required to include a list describing all the symbols and abbreviations in the paper. Use of the international system of measurement units is mandatory.

- On-line submission of manuscripts results in faster publication process and is recommended. Instructions are given in the IJE web sites: www.ije.ir-www.ijeir.info
- Hardcopy submissions must include MS Word and jpg files.
- Manuscripts should be typewritten on one side of A4 paper, double-spaced, with adequate margins.
- References should be numbered in brackets and appear in sequence through the text. List of references should be given at the end of the paper.
- Figure captions are to be indicated under the illustrations. They should sufficiently explain the figures.
- Illustrations should appear in their appropriate places in the text.
- Tables and diagrams should be submitted in a form suitable for reproduction.
- Photographs should be of high quality saved as jpg files.
- Tables, Illustrations, Figures and Diagrams will be normally printed in single column width (8cm). Exceptionally large ones may be printed across two columns (17cm).

PAGE CHARGES AND REPRINTS

The papers are strictly limited in length, maximum 8 journal pages (including figures and tables). For the additional to 8 journal pages, there will be page charges. It is advised to keep papers limited to 3500 words.

Page Charges for Papers More Than 8 Pages (Including Abstract)	
For International Author ***	**$55 / per page**
For Local Author	**100,000 Toman / per page**

AUTHOR CHECKLIST

- Author(s), bio-data including affiliation(s) and mail and e-mail addresses).
- Manuscript including abstracts, key words, illustrations, tables, figures with figure captions and list of references.
- MS Word files of the paper.

International **J**ournal of **E**ngineering, P.O. Box 13145-1659, Tehran, I.R. Iran
Materials and Energy Research Center, 5 Ahuramazda St., Alvand Ave., Argentina Sq., Tehran, Islamic Republic of Iran
www.merc.ac.ir - www.emerc.ac.ir

THOMSON REUTERS

WEB OF SCIENCE

Scopus®

CAS®
A DIVISION OF THE
AMERICAN CHEMICAL SOCIETY

Google
Scholar